<u>Impacts of Tidal Currents on the Assessment of the Wave Energy Resource of the West Coast of
Canada</u>

by

Ignacio Beya

Civil Engineer, Universidad de Chile, 2010

A Thesis Submitted in Partial Fulfillment

of the Requirements for the Degree of

MASTER OF APPLIED SCIENCE

in the Department of Mechanical Engineering

© Ignacio Beya, 2020

University of Victoria

# Supervisory Committee

Impacts of Tidal Currents on the Assessment of the Wave Energy Resource of the West Coast of Canada

by

Ignacio Beya

Civil Engineer, Universidad de Chile, 2010

**Supervisory Committee**

Dr. Bradley Buckham, Department of Mechanical Engineering.

**Co-Supervisor**

Dr. Bryson Robertson, Department of Civil & Construction Engineering, Oregon State University.

**Co-Supervisor**

**Supervisory Committee**

Dr. Bradley Buckham, Department of Mechanical Engineering, University of Victoria.
**Co-Supervisor**

Dr. Bryson Robertson, Department of Civil & Construction Engineering, Oregon State University.
**Co-Supervisor**

# Abstract

Numerous studies have identified the west coast of Canada as an attractive place for the development of wave energy projects. To evaluate the viability of these projects, an accurate description of the wave resource is crucial. Most of the previous efforts to characterize the wave climate in B.C. at shallower waters, where wave energy converters (WECs) are most likely to be deployed, lack the necessary nearshore spatial resolution, and were driven by overly simplistic wave boundary conditions. In addition, none of the previous studies have included the effect of tidal currents, which have been proven to be significant in wave resource characterizations in other locations.

This work increased the fidelity of the wave resource characterization and developed an understanding of the impact of tidal currents on the wave conditions in this region by generating two most accurate, long-term (14 years, 2004 to 2017), high resolution (in space and time) datasets of the wave resource for the west coast of Canada. The two datasets were generated using nearly identical SWAN wave models, which their only difference was that one of them (V5), did not incorporate the effect of currents, while the other (V6) included tidal currents as forcing. Thus, the pure influence of the tidal currents on the wave characteristics was able to be identified when comparing the two wave model results.

This study developed simple, robust, and objective metrics to support the calibration process and to evaluate the performance of the models. Utilizing these metrics, the V5 and V6 models presented substantial improvements in reproducing the wave conditions of about 18% and 20%, respectively and in relation to the previous most complete and accurate wave model of the region

(V4). Their better performance was largely achieved by a significant increment in their ability to reproduce the significant wave height ($H_{m0}$) and energy period ($T_e$).

The inclusion of tidal currents in the wave model increased the accuracy of the wave resource characterization, mainly by improving the model's ability in simulating $T_e$ by 5.1%. The most sensitive wave parameter to the tidal currents was the peakedness of the wave spectrum ($Q_p$), which was consistently and significantly reduced by values even larger than 2.5. In some regions, directions characterized by the mean wave direction ($D_m$) and the directional spreading ($D_{spr}$) were also noticeably very sensitive to the currents, which even deflected $D_m$ to its opposite direction and drove changes in $D_{spr}$ that reached values of up to 40°. However, these significant transformations were less frequent and reduced in magnitude at exposed (to swell-waves) sites, where strong currents have affected waves in a reduced part of their trajectory.

Typically, tidal currents had the effect of reducing the wave power density ($P$), but in a relatively small amount, however, during rare events, tidal currents were able to induce changes in this parameter ranging -140 kW/m to 75 kW/m. At these extreme events, it was observed that the peak of the wave spectra became flatter, with some of its wave height variance redistributed to near increasing and decreasing frequencies and directions, regardless to the magnitude and direction of the local tidal currents.

Impacts of the tidal currents on $P$ were largely attributed to the induced changes in $H_{m0}$ and $T_e$. Although $D_{spr}$ and $Q_p$ were greatly transformed by the action the tidal currents, they account very little in explaining the variations in $P$. These four wave parameters together, and how they are transformed under the presence of currents, can explain a large part of the changes in $P$, however, other transformations of the wave spectrum due to the currents, not investigated in this study, must account for a considerable part of the changes in $P$.

# **Table of Contents**

# List of Tables

# List of Figures

# Acknowledgments

I would like to express my most sincere gratitude to my supervisors, Dr. Buckham and Dr. Robertson, for those countless hours spent reviewing my thesis, and for their constant support and always cordial constructive criticism and advice. I am also grateful to Barry Kent for his support in setting up the computers where I ran my simulations and providing me access to lots of digital storage space for the information generated. I would also like to extend my gratitude to my youngest brother Victor, for his dedication in reviewing with me the wording and for his valuable practical suggestions. Special thanks to the National Research Council Canada and Julien Cousineau for providing the tidal current information included in one of my models, and the Canadian Hydrographic Service and Kim Tenhunen for preparing for this study the most reliable and high resolution bathymetric information of the Canadian west coast implemented in my models mesh. To my parents Marilyn and Francisco, and my siblings Victor, Rocio and Jose for their emotional support, and to my friends from here and from far way for all the fun and laughter. Finally, I gratefully acknowledge the financial support provided by the West Coast Wave Initiative and by the Department of Mechanical Engineering, both from the University of Victoria.

# Chapter 1 Introduction

With population growth and industrialized societies, rates of environmental degradation and climate change have increased dramatically to unprecedented levels, and this has led to an ecological crisis (IPCC, 2014; Brüggemeier, 2001). In this crisis, energy production and use are playing a major role, contributing 78% of the global anthropogenic greenhouse-gas (GHG) emissions. In Canada, this number is over 81% (ECCC, 2018).

Consistent with global efforts to reduce our contribution to the environmental crisis, in May 2015, Canada indicated its intent to reduce its GHG emissions by 30% below 2005 levels by 2030. In December 2016, the Pan-Canadian Framework on Clean Growth and Climate Change presented a comprehensive plan to achieve this intention through: carbon pricing, increasing efficiency, switching to and expanding the use of clean electricity and low-carbon technologies, reforestation and enhancing carbon sinks (ECCC, 2016). Within the Pan-Canadian Framework, provinces have set their own goals and pathways to cut down their emissions. In 2018, the province of British Columbia (BC) presented its CleanBC plan, aiming to reduce its GHG emissions by 40%, 60% and 80% (relative to 2007 GHG emissions) by 2030, 2040 and 2050, respectively. A large part of the emission reduction is planned to be achieved by switching to and expanding the use of clean electricity, providing great opportunities to the renewable energy generation industry (solar, wind, biomass, hydro, tides, waves among others).

The viability of a renewable energy project primarily depends on three factors: the characteristics of the natural resource (e.g. availability, accessibility, predictability, variability, consistency), the cost (e.g. initial, operational) and performance (e.g. energy conversion efficiency, material intensity, lifetime) associated to the technology used to extract the natural energy and convert it into a usable form (e.g. electricity, compressed air, pumped hydro storage, etc).

With respect to its natural characteristics, wave energy possesses several advantages. Numerous global studies have identified the west coast of Canada as one of the most energetic places in the world, with an average annual wave power density of 40-50 kW/m at the continental shelf (Gunn and Stock-Williams, 2012; Arinaga and Cheung, 2012; Cornett, 2008). Generally, the energy density in ocean waves is higher, more predictable and less variable than wind and solar (Robertson et al., 2017). Although waves are not equally consistent over the seasons in BC, their

greater availability coincides with the increase in the energy demand during colder seasons. This energetic climate has the potential to satisfy the electric demands on Vancouver Island and numerous coastal remote communities (Xu, 2018).

The energy from the waves can be converted into a usable form by Wave Energy Converters (WECs). Since the first patent of a WEC, presented in 1799, several hundreds of patents related to WECs have been filled. However, only after the 1960s serious research on wave energy systems allowed progress from conceptual ideas to full scale operational units. Numerous WEC concepts have been proposed and studied, each with different efficiencies and based on different physical principles (Aderinto & Li, 2018).

Despite the abundance of the wave resource and the progress on WEC technologies, maturation of the wave energy industry in Canada has been slow, with only one company (NeptuneWAVE[1], based in B.C.) that has successfully deployed a prototype WEC (MRC, 2018). Among the many challenges affecting the low penetration of ocean wave energy, strategic development of wave energy projects have been hindered by a lack of appropriate assessments of the wave resource in near-shore areas (Robertson et al., 2016). It is in these near-shore areas that wave energy projects are most likely be located in the future (Cornett, 2008). Long-term, high resolution (in space and time), detailed and accurate wave resource characterization is crucial to evaluating these projects; particularly, in the context of integrating them to energy demand centers, such as populated centers (cities, towns and communities) and industries. Wave resource characterization is essential for selecting the project location, designing / selecting the optimal WEC for the wave conditions (optimal performance for operational wave conditions, and survivability for extreme sea states), and for estimating the electrical energy generation from WEC farms and their economic viability (Robertson et al., 2014).

## 1.1 Problem statement

In addition to the numerous studies that have been conducted to estimate the wave power potential globally, several regional and more detailed wave resource assessments have been carried

---

[1] https://www.neptunewave.ca/

out for the B.C. coast (Robertson et al., 2016; Robertson et al., 2014; Kim et al., 2012; Cornett & Zhang, 2008; Cornett, 2006). Despite these studies, efforts to characterize the wave climate in B.C. along the coastline at shallower waters (< 100 – 200 m) and greater spatial and temporal resolution (~50 m and ~1 hr, needed for wave energy project development) have been limited. Some of these studies (Robertson et al., 2014; Kim et al., 2012; Cornett & Zhang, 2008; Cornett, 2006) lack the necessary nearshore spatial resolution and were driven by overly simplistic wave boundary conditions. None of these numerical studies have included the effect of currents.

The latest regional effort covering the whole B.C coastline and including shallower waters at high resolution detail was carried out by Robertson et al. (2016). Although Robertson et al. (2016) completed a significant step towards characterizing the wave climate over the west coast of Canada, greater improvements in accuracy and detail could be achieved; mainly by enlarging the model domain, increasing the temporal and spatial resolution, taking advantages of new features included in more recently released wave models, and including currents as forcing.

It is important to mention that there is evidence that tidal currents can greatly influence the wave resource and many authors have recommended including them in numerical studies (e.g. IEC, 2015; Saruwatari et al., 2013; EquiMar, 2011). For example, Barbariol et al. (2013) compared the results of numerical models that included (2WCM) and excluded (WM) wave-current interactions against measurements in the northern Adriatic Sea. They found that, at the measurement location, the 2WCM increased the accuracy on the wave power by 11% in comparison to the WM. Then, assuming the 2WCM as the reference, the WM model overestimated the mean wave power by up to 30%. Saruwatari et al. (2013) compared the results of the wave characteristics around Orkney Islands, UK from two simulations. The first simulation did not include tidal currents as forcing. The most extreme differences in wave power oscillated between -60% and + 60% at the site with the strongest currents (up to 3 m/s). They observed increases in wave height of 150 – 200% when waves encounter opposing currents, leading to increases in the available wave power of over 100 kW/m.

## 1.2 Technical Objectives

The main objectives of this work are: (1) build and run a numerical model able to reproduce accurately the wave characteristics along the west coast of Canada, and create a detailed and long

term wave database; (2) quantify the influence of tidal currents on the wave characteristics and wave power; (3) quantify the improvements in accuracy of this new database with respect to the latest previous results produced by Robertson et al. (2016). To achieve these proposed objectives, the following specific goals were defined:

- Chose an appropriate numerical model to simulate accurately 14 years of wave conditions along the whole west coast of Canada.

- Gather, analyze and process detailed information needed to develop the numerical model. This information includes boundary conditions, forcings (winds and tidal currents), calibration and validation data, topo-bathymetry, etc.

- Select, through a calibration process, the setting of the numerical model for the long-term simulation. This model will not include tidal currents as forcing.

- Develop and run a second new model that includes tidal currents as forcing.

- Evaluate the performance of the new models developed in this work against the model produced by Robertson et al. (2016).

- Quantify the influence of the tidal currents on the wave characteristics and wave power by comparing the results between the two models developed in this work.

It is worth mentioning that Robertson et al. (2016) and Robertson et al. (2014) were efforts conducted at the West Coast Wave Initiative (WCWI)[2], and are based on their third (WCWI-v3) and fourth (WCWI-v4) wave model versions, respectively. As well as Robertson et al. (2016) and Robertson et al. (2014), this work is conducted at the WCWI and builds up on WCWI-v4 (or V4). Thus, the new model that does not include wave-current interactions will be named WCWI-v5 (or V5), while the model that include tidal currents as forcing will be called WCWI-v6 (or V6).

---

[2] The WCWI is a multi-disciplinary group of academics and industry members aiming to contribute the development of the wave energy industry in B.C. The group develops wave energy resource assessments, simulations of Wave Energy Converters (WEC) and grid integration analysis to create the most accurate possible assessment of the feasibility of wave energy conversion in British Columbia.

## 1.3 Contributions

Aiming to contribute to the development of the wave energy industry in BC, and thus, to the Canadian and global efforts in reducing the GHG emissions and stopping the environmental crisis, this study generated two most accurate, extended, long-term, high resolution (in space and time) datasets of the wave characteristics of the west coast of Canada.

This dataset cannot only be used to better evaluate wave energy generation projects (e.g. selecting the optimal location, estimating the electrical energy generation and the extreme wave conditions for WEC survivability), but also to inform a myriad of other topics in ocean and coastal engineering; for example, the model outputs could drive the estimation of: extreme and operational forcing in marine structures (seawalls, breakwater, platforms, etc.) and floating bodies (e.g. fish-farms), the response of natural and artificial coastal systems (e.g. beaches, harbor basins), the movement of vessels and the induced forces on mooring lines, bollard and fenders in a harbors, etc.

The dataset was created using the most recently available spectral wave model (SWAN 41.31). To improve the accuracy of the dataset (in comparison to previous studies), the model domain was extended, and the temporal and spatial resolution was increased. The model was also calibrated and validated thoroughly, and beside other forcings, it was run with and without including tidal currents. The comparison between the results from these two models allowed to extensively investigate the influence of tidal currents on the wave characteristics and wave power, which to the best knowledge of the author, is done for the first time for the B.C. coast.

To calibrate and assess the performance of the models (with and without tidal currents, i.e. WCWI-v6 and WCWI-v5, respectively), a simple, but robust, systematic and objective methodology and performance metrics were proposed and applied. This methodology and metrics can be replicated (or serve as a base) in other wave characterization studies.

## 1.4 Background

This section introduces some concepts and relevant information related to water and ocean waves, the phenomena that generate and transform them, and how are they characterized and

studied. Special consideration on wave-current interactions, numerical models and recommendations for producing wave resource studies is taken.

### 1.4.1 Water waves

Water waves are oscillations or periodic disturbances of a water interface. An individual wave can be described by their height (or amplitude), period (or frequency), wave length and direction (see Figure 1-1). Depending on the type of interface, water waves can be classified as surface waves at the air-water interface, or internal waves when the oscillations travel within layers of stratified fluid (i.e. different densities typically due to temperature and/or salinity).
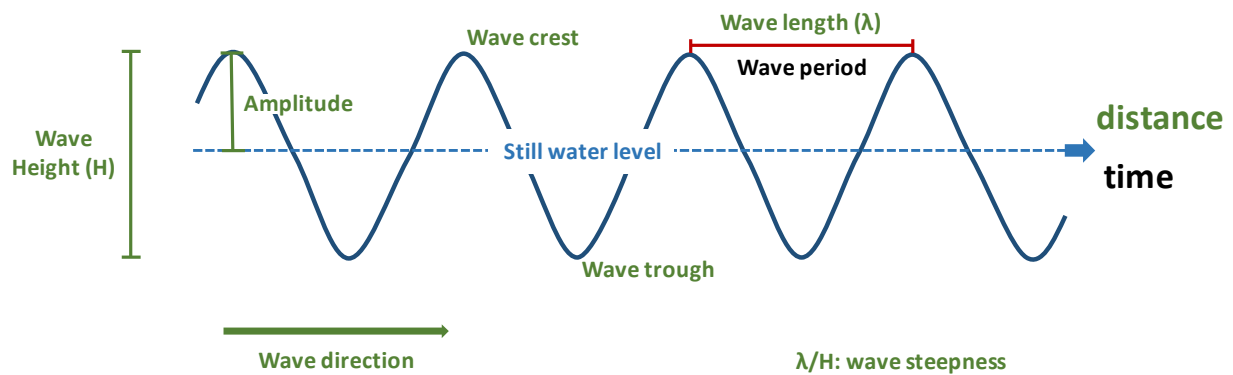


Figure 1-1 Wave characteristics.

For a wave to exist there must be an initial equilibrium state, which is perturbed by a generating force and compensated by a restoring force. Generating mechanisms include local wind, earthquakes, atmospheric pressure gradients, and gravitational forces of celestial bodies (e.g. Sun, Moon), among others. These forces are compensated by gravity (exerted by the Earth), surface tension and the Coriolis force (Toffoli & Bitner-Gregersen, 2017).

Surface ocean waves can also be classified in several ways. The most intuitive and commonly used classification is based on the wave period or the associated wavelength (Toffoli & Bitner-Gregersen, 2017; Holthuijsen, 2007). Table 1-1 present this classification with respect to wave period, as well as with the associated main generating and restoring forces. A graphical representation of an idealized wave amplitude spectrum is provided in Figure 1-2.

This work focuses only on surface gravity waves (wind-generated gravity waves) with periods ranging from ~1 s to ~20 s.

Table 1-1 Ocean wave classification (Toffoli & Bitner-Gregersen, 2017).

| Classification | Period band | Main generating forces | Main restoring forces |
| --- | --- | --- | --- |
| Capillary waves | < 0.1 s | Wind | Surface tension |
| Ultragravity waves | 0.1 - 1 s | Wind | Surface tension and gravity |
| Gravity waves | 1 - 20 s | Wind | Gravity |
| Infragravity waves | 20 s to 5 min | Wind and atmospheric pressure gradients | Gravity |
| Long-period waves | 5 min to 12 h | Atmospheric pressure gradients and earthquakes | Gravity |
| Ordinary tidal waves | 12 - 24 h | Gravitational attraction | Gravity and Coriolis force |
| Transtidal waves | > 24 h | Storms and gravitational attraction | Gravity and Coriolis force |
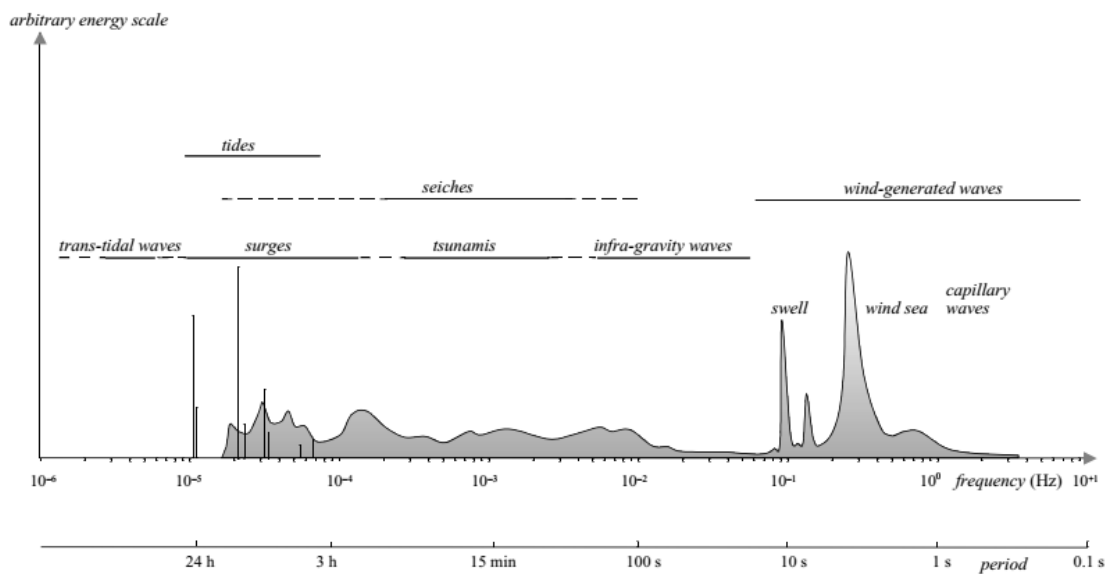


Figure 1-2 Frequencies and periods of the vertical motions of the ocean surface (Holthuijsen, 2007).

## 1.4.2 Wind-generated gravity waves

Wind-generated waves originate in windy regions of water bodies (oceans, seas and lakes). They can travel across great expanses of open waters until they release their energy by breaking against the shore.

As the wind blows over the water surface, it creates pressure stress forming ripples (capillary waves), allowing to transfer more efficiently the energy from the wind into the water. As more energy is transferred, gravity waves develops, increasing in height, length and speed of propagation. Thus, the factors that determine the amount of energy in waves are the wind speed, the time that the wind blows in one direction, and the fetch (distance over which the wind blows in one direction). However, waves cannot grow indefinitely after an equilibrium condition called 'fully developed sea' has been achieved. As the energy of waves increases, so does their steepness, until they reach a critical value of 1/7 at which point waves will break forming whitecaps (whitecapping), losing some of their energy (Thurman & Trujillo, 2002).

Waves in the generation zone are called 'sea' or 'sea-waves', and are characterized by choppiness and waves travelling in many directions. Waves in this zone also have a variety of periods and wavelength (most of them short) due to frequently changing wind speed and direction. When waves move away from the generation zone, wind speed diminish and waves eventually move faster than the wind. When this occurs, wave steepness decreases, and waves become long-crested waves called 'swells' or 'swell-waves'. Swells are characterized by a narrower range of frequencies and directions, and a more regular shape of the waves. This kind of waves can travel with little loss of energy over large stretches of the ocean surface (Thurman & Trujillo, 2002).

The combination of the many waves travelling with different heights, periods, and directions in a specific location and moment is called 'sea state' or simply 'ocean waves', and are affected and transformed by numerous phenomena. The most significant mechanisms for transformation are listed below (Holthuijsen, 2007). The relative importance of these mechanisms in oceanic and coastal waters is presented in Table 1-2.

- Wind wave generation and growth: the development of surface gravity waves caused by the transfer of energy from the wind to the ocean surface.

- Frequency-dispersion: In deep waters, longer waves (lower-frequency waves) travel faster than shorter waves (higher-frequency waves), and thus, a sorting process of waves by their wavelength occur with the low frequencies in the lead and the high frequencies in the trailing edge. The equation that describe this phenomenon is presented in Eq. 1.1.

$$\sigma^2 = g|\vec{k}| \, tanh(|\vec{k}|d) \qquad\qquad 1.1$$

Where $\sigma$ is the relative (to the moving water) angular frequency. $g$ is the gravitational acceleration. $\vec{k}$ is the wave number vector defined as $k = 2\pi/\lambda$ with the same direction as the wave. $d$ is the water depth. The absolute angular frequency is defined as $\omega = \sigma + \vec{k} \cdot \vec{U}$, with $\vec{U}$ the ambient current.

- <u>Direction-dispersion</u>: In the generation area, and because of the fluctuations of the wind velocity, waves travel in a range of directions. Away from the generation area (where the wind speed has diminished), waves travel in a more reduced range of directions. Frequency- and direction-dispersion occur simultaneously and are more noticeable further from the generation zone, transforming the short-crested waves into long-crested waves.

- <u>Quadruplet wave-wave interaction</u>: exchange of energy through resonance between two pairs of wave components of the sea state. To this to happens, specific conditions of the frequencies, directions and wave numbers of the pair of wave components need to meet.

- <u>Triad wave-wave interaction</u>: exchange of energy by resonance between three wave components of the sea state. For this energy exchange to occur, specific conditions of the frequencies, directions and wave numbers of the pair of wave components need to meet. Triad wave-wave interaction cannot occur in deep water ($> \lambda/2$).

- <u>Shoaling</u>: a process whereby the wavelength and wave speed decreases, and the wave height increases due to a decrease in water depth (as described by the dispersion relationship in Eq. 1.1) (SWAN, 2019b). During this process, frequency remains constant.

- <u>Refraction</u>: change in direction of the waves due to changes in the wave speed along the wave front. In shallow water, refraction tends to line up wave fronts with bathymetric contours.

- <u>Diffraction</u>: a process which spreads wave energy laterally, extending the wave front. This phenomenon occurs when waves encounter and pass obstacles.

- <u>Reflection</u>: a change in direction of a wave front when collide with a solid obstacle. After the collision, waves return into the water.

- <u>Bottom friction</u>: a mechanism that dissipates energy and momentum from the motion of the water particles to the turbulent boundary layer at the sea bottom.

- Wave breaking: wave energy dissipation due to the turbulent mixing which occurs when wave steepness surpasses a critical value, causing the water to spill off the top of a wave crest. It is a complicated phenomenon that involve highly nonlinear hydrodynamics on a wide range of scales, from gravity surface waves to capillary waves, down to turbulence. There are two types of wave breaking: Whitecapping and Bottom-induced wave breaking. The first occur in deep water during 'fully developed sea' conditions. The second happen due to shoaling in shallow water.

- Wave-current interaction: changes in wave amplitude, frequency and direction. The wave amplitude is affected by a shoaling process caused by current related change in propagation speed, while changes in frequency and direction are due to the Doppler effect and current induced refraction, respectively.

Table 1-2 Relative importance of the various process affecting the evolution of waves in oceanic and coastal waters (Holthuijsen, 2007).

| Process | Oceanic waters | Coastal waters | | |
|---|---|---|---|---|
| | | Shelf seas | Nearshore | Harbour |
| Wind generation | ●●● | ●●● | ● | ○ |
| Quadruplet wave–wave interactions | ●●● | ●●● | ● | ○ |
| White-capping | ●●● | ●●● | ● | ○ |
| Bottom friction | ○ | ●● | ●● | ○ |
| Current refraction / energy bunching | ○/● | ● | ●● | ○ |
| Bottom refraction / shoaling | ○ | ●● | ●●● | ●● |
| Breaking (depth-induced; surf) | ○ | ● | ●●● | ○ |
| Triad wave–wave interactions | ○ | ○ | ●● | ● |
| Reflection | ○ | ○ | ●/●● | ●●● |
| Diffraction | ○ | ○ | ● | ●●● |

●●● = dominant, ●● = significant but not dominant, ● = of minor importance, ○ = negligible.

### 1.4.3 Wave-current interactions

Waves are influenced by currents and vice versa. These currents can be tidal, ocean, local wind generated, river, and wave generated currents, or a combination of them. The theoretical description of these interactions was first presented by Longuet-Higgins and Stewart (1960, 1961, 1962; in SWAN, 2019a). Since then, many other studies on wave-current interactions have been published.

The effect of current on waves can be summarized as follow (Wolf & Pradle, 1999):

- <u>Energy transfer from wind to waves</u>: the effective wind energy transferred to the waves is relative to the surface current, i.e. in opposing wind-current velocities, the energy transfer is greater. In addition, surface roughness changes in the present of current, which also affect the quantity on the wind energy that is transferred to the waves.

- <u>Current refraction</u>: waves are deflected toward the current direction.

- <u>Doppler shift</u>: waves of the same absolute frequency ($\omega$) will have a lower relative frequency ($\sigma$) in favorable following currents and a higher relative frequency in an opposing current.

- <u>Wave height, wavelength and wave steepness change</u>: due to the wave action conservation and the Doppler shift effect, wavelength shorten, waves get higher and wave steepness increase in opposing currents. The opposite occurs in favorable currents.

- <u>Wave-current bottom friction</u>: empirical studies of the bottom boundary layer have shown that the friction coefficient is larger in presence of currents than in a no current ambient.

- <u>Modulation of frequencies</u>: the absolute frequency is modulated by unsteady currents, i.e. $\omega$ varies according to the variations of the unsteady current. In non-uniform current fields, $\sigma$ is modulated while propagating. If the current is steady $\omega$ should be constant, if the current is homogeneous $\sigma$ should be constant.

- <u>Whitecapping</u>: in strong enough opposite current, whitecapping could occur (SWAN, 2019a).

- <u>Non-linear wave energy transfer</u>: the wave action at the blocking frequency is partially transferred away to higher and lower frequencies by nonlinear wave-wave interactions (Ris, 1997; in SWAN, 2019a).

The effect of waves on current is summarized below (Wolf & Pradle, 1999):

- Radiation stress: this term describes the additional horizontal momentum (depth integrated and phase averaged) due to the presence of waves. Spatial variation in the radiation stress (as a result of spatial variations in wave conditions) induce changes in the mean flow (wave-induced currents) and mean surface elevation (wave setup / setdown).

- Energy transfer from wind to current: the effective drag coefficient for wind-driven currents change in the presence of waves.

- Wave-current bottom friction: the bottom friction coefficient for currents is modified in the presence of waves.

### 1.4.4 Ocean waves characterization

A sea state is composed of waves of different heights and periods, coming from different directions, and its conventional short-term characterization requires a statistical approach. This statistical approach also requires statistical stationarity. Therefore, a time record of actual ocean waves needs to be as short as possible, however, a reliable statistical characterization requires averaging over a duration that is as long as possible. The compromise at sea is typically a record length in the range of 15–30 min (Holthuijsen, 2007).

The wave condition in a stationary record can be characterized with average wave parameters computed after defining each wave using a zero up- or down-crossing method. The most typical statistical wave parameters are:

- $H_z$ and $T_z$: mean wave height and period, respectively.

- Significant wave height ($H_s$) and significant wave period ($T_s$): mean wave height and period of the highest third of the waves, respectively. $H_s$ correlates well with the wave height estimated visually by experimented observers.

- $H_{1/10}$: mean wave height of the highest tenth of the waves.

- $H_{max}$ and $H_{rms}$: maximum wave height and root mean square of wave height.

A more complete description of the wave condition is obtained by approximating the surface elevation time series as the sum of harmonic waves (wave components) as presented in Eq. 1.2. This type of description leads to the concept of the wave height variance density spectrum (one-dimensional spectrum), which shows how the variance of the sea-surface elevation is distributed over the frequencies. The wave height variance density spectrum (wave spectrum) concept can be extended to the directional wave spectrum (two-dimensional wave spectrum, $E$), which shows also the wave height variance of each wave component propagating in all directions across the sea surface. Figure 1-3 shows an example of a variance density spectrum.

If the surface elevations are Gaussian distributed and the sea state is stationary, the wave spectrum provides a complete statistical description of the waves. The frequency spectrum ($E_\omega$, see Eq. 1.3) and a direction spectrum ($E_\theta$, see Eq. 1.4) can be obtained from the two-dimensional spectrum (directional spectrum, $E$) by integration over all directions, and over all frequencies, respectively. When multiplied by the density of the water ($\rho_w$) and the gravitational acceleration ($g$), the wave spectrum becomes the energy density spectrum, showing how the energy of the waves is distributed over the frequencies (and directions) (Holthuijsen, 2007).

$$\eta(t) = \sum_i a_i \cos(\omega_i t + \alpha_i)$$

1.2

Where $\eta(t)$ is the surface elevation at the instant $t$, $a_i$, $\sigma_i$ and $\alpha_i$ are the amplitude, absolute angular frequency and phase of the $i$th wave component.
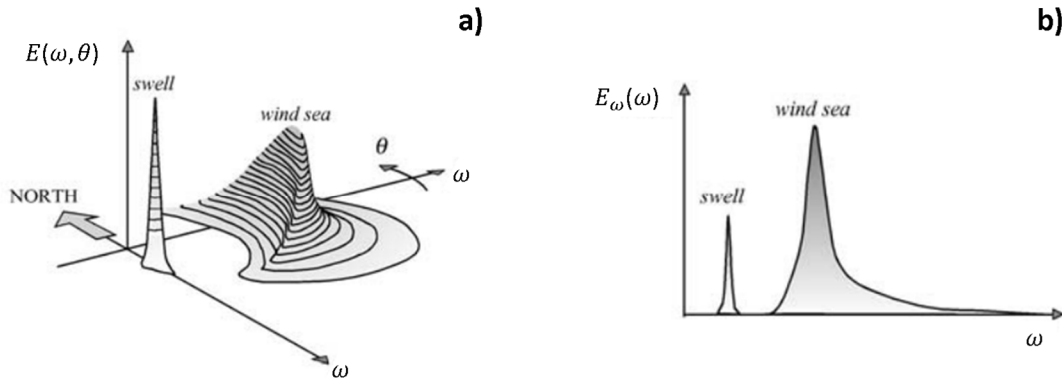


Figure 1-3 Wave height variance density spectrum: a) 2D wave spectrum. b) 1D wave spectrum obtained from the 2D spectrum (modified from Holthuijsen, 2007).

$$E_\omega(\omega) = \int_0^{2\pi} E(\omega, \theta)\, d\theta \qquad\qquad 1.3$$

$$E_\theta(\theta) = \int_0^\infty E(\omega, \theta)\, d\omega \qquad\qquad 1.4$$

Characteristic wave parameters can also be estimated from the wave spectrum. The most commonly used are presented and defined below, based on the $n$th spectral moment (Eq. 1.5) and the directional variance spectrum $E(\omega, \theta)$ as a function of the absolute angular frequency $\omega$ and direction $\theta$ of the wave components, or as a function of the relative angular frequency ($\sigma$) and $\theta$, $E(\sigma, \theta)$ (SWAN, 2019b).

- Significant wave height estimated from the spectrum ($H_{m0}$, see Eq. 1.6).

- Energy period ($T_e$, see Eq. 1.7).

- Mean wave period ($T_{m01}$, see Eq. 1.8, or $T_{m02}$, see Eq. 1.9).

- Peak period ($T_p$, see Eq. 1.10).

- Mean direction ($D_m$, see Eq. 1.11).

- Peak direction ($D_p$, see Eq. 1.12).

- Directional spreading ($D_{SPR}$, see Eq. 1.13).

- Peakedness of the wave spectrum ($Q_p$, see Eq. 1.14).

- Wave steepness ($S$, see Eq. 1.15).

- Energy transport (power) per linear meter in the $x$- and $y$-direction ($P_x$ and $P_y$, respectively; see Eq. 1.16 and 1.17).

$$m_n = \int_0^{2\pi} \int_0^\infty \omega^n E(\omega, \theta)\, d\omega d\theta \qquad\qquad 1.5$$

$$H_{m0} = 4\sqrt{m_0} \qquad\qquad 1.6$$

$$T_e = T_{m-10} = 2\pi \frac{m_{-1}}{m_0} \qquad (1.7)$$

$$T_{m01} = 2\pi \left(\frac{m_1}{m_0}\right)^{-1} \qquad (1.8)$$

$$T_{m02} = 2\pi \left(\frac{m_2}{m_0}\right)^{-1/2} \qquad (1.9)$$

$$T_p = \frac{2\pi}{\omega_p} \qquad (1.10)$$

$$D_m = \operatorname{atan}\left(\frac{\int_0^{2\pi} \int_0^\infty \sin(\theta) E(\sigma, \theta) \, d\sigma d\theta}{\int_0^{2\pi} \int_0^\infty \cos(\theta) E(\sigma, \theta) \, d\sigma d\theta}\right) \qquad (1.11)$$

$$D_p = \theta_p \qquad (1.12)$$

$$D_{SPR} = \sqrt{\left(\frac{180}{\pi}\right)^2 \int_0^{2\pi} \left(2 \sin\left(\frac{\theta - D_m}{2}\right)\right)^2 E_\theta(\theta) d\theta} \qquad (1.13)$$

$$Q_p = 2 \frac{\int_0^{2\pi} \int_0^\infty \sigma E^2(\sigma, \theta) \, d\sigma d\theta}{\left(\int_0^{2\pi} \int_0^\infty E(\sigma, \theta) \, d\sigma d\theta\right)^2} \qquad (1.14)$$

$$S = \frac{H_{m0}}{\lambda_m} \qquad (1.15)$$

$$P_x = \rho g \int_0^{2\pi} \int_0^\infty c_x E(\sigma, \theta) \, d\sigma \, d\theta \qquad (1.16)$$

$$P_y = \rho g \int_0^{2\pi} \int_0^\infty c_y E(\sigma, \theta) \, d\sigma \, d\theta \qquad (1.17)$$

$\omega_p$ is the frequency at the peak of $E_\omega$. $\theta_p$ is direction at the peak of $E_\theta$. $\rho$ and $g$ are the density of the water and the gravitational acceleration. $c_x$ and $c_y$ are the propagation velocity of energy in the $x$ and $y$ direction (see Eq. 1.18 and Eq. 1.19).

$$\left(c_x, c_y\right) = \frac{d\vec{x}}{dt} = \vec{c}_g + \vec{U} \qquad \text{1.18}$$

$$\vec{c}_g = \frac{1}{2}\left(1 + \frac{2|\vec{k}|d}{\sinh(2|\vec{k}|d)}\right)\frac{\sigma\vec{k}}{|\vec{k}|^2} \qquad \text{1.19}$$

Beside the wave parameters presented in Eq. 1.6 to 1.17, wave parameters from regions of the 2D spectrum can also be computed. These regions of the wave spectrum are called partitions and are sections of the spectrum associated to different wave systems (waves that can be linked to different wave-originating storms). In case of multi-wave system spectra, partition parameters can be used to recreate the spectrum more accurately than with only global parameters, without having to store the full wave spectra which require considerably more data storage space.

It is worth mentioning that, when having limited information, wave power can be approximated using Eq. 1.20, which in deep water ($d > \lambda/2$) becomes Eq. 1.21.

$$P \approx \frac{\rho g}{16} H_{m0}{}^2 C_g(T_e, d) \qquad \text{1.20}$$

$$P_0 \approx \frac{\rho g^2}{64\pi} H_{m0}{}^2 T_e \qquad \text{1.21}$$

### 1.4.5 Ocean waves estimation

Wave characteristics (spectra and/or parameters) at particular locations can be estimated mainly through four methods. These methods are described below, including their main advantages and disadvantages.

**Measurements**

Measurement techniques can be classified into two categories; in-situ techniques (instruments deployed in the water), or remote-sensing techniques (instruments installed at some distance above the water). Currently, common in-situ instruments include wave buoys and acoustic Doppler current profilers (ADCPs), which are directional wave measurement instruments. The most common remote-sensing technique is the radar, which is based on the emission of electro-magnetic radiation and the analysis of the backscatter reflected by the sea surface. Radars may be

installed at the coast (e.g. High Frequency Radar), in fixed platforms, or in moving platforms (airplanes and satellites; e.g. Synthetic Aperture Radar, SAR) (Robertson, 2017 in Yang & Copping, 2017; Pandian et al., 2010; Holthuijsen, 2007).

Each measurement technique has its own advantages and disadvantages regarding to operational performance, accuracy, maintenance, cost and reliability (Robertson, 2017; Pandian et al., 2010; Holthuijsen, 2007). But in general, remote-sensing instruments are better suited for measuring larger spatial distributions of the wave field, however, they are not as precise and accurate as in-situ instruments. On the other hand, oceanographic buoys have proven to be cost-effective and are usually the principal instrument for national wave measurement programs in many countries (Pandian et al., 2010), but they as well ADCPs and other in-situ techniques can only measure the wave characteristics at only one location.

For the wave energy industry, buoys are also preferred mainly because their ease of deployment and capabilities for long-term data collection (Robertson, 2017). Normally, measurements are considered to be the best data (Goda, 2010; Dalrymple, 1985 in Huges, 1996), but field studies are commonly expensive, and the spatial and temporal resolution is limited (Pandian et al., 2010). Thus, measured wave data is usually used to specify hydrodynamic forcing conditions and/or to verify the estimations made using numerical or physical models (Hughes, 1996).

**Physical models (laboratory experiments)**

Physical models are smaller and are a simplified physical representation of a physical system. They integrate the appropriate 'governing equations' without simplifications or assumptions needed to be made by numerical models or analytical expressions. The small size of the model allows coast-effective, easier and simultaneous data collection whereas field measurements are more expensive and difficult to obtain. Physical models have a high degree of experimental control allowing to study varied conditions at the convenience of the researcher. However, they are almost exclusively used for short-term analysis, small areas of interest and the study of complicated phenomena or interactions (e.g. wave-structure interactions). This, because they are usually more expensive than the operation of numerical models (where numerical models give reliable results), and they have scale effects that become more important when reducing the scale to simulate larger domains. Laboratory effects are also present and can influence the process

being simulated. Typical laboratory effects include the inability to generate multidirectional wave spectra at the offshore boundary and to incorporate a wind field (Hughes, 1996).

**Analytical expression**

Mathematical expression generally obtained by correlating measurements of different physical parameters and/or by simplifying fundamental physics equations. They are simple to use and results can be obtained quickly, but less accurate than the other methods. Typically, gross estimations and/or assumptions need to be done on the independent variables values. An example of an analytical expression for the estimation of a fetch-limited seas spectrum can be found in Hasselmann et al. (1973).

**Numerical models**

Numerical models are a simplified mathematical representation of a physical system solved by numerical methods. They are based on fundamental physics equations or simplifications of them. These equations need to be discretized over the model domain and simulation time to be solved.

Numerical models have shown steady growth and utility over the years thanks to increasing computing power. For simulating surface wave processes, basically two types of numerical models can be distinguished: Phase-resolving and Phase-averaged models.

Phase-resolving models solve the water surface elevation and the horizontal (and some of them the vertical) flow velocity. They are especially suitable for resolving radiation and diffraction, among other wave transformation phenomena, however they do not include wave generation and growth processes. Phase-resolving models are based on the fundamental mass and momentum balance equations. To compute the evolution of the sea surface, a grid with a resolution finer than the wavelength and time steps much shorter than the wave period are needed. The high computational requirements of these models limit their applications to small areas and simulation times, making them impractical for high-resolution, long-term, regional hindcast or / and for simulating multiple scenarios.

Phase-averaged models are based on the wave energy balance equation and provide a statistical description (wave spectrum) of the wave conditions in space and time. In addition to the wave transformation, they include wave generation and growth processes. These models have

global, regional and local applications and can be used for several years to decades' simulation timeframes. These types of models are the only practical models that can be employed for wave climate characterization and wave energy assessment projects (Robertson, 2017; Neary et al., 2016; Liu and Losada, 2002).

As mentioned previously, numerical models incorporate the physical concepts of the phenomena within their governing equations. So, their performance depends on these governing equations, but also on the numerical schemes to solve them, the space and time discretization, the quality of the input data (e.g. wave boundary conditions, wind field, currents, etc), and for the case of spectral wave models (Phase-averaged), the frequency and directional discretization of the energy density wave spectrum.

It is important to mention that, although both types of numerical models use governing equations that follow physical principles, none of them considers all physical processes involved (Liu & Losada, 2002). Some terms are neglected, simplified and / or parametrically modeled (e.g. source-sink terms related to energy transference wind-water and energy dissipation through whitecapping, wave breaking, etc), so, the parameters involved need to be carefully chosen, usually based on experiments and measurements. However, for the models to be reliable, their parameters need to be adjusted in a calibration and validation process involving a comparison of their results against measurements.

## 1.5 Wave energy resource assessment standards

Among the different methods to estimate the ocean waves characteristics, numerical models standout as a powerful tool for the study of surface water waves (Janssen, 2008; in Thomas and Dwarakish, 2015). In occasions (as for the present work), they are the only feasible method under economical, accuracy and time restrictions, and coverage and extension requirements. Moreover, the International Electrotechnical Commission in its 'Technical Specification on Wave Energy Resource Assessment and Characterization' (IEC, 2015), which provides guidance to perform wave resource assessments, relies its recommended methodology primarily on spectral wave (phase-averaged) models.

IEC (2015) divide wave resource assessments into three distinct types: Class 1 for reconnaissance, Class 2 for feasibility, and Class 3 for design studies. Class 1 studies are

commonly carried out at low to medium resolution, while Class 2 and especially Class 3 usually focus on smaller areas and employ higher resolution to generate more accurate estimations of the wave resource. The most important suggestions on how to conduct every type of wave resource assessment using numerical models are presented below.

- Wave boundary condition using directional wave spectra.

- Include the physical process of wind-wave growth, whitecapping, quadruplet interactions, depth induced wave breaking, bottom friction, triad interactions, diffraction and refraction, wave-current interactions. However, depth induced wave breaking, bottom friction and triad interactions can be excluded in reconnaissance studies.

- Bathymetric data resolution at depths greater than 200 m, at the range between 20 m to 200 m, and at less than 20 m should be greater than 5 km, 500 m and 100 m respectively for reconnaissance studies; 2 km, 100 m and 50 m respectively for feasibility studies; and 1 km, 25 m and 10 m respectively for design studies.

- The numerical simulations should produce a minimum of 10 years of sea state data.

- The frequency range of the model output should cover at least 0,04 Hz to 0,5 Hz.

- The numerical model should be calibrated and validated using measured wave data (a procedure is suggested).

- Estimates of the uncertainty of the wave resource shall be provided for at least $H_{m0}$, $T_e$ and the annual average wave power.

Although the IEC standards (IEC, 2015) suggests to review, describe and assess the influence of tidal currents, as well as other forcing (e.g. water level fluctuations, non-tidal currents), and include them when their influence is likely to be significant, no specific threshold for 'significance' is presented. EquiMar (2011) recommends, for more advanced stages of modelling studies, to include currents if they are higher than 2-3% of the local group velocity of the dominant waves. EquiMar (2011) also suggest that wind should always be included when available, and tides (water surface fluctuations) may be excluded if in the area of interest, the water depth is modified by less than 5%.

## 1.6 Thesis outline

The remainder of this thesis lay out is as follows:

Chapter 2 presents an overview of the fundamentals of phase-averaged numerical wave models, and the rationale behind the choice of a particular model called SWAN for this work. Chapter 2 also summarize previous wave resource assessments developed for the BC coast, as well as methodologies to evaluate the performance of different candidate numerical models.

Chapter 3 describes all the data analyzed and employed to build, run and calibrate the numerical wave models (with and without currents, i.e. WCWI-v6 and WCWI-v5, respectively) of the B.C. coast. The data analyzed include bathymetry, waves, wind and currents, among others.

Chapter 4 reviews the processes of building the wave models. These processes consist of the construction of the model mesh, calibration and the definition of the final models setup.

Chapter 5 presents the results and discussion of the results, including a performance analysis of the two models, a comparison on the wave characteristics and power as a results of the influence of the tidal currents, and a wave resource characterization.

Chapter 6 summarizes the findings and conclusions of this thesis and presents recommendations for future wave resource assessment for the west coast of Canada.

# Chapter 2 Literature review

As presented in Chapter 1, phase-averaged models are the standard tool used in wave energy resource assessment and wave characterization studies. Furthermore, they are usually the only feasible method under economical, accuracy and time restrictions, and coverage and extension requirements, as it is for the present study. Thus, the wave energy resource assessment of the west coast of Canada developed in this thesis is based on the results of numerical wave models.

This chapter presents an overview of wave models (phase-averaged ocean wave models), previous work related to the wave resource assessment for the B.C. coast, as well as methodologies to evaluate the performance of numerical (wave) models.

## 2.1 Phase-averaged ocean waves models

In the 1950s, researchers began to recognize that the wave generation and propagation processes are best described as a spectral phenomenon. Based on advances on spectral wave growth due to wind inputs, and energy dissipation, the first-generation spectral wave model was developed by Gelci et al. (1957) (USACE 2008; Mitsuyasu 2001). The first-generation models limit the shape of the spectrum to a parametric form (e.g. Pierson-Moskowitz). No nonlinear wave-wave interaction, or a very simple formulation of it were taken into account (USACE, 2008).

In the late 1960s, improvements on the understanding of wave generation and propagation led to the development of second-generation spectral wave models. Second-generation models incorporated a parametric nonlinear wave-wave interaction theory developed by Hasselmann (1961), allowing the spreading of the spectral energy to less energetic areas of the spectrum (USACE, 2008).

In the mid-1980s, third-generations wave models appeared. These new models, based on Hasselmann et al. (1985) (Fradon et al., 1999), use a more detailed and explicit nonlinear wave-wave interaction source terms and relax most of the constrains on the spectral shape (USACE, 2008; Fradon et al., 2000). As a consequence, and because the physics of wind-waves are universal, these models can be applied anywhere (with the appropriate bathymetry, grid extension and resolution, and suitable wind data) (EquiMar, 2011). Further improvements continue, for example: including better capabilities in coastal areas (e.g. including triad nonlinear wave-wave interactions,

bottom frictions, depth-induced breaking, current-inputs, diffraction) or improving the numerical schemes, parametrization of source-sinks terms or making more flexible the spatial grid discretization (e.g. from structured to curvilinear and unstructured grids).

Over the last twenty years, and for the case of wind wave generation and propagation, phase-averaged models based on the spectral wave action balance equation (Eq. 2.1, or some adaptation of it) have gained extensive usage in both scientific and engineering applications. This type of models has displaced the former preferred method based on energy conservation and ray tracing (Ardhuin and Roland, 2014; Liu and Losada, 2002), which although is much less computationally expensive, is limited to bulk descriptions of wave conditions (e.g., significant wave height, peak period, mean direction), or bulk descriptions of each wave partition, lacking spectral details (Ardhuin and Roland, 2014).

$$\frac{\partial N}{\partial t} + \vec{\nabla}_{\vec{x}} \left[ \frac{d\vec{x}}{dt} N \right] + \frac{\partial c_\sigma N}{\partial \sigma} + \frac{\partial c_\theta N}{\partial \theta} = \frac{S_{tot}}{\sigma} \qquad \text{2.1}$$

Where $N = N(\sigma, \theta, x, y, t)$ is the wave action density defined as $N = E/\sigma$ for the frequency $\sigma$, propagation direction $\theta$, two horizontal spatial coordinates $x$ and $y$, and time $t$. $\frac{d\vec{x}}{dt}$ is the propagation velocity of energy defined as in Eq. 1.18. $c_\sigma$ and $c_\theta$ are the propagation velocities in the spectral frequency-space (see Eq. 2.2) and direction-space (see Eq. 2.3), respectively. $S_{tot}(f, \theta, x, y, t)$ is a non-conservative term representing all physical process which generate, dissipate, or redistribute wave energy (source / sink terms, see Eq. 2.4). The left hand side of Eq. 2.1 represent the kinematics of the wave action density. The second term represent the propagation of wave energy in the two-dimensional geographical space, including wave shoaling. The third term accounts for the effect of shifting of the frequency due to variations in depth and current. The fourth term represents depth-induced and current-induced refraction.

$$c_\sigma = \frac{d\sigma}{dt} = \frac{\partial \sigma}{\partial d} \left( \frac{\partial d}{\partial t} + \vec{U} \cdot \nabla_{\vec{x}} d \right) - c_g \vec{k} \frac{\partial \vec{U}}{\partial s} \qquad \text{2.2}$$

$$c_\theta = \frac{d\theta}{dt} = -\frac{1}{|\vec{k}|} \left( \frac{\partial \sigma}{\partial d} \frac{\partial d}{\partial m} + \vec{k} \cdot \frac{\partial \vec{U}}{\partial m} \right) \qquad \text{2.3}$$

$$S_{tot} = S_{in} + S_{nl3} + S_{nl4} + S_{ds,w} + S_{ds,b} + S_{ds,br} \qquad\qquad 2.4$$

Where $\vec{c}_g = \partial\sigma/\partial k$ is the group celerity (see Eq. 1.19 for an expanded definition). $s$ and $m$ are the space coordinate in the wave propagation direction $\theta$ and perpendicular to it, respectively. $S_{in}$ is the wave growth by wind, $S_{nl3}$ and $S_{nl4}$ are the non-linear transfer of wave energy through three-wave and four-wave interactions (Triad and Quads), respectively. $S_{ds,w}$, $S_{ds,b}$ and $S_{ds,b}$ are the wave decay due whitecapping, bottom friction and depth-induced wave breaking, respectively.

As this work consider the evaluation of wave models that include and exclude tidal currents as forcing, it is worth noticing that currents play an important role in the action balance equation (Eq. 2.1). This equation, without ambient current (and invariant bathymetry), can be reduced as in Eq. 2.5. The consequences of having ambient currents on the wave characteristics and wave variance spectrum are discussed in sub-section 1.4.3.

$$\frac{\partial N}{\partial t} + \vec{\nabla}_{\vec{x}}\left[\vec{c}_g N\right] + \frac{\partial \hat{c}_\theta N}{\partial \theta} = \frac{S_{tot}}{\sigma} \qquad\qquad 2.5$$

With $\hat{c}_\theta = -\frac{1}{|\vec{k}|}\left(\frac{\partial\sigma}{\partial d}\frac{\partial d}{\partial m}\right)$.

There are two ways to include currents in a spectral wave model: in a one-way-coupling (a parametric way), and in a two-way-coupling. With the first alternative, currents are estimated previously (e.g. using a hydrodynamic model) and included as parameters that are not affected by the wave-current interactions. The second alternative (two-way-coupling), currents are dynamically included by the interaction of the spectral wave model with a hydrodynamic model. In this second alternative, both models interact and are fed by the results of the other at each time step, resolving the two-way wave-current interactions. Two-way-coupling is normally restricted to short-term and / or small model domains as hydrodynamic models, included in the phase resolving type of models, are very computationally expensive. Thus, for long term numerical simulations, currents can be included in a parametric form (EquiMar, 2011).

### 2.1.1 Third-generation spectral wave models

Since the first third-generation spectral wind-wave model WAM (Group, 1988) appeared, a number of other models have been developed. WAVEWATCH III (WW3), TOMAWAC, MIKE

21 SW, STWAVE and SWAN are some of the most popular. Although all these models solve the spectral action balance equation (Eq. 2.1) without any a priori restrictions on the spectral shape, they differ in their numerical implementation and the parametrization of the source-sink terms (e.g. wind forcing, whitecapping). WAM and WW3 have been typically used in regional to global applications because they lack(ed) or have(had) fairly rudimentary additional formulations for shallow waters. However, WW3 in their last versions has included shallow water capabilities (WW3DG, 2019; Robertson, 2017) and the ability to handle unstructured grids, preferred for coastal areas as the grid spacing can be optimized to better describe the bathymetric changes that affect the wave field. TOMAWAC, MIKE 21 SW, STWAVE and SWAN are typically used in local to regional application (as for the present work) as they have implemented these shallow water features (SWAN, 2019b; Ponce de León, 2018; Robertson, 2017; Fonseca et al. 2017; Roland and Ardhuin, 2014; Ueno and Kohno, 2004).

TOMAWAC and STWAVE are more simplified models and run faster. For example, TOMAWAC uses a ray-integration method which incorporates undesired diffusion (Roland and Ardhuin, 2014), while STWAVE is a steady-state model, simpler in terms of formulations and parameter choices, and can only generate and propagate wave characteristics from a direction range up to 180° (Fonseca et al. 2017; Neary et al., 2016). SWAN and MIKE 21 SW are similar models in terms of complexity (Fonseca et al., 2017), with the difference that MIKE 21 SW is a commercial software and SWAN is freely available as an open-source software.

It is worth mentioning that all these numerical models include multiple formulations for modelling the physics of the source-sink terms. The user can select a formulation, from more simplistic to more realistic, or for different applications. Each formulation will impact on the computational cost, accuracy, stability, etc. Improvements of these models are constantly being released, so some of the mentioned above could be out-of-date regarding to their latest versions.

Due to all the previously discussed benefits, its popularity among both the scientific community and industry, and since it is the only documented third-generation spectral wave model to be specifically developed for nearshore applications (Neary et al., 2016), the SWAN model was chosen as the modelling tool for this work.

## 2.1.2 SWAN model

SWAN (Simulating WAves Nearshore) is a third-generation wave software, developed by the Delft University of Technology in the Netherlands, and can be freely used under the terms of the general public license (GNU). It computes random, short-crested wind-generated waves in coastal regions and inland waters from given wind, bottom and current conditions by solving the stationary or nonstationary spectral action balance equation (Eq. 2.1).

SWAN can be employed on any scale relevant for wind-generated surface gravity waves using structured, curvilinear or unstructured discretization of the model domain (mesh), in cartesian or spherical coordinates. It employs implicit numerical schemes, making it more robust and computationally more economical in shallow waters, but generally less efficient on oceanic scales than models that use explicit schemes (SWAN, 2019a; SWAN, 2019b). The physical processes that SWAN can reproduce are the following:

- Generation and growth by wind ($S_{in}$).

- Spatial propagation from deep water to the surf zone.

- Refraction due to spatial variations of the bottom and currents.

- Diffraction.

- Blocking and reflection by, and transmission through opposing currents and obstacles.

- Dissipation by whitecapping ($S_{ds,w}$), bottom friction ($S_{ds,b}$) and depth-induced wave breaking ($S_{ds,br}$).

- Wave-wave interaction in both, deep (quadruplets, $S_{nl4}$) and shallow (triads, $S_{nl3}$) water.

- Wave-induced set-up.

The process described above can be estimated in some cases by choosing from several parametric formulations developed by different authors. Some of these formulations are presented in Table 2-3.

Table 2-3 Overview of the physical processes represented in SWAN and some of the formulations available to estimate their effect on the wave energy balance equation (SWAN, 2019b).

| process | authors | generation mode | | |
|---|---|---|---|---|
| | | 1st | 2nd | 3rd |
| Linear wind growth | Cavaleri and Malanotte-Rizzoli (1981) (modified) | × | × | |
| | Cavaleri and Malanotte-Rizzoli (1981) | | | × |
| Exponential wind growth | Snyder *et al.* (1981) (modified) | × | × | |
| | Snyder *et al.* (1981) | | | × |
| | Janssen (1989, 1991) | | | × |
| | Yan (1987) (modified) | | | × |
| Whitecapping | Holthuijsen and De Boer (1988) | × | × | |
| | Komen *et al.* (1984) | | | × |
| | Janssen (1991) | | | × |
| | Alves and Banner (2003) | | | × |
| Quadruplets | Hasselmann *et al.* (1985) | | | × |
| Triads | Eldeberky (1996) | × | × | × |
| Depth-induced breaking | Battjes and Janssen (1978) | × | × | × |
| Bottom friction | JONSWAP (1973) | × | × | × |
| | Collins (1972) | × | × | × |
| | Madsen *et al.* (1988) | × | × | × |
| Obstacle transmission | Seelig (1979), d'Angremond (1996) | × | × | × |
| Wave-induced set-up | | × | × | × |
| Vegetation dissipation | Dalrymple (1984) | × | × | × |
| Mud dissipation | Ng (2000) | × | × | × |
| Sea ice dissipation | Collins and Rogers (2017), Rogers (2019) | × | × | × |
| Turbulence dissipation | | × | × | × |

## 2.2 Previous wave resource assessment studies in B.C.

Several wave resource assessments have been performed for the coast of British Columbia (B.C.). Relevant initial works such as Baird and Mogridge (1976), and Allievi and Bhuyan (1994) quantified the wave power from buoy measurements at two and eleven locations, respectively. Between 1991-1993, Transport Canada funded and published a four volume Wind and Wave Climate Atlas of Canada. This atlas presented detailed information on wind speeds, wave heights and wave periods, but no information was given on wave power. In 2006, Cornett (2006) quantified the wave resource in both Canada's Pacific and Atlantic waters by analyzing the data from three

sources: direct wave measurements and two wind-wave hindcast models built using the OWI3G[3] and WW3 model frameworks. The calculation of wave power was performed using a simplified equation based on $H_{m0}$ and $T_e$ (see Eq. 1.20) at 3-hour intervals and at a maximum spatial resolution of 0.25°x0.25°. The data generated by Cornett (2006) provided a reasonable estimation of the off-shore wave energy resource, but both models lacked precision in coastal water areas due to the coarseness of the model grid. Additionally, the two models considered a relatively short period of time: from October 2002 to September 2005.

More detailed wave resource assessments in near-shore B.C. waters were completed by Robertson et al. (2014), Kim et al. (2012) and Cornett and Zhang (2008). However, all of these studies still lack the necessary near-shore spatial resolution and were driven by parametric wave spectra at the offshore boundary (Robertson et al., 2016). Kim et al. (2012) and Cornett and Zhang (2008) used a simplified equation to compute the wave power (Eq. 1.20) over a simulations period of only 5 years and 3-hour interval, and a spatial resolution of 1000 and ~275 m, respectively. Robertson et al. (2014) simulated in SWAN wave conditions for only 8 years (2005 to 2012) at 3-hour resolution in a non-stationary mode using an irregular grid (see Figure 2-1 a).

The latest regional effort to assess the wave resource in B.C. at near-shore waters was carried out by Robertson et al. (2016). In this work, a simulation of 10 years (2004 to 2013) at 3-hour interval was performed using the SWAN wave modelling software in its non-stationary mode. It utilized an irregular grid formed by 191,815 elements and 100,658 nodes that encompasses an area of 410,000 km$^2$ and 1500km of the Western Canadian coastline. The grid has maximum resolution of ~50 m at shallower waters and a minimum resolution of ~40 km in deep water (see Figure 2-1 b). The model was driven at the off-shore boundary by 2D wave spectra obtained at 3-hour resolution from the European Centre for Medium Range Weather Forecasts (ECMWF) WAM model at eight locations, and wind fields (3-hour and 0.2° resolution) obtained from the Coupled Ocean / Atmosphere Mesoscale Prediction System (COAMPS).

None of the previous studies included any of the mechanics of wave-current interactions described in sub-section 1.4.3.

---

[3] Third generation wave model: https://www.oceanweather.com/research/NumericalModeling.html
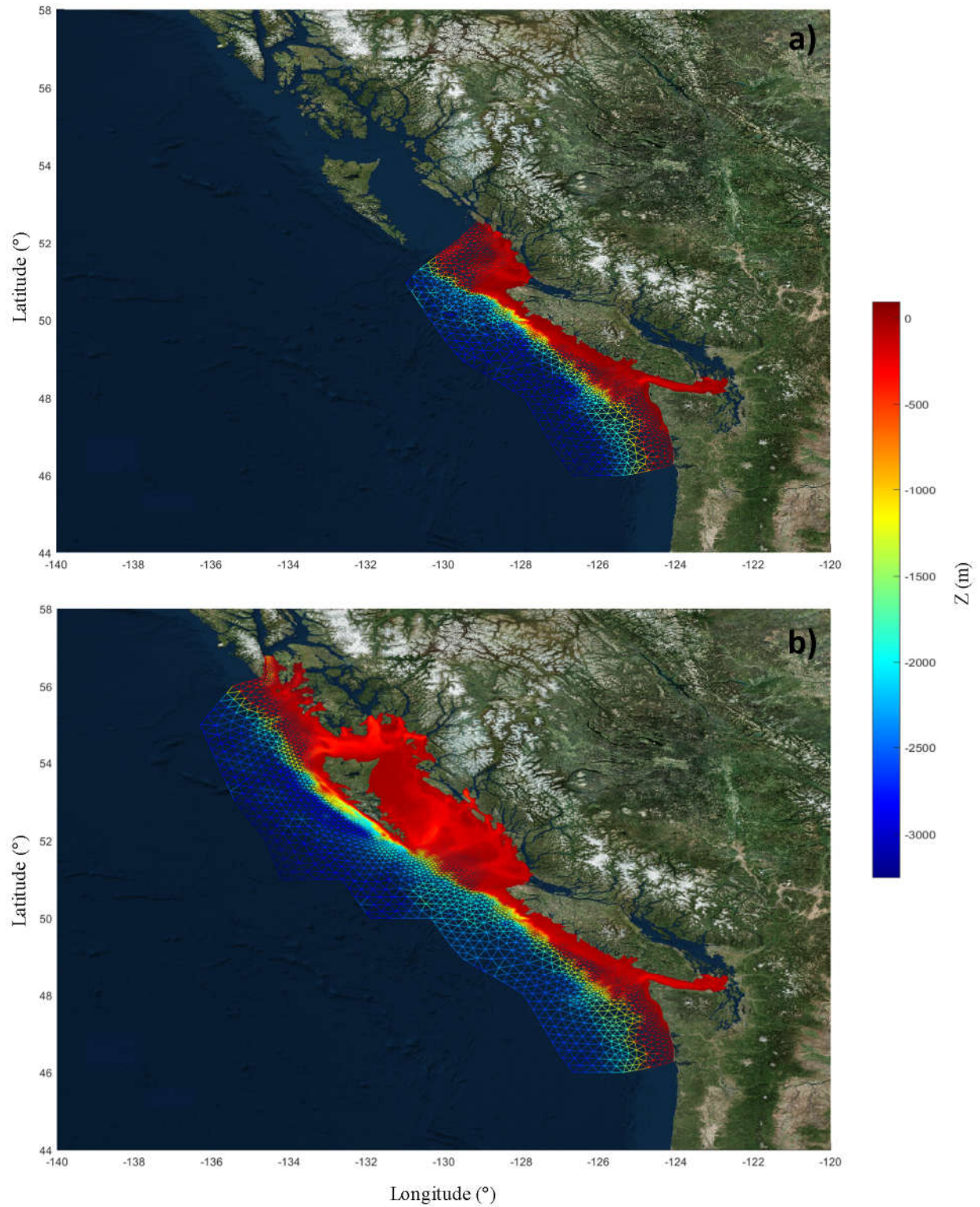
Figure 2-1 Mesh and digital elevation model (DEM) of the West Coast Wave Initiative (WCWI) SWAN model. a) WCWI-v3 utilized by Robertson et al. (2014). b) WCWI-v4 utilized by Robertson et al. (2016).

## 2.3 Evaluation of model performance

One of the main objectives of model performance analysis is to quantify the accuracy of the model results with respect to 'true' values (usually estimated from field measurements), as the accuracy dictates the usefulness of the model (Tian et Al. 2015). Quantification of accuracy is performed by characterizing the error ($\varepsilon$) of the modeled parameters through error metrics. When evaluating model performance, two types of error can be observed: systematic errors (shift of the model results in a consistent way) associated to the bias, and random errors (unpredictable variation of the model results) associated to precision. Researchers must select carefully the most appropriate(s) error metric(s) to properly quantify the accuracy of a model on a case to case basis according to the objectives of the model (Chai and Draxler, 2014).

Wave resource is defined by several parameters, and error metrics can be computed for each of them (when measurements are available). The choice of the wave parameters for which error should be characterized depends on the purpose of the study. IEC (2015) recommends to quantify accuracy as uncertainty and report it at least for $H_{m0}$, $T_e$ and the annual average wave power in wave energy resource assessment studies. Uncertainty $u_p$ define a confidence interval that bound the errors ($[\varepsilon s - u_p, \varepsilon s + u_p]$) with the probability $p$. $\varepsilon s$ represents the systematic error and $u_p$ is commonly estimated by the standard deviation of the random error, or a multiple of it. When uncertainty is characterized by the standard deviation of the random error ($\sigma$), it is called standard uncertainty, and define the interval of 68.26% of confidence if the random error ($\varepsilon r$) follows a normal distribution. As an example, Figure 2-2 present different confidence intervals defined by multiples of $\sigma$ when $\varepsilon r$ follows a normal distribution. As can be noticed from the previously discussed, the systematic error ($\varepsilon s$) can contribute significantly to the error characterization, and thus should also be included in the analysis.

$P(\varepsilon)$

68.26%

95.45%

99.73%

$\varepsilon s - 3\sigma$  $\varepsilon s - 2\sigma$  $\varepsilon s - \sigma$  $es$  $\varepsilon s + \sigma$  $\varepsilon s + 2\sigma$  $\varepsilon s + 3\sigma$  $\varepsilon$
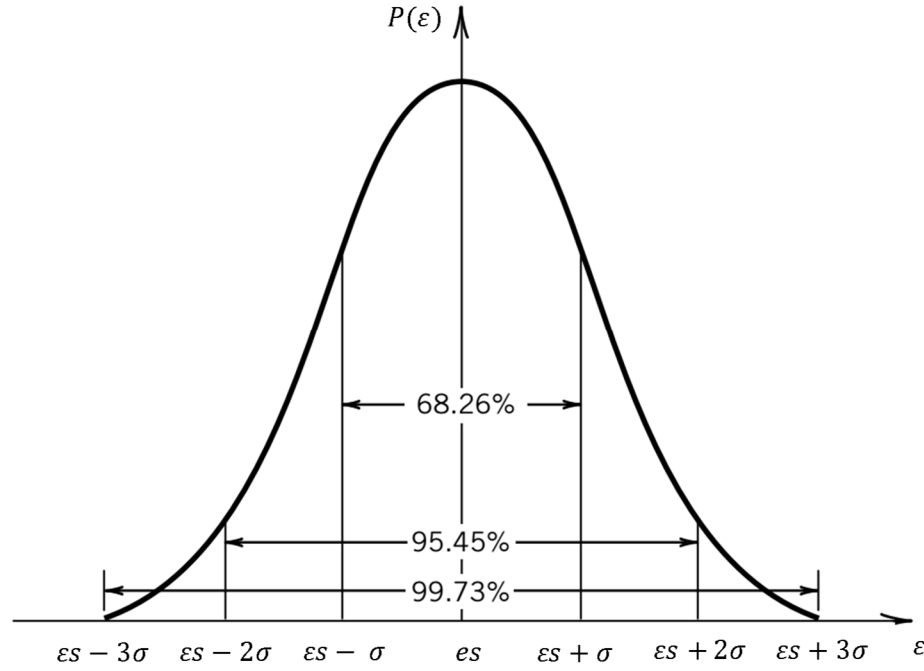
Figure 2-2 Confidence intervals of the total error ($\varepsilon$) defined by multiples of the standard deviation of the random error ($\sigma$) when the latter follows a normal distribution (adapted from Figliola and Beasley, 2010).

Several methodologies to quantify the performance of models and instruments in different areas have been developed. In the following sub-sections, a description of the methodologies commonly used to characterize the error of numerical wave models is presented.

**2.3.1 Statistical error parameters**

Common practice to characterize the error of numerical models is to compute a set of statistical error parameters that summarize the similarity (or difference) between measurements and model results. Statistical error parameters most commonly used to evaluate the performance of numerical wave models are the mean error ($ME$, Eq. 2.6), mean square error ($MSE$, Eq. 2.7), correlation coefficient ($CC$, Eq. 2.8), root mean square error ($RMSE$, eq 2.9), standard deviation of the total error ($SDe$, eq 2.10), mean absolute error ($MAE$, Eq. 2.11), coefficient of determination ($CoD$, Eq. 2.12), skill score based on the $RMSE$ ($SS_{RMSE}$, Eq. 2.13) and scatter index ($SI$, Eq. 2.14).

$$ME = \frac{1}{N}\sum_{i=1}^{N} y_i - x_i \qquad\qquad 2.6$$

$$MSE = \frac{1}{N}\sum_{i=1}^{N} (y_i - x_i)^2 \qquad\qquad 2.7$$

$$CC = \frac{\sum_{i=1}^{N}(x_i - \bar{x})(y_i - \bar{y})}{\sqrt{\sum_{i=1}^{N}(x_i - \bar{x})^2}\sqrt{\sum_{i=1}^{N}(y_i - \bar{y})^2}} \qquad\qquad 2.8$$

$$RMSE = \sqrt{\frac{1}{N}\sum_{i=1}^{N}(y_i - x_i)^2} \qquad\qquad 2.9$$

$$SDe = \frac{1}{N}\sum_{i=1}^{N}(y_i - x_i - ME)^2 \qquad\qquad 2.10$$

$$MAE = \frac{1}{N}\sum_{i=1}^{N}|y_i - x_i| \qquad\qquad 2.11$$

$$CoD = \frac{[\sum_{i=1}^{N}(x_i - \bar{x})(y_i - \bar{y})]^2}{\sum_{i=1}^{N}(x_i - \bar{x})^2 \sum_{i=1}^{N}(y_i - \bar{y})^2} \qquad\qquad 2.12$$

$$SS_{RMSE} = 1 - \sqrt{\frac{\sum_{i=1}^{N}(y_i - x_i)^2}{\sum_{i=1}^{N}(x_i - \bar{x})^2}} \qquad\qquad 2.13$$

$$SI = \sqrt{\frac{\sum_{i=1}^{N}\left((y_i - \bar{y}) - (x_i - \bar{x})\right)^2}{\sum_{i=1}^{N}(x_i)^2}} \qquad\qquad 2.14$$

Where $x_i$ and $y_i$ are the $i^{th}$ measured and modeled data values, respectively; while $\bar{x}$ and $\bar{y}$ are their respective average.

Sangalugeme et al. (2018) evaluated the performance of the WAVE WATCH III wave model over the South West Indian Ocean, forced by two different wind data set, GFS and ECMWF. They concluded that the model performs better when forced by ECMWF winds using the $ME$, $RMSE$, $SDe$ and $CC$ as metrics for the significant wave height ($H_{m0}$) and wavelength ($\lambda$) in three locations.

Beya et al. (2017) used a multi-criteria analysis summarized in a global performance score (GPS) to quantitatively evaluate the performance, calibrate and validate 35-years wave hindcast databases created using four different calibration criteria. The calibration criteria consisted on assigning more or less importance to different types of wave climate (e.g. mean waves, extreme wave), different calibration data type (e.g. oceanographic buoys or satellite measurements) and different wave parameters. Different settings and wind data source were tested, including ERA-Interim, NOAA CFSR and NOAA CFSv2. Based on the GPS, defined as a linear combination of five performance metrics of three wave parameters and several locations, they concluded that the best performance was achieved using the ERA-Interim winds. The performance metrics were normalized version of the $MAE$, $CoD$, $RMSE$, $SS_{RMSE}$ and $ME$, all weighing the same in the $GPS$. The wave parameters considered in the analysis were the $H_{m0}$, mean wave period ($T_{m01}$) and the mean wave direction ($D_m$). The weights associated to each of these wave parameters in the $GPS$ and for every calibration criteria is presented in Table 2-4.

Table 2-4 Relative weight factors for wave parameters and different criteria used in Beya et al. (2017).

| Parameter | Calibration criteria | | | |
| --- | --- | --- | --- | --- |
| | Global | Extreme waves | Mean waves | Global enhanced |
| $H_{m0}$ | 0.33 | 0.33 | 0.33 | 0.5 |
| $T_{m01}$ | 0.33 | 0.33 | 0.33 | 0.25 |
| $D_m$ | 0.33 | 0.33 | 0.33 | 0.25 |

Fonseca (2017) compared the performance of three very well-known third-generation spectral wave models: MIKE 21 SW, SWAN and STWAVE in shallow waters (coastal areas). Several target areas in the Portuguese coast were considered. The performance metrics used were the $ME$, $RMSE$, $SI$ and $CC$ calculated for $H_{m0}$, peak period ($T_p$) and $D_m$. Fonseca (2017) also compared the range of directions and the energy density at the peak of the spectrum at one specific

time and two locations. No final conclusion on which model performed the best was made as the different performance metrics were not all consistent.

Robertson et al. (2016) investigated the performance of the WCWI-v4 model when forced by a combination of wave (at the boundary condition) and wind data in a calibration process. Two 2D wave spectra data source were considered: from the NOAA's WW3 at five buoy locations and 3-hour interval, and from the European Centre for Medium Range Weather Forecasts (ECMWF) WAM model at eight locations and 6-hour interval. Also, two wind field data were examined: from the Global Forecast System (GFS) at 3-hour and 0.5° resolution, and from the Coupled Ocean / Atmosphere Mesoscale Prediction System (COAMPS) at 3-hour and 0.2° resolution. The calibration was performed by comparing the $ME$, $RMSE$ and $CC$ for $H_{m0}$ and $T_p$ at six locations.

Robertson et al. (2014) calibrated and then quantified the accuracy of the WCWI-v3 by comparing time series of measured and modeled $H_{m0}$ and $T_p$ wave parameters, and the by analyzing the $ME$, $SI$ and $CC$ of the same wave parameters at two locations. They also validated their results by comparing the measured and modeled frequency wave spectrum at the same two locations at two specific times. This later comparison revealed the inadequacy of modelling the wave boundary conditions by reconstructing the wave spectra from wave parameters using the parametric JONSWAP spectrum.

Kumar and Naseef (2015) evaluated the performance of the ERA-Interim wave data in the nearshore waters around India. They compute the same statistical parameters as in Fonseca (2017) ($ME$, $RMSE$, $SI$ and $CC$) for the $H_{m0}$ and wave energy period ($T_e$) at six shallow-water locations. Annual means, annual maximums and percentiles of $H_{m0}$ and $T_e$, and monthly average of the $ME$ and $CC$ for $H_{m0}$ were also analyzed.

Statistical error parameters condense a large amount of data into a single value, and most of them combining different types of errors (systematic and random), but emphasizing a certain aspect of them. With the exception of $SDe$, which is only useful to calculate uncertainty when the total error ($\varepsilon$) follows a normal distribution, none of these statistical error parameters (or a combination of them) give uncertainty information. Moreover, even when using a set of them, the use of statistical error parameters presents several limitations (Tian et Al. 2015):

- Interdependence: Most of these performance metrics are not independent. The relationship among these metrics indicate redundancy and leads to ambiguity in the interpretation of error characteristics.

- Underdetermination: Even when used collectively, these metrics do not describe unique error characteristics.

- Incompleteness: There are not well-accepted guidelines on which and how many of these parameters are sufficient.

## 2.3.2 Error characterization with an error model

Error characterization using an error model allows to differentiate the systematic and random errors and correct the model results, reducing the uncertainty of the corrected data. Error models assume a parametric relationship between 'true' or reference ($x_i$, e.g. measurements) and modeled ($y_i$) data, where the parameters are associated to the systematic or random error. A simple but widely used / assumed error model is the linear version presented in Eq. 2.15 (Tian et Al., 2015).

$$y_i = mx_i + \delta + \varepsilon r_i \qquad\qquad 2.15$$

Where $x_i$ and $y_i$ are the 'true' (or reference) and modeled data values, respectively. $m$ characterize a scale error ($m - 1$) and $\delta$ represents a constant deviation or displacement error, which together quantify the systematic error $\varepsilon s_i$ (error of the error model regarding to the perfect relationship between measured and modeled data $y_i = x_i$, see Eq. 2.16). $\varepsilon r_i$ is a stochastic variable assumed to follow a specific probability distribution function (PDF) and represent the random error. $\varepsilon r_i$ (see Eq. 2.17) is typically assumed to be independent and identically distributed, with zero mean value and a standard deviation $\sigma$. If Eq. 2.15 is the correct error model, $m$, $\delta$ and $\sigma$ capture all the error characteristics. The three parameters of the error model ($m$, $\delta$ and $\sigma$) can be estimated using a number of methods, including the least squares, the maximum likelihood or the Bayesian method. In addition, they can easily and intuitively be roughly estimated by observing a scatter plot (Tian et Al. 2015). Equations 2.18, 2.19 and 2.20 present the parameters $\lambda$, $\delta$ and $\sigma$ computed using the least squares method.

$$\varepsilon s_i = (m-1)x_i + \delta \qquad\qquad 2.16$$

$$\varepsilon r_i = y_i - mx_i - \delta \qquad\qquad 2.17$$

$$m = \frac{\sum_{i=1}^{N}(x_i + \bar{x})(y_i + \bar{y})}{\sum_{i=1}^{N}(x_i + \bar{x})^2} \qquad\qquad 2.18$$

$$\delta = \bar{y} - m\bar{x} \qquad\qquad 2.19$$

$$\sigma = \frac{1}{N}\sum_{i=1}^{N}\varepsilon r_i^2 \qquad\qquad 2.20$$

Conventional performance metrics (statistical error parameters) can be computed from $m$, $\delta$ and $\sigma$. Table 2-5 presents some of these relationships, showing that all but the $ME$ are metrics that combine both, systematics and random errors, leading to redundancy and ambiguity in the interpretation of error characteristics. The $ME$ reflects the combination of both inherent flaws in the linear error model (the scale error $m-1$, and the displacement error $\delta$), but even with no displacement error ($\delta = 0$), a scale error different than zero will be interpreted as a constant 'bias', which may lead to the development of poor 'bias' correction strategies (Tian et Al., 2015).

Table 2-5 Relationship of some statistical error parameters with the three error model parameters ($\lambda$, $\delta$ and $\sigma$) (Tian et Al., 2015).

| Parameter | Derivation from the three error model parameters |
|---|---|
| mean error ($ME$) | $(m-1)\bar{x} + \delta$ |
| Mean square error ($MSE$) | $[(m-1)\bar{x} + \delta]^2 + (m-1)^2\sigma_x^2 + \sigma^2$ |
| Linear correlation coefficient ($CC$) | $m\sqrt{\dfrac{\sigma_x^2}{m^2\sigma_x^2 + \sigma^2}}$ |
| Coefficient of determination ($CoD$) | $\dfrac{m^2\sigma_x^2}{m^2\sigma_x^2 + \sigma^2}$ |
| Skill score based on the MSE ($SS_{MSE}$) | $1 - \dfrac{[(m-1)\bar{x} + \delta]^2 + (m-1)^2\sigma_x^2 + \sigma^2}{\sigma_x^2}$ |

Although widely adopted, the linear error model (Eq. 2.15) is not always appropriate, but once the analytical form of the error model is given, the error information is fully captured by the error model parameters. Examples of the application of nonlinear error models are presented in

Tian et al. (2013) and Tang et al. (2015) (Tian et Al., 2015). They proved that a nonlinear, multiplicative error model (Eq. 2.21) is more appropriated to describe high-resolution precipitation (Tian et Al. 2015).

$$y_i = \alpha x_i{}^\beta \varepsilon r_i \qquad\qquad 2.21$$

Where $\alpha$ and $\beta$ together represent the systematic error, and $\varepsilon r_i$ the random error, which in these particular cases is no longer Gaussian but rather Lognormal.

Fewer works associated with the quantification of the performance, calibration and / or validation of wave models using error model parameters can be found in the literature. An example can be found in Van Vledder and Akpınar (2015) who evaluated the performance of SWAN on predicting both, normal and extreme wave conditions in the Black Sea for different wind data sets: NCEP CFSR, NASA MERRA, JRA-25, ECMWF Operational, ECMWF ERA40, and ECMWF ERA-Interim. They concluded that NCEP CFSR is the most suitable. The performance was quantified in terms of many statistical error parameters ($CC$, $RMSE$, $SI$, $ME$, systematic and unsystematic $RMSE$, and directional version of the $ME$ and $RMSE$) and error model parameters ($m$, $\delta$ and $m_{\delta=0}$) for three wave parameters, $H_{m0}$, mean wave period ($T_{m02}$) and $D_m$. In spite of the many performance metrics, they did not summarize them in a global performance metric as in Beya et al. (2017), making it difficult to evaluate and rank the calibration tests based on the different performance metrics used.

Modeled data can easily be corrected using $m$ and $\delta$ to eliminate the systematic error. However, this corrections are only valid at the locations where $m$ and $\delta$ were computed (where measurements are available), so in general, wave model results cannot be corrected, and both types of errors have to be considered. In addition, the method assumes that the random error follows a normal distribution. When the latter is not satisfied, $\sigma$ cannot be used as an estimator of the uncertainty. Therefore, uncertainty of the total error is a better error metric that needs to be estimated using a different method.

### 2.3.3 Non-parametric statistics

To overcome the limitations regarding to the use of statistical error parameters and error models in characterizing the error and estimating uncertainty, non-parametric methods can be

used. Non-parametric methods make no assumptions about the shape of the underlying probability distribution of the variables being assessed. Error metrics are based on the calculation of the empirical PDF (or cumulative distribution function CDF). From the empirical PDF / CDF, uncertainty at any confidence level ($u_p$) can be obtained directly.

To the authors knowledge, non-parametric statistics have not been applied to the estimation of uncertainty of spectral wave models.

### 2.3.4 Other methods

Many other enhanced techniques and metrics have been proposed, including decomposition schemes of the conventional metrics and object-oriented metrics. However, they are not discussed in this work due to their relatively more complex statistical analysis, their absence from specialized literature associated to the evaluation of wave models (to this author best knowledge), and that it is doubtful that they will replace linear performance metrics (Tian et Al. 2015).

# Chapter 3 Source of data

As can be inferred from section 2.1, numerical wave models require a set of input data that allow them to compute the wave field over the discretized model domain (space and time). These input data are associated to the wave generation, propagation and transformation forces, and the boundary conditions which characterize the sea state along the offshore frontier that then are propagated inside the model domain. In addition to the input data, a model mesh that discretizes the model domain needs to be provided. As well as the governing equations and the numerical techniques to solve these equations, the quality of both, the input data and the model mesh are essential for obtaining accurate results.

The information presented in this chapter was utilized to build, calibrate, run and validate the wave models WCWI-v5 and WCWI-v6. Topo-bathymetric data, tides, coastlines, and location of cities, towns and communities in B.C. were used to generate the wave models mesh (WMMesh) and its digital elevation model (DEM). Offshore directional wave spectra, wind fields and tidal currents are the ambient forcings utilized to run the simulations, while wave measurements were necessary to calibrate and validate the models. All this information is presented and detailed in the following sections.

## 3.1 Topo-bathymetry

The shape of the sea floor (bathymetry or water depths) induces important transformations on waves while propagating (see sub-section 1.4.2) over intermediate and shallow waters ($d \leq \lambda/2$). Water depth information is needed to be incorporated to the model at every node of the model mesh, usually through an interpolation method from a DEM. Topographic information is not strictly necessary but it is useful for interpolation purposes, as bathymetry is not usually available at the surf zone. Topo-bathymetry is also the main information needed to build a more optimal model grid (see section 4.2).

To obtain topo-bathymetric information to cover the whole model domain (see section 4.1), a large amount of data was collected from six different sources. This information was used to build the DEM needed to interpolate water depths into the nodes of the models mesh. Figure 3-1 shows a summary of the data extension and resolution, while Table 3-6 summarizes the different

coordinate systems used by each source. A detailed description of each source and the creation of the DEM are presented in the following sub-sections.
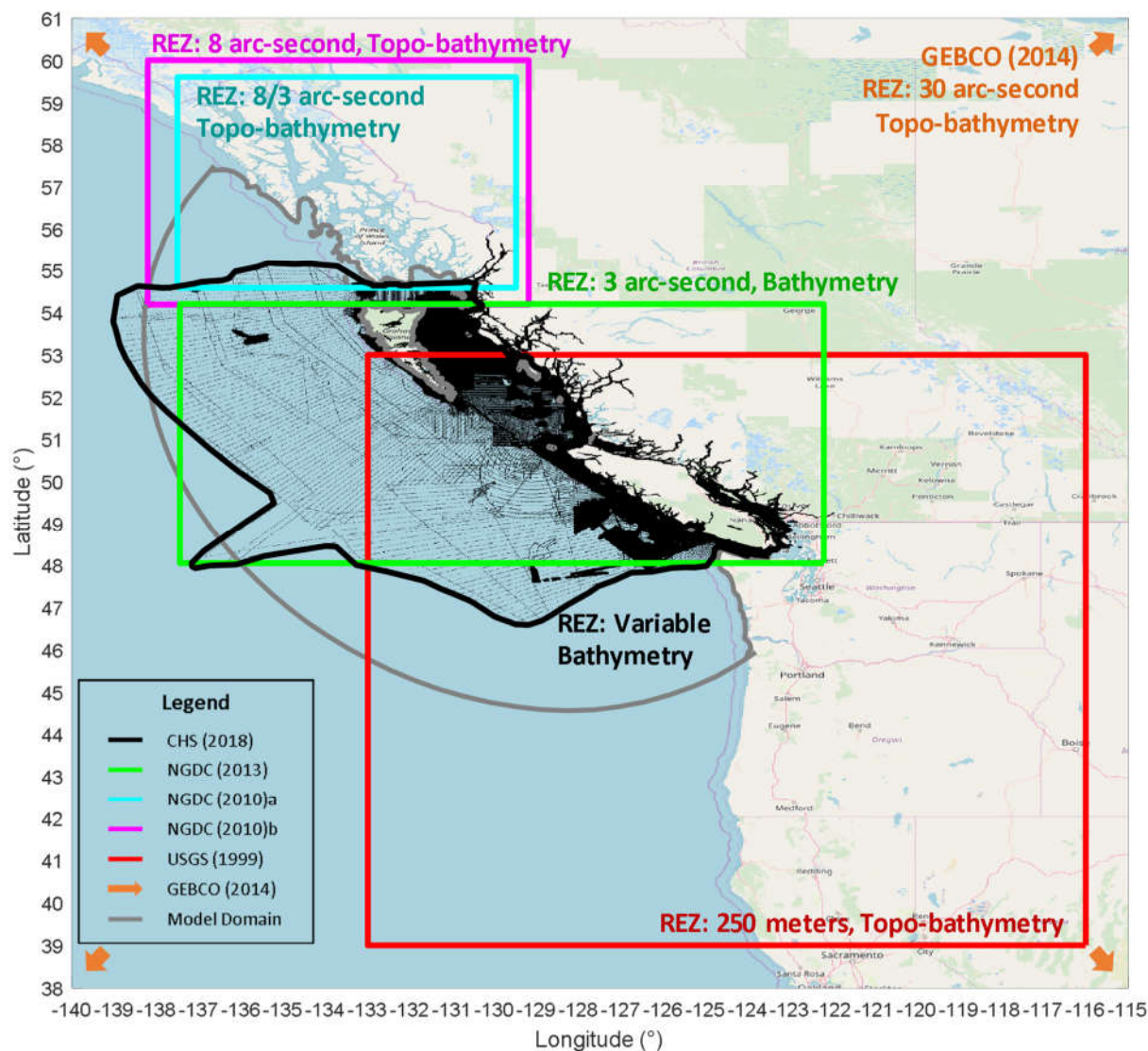


Figure 3-1 Topo-bathymetry data source: Area and resolution.

Table 3-6 Summary of the topo-bathymetry data specifications.

| Source | Type | Coverage | | Resolution | Coordinate system | | |
| | | Latitude | Longitude | | Horizontal coordinates | Datum | |
| | | | | | | Horizontal | Vertical |
|---|---|---|---|---|---|---|---|
| CHS (2018) | Bathymetry | As presented in Figure 3-1 | | >= 50 m | Geographic | WGS84 | CD (LLWLT) |
| NGDC (2013) | Bathymetry | 48.50N - 54.20N | 122.20W - 137.45W | 3 arc-sec | Geographic | WGS84 | MHHW |
| NGDC (2010 a) | Topo-bathymetry | 54.59N – 59.61N | 129.49W – 137.51W | 8/3 arc-sec | Geographic | WGS84 | MHHW |
| NGDC (2010 b) | Topo-bathymetry | 54.19N – 60.01N | 129.19W – 138.21W | 8 arc-sec | Geographic | WGS84 | MHHW |
| USGS (1999) | Topo-bathymetry | 39.00N - 53.00N | 116.00W - 133.00W | 250 m | Lambert Conformal Conic | NAD27 | MLLW*, MSL** |
| GEBCO (2014) | Topo-bathymetry | Global | | 30 arc-sec | Geographic | WGS84 | MSL |

**Canadian Hydrographic Service**

The Canadian Hydrographic Service (CHS)[4] collects, processes and compiles bathymetric information to develop navigational charts. The CHS is a division of the Science Branch of the Department of Fisheries and Oceans Canada (DFO), with access to Canadian Coast Guard ships to take hydrographic and oceanographic measurements. In October 2018, CHS kindly prepared a bathymetric dataset especially for this work. This data set, CHS (2018), is presented in geographic coordinates with WGS84 horizontal datum and Chart Datum (CD) for the vertical datum. The information used to generate this dataset comes from multiple single and multi-beam bathymetric surveys carried out in different years. To be able to handle this information, the highest resolution of the data was truncated to 50x50 meters (where multi-beam surveys are available). It is important to mention that on most Canadian charts, the Lower Low Water Large Tide (LLWLT) has been adopted as Chart Datum, while a variety of other choices have been made on some older charts (DFO, 2018).

**General Bathymetric Chart of the Oceans**

General Bathymetric Chart of the Oceans (GEBCO)[5] is a global gridded topo-bathymetry data with a resolution of 30 arc-second. GEBCO is a non-profit organization and operates under the auspices of the International Hydrographic Organization (IHO) and the Intergovernmental Oceanographic Commission (IOC) of UNESCO. Its main objective is to provide the most authoritative publicly-available bathymetry of the world's oceans, and its latest release was published in 2014. The DEM, GEBCO (2014), was generated by combining quality-controlled depth soundings from ships and sounding points guided by satellite-derived gravity data. It is developed using geographical coordinate system with the WGS84 horizontal datum and the Mean Sea Level (MSL) as vertical datum. In some shallow water areas, the grid include data from sources having a vertical datum other than MSL.

---

[4] http://www.charts.gc.ca/

[5] https://www.gebco.net/

**National Geophysical Data Center, U.S.**

Three DEMs generated by the U.S. National Oceanic and Atmospheric Administration (NOAA)'s National Geophysical Data center (NGDC) were collected. The first DEM, NGDC (2013)[6], was generated for NOAA's West Coast and Alaska Tsunami Warning Center (WC/ATWC) and the Pacific Marine Environmental Laboratory (PMEL) to be used to support the improvement of the coastal tsunami inundation forecasts. It has a 3 arc-second resolution and covers the latitudes 48.50N to 54.20N, and longitudes 122.20W to 137.45W. The DEM was generated in the year 2013 in geographical coordinate system using the WGS84 horizontal datum and the Mean Higher High Water (MHHW) as vertical datum. The DEM include data from NOAA's agencies, CHS, NGDC, U.S. Geological Survey (USGS), the British Columbia Marine Conservation Analysis and the National Geospatial-Intelligence Agency (NGA). It does not contain topographic data. A Detailed documentation on the creation of this DEM can be found in NGDC (2013).

The two other DEMS, NGDC (2010)(a & b), were generated in the year 2010 for the National Tsunami Hazard Mitigation Program (NTHMP) in support of the State of Alaska's tsunami inundation modeling efforts led by the Geophysical Institute at the University of Alaska at Fairbanks (UAF). NGDC (2010a) [7] has a 8/3 arc-second resolution and covers the latitudes 54.59N to 59.61N, and longitudes 129.49W to 137.51W. NGDC (2010b)[8] has 8 arc-second resolution and covers the latitudes 54.19N to 60.01N, and longitudes 129.19W to 138.21W. The DEMs were developed in geographical coordinate system using the WGS84 horizontal datum and the Mean Higher High Water (MHHW) as vertical datum. The DEM include data from NOAA's agencies (NGDC and OCS), CHS, U.S. Army Corps of Engineers (USACE), City of Juneau, National Aeronautics and Space Administration (NASA). Detailed documentation on the creation of these two DEMs can be found in NGDC (2010).

---

[6] https://www.ncei.noaa.gov/metadata/geoportal/rest/metadata/item/gov.noaa.ngdc.mgg.dem:4956/html

[7] https://www.ncei.noaa.gov/metadata/geoportal/rest/metadata/item/gov.noaa.ngdc.mgg.dem:715/html

[8] https://www.ncei.noaa.gov/metadata/geoportal/rest/metadata/item/gov.noaa.ngdc.mgg.dem:575/html

**U.S. Coast and Geodetic Survey**

The U.S. Coast and Geodetic Survey (USGS) generated in the year 1999 a DEM, USGS (1999)[9], with a 250 m resolution of the Cascadia bioregion (latitude 39N - 53N, longitude 116W - 133W). The DEM contains rounded elevations to the nearest integer and was developed with the Lambert conformal conic projection and the NAD27 horizontal datum (Clarke 1866 ellipsoid). Marine depths are relative to the Mean Lower Low Water (MLLW), whereas terrestrial elevations are relative to datums which are approximately equivalent to the Mean Sea Level (MSL). The usage of these two vertical datums can lead to differences up to about 2 meters. The DEM include data from the NGDC, PMEL, U.S. Defense Mapping Agency (DMA), Oregon State University (Chris Goldfinger, personal communication), U.S. Coast and Geodetic Survey (USCGS), USGS (Myrtle Jones, personal communication), Geological Survey of Canada (Dave Seeman and Tark Hamilton, personal communication), CHS and ETOPO5 (NGDC). Detailed documentation on the creation of this DEM can be found in USGS (1999).

### 3.1.2 Digital elevation model

Using the topo-bathymetric data described above, a DEM (WMDEM) for the wave models (WCWI-v5 and WCWI-v6) was created by combining the topo-bathymetric information from the different sources. The combination was performed as follows.

First, the coordinates were transformed (when necessary) to a common coordinate system. The choice for the common horizontal and vertical coordinate system was the Geographic WGS84 and Chart Datum (CD), as they were used to generate the main bathymetric dataset of this work: CHS (2018). The horizontal transformation was performed using the software CARIS[10], developed by Teledyne CARIS[TM]. For the vertical transformation, NGDC (2013) and NGDC (2010) (a & b) were shifted down by an estimation of MHHW, GEBCO (2014) by an estimation of MSL and USGS (1999) by an estimation of MLLW. The estimation of this three vertical datums (MHHW, MSL and MLLW) is presented in section 3.2. It is important to mention that this process was aimed to reduce the errors when combining the different source data, not to eliminate them. The values

---

[9] https://pubs.er.usgs.gov/publication/ofr99369

[10] https://www.teledynecaris.com/en/home/

obtained here are only estimations of the original vertical datums used at each DEM, which also varies from sector to sector within the DEMs.

Second, data was merged keeping only data from sources with higher priority rank and filling any gaps with the information from the lower ranks needed. Due to the nature of the information, date of development and resolution, the topographic and bathymetric data was prioritized as presented in Table 3-7.

Table 3-7 Bathymetry and topography priorization.

| Priority ranking | Bathymetry | Topography |
|:---:|:---:|:---:|
| | Source | Source |
| 1 | CHS (2018) | NGDC (2010)a |
| 2 | NGDC (2013) | NGDC (2010)b |
| 3 | NGDC (2010)a | GEBCO (2014) |
| 4 | NGDC (2010)b | USGS (1999) |
| 5 | USGS (1999) | N/A |
| 6 | GEBCO (2014) | N/A |

Thirdly, a quality control of the merging process was performed to ensure that no unnatural discontinuities were present, especially at the merging boundaries. This process was carried out by examining visually contour maps and vertical profiles.

Although the processes of producing WMDEM can have flaws, especially related to the combination of information with different vertical datums within and among the data sources, it can be said that WMDEM is sufficiently accurate and fine for the following reasons.

A huge amount of topo-bathymetric information was gathered, processed and combined. The information has a variety but relatively high resolutions, and for the area of interest (B.C. coast near shore area) the information comes directly from field surveys (CHS, 2018).

Differences in elevation among the DEMs were reduced by transforming the information to the CD vertical datum. The CD is the LLWLT for every navigational chart zone and the difference among LLWLTs depends on the tidal range of the zones that are compared. The variations in

LLWLTs tends to zero as the tidal ranges are similar, which is the case of areas exposed to swell waves.

In Deeper waters, not only the relative deviation in elevation due to the use of different vertical datums is negligible, but also the bathymetry in these areas do not induce wave transformations.

Outside the area of interest, the influence of bathymetric differences is only important in shallower waters, where the principal wave systems travel toward shore, so its effect on the wave propagation to the area of interest is negligible.

The final DEM (WMDEM) used to build the mesh for the SWAN models is presented in Figure 3-2.
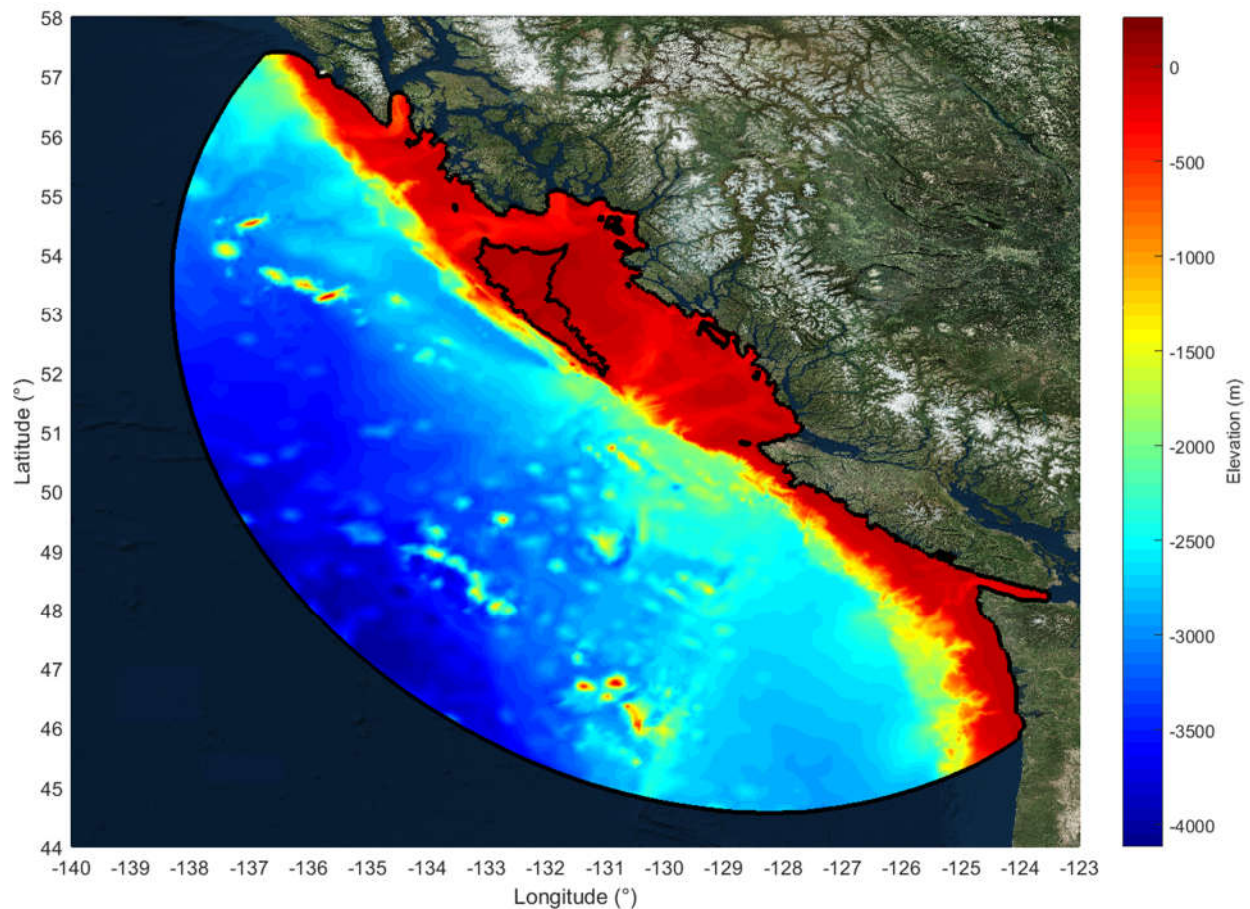


Figure 3-2 DEM used to build the mesh of the SWAN models (WMDEM).

## 3.2 Tides

Tidal elevation information was collected to estimate a value for the vertical datums: MHHW, MSL and MLLW, and to transform the elevations on the separate source DEMs to a common reference, the CD. To properly transform the elevations to the CD (LLWLT) reference, tidal data used to generate the topo-bathymetric information is required. This tidal data is not accessible or of easy access, and is of difficult interpretation because different zones and bathymetric surveys used within a DEM can have different tidal information. As mentioned in section 3.1, an exact correction is not possible neither necessary for the aim this work. Thus, the estimation of MHHW, MSL and MLLW to reduce undesired differences in the elevations when combining the topo-bathymetric information from the different sources, was not performed rigorously.

The tidal data was obtained from the Canadian Station Inventory and Data Download[11] of the FOC for six stations along the B.C. coast (see Figure 3-3) at 1-hour interval, selected because the following reasons:

- Their little influence from tide transformations due to geographic feature like channels and fjords.

- Location, so the information cover most of the area of interest.

- When possible: relatively recent (last 10 years) and long term (10 years) measurements.

Figure 3-4 present the time series of the water surface elevations and the estimate of the tidal datums (referenced to CD) at every stations and their average (values used for transforming to the common vertical reference), while Table 3-8 present also their location and data extension. The computation of this three values (MHHW, MSL and MLLW) was performed following the tidal datums definition[12] by the NOAA, with the exception of the time extension required (only the data collected and presented here was used). These definitions are presented below:

---

[11] http://www.meds-sdmm.dfo-mpo.gc.ca/isdm-gdsi/twl-mne/inventory-inventaire/list-liste-eng.asp?user=isdm-gdsi&region=PAC&tst=1

[12] https://tidesandcurrents.noaa.gov/datum_options.html

- MHHW: The average of the higher high water height of each tidal day observed over the National Tidal Datum Epoch.

- MSL: The arithmetic mean of hourly heights observed over the National Tidal Datum Epoch.

- MLLW: The average of the lower low water height of each tidal day observed over the National Tidal Datum Epoch.
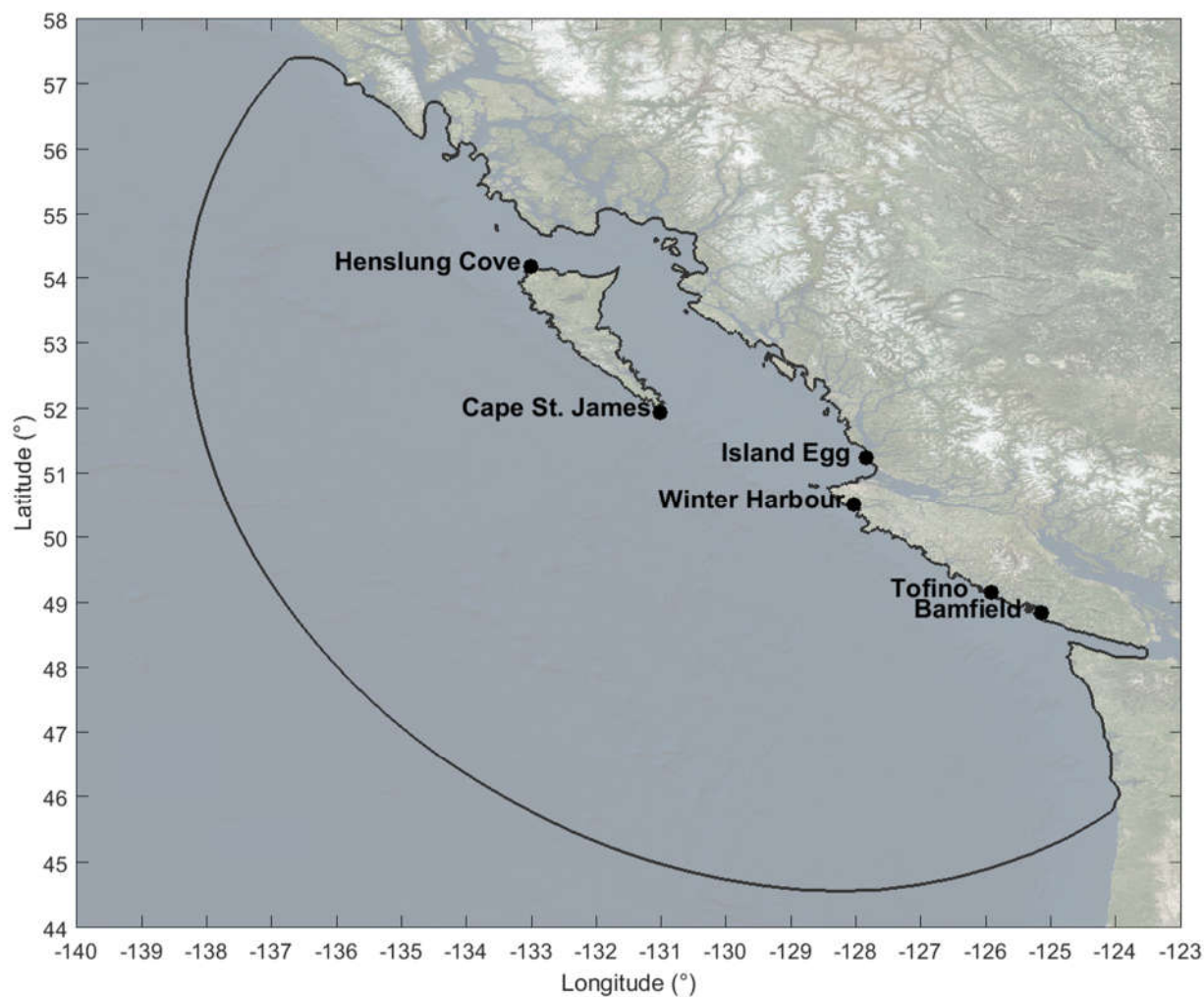


Figure 3-3 Location of the Tidal stations used.
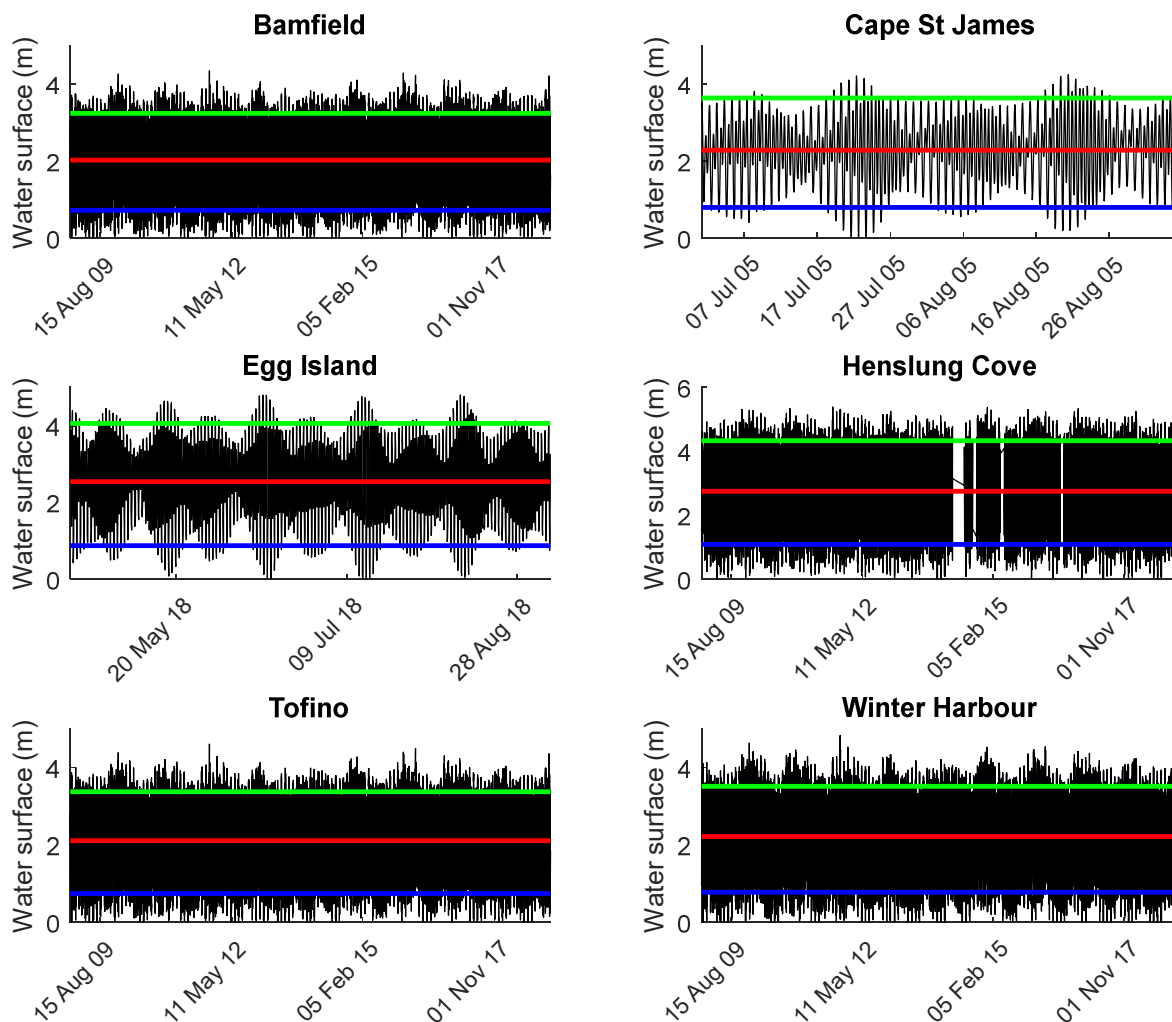
Figure 3-4 Time series of the water surface elevation (black) and datums estimates (MHHW in green, MSL in red and MLLW in blue) at every tidal station.

Table 3-8 Tidal stations data and vertical datum estimates.

| Station | Coordinates (Geographic, WGS84) | | Data extension (used) | | Datum referenced to CD (m) | | |
|---|---|---|---|---|---|---|---|
| | Latitude (°) | Longitude (°) | Start date | End date | MHHW | MSL | MLLW |
| Bamfield | 48.8361 | -125.1358 | 1/1/2009 | 1/1/2019 | 3.24 | 2.03 | 0.71 |
| Cape St. James | 51.9380 | -131.0150 | 1/7/2005 | 4/9/2005 | 3.64 | 2.28 | 0.79 |
| Henslung Cove | 54.1897 | -133.0053 | 1/1/2009 | 1/1/2019 | 4.32 | 2.75 | 1.08 |
| Island Egg | 51.2490 | -127.8360 | 18/4/2018 | 6/9/2018 | 4.05 | 2.54 | 0.87 |
| Tofino | 49.1536 | -125.9125 | 1/1/2009 | 1/1/2019 | 3.37 | 2.10 | 0.75 |
| Winter Harbour | 50.5131 | -128.0289 | 1/1/2009 | 1/1/2019 | 3.51 | 2.21 | 0.78 |
| **Average** | **-** | **-** | | | **3.69** | **2.32** | **0.83** |

## 3.3 Coastline

The coastline of the west coast of Canada and the United States was used to delimit the model domain on the shore side and define islands (see section 4.1). The objective of delimiting the model domain and the definition of island is to reduce the number of elements and nodes, and therefore to reduce the runtimes. The definition of the coastline could have been done simply by interpolating WMDEM at certain elevation (topographic contour), but topo-bathymetry in coastal areas near the shore is unreliable. Bathymetry in the surf zone is usually interpolated and sandy beaches are highly affected by natural morphodynamic processes induced by waves, currents and wind. Defining the inshore boundary of the model domain following the coastline of a satellite image is a common practice and is only relevant to present nicer figures of the model domain, mesh and results. The accuracy of the model results should not be determined by the inshore limit, but by the quality of the topo-bathymetric information, offshore boundary conditions, forcings (winds, currents, etc.), discretization of the model domain (space and time), governing equations, and the numerical schemes used to solve the governing equations.

To simplify the process of defining the inshore limits of the model, three different coastlines (OMS, GSHHG and NGD) were gathered, analyzed and compared visually to a satellite image. Figure 3-5 presents an example-area showing the accuracy of these three different shorelines in following the coastline of the satellite image. The comparison was performed over the entire area of interest (B.C. coast). OSM (2018) was chosen to be the base line to delimit the in-land model domain, as it best follows the coastline of the satellite images. However, it was corrected in some areas with disagreement with the satellite images, and smoothed in some others for modelling purpose (see section 4.1). The satellite image was obtained from the World Imagery[13], which provides satellite and aerial imagery worldwide with a resolution of up to one-meter. A detailed description of the three coastlines is presented below.

---

[13] https://esri.ca/en/products/imagery
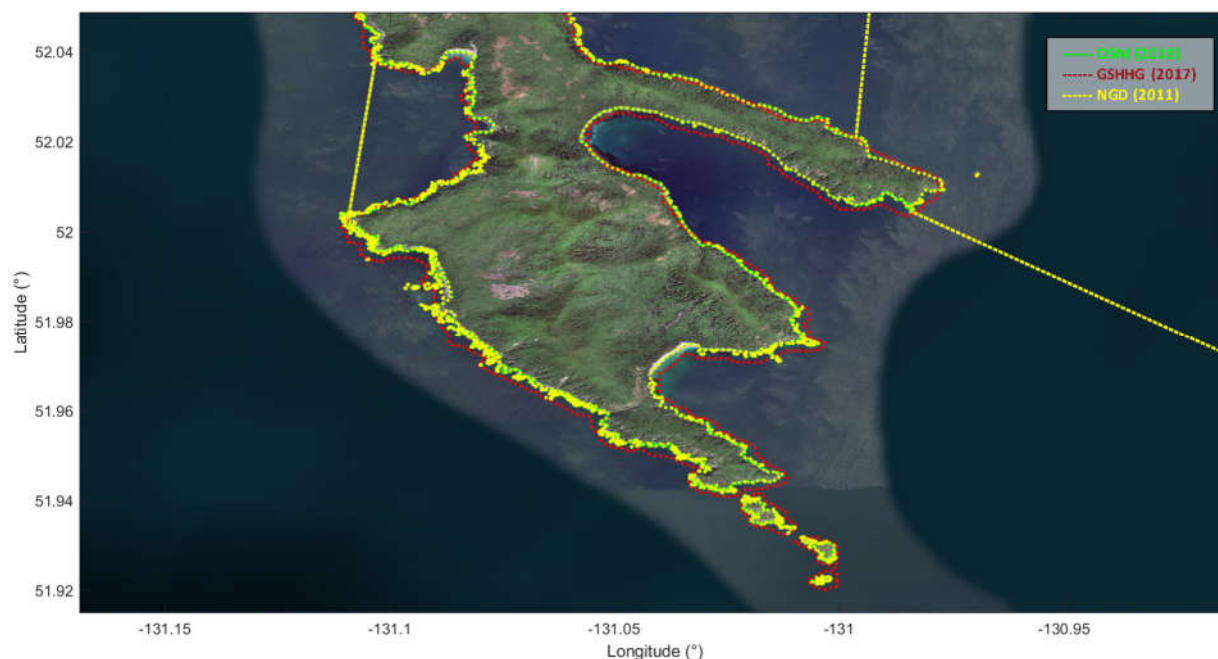
Figure 3-5 Comparison example of the different shoreline data.

**OpenStreetMap**

OpenStreetMap (OSM) [14] collects large amount of geodata, process it and makes it publicly and freely available (licensed on terms of the Open Database License, 'ODbL' 1.0). The service was created by Jochen Topf and Christoph Hormann for the OpenStreetMap community and the general public. The coastline information was downloaded in July (2018).

**Global Self-consistent, Hierarchical, High-resolution Geography**

The Global Self-consistent, Hierarchical, High-resolution Geography (GSHHG) [15] Database was developed and maintained by Paul Wessel, SOEST, University of Hawaii, and Walter H. F. Smith, NOAA Geosciences Lab, National Ocean Service. The shoreline was downloaded from GSHHG Version 2.3.7, and was released in June 15, 2017 under the Lesser GNU Public License.

---

[14] http://openstreetmapdata.com/

[15] http://www.soest.hawaii.edu/wessel/gshhg/

**Canadian National Geographic Database**

The Canadian National Geographic Database (NGD)[16] is a joint Statistics Canada and Elections Canada initiative to develop and maintain a spatial database which serves the needs of both organizations. The focus of the NGD is the continual improvement of quality and currency of spatial coverage using updates from provinces, territories and local sources. The Coastline from the 2011 Census Boundary Files depict boundaries of standard geographic areas established for the purpose of disseminating census data.

## 3.4 Cities, towns and communities

As discussed in Chapter 1, wave energy projects are most likely to be located near-shore, close to energy demand centers such as populated areas and industries. To evaluate wave energy projects viability, long-term, high resolution (in space and time), detailed and accurate wave resource characterization is crucial. To increase the space resolution, and with it also the accuracy of the wave models in areas likely to be of the interest of the wave energy industry, a meshing rule that uses the location of cities, towns and communities along the B.C. coast was implemented (see section 4.2).

The location of cities, towns and communities along the B.C. coast was obtained from 2 different sources (GND and RCED). Figure 3-6 presents graphically the populated sites from these two sources in the area of interest. A description of each source is presented below. Populated sites in the US were not included, as they are not in the area of interest.

---

[16] https://www12.statcan.gc.ca/census-recensement/2011/geo/bound-limit/bound-limit-2016-eng.cfm
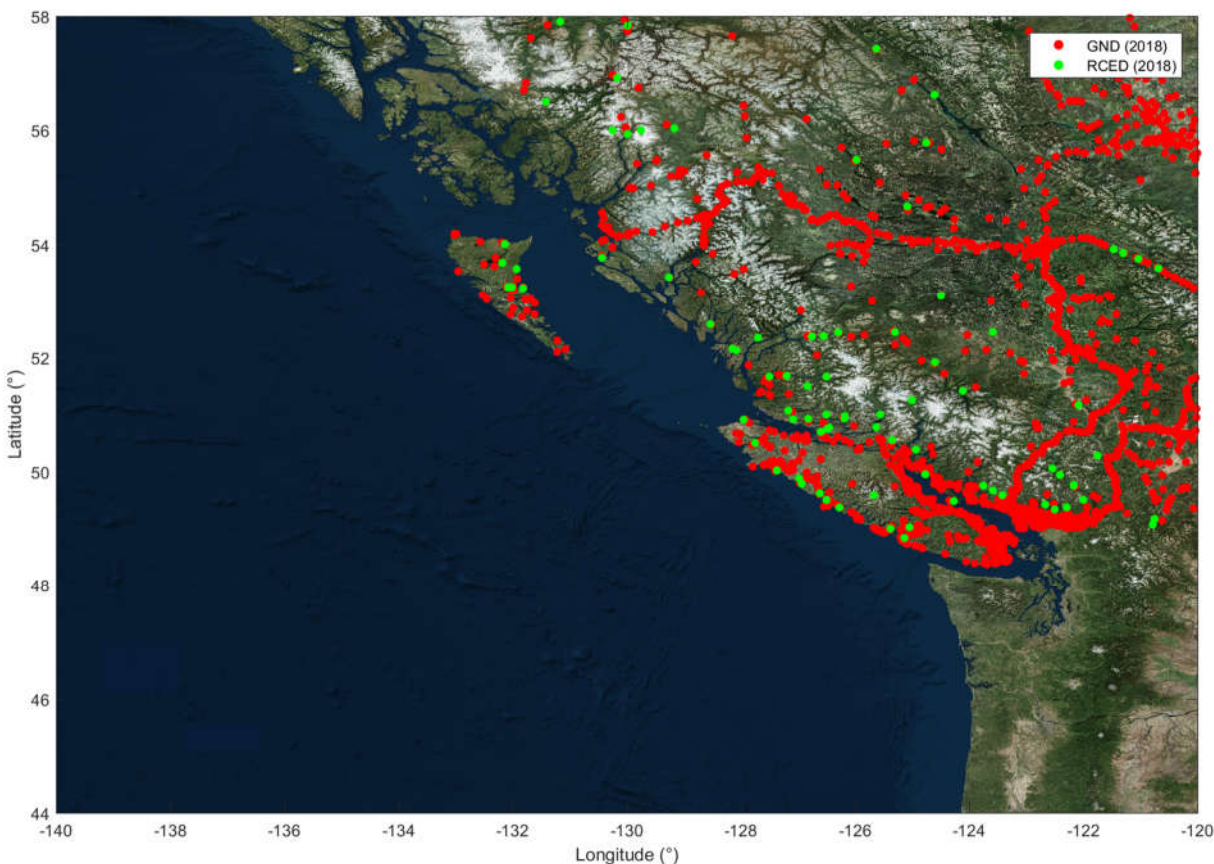
Figure 3-6 Cities, towns and communities in the area of interest.

**Geographical Names Data**

Geographical Names Data (GND) [17] are files that contain georeferenced names recognized by the Geographical Names Board of Canada. The dataset includes the names of populated places and administrative areas, water features such as lakes, rivers and bays, and terrain features like mountains, capes and valleys. The data is provided by provincial, territorial and federal naming authorities, and managed by the Geographical Names Board of Canada Secretariat at Natural Resources Canada. The file containing this information was downloaded from the Natural Resources Canada web page (www.nrcan.gc.ca/) in October 2018.

---

[17] https://www.nrcan.gc.ca/earth-sciences/geography/download-geographical-names-data/9245

**Remote Communities Energy Database**

Remote Communities Energy Database (RCED)[18] is the most recent dataset of remote communities, i.e. communities that are not currently connected to the North-American electrical grid nor to the piped natural gas network; and are a permanent or long-term (5 years or more) settlement with at least 10 dwellings. This dataset was downloaded from the Natural Resources Canada web page (www.nrcan.gc.ca) in October 2018.

## 3.5 Waves

The most complete representation of a sea state is through directional wave spectrum (2D spectrum) (Caires, S. et al., 2005), and is this type of information that is recommended to be used as offshore wave boundary condition in wave energy assessment studies (IEC, 2015). 2D spectra could be obtained from specialized measuring instruments (e.g. oceanographic buoys, Acoustic Doppler Current Profiler), or numerical simulation (hopefully calibrated and validated). Generally, measured wave data is considered more precise and numerical models use this information to calibrate / validate their results.

For regional to local simulations, wave information is usually needed along the open boundary of the model domain. Generally, and as is the case for this work, measured wave data is not available along the open boundary, has temporal gaps, do not cover the whole period of simulation and / or is not directional spectra, so wave information from other (global to regional) numerical simulations must be used.

Directional wave spectra from a global hindcast simulation (ECMWF) was considered as the information to be implemented as boundary condition, while three different wave measurement sources (DFO, NDBC and WCWI) were used to calibrate / validate the models. Figure 3-7 and Figure 3-8 show the locations of the wave information for these four data sources, while Figure 3-9 present graphically the extension and gaps of the wave information. Table 3-9 and Table 3-10 present a summary of the wave data used as boundary conditions, and used to calibrate / validate the model, respectively.

---

[18] https://atlas.gc.ca/rced-bdece/en/index.html

The following sub sections describe in detail the wave information gathered for this work.
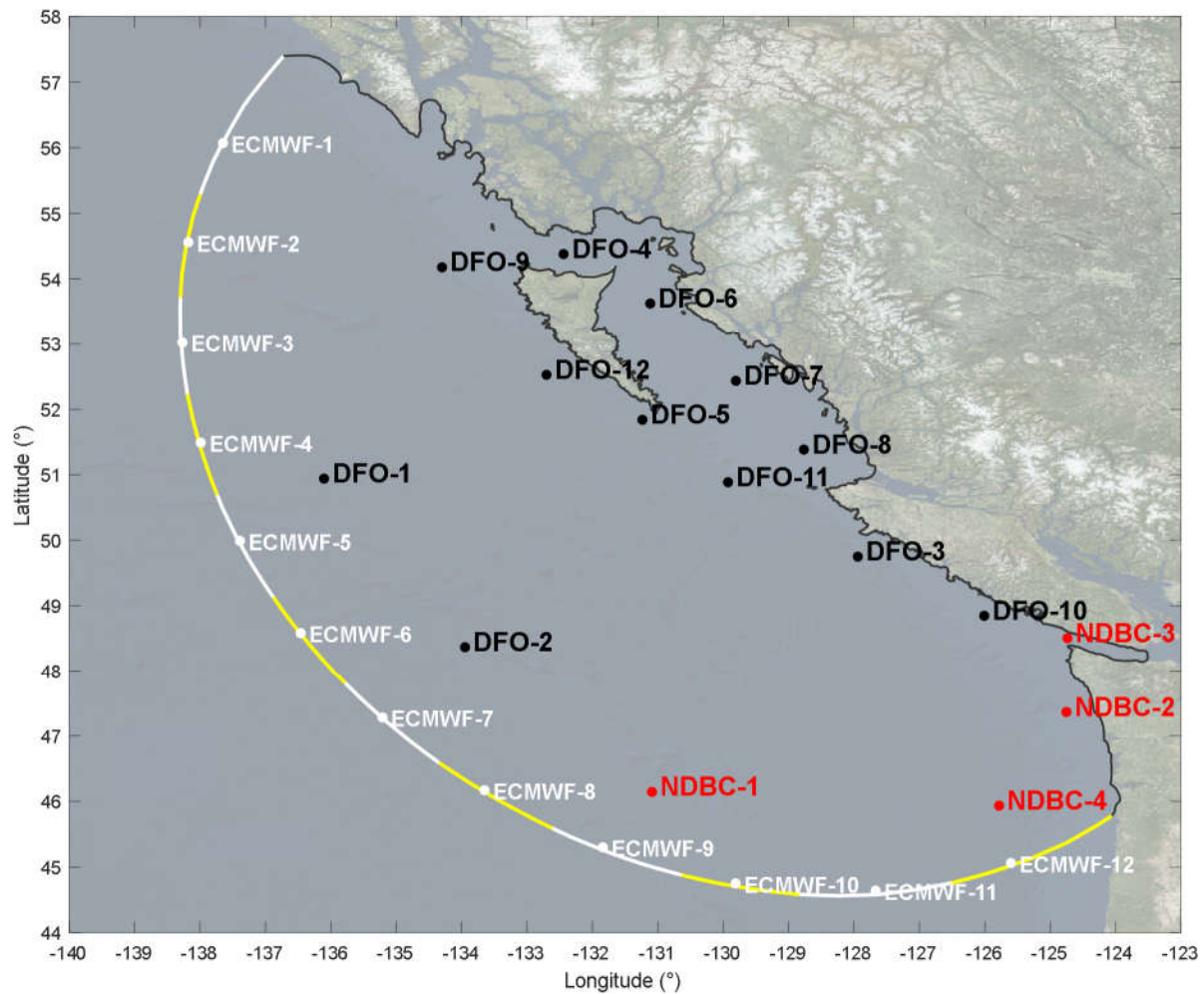


Figure 3-7 Location of the wave information for three data sources (ECMWF, FOC and NDBC, see sub-section 3.5.1 and 3.5.2 for the description).
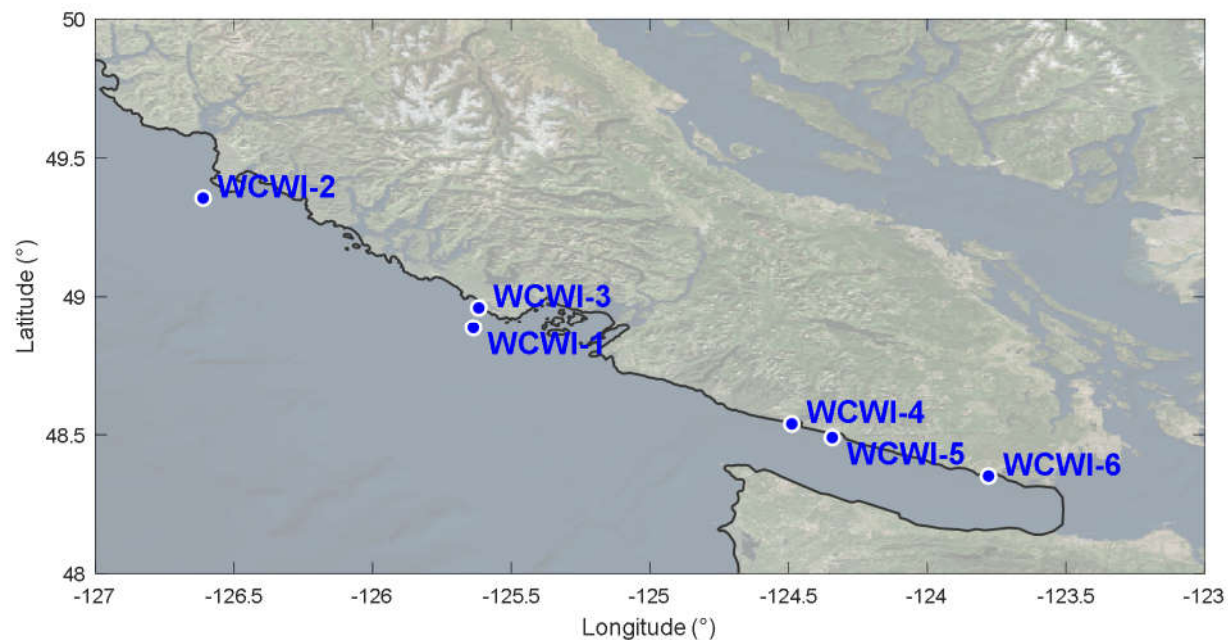
Figure 3-8 Location of the wave information from WCWI data sources (see sub-section 3.5.2 for the description).
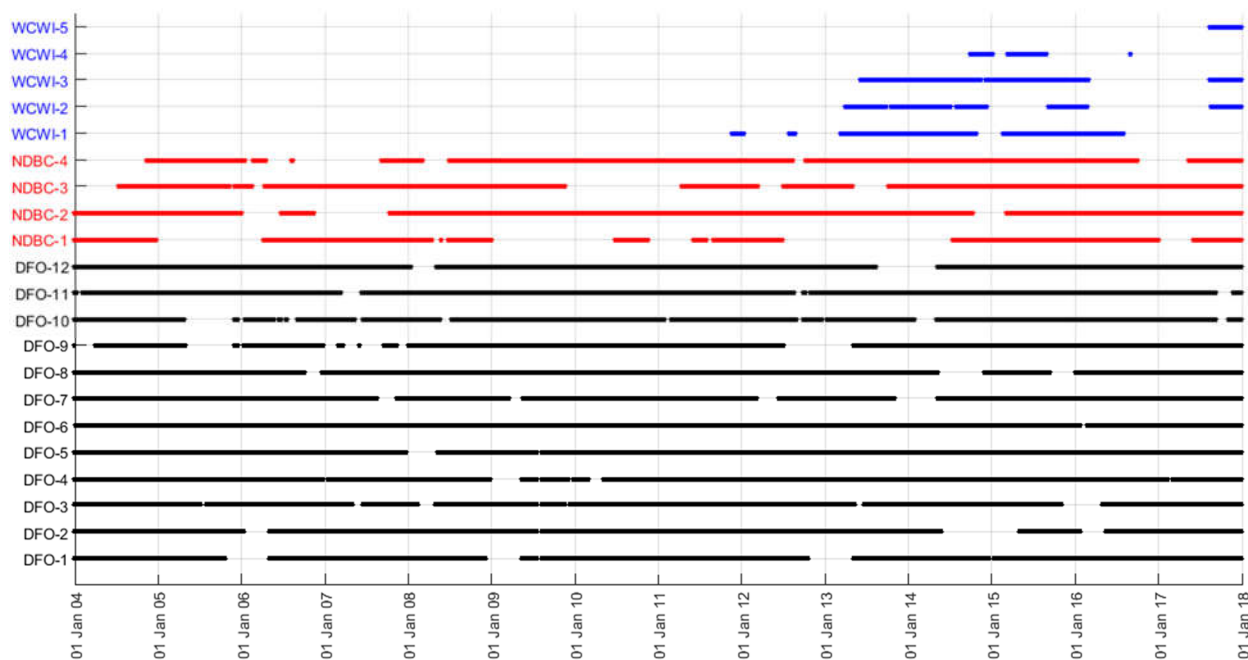


Figure 3-9 Wave data extension and gaps of information (gathered for this work).

Table 3-9 Summary of the boundary condition wave data (ECMWF).

| Buoy Name | Coordinates | | Data | Data extension (used) | | Resolution |
| --- | --- | --- | --- | --- | --- | --- |
| | Lon. (°) | Lat. (°) | | Start date | End date | |
| ECMWF-1 | -137.640 | 56.060 | 2D spec. | 1/01/2004 | 1/01/2018 | 1 hr |
| ECMWF-2 | -138.170 | 54.550 | 2D spec. | 1/01/2004 | 1/01/2018 | 1 hr |
| ECMWF-3 | -138.260 | 53.010 | 2D spec. | 1/01/2004 | 1/01/2018 | 1 hr |
| ECMWF-4 | -137.980 | 51.480 | 2D spec. | 1/01/2004 | 1/01/2018 | 1 hr |
| ECMWF-5 | -137.380 | 49.980 | 2D spec. | 1/01/2004 | 1/01/2018 | 1 hr |
| ECMWF-6 | -136.450 | 48.570 | 2D spec. | 1/01/2004 | 1/01/2018 | 1 hr |
| ECMWF-7 | -135.200 | 47.270 | 2D spec. | 1/01/2004 | 1/01/2018 | 1 hr |
| ECMWF-8 | -133.640 | 46.160 | 2D spec. | 1/01/2004 | 1/01/2018 | 1 hr |
| ECMWF-9 | -131.830 | 45.290 | 2D spec. | 1/01/2004 | 1/01/2018 | 1 hr |
| ECMWF-10 | -129.800 | 44.740 | 2D spec. | 1/01/2004 | 1/01/2018 | 1 hr |
| ECMWF-11 | -127.660 | 44.630 | 2D spec. | 1/01/2004 | 1/01/2018 | 1 hr |
| ECMWF-12 | -125.590 | 45.050 | 2D spec. | 1/01/2004 | 1/01/2018 | 1 hr |

Table 3-10 Summary of the measured (buoy) wave data.

| Buoy Name | Institution's given name | Coordinates | | Data | Data extension (used) | | Resolution |
|---|---|---|---|---|---|---|---|
| | | Lon. (°) | Lat. (°) | | Start date | End date | |
| DFO-1 | Middle Nomad | -136.095 | 50.930 | Params. + 1D spec. | 1/01/2004 | 1/01/2018 | 1 hr |
| DFO-2 | South Nomad | -133.938 | 48.355 | Params. + 1D spec. | 1/01/2004 | 1/01/2018 | 1 hr |
| DFO-3 | South Brooks | -127.932 | 49.738 | Params. + 1D spec. | 1/01/2004 | 1/01/2018 | 1 hr |
| DFO-4 | Central Dixon Entrance | -132.431 | 54.371 | Params. + 1D spec. | 1/01/2004 | 1/01/2018 | 1 hr |
| DFO-5 | South Moresby | -131.225 | 51.828 | Params. + 1D spec. | 1/01/2004 | 1/01/2018 | 1 hr |
| DFO-6 | North Hecate Strait | -131.105 | 53.617 | Params. + 1D spec. | 1/01/2004 | 1/01/2018 | 1 hr |
| DFO-7 | South Hecate Strait | -129.796 | 52.423 | Params. + 1D spec. | 1/01/2004 | 1/01/2018 | 1 hr |
| DFO-8 | West Sea Otter | -128.756 | 51.373 | Params. + 1D spec. | 1/01/2004 | 1/01/2018 | 1 hr |
| DFO-9 | West Dixon Entrance | -134.289 | 54.169 | Params. + 1D spec. | 1/01/2004 | 1/01/2018 | 1 hr |
| DFO-10 | La Perouse Bank | -125.998 | 48.835 | Params. + 1D spec. | 1/01/2004 | 1/01/2018 | 1 hr |
| DFO-11 | East Dellwood | -129.915 | 50.875 | Params. + 1D spec. | 1/01/2004 | 1/01/2018 | 1 hr |
| DFO-12 | West Moresby | -132.692 | 52.515 | Params. + 1D spec. | 1/01/2004 | 1/01/2018 | 1 hr |
| NDBC-1 | West Washington | -131.079 | 46.134 | 1D spec. | 1/01/2004 | 1/01/2018 | 1 hr |
| NDBC-2 | Cape Elizabeth | -124.742 | 47.353 | 1D spec. | 1/01/2004 | 1/01/2018 | 1 hr |
| NDBC-3 | Neah Bay | -124.726 | 48.493 | 1D spec. | 9/07/2004 | 1/01/2018 | 1 hr/30 min |
| NDBC-4 | Tillamook | -125.771 | 45.925 | 1D spec. | 10/11/2004 | 1/01/2018 | 1 hr |
| WCWI-1 | Amphitrite | -125.634 | 48.884 | Params. + 2D spec. | 19/11/2011 | 31/07/2016 | 1 hr |
| WCWI-2 | Estevan | -126.608 | 49.353 | Params. + 2D spec. | 28/03/2013 | 1/01/2018 | 1 hr |
| WCWI-3 | Florencia | -125.614 | 48.957 | Params. + 2D spec. | 4/06/2013 | 1/01/2018 | 1hr/20min |
| WCWI-4 | Renfrew | -124.486 | 48.536 | Params. + 2D spec. | 26/09/2014 | 2/09/2016 | 1hr/20min |
| WCWI-5 | Sombrio | -124.340 | 48.487 | Params. + 2D spec. | 11/08/2017 | 1/01/2018 | 1 hr |

### 3.5.1 Wave boundary condition

The data set used as boundary condition is ECMWF (2018). ECMWF (2018) are directional wave spectra from the European Centre for Medium-Range Weather Forecasts (ECMWF)[19] at twelve points (nodes) along the open boundary of the model (see Figure 3-7), from the 1st of January 2004 to 31th of December 2017 and at 1-hour interval. This data comes from the ERA5[20] reanalysis dataset which combines vast amounts of historical observations into global estimates using advanced modelling and data assimilation systems. The data was provided by Jean Bidlot (ECMWF, Research Department, Marine Aspects Section) especially for this work. The Spectra are discretized in 30 frequencies and 24 directions (see Table 3-11), which combined give a total of 720 (30x24) values of variance of the sea surface elevation at each time interval and node.

Table 3-11 Spectral discretization of ECMWF wave data.

| N# | Frequency (hz) | Direction (°) | N# | Frequency (hz) | Direction (°) |
|----|----------------|---------------|----|----------------|---------------|
| 1  | 0.0345 | -172.5 | 16 | 0.1442 | 52.5  |
| 2  | 0.038  | -157.5 | 17 | 0.1586 | 67.5  |
| 3  | 0.0418 | -142.5 | 18 | 0.1745 | 82.5  |
| 4  | 0.0459 | -127.5 | 19 | 0.1919 | 97.5  |
| 5  | 0.0505 | -112.5 | 20 | 0.2111 | 112.5 |
| 6  | 0.0556 | -97.5  | 21 | 0.2323 | 127.5 |
| 7  | 0.0612 | -82.5  | 22 | 0.2555 | 142.5 |
| 8  | 0.0673 | -67.5  | 23 | 0.281  | 157.5 |
| 9  | 0.074  | -52.5  | 24 | 0.3091 | 172.5 |
| 10 | 0.0814 | -37.5  | 25 | 0.34   | -     |
| 11 | 0.0895 | -22.5  | 26 | 0.374  | -     |
| 12 | 0.0985 | -7.5   | 27 | 0.4114 | -     |
| 13 | 0.1083 | 7.5    | 28 | 0.4526 | -     |
| 14 | 0.1192 | 22.5   | 29 | 0.4979 | -     |
| 15 | 0.1311 | 37.5   | 30 | 0.5476 | -     |

[19] https://www.ecmwf.int/

[20] The ERA5 reanalysis data set provides hourly estimates of a large number of atmospheric, land and oceanic climate variables. The data cover the Earth on a 30km grid and resolve the atmosphere using 137 levels from the surface up to a height of 80km. It also includes information about uncertainties for all variables at reduced spatial and temporal resolutions.

**3.5.2 Calibration and validation data sets**

As mentioned previously, three data source of wave measurements (DFO, NDBC and WCWI) were collected, each of these three sources containing information at different locations. A full description of the wave measurement data is presented below.

**Fisheries and Oceans Canada**

Environment Canada and Fisheries and Oceans Canada (DFO) [21] in association with Axys Technologies maintain several oceanographic buoys over Canadian territorial waters. In British Columbia, inside the model domain there are twelve of them. The data available consist of wave parameters and 1D spectra, this later discretized at the frequencies presented in Table 3-12. General weather information (wind included) is also available. The data collected is reported to Environment Canada via satellite. Figure 3-7 presents the locations these buoys.

Table 3-12 Frequency discretization of DFO wave data.

| N# | Frequency (hz) | N# | Frequency (hz) | N# | Frequency (hz) | N# | Frequency (hz) |
|---|---|---|---|---|---|---|---|
| 1 | 0.003906 | 12 | 0.046880 | 23 | 0.089840 | 34 | 0.169900 |
| 2 | 0.007813 | 13 | 0.050780 | 24 | 0.093750 | 35 | 0.187500 |
| 3 | 0.011720 | 14 | 0.054690 | 25 | 0.097660 | 36 | 0.209000 |
| 4 | 0.015630 | 15 | 0.058590 | 26 | 0.101600 | 37 | 0.234400 |
| 5 | 0.019530 | 16 | 0.062500 | 27 | 0.105500 | 38 | 0.267600 |
| 6 | 0.023440 | 17 | 0.066410 | 28 | 0.111300 | 39 | 0.308600 |
| 7 | 0.027340 | 18 | 0.070310 | 29 | 0.119100 | 40 | 0.365200 |
| 8 | 0.031250 | 19 | 0.074220 | 30 | 0.127000 | 41 | 0.451200 |
| 9 | 0.035160 | 20 | 0.078130 | 31 | 0.134800 | | |
| 10 | 0.039060 | 21 | 0.082030 | 32 | 0.144500 | | |
| 11 | 0.042970 | 22 | 0.085940 | 33 | 0.156300 | | |

---

[21] http://www.meds-sdmm.dfo-mpo.gc.ca/isdm-gdsi/waves-vagues/data-donnees/index-eng.asp

**National Data Buoy Center, U.S.**

The National Data Buoy Center (NDBC) [22], which is part of the National Ocean and Atmospheric Administration (NOAA), maintain several buoys and their historical data over the territorial waters of the U.S., four of them in the Pacific Ocean coast in side this work's model domain. The data available corresponds to 1D wave spectra. The spectra are discretized in 47 frequencies as presented in Table 3-13. However, for NDBC-1 and NDBC-2, and just for the period before September 9th 2004 and December 30th 2005, respectively, the spectra are discretized in 38 frequencies as presented in Table 3-14. General weather information (wind included) is also available. Figure 3-7 present the location of the buoys used.

Table 3-13 Frequency discretization of NDBC wave data - a.

| N# | Frequency (hz) | N# | Frequency (hz) | N# | Frequency (hz) | N# | Frequency (hz) |
|----|----------------|----|----------------|----|----------------|----|----------------|
| 1 | 0.0200 | 13 | 0.0875 | 25 | 0.2000 | 37 | 0.3200 |
| 2 | 0.0325 | 14 | 0.0925 | 26 | 0.2100 | 38 | 0.3300 |
| 3 | 0.0375 | 15 | 0.1000 | 27 | 0.2200 | 39 | 0.3400 |
| 4 | 0.0425 | 16 | 0.1100 | 28 | 0.2300 | 40 | 0.3500 |
| 5 | 0.0475 | 17 | 0.1200 | 29 | 0.2400 | 41 | 0.3650 |
| 6 | 0.0525 | 18 | 0.1300 | 30 | 0.2500 | 42 | 0.3850 |
| 7 | 0.0575 | 19 | 0.1400 | 31 | 0.2600 | 43 | 0.4050 |
| 8 | 0.0625 | 20 | 0.1500 | 32 | 0.2700 | 44 | 0.4250 |
| 9 | 0.0675 | 21 | 0.1600 | 33 | 0.2800 | 45 | 0.4450 |
| 10 | 0.0725 | 22 | 0.1700 | 34 | 0.2900 | 46 | 0.4650 |
| 11 | 0.0775 | 23 | 0.1800 | 35 | 0.3000 | 47 | 0.4850 |
| 12 | 0.0825 | 24 | 0.1900 | 36 | 0.3100 | | |

---

[22] https://www.ndbc.noaa.gov/

Table 3-14 Frequency discretization of NDBC wave data - b.

| N# | Frequency (hz) | N# | Frequency (hz) | N# | Frequency (hz) | N# | Frequency (hz) |
|---|---|---|---|---|---|---|---|
| 1 | 0.03 | 11 | 0.13 | 21 | 0.23 | 31 | 0.33 |
| 2 | 0.04 | 12 | 0.14 | 22 | 0.24 | 32 | 0.34 |
| 3 | 0.05 | 13 | 0.15 | 23 | 0.25 | 33 | 0.35 |
| 4 | 0.06 | 14 | 0.16 | 24 | 0.26 | 34 | 0.36 |
| 5 | 0.07 | 15 | 0.17 | 25 | 0.27 | 35 | 0.37 |
| 6 | 0.08 | 16 | 0.18 | 26 | 0.28 | 36 | 0.38 |
| 7 | 0.09 | 17 | 0.19 | 27 | 0.29 | 37 | 0.39 |
| 8 | 0.1 | 18 | 0.2 | 28 | 0.3 | 38 | 0.4 |
| 9 | 0.11 | 19 | 0.21 | 29 | 0.31 | | |
| 10 | 0.12 | 20 | 0.22 | 30 | 0.32 | | |

**West Coast Wave Initiative**

The West Coast Wave Initiative (WCWI) [23] at the University of Victoria maintains 5 oceanographic buoys in the B.C. coast. Wave parameters and 2D spectra are available. The spectra's frequency resolution is 0.005 hz, ranging from 0.055 to 0.5 hz. The spectra direction resolution is 3°, ranging from 0° to 360°. Figure 3-8 presents the locations of these buoys.

## 3.6 Winds

As presented in sub-sections 1.4.2 and section 2.1, wind data is of vital importance for wind-wave generation and propagation models such as SWAN. Because of the great extension of the model domain (see section 4.1), wind fields are needed for improving the performance of the wave model. For this purpose, two different datasets of wind fields were gathered as possible candidates to force the model. Both datasets where used as wind inputs during the calibration process (see sub-chapter 4.3).

A comparison of these two datasets against wind measurements was also performed. Thus, two types of wind data were collected: wind fields for forcing the wave model, and wind measurements to assess the accuracy of the previous type of data. The following sub sections

---

[23] https://www.uvic.ca/research/projects/wcwi/

describe in detail the wind information gathered for this work and the comparison analysis performed to the wind fields candidates (inputs for the wave models).

### 3.6.1 Wind data for model input

Two wind data source were considered as forcing of the wave model (NWW3 and ERA5). Figure 3-10 shows the location and spatial resolutions of the wind fields data considered for this study. These datasets where selected because of their popularity as wind inputs among wave climate characterization studies and are freely available. A description of the two datasets is presented below.
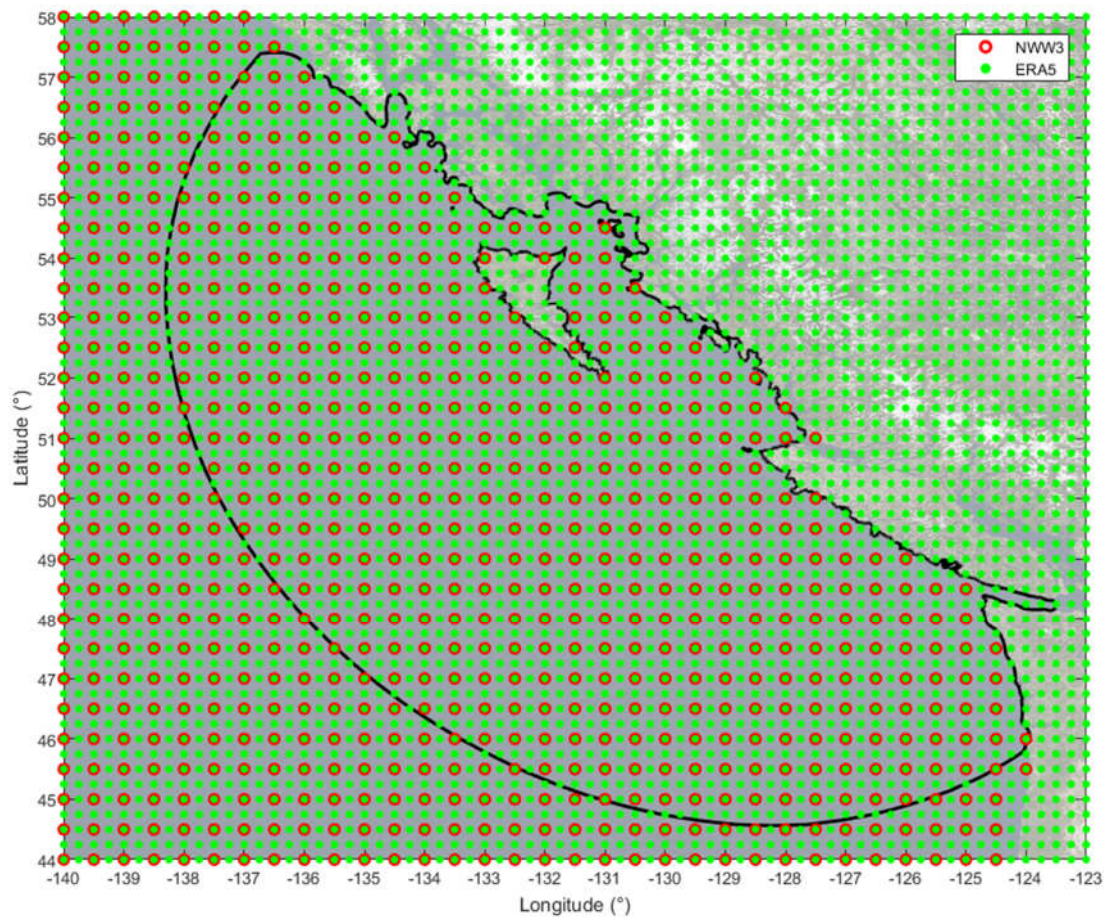


Figure 3-10 Wind field data.

**NOAA WAVEWATCH III**

NOAA WAVEWATCH III (NWW3)[24] is a global wave numerical model operated by the NOAAS's Environmental Modeling Center used to produce hindcast estimates of wave parameters (and wave spectra for some specific locations). It uses global wind fields (vectors) at 10-meter height from the operational Global Forecast System (GFS)[25] to force the model. As well as wave parameters (outputs of the model), wind data (input of the model) is available from February 2005 to December 2018 (at the moment of the last access in January 2018) at 3-hour interval, with a spatial resolution of 0.5° of arc (latitude and longitude). To complete the data needed for the simulation period (2004-2017), data from the same source (GFS) but used in an earlier version of the NWW3 model was also collected. This data is available from July 1999 to November 2007 at 3-hours interval with a spatial resolution of 1.00° and 1.25° of arc in latitude and longitude, respectively.

**ERA5**

The ERA5[26] is a reanalysis dataset generated through advanced modelling and data assimilation systems by the European Centre for Medium-Range Weather Forecasts (ECMWF)[27]. It provides hourly estimates of a large number of atmospheric, land and oceanic climate variables. The data cover the Earth on a 30km grid and resolve the atmosphere using 137 levels from the surface up to a height of 80km. The global wind fields (vectors) are at 10-meter height, and are available from 1979 to the present at 1-hour interval with a spatial resolution of 0.25° of arc (latitude and longitude).

**3.6.2 Wind measurements for wind input data verification**

Wind measurements to evaluate the accuracy of the model inputs comes from the same oceanographic buoys maintained by DFO and NDBC presented in sub-chapter 3.5.2. For both sources, the data available correspond to wind speed and direction. The resolution of FOC wind

---

[24] https://polar.ncep.noaa.gov/waves/

[25] https://www.ncdc.noaa.gov/data-access/model-data/model-datasets/global-forcast-system-gfs

[26] https://www.ecmwf.int/en/forecasts/datasets/reanalysis-datasets/era5

[27] https://www.ecmwf.int/

data is 1-hour while NDBC has initial periods with 1-hour data intervals and later periods with 10-minutes resolution. Their location, data extension and blanks of information is the same as for the wave information presented in Figure 3-7, Table 3-10 and Figure 3-9.

### 3.6.3 Accuracy evaluation of the wind data for model input

To evaluate the accuracy of the wind model inputs, and following the arguments presented in sub-section 2.3.2, an empirical cumulative distribution function (CDF) of the absolute total error ($|\varepsilon|$) was computed for each dataset, for the two components of the wind velocity ($V_x$ and $V_y$), and at every location where measurements are available. From the CDFs, the uncertainty of $|\varepsilon|$ associated to the 95% confidence level ($u_{95}$) was computed as the performance metric. Then, the average $u_{95}$ at each location and the global $u_{95}$ average of each wind field source were compared (see Table 3-15). It is worth noticing that $u_{95\%}$ consider both, systematic and random errors.

As can be noticed from Table 3-15, NWW3 has a slightly lower total $u_{95}$ average than ERA5 of 8.5% (3.87 and 4.23 m/s, respectively). This minor better average representation of the wind field, as can be seen in section 4.3, has a significant impact on the better calibration test results when using NWW3 as forcing.

Finally, some locations near the shore (DFO-4, DFO-10 and NDBC-3) were not used in this evaluation, since for the NWW3 data, interpolation of the wind field cannot be computed due to blanks in the information in the land area surrounding these buoy locations.

Table 3-15 Uncertainty of the absolute total error ($|\varepsilon|$) associated to the 95% confidence level ($u_{95}$) - Wind field data sources.

| Name | Institution's given name | $u_{95} - V_x$ | | $u_{95} - V_y$ | | Averege $u_{95}$ | |
|---|---|---|---|---|---|---|---|
| | | NWW3 | ERA5 | NWW3 | ERA5 | NWW3 | ERA5 |
| DFO-1 | Middle Nomad | 3.41 | 3.30 | 3.28 | 3.09 | 3.34 | 3.19 |
| DFO-2 | South Nomad | 3.28 | 3.22 | 3.18 | 3.01 | 3.23 | 3.11 |
| DFO-3 | South Brooks | 4.89 | 6.14 | 4.25 | 4.72 | 4.57 | 5.43 |
| DFO-5 | South Moresby | 3.74 | 4.05 | 3.72 | 4.28 | 3.73 | 4.16 |
| DFO-6 | North Hecate Strait | 4.72 | 5.97 | 4.42 | 4.87 | 4.57 | 5.42 |
| DFO-7 | South Hecate Strait | 4.33 | 4.61 | 4.13 | 4.36 | 4.23 | 4.49 |
| DFO-8 | West Sea Otter | 4.42 | 5.81 | 4.07 | 5.23 | 4.25 | 5.52 |
| DFO-9 | West Dixon Entrance | 3.48 | 3.54 | 3.26 | 3.37 | 3.37 | 3.46 |
| DFO-11 | East Dellwood | 6.17 | 6.01 | 5.88 | 5.99 | 6.03 | 6.00 |
| DFO-12 | West Moresby | 3.61 | 4.27 | 3.28 | 3.45 | 3.44 | 3.86 |
| NDBC-1 | West Washington | 2.76 | 2.88 | 2.80 | 2.79 | 2.78 | 2.83 |
| NDBC-2 | Cape Elizabeth | 3.83 | 4.41 | 3.36 | 3.75 | 3.60 | 4.08 |
| NDBC-4 | Tillamook | 3.16 | 3.61 | 3.25 | 3.36 | 3.20 | 3.48 |
| Total average | | **3.99** | **4.45** | **3.76** | **4.02** | **3.87** | **4.23** |

## 3.7 Tidal currents

Current forcing was incorporated in the version 6 of the WCWI SWAN model (WCWI-v6). The current data collected correspond to the full tidal model results of the National Research Council Canada (NRCC), given for the aim of this work by Julien Cousineau (Research engineer; Ocean, Coastal and River Engineering NRCC). The results include water surface elevations and current velocity at 10-minutes interval for 35 days, from January 8th 2013 to February 12th 2013, for all of the 2,338,104 nodes of the model mesh (see Figure 3-11). The model was developed in TELEMAC-MASCARET[28] free-surface flow solver suit, using the UTM Zone 9 and WGS84 coordinate system.

---

[28] http://www.opentelemac.org/
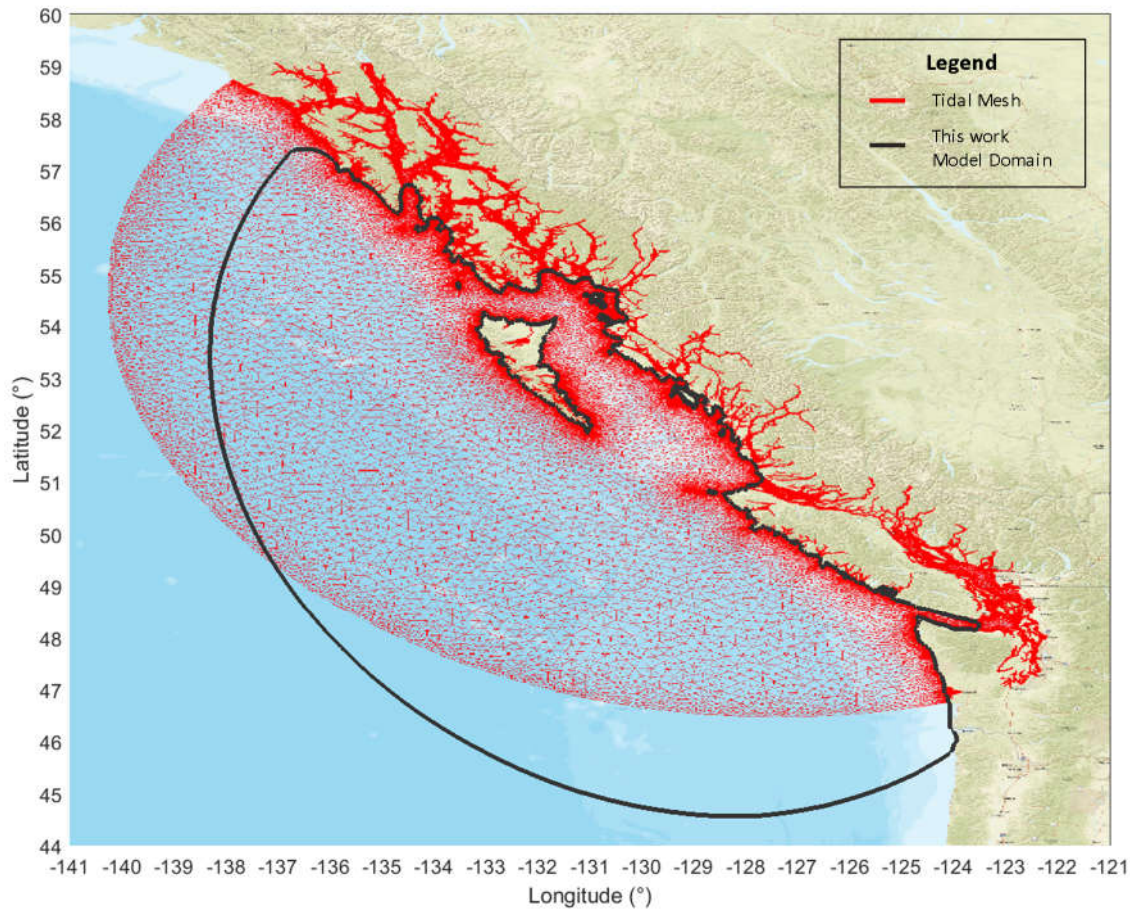
Figure 3-11 Mesh of the National Research Council Canada (NRCC) tidal model.

The tidal current information was space-interpolated to wave model mesh (WMMesh, see section 4.2) and then time-extrapolated to cover the simulation period (2004-2017). The space-interpolation was performed using a linear method over the two components of the currents (Vx, Vy), while the time-extrapolation was performed using the 't_tide'[29] algorithm implemented in Matlab by Rich Pawlowicz based on Pawlowicz (2002). As can be seen from Figure 3-11, an area of the wave model domain does not possess tidal current information, thus, points with zero velocity along the external boundary of the wave model domain were added, so the interpolation could be performed to complete the information in the blank area. This interpolation methodology is justified due to the very low velocities in the deep water area of the tidal model, ranging 0.05 – 0.11 m/s at the boundary of the blank area with the tidal model domain (see Figure 3-12). Stronger

---

[29] https://www.eoas.ubc.ca/~rich/#T_Tide

currents in shallower zones of the blank area (U.S. coast) could exist but they are not important as these zones do not have an influence over the wave field in the area of interest (B.C. coast).

As well as for the wind fields, the quality of the extrapolated time series at every node of WMMesh was assessed by analyzing the uncertainty of the absolute total error ($|\varepsilon|$) associated to the 95% confidence level ($u_{95}$) for both velocity component ($V_x$, $V_y$). Figure 3-13 and Figure 3-14 shows $u_{95}$ for $V_x$ and $V_y$, respectively. As can be noticed from the figures, large $u_{95}$ values, of up to 0.36 m/s and 0.35 m/s for $V_x$ and $V_y$, respectively, are found over the domain. Most of the largest values are located in sheltered (from swell waves) areas such as in Juan de Fuca strait and some areas in Hecate strait. Larger $u_{95}$ can also be found in very small areas between isles, and in zones at the intersection of the blank area and the tidal mesh. All high $u_{95}$ values located mainly where there are strong tidal currents, representing a small error in comparison with the maximum current in the site; at the blank area boundary with $u_{95} < 0.035$ m/s; or at the blank area boundary in shallow waters in U.S. territory where currents do not influence the wave field in the area of interest. Thus, and as per the data available (NRCC tidal model), it can be said that the representation of the currents is sufficiently accurate for the aim of this work.

It is important to mention that, with the 35 days of data available, harmonics constituent with periods up to 35 days can be estimated, so the extrapolation neglects longer-period constituents. These longer period constituents have a minor importance and usually are not considered in tidal studies, such as for the computation of vertical datum in bathymetric surveys.
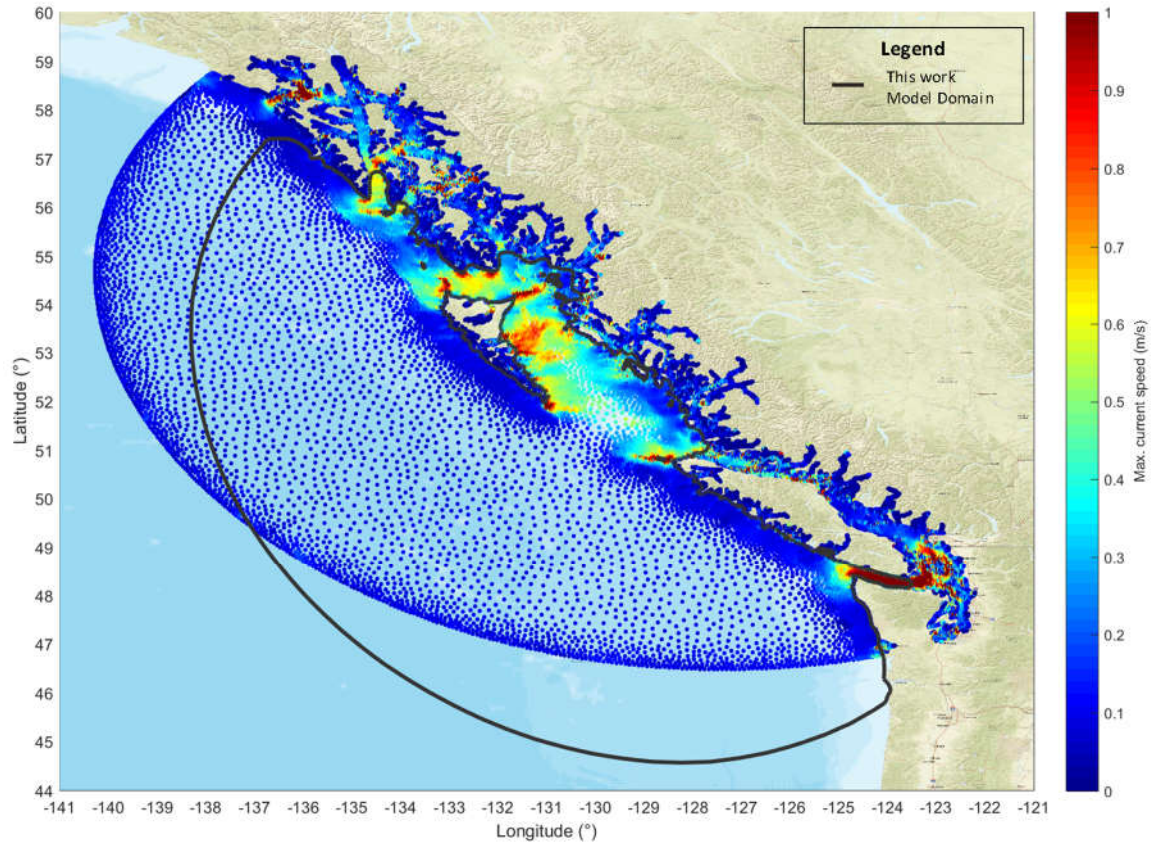
Figure 3-12 Maximum current speed in NRCC tidal model (35 days model results, color-map has been truncated to 1 m/s).
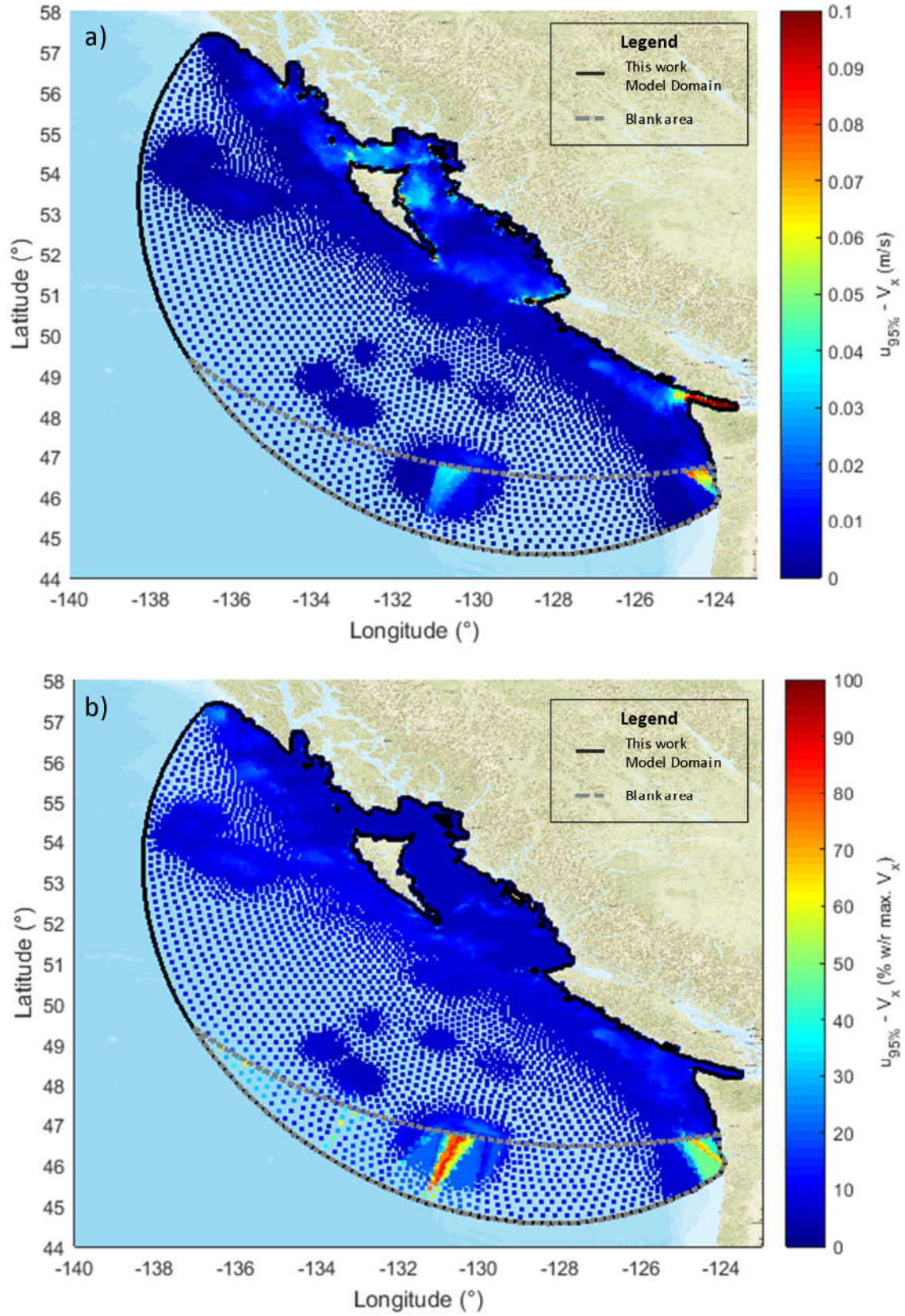
Figure 3-13 $u_{95}$ for $V_x$. a) absolute value. b) percentage with respect maximum $|V_x|$.
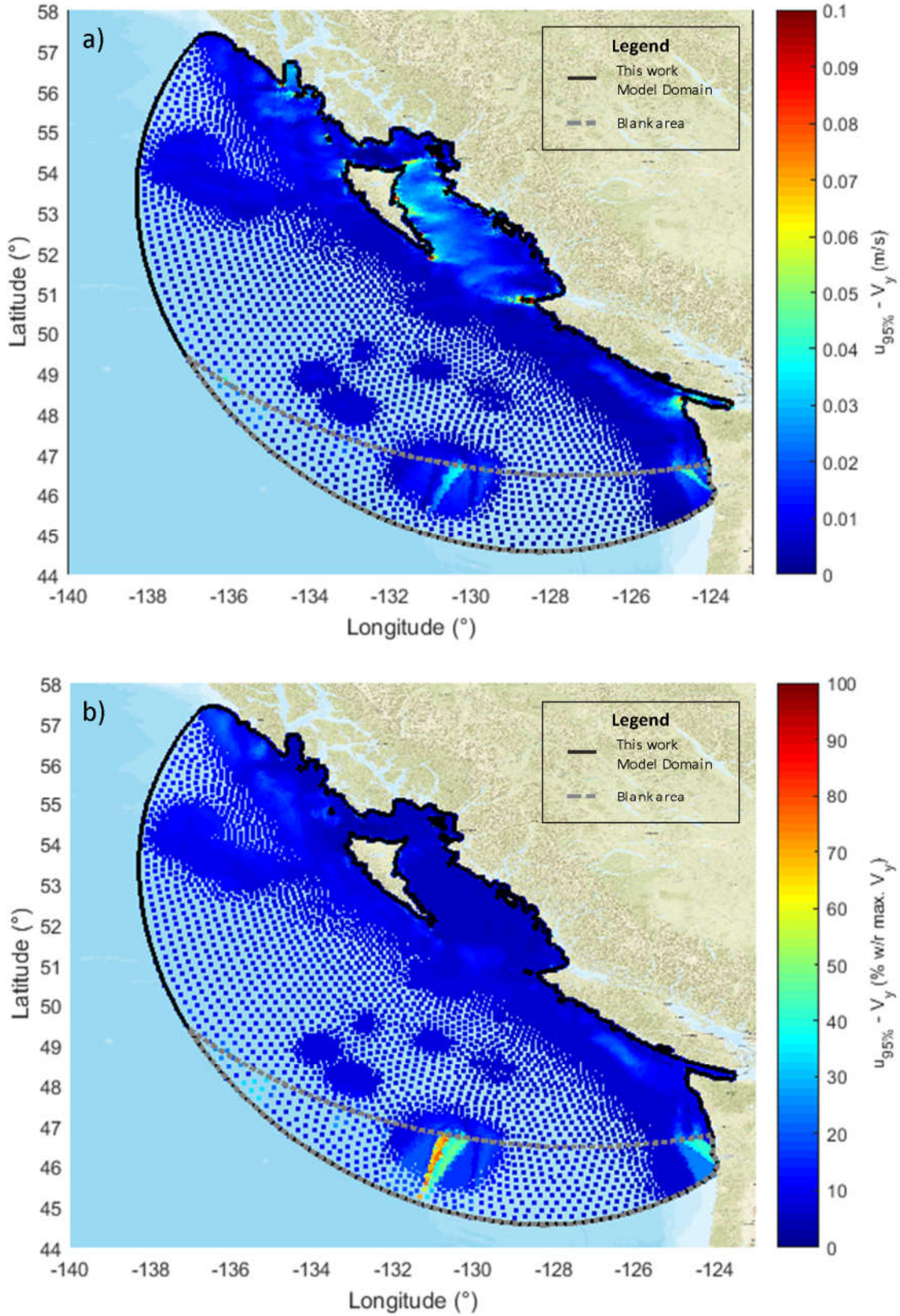
Figure 3-14 $u_{95}$ for $V_y$. a) absolute value. b) percentage with respect maximum $|V_y|$.

# Chapter 4 Model setup

As mentioned in section 2.1, the spectral wave model selected to simulate the wave conditions for this work was the latest available version of the spectral wave model SWAN (version 40.31). The reasons for this choice are mainly that SWAN is the only documented third-generation spectral wave model to be specifically developed for nearshore applications (Neary et al., 2016), its use is very well documented in both scientific and industry studies, is freely available as an open-source software, and its latest release (version 40.31) implements state of the art features.

The setup of the model includes physical and numerical definitions that need to be provided or defined. The physical definitions comprise the model domain, the boundary conditions, forcings, initial conditions, state conditions and the parametric characterization (formulations) of the source-sink terms in the wave action balance equation (see Eq. 2.1 and 2.4). Numerical definitions include the temporal, spatial and wave spectra discretization, and the parameters used by the numerical schemes to solve the governing equations.

Boundary conditions and forcing (wind and tidal currents) information were presented in Chapter 3, as well as the information necessary to define the state conditions: the sea level surface elevation and topo-bathymetry. The other definitions needed to be provided, such as the formulations (and their parameters) to compute the source-sink terms of the wave action balance equation, the temporal, spatial and wave spectra discretization, and the numerical schemes (and their parameters) are discussed and presented in the following sections.

From all the definitions left to be provided, the model domain and its spatial discretization (mesh) are of critical importance to obtain accurate and high resolution results (wave characteristics) at the areas of interest. Thus, a comprehensive description and the considerations taken for their conception is presented in section 4.1 (model domain) and 4.2 (mesh).

As any other spectral wave model, SWAN has several formulations for modeling the physics of the source-sink terms of the wave action balance equation to choose from, and each of them include parameters whose values need to be specified. Moreover, there are many parameters that control the numerical schemes (methods) used to solve the governing equations that also need to be specified. Default settings for both, the physics for the source-sink terms and numerical schemes

and parameters, are already defined within SWAN. However, to ensure the models be accurate, they need to be adjusted or validated in a calibration process involving a comparison of the model results against measurements. Such process was carried out and presented in section 4.3.

Lastly, after defining all the physical and numerical aspects of the model, a summary of the final settings employed in WCWI-v5 and WCWI-v6 are presented in section 4.4. This section also defines the locations where wave parameters, wave power and wave spectra will be requested, and which, from all of the available wave parameters will be saved.

## 4.1 Model domain

The model domain was defined considering (1) the goals of the numerical modelling of having valid results all along the west coast of Canada, (2) including important geomorphological features that could affect the wave field in the area of interest (and missing in coarse global models), (3) the available boundary conditions and (4) the physical processes of wave transformation to occur away from the offshore boundary in order to have 'relatively independent' results in the area of interest from the wave boundary conditions.

Due to submarine mountains (see Figure 4-1), it was decided to extend the domain offshore to include them. The reason for this decision is that the effect of these submerged mounts on the wave field is probably not captured by the global hindcast model used to obtain the wave boundary conditions (ECMWF, see sub-section 3.5.1) due to the coarseness of its grid.

The inshore limit of the domain was defined using the shoreline OSM (2018, described in section 3.3). This shoreline was corrected in some areas using satellite images as reference, and modified and / or smoothed in some others for modelling purpose, such as to reduce the number of unnecessary elements in the mesh. Some very small islands, with areas less than 3 km$^2$ were not considered as such (excluded from the model domain), or combined where near other land masses. It is important to mention that including or excluding islands in the mesh should not affect the model results, as the wave transformations induced by the presence of islands should be controlled purely by the bathymetry. The definition of the inshore limit of the model and islands aims to decrease the number of elements and nodes, and therefore to reduce the amount of Random-Access-Memory (RAM) usage of the computer when running the simulations, and the amount of data (results) finally stored. These two reasons are associated to reduce the runtimes.

Figure 4-1 presents the limits (offshore, inshore and islands) of the model domain. The color-map associated to the DEM was truncated to show better the submerged mountains, which have peaks as high as -25 m (north-western mount) and -100 m (southern mount) according to WMDEM (see section 3.1).
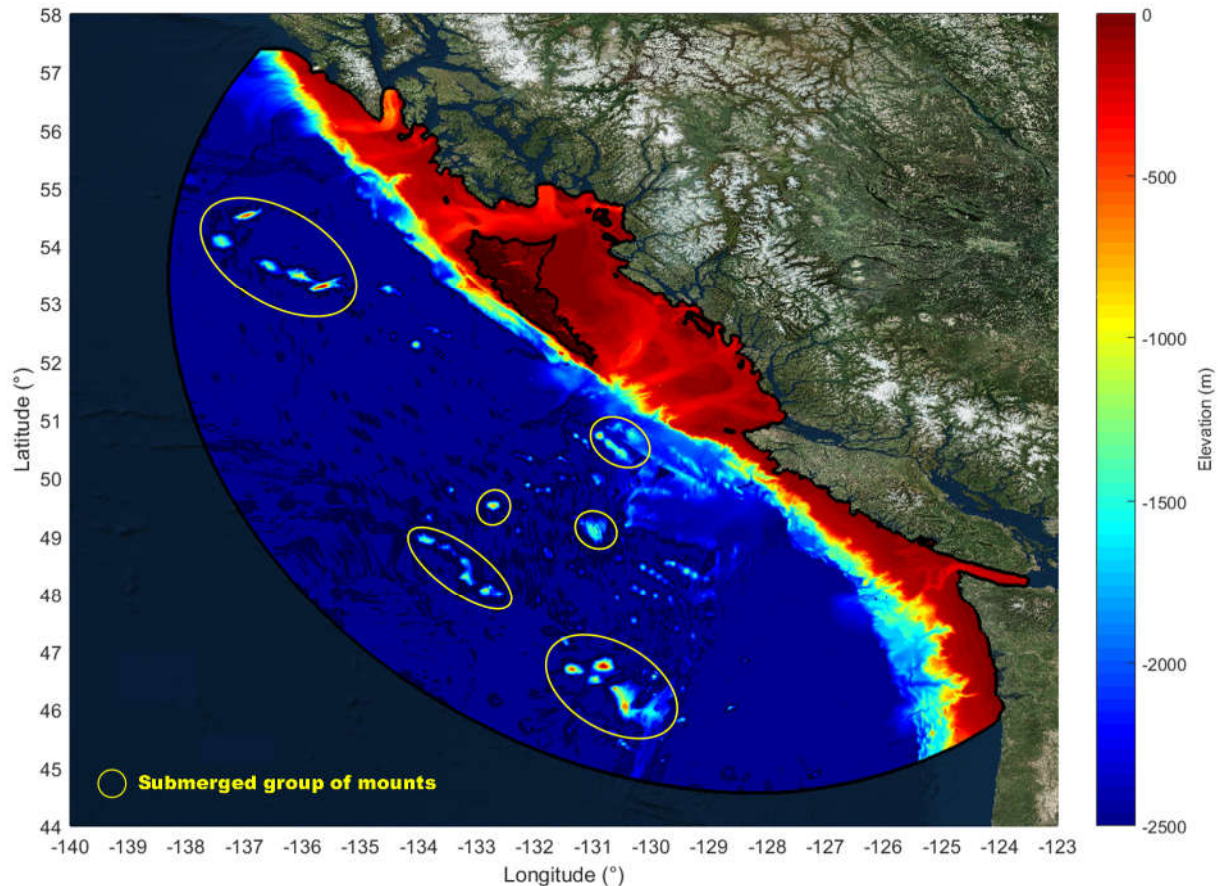


Figure 4-1 Submerged mounts in the model domain and truncated topo-bathymetry.

## 4.2 Mesh

Generation of the mesh and its interpolated digital elevation model (topo-bathymetry) is a critical step in the accuracy, stability and efficiency of most of the hydrodynamic numerical models, including those based on the wave action balance equation (such as SWAN). This is particularly true when simulating waves on intermediate and shallow waters ($d \leq \lambda/2$), where geographical features can induce important transformations on the wave field. In addition to the geographical features, forcings (e.g. wind, tidal currents) also need to be well represented within

the model. Thus, a proper spatial discretization (mesh) need to be defined (in addition to providing accurate topo-bathymetric and forcing information).

SWAN can handle two types of grids (meshes): structured and unstructured. Structured grids could be rectilinear or curvilinear (based on quadrilateral elements), while unstructured meshes in SWAN are based on triangular elements. Because of the intrinsic greater flexibility with respect to the mesh node distribution of unstructured grids, a far more optimal mesh compared to structured grids can be achieved. For this reason, unstructured meshes have been used in the previous SWAN models at the WCWI, as well as for these new versions of the wave model (WCWI-v5 and WCWI-v6).

The concept of mesh optimality is subjective and vary from case to case depending on the modeler needs and criteria. Generally, there is a compromise between two opposing objectives for the model, being able to represent the wave field accurately and with the desired resolution (and thus all the forcings that affect it need to be represented properly), and to obtain simulation results in reasonable times (reasonable runtimes). Nonetheless, other factors may also influence the space discretization (e.g. outputs storage restrictions).

Normally, it is preferred to have higher spatial resolution in intermediate and shallow waters ($d < \lambda/2$) and especially where the bathymetry changes rapidly. In shallower waters, such rapid changes in bathymetry could induce significant transformations in the waves over short distances. Thus, bathymetry is a dominant factor in determining the mesh refinement. Some of the most common depth-dependent considerations for defining the nodes distribution are related to: the wavelength of the waves expected in the area, and the slope or steepness of the seafloor. Other dominant factors are the resolution and better representation of the wave field needed at specific areas of interest, and the model execution time (runtime) which increases with the number of mesh elements.

Taking into account the considerations presented above, the node spacing to build the model mesh (WMMesh) was defined according to a master meshing rule designed to control the element size during the meshing process. This master rule was created as a combination of five 'lower rank' meshing rules ($\alpha$s) that represent the different factors considered to obtain a more optimal mesh. As discussed previously, these factors are associated to the following.

- Wavelength: Areas with shorter wavelengths need higher spatial resolution.

- Steepness of the seafloor: Areas with greater slopes need higher spatial resolution.

- Distance from areas of interest: For the purpose of this work, potential sites for the deployment of Wave Energy Converters (WECs) are considered as areas of interest. These areas are associated to the closeness to energy consumption centers (populated areas) in unsheltered coastline. Areas closer to these locations need higher spatial resolution.

- Mesh resolution smoothing: It is preferred to have smooth changes of the elements size over the mesh to avoid numerical instabilities within the schemes used to solve the (discretized) governing equations of the SWAN software.

- Limits on minimum and maximum distance between nearest nodes, allows for a good representation of the wave field and reasonable computational runtimes.

Both, master and lower rank rules were defined as values over a grid covering the model domain. The values of the lower rank rules where defined between 0 and 1, representing normalized desired element size, where smaller values define a finer element size, and greater values define a coarser mesh. These lower rank rules were combined into a normalized master rule, which then was transformed into the final master rule by adjusting the range of its values from a desired minimum to a desired maximum distance between neighboring nodes. The resolution of the grid used to define the meshing rules was set to 500x500-meters (GRID_500x500) so the meshing process did not crash, but was still able to represent properly the bathymetric features (needed for the wavelength and seafloor slope rules). In the majority of the model domain, this grid is coarser than the bathymetric data available, but is sufficiently fine for the meshing purpose, as the mesh should then be smoothed to avoid numerical problems within the SWAN numerical scheme, blurring bathymetric details anyways.

To define the bathymetric dependent rules, a DEM with nodes at the exact same coordinates as GRID_500x500 (DEM_500x500) was interpolated from the WMDEM.

Note that GRID_500x500 and DEM_500x500 are used purely for the generation of the meshing rules.

Definition of the lower and master meshing rule ($\alpha$s), the smoothing process and the generation of the final mesh (WMMesh) to be used in WCWI-v5 and WCWI-v6 is presented in the following sub-sections.

### 4.2.1 Lower rank meshing rule: distance from points of interest

From the populated areas data (GND, 2018 and RCED, 2018; see section 3.4) and the shoreline OSM (2018) data (see section 3.3), three $\alpha$ rules where defined. First, the minimum distance of every point in GRID500x500 to any populated centers, and exposed coastline were computed. These distances were used to assign the values of the three different but similar normalized rules. The first rule ($\alpha_{Dist1}$, Eq. 4.1) is related to the distance to exposed coastline and was normalized to a distance of 20 km. The second rule ($\alpha_{Dist2}$, Eq. 4.2) is related to the distance to the populated areas. In this second rule, distances were normalized to a distance of 30 km. Lastly, a smoothing rule ($\alpha_{Dist3}$, Eq. 4.3) was defined by normalizing the distances to the exposed coastline by 600 km. All the values for these three rules where truncated to 1. The choice of the values used to normalize $\alpha_{Dist1}$ and $\alpha_{Dist2}$ was somehow arbitrary, but trying to account for the importance of nearshore locations and the closeness to energy demand centers for the development of wave energy projects. The normalizing value for $\alpha_{Dist3}$ smoothens the values of the master rule over the whole domain, but also gives more resolution to the exposed nearshore areas.

To speed up the distance computation at every grid point, populated areas located further than 40 km inland or along sheltered coastline were eliminated. Additionally, a couple of them where slightly displaced (less than 10 km) to influence a greater area of the model domain.

$$\alpha_{Dist1}(i,j) = min\left[\frac{D_c(i,j)}{20}, 1\right] \qquad 4.1$$

$$\alpha_{WL}(i,j) = min\left[\frac{D_p(i,j)}{30}, 1\right] \qquad 4.2$$

$$\alpha_{WL}(i,j) = min\left[\frac{D_c(i,j)}{600}, 1\right] \qquad 4.3$$

Where $D_c(i,j)$ and $D_p(i,j)$ are the distance to the nearest exposed coastline point and distance to the nearest populated area at the $(i,j)$ grid point.

**4.2.2 Lower rank meshing rule: wavelength**

From DEM_500x500 and using the frequency dispersion equation (Eq. 4.4: adapted from Eq. 1.1), the wavelength at every grid point was computed for a regular wave with a period of 30 s. The 30 s period was selected as it is approximately the longest period of the discretized wave spectra of the SWAN model (see Table 4-17). Using this longer period, a broader range of wavelengths can be obtained, expanding the area where this rule is differentiable from its maximum value. The wavelengths calculated at each grid point were then normalized by the largest wavelength ($\lambda_{max}$, which correspond to a 30 s period wave in deep water), creating the normalized wavelength rule ($\alpha_{WL}$) as shown in Eq. 4.5.

$$\lambda = \frac{g}{2\pi}T^2\tanh(\frac{2\pi d}{\lambda})$$

<div style="text-align:right">4.4</div>

$$\alpha_{WL}(i,j) = \frac{\lambda(i,j)}{\lambda_{max}}$$

<div style="text-align:right">4.5</div>

Where $\lambda$ is the wavelength, $g$ is the gravity acceleration constant, $T$ is the wave period and $d$ is the depth.

**4.2.3 Lower rank meshing rule: seafloor slope**

Then, the absolute value of the slopes was computed using the Matlab® functions 'grad()' and 'abs()' at every grid point. Slopes at depths greater than $\lambda_{max}$ were replaced by 0.001 m/m and slopes smaller than 0.001 m/m were truncated to this same value. The reason for the above are twofold. The first is that wave transformations induced by the sea bottom do not occur at depths greater than $\lambda/2$ (as per the linear wave theory), but for meshing purposes it is desired to apply this rule from deeper sectors to have a smooth transmission of the elements size in the area where wave transformation is influenced by the bathymetry. The second reason is that very small slopes will tend to lead to numerical errors as shown by the slope rule ($\alpha_S$) in Eq. 4.6.

$$\alpha_S(i,j) = \frac{\min_{i,j}\left(|\hat{S}(i,j)|\right)}{|\hat{S}(i,j)|}$$

<div style="text-align:right">4.6</div>

Where $|\hat{S}(i,j)|$ is the truncated absolute value of the slope at the $(i,j)$ grid point.

## 4.2.4 Master rule, smoothing and final mesh

A combined normalized rule ($\alpha_C$) was defined by the amalgamation of the five normalized rules mentioned above as presented in Eq. 4.7.

$$\alpha_C(i,j) = \alpha_{WL}(i,j)^{b1} \cdot \alpha_S(i,j)^{b2} \cdot \alpha_{Dist1}(i,j)^{b3} \cdot \alpha_{Dist2}(i,j)^{b4} \cdot \alpha_{Dist3}(i,j)^{b5} \qquad 4.7$$

Where $b1$, $b2$, $b3$, $b4$, $b5$ are parameters that define the importance of the rules in the combination. Table 4-1 shows the values of each parameter used in the combination, while Figure 4-2 depicts all lower rank normalized rules ($\alpha_{Dist1}$, $\alpha_{Dist2}$, $\alpha_{Dist3}$, $\alpha_{WL}$ and $\alpha_S$), and the amalgamation normalized rule $\alpha_C$.

Table 4-1 Weighting parameters used in the rules amalgamation.

| Parameter | Value | Description |
|---|---|---|
| $b1$ | 0.65 | Related to the wavelength |
| $b2$ | 0.35 | Related to the steepness of the seafloor |
| $b3$ | 0.35 | Related to the distance to exposed coastline |
| $b4$ | 0.35 | Related to the distance to populated areas |
| $b5$ | 0.35 | Related to the smoothing rule (distance to exposed coastline) |
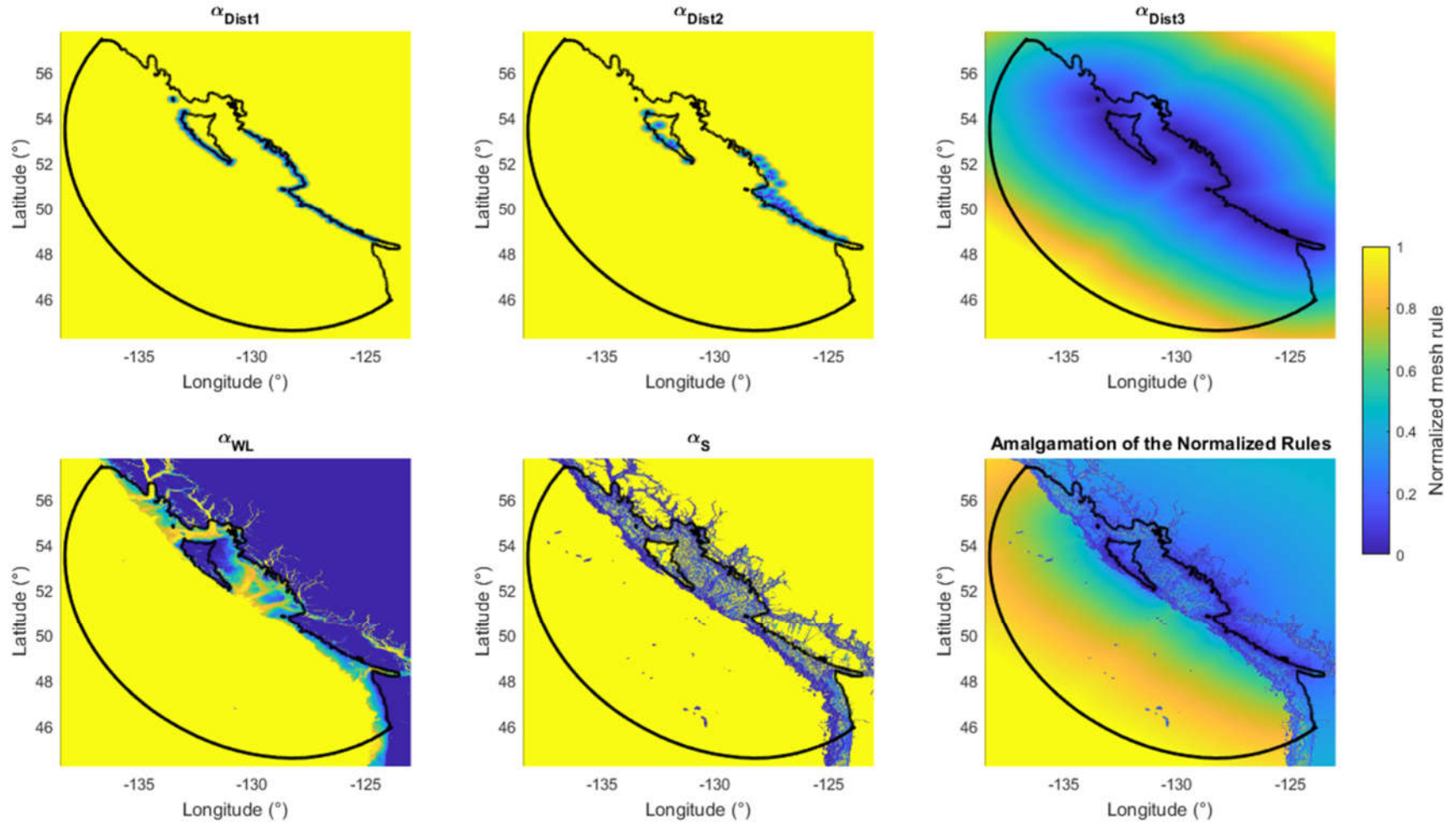
Figure 4-2 Normalized rules: a) $\alpha_{Dist1}$ related to the distance to the exposed coastline. b) $\alpha_{Dist2}$ related to the distance to populated areas. c) $\alpha_{Dist3}$ smoothing rule. d) $\alpha_{WL}$ related to the wavelength. e) $\alpha_S$ related to the seafloor slope. f) Amalgamation of the normalized rules ($\alpha_C$).

After the amalgamation, and in addition to the smoothing rule ($\alpha_{Dist3}$) presented in Eq. 4.3, an additional smoothing procedure was performed. This smoothing procedure was carried out by an iterative process using the 2D Gaussian smoothing filter implemented in Matlab® (*imgaussfilt*) with a variable standard deviation value. This iterative process is explained in the scheme presented in Figure 4-3, while Figure 4-4 shows the results on the smoothed combined normalized rule ($\widetilde{\alpha_C}$) during the iterative smoothing process at different stages ($k$ values).

$$N = 30$$
$$k = 1$$
$$\textit{Repeat N times} \quad \left[ \begin{array}{c} \widetilde{\alpha_c}(i,j) = \min(\widetilde{\alpha_c}(i,j), \alpha_c(i,j)) \\[1em] \widetilde{\alpha_c} = imgaussfilt\left(\widetilde{\alpha_c}, 2(N - (k-1))\right) \\[1em] k = k + 1 \end{array} \right.$$
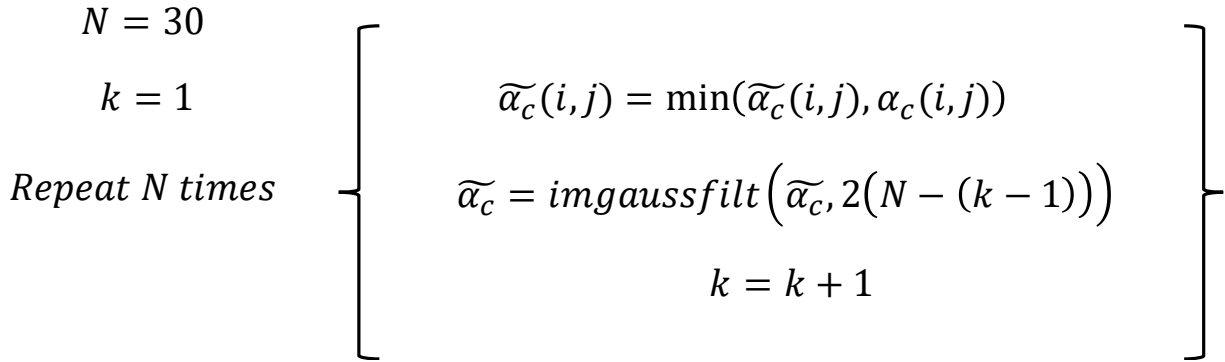
Figure 4-3 Smoothing procedure using the Matlab® Gaussian filter imgaussfilt.
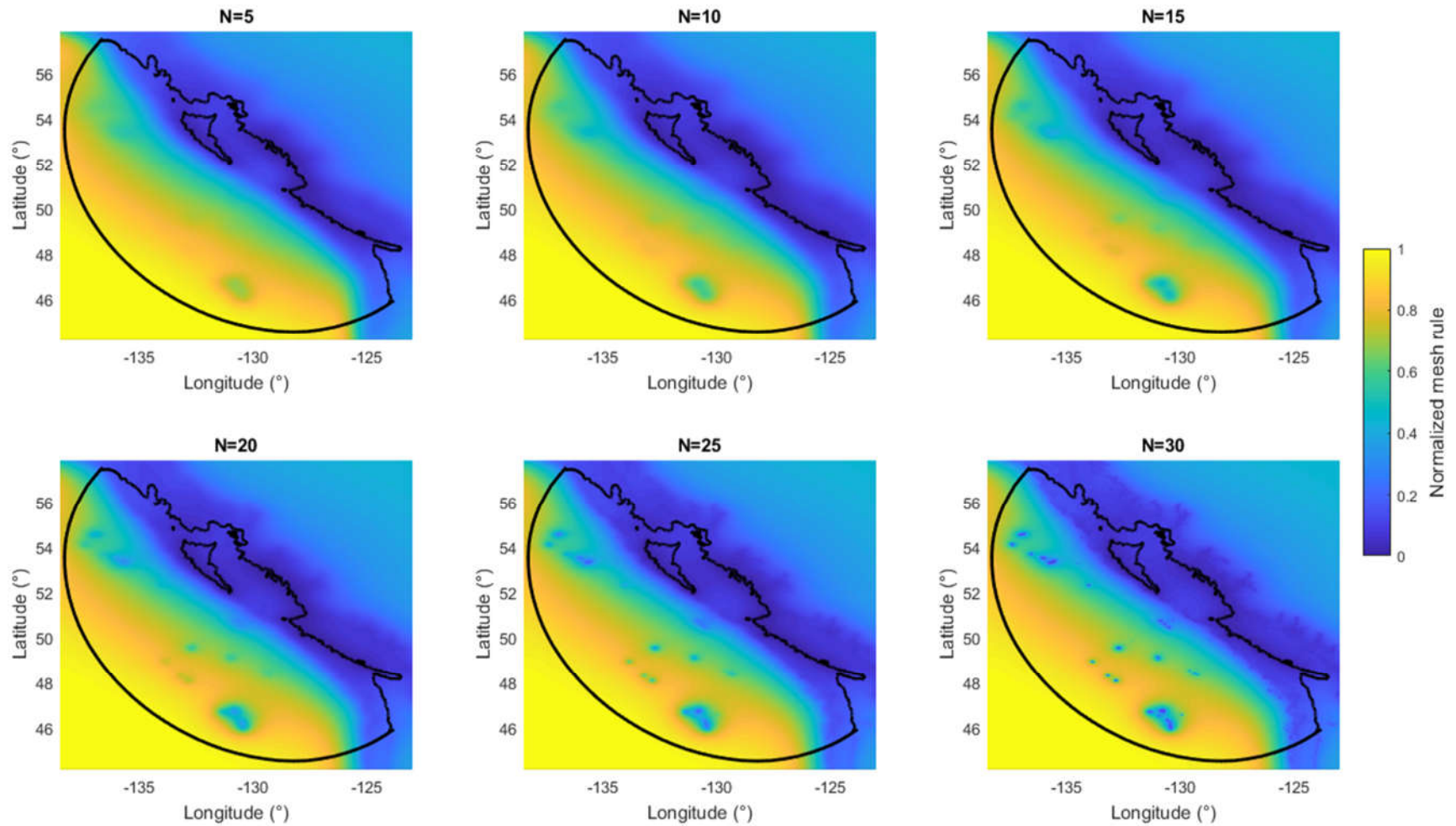
Figure 4-4 Smootheed normalized combined rule ($\widetilde{\alpha_C}$) during the iterative smoothing process at different stages ($k$ values).

Finally, $\widetilde{\alpha_C}$ was transformed into the master rule ($\alpha_M$) by applying a linear function presented in Eq. 4.8, changing the range of the values from $\widetilde{\alpha_C}(i,j) \in [0,1]$ to $\alpha_M(i,j) \in [m_{min}, m_{max}]$, where the parameter $m_{min}$ and $m_{max}$ are the minimum and maximum distance between the nearest nodes in the mesh, respectively. These parameters, like the $b$ parameters, were defined using a trial and error method until an acceptable number of elements and nodes, and a 'good mesh resolution' was found. The $m_{min}$ and $m_{max}$ parameters finally used are 150 m and 25,000 m.

Figure 4-5 presents the final mesh (WMMesh), formed by 348,364 elements and 177,945 nodes, and the elevation model interpolated from WMDEM. Figure 4-6 presents some statistics of WMMesh related to the area, minimum angle, maximum slope between connected nodes and average depth of the elements.

$$\alpha_M = A \cdot \widetilde{\alpha_C} + B \tag{4.8}$$

Where: $A = \dfrac{m_{max} - m_{min}}{\widetilde{\alpha_C}_{max} - \widetilde{\alpha_C}_{min}}$, $B = \dfrac{(m_{max} + m_{min}) - A \cdot (\alpha_{C max} + \alpha_{C min})}{2}$. $\widetilde{\alpha_C}_{max}$ and $\widetilde{\alpha_C}_{min}$ are maximum and minimum value of $\widetilde{\alpha_C}$, respectively.

It is important to mention that the definition of a 'good mesh resolution' and the meshing rules defined above are based on experience, taking into account the goals of this work and limiting the runtime of the simulations to a reasonable time. Some areas of the mesh were manually optimized to increase its resolution, specifically where the submerged mounts are located (shown in Figure 4-1), so bathymetry-induced wave transformation in these areas can be modeled properly. Also, the maximum resolution required for reconnaissance studies as recommended by IEC (2015) at depths shallower than 20 m (100 m node spacing) was not met due to the increasing number of nodes, which made impractical long-term simulations for this work (excessive computational cost). However, spectral data was requested along the coast at ~500 m depth (section 4.4), so more detailed numerical models can be generated from the results of this work at shallower depths.
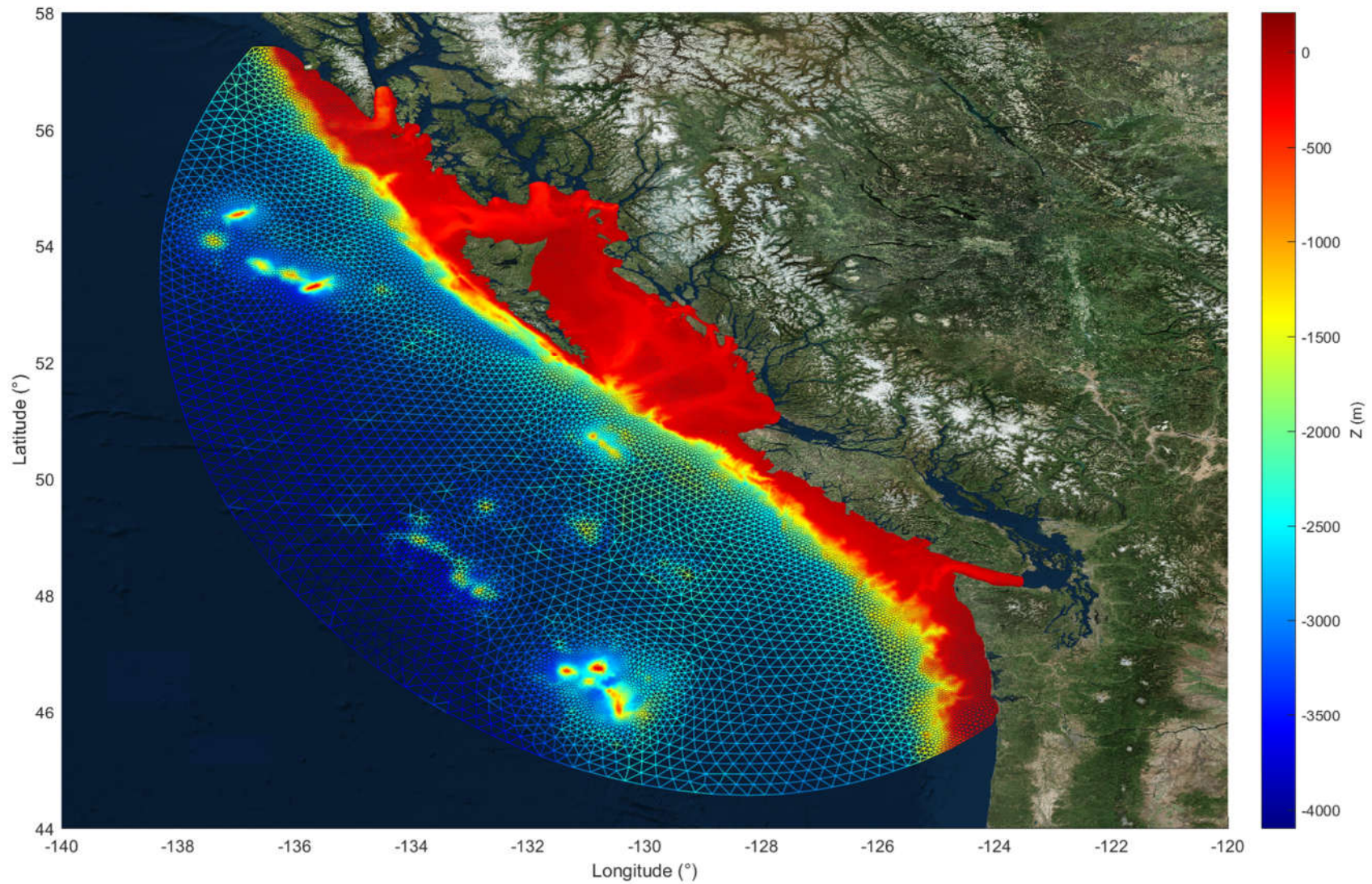
Figure 4-5 Mesh of the SWAN model WCWI-v5 and WCWI-v6 (WMMesh).
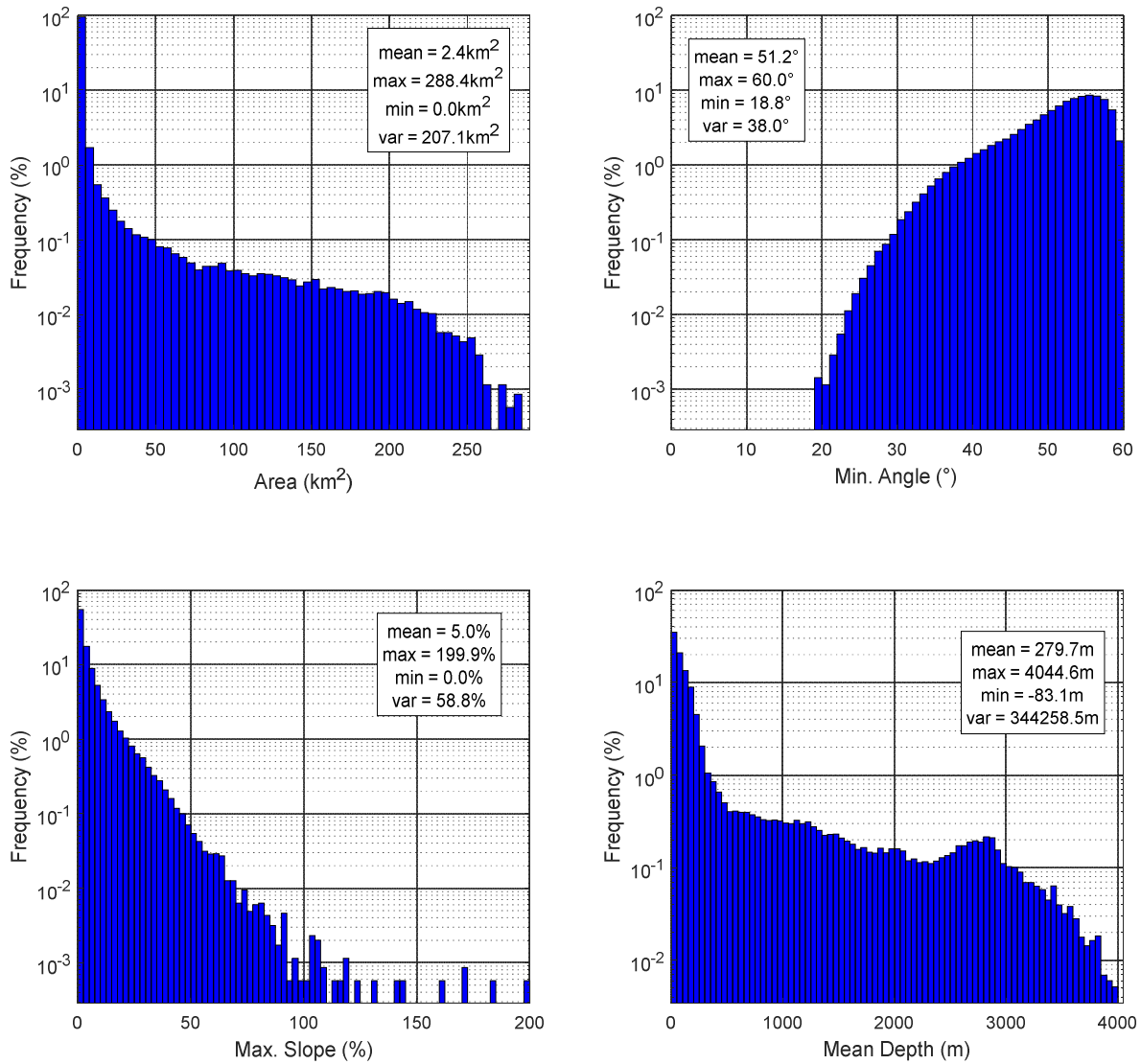
Figure 4-6 Statistics of the WCWI-v5 and WCWI-v6 mesh (WMMesh).

## 4.3 Calibration

Numerous settings and two different wind forcing conditions (see sub-section 4.3.1) were used to run various model candidates (calibration tests). First, a set of preliminary calibration tests were run over 1 month and an initial comparison of the results with oceanographic buoy measurements was performed to evaluate the accuracy. Based on this initial comparison, several calibration tests were proposed as candidates for a more extensive performance analysis against a

wider range of a metrics to finally find the settings of the SWAN model WCWI-v5 (and WCWI-v6).

The spectral discretization (wave frequency and direction) was defined prior to the definition of any of the calibration tests and kept untouched throughout the calibration process. The characteristics of the discretization were determined using recommendations from SWAN (2019b) and IEC (2015), while also considering the runtimes for the complete simulation period (14 years, 2014-2017) for both wave models. Table 4-17 presents the spectra discretization for the two wave models.

Table 4-17 WCWI-v5 and WCWI-v6 spectra discretization.

| N# | Frequency (hz) | Direction (°) | N# | Frequency (hz) | Direction (°) | N# | Frequency (hz) | Direction (°) |
|---|---|---|---|---|---|---|---|---|
| 1 | 0.0345 | 265 | 13 | 0.1013 | 145 | 25 | 0.2973 | 25 |
| 2 | 0.0377 | 255 | 14 | 0.1108 | 135 | 26 | 0.3252 | 15 |
| 3 | 0.0413 | 245 | 15 | 0.1212 | 125 | 27 | 0.3557 | 5 |
| 4 | 0.0452 | 235 | 16 | 0.1326 | 115 | 28 | 0.3891 | -5 |
| 5 | 0.0494 | 225 | 17 | 0.145 | 105 | 29 | 0.4256 | -15 |
| 6 | 0.054 | 215 | 18 | 0.1586 | 95 | 30 | 0.4656 | -25 |
| 7 | 0.0591 | 205 | 19 | 0.1735 | 85 | 31 | 0.5093 | -35 |
| 8 | 0.0647 | 195 | 20 | 0.1898 | 75 | 32 | 0.5571 | -45 |
| 9 | 0.0707 | 185 | 21 | 0.2076 | 65 | 33 | 0.6094 | -55 |
| 10 | 0.0774 | 175 | 22 | 0.2271 | 55 | 34 | 0.6666 | -65 |
| 11 | 0.0846 | 165 | 23 | 0.2484 | 45 | 35 | N/A | -75 |
| 12 | 0.0926 | 155 | 24 | 0.2717 | 35 | 36 | N/A | -85 |

As can be observed, the frequency discretization is coarser at higher frequencies, however, in terms of periods, the coarser discretization of the wave periods occurs at lower frequencies, with 2.5 s at the highest wave period of 28.9 s. The finest discretization is about 0.15 s at the smallest wave period of 1.5 s. At an average peak period of about 10.6 s (as per the wave data from the buoys), the period discretization is smaller than 1.0 s, which is sufficiently fine to represent the shape of the spectrum. The frequency limits allow proper characterization of the sea states with peak periods between 3.8 s and 20.3 s, this represents at least 99.1% of the cases observed across all buoy locations. On the other hand, the whole range of wave directions can be represented in the model, with a directional discretization of 10°. Although 10° is sufficiently fine to characterize

the wave spectrum of sea-waves, with typical directional spreading ($D_{spr}$) of about 30°, it may not be sufficient for swell-waves which come from a much narrower directional range. For these later cases, SWAN (2019b) recommends a directional discretization of about 2° or smaller. However, with this fine representation of the directional space (~2°), the spectral space gets too big for long-term simulations of regional domains, obtaining runtimes that are not permissible for this work. Thus, it was decided to utilize the same directional space employed by WCWI-v4. Exploring improvements in the accuracy of the models by increasing the resolution of the spectral space, and particularly directional space is something that should be investigated in future work.

The settings that where varied during the calibration process are introduced in sub-section 4.3.1. Calibration tests and the methodology used to evaluate their performance is presented in sub-chapter 4.3.2, while the performance results and analysis are reported in sub-section 4.3.3. Final settings for WCWI-v5 and WCWI-v6 are presented in section 4.4.

### 4.3.1 Settings varied during the calibration process

The following settings were varied to create the model candidates (calibration tests).

**Wind forcing conditions (Winds)**

Two different wind field datasets were tested, ERA5 and NWW3 (see sub-section 3.6.1).

**Third generation Physics (GEN3)**

The simulations were all run in third-generation mode (see section 2.1). Four different physic packages that control wind energy transfer, quadruplet interactions and whitecapping are available: Jansen, Komen, Westhuysen (WES) and ST6 (refer to SWAN, 2019a for a detailed description). From the available options, only WES and ST6 were tested because WES was the physics package used in WCWI-v4, and ST6 is a relatively new physics package that has been tested in SWAN obtaining better agreement against measurements than other options (e.g. Lavidas and Polinder, 2019; Aijaz et al., 2016).

**Quadruplets computation (iquad)**

There are several choices on how the non-linear quadruplets wave interaction is computed. Some examples are: semi-implicit computation of the nonlinear transfer with Discrete Interaction

Approximation (DIA) per sweep (iquad=1), fully explicit computation of the nonlinear transfer with DIA per sweep (iquad=2), fully explicit computation of the nonlinear transfer with DIA per iteration (iquad=3), Multiple DIA (iquad=4), and XNL for finite depth transfer (iquad=53). The DIA has been found to be successful in describing the essential features of a developing wave spectrum, however for uni-directional waves, this approximation is not valid and, in some cases the DIA technique may not be accurate enough. Multiple DIA was developed to increase the accuracy of the quadruplets wave-wave interaction estimation by increasing the number of quadruplet configurations without increasing excessively the computational cost. XNL computes the exact four wave-wave interactions, but the computation cost is too high for long term and regional applications (SWAN, 2019a; SWAN, 2019b). The default option and the one used in WCWI-v4 is iquad=2. In this work iquad=2, iquad=3 and iquad=4 were tested, however iquad=4 was then discarded because parallel computing is not allowed, and runtimes were impermissible for the time frame of this study. iquad=2 was also discarded for the final settings as the numerical method is not conservative for simulations that include current interactions, so the pure influence of the tidal currents on the wave characteristics could not be evaluated fairly when comparing WCWI-v5 and WCWI-v6. However, results using iquad=2 are still presented as it is the default setting in SWAN, and finally used in WCWI-v4.

**Time step ($\Delta t$)**

The time step ($\Delta t$) is the time discretization of the simulation time (non-stationary simulations only). SWAN is based on implicit numerical schemes, thus the Courant stability criterion ($CFL \leq 1$, see Eq. 4.9) does not need to be satisfied. However, the accuracy of the model results is still affected by the time step. It is recommended to choose time steps such that the Courant number is smaller than 10 for the fastest (or dominant) wave, and be at most 10 min.

$$CFL = U \frac{\Delta t}{\Delta x}$$
\hfill 4.9

It is also necessary that $\Delta t$ be small enough to resolve the time variations of the wave field (SWAN, 2019b). Due to the higher mesh resolution required in shallower waters, the time step required to meet the recommendations is very small (< 1.5 min, see Figure 4-7 for an example of the time steps required at every node to satisfy $CFL = 10$), leading to excessively long runtimes.

Thus, it was decided to ignore the Courant number recommendation ($CFL \leq 10$), and in many test cases, the 10 min limit. Several time steps were tested: 5, 10, 20, 30 and 60 min.
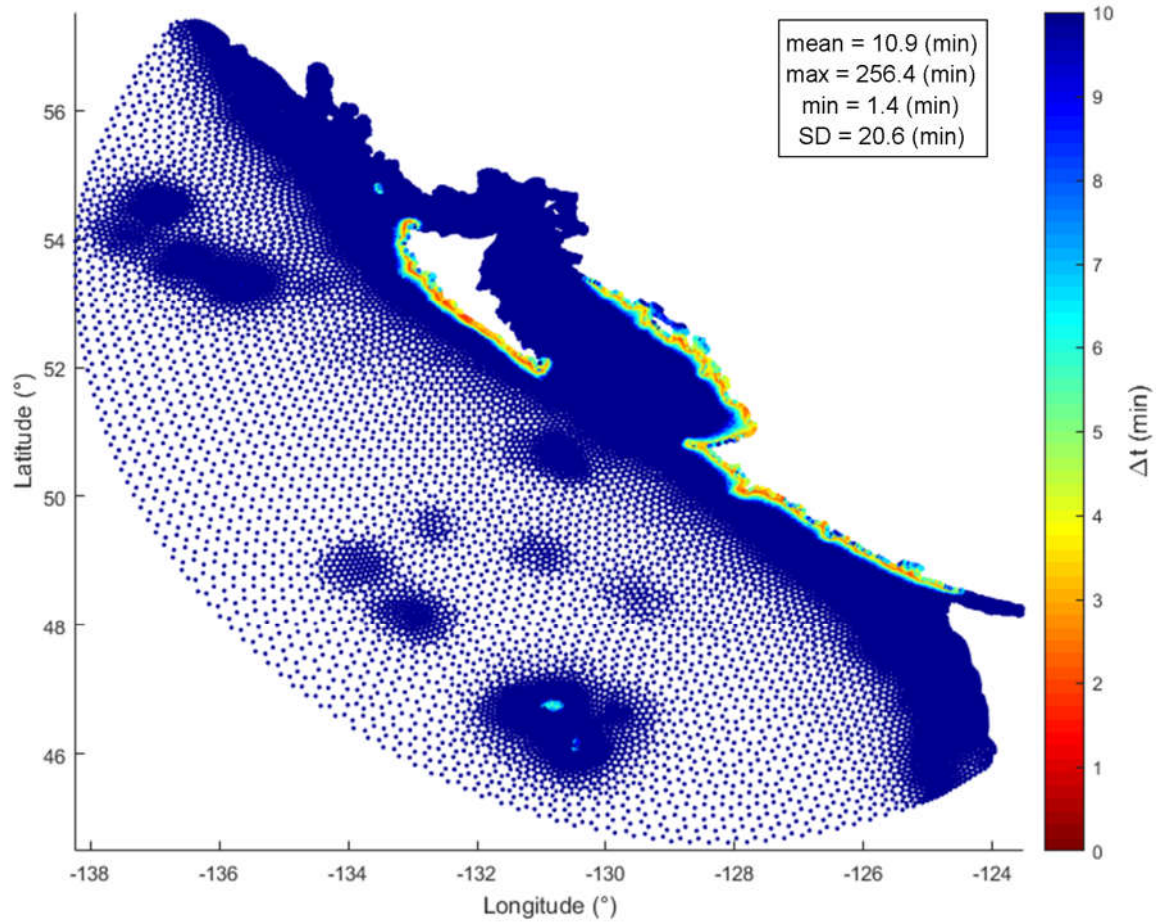


Figure 4-7 Time step required to satisfy $CFL = 10$ (truncated at 10 min).

**Maximum number of iterations (MNI)**

Energy propagates along wave rays and the computation of this propagation need to be completed in an iterative process when the rays are curved (SWAN, 2019a). This parameter controls the maximum number of iterations per time step for nonstationary computations (there is a similar parameter for stationary computations). For sufficiently small time steps ($\leq 10$ min), no more than 1 iteration per time step is recommended. However, as the time step recommendations are not fulfilled, three iteration limits were tested, MNI=1, MNI=2 and MNI=40. The later MNI value is an excessive number used in WCWI-v4, but iterations generally stop at a much lower number, depending on the wave conditions and other settings.

**Whitecapping (WCP)**

Beside the whitecapping formulations included in the different GEN3 physics, SWAN can be forced to compute the deep water breaking according to Komen et al. (1984) (SWAN, 2019b). Calibration test using Komen et al. (1984) were included in the analysis.

### 4.3.2 Calibration tests and performance metric

The model candidates (calibration tests), presented and described in Table 4-3, were run over a one-year period. The naming convention for the calibration tests starts with the source of wind data used to force the model, and follows with the physics package that control wind energy transfer and whitecapping. Then, the iquad option, the physics package that control the quadruplet interactions, the maximum number of iterations, and lastly, the time step expressed in minutes. All components of the calibration test label are separated by a hyphen.

The performance of these model candidates was assessed in comparison to WCWI-v4's ability to represent measured wave conditions. The wave conditions were represented by three wave parameter that characterize the wave spectrum: the significant wave height ($H_{m0}$), the energy period ($T_e$) and the peak wave direction ($D_p$) (when available). To evaluate their performance, and based on the ideas presented in Beya et al. (2017), a performance metric based on the uncertainty of the absolute total error ($|\varepsilon|$) associated to the 95% confidence level ($u_{95}$) was defined. This performance metric, called Global Performance Score ($GPS$, Eq. 4.10), is a scalar metric that compare the global accuracy of the calibration test in relation to WCWI-v4, and is formed by Local Performance Scores ($LPS$s, Eq., 4.11), which in turns are computed from a linear combination of Variable Performance Scores ($VPS$s, Eq. 4.12). $VPS$s are defined for every wave parameter considered, and at every location where there are simultaneous measurements and WCWI-v4 results (see Table 4-4), and it represents the percentage of improvement (or retrogression) in modelling the wave parameter with respect to WCWI-v4. Therefore, $LPS$ and $GPS$ represent the improvement (in relation to WCWI-v4) in simulating the sea state in a particular location and globally, respectively. For any of the performance score ($GPS$, $LPS$ and $VPS$), negative values mean a poorer performance, while higher positive values mean better performance than V4 (by definition, V4's performance scores are all 0.0%).

$$GPS_s = \frac{1}{L}\sum_{l=1}^{L} LPS_{S,l} \qquad\qquad 4.10$$

$$LPS_{S,l} = \sum_{v=1}^{V} \alpha_v \cdot VPS_{S,l,v} \qquad\qquad 4.11$$

$$VPS_{S,l,v} = 1 - \frac{u_{S,l,v}}{u_{V4,l,v}} \qquad\qquad 4.12$$

Where $s$, $v$ and $l$ represent the specific calibration test, variable, and location, respectively. $u_{s,l,v}$ is the uncertainty of $|\varepsilon|$ with a confidence level of 95% for the calibration test $s$, location $l$ and wave parameter $v$. $u_{V4,l,v}$ is the uncertainty of $|\varepsilon|$ with a 95% confidence level for WCWI-v4 at the location $l$ and wave parameter $v$. $\alpha_v$ is the weight of the wave parameter $v$ in the $LPS$, with values of 0.5, 0.3 and 0.2 for $H_{m0}$, $T_e$ and $D_p$, respectively. At the locations where $D_p$ is not available, the $\alpha_v$ takes the values 0.625 and 0.375 for $H_{m0}$ and $T_e$, respectively. These $\alpha_v$ values were chosen to represent their general relative importance for a generic WEC.

It worth mentioning that the mean wave direction ($D_m$) is a better wave parameter than $D_p$ for assessing the performance of the models, as $D_m$ is more stable (vary more gradually). This is especially true for measurements, and in multi wave-systems where the energy of the peaks of at least two of the wave systems are similar. However, $D_m$ is not available for WCWI-v4 and thus $D_p$ had to be used instead.

The simulation period was selected to be the year 2015, as this year presents the most extensive measurement dataset distributed among all the oceanographic buoys able to be used in the calibration. Also, only the closest (in time) data point was kept for every single hour. Table 4-4 presents the data points available for calibration per year and buoy.

The simulation tests were run progressively, comparing first the different wind fields sources and third generation physics packages. Then, other settings were tested as new performance information were obtained from previous calibration tests. Several calibration tests are not presented, as they are irrelevant to show the importance of the settings that were varied in order to obtain a better performance.

Table 4-3 Settings and boundary conditions varied in the calibration test.

| Calibration test | Winds | GEN3 | MNI | WCP | iquad | Δt (min) |
|---|---|---|---|---|---|---|
| *WCWI-v4 | COAMPS | WESTH | 40 | WESTH | 2 | 180 |
| ERA5-ST6-2-Komen-2-10m | ERA5 | ST6 | 2 | Komen | 2 | 10 |
| ERA5-ST6-2-ST6-3-20m | ERA5 | ST6 | 2 | ST6 | 3 | 20 |
| ERA5-WES-2-WES-3-20m | ERA5 | WESTH | 2 | WESTH | 3 | 20 |
| NWW3-ST6-1-ST6-3-20m | NWW3 | ST6 | 1 | ST6 | 3 | 20 |
| NWW3-ST6-2-Komen-2-05m | NWW3 | ST6 | 2 | Komen | 2 | 5 |
| NWW3-ST6-2-Komen-2-10m | NWW3 | ST6 | 2 | Komen | 2 | 10 |
| NWW3-ST6-2-ST6-2-20m | NWW3 | ST6 | 2 | ST6 | 2 | 20 |
| NWW3-ST6-2-ST6-3-05m | NWW3 | ST6 | 2 | ST6 | 3 | 5 |
| NWW3-ST6-2-ST6-3-10m | NWW3 | ST6 | 2 | ST6 | 3 | 10 |
| NWW3-ST6-2-ST6-3-20m | NWW3 | ST6 | 2 | ST6 | 3 | 20 |
| NWW3-ST6-2-ST6-3-30m | NWW3 | ST6 | 2 | ST6 | 3 | 30 |
| NWW3-ST6-40-ST6-3-20m | NWW3 | ST6 | 40 | ST6 | 3 | 20 |
| NWW3-ST6-40-ST6-3-60m | NWW3 | ST6 | 40 | ST6 | 3 | 60 |
| NWW3-WES-2-WES-2-20m | NWW3 | WESTH | 2 | WESTH | 2 | 20 |

* This model is not a calibration test, but rather is the final model built and run by Robertson et al. (2016) at the West Coast Wave Initiative (WCWI).

Table 4-4 Data available for calibration per year and buoy.

| Name | Year | | | | | | | | | | | | | |
|---|---|---|---|---|---|---|---|---|---|---|---|---|---|---|
| | 2004 | 2005 | 2006 | 2007 | 2008 | 2009 | 2010 | 2011 | 2012 | 2013 | 2014 | 2015 | 2016 | 2017 |
| DFO-1* | 7840 | 5302 | 4963 | 8077 | 7722 | 5040 | 8666 | 8639 | 6830 | 4993 | 7839 | 7773 | 8128 | 4397 |
| DFO-2* | 8399 | 8647 | 5266 | 8201 | 8714 | 8157 | 8659 | 8651 | 8404 | 8184 | 3172 | 5276 | 5799 | 7871 |
| DFO-3 | 8111 | 8065 | 7385 | 5755 | 6445 | 7727 | 7391 | 6270 | 6642 | 6522 | 7785 | 6582 | 5330 | 8165 |
| DFO-4 | 7893 | 8643 | 7256 | 7863 | 8552 | 4651 | 6981 | 7691 | 7580 | 8381 | 8483 | 8753 | 8470 | 7820 |
| DFO-5 | 8493 | 8686 | 7447 | 8055 | 5720 | 8159 | 8287 | 7437 | 7257 | 6000 | 7911 | 8284 | 8466 | 8192 |
| DFO-6 | 7321 | 7982 | 7134 | 7436 | 7889 | 7538 | 7971 | 6345 | 7194 | 7891 | 7790 | 8030 | 7334 | 7771 |
| DFO-7 | 8465 | 8655 | 7590 | 5440 | 8565 | 6643 | 8216 | 7982 | 6028 | 6640 | 5064 | 7970 | 8034 | 8035 |
| DFO-8 | 8486 | 8473 | 5554 | 8236 | 8519 | 8416 | 8098 | 7393 | 7964 | 7906 | 3469 | 4750 | 8339 | 8011 |
| DFO-9 | 6207 | 2977 | 5181 | 1138 | 7417 | 8312 | 8230 | 8264 | 4342 | 5243 | 8130 | 8125 | 8365 | 8096 |
| DFO-10 | 7350 | 2186 | 3454 | 7144 | 7325 | 7904 | 7848 | 7569 | 6746 | 8180 | 6086 | 8291 | 7860 | 6400 |
| DFO-11 | 7681 | 8609 | 7356 | 6408 | 8728 | 8513 | 8503 | 8150 | 7214 | 8088 | 6887 | 8137 | 8105 | 6180 |
| DFO-12 | 8513 | 8570 | 6802 | 6971 | 6050 | 8516 | 7896 | 5905 | 6311 | 4737 | 5375 | 7948 | 8251 | 8202 |
| NDBC-1* | 8608 | 0 | 6422 | 8684 | 6773 | 0 | 3289 | 4277 | 4361 | 0 | 4144 | 8735 | 8739 | 5155 |
| NDBC-2 | 8744 | 8686 | 3508 | 1902 | 8746 | 8489 | 8240 | 8356 | 8535 | 8606 | 6730 | 7218 | 8732 | 8682 |
| NDBC-3 | 4208 | 7872 | 6451 | 8614 | 6015 | 7505 | 0 | 5391 | 5450 | 4474 | 8686 | 8729 | 8780 | 8726 |
| NDBC-4 | 1169 | 8019 | 712 | 2578 | 5128 | 6575 | 7885 | 8197 | 7363 | 8698 | 8699 | 8716 | 6541 | 5589 |
| WCWI-1 | 0 | 0 | 0 | 0 | 0 | 0 | 0 | 1009 | 940 | 6329 | 6830 | 7533 | 4737 | 0 |
| WCWI-2 | 0 | 0 | 0 | 0 | 0 | 0 | 0 | 0 | 0 | 5786 | 6711 | 2836 | 1369 | 3205 |
| WCWI-3 | 0 | 0 | 0 | 0 | 0 | 0 | 0 | 0 | 0 | 5000 | 8028 | 8760 | 1477 | 3320 |
| WCWI-4 | 0 | 0 | 0 | 0 | 0 | 0 | 0 | 0 | 0 | 0 | 2311 | 4301 | 31 | 0 |
| WCWI-5* | 0 | 0 | 0 | 0 | 0 | 0 | 0 | 0 | 0 | 0 | 0 | 0 | 0 | 3400 |
| Total | 117488 | 111372 | 92481 | 102502 | 118308 | 112145 | 116160 | 117526 | 109161 | 121658 | 130130 | 146747 | 132887 | 127217 |
| Total** | 92641 | 97423 | 75830 | 77540 | 95099 | 98948 | 95546 | 95959 | 89566 | 108481 | 114975 | 124963 | 110221 | 106394 |

* Data not available for WCWI-v4, see also Figure 4-9.
** Total excluding buoys that are not available for WCWI-v4, and thus, for the $GPS$ computation.

### 4.3.3 Performance analysis results

Figure 4-27 and Table 4-5 show the *GPS* and the average *VPS* ($\overline{VPS}$) for every wave parameter considered.

As can be noticed, calibration tests forced by NWW3 winds have a significantly higher performance than the calibration tests using ERA5 wind fields.

Also, ST6 GEN3 physics produced considerably better results than WESTH, thus, many calibration tests were ran using the former physics package and the NWW3 wind fields. Quadruplets interactions using the fully explicit computation of the nonlinear transfer with DIA per sweep (iquad=2) generated slightly superior outputs than fully explicit computation of the nonlinear transfer with DIA per iteration (iquad=3). However, iquad=3 had to be chosen for the final settings to compare the pure influence of tidal currents on wave characteristics between WCWI-v5 and WCWI-v6, as iquad=2 is not conservative when currents are included.

The maximum number of iteration (MNI) allowed per time step has a significant influence when varied from 1 to 2, but a very small impact on the performance when then increased to 40. MNI=2 presented the best results between comparable calibration tests (NWW3-ST6-1-ST6-3-20m, NWW3-ST6-2-ST6-3-20m and NWW3-ST6-40-ST6-3-20m).

Regarding to the time steps, surprisingly, greater time steps produced slightly better global performance due mainly to significant better representation of the wave period ($T_e$) expressed as $\overline{VPS}$, from 9.3% for NWW3-ST6-2-ST6-3-05m to 18.3% for NWW3-ST6-40-ST6-3-60m. In addition to its slightly lower *GPS*, runtimes of NWW3-ST6-2-ST6-3-05m were inadmissible for the long-term simulations, thus, was discarded. Despite the slightly higher *GPS*s and smaller runtimes of NWW3-ST6-2-ST6-3-30m and NWW3-ST6-40-ST6-3-60m, the settings of NWW3-ST6-2-ST6-3-20m, with a *GPS* of 17.9%, were finally selected for WCWI-v5 and WCWI-v6. This decision was taken because NWW3-ST6-2-ST6-3-20m settings are closer to the recommendations stated in SWAN (2019b), and its global performance is comparable to the best performed calibration test: NWW3-ST6-2-ST6-3-30m with *GPS*s of 18.8%.
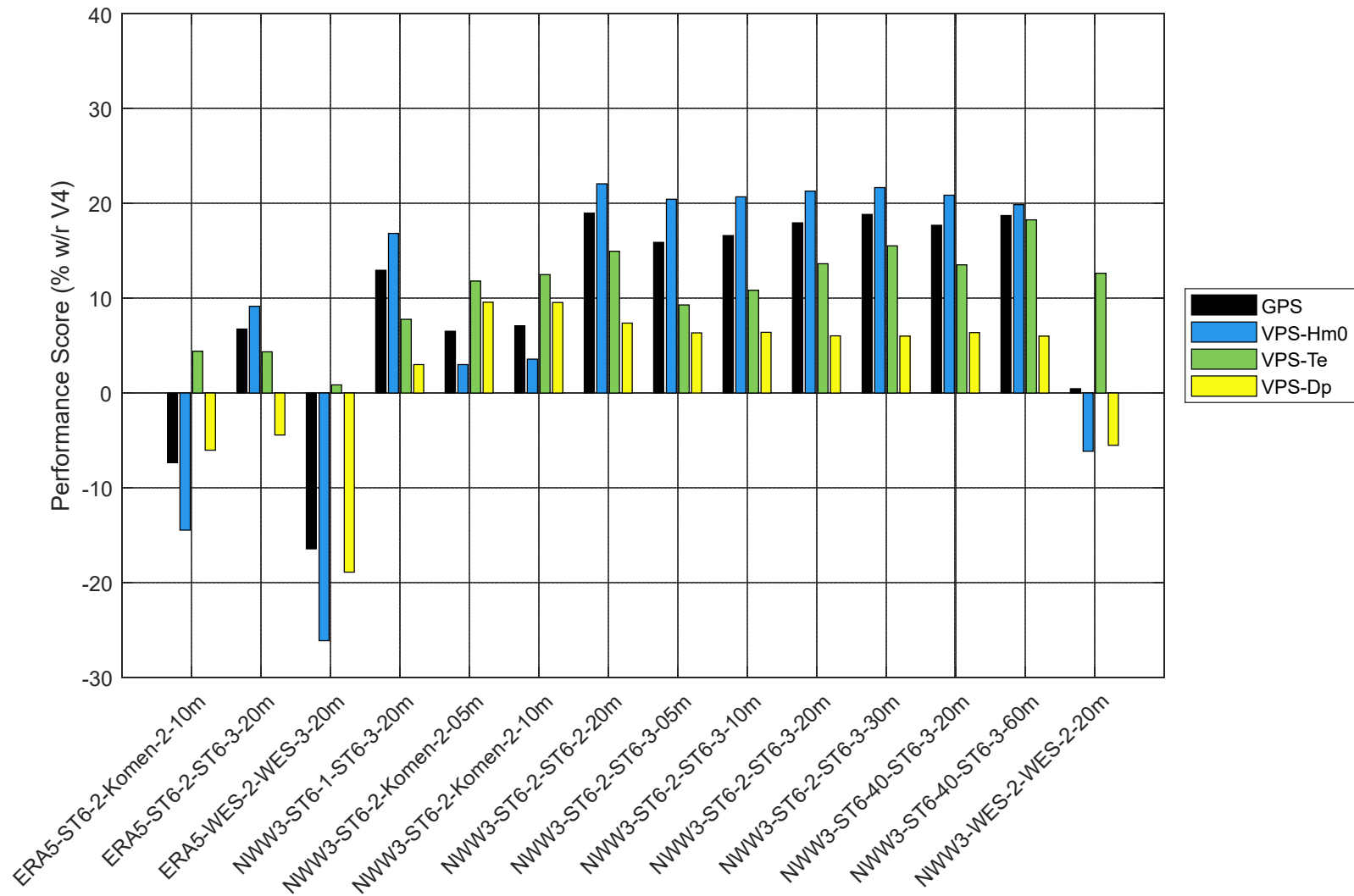
Figure 4-27 Global Performance Scores ($GPS$) and average variable performance score ($\overline{VPS}$) – Calibration tests.

Table 4-5 Global Performance Score ($GPS$) and averaged Variable Performance Score ($\overline{VPS}$) for every calibration test.

| Calibration test | $\overline{VPS}$ (%) | | | $GPS$ (%) |
|---|---|---|---|---|
| | $H_{m0}$ | $T_e$ | $D_p$ | |
| ERA5-ST6-2-Komen-2-10m | -14.5 | 4.4 | -6.0 | -7.4 |
| ERA5-ST6-2-ST6-3-20m | 9.1 | 4.3 | -4.4 | 6.7 |
| ERA5-WES-2-WES-3-20m | -26.1 | 0.8 | -18.9 | -16.4 |
| NWW3-ST6-1-ST6-3-20m | 16.8 | 7.8 | 3.0 | 13.0 |
| NWW3-ST6-2-Komen-2-05m | 3.0 | 11.8 | 9.6 | 6.5 |
| NWW3-ST6-2-Komen-2-10m | 3.6 | 12.5 | 9.5 | 7.1 |
| NWW3-ST6-2-ST6-2-20m | 22.1 | 14.9 | 7.4 | 19.0 |
| NWW3-ST6-2-ST6-3-05m | 20.4 | 9.3 | 6.3 | 15.9 |
| NWW3-ST6-2-ST6-3-10m | 20.7 | 10.8 | 6.4 | 16.6 |
| NWW3-ST6-2-ST6-3-20m | 21.3 | 13.6 | 6.0 | 17.9 |
| NWW3-ST6-2-ST6-3-30m | 21.6 | 15.5 | 6.0 | 18.8 |
| NWW3-ST6-40-ST6-3-20m | 20.9 | 13.5 | 6.4 | 17.7 |
| NWW3-ST6-40-ST6-3-60m | 19.9 | 18.3 | 6.0 | 18.7 |
| NWW3-WES-2-WES-2-20m | -6.1 | 12.6 | -5.5 | 0.5 |

## 4.4 Final settings for WCWI-v5 and WCWI-v6

After gathering and processing the wave boundary conditions, topo-bathymetry, and the wind and tidal current forcings in Chapter 3; defining the model domain and spatial discretization (in sections 4.1 and 4.2, respectively); and adjusting and ratifying the physical and numerical formulations, parameters and methods that define and solve the governing equations of the model (through a calibration process described in section 4.3); the complete definition of the model settings for WCWI-v5 and WCWI-v6 was determined. Table 4-6 summarize the most important settings of the SWAN model WCWI-v5 (V5) and WCWI-v6 (V6) (other settings were left as default).

It is important to highlight that the only difference between these two wave models is that one of them, WCWI-v5, did not incorporate the effect of currents, while the other, WCWI-v6, included tidal currents as forcing. Thus, the pure influence of the tidal currents on the wave characteristics can be evaluated fairly when comparing the two wave model results. Also, the settings finally used do not include diffraction, as it is recommended to be considered by IEC (2015). The above, due to the inclusion of this physical process

(diffraction) require a much finer discretization in the regions were this phenomenon occurs, which make impractical long-term simulations (excessive computational cost). Triads, which are required to be included in feasibility and design studies, were also neglected as it inclusion caused instabilities in the model.

Table 4-6 SWAN v5 and v6 set-up summary.

| Physical definitions |
|---|

**State conditions**

Sea level at 2.2 m above chart datum (CD) associated to the mean sea level (as per the tidal data presented in section 3.2).
Topo-bathymetry from WMDEM (see section 3.1).

**Boundary conditions**

2D spectra at 12 locations defined at 1-hour interval (see sub-section 3.5.1).

**Initial conditions**

Stationary computation of the wave spectra based on the wind field.

**Characterization of the source-sink terms**

Wind field from NWW3 (see sub-section 3.6.1).
Tidal currents from the NRCC model (only for WCWI-v6, see section 3.7)
Generation 3 mode using the ST6 physics for parametrization of wind inputs, whitecapping and swell dissipation (a1sds=2.8E-6, a2sds=3.5E-5, U10Proxy=32, AGROW; ZIEGER = 0.00025 with negative wind input, rdcoef=0.04).
Quadruplets: fully explicit computation of the nonlinear transfer with DIA per iteration (iquad=3).

Breaking: Default settings using a constant breaker index (alpha=1.0, gamma=0.73).
Friction: Default settings according to the semi-empirical expression derived from JONSWAP results (Hasselmann et al., 1973).

Triads: neglected (default).

Diffraction: neglected (default).
Turbulent viscosity: neglected for WCWI-v5 (default). Default Computation for WCWI-v6 (tbcur=0.004).

| Numerical definitions |
|---|

**Spatial discretization (mesh)**

Spherical coordinates, unstructured grid (see section 4.2).

**Time discretization**

Time step = 20 min.

**Spectra discretization**

34 frequencies, from 0.0345 to 0.6666 hz (see Table 4-17).

36 directions, 10° spacing (see Table 4-17).

**Constrains**

Maximum number of iterations per time step = 2 (see section 4.3).

For a full description of these and other settings, refer to SWAN (2019a) and SWAN (2019b)

Finally, with respect to the outputs of the models, two types of results were requested, wave parameters and wave spectra. Also, two kind of wave parameters were obtained: global (spectrum sense), and partition parameters (for the first ten partitions). Both kinds of wave parameters were obtained at every node of the mesh (177,945 nodes). In addition, global wave parameters were also requested at every calibration buoy location (see section 3.5), so the calibration and comparison process could be performed faster and more easily. The global wave parameters saved are: $H_{m0}$, $T_e$, $T_{m01}$, $T_{m02}$, $T_p$, $D_m$, $D_p$, $D_{SPR}$, $Q_p$, $P_x$ and $P_y$, while the partition parameters are: $H_{m0}$, $T_p$, $\lambda_m$, $D_p$, $D_{SPR}$, $Q_p$, $S$ (see sub-section 1.4.4 for parameter description).

Directional spectra were requested at every calibration buoy location, 11 locations defined as energetic sites from WCWI-v4 (hotspots or HS, see Table 4-7 and Figure 4-9) and at 231 additional points along the coast at a ~500 m depth. These later additional points could be used in future studies to feed (as wave boundary conditions) local and more spatially resolved numerical models, while spectra at buoys and hotspot locations were used to compare differences on the wave characteristics and power due to the influence of tidal currents.

Table 4-7 Location of the hotspots (HS) selected from WCWI-v4.

| Name | Coordinates | |
| --- | --- | --- |
| | Lon. (°) | Lat. (°) |
| HS-1 | -129.136 | 50.867 |
| HS-2 | -127.562 | 49.921 |
| HS-3 | -133.342 | 53.947 |
| HS-4 | -131.584 | 52.339 |
| HS-5 | -131.401 | 52.199 |
| HS-6 | -127.235 | 49.782 |
| HS-7 | -128.274 | 50.506 |
| HS-8 | -127.938 | 50.154 |
| HS-9 | -132.169 | 52.767 |
| HS-10 | -125.684 | 48.833 |
| HS-11 | -132.752 | 53.261 |
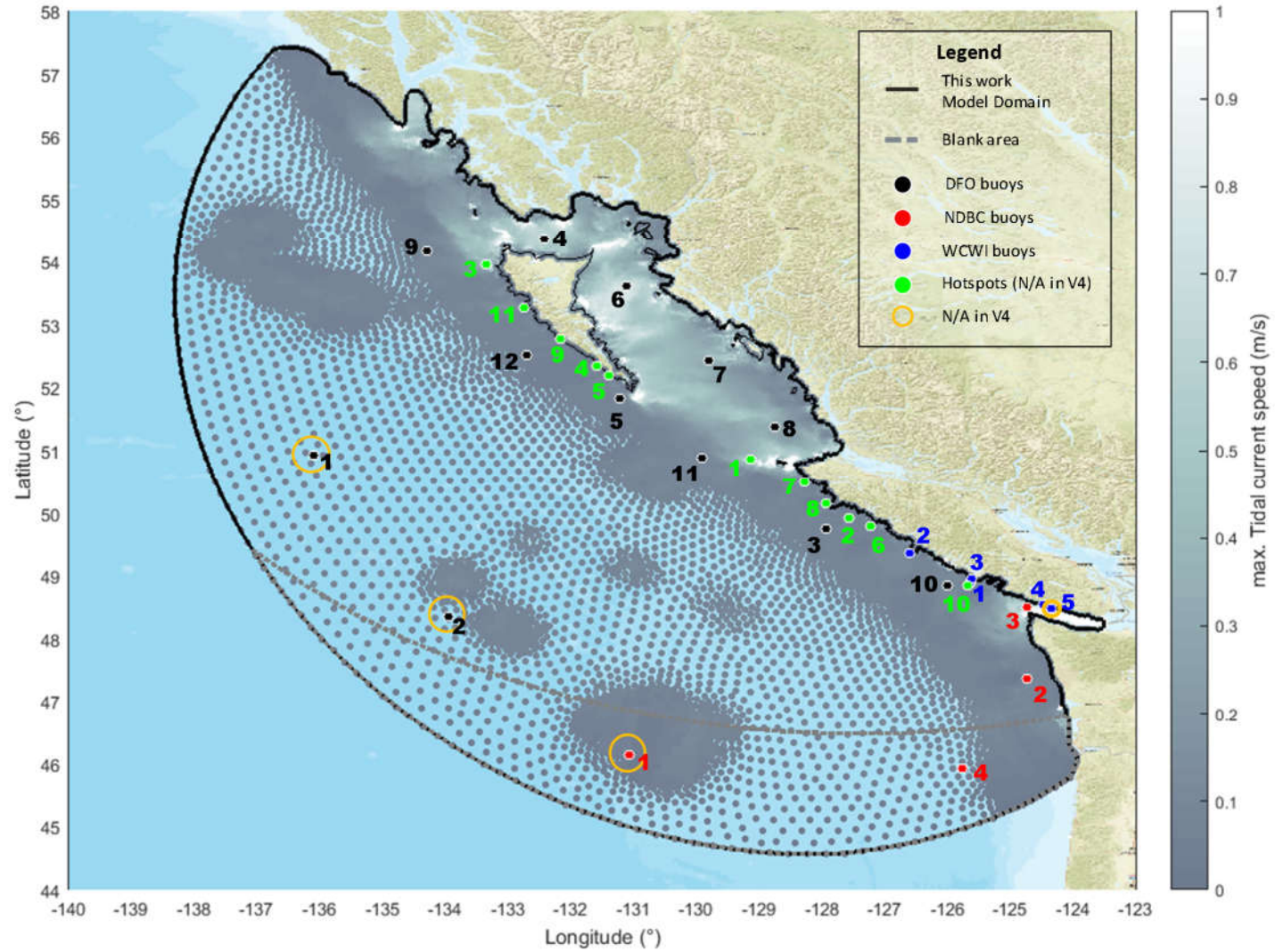
Figure 4-9 Locations where wave spectra was requested (WCWI-v5 and WCWI-v6).

# Chapter 5 Results and discussion

The two models developed in Chapter 4 (settings summarized in section 4.4), and which their only difference is that WCWI-v5 does not include the effect of currents, while WCWI-v6 includes tidal currents as forcing, were run over a period of 14 years, from 2004 to 2017.

This long-term simulation period will allow to consider the variability of the wave resource, critical for the estimation of the energy production and financial viability of a wave energy project, and to estimate the probabilities of the wave characteristics during extreme events with a reduced uncertainty, essential for risk analysis of the survivability of the wave energy converts (WECs).

On the other hand, as discussed in Chapter 1, there is evidence that tidal currents can greatly influence the wave resource, and many authors, including the wave resource assessment standard (IEC, 2015), recommend including them when their influence is likely to be significant. The similarities of the two models, developed and run in this work, enable the evaluation of the pure influence and significance of the tidal currents on the wave resource, which to the authors knowledge, is done for the first time for the B.C. coast.

It is also crucial to evaluate the performance of the models, and estimate the uncertainty of their results. This was carried out using the performance metrics described in sub-section 4.3.2 ($GPS$, $LPS$ and $VPS$) and the error metrics presented in sub-sections 2.3.2 and 2.3.3 ($m$, $\delta$, $\sigma$, $u_p$).

The following sections present the most important results, and their discussion, of this work. A performance analysis and validation of the wave models WCWI-v5 and WCWI-v6 can be found in sections 5.1 and 5.2, respectively. A descriptive analysis of the wave characteristics and power is presented in section 5.4, and a comprehensive investigation to quantify the tidal currents influence on the wave resource (by comparing the results from WCWI-v5 and WCWI-v6) is delivered in section 5.3.

## 5.1 Performance analysis

Both of WCWI-v5 (V5) and WCWI-v6 (V6) were compared against WCWI-v4 (V4) using the whole extension of the simulation results (14 years, from 2004 to 2017). This comparison relied on the performance metrics described in sub-section 4.3.2: the Global Performance Score ($GPS$), the Local Performance Score ($LPS$) and Variable Performance Score ($VPS$). The $GPS$ and $LPS$ represent the improvement, with respect to V4, in simulating the sea state (characterized by $H_{m0}$, $T_e$ and $D_p$) globally and locally, respectively, while $VPS$ does it for a particular wave parameter at a specific location.

Figure 5-29 presents the $VPS$s for every location and for the three wave parameter considered, $H_{m0}$, $T_e$ and $D_p$. Figure 5-30 shows the summarized performance score for every location ($LPS$), and Figure 5-31 presents the global improvement ($GPS$) and the averaged $VPS$s ($\overline{VPS}$s) for both models, V5 and V6.

As can be observed, V5 and V6 show significantly better performance in comparison to V4, with $GPS$s of 17.7% and 19.9%, respectively. Their better performance is achieved mainly by a substantial increment in their ability to reproduce $H_{m0}$ and $T_e$, with $\overline{VPS}$s of 19.7% and 15.6% for V5, and 20.3% and 20.7% for V6, for $H_{m0}$ and $T_e$, respectively. On the other hand, the models show just a moderate global improvement in representing wave direction, with $D_p$'s $\overline{VPS}$s of 5.0% for V5 and 5.6% for V6. The V5 and V6 models outperform V4 at every location, having $LPS$s ranging from 2.4% to 29.1% for V5, and 6.7% to 31.8% for V6. In general, both models have a superior accuracy in modelling $H_{m0}$, $T_e$ and $D_p$, however, there are few locations where the new models perform worse than V4 in simulating some wave parameters. The V5 model has a slightly poorer representation of $H_{m0}$ and $T_e$ at NDBC-3 and WCWI-1, respectively, with $VPS$s for each of those wave parameters and locations of -2.6% and -0.9%. V6 has a considerably poorer representation for only $D_p$ at just one location (WCWI-4) with a $VPS$ of -9.5%.

The better performance of V6 with respect to V5 can be attributed mainly to its superior global representation of the energy period ($T_e$) with a 5.1% higher $\overline{VPS}$ for $T_e$. The other $\overline{VPS}$s, for $H_{m0}$ and $D_p$, show both a minor improvement of only 0.6% (V6 over V5) for both parameters.

As per the *LPS*s (Figure 5-30), V6 is superior at every location with the exception of DFO-4, where both *LPS*s are virtually equal (13.1% and 12.8% for V5 and V6, respectively). Comparing V5's and V6's *VPS*s show that both have very similar performance in simulating $H_{m0}$. However, greater differences can be noticed when comparing $T_e$ and $D_p$'s *VPS*s. Regarding to $T_e$'s *VPS*s, V6 has a consistent better performance across every location. With respect to $D_p$'s *VPS*, V6 has a superior performance at WCWI-1 and WCWI-2, while V5 has a better performance at WCWI-3 and WCWI-4 (there are only four locations with directional information). The two location where V6's representation of $D_p$ is poorer than V5's are closer to shore than the other two locations where V6 is superior. It is possible that the tidal currents used in the simulations do not represent the current conditions accurately at WCWI-3 and WCWI-4 (and possibly other) locations due to geographical features that are not well represented in the tidal model (e.g. coarseness of the mesh, poor bathymetric information).
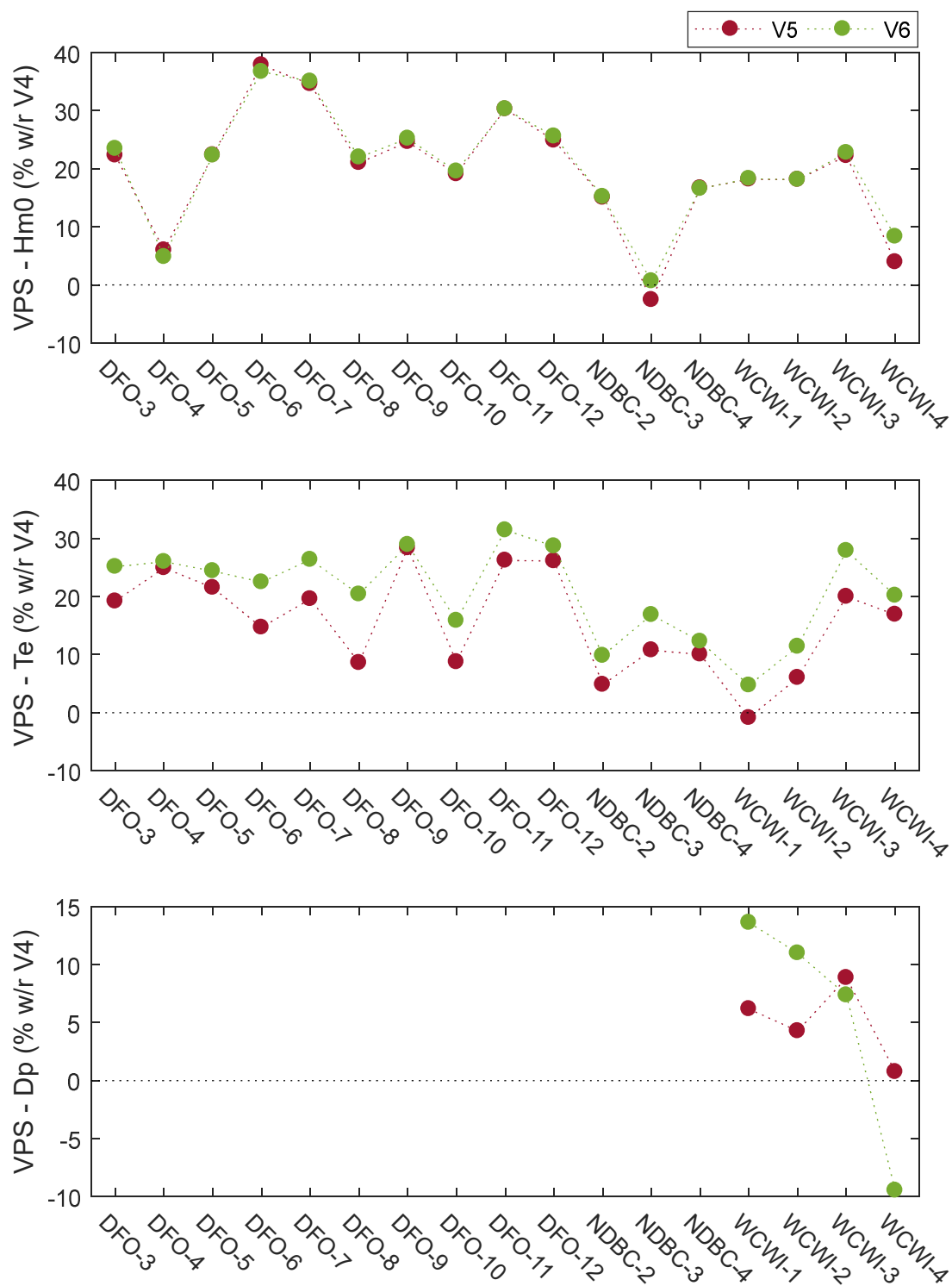
Figure 5-29 Variable Performance Score ($VPS$) for $H_{m0}$, $T_e$ and $D_p$ at every location – V5 and V6.
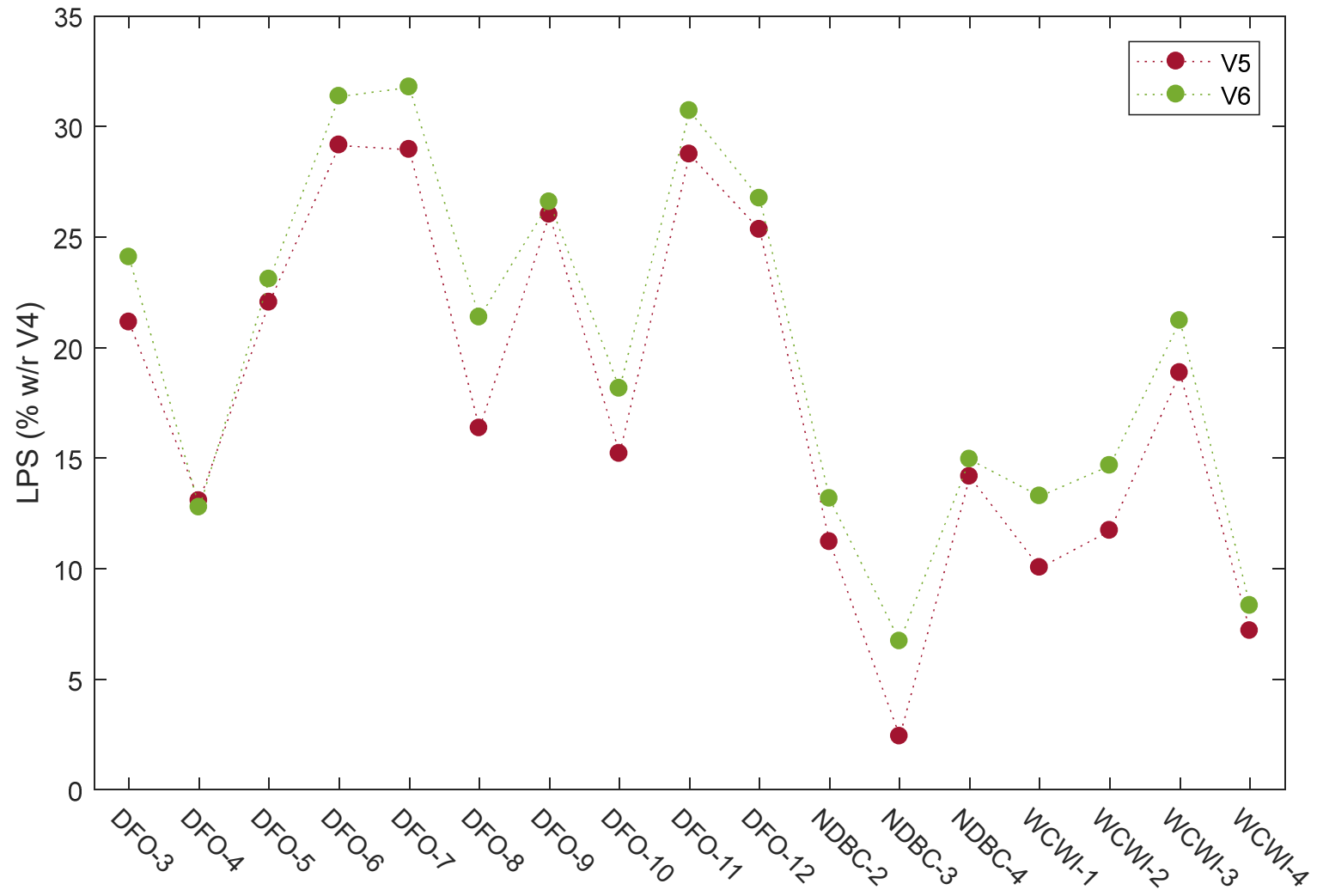
Figure 5-30 Local Performance Score (*LPS*) at every location – V5 and V6.
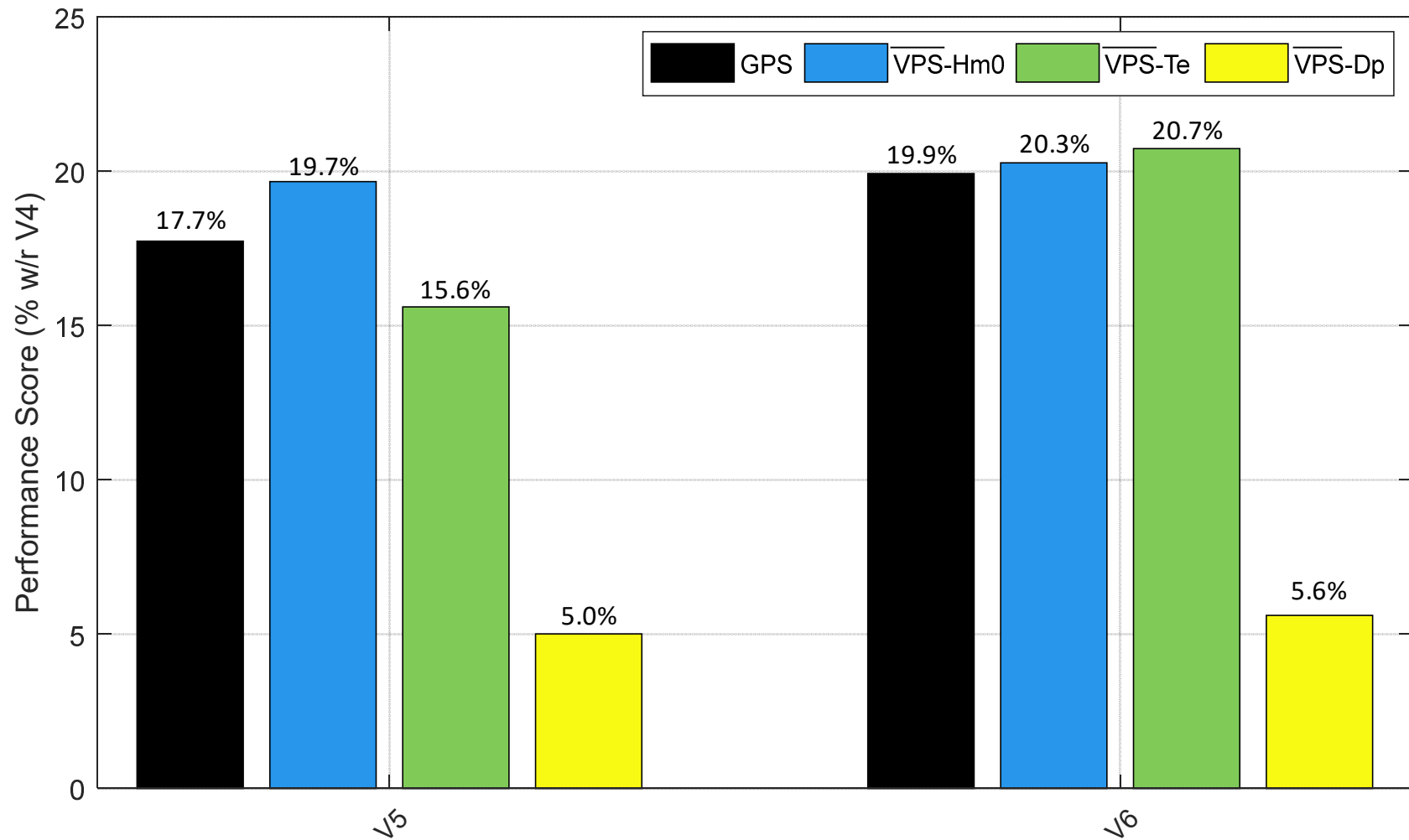
Figure 5-31 Global Performance Scores ($\boldsymbol{GPS}$s) and average Variable Performance Scores ($\overline{\boldsymbol{VPS}}$s) – V5 and V6.

## 5.2 Validation

As presented in section 1.5, the wave resource assessment standards (IEC, 2015) require uncertainty estimates to be provided. Thus, this work utilizes uncertainty estimates to validate WCWI-v5 (V5) and WCWI-v6 (V6). Also, and as discussed in section 2.3, uncertainty of the total error, or the absolute value of it (as has been applied throughout the thesis), is a more convenient performance metric than the many other error characterization metrics presented in the same section. However, some of these other error metrics can give valuable insight about the model performance. Therefore, a set of error parameters and uncertainties were computed to validate the two wave models, V5 and V6.

The error parameters considered are the linear error model parameters $m$, $\delta$ and $\sigma$ (discussed in sub-section 2.3.2). Parameters $m$, $\delta$ can be used to estimate the systematic error ($\varepsilon s$) using Eq. 2.16, or from the model estimate ($y_i$) using Eq. 5.1 (adapted from Eq. 2.15 and Eq. 2.16). The $\sigma$ parameter characterize the random error ($\varepsilon r$). It is an estimate of the uncertainty of $\varepsilon r$ with a confidence level of 68.26% and is also known as the standard uncertainty. Its confidence level is only valid when the $\varepsilon r$ follows a normal distribution.

$$\varepsilon s_i = \left(1 - \frac{1}{m}\right) y_i - \frac{\delta}{m} \qquad \qquad 5.1$$

On the other hand, two uncertainty estimates are provided. The uncertainty of the absolute total error ($|\varepsilon|$) with a 95% confidence level ($u_{95}$), which is used to characterize the total error, and the uncertainty of the random error with a confidence level of 68.26% ($u_\sigma$), used to characterize the random error and to be compare to the standard uncertainty ($\sigma$). These two uncertainties ($u_{95}$ and $u_\sigma$) were computed from the empirical cumulative distribution functions (CDFs), giving a more reliable estimate as the errors do not need to follow any specific parametric CDF.

The wave parameters selected to characterize the sea state for this validation process are $H_{m0}$, $T_e$ and $D_m$, and the computation of the error metrics is provided at every buoy location. Table 5-8, Table 5-9 and Table 5-10 present the error parameters and uncertainty estimates at every location for $H_{m0}$, $T_e$ and $D_m$, respectively. Figure 5-32, Figure 5-33 and

Figure 5-34 show scatter plots of measurements versus modeled wave parameters at the locations with the poorest performance (as per $u_{95}$) in simulating $H_{m0}$, $T_e$ and $D_m$, respectively. See Appendix A for the complete set of scatter plots (at every location and for both, V5 and V6 models).

As expected, and can be noticed from the tables, both models have similar error metrics. Focusing on the $m$ and $\delta$ values, and the actual range of the wave parameters, in general both models tend to underestimate $H_{m0}$, overestimate lower $T_e$ values and underestimate higher $T_e$ values. Also, both models tend to reduce de range of directions.

Regarding to the random errors, $\sigma$ and $u_\sigma$ values are significantly different (at very location and wave parameter considered), implying that $\varepsilon r$s do not follow a normal distribution as typically assumed, and thus, $\sigma$ cannot be used as a measure of the uncertainty. Relative to the total uncertainty, values of $u_{95}$ show that V5 and V6 have relatively small (considering that the confidence level is very high) total error when simulating $H_{m0}$, with a maximum uncertainty of 0.85 m at DFO-5 for both models, and an averaged $u_{95}$ of 0.68 m and 0.67 m for V5 and V6, respectively. The $u_{95}$ values for $T_e$ also show relative small errors, with a maximum of 2.97 s and 2.85 s at WCWI-4, and a mean of 1.77 s and 1.67 s for V5 and V6, respectively. On the other hand, $u_{95}$ values for $D_m$ show significant uncertainty, with maximum and mean values of about 65° and 50°, respectively, for both models.

Table 5-8 Error parameters and uncertainty estimates for $H_{m0}$.

| Location | $m$ (m/m) | | $\delta$ (m) | | $\sigma$ (m) | | $u_\sigma$ (m) | | $u_{95}$ (m) | |
|---|---|---|---|---|---|---|---|---|---|---|
| | V5 | V6 | V5 | V6 | V5 | V6 | V5 | V6 | V5 | V6 |
| DOF-1 | 0.95 | 0.94 | 0.18 | 0.19 | 0.3 | 0.3 | 0.24 | 0.24 | 0.64 | 0.64 |
| DOF-2 | 0.95 | 0.95 | 0.16 | 0.18 | 0.3 | 0.3 | 0.25 | 0.25 | 0.64 | 0.64 |
| DOF-3 | 0.92 | 0.91 | 0.22 | 0.25 | 0.33 | 0.32 | 0.26 | 0.25 | 0.69 | 0.68 |
| DOF-4 | 0.82 | 0.81 | 0.21 | 0.23 | 0.31 | 0.31 | 0.24 | 0.24 | 0.76 | 0.77 |
| DOF-5 | 0.89 | 0.88 | 0.22 | 0.25 | 0.37 | 0.36 | 0.3 | 0.3 | 0.85 | 0.85 |
| DOF-6 | 0.93 | 0.91 | 0.04 | 0.05 | 0.27 | 0.27 | 0.2 | 0.2 | 0.58 | 0.59 |
| DOF-7 | 0.92 | 0.9 | 0.23 | 0.26 | 0.32 | 0.32 | 0.22 | 0.22 | 0.67 | 0.66 |
| DOF-8 | 0.91 | 0.89 | 0.24 | 0.27 | 0.32 | 0.31 | 0.25 | 0.24 | 0.69 | 0.68 |
| DOF-9 | 0.91 | 0.9 | 0.2 | 0.23 | 0.34 | 0.33 | 0.26 | 0.25 | 0.73 | 0.72 |
| DOF-10 | 0.89 | 0.87 | 0.26 | 0.28 | 0.3 | 0.29 | 0.24 | 0.23 | 0.65 | 0.65 |
| DOF-11 | 0.92 | 0.91 | 0.22 | 0.25 | 0.33 | 0.33 | 0.27 | 0.26 | 0.71 | 0.71 |
| DOF-12 | 0.93 | 0.92 | 0.16 | 0.2 | 0.33 | 0.33 | 0.27 | 0.26 | 0.73 | 0.73 |
| NDBC-1 | 0.91 | 0.91 | 0.18 | 0.2 | 0.31 | 0.3 | 0.23 | 0.23 | 0.68 | 0.68 |
| NDBC-2 | 0.89 | 0.87 | 0.24 | 0.26 | 0.3 | 0.3 | 0.24 | 0.23 | 0.69 | 0.69 |
| NDBC-3 | 0.91 | 0.89 | 0.16 | 0.18 | 0.39 | 0.37 | 0.31 | 0.3 | 0.83 | 0.8 |
| NDBC-4 | 0.9 | 0.9 | 0.2 | 0.22 | 0.3 | 0.3 | 0.24 | 0.24 | 0.67 | 0.67 |
| WCWI-1 | 0.88 | 0.86 | 0.27 | 0.28 | 0.27 | 0.26 | 0.2 | 0.19 | 0.61 | 0.61 |
| WCWI-2 | 0.84 | 0.83 | 0.29 | 0.31 | 0.31 | 0.3 | 0.24 | 0.24 | 0.78 | 0.78 |
| WCWI-3 | 0.89 | 0.88 | 0.23 | 0.24 | 0.24 | 0.23 | 0.17 | 0.17 | 0.51 | 0.51 |
| WCWI-4 | 0.95 | 0.92 | 0.12 | 0.16 | 0.21 | 0.2 | 0.17 | 0.16 | 0.47 | 0.45 |
| WCWI-5 | 0.74 | 0.72 | 0.31 | 0.31 | 0.26 | 0.25 | 0.22 | 0.2 | 0.61 | 0.6 |
| **Average** | **0.9** | **0.88** | **0.21** | **0.23** | **0.31** | **0.3** | **0.24** | **0.23** | **0.68** | **0.67** |
| **Max.** | **0.95** | **0.95** | **0.31** | **0.31** | **0.39** | **0.37** | **0.31** | **0.3** | **0.85** | **0.85** |
| **Min.** | **0.74** | **0.72** | **0.04** | **0.05** | **0.21** | **0.2** | **0.17** | **0.16** | **0.47** | **0.45** |

Table 5-9 Error parameters and uncertainty estimates for $T_e$.

| Location | $m$ (s/s) | | $\delta$ (s) | | $\sigma$ (s) | | $u_\sigma$ (s) | | $u_{95}$ (s) | |
|---|---|---|---|---|---|---|---|---|---|---|
| | V5 | V6 | V5 | V6 | V5 | V6 | V5 | V6 | V5 | V6 |
| DOF-1 | 1.03 | 1.02 | -0.7 | -0.6 | 0.54 | 0.53 | 0.48 | 0.48 | 1.3 | 1.3 |
| DOF-2 | 1.01 | 1 | -0.4 | -0.4 | 0.53 | 0.53 | 0.46 | 0.46 | 1.22 | 1.22 |
| DOF-3 | 0.9 | 0.88 | 1.18 | 1.3 | 0.57 | 0.54 | 0.51 | 0.48 | 1.36 | 1.26 |
| DOF-4 | 0.94 | 0.89 | 0.3 | 0.55 | 0.85 | 0.78 | 0.71 | 0.65 | 1.77 | 1.74 |
| DOF-5 | 0.9 | 0.88 | 0.98 | 1.11 | 0.55 | 0.53 | 0.49 | 0.47 | 1.18 | 1.14 |
| DOF-6 | 0.96 | 0.91 | -0 | 0.31 | 1.05 | 0.95 | 0.65 | 0.61 | 2.05 | 1.86 |
| DOF-7 | 0.9 | 0.84 | 1.09 | 1.48 | 0.85 | 0.76 | 0.7 | 0.66 | 1.91 | 1.75 |
| DOF-8 | 0.88 | 0.85 | 1.55 | 1.62 | 0.66 | 0.61 | 0.59 | 0.54 | 1.71 | 1.49 |
| DOF-9 | 0.87 | 0.85 | 1.22 | 1.29 | 0.64 | 0.62 | 0.51 | 0.49 | 1.24 | 1.23 |
| DOF-10 | 0.83 | 0.8 | 2 | 2.12 | 0.66 | 0.62 | 0.54 | 0.51 | 1.69 | 1.56 |
| DOF-11 | 0.92 | 0.89 | 0.88 | 1.01 | 0.52 | 0.49 | 0.47 | 0.44 | 1.14 | 1.06 |
| DOF-12 | 0.93 | 0.9 | 0.71 | 0.85 | 0.53 | 0.5 | 0.46 | 0.44 | 1.11 | 1.07 |
| NDBC-1 | 0.67 | 0.66 | 2.91 | 2.98 | 0.88 | 0.86 | 0.66 | 0.65 | 2.25 | 2.26 |
| NDBC-2 | 0.75 | 0.72 | 2.63 | 2.77 | 0.77 | 0.73 | 0.58 | 0.55 | 1.83 | 1.73 |
| NDBC-3 | 0.8 | 0.78 | 2.03 | 2.14 | 0.71 | 0.66 | 0.59 | 0.54 | 1.68 | 1.56 |
| NDBC-4 | 0.81 | 0.77 | 2.11 | 2.31 | 0.61 | 0.59 | 0.54 | 0.53 | 1.65 | 1.61 |
| WCWI-1 | 0.76 | 0.75 | 2.98 | 2.99 | 0.79 | 0.76 | 0.68 | 0.65 | 2.41 | 2.28 |
| WCWI-2 | 0.76 | 0.75 | 2.63 | 2.64 | 0.66 | 0.63 | 0.59 | 0.56 | 1.86 | 1.75 |
| WCWI-3 | 0.76 | 0.74 | 2.83 | 2.84 | 0.84 | 0.79 | 0.7 | 0.65 | 2.16 | 1.95 |
| WCWI-4 | 0.63 | 0.6 | 3.44 | 3.61 | 1.01 | 0.94 | 0.85 | 0.81 | 2.97 | 2.85 |
| WCWI-5 | 0.74 | 0.72 | 2.33 | 2.38 | 1.08 | 0.95 | 0.87 | 0.76 | 2.66 | 2.43 |
| Average | 0.85 | 0.82 | 1.55 | 1.68 | 0.73 | 0.68 | 0.6 | 0.57 | 1.77 | 1.67 |
| Max. | 1.03 | 1.02 | 3.44 | 3.61 | 1.08 | 0.95 | 0.87 | 0.81 | 2.97 | 2.85 |
| Min. | 0.63 | 0.6 | -0.7 | -0.6 | 0.52 | 0.49 | 0.46 | 0.44 | 1.11 | 1.06 |

Table 5-10 Error parameters and uncertainty estimates for $D_m$.

| Location | $m$ (°/°) | | $\delta$ (°) | | $\sigma$ (°) | | $u_\sigma$ (°) | | $u_{95}$ (°) | |
|---|---|---|---|---|---|---|---|---|---|---|
| | V5 | V6 | V5 | V6 | V5 | V6 | V5 | V6 | V5 | V6 |
| DOF-1 | N/A | N/A | N/A | N/A | N/A | N/A | N/A | N/A | N/A | N/A |
| DOF-2 | N/A | N/A | N/A | N/A | N/A | N/A | N/A | N/A | N/A | N/A |
| DOF-3 | N/A | N/A | N/A | N/A | N/A | N/A | N/A | N/A | N/A | N/A |
| DOF-4 | N/A | N/A | N/A | N/A | N/A | N/A | N/A | N/A | N/A | N/A |
| DOF-5 | N/A | N/A | N/A | N/A | N/A | N/A | N/A | N/A | N/A | N/A |
| DOF-6 | N/A | N/A | N/A | N/A | N/A | N/A | N/A | N/A | N/A | N/A |
| DOF-7 | N/A | N/A | N/A | N/A | N/A | N/A | N/A | N/A | N/A | N/A |
| DOF-8 | N/A | N/A | N/A | N/A | N/A | N/A | N/A | N/A | N/A | N/A |
| DOF-9 | N/A | N/A | N/A | N/A | N/A | N/A | N/A | N/A | N/A | N/A |
| DOF-10 | N/A | N/A | N/A | N/A | N/A | N/A | N/A | N/A | N/A | N/A |
| DOF-11 | N/A | N/A | N/A | N/A | N/A | N/A | N/A | N/A | N/A | N/A |
| DOF-12 | N/A | N/A | N/A | N/A | N/A | N/A | N/A | N/A | N/A | N/A |
| NDBC-1 | N/A | N/A | N/A | N/A | N/A | N/A | N/A | N/A | N/A | N/A |
| NDBC-2 | N/A | N/A | N/A | N/A | N/A | N/A | N/A | N/A | N/A | N/A |
| NDBC-3 | N/A | N/A | N/A | N/A | N/A | N/A | N/A | N/A | N/A | N/A |
| NDBC-4 | N/A | N/A | N/A | N/A | N/A | N/A | N/A | N/A | N/A | N/A |
| WCWI-1 | 0.57 | 0.55 | 115 | 119 | 10.8 | 10.3 | 8.8 | 8.5 | 44.9 | 44.7 |
| WCWI-2 | 0.68 | 0.67 | 86.7 | 89.5 | 11.0 | 10.7 | 9.3 | 8.9 | 42.5 | 42.4 |
| WCWI-3 | 0.59 | 0.58 | 104 | 108 | 15.0 | 14.7 | 8.5 | 8.1 | 39.8 | 40.6 |
| WCWI-4 | 0.41 | 0.38 | 151 | 157 | 11.9 | 10.9 | 8.6 | 7.1 | 55.1 | 58.0 |
| WCWI-5 | 0.45 | 0.44 | 151 | 153 | 17.9 | 16.7 | 8.9 | 8.0 | 64.8 | 65.3 |
| **Average** | **0.54** | **0.52** | **122** | **125** | **13.3** | **12.7** | **8.8** | **8.1** | **49.4** | **50.2** |
| **Max.** | **0.68** | **0.67** | **151** | **157** | **17.9** | **16.7** | **9.3** | **8.9** | **64.8** | **65.3** |
| **Min.** | **0.41** | **0.38** | **86.7** | **89.5** | **10.8** | **10.3** | **8.5** | **7.1** | **39.8** | **40.6** |

**DFO-5 - H$_s$ (m)** (V5)

$\lambda = 0.89$
$\delta = 0.22$
$\sigma = 0.37$
$u_\sigma = 0.30$

**DFO-5 - T$_e$ (s)** (V5)

$\lambda = 0.90$
$\delta = 0.98$
$\sigma = 0.55$
$u_\sigma = 0.49$

**DFO-5 - D$_m$ (°)**

No data available

**DFO-5 - H$_s$ (m)** (V6)

$\lambda = 0.88$
$\delta = 0.25$
$\sigma = 0.36$
$u_\sigma = 0.30$

**DFO-5 - T$_e$ (s)** (V6)

$\lambda = 0.88$
$\delta = 1.11$
$\sigma = 0.53$
$u_\sigma = 0.47$

**DFO-5 - D$_m$ (°)**
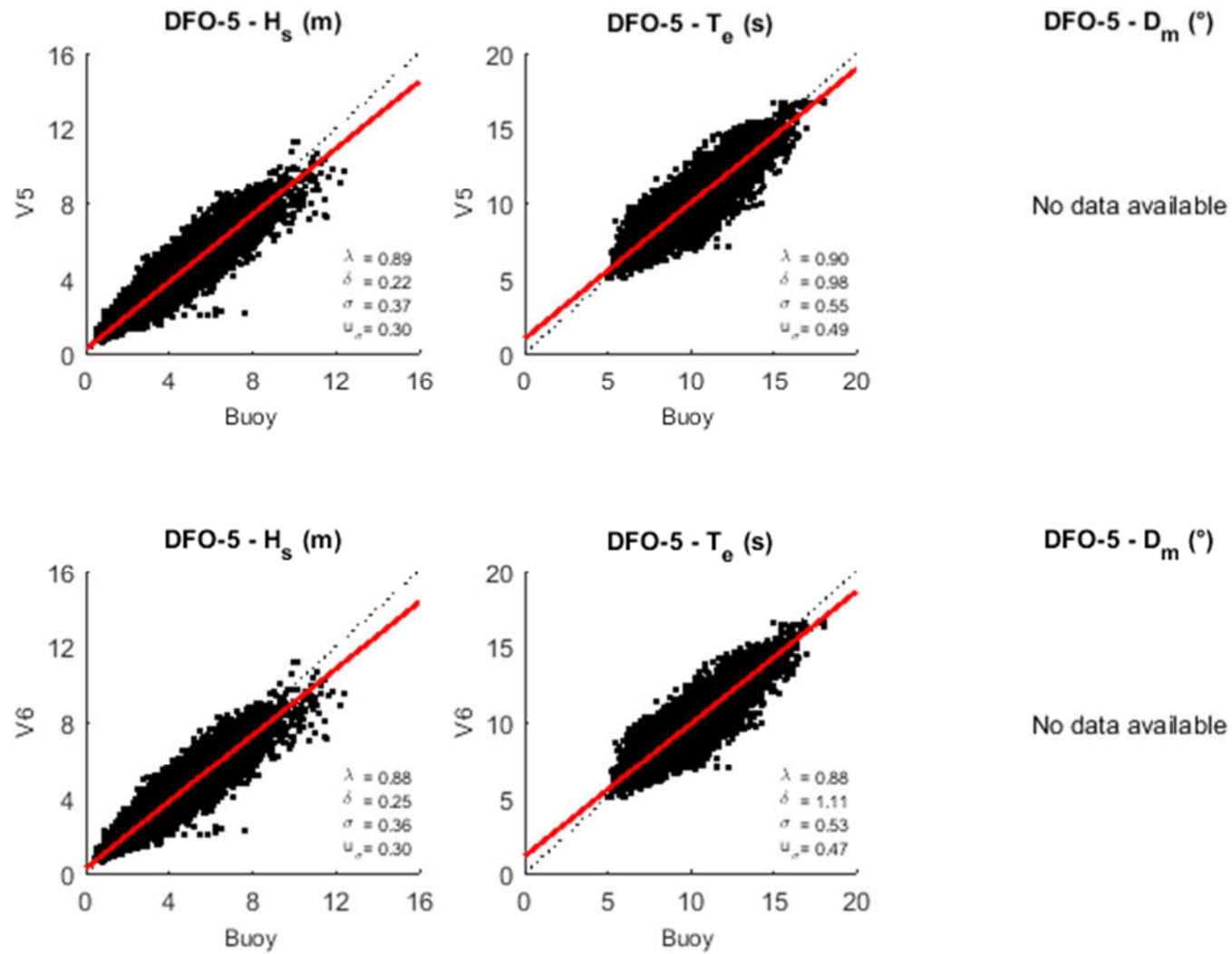
No data available

Figure 5-32 Scatter plots and error parameters for V5 and V6 models, and $H_{m0}$, $T_e$ and $D_m$ at DFO-5 buoy location.
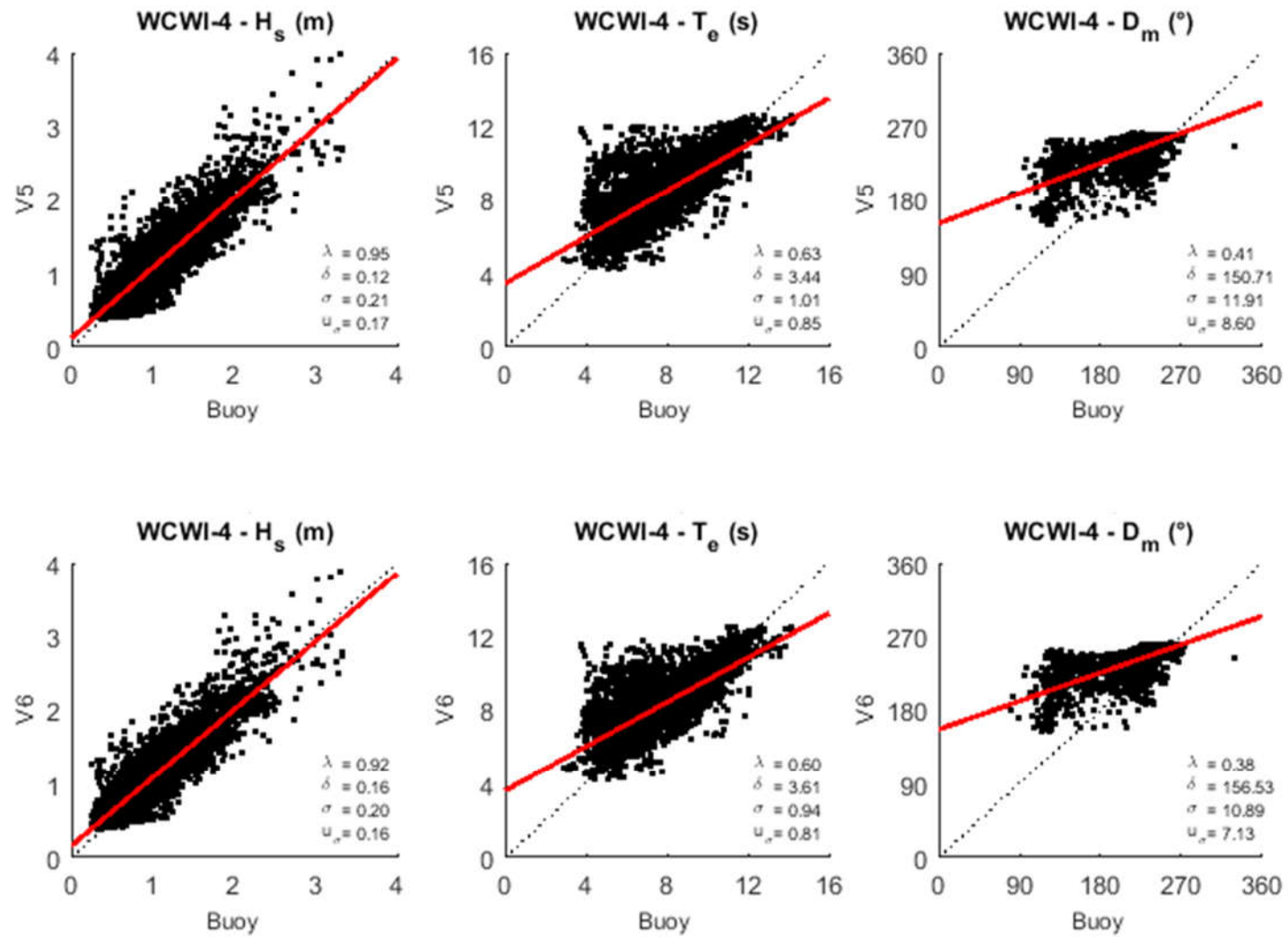
Figure 5-33 Scatter plots and error parameters for V5 and V6 models, and $H_{m0}$, $T_e$ and $D_m$ at WCWI-4 buoy location.
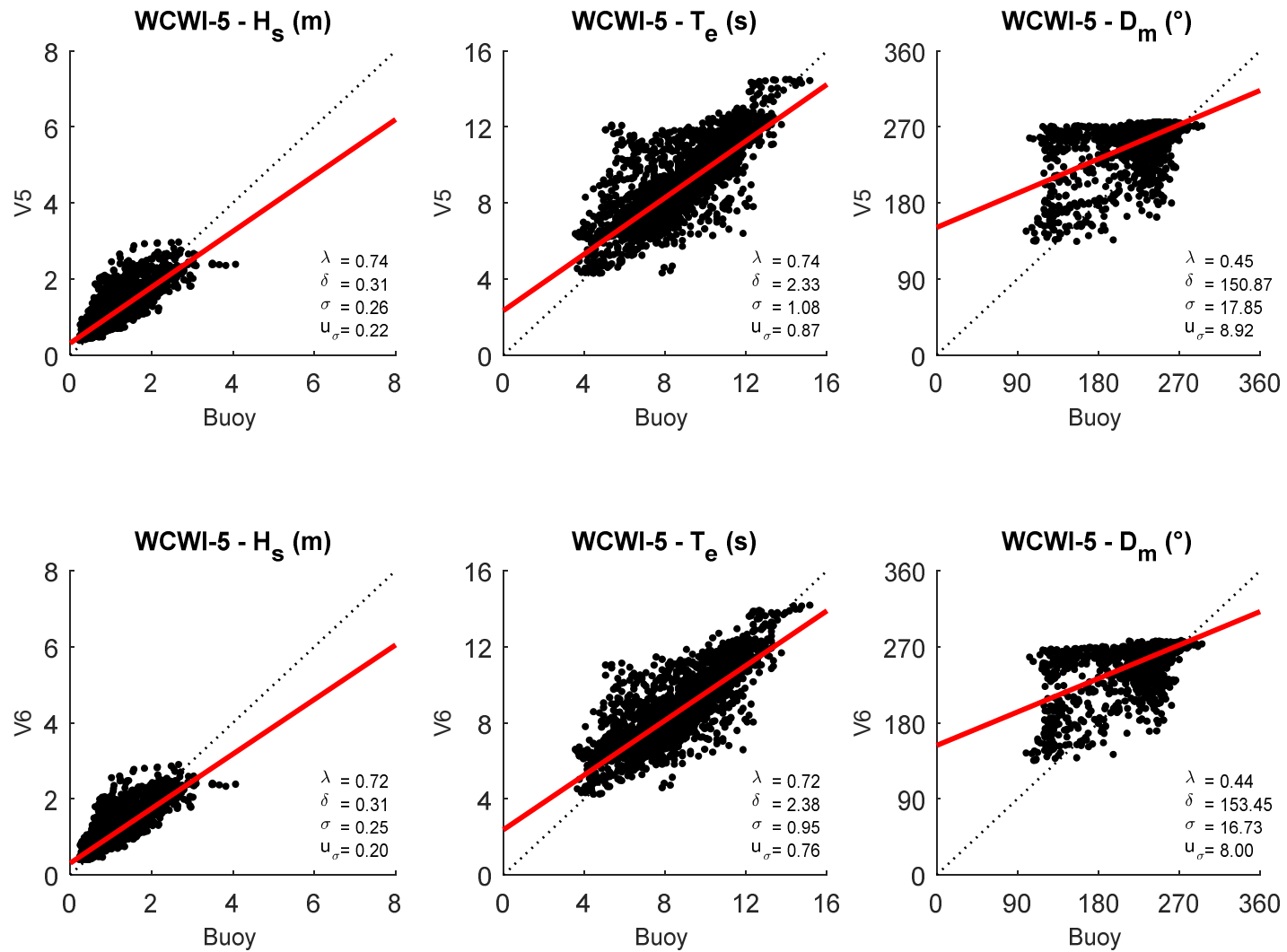
Figure 5-34 Scatter plots and error parameters for V5 and V6 models, and $H_{m0}$, $T_e$ and $D_m$ at WCWI-5 buoy location.

From the scatter plots (see Appendix A for the complete set of scatter plots), it is noticeable that random errors are not equally distributed over the values of the wave parameters. This suggest that a more accurate characterization of the random error, and thus of the total error, can be performed in a piecewise manner. In general, random errors ($\varepsilon r$s) of $H_{m0}$ tend to be significantly smaller at lower values of $H_{m0}$. Uncertainty of $T_e$ usually has its maximum at mid-range, while for $D_m$, $\varepsilon r$s do not follow any general distribution shape throughout the different locations.

It is important to mention that the error metrics used in this work assume that measurements provide the 'true' value of the wave characteristic. Although specification of the measurement instruments (in this case oceanographic buoys) declare very accurate sensors (e.g. <1% for heave, <1% for wave period and ±3° for wave direction for the Triaxys$^{TM}$ buoy used by the WCWI; Axys, 2016. ±0.2 m for wave heights, ±1 s for wave periods and ±10° for wave directions in NDBC buoys; NDBC, 2020), and calibration procedures claim very small errors (less than 2% for $H_{m0}$; e.g. Van Essen et al., 2018); accuracy of moored buoys under environmental conditions (e.g. real ocean waves, wind, currents, biofouling formation) is unknown. Moreover, errors in the estimation of some wave characteristics can vary greatly and differently under operational conditions, especially for the wave direction under current and / or wind.

## 5.3 Influence of tidal currents on wave characteristics and power

As discussed in Chapter 1, there is evidence that tidal currents can greatly influence the wave resource, supporting the recommendation of many authors, including the wave resource assessment standard (IEC, 2015), to include them when their influence is likely to be significant.

To characterize the influence of tidal currents on the wave characteristics and wave power, a five stage analysis was conducted, all involving a comparison between the results from WCWI-v5, which does not include currents as forcing, and WCWI-v6, which it does.

First, a global comparison of the wave power density ($P$) over the entire model domain is presented in sub-section 5.3.1. The other four levels of analysis were performed only at the buoy and hotspot locations (see Figure 4-9). The comparison analyses

performed at these specific locations are: (1) scatter plots and error model parameters ($m$, $\delta$ and $\sigma$) comparing different wave parameters; (2) time series of wave parameters showing the biggest positive and negative differences in $P$ between the two models ($\Delta P$); (3) directional wave spectra at the times of the largest positive and negative $\Delta P$; and (4) an investigation on the impact of the wave parameters' differences due to the tidal currents on $\Delta P$; all presented in sub-sections 5.3.2, 5.3.3, 5.3.4 and 5.3.5, respectively.

The wave parameters considered for the scatter plots and time series analysis are the wave power density ($P$), the significant wave height ($H_{m0}$), the energy period ($T_e$), the mean wave direction ($D_m$), the directional spreading ($D_{spr}$), and the peakedness of the wave spectrum ($Q_p$). For the correlation analysis between variables, only $D_m$ was excluded as, although it can be correlated to $\Delta P$, $D_m$ is not associated to changes in the wave spectra that can affect the omnidirectional wave power.

It is important to note that the way in which wave parameters ($P$, $H_{m0}$, $T_e$, $D_m$, $D_{spr}$, $Q_p$ and others), environmental conditions (e.g. currents, wind, tides, biofouling) and mooring systems affect the energy production will be specific to the individual design of each WEC. Thus, in addition to site-specific characterization of the ambient factors, WEC-specific analysis on the energy production and survivability needs to be carried out prior to any wave energy development. Including a more complete representation of the environmental conditions can lead, for instance, to major differences on the estimation of WECs power outputs and mooring tensions, compared to more classical estimations that rely primarily on $H_{m0}$ and $T_e$ to characterize the wave conditions. These and other misrepresentations can seriously impact the viability of wave energy projects. For example, Robertson et al. (2019) found that a more complete ambient characterization could reduce the estimates of the mean power production by 11.6%, increase the maximum production by 328%, and decreased the mean and maximum mooring tensions by 182% and 729%, respectively.

In addition to the sensitivities of wave energy technologies to a full range of ambient conditions, the condensation of fulsome descriptions of complete wave descriptions (a directional wave spectrum) into summary statistical parameters can significantly obscure the true wave conditions and introduce uncertainty in any prediction of technology

performance. However, use of statistical parameters allows researchers to study the wave conditions systematically through a manageable set of variables.

Only figures illustrating results for the comparative analysis of the models at HS-1 are presented in this section (figures for every location are presented in the Appendices). The choice of HS-1 as the example location for presenting the different analysis was taken because this location possesses both, strong tidal currents and an energetic wave climate.

For the following sub-sections, differences between wave parameter are expressed as $\Delta X$, meaning that the wave parameter from WCWI-v6 is subtracted by the same parameter from WCWI-v5 ($X_{v6,t}$-$X_{v5,t}$) at the coincident time $t$, where $X$ is any of the wave parameters considered in the analysis ($P$, $H_{m0}$, $T_e$, $D_m$, $D_{spr}$ and $Q_p$). Absolut values of $\Delta X$ were expressed as $|\Delta X|$.

### 5.3.1 Global comparison of the wave power density

A global comparison of the mean, minimum, maximum, and the 50th, 70th and 90th percentiles of the wave power density ($P$) estimates from WCWI-v5 and WCWI-v6, and their difference ($\Delta P$), are presented in Figure 5-35 and Figure 5-36, respectively. These statistical estimates were computed at every single node of the model domain, considering the whole population of $P$ results over the simulation period.

From Figure 5-35 it can be observed that, in general, $P$ was reduced by the action of tidal currents. This is especially true in deep waters, where contour lines of the mean, and of the different percentiles are displaced offshore (in relation to V5 results). At increasing percentiles, the differences in the contour lines are more prominent, which suggest that bigger differences in $P$ occur in more energetic sea states. These bigger differences get reduced at near-shore locations. Also, for the maximum $P$ values, contour lines from the two models are very similar, suggesting that $\Delta P$ represent a minor percentage during extreme events.

Figure 5-36 shows that, in general, $\Delta P$ are relatively small. This can be observed, for example, from the mean $\Delta P$ values, which are bounded by a very reduced range of about -2.5 kW/m and +2.5 kW/m, and from the 90th percentile of $|\Delta P|$, which present numbers

not greater than 7.5 kW/m. However, there were relatively few extreme events where the tidal currents considerably affected the wave power. The maximum positive $\Delta P$s can exceed 75 kW/m, while the maximum negative $\Delta P$s could reach values of about -140 kW/m in some regions.
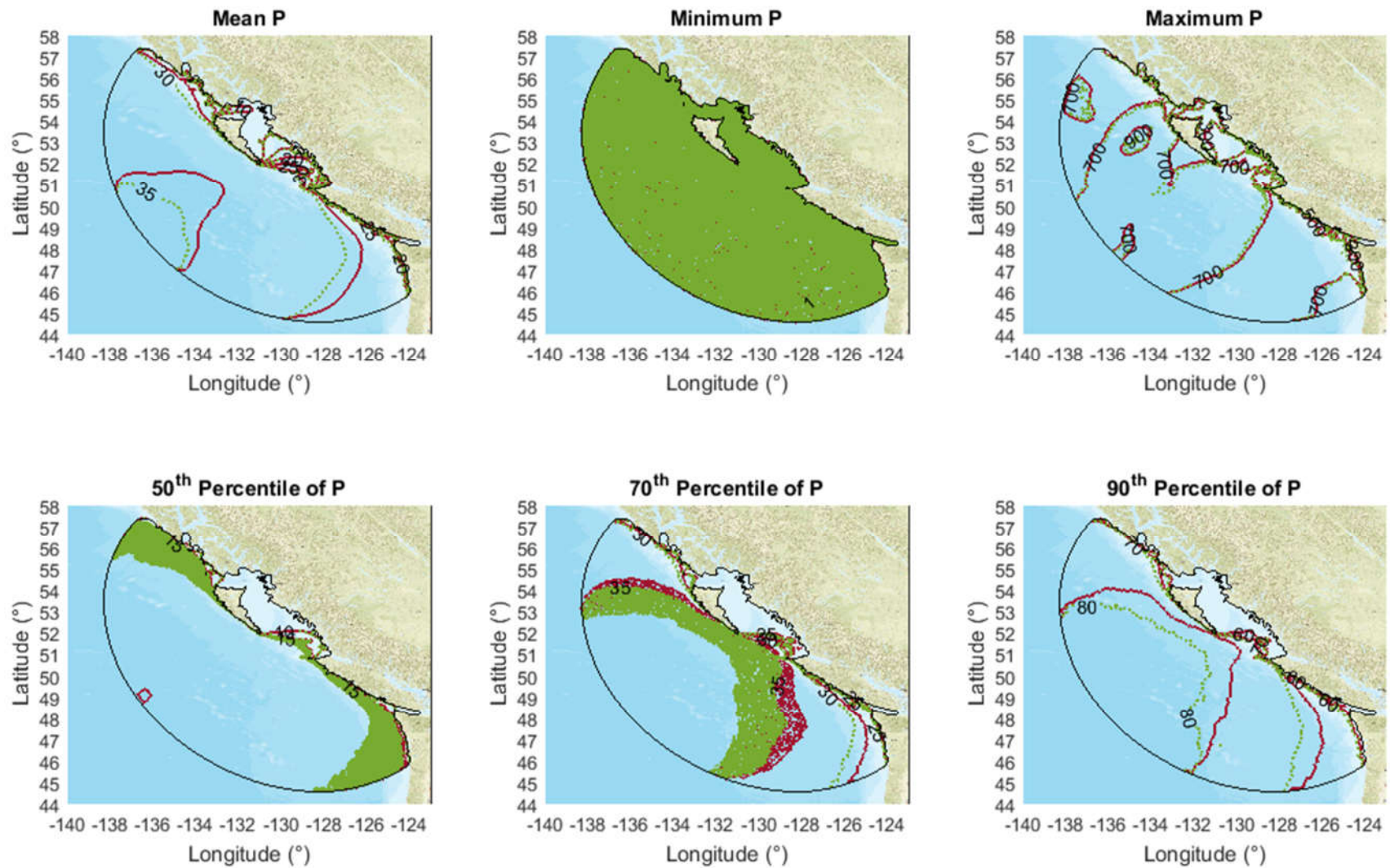
Figure 5-35 Wave power density (in kW/m) over the models domain: V5 (in solid red lines) and V6 (in dashed green lines).
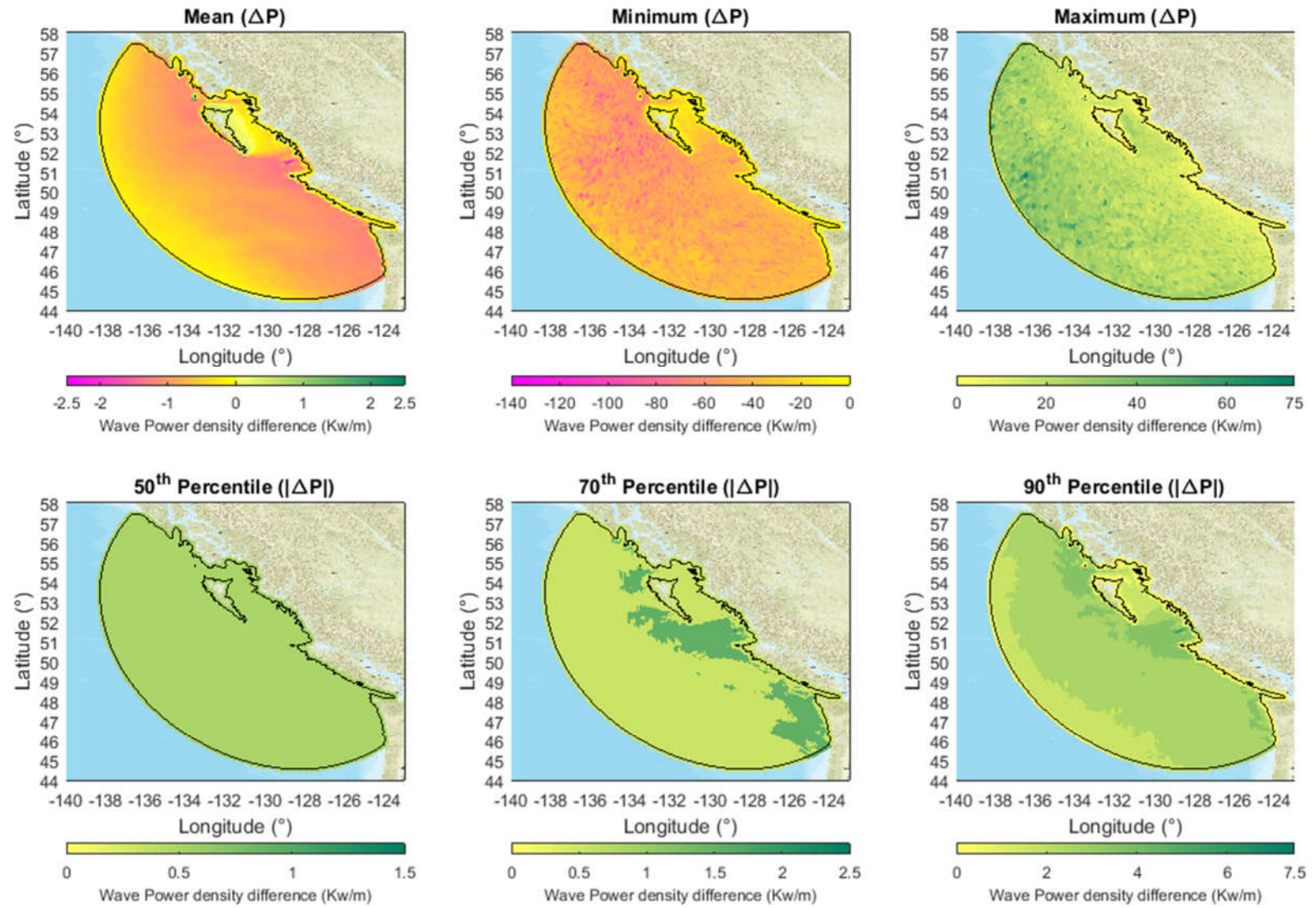
Figure 5-36 Wave power density difference ($\Delta P$) between V6 and V5 over the models domain.

**5.3.2 Local comparison of wave parameters and power: scatter plots**

Comparison between the wave parameters ($H_{m0}$, $T_e$, $D_m$, $D_{spr}$, $Q_p$ and $P$) of the two models at HS-1 is presented in scatter plots in Figure 5-37 (see Appendix B for the complete set of similar figures covering all sites shown in Figure 4-9).

There are several locations were tidal currents induced significant changes on the wave parameters. These locations do not only have strong currents, but also rapid currents occurring over a considerable length of the waves' trajectory (Juan the Fuca Strait: WCWI-4, WCWI-5, NDBC-3; Hecate Strait: DFO-6, DFO-7; Dixon Entrance: DFO-4). With the exception of NDBC-3, these locations are all protected from swell-waves, or at least from a large portion of their directions. At these sites, the scatter plots show considerably higher dispersion (characterized by $\sigma$) and extreme maximum differences between the wave parameters of the two models.

In general, $H_{m0}$ and $P$ are consistently and slightly reduced by the effect of the tidal currents. However, cases with increased $H_{m0}$ and $P$ are not rare, but normally these differences are smaller in magnitude. Both parameters have little dispersion when comparing the results between the two models, even at locations where strong tidal currents can affect waves along a considerable length of their path. At the most extreme case (at WCWI-5), the average reduction in $H_{m0}$ and $P$ did not exceed 4% and 9%, respectively (estimated from the $m$ and $\delta$ values). However, when considering only exposed (to swell-waves) sites, these reductions do not exceed 2% and 5%, respectively.

Contrary to the significant and consistent improvement of V6 over V5 in characterizing $T_e$ at every location (as discussed in the performance analysis found in section 5.1), in general, $T_e$ was barely affected at exposed (to swell-waves) sites. However, at locations in Juan the Fuca Strait, Hecate Strait and Dixon Entrance, low values of $T_e$ were typically increased, and higher values reduced. At the location with the most extreme influence of the tidal currents on this wave parameter (DFO-6), $T_e$ presents the higher dispersion, with $\sigma$ values of up to 0.36 s and extreme $|\Delta T_e|$ values greater than 5 s.

Directions, characterized by $D_m$ and $D_{spr}$, are noticeably more sensitive to the currents, which were able to transform $D_m$ to its opposite direction ($|\Delta D_m| \sim 180°$), and

drove changes in $D_{spr}$ that reached values of up to 40°. Significant changes of these two parameters can also be observed at some exposed site, but these changes are less frequent and reduced in magnitude.

The most sensitive wave parameter to the tidal currents is $Q_p$, which is consistently and significantly reduced by them at every location, spreading the wave height variance of the wave spectra over the frequencies. Although, there are few events at some locations where $Q_p$ increased its value in the presence of currents, these increments are very small and rare over the time frame of the simulation period. At the site with the higher dispersion (DFO-6), extreme $Q_p$ reductions reached values that exceed 2.5.
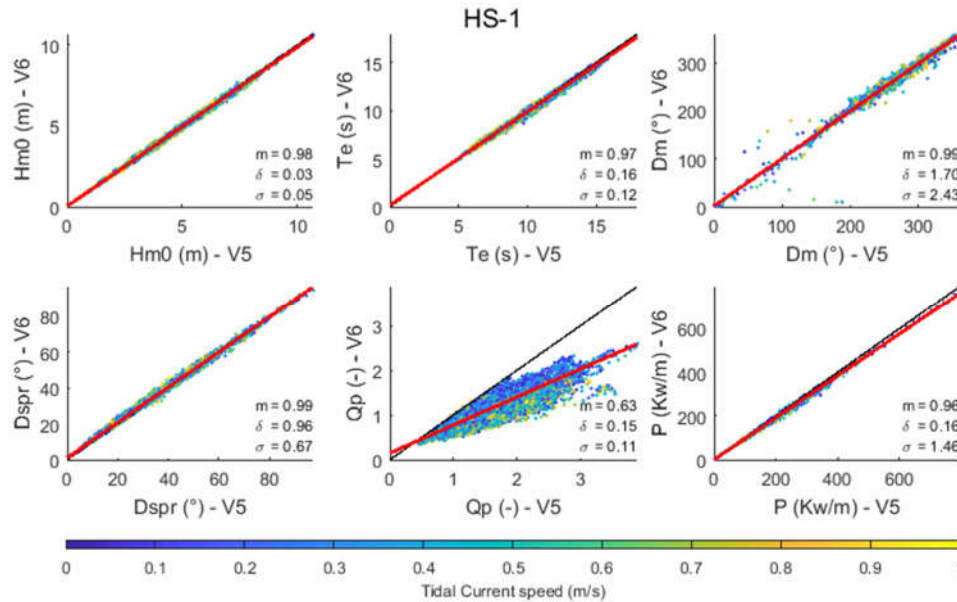


Figure 5-37 Scatter plots for different wave parameters at HS-1 – V6 vs V5.

### 5.3.3 Local comparison of wave parameters: time series semi-centered at the biggest positive and negative difference in wave power density between models

Time series for different wave parameters at HS-1, spanning 5 days and semi-centered at the moment of the biggest positive and negative $\Delta P$ are shown in Figure 5-38 and Figure 5-39, respectively. These figures depict also the tidal currents (TC), and the dot-product between TC and the unit-vector pointing towards the mean wave direction of the travelling waves (w·TC). The former parameter (w·TC) characterize the TC in terms of the

wave direction, with positive values when a component of the TC points towards the mean direction of the travelling waves (having a favorable following currents with respect to the waves). Likewise, w·TC present negative values when the currents oppose waves. The same type of time series for every location can be found in Appendix C .

As can be observed from the figures, the biggest increase in $P$ when including currents, coincide with local peaks of the $\Delta H_{m0}$. Similarly, the biggest decrease in $P$ coincide with local troughs in $\Delta H_{m0}$. Also, the biggest $\Delta P$ generally occur at relatively high $T_e$ values, and when there are considerable differences in $D_{spr}$ and / or $Q_p$, although these former conditions are not always present throughout the different locations. At the maximum positive and negative $\Delta P$, the majority of $\Delta H_{m0}$'s peaks and trough are small, with maximum positive and negative differences among all locations of +0.48 m and -0.56 m, respectively. These small differences could account for important variations in $P$, as can be estimated using the wave power density approximation for deep water waves ($P_0$, see Eq. 1.21) for example. Differences in $T_e$ are also important but in a minor way (as per Eq. 1.21).

On the other hand, tidal currents at the specific location do not seem to present a clear pattern on how they affect the wave parameters. Local peaks and troughs of $\Delta P$ occurs during strong and weak currents, with following and opposing flows (with respect to the waves). The most likely explanation for this is that waves are transformed by the aggregated effect of the currents all along their trajectory, from the offshore boundary of the model domain to the shore, passing through the location where this analysis is being performed. In addition, at every specific location, the sea state is composed by waves traveling with different directions and having different frequencies, thus, the currents along the trajectory of different groups of waves (represented by every single bin in the directional spectrum) are not the same. Therefore, considering how currents induce wave transformations, it is impossible to fully describe the differences on the wave parameters between these two wave models by only considering local current conditions.

Figure 5-38 Time series of wave parameters, wave power and tidal currents including the maximum positive difference in wave power density between V6 and V5 (purple line) at HS-1.
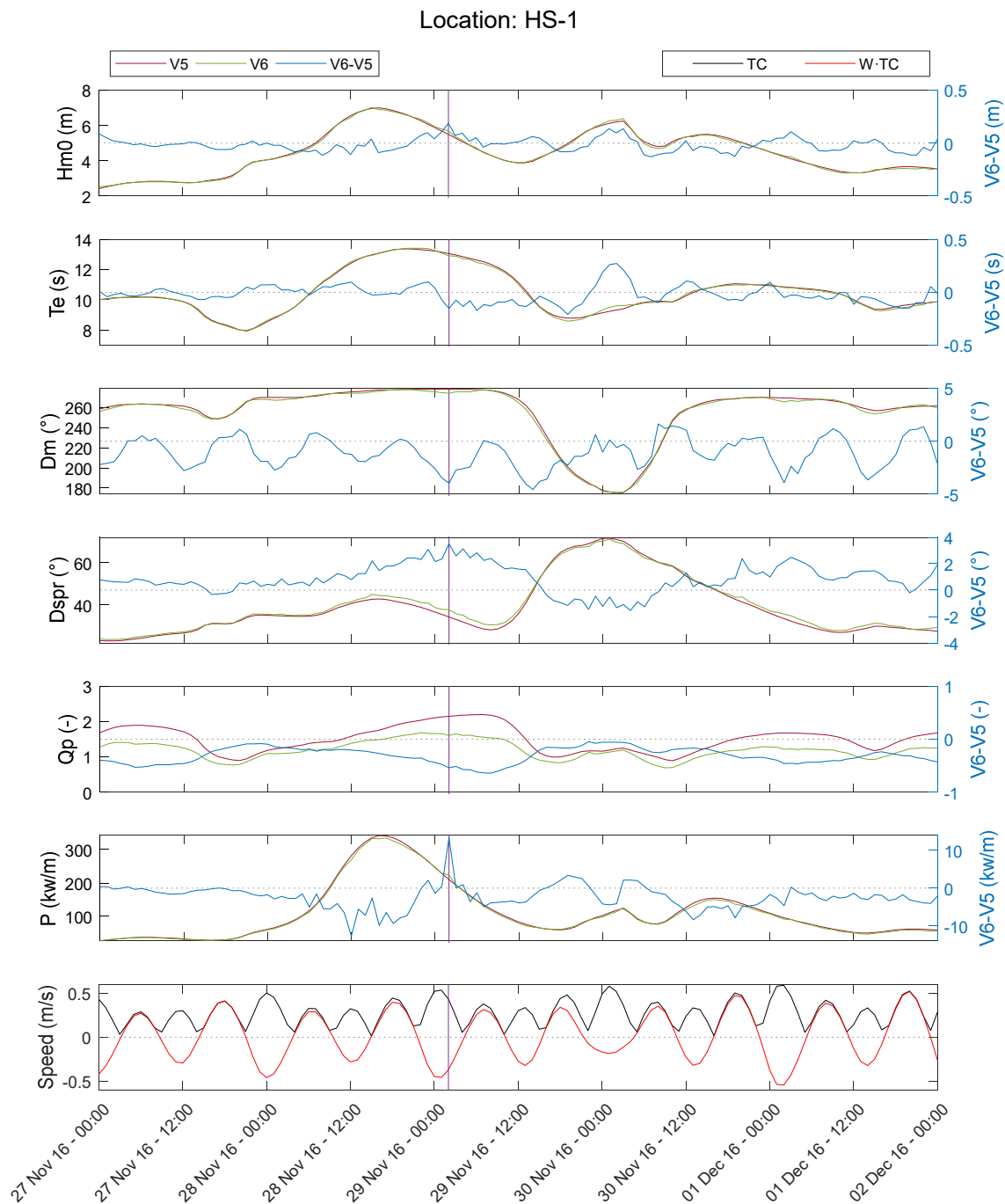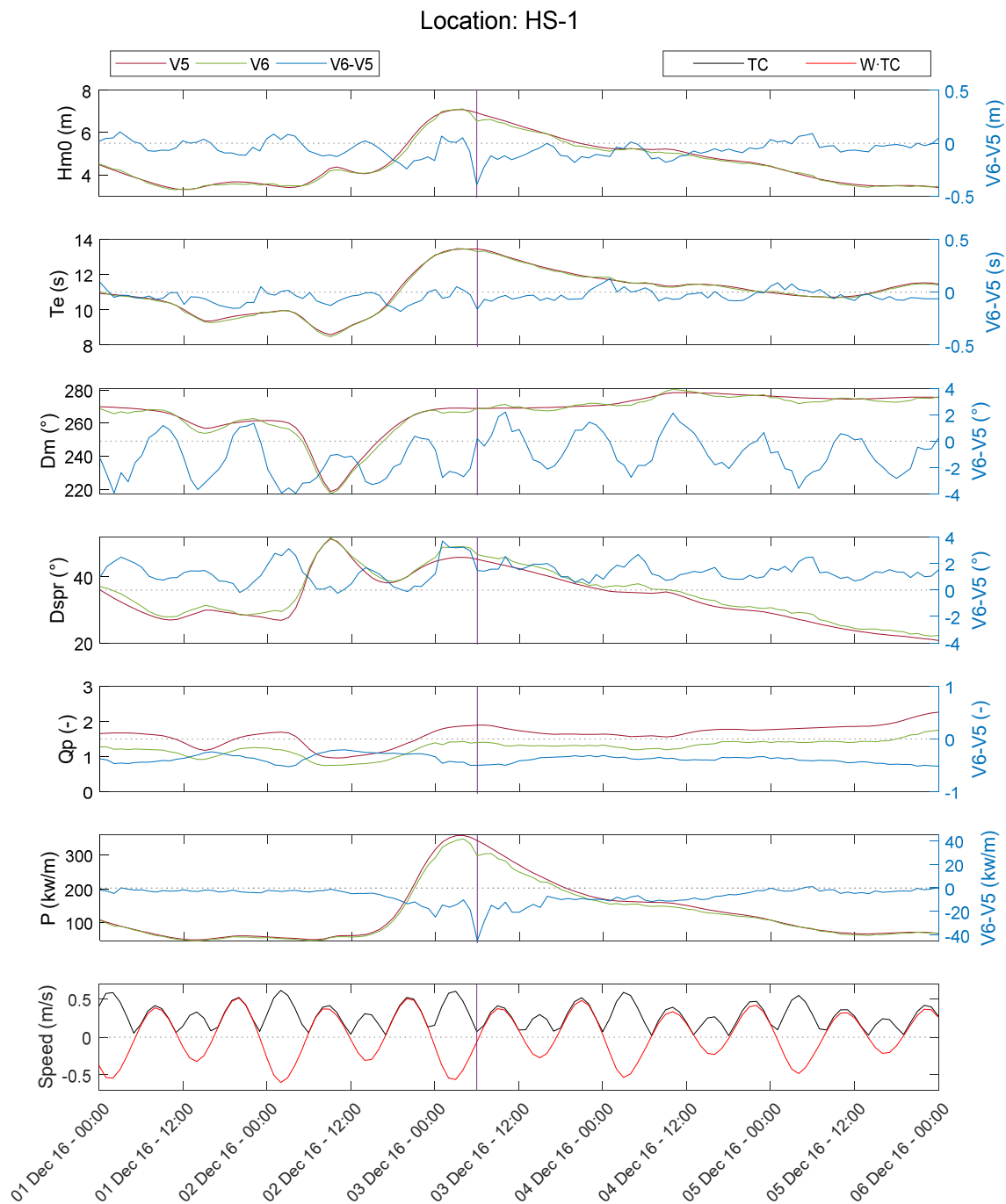
Figure 5-39 Time series of wave parameters, wave power and tidal currents including the maximum negative difference in wave power density between V6 and V5 (purple line) at HS-1.

### 5.3.4 Local comparison of directional wave spectra at the biggest positive and negative differences of wave power density between models

Directional wave spectra for V6 and the difference between the V6's and V5's spectra, at the biggest positive and negative difference between the wave power density ($\Delta P$), for the location HS-1 are shown in Figure 5-40. The same type of figures for every location can be found in Appendix D .

At these specific times (and generally throughout the simulation period as is evidenced by the significant and consistent reduction of $Q_p$), currents have the effect of flattening the peak of the wave spectra. At the maximum increment of $P$, the flattening of the peak is due to a redistribution of the wave height variance over the frequencies and directions near the peak. At the maximum decrement of $P$, the flattening of the peak is still due to a redistribution of the wave height variance over the frequencies and directions near the peak, but also accompanied by a noticeable loss of the total wave height variance. In both cases (maximum positive and negative $\Delta P$), the redistribution and loss of the wave height variance do not follow an easy-to-interpret pattern with the currents at the specific location, as the redistribution of variance occur over increasing and decreasing frequencies and directions, regardless of the magnitude and direction of the local currents.

As discussed in sub-section 5.3.3, the most likely explanation for this is that different groups of waves are affected differently and by different currents along their trajectory. This phenomenon makes it difficult to interpret the differences in the spectral shape by only considering local current conditions.
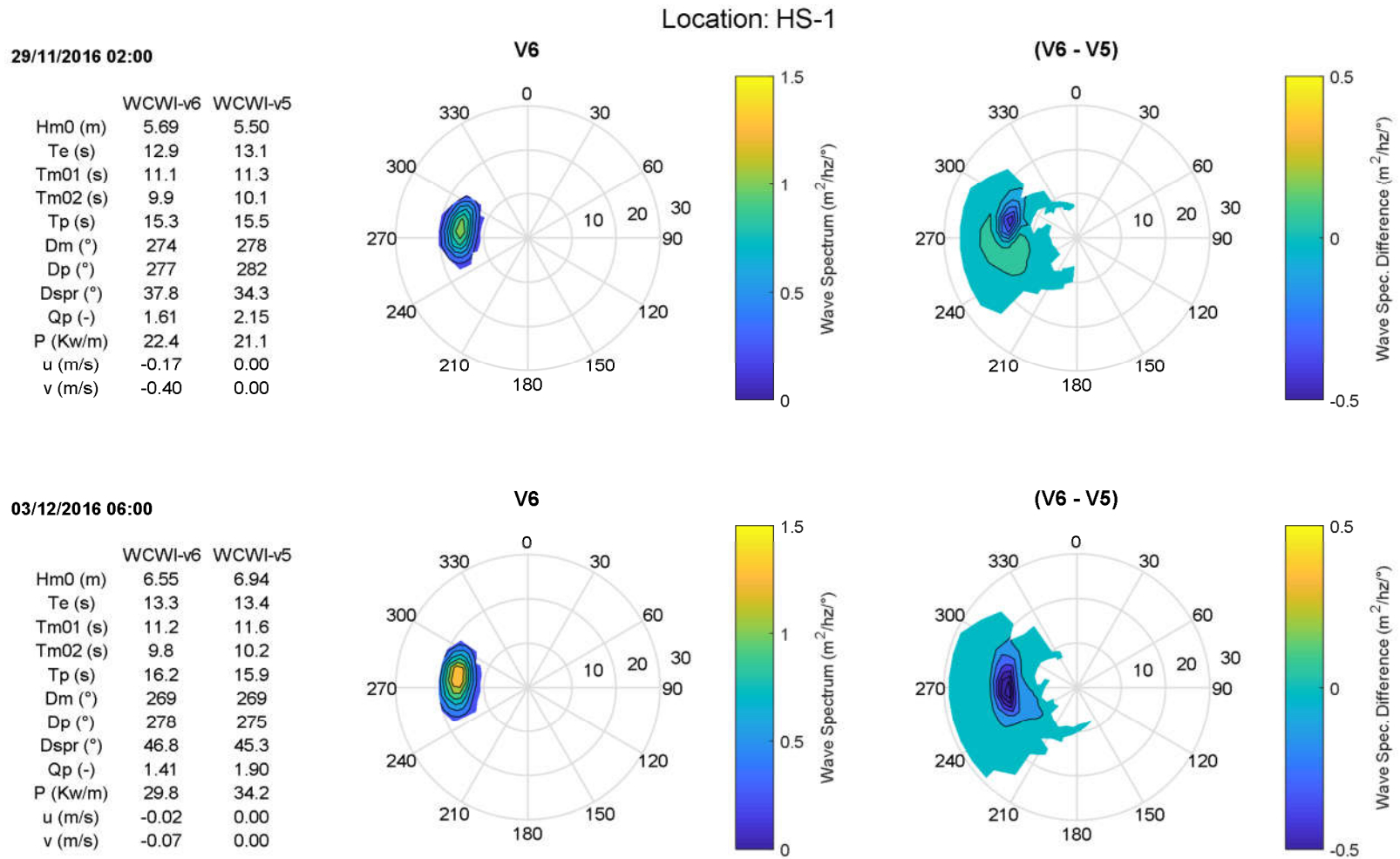
Figure 5-40 V6's wave spectrum, and difference between V6's and V5's wave spectra at the maximum positive (top plots) and negative (bottom plots) difference in wave power density between the two models – HS-1

**5.3.5 Impact of the wave parameters' differences due to tidal currents on the wave power density**

As discussed in sub-section 5.3.3, the biggest differences in $P$ occur at local peaks or troughs of $\Delta H_{m0}$, and at relatively high values of $T_e$. Also, at many locations, significant differences in $D_{spr}$ and $Q_p$ accompany these extreme events, however this is not always the case, and in general, there is no clear relationship between these two wave parameters and $\Delta P$.

To verify the importance of $H_{m0}$, $T_e$ and their respective differences ($\Delta H_{m0}$ and $\Delta T_e$) on how $P$ is modified with the presence of currents, a comparison between $\Delta P$ and $\Delta P_0$ was carried out at every location, and presented in Figure 5-41. From Figure 5-41, it seems clear that $H_{m0}$, $T_e$, $\Delta H_{m0}$ and $\Delta T_e$ account for the major part of $\Delta P$, especially at the locations where the tidal currents are milder (e.g. DFO-1, NDBC-1 and WCWI-3 among others). At locations where tidal currents are stronger (e.g. HS-1, DFO-6, NDBC-3 and WCWI-5), $H_{m0}$, $T_e$, $\Delta H_{m0}$ and $\Delta T_e$ still have an important influence on $\Delta P$, but the scatter plots of $\Delta P_0$ against $\Delta P$ present significant more dispersion, suggesting that other differences in the spectral shape are probably responsible for a considerable part of $\Delta P$.

As presented in sub-section 5.3.3, the other wave parameters, especially $D_{spr}$ and $Q_p$, which characterize important features of the spectrum shape, are significantly impacted, but they do not present an easy-to-interpret effect on $\Delta P$. Thus, to investigate more thoroughly the impact of the difference in $D_{spr}$ and $Q_p$ (and $H_{m0}$, $T_e$ as well), a correlation analysis between $\Delta P$ and an estimated value of $\Delta P$ using neural network ($\Delta P_{nn}$) was performed at HS-1 and presented in Figure 5-42 (same analysis for every location is presented in Appendix E ). The neural networks (NNs) used in each comparison utilize a combination of different wave parameters, and always from both wave models, to get $\Delta P_{nn}$. The NNs employed in this analysis possess three layers. The first layer to receive the input variables (wave parameters), the second layer composed by 30 'neurons', and the third layer which outputs the estimation of $\Delta P$ based on the input variables ($\Delta P_{nn}$).

As can be observed, and already discussed in previous analysis, $H_{m0}$ and $T_e$ and their differences explain the largest percentage of $\Delta P$. The NN based on this two parameters

$(NN(H_{m0}, T_e))$ produce a $\Delta P_{nn}$ with a high linear correlation coefficient ($CC$) of 0.85, but significant dispersion, with a $\sigma$ value of 1.17 kW/m. $NN(D_{spr})$ and especially $NN(Q_p)$ estimate $\Delta P$ very poorly, showing $CC$ values of 0.63 and 0.31, and $\sigma$ values of 1.74 kW/m and 2.13 kW/m, respectively. Surprisingly, $Q_p$, which is the wave parameter that has a more consistent and notorious change in the presence of currents, do not account significantly to explain the wave power changes. However, when $D_{spr}$ and $Q_p$ are separately combined with $H_{m0}$ and $T_e$ to compute $\Delta P_{nn}$ ($NN(H_{m0}, T_e, D_{spr})$ and $NN(H_{m0}, T_e, Q_p)$, respectively), $CC$ gets increased and $\sigma$ gets reduced to the same values, 0.88 and 1.06 kW/m, respectively. This suggest that both wave parameters contribute similarly on explaining $\Delta P$, contrary to what can be extracted when analyzing the correlation and dispersion metrics from $NN(D_{spr})$ and $NN(Q_p)$. The improvement of $NN(H_{m0}, T_e, D_{spr})$ and $NN(H_{m0}, T_e, Q_p)$ on estimating $\Delta P$ is minor compared to the performance of $NN(H_{m0}, T_e)$. When including every wave parameter considered in this analysis into a NN ($NN(H_{m0}, T_e, Q_p, D_{spr})$), correlation and dispersion between $\Delta P$ and $\Delta P_{mm}$, improves slightly, obtaining a $CC$ equal to 0.9 and a $\sigma$ value of 1.00 kW/m.

Considering the results from the previous analysis, it is clear that that $D_{spr}$ and $Q_p$ provide some information on how the wave power is affected by the currents, yet, this information is limited compared to the information provided by $H_{m0}$ and $T_e$. Even though $H_{m0}$ and $T_e$ complemented with $D_{spr}$ and $Q_p$ can explain much of the difference in wave power when currents are present, there is still high dispersion between $\Delta P$ and $\Delta P_{mm}$, suggesting that other features of the wave spectrum shape need to be included to fully explain how the tidal currents affect the sea state, and thus, the wave power.

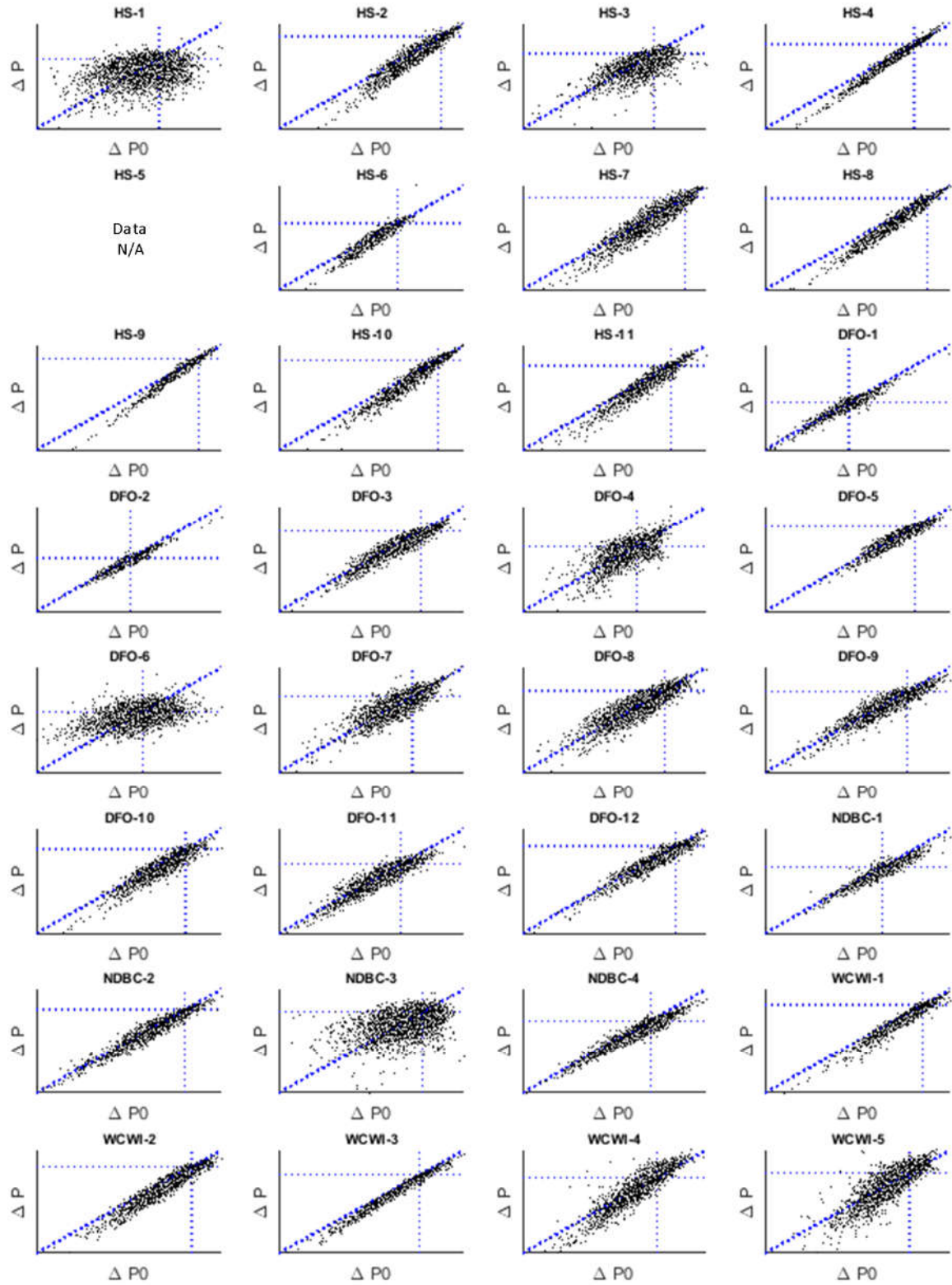Figure 5-41 Comparison between $\Delta P$ and $\Delta P_0$ at every location.
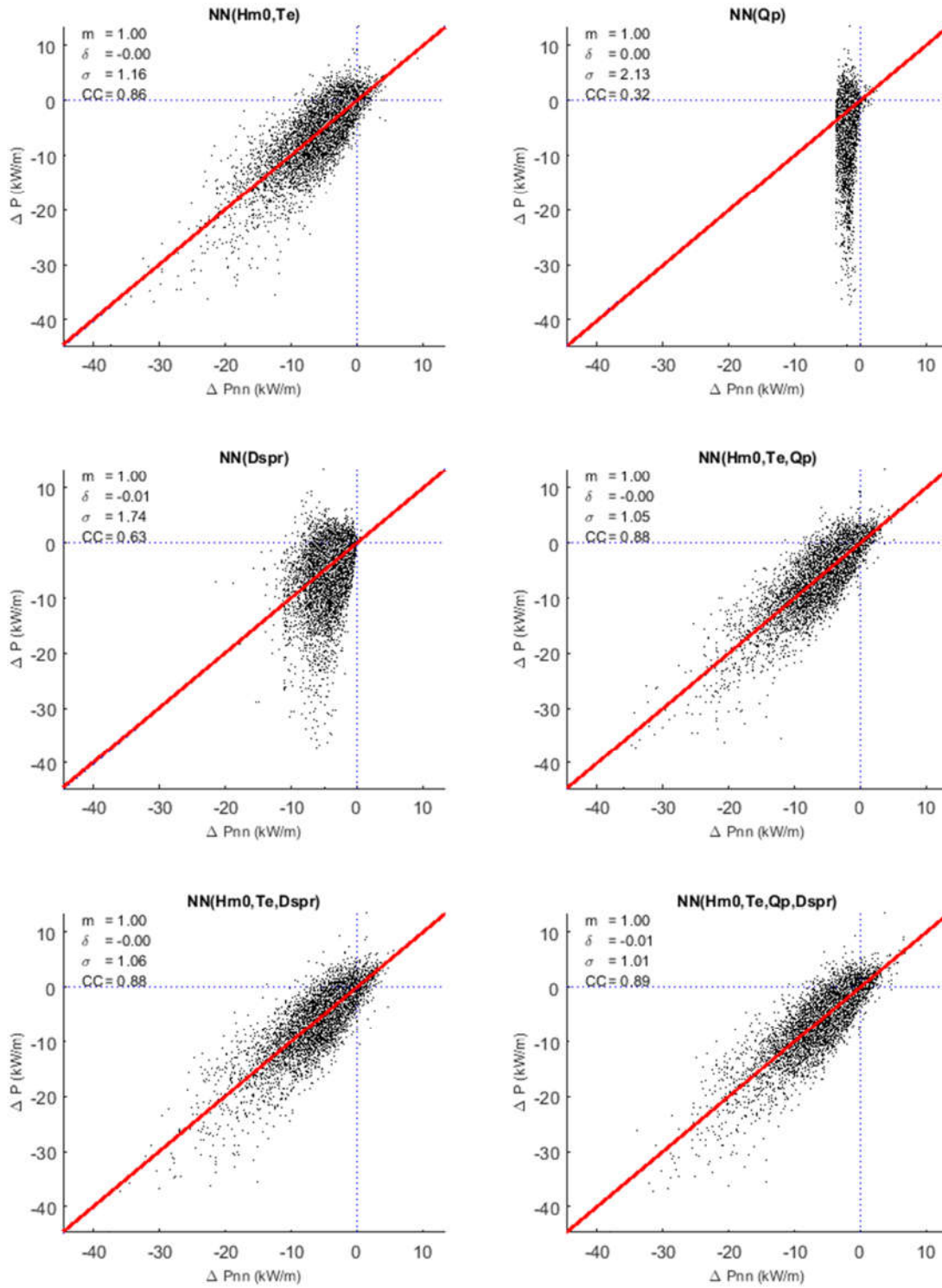
Figure 5-42 Correlation analysis of $\Delta P$ and an estimation of $\Delta P$ using neural networks ($\Delta P_{nn}$) and different wave parameters from both wave models – HS-1.

## 5.4 Wave characteristics and wave power

This section offers a descriptive analysis of a set of statistical values for different wave parameters (including the wave power density) for WCWI-v6.

The choice of presenting results only for WCWI-v6 (V6) is that this model, and according to the performance and validation analysis presented in sections 5.1 and 5.2, respectively, describe better the wave characteristics over the domain than WCWI-v5 (V5). This better description of the wave characteristics over the whole domain is well summarized by the Global Performance Score ($GPS$) and the averaged Variable Performance Scores ($\overline{VPS}$s) computed in section 5.1. The $GPS$ showed a global improvement on the wave resource characterization of about 19.9% for V6, versus 17.7% for V5. The V6's $\overline{VPS}$s for $H_{m0}$, $T_e$ and $D_m$ present improvements of 0.6%, 5.1% and 0.6% over the V5's $\overline{VPS}$s, respectively.

Thus, Figure 5-43, Figure 5-44 and Figure 5-45 present statistical values over the whole domain for $H_{m0}$, $T_e$ and $P$, respectively. Figure 5-46 to Figure 5-51 depict the empirical probability distribution functions (PDFs) and cumulative distribution functions (CDFs) for the significant wave height ($H_{m0}$), the energy period ($T_e$), the mean wave direction ($D_m$), the directional spreading ($D_{spr}$), the peakedness of the wave spectrum ($Q_p$) and the wave power density ($P$) (see sub-section 1.4.4 for a full description of each of these parameters).

The choice of these parameters is associated to the major characteristics of the sea state that they represent, and which can greatly affect the energy production and survivability of WECs. However, for the evaluation of a particular wave energy project, the characterization of other wave parameters might be necessary.
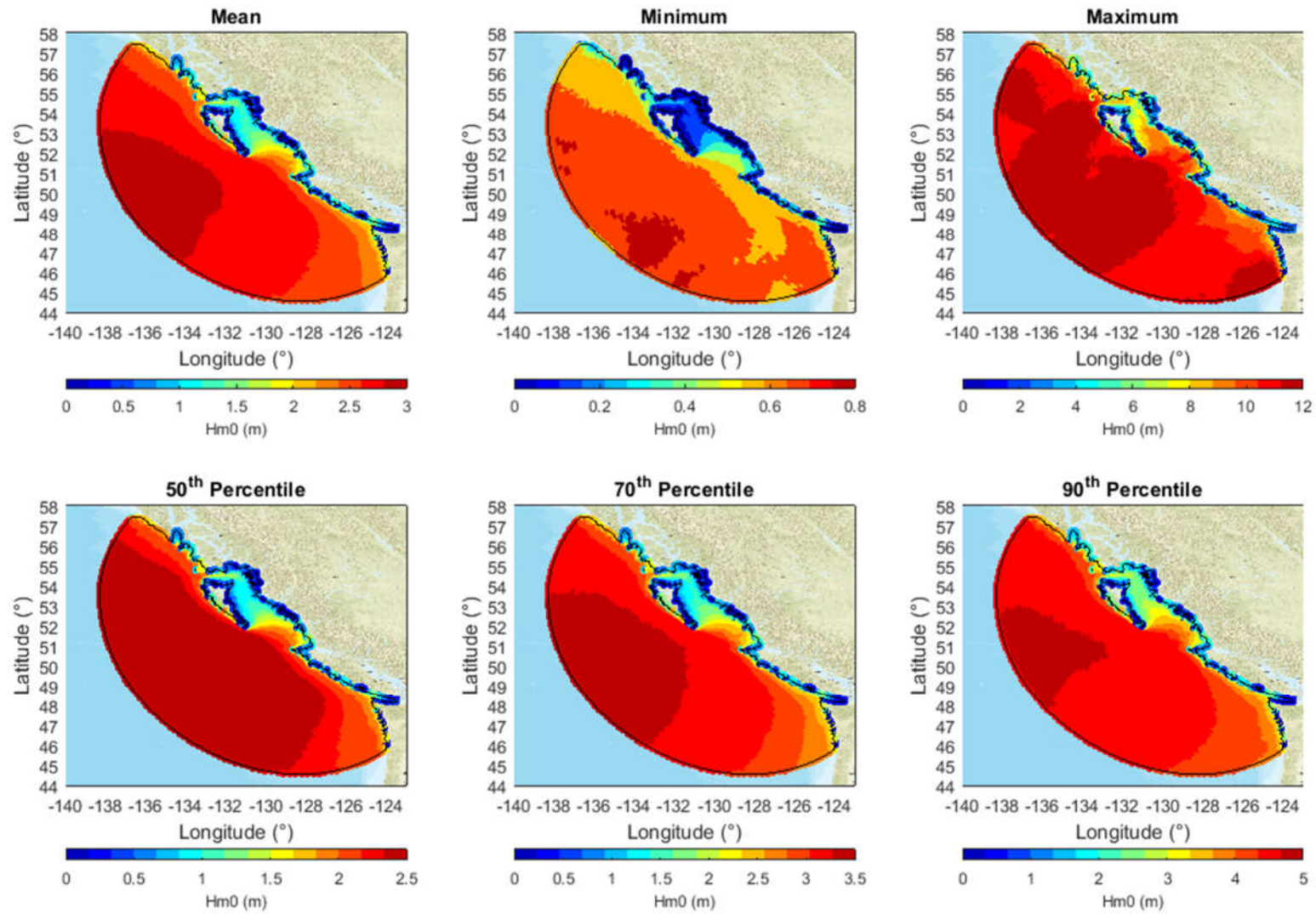
Figure 5-43 Statistical values of $H_{m0}$ over the whole domain – WCWI-v6.
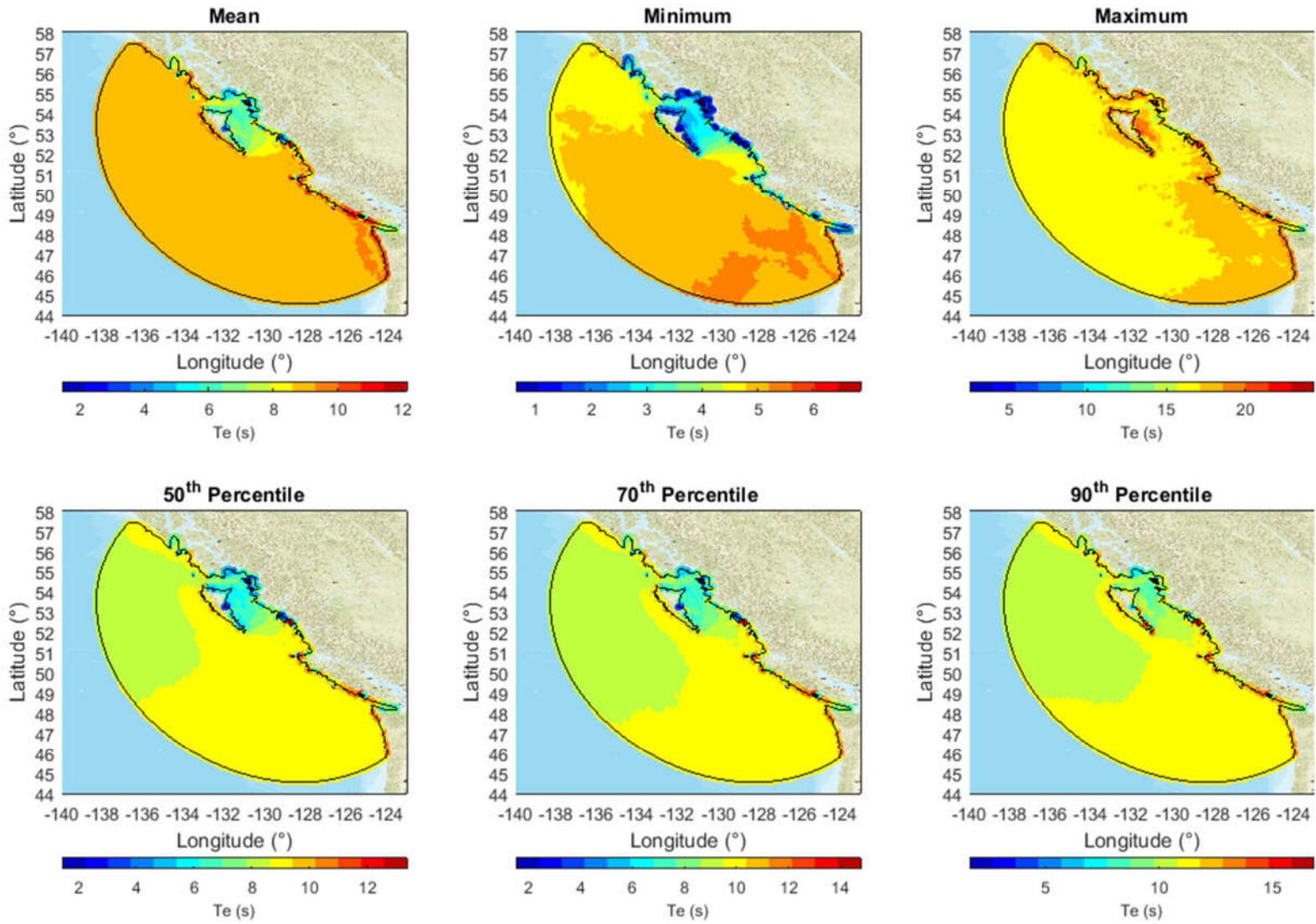
Figure 5-44 Statistical values of $T_e$ over the whole domain – WCWI-v6.
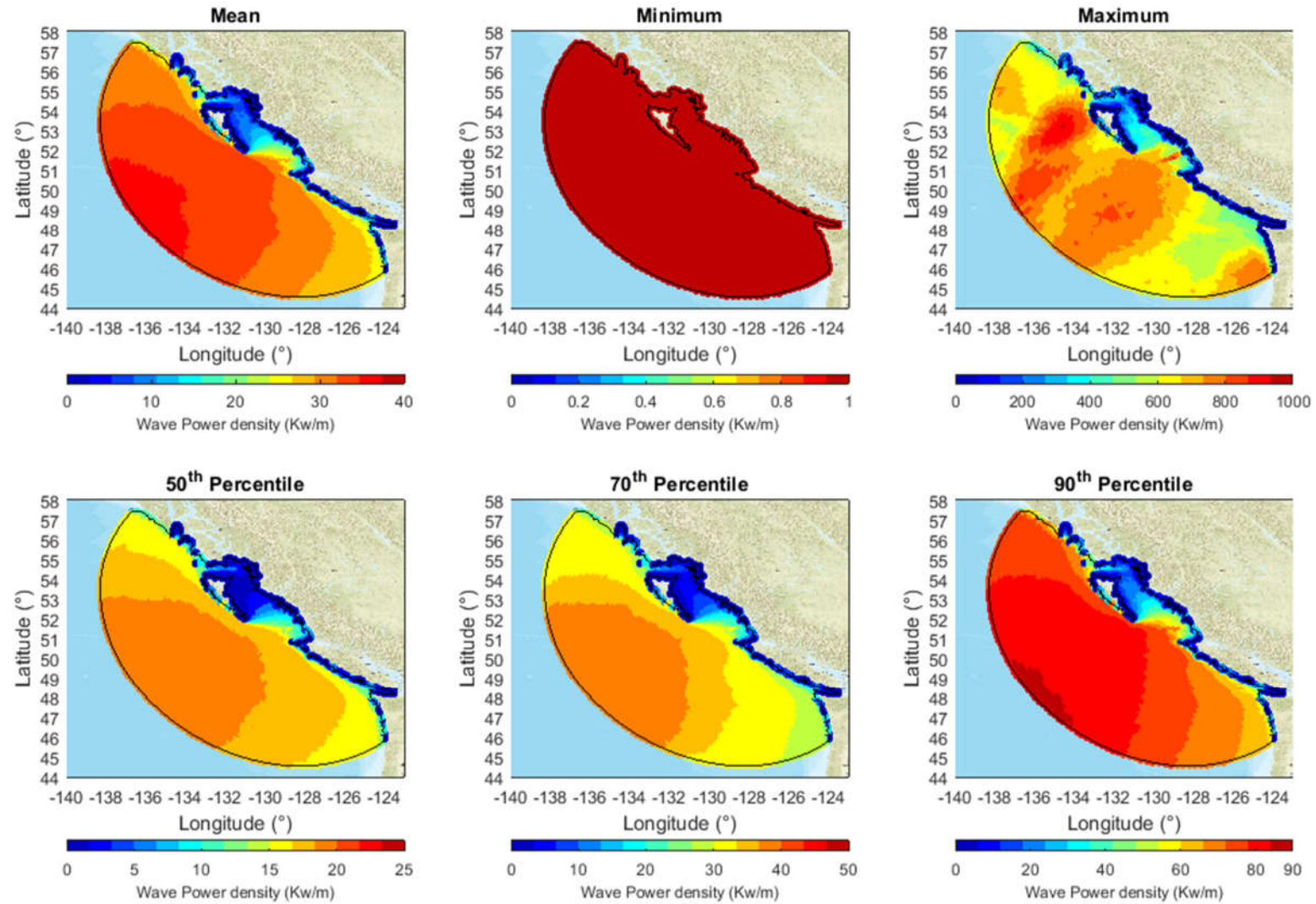
Figure 5-45 Statistical values of *P* over the whole domain – WCWI-v6.
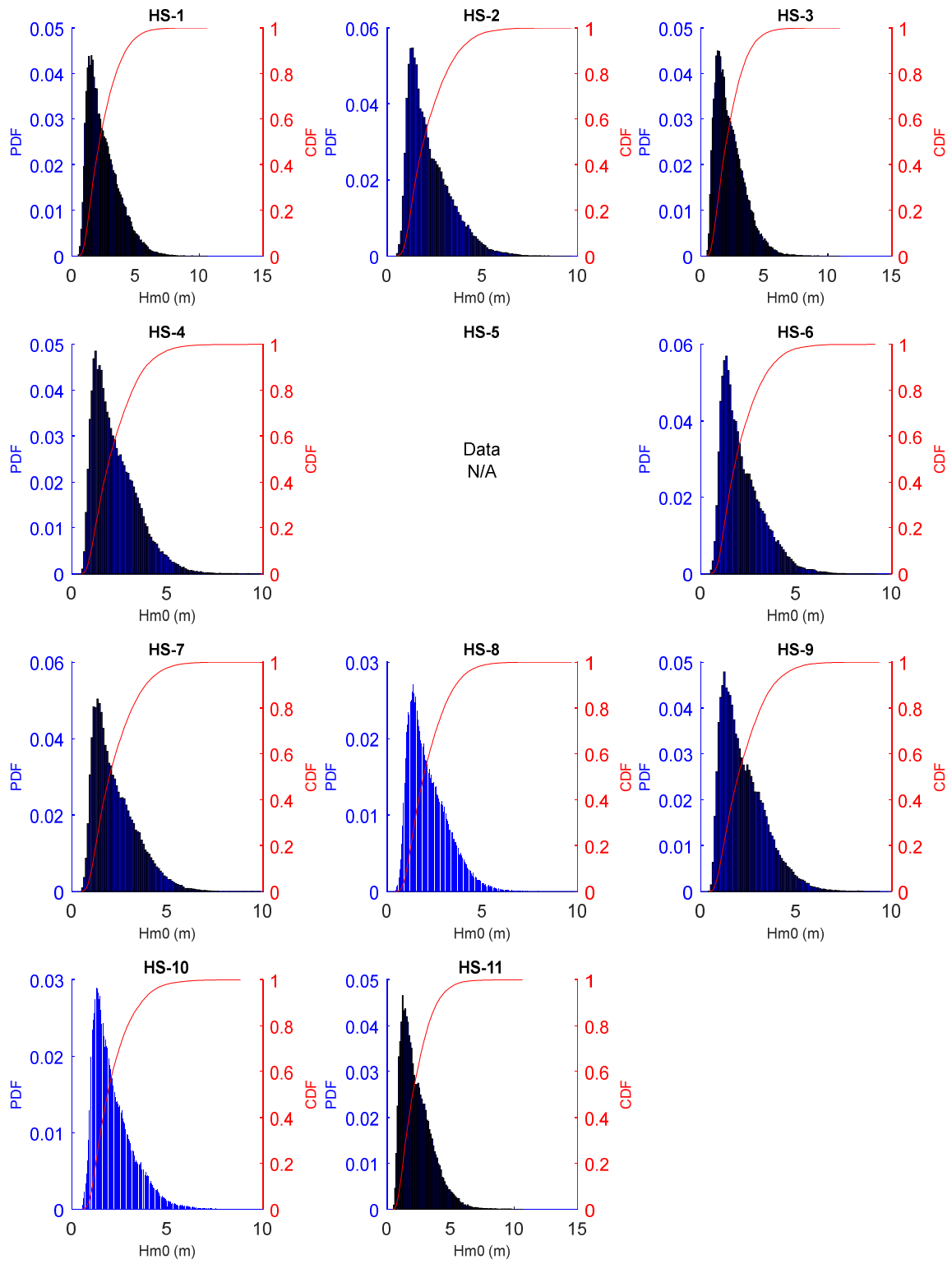
Figure 5-46 Empirical probability distribution function (PDF) and empirical cumulative distribution function (CDF) for $H_{m0}$ at different hotspots (HS) locations.
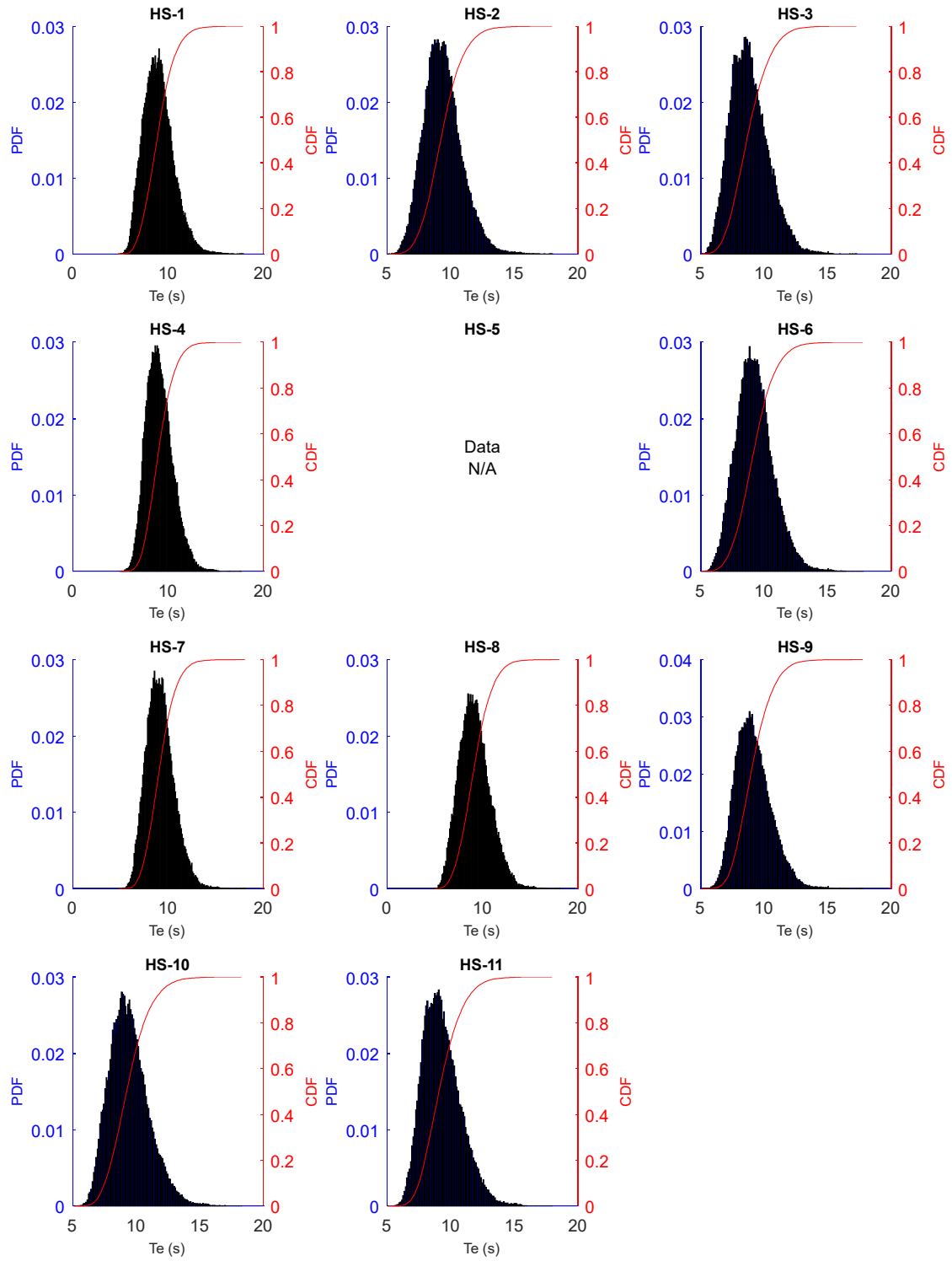
Figure 5-47 Empirical probability distribution function (PDF) and empirical cumulative distribution function (CDF) for $T_e$ at different hotspots (HS) locations.
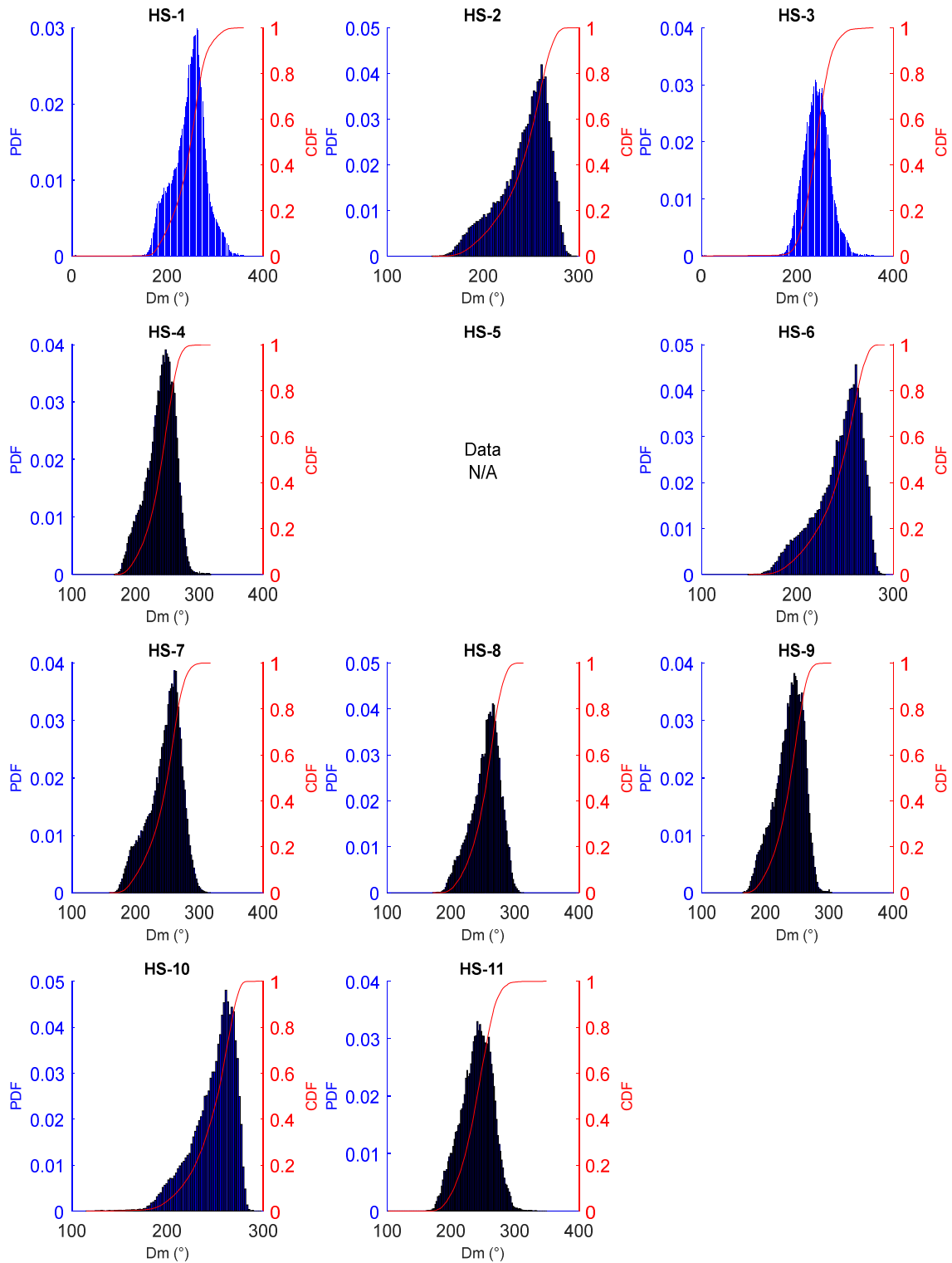
Figure 5-48 Empirical probability distribution function (PDF) and empirical cumulative distribution function (CDF) for $D_m$ at different hotspots (HS) locations.
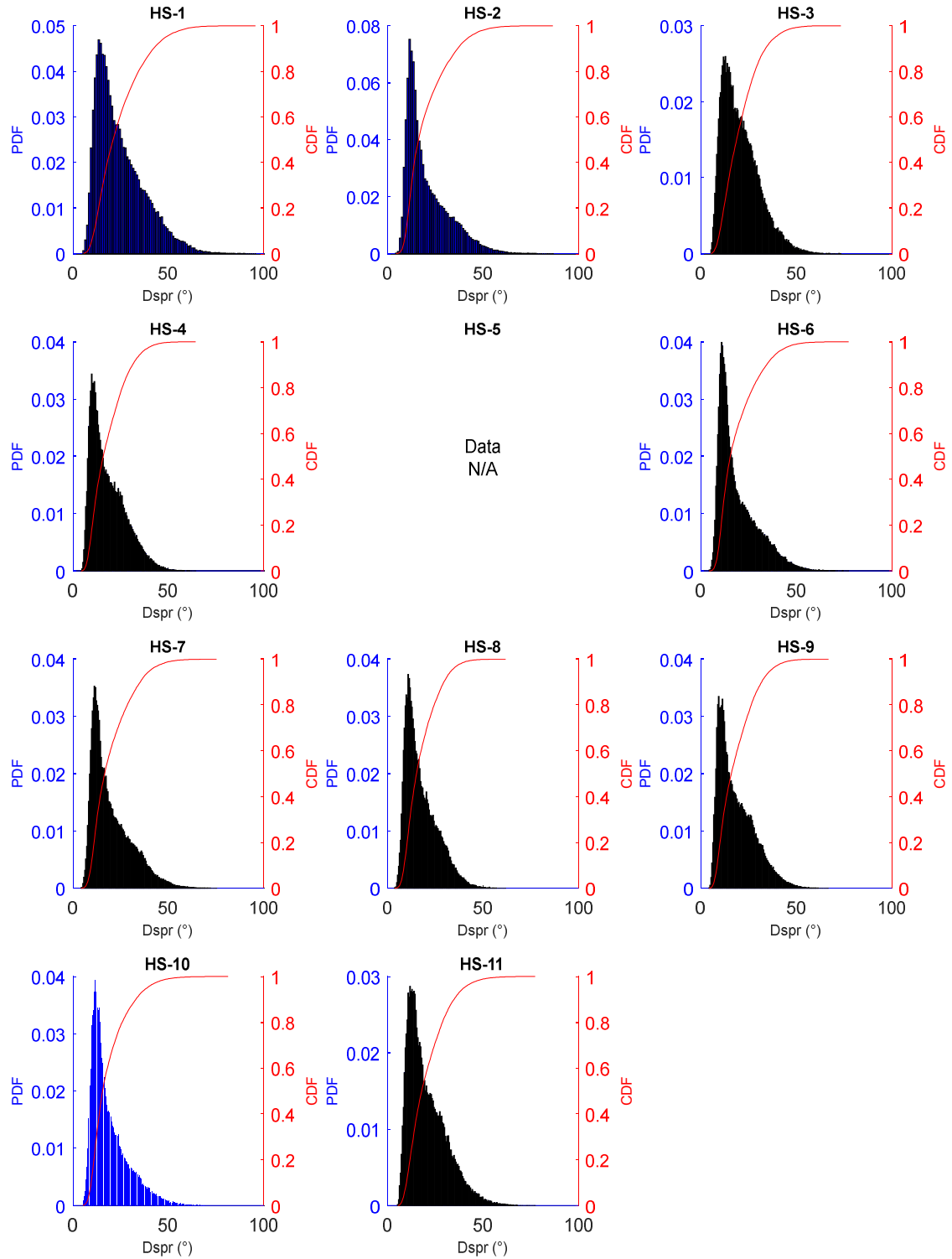
Figure 5-49 Empirical probability distribution function (PDF) and empirical cumulative distribution function (CDF) for $D_{spr}$ at different hotspots (HS) locations.
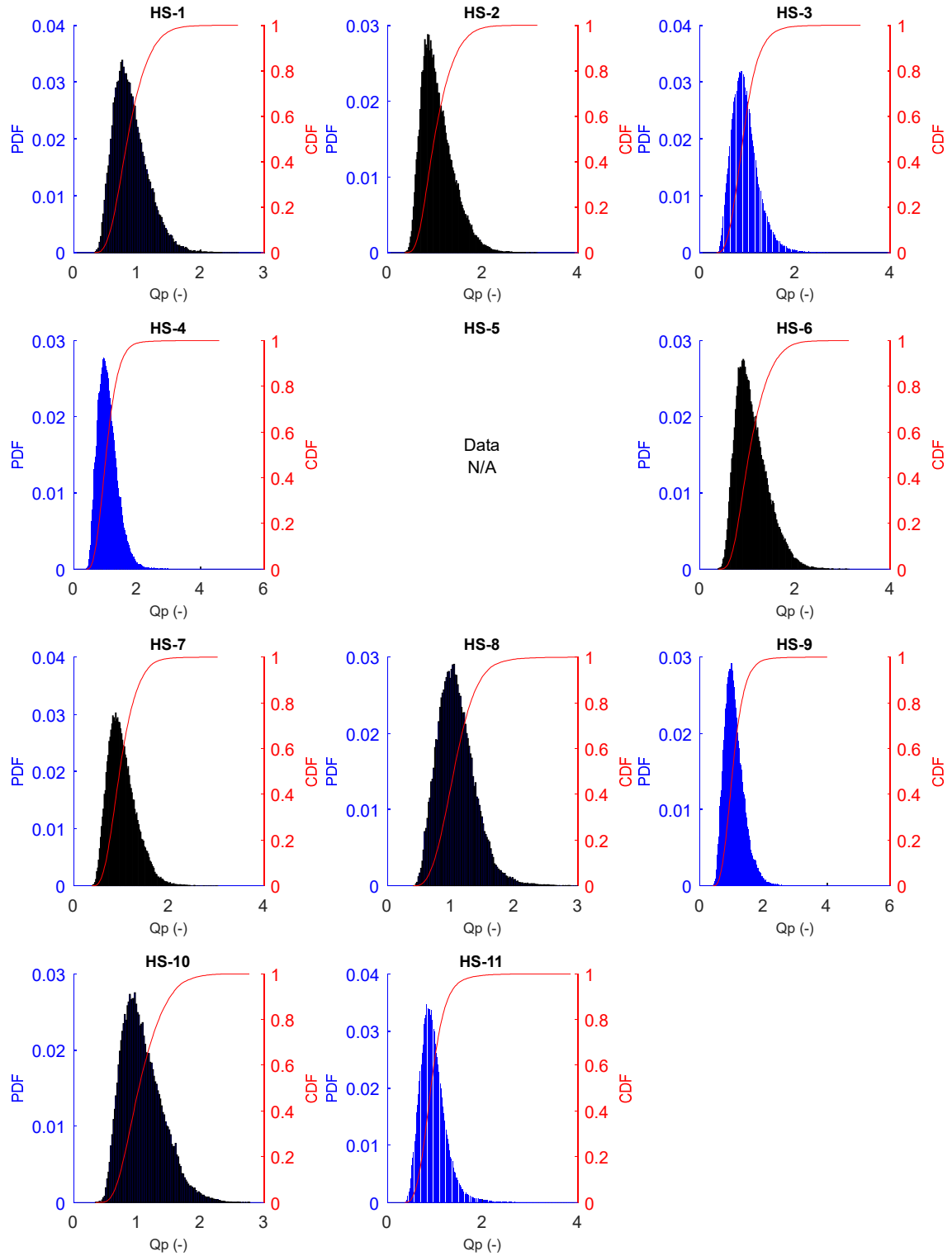
Figure 5-50 Empirical probability distribution function (PDF) and empirical cumulative distribution function (CDF) for $Q_p$ at different hotspots (HS) locations.
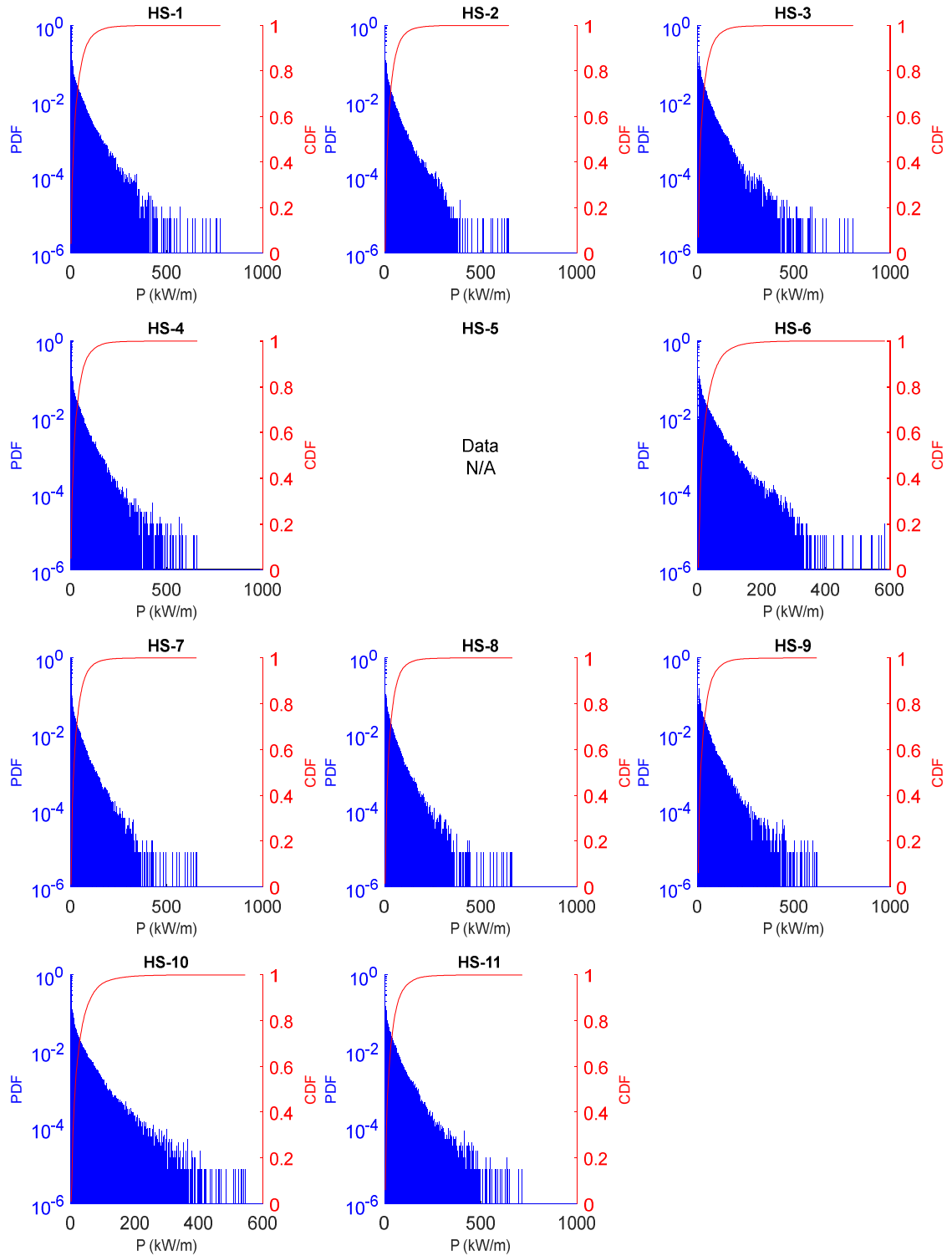
Figure 5-51 Empirical probability distribution function (PDF) and empirical cumulative distribution function (CDF) for *P* at different hotspots (HS) locations.

# Chapter 6 Conclusions

Aiming to contribute to the development of the wave energy industry in B.C., and thus, to the Canadian and global efforts in reducing the GHG emissions, this work generated two most accurate, long-term (14 years, 2004 to 2017), high resolution (in space and time) datasets of the wave resource for the west coast of Canada.

These datasets improve knowledge on the wave resource and developed an understanding of the impact of tidal currents on the wave characteristics in this region. They can be used in support of siting wave energy generation projects, assessing the electrical energy generation for such projects, and identifying the extreme wave conditions needed to complete survivability analyses. In addition, the wave data generated in this work might be also useful to inform a myriad of other topics in ocean and coastal engineering.

The two datasets were generated using nearly identical numerical spectral wave models, developed using the most recently available Simulating WAves Nearshore software (SWAN, version 41.31). The only difference between these two models was that one of them, WCWI-v5 (V5), did not incorporate the effect of currents, while the other, WCWI-v6 (V6), included tidal currents as forcing. Thus, the pure influence of the tidal currents on the wave characteristics was able to be identified when comparing the two wave model results. This comparison allowed an extensive investigation of the influence of tidal currents on the wave characteristics and wave power, which to the best knowledge of the author, was the first such study for the B.C. coast.

The increased fidelity of the datasets in representing the sea states (in comparison to previous studies) was achieved mainly by: (1) extending the model domain, (2) increasing the temporal resolution, (3) implementing a tailored, well-suited (in accordance to the objectives of this thesis) spatial discretization (mesh) to faithfully reproduce the wave conditions at high resolution, (4) utilizing high quality data to be incorporated in the models, (6) taking advantage of new features of the SWAN model, leading to the use of a more recently developed physics package (ST6; not available for the previous wave resource assessments developed for the region), (7) optimizing the model settings through

a thorough calibration process, and (8) including tidal currents as forcing (for the V6 model).

This study developed three simple, robust, and objective metrics to support the calibration process and to evaluate the performance of the models. These metrics were the Global Performance Score ($GPS$), the Local Performance Score ($LPS$), and the Variable Performance Score ($VPS$), which represent the improvement respect to V4[30] in simulating the sea state (characterized by $H_{m0}$, $T_e$ and $D_p$) globally, locally and for a particular wave parameter and location, respectively. Relying on these metrics, the settings for V5 and V6 were selected from the best performed model candidates. These metrics can be replicated (or serve as a base) for other wave characterization studies.

Equipped with these performance metrics ($GPS$, $LPS$ and $VPS$), the performance of V5 and V6 was evaluated considering the whole extension of the simulation results (14 years). Both models, V5 and V6, present substantial improvements in relation to V4, with $GPS$s of about 18% and 20% respectively. Their better performance was achieved mainly by a significant increment in their ability to reproduce $H_{m0}$ and $T_e$, with averaged $VPS$s ($\overline{VPS}$s) of 19.7% and 15.6% for V5, and 20.3% and 20.7% for V6, for $H_{m0}$ and $T_e$ correspondingly. On the other hand, the models showed just a moderate global improvement in representing the wave directions, with $\overline{VPS}$s for $D_p$ of 5.0% and 5.6% for V5 and V6, respectively. Both models outperform V4 at every buoy location, having $LPS$s ranging from 2.4% to 29.1% for V5, and 6.7% to 31.8% for V6.

In spite of the substantial improvements in the fidelity of these two models, V5 and V6 tend to underestimate $H_{m0}$, overestimate lower $T_e$ values and underestimate higher $T_e$ values. The total uncertainty estimates ($u_{95}$) show that both, V5 and V6, have relatively small total error when simulating $H_{m0}$ and $T_e$, with maximum values not greater than 0.85 m and 3.0 s, respectively. However, as can be estimated with the deep water wave power density approximation, small misrepresentation of these two wave parameters can lead to

---

[30] Previous most complete, long-term and high resolution wave resource characterization for the British Columbia coast, developed by Robertson et al. (2016) at the West Coast Wave Initiative at the University of Victoria.

important errors in the estimation of the wave power density ($P$). On the other hand, these models tend to reduce the range of directions, and present significant uncertainties for the mean wave direction ($D_m$), with maximum and mean $u_{95}$ values of about 65° and 50°, respectively. Although characterizing the directionality of the sea state is not important regarding to the available wave power on a site basis, in the model, it affects the accuracy of the wave energy propagation, and the performance of some WECs can be very sensitive to this property. Thus, the characteristics of the error of these (and others) wave parameters need to be taken into account when assessing the energy production and performing survivability analyses when evaluating wave energy projects.

The inclusion of tidal currents in the wave model increased the accuracy of the wave resource characterization, mainly by improving the model's ability in simulating the wave periods by 5.1% (as per the $\overline{VPS}$ for $T_e$). This better representation of the wave periods was consistent across all the buoy locations.

The comparison between the two models, V5 and V6, permitted to identify the important transformations induced by the tidal current on the wave characteristics and wave power.

In general, tidal currents had the effect of reducing $P$, yet, they also were able to increase $P$, but less frequently and by a reduced magnitude. Typically, their effect on $P$ was relatively small, showed for example by the 90th percentile of the absolute value of the difference in $P$ between the two models, which did not exceeded 7.5 kW/m over the whole model domain. However, during rare events, tidal currents were able to induce increases and decreases in $P$ of about 75 kW/m and -140 kW/m, respectively, in some regions.

The locations where tidal currents impacted wave parameters the most are not only those locations with stronger tidal currents, but also rapid currents (~>0.5 m/s) occurring over a larger length of the waves' trajectory (in comparison to more exposed to swell-waves sites, e.g. Juan the Fuca Strait, Hecate Strait, Dixon Entrance). In general, these regions are not attractive for the development of wave energy projects as they possess a much reduced wave power density for being protected from swell-waves, or at least from a large portion of their directions.

The most sensitive wave parameter to the tidal currents was the peakedness of the wave spectrum ($Q_p$), which was consistently and significantly reduced at every location, spreading the wave height variance of the wave spectrum over the frequencies. At the site most affected, $Q_p$ got reduced by values even larger than 2.5.

Directions, characterized by $D_m$ and $D_{spr}$ (directional spreading), were noticeably very sensitive to the currents at locations in Juan the Fuca Strait, Hecate Strait, Dixon Entrance, which even deflected $D_m$ to its opposite direction and drove changes in $D_{spr}$ that reached values of up to 40°. Significant changes of $D_m$ and $D_{spr}$ can also be observed at some exposed site, but these changes are less frequent and reduced in magnitude.

Typically, $H_{m0}$ and $P$ were consistently decreased, reaching average reductions of up to 4% and 9%, respectively, but when considering only exposed sites, these reductions do not exceed 2% and 5%, respectively. $T_e$ was barely affected at exposed sites, however at locations in Juan the Fuca Strait, Hecate Strait and Dixon Entrance, low values of $T_e$ were normally increased and higher values reduced, but not consistently with the magnitude and direction of the local currents. Extreme tidal current impacts show that $T_e$ can be modified by more than 5 s.

Influence of the tidal currents on $P$ were largely attributed to the induced changes in $H_{m0}$ and $T_e$. And, in spite of $D_{spr}$ and $Q_p$ were greatly transformed by the action the tidal currents, they account very little in explaining the variations in $P$. Although, these four wave parameters together, and how they change under the presence of currents, can explain a large part of the changes in $P$, they are still unable to explain a considerable part of them. Thus, other features of the wave spectrum must be accounting for the changes in wave power when tidal currents are present.

At events of extreme tidal current impacts on $P$ (and most likely in the majority of cases), the peak of the wave spectra became flatter, with some of its wave height variance redistributed to near increasing and decreasing frequencies and directions, regardless to the magnitude and direction of the local tidal currents (where the analysis is being performed).

The impacts of tidal currents on the wave parameters, and spectral shape found in this work are not only significant for a better characterization of the wave resource, but

more importantly, they can be significant when evaluating the wave energy production of WECs, especially those sensitive to the wave direction, and how the wave height variance of the spectrum is distributed over the direction and frequency space.

## 6.1 Recommendations

In order to further support the wave energy industry, and other branches of the ocean and coastal engineering that require a long-term and spatially distributed characterization of the wave climate, this work can provide several recommendations.

Use an appropriate wave model that consider all the important physical phenomena affecting the variables being studied. Feed the model with the most reliable information (wave boundary conditions, wind fields, currents, topo-bathymetry, etc.) available, and consider to include as much forcings that affect the physics of the phenomena in study as possible. In addition, and whenever possible (when there are measurements available), numerical tools need to be calibrated and validated to ensure accurate (or at least with known uncertainties) results. It is also worth considering the latest available version of the model, which might include state of the art capabilities, and fixed bugs present in previous versions.

For the calibration and validation processes, identify the most important variables, and use meaningful error metrics to create tailored (for your application) performance metrics in order to support your decisions on the best settings for your model, and to provide uncertainty estimates and other error characterization metrics for the results. For example, this work utilizes the $GPS$, $LPS$ and $VPS$ as metrics to evaluate the performance of the models. These metrics are all based on the $u_{95}$, which describe relatively high but rare errors. Other error metrics, such as the $RMSE$, which describe the general behavior of the errors (weighing more the larger over the smaller ones), can also be used to compute these ($GPS$, $LPS$ and $VPS$) or other performance scores. Thus, focusing in other aspects of the errors.

Although this work did not follow some of the recommendation presented in the 'Technical Specification on Wave Energy Resource Assessment and Characterization' (IEC, 2015) and in the user manual of the SWAN software, it is suggested that whenever

possible, follow the recommendations stated in the numerical model's manual, and the guidelines associated to the type of study being conducted (e.g. IEC, 2015; EquiMar, 2011). When this is not achievable, sensitivity studies around the recommendations that are not being followed might be required.

Spatial discretization (mesh) and its interpolated topo-bathymetric information is a critical definition that affect in the accuracy, stability and efficiency of most of the hydrodynamic numerical models (including those based on the wave action balance equation, such as SWAN). This is particularly true when simulating waves on intermediate and shallow waters, where geographical features can induce important transformations on the wave field. Thus, an appropriate and custom-made mesh, that take into account the objectives of the study, the areas of interest and the topo-bathymetric features of the model domain, should be consider.

## 6.2 Future work

This improved, more accurate, and higher resolution (in space and time) characterization of the wave resource, can be used to update the study carried out by Xu (2018) which identified strategically important wave energy sites in B.C. assuming an overly simplistic shape of the wave spectrum. Although the datasets generated in this work do not include wave spectra at node of the model mesh, a more informed reconstruction of the wave spectra can be performed using the wave parameters from the partitions. In addition, the spectral data generated at intermediate-depth waters all along of the west coast of Canada, can be utilized to develop local and higher resolution wave characterization at sites that can be identified as of interest in the future.

In spite of the significant improvements in characterizing the wave energy resource achieved by this work, further investigation on increasing the accuracy of the wave modelling tool can be performed through a more extensive calibration process. In this sense, it may be worth considering to follow the recommendations presented in the SWAN software's manual, and refine the spectral discretization, especially over the directional space. This spectral discretization refinement might allow to model narrow directional-wise wave systems, such as swell-waves, in more detail. Furthermore, SWAN (as well as

other spectral wave models), include numerous formulations, parameters and numerical schemes that define the governing equations and how they are solved. In this work, a limited set of settings where varied to explore improvements in the numerical modelling tool. Proposed settings to include in a further investigation are the physics that controls the wind-to-wave energy transfer, the two physical processes recommended to be included in wave resource assessments by the IEC (2015), the non-linear wave-wave interactions in shallower waters (triads) and the wave diffraction.

As noticed from the results of this (and other works), tidal currents can induce significant transformations to the wave characteristics and wave power. Thus, it may be worth exploring improvements in the estimates of the tidal currents, as well as investigating the influence of currents associated to other phenomena, such as oceanic currents, and currents induced by waves and wind.

The error and performance metrics used in this work assume that measurements provide the 'true' value of the wave characteristics. Although specification of the measurement instruments (in this case oceanographic buoys) declare very accurate sensors, and calibration procedures claim very small errors; accuracy of moored buoys under environmental conditions is unknown. Thus, efforts in estimating the uncertainty of the measurements need to be conducted in order to fully characterize the uncertainty of the model estimates.

Finally, this study explored the influence of the tidal currents on the wave power, on a limited set of wave parameters, and on the wave spectrum at only few extreme events. To further improve the characterization of the tidal current influence on the wave resource, a broader set of wave parameters and a more complete set of events can be included. For example, good candidates to be considered could be: other wave periods, wave steepness and wave parameters obtained from the partitions of the wave spectrum. Furthermore, changes of the wave spectrum at different events related to the magnitude and direction of the tidal currents with respect to the waves can also be investigated. It would also be interesting to explore how the trajectories of the wave components are changed due to the action of currents. However, this analysis will require to modify the source code of the

SWAN software to track how the wave height variance at every bin of the spectrum is modified through time and space.

# Bibliography

Aderinto, T., Li, H., 2018. Ocean Wave Energy Converters: Status and Challenges. Energies 2018, 11 (5), 1250. doi:10.3390/en11051250.

Aijaz, S., Rogers, W.E., Babanin, A.V., 2016. Wave spectral response to sudden changes in wind direction in finite-depth waters. Ocean Modelling 103 (2016), 98–117.

Allievi, A., Bhuyan, G., 1994. Assessment of Wave Energy Resources for the West Coast of Canada. Department of Mechanical Engineering, University of British Columbia, Vancouver.

Ardhuin, F., Roland A., 2014. The Development of Spectral Wave Models: Coastal and Coupled Aspects. Coastal Dynamics 64, 833–846. https://doi.org/10.1007/s10236-014-0711-z.

Arinaga, R.A., Cheung, K.F., 2012. Atlas of global wave energy from 10 years of reanalysis and hindcast data. Renewable Energy 39(1), 49–64.

Axys (Axys Technologuies Inc.), 2016. Triaxys$^{TM}$ Directional wave buoy brochure. https://axystechnologies.com/wp-content/uploads/2016/08/TRIAXYS-Directional-Wave-Buoy.pdf. Web page last visited on May 2020).

Baird W., Mogridge, G., 1976. Estimates of the Power of Wind-Generated Water Waves at Some Canadian Coastal Locations. National Research Council of Canada, Hydraulics Laboratory Report LTR-HY-53, Ottawa, Ontario, Canada KlA OR6 (1976).

Barbariol F., Benetazzo A., Carniel S., Sclavo M., 2013. Improving the assessment of wave energy resources by means of coupled wave-ocean numerical modeling. Renewable Energy 60 (2013), 462-471.

Beyá, J., Álvarez, M., Gallardo, A., Hidalgo, H., Winckler, P., 2017. Generation and validation of the Chilean Wave Atlas database. Ocean Model. 116 (2017), 16–32.

Brüggemeier, F.J., 2001. Environmental History. In: Smelser, N.J. and Baltes, P.B. (Ed.), International Encyclopedia of the Social & Behavioral Sciences. Elsevier, 2001, Pergamon, pp. 4621-4627.

Caires, S., Sterl, A., Gommenginger, C.P., 2005. Global ocean mean wave period data: Validation and description. Journal of Geophysical Research: Oceans 110 (C2). doi:10.1029/2004JC002631.

Chai, T., Draxler, R.R., 2014. Root mean square error (RMSE) or mean absolute error (MAE)? – Arguments against avoiding RMSE in the literature. Geosci. Model Dev., 7 (2014), 1247–1250.

Cornett, A. 2006. Inventory of Canada's Offshore Wave Energy Resources. Ocean Eng. Polar Arct. Sci. Technol., 2 (2006), 353–362.

Cornett, A. 2008. A global wave energy resource assessment. National Research Council – Canadian Hydraulics Centre.

Cornett, A., Zhang, J., 2008. Nearshore Wave Energy Resources, Western Vancouver Island, B.C. Canadian Hydraulics Centre.

DFO (Department of Fisheries and Oceans Canada), 2018. https://www.tides.gc.ca/eng/info/verticaldatums. Web page last visited on December 15th, 2018.

ECCC (Canada. Environment and Climate Change Canada), 2016. Pan-Canadian Framework on Clean Growth and Climate Change: Canada's plan to address climate change and grow the economy. ISBN: 978-0-660-07023-0.

ECCC (Environment and Climate Change Canada), 2018. National Inventory Report 1990-2016 - Greenhouse Gas Sources and Sinks in Canada: Executive Summary. ISSN: 2371-1329.

EquiMar (Equitable Testing & Evaluation Of Marine Energy Extraction Devices in Terms of Performance, Cost and Environmental Impact), 2011. Protocols for the Equitable Assessment of Marine Energy Converters.

Figliola, R. S., Beasley, D. E., 2010. Theory and design for mechanical measurements. Hoboken, N.J., John Wiley.

Fonseca, R.B., Gonçalves, M., Guedes Soares, C., 2017. Comparing the performance of spectral wave model for coastal areas. Journal of Coastal Research, 33(2), 331–346. https://doi.org/10.2112/JCOASTRES-D-15-00200.1.

Fradon, B., Hauser, D., Lefevre, J.M., 2000. Comparison Study of a Second-Generation and of a Third-Generation Wave Prediction Model in the Context of the SEMAPHORE Experiment. Journal of Atmospheric and Oceanic Technology 17 (2), 197-214.

Goda, Y., 2010. Random Seas and Design of Maritime Structures. Advanced Series on Ocean Engineering: Volume 33. World Scientific, Singapore. https://doi.org/10.1142/7425.

Group, T. W., 1988. The WAM Model—A Third Generation Ocean Wave Prediction Model. J. Phys. Oceanogr., 18 (12), 1775–1810, https://doi.org/10.1175/1520-0485(1988)018<1775:TWMTGO>2.0.CO;2.

Gunn K., Stock-Williams C., 2012. Quantifying the global wave power resource. Renewable Energy 44 (2012), 296-304.

Gunn, K., Stock-Williams, C., 2012. Quantifying the global wave power resource. Renewable Energy 44 (2012), 296-304.

Hasselmann, K., Barnett, T.P., Bouws, E., Carlson, H., Cartwright, D.E., Enke, K., Ewing, J.A., Gienapp, H., Hasselmann, D.E., Kruseman, P., Meerburg, A., Muller, P., Olbers, D.J., Richter, K., Sell, W., Walden, H., 1973. Measurements of wind-wave growth and swell decay during the Joint North Sea Wave Project (JONSWAP). Deutsches Hydrographisches Institut, Hamburg.

Holthuijsen, L., 2007. Description of ocean waves. In Waves in Oceanic and Coastal Waters, pp. 24-55. Cambridge University Press. doi:10.1017/CBO9780511618536.004.

Huges, S.A., 1996. Physical models and laboratory techniques in coastal engineering. Advanced series on ocean engineering. World Scientific, Singapore.

IEC (International Electrotechnical Commission), 2015. Wave Energy Resource Assessment and Characterization. Marine Energy – Wave, Tidal and Other Water Current Canverters. Technical Specification. IEC TS 62600-101.

IPCC (Intergovernmental Panel on Climate Change), 2014. Climate Change 2014 Synthesis Report Summary for Policymakers.

Kim, C.-K., Toft, J.E., Papenfus, M., Verutes, G., Guerry, A.D., et al., 2012. Catching the right wave: evaluating wave energy resources and potential compatibility with existing marine and coastal uses. PLoS ONE 7 (11), e47598. doi:10.1371/journal.pone.0047598.

Kumar, S.V., Naseef T.M., 2015: Performance of ERA-Interim Wave Data in the Nearshore Waters around India. J. Atmos. Oceanic Technol., 32 (2015), 1257–1269. https://doi.org/10.1175/JTECH-D-14-00153.1.

Lavidas, G., Polinder, H., 2019. North Sea Wave Database (NSWD) and the Need for Reliable Resource Data: A 38 Year Database for Metocean and Wave Energy Assessments. Atmosphere 2019, 10 (9), 551. doi:10.3390/atmos10090551.

Liu, P., Losada, I., 2002. Wave propagation modeling in coastal engineering. Journal of Hydraulic Research, 40 (3), 229-240, DOI: 10.1080/00221680209499939.

Mitsuyasu, H., 2001. A Historical Note on the Study of Ocean Surface Waves. Journal of Oceanography, 58 (2002), 109 -120.

MRC (Marine Renewables Canada), 2018. Marine Renewable Energy in Canada. 2018 State of the Sector Report.

NDBC (U.S. National Data Buoy Center), 2020. https://www.ndbc.noaa.gov/rsa.shtml. Web page last visited on May 29th, 2020.

Neary, V.S., Gunawan, B., Yang, Z., Dallman, A.R., Wang, T., 2016. Model Test Bed for Evaluating Wave Models and Best Practices for Resource Assessment and Characterization. Richland, WA, Pacific Northwest National Laboratories, and Sandia National Laboratories, (SAND2016-8497R; PNNL-25385).

NGDC, 2010 a&b. Digital elevation models of Juneau and southeast Alaska: procedures, data sources and analysis. NOAA Technical Memorandum NESDIS NGDC-53.

NGDC, 2013. Bathymetric Digital Elevation Model of British Columbia, Canada: Procedures, Data Sources, and Analysis.

Pandian, P.K., Osalusi, E., Ruscoe, J.P., Side, J.C., Harris, R.E., Bullen, C.R., 2010. An overview of recent technologies on wave and current measurement in coastal and marine applications. J. Oceanogr. Mar. Sci., 1 (2010), pp. 1-10.

Pawlowicz, R., Beardsley B., Lentz, S., 2002. Classical tidal harmonic analysis including error estimates in MATLAB using T_TIDE. Computers and Geosciences 28 (2002), 929-937.

Ponce de León, S., Bettencourt, J., Van Vledder, G. Ph., Doohan, P., Higgins, C., Guedes, C., Dias, F., 2018. Performance of WAVEWATCH-III and SWAN Models in the North Sea. In: Proceedings of the ASME 2018 37th International Conference on Ocean, Offshore and Arctic Engineering, Madrid, Spain.

Robertson, B., 2017.Marine Renewable Energy: Resource Characterization and Physical Effects. In: Yang, Z., Copping, A. (Eds.). Springer International Publishing. DOI 10.1007/978-3-319-53536-4.

Robertson, B., Bailey H., Buckham B., 2019. Resource assessment parameterization impact on wave energy converter power production and mooring loads. Applied Energy 244 (2019), 1–15.

Robertson, B., Bailey, H., Buckham, B., 2017. Wave energy, a primer for British Columbia. Pacific Institute for Climate Solutions.

Robertson, B., Hiles, C., Buckham, B., 2014. Characterizing the near shore wave energy resource on the west coast of Vancouver Island, Canada. Renewable Energy 71 (2014), 665–678.

Robertson, B., Hiles, C., Luczko, E., Buckham, B., 2016. Quantifying wave power and wave energy converter array production potential. International Journal of Marine Energy 14 (2016), 143–160.

Roland A., Ardhuin, F., 2014. On the developments of spectral wave models: numerics and parameterizations for the coastal ocean. Ocean Dynamics 64 (6), 833-846.

Sangalugeme C., Luhunga P., Kijazi A., Kabelwa H., 2018. Validation of operational WAVEWATCH III Wave Model Against Satellite Altimetry Data Over South West Indian Ocean Off-Coast of Tanzania. Appl Phys Res. 10(4), 55-65. https://doi.org/10.5539/apr.v10n4p5525.

Saruwatari, A., Ingram, D.M., Cradden, L., 2013. Wave–current interaction effects on marine energy converters. Ocean Engineering 73 (2013), 106–118.

SWAN, 2019a. Scientific and Technical Documentation. SWAN Cycle III version 41.31, Delft University of Technology. Faculty of Civil Engineering and Geosciences. Environmental Fluid Mechanics Section.

SWAN, 2019b. User Manual. SWAN Cycle III version 41.31. Delft University of Technology. Faculty of Civil Engineering and Geosciences. Environmental Fluid Mechanics Section.

Thomas T.J., Dwarakish, G.S., 2015. Numerical Wave Modelling–A Review. Aquatic Procedia. 4 (2015), 443– 448.

Thurman, H., Trujillo, A., 2002. Essentials of Oceanography. Upper Saddle River, N.J., Pearson Prentice Hall, pp. 236-264.

Tian, Y., Nearing, G., Peters-Lidard, C.D., Harrison, K.W., Tang, L., 2015. Performance Metrics, Error Modeling, and Uncertainty Quantification. Mon. Wea. Rev., 144 (2), 607–613. DOI: 10.1175/MWR-D-15-0087.1.

Toffoli, A., Bitner-Gregersen, E., 2017. Types of ocean surface waves, wave classification. Encyclopedia of Maritime and Offshore Engineering. DOI: 10.1002/9781118476406.emoe077.

Ueno, K., Kohno, N., 2004. The development of the third generation model MRI-III for operational use. In: Proc. 8th Int. Workshop on Wave Hindcasting and Forecasting, G2, 1–7.

USACE (U.S. Army Corps of Engineers), 2008. Coastal engineering manual, Part II-Chapter 2, Meteorology and Wave.

USGS, 1999. Digital elevation model (DEM) of Cascadia, latitude 39N-53N, longitude 116W-133W, Readme.txt file. https://doi.org/10.3133/ofr99369.

Van Essen, S., Ewans, K., McConochie, J., 2018. Wave buoy performance in short and long waves, evaluated using tests on a hexapod. In: Proceedings of the ASME 2018 37th International Conference on Ocean, Offshore and Arctic Engineering OMAE2018.

Van Vledder, G.pH, Akpınar, A., 2015. Wave model predictions in the Black Sea: sensitivity to wind fields. Applied Ocean Research 53 (2015), 161–178.

Wolf, J., Prandle, D., 1999. Some observations of wave–current interaction. Coastal Engineering 37 (1999), 471–485.

WW3DG (WAVEWATCH III development group), 2019. User manual and system documentation of WAVEWATCH III®, version 6.07. Technical note 333, NOAA/NWS/NCEP/MMAB, College Park, MD, USA, 465 pp.

Xu, X., 2018. Identifying British Columbia's Strategically Important Wave Energy Sites. A thesis submitted in partial fulfillment of the requirements for the degree of Master of Applied Science in the Department of Mechanical Engineering, University of Victoria.

# Appendices

# Appendix A  Scatter plots: measurements vs model results

**WCWI-v5:**



Figure A-1 Scatter plots for WCWI-v5, and $H_{m0}$, $T_e$ and $D_m$ – A.

## V5

**DFO-5 - H$_s$ (m)**

**DFO-5 - T$_e$ (s)**

**DFO-5 - D$_m$ (°)**

$\lambda$ = 0.89
$\delta$ = 0.22
$\sigma$ = 0.37
u$_\sigma$ = 0.30

$\lambda$ = 0.90
$\delta$ = 0.98
$\sigma$ = 0.55
u$_\sigma$ = 0.49

No data available

**DFO-6 - H$_s$ (m)**

**DFO-6 - T$_e$ (s)**

**DFO-6 - D$_m$ (°)**

$\lambda$ = 0.93
$\delta$ = 0.04
$\sigma$ = 0.27
u$_\sigma$ = 0.20

$\lambda$ = 0.95
$\delta$ = -0.04
$\sigma$ = 1.05
u$_\sigma$ = 0.65

No data available

**DFO-7 - H$_s$ (m)**

**DFO-7 - T$_e$ (s)**

**DFO-7 - D$_m$ (°)**

$\lambda$ = 0.92
$\delta$ = 0.23
$\sigma$ = 0.32
u$_\sigma$ = 0.22

$\lambda$ = 0.90
$\delta$ = 1.09
$\sigma$ = 0.85
u$_\sigma$ = 0.70

No data available

**DFO-8 - H$_s$ (m)**

**DFO-8 - T$_e$ (s)**

**DFO-8 - D$_m$ (°)**

$\lambda$ = 0.91
$\delta$ = 0.24
$\sigma$ = 0.32
u$_\sigma$ = 0.25

$\lambda$ = 0.88
$\delta$ = 1.55
$\sigma$ = 0.66
u$_\sigma$ = 0.59

No data available
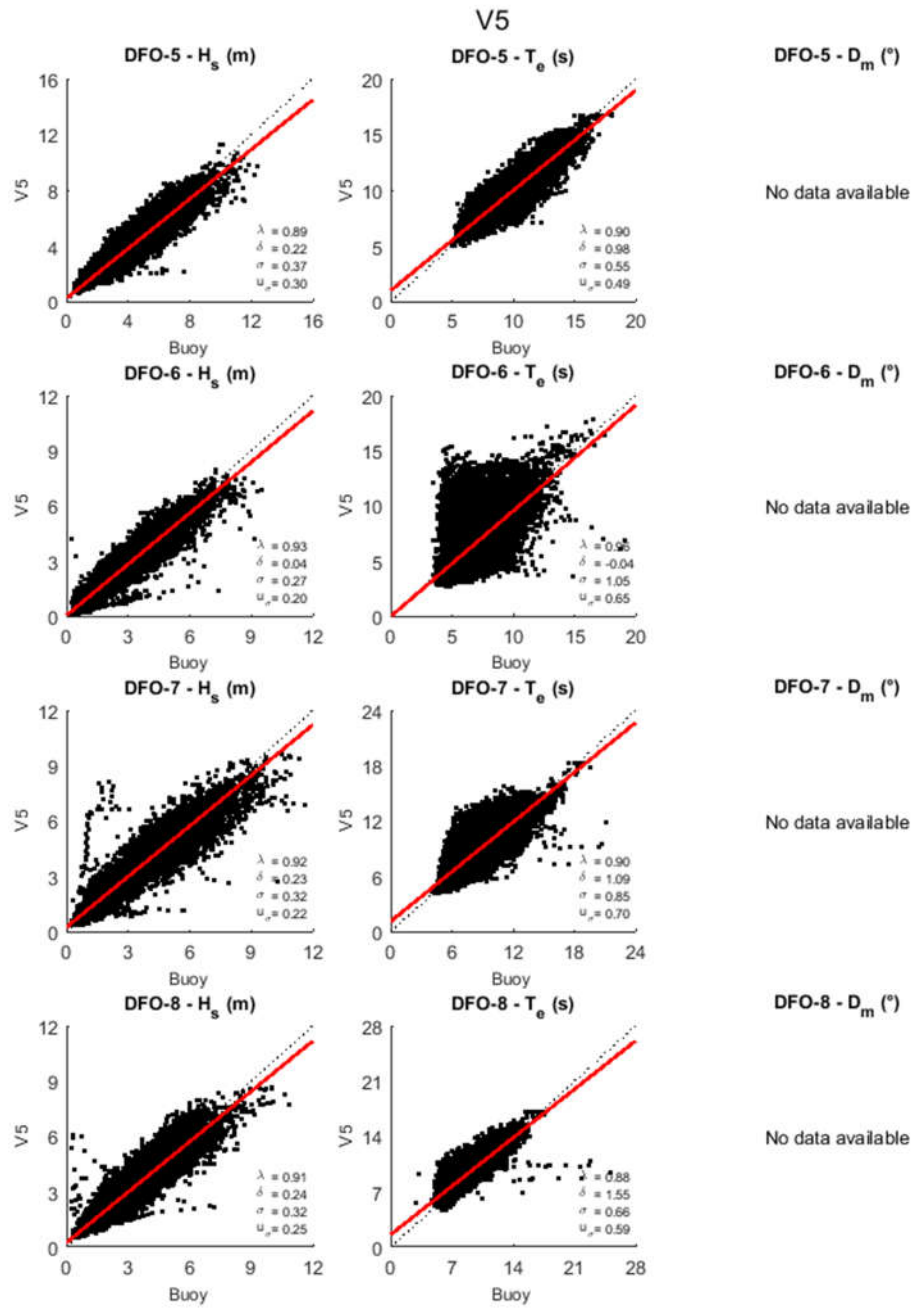
Figure A-2 Scatter plots for WCWI-v5, and $H_{m0}$, $T_e$ and $D_m$ – B.
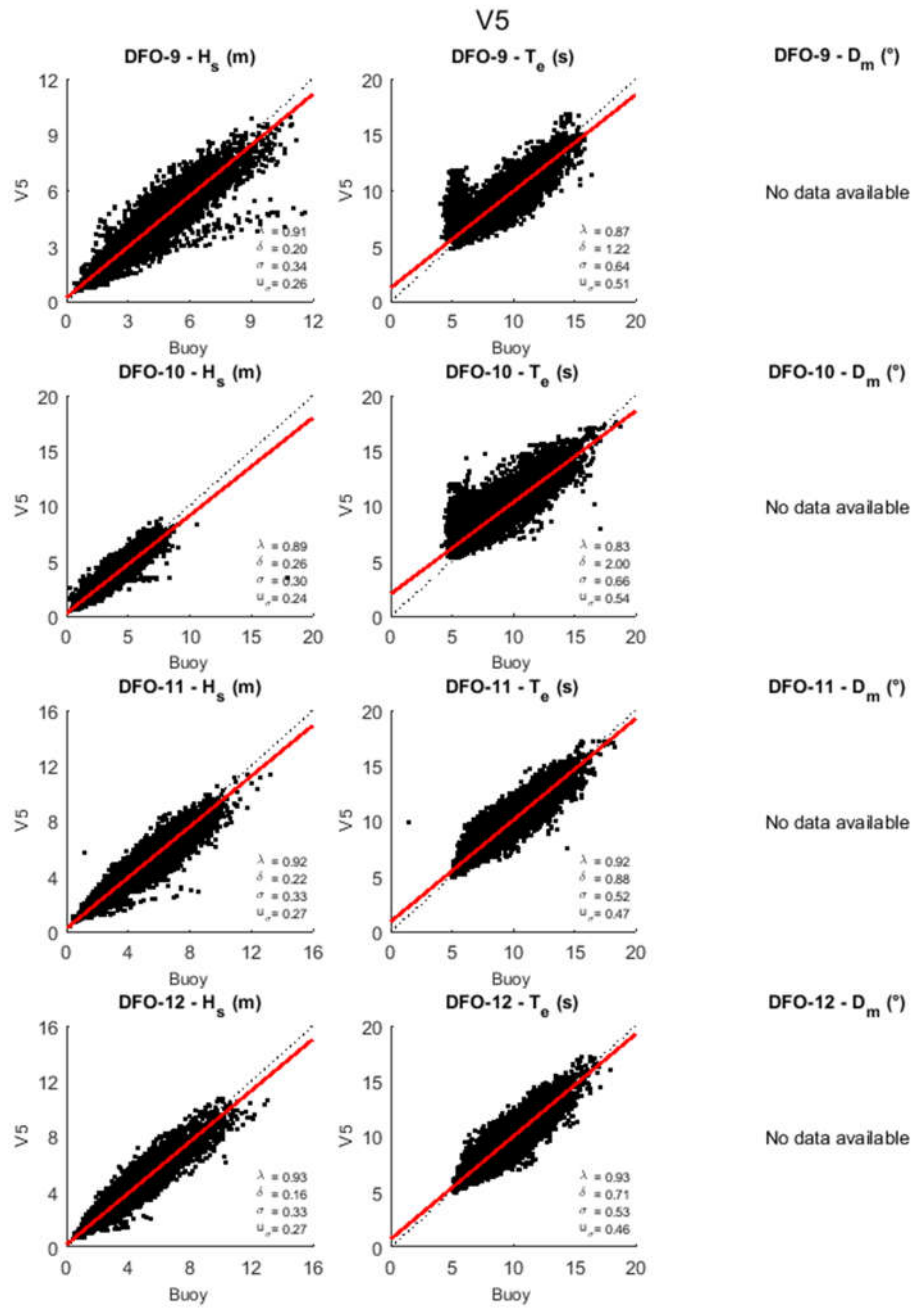
Figure A-3 Scatter plots for WCWI-v5, and $H_{m0}$, $T_e$ and $D_m$ – C.
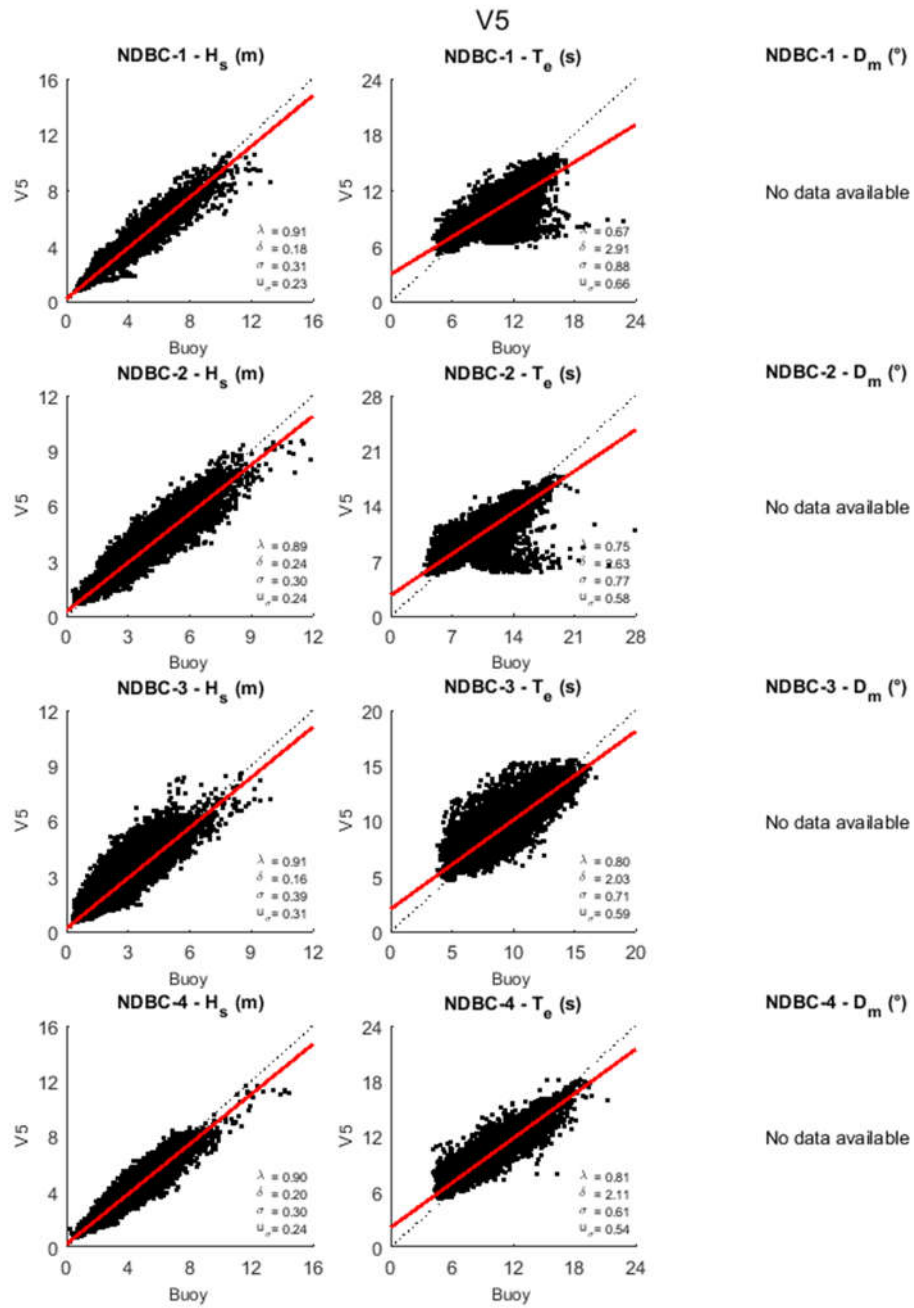
Figure A-4 Scatter plots for WCWI-v5, and $H_{m0}$, $T_e$ and $D_m$ – D.
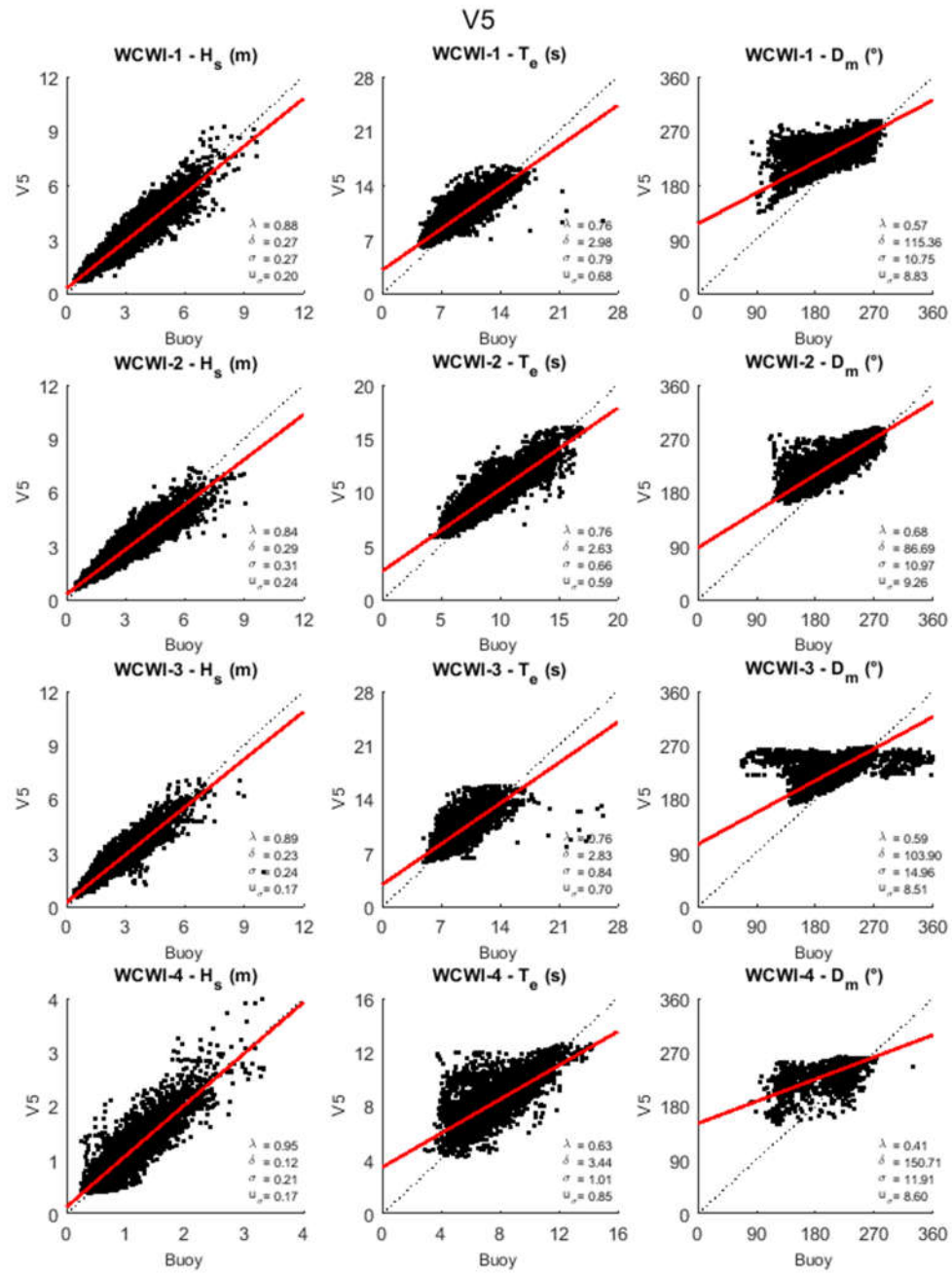
Figure A-5 Scatter plots for WCWI-v5, and $H_{m0}$, $T_e$ and $D_m$ – E.
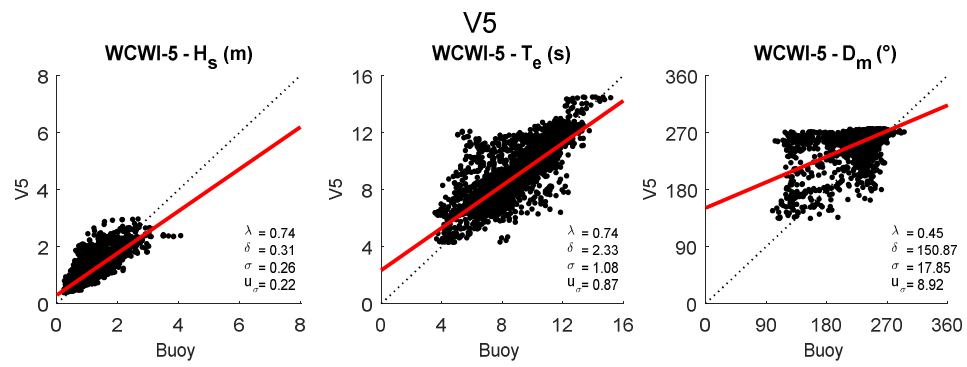
Figure A-6 Scatter plots for WCWI-v5, and $H_{m0}$, $T_e$ and $D_m - F$.

**WCWI-v6:**
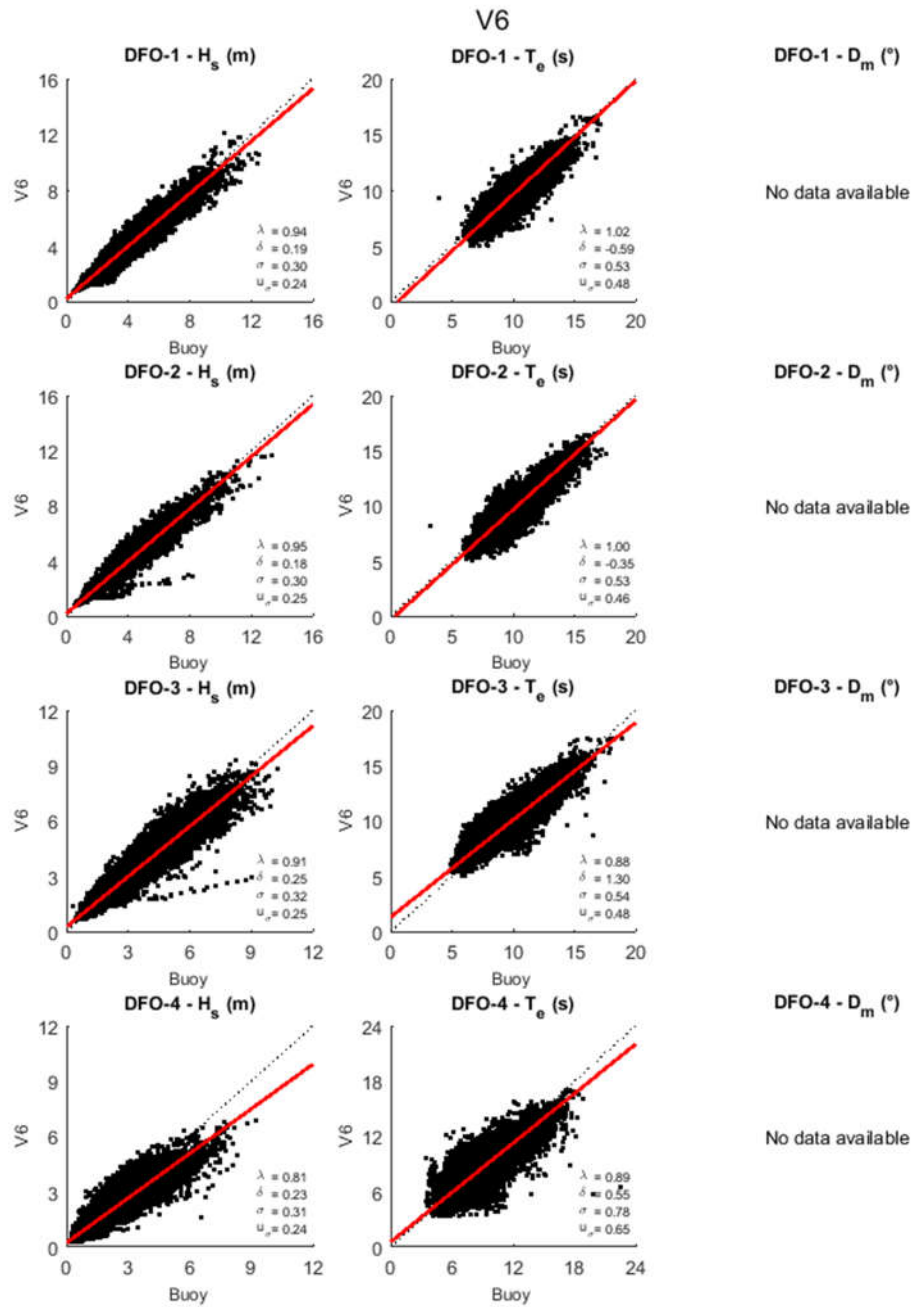


Figure A-7 Scatter plots for WCWI-v6, and $H_{m0}$, $T_e$ and $D_m$ – A.
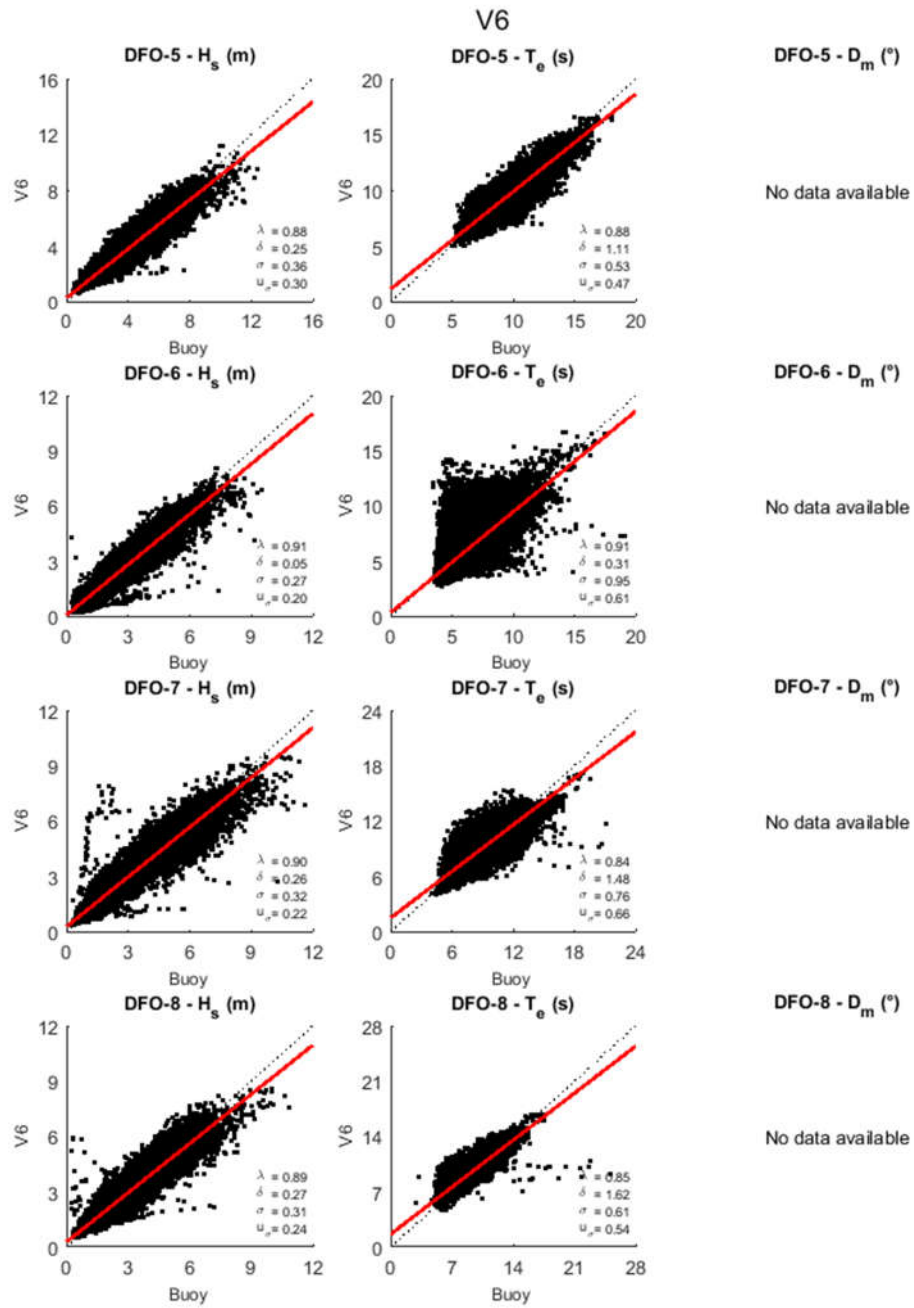
Figure A-8 Scatter plots for WCWI-v6, and $H_{m0}$, $T_e$ and $D_m$ – B.
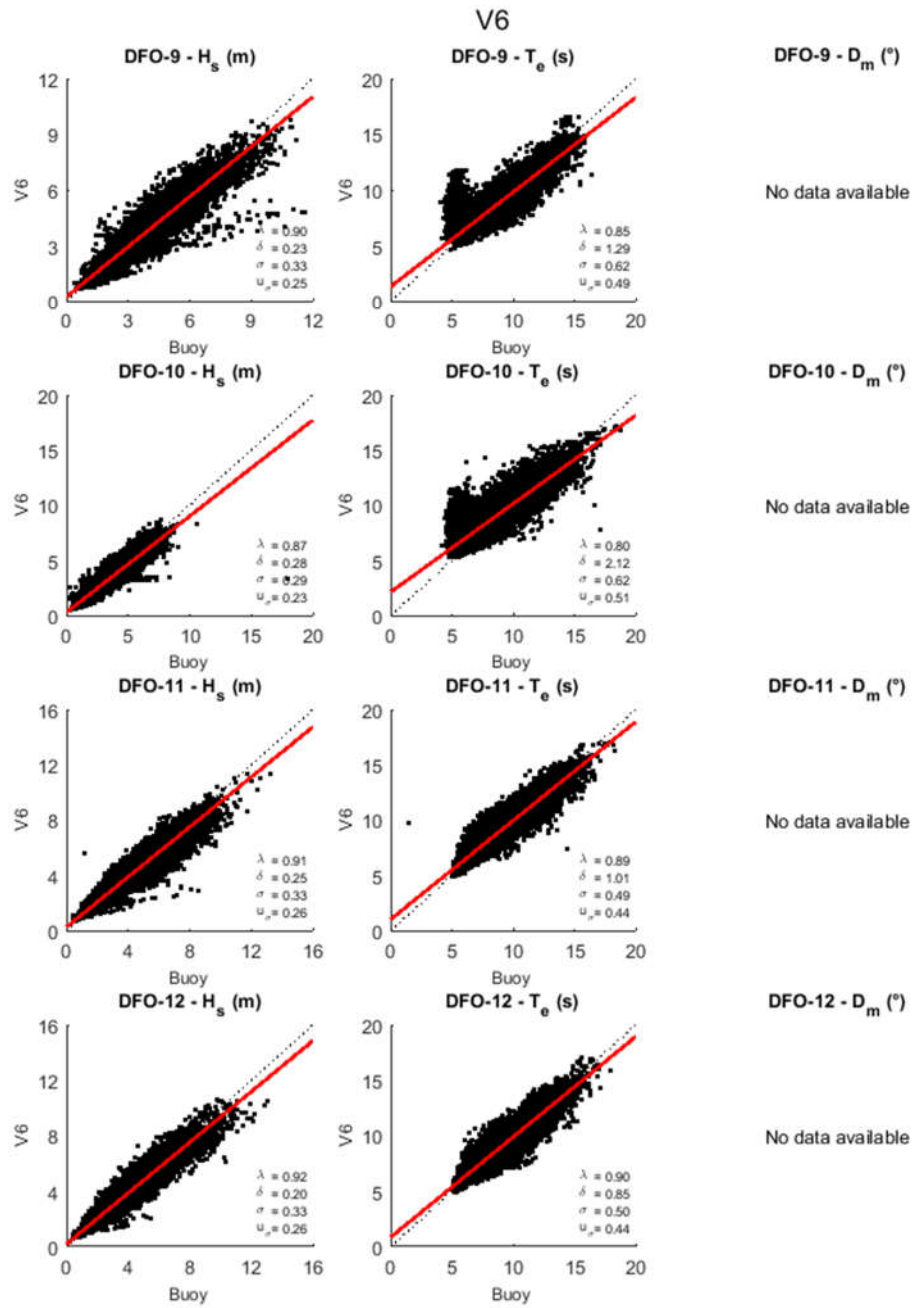
Figure A-9 Scatter plots for WCWI-v6, and $H_{m0}$, $T_e$ and $D_m$ – C.

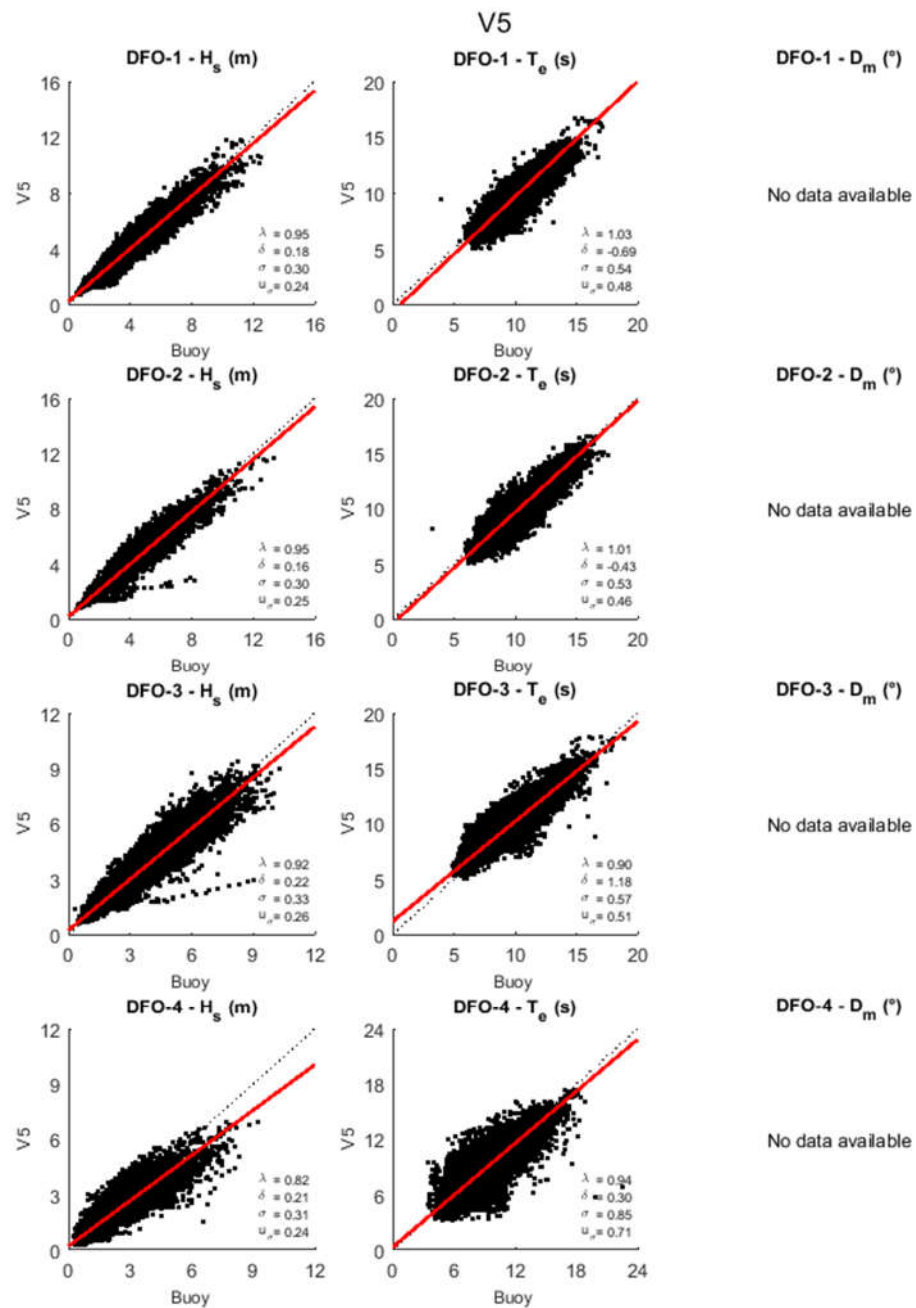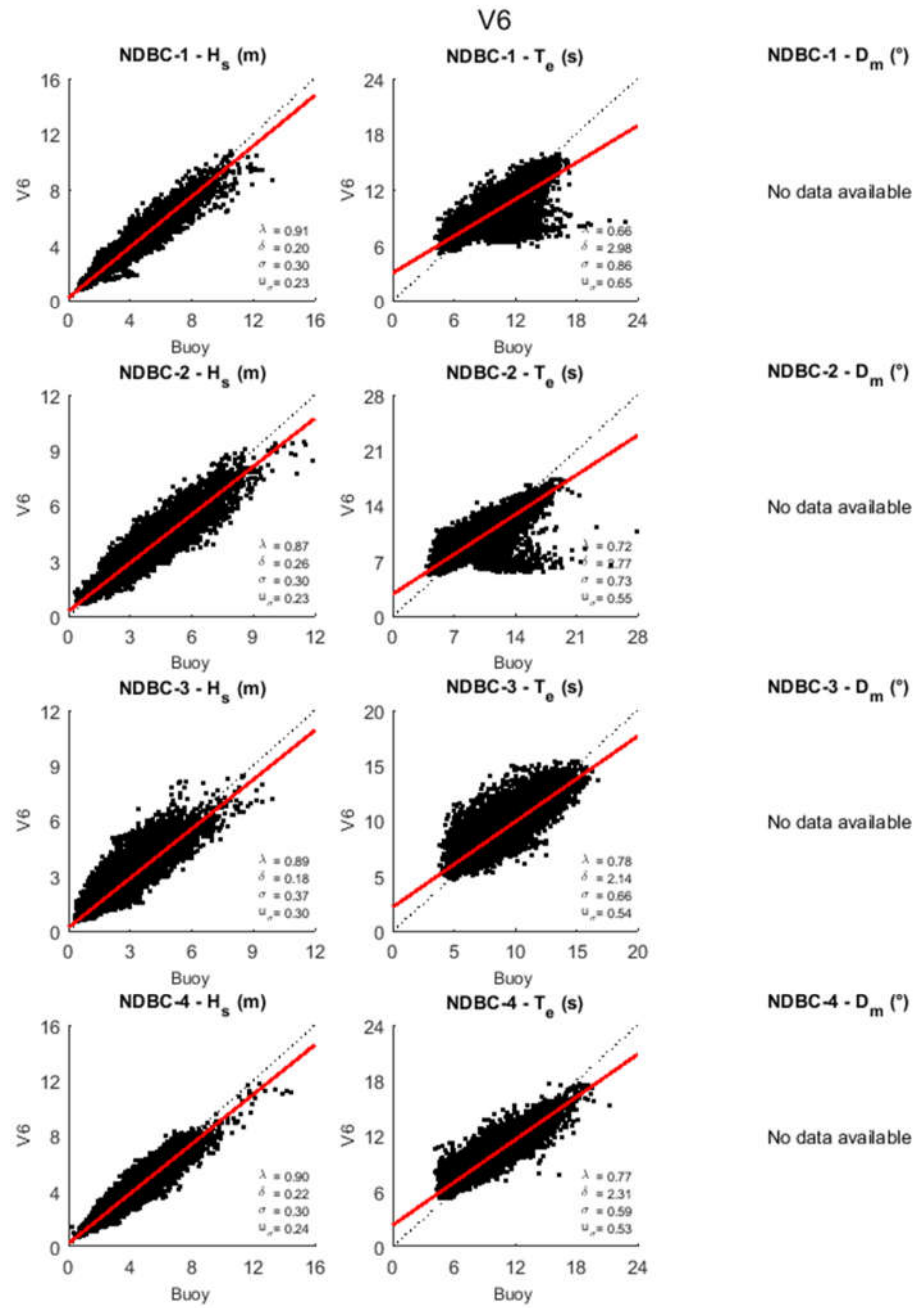Figure A-10 Scatter plots for WCWI-v6, and $H_{m0}$, $T_e$ and $D_m$ – D.
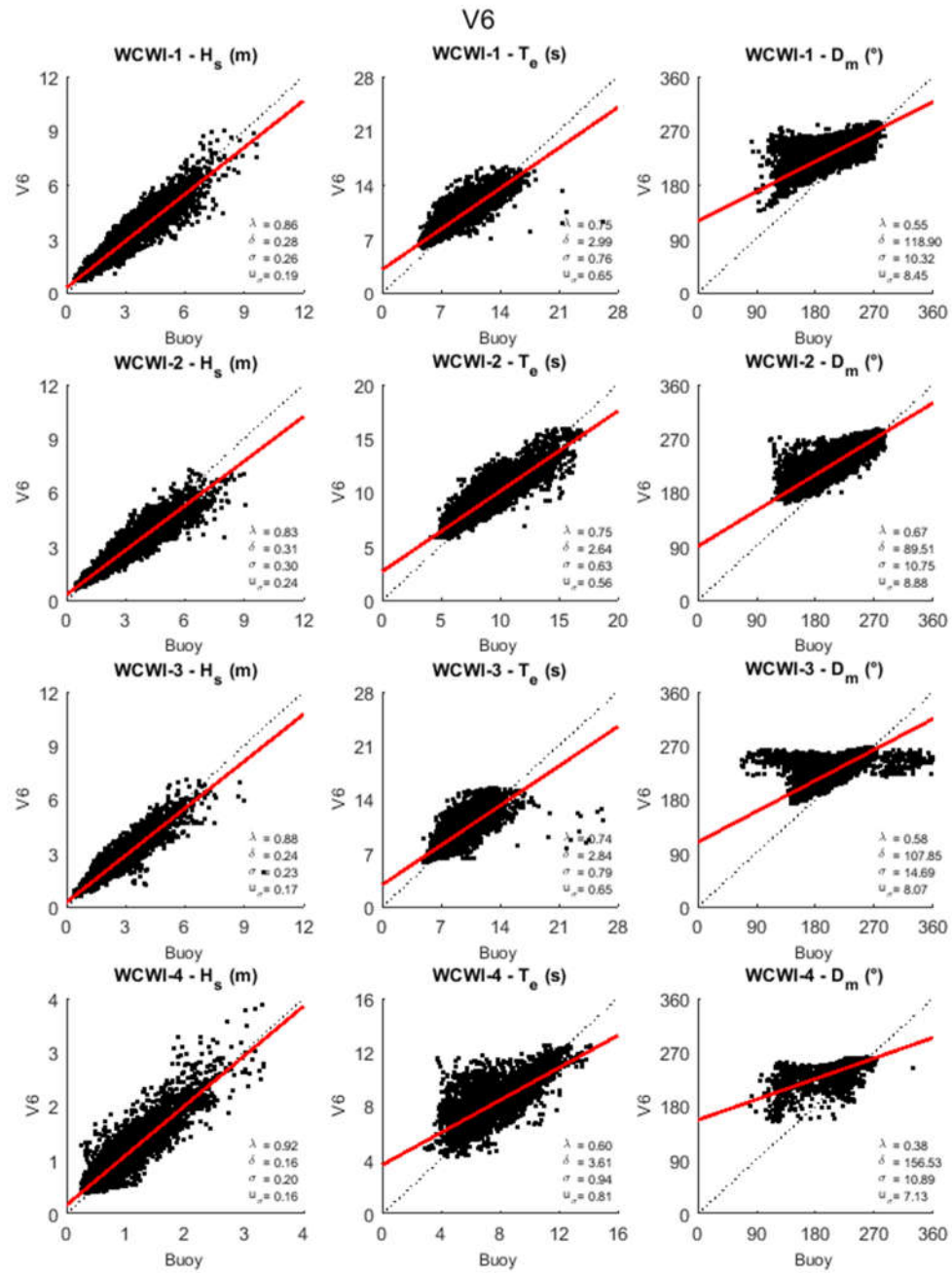
Figure A-11 Scatter plots for WCWI-v6, and $H_{m0}$, $T_e$ and $D_m$ – E.
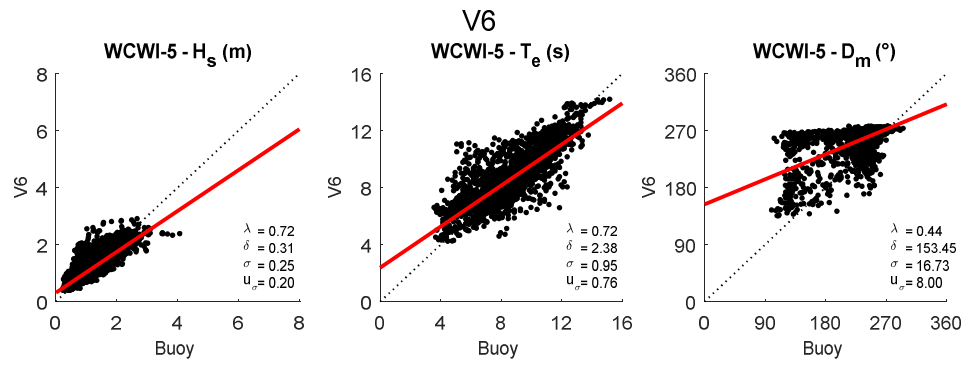
Figure A-12 Scatter plots for WCWI-v6, and $H_{m0}$, $T_e$ and $D_m$ − F.

# Appendix B  Scatter plots: WCWI-v6 vs WCWI-v5
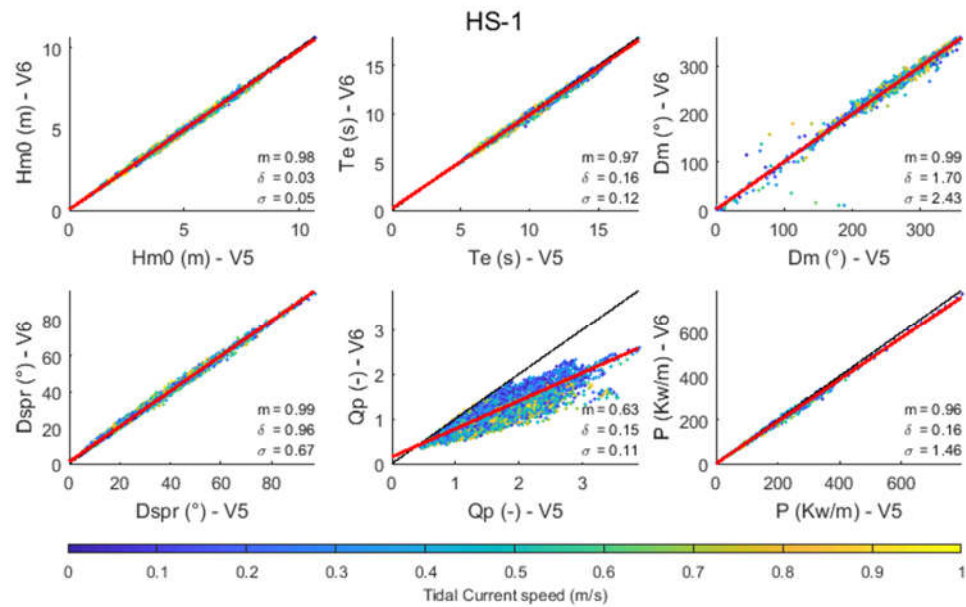


Figure B-1 Scatter plots for different wave parameters at HS-1 – V6 vs V5.
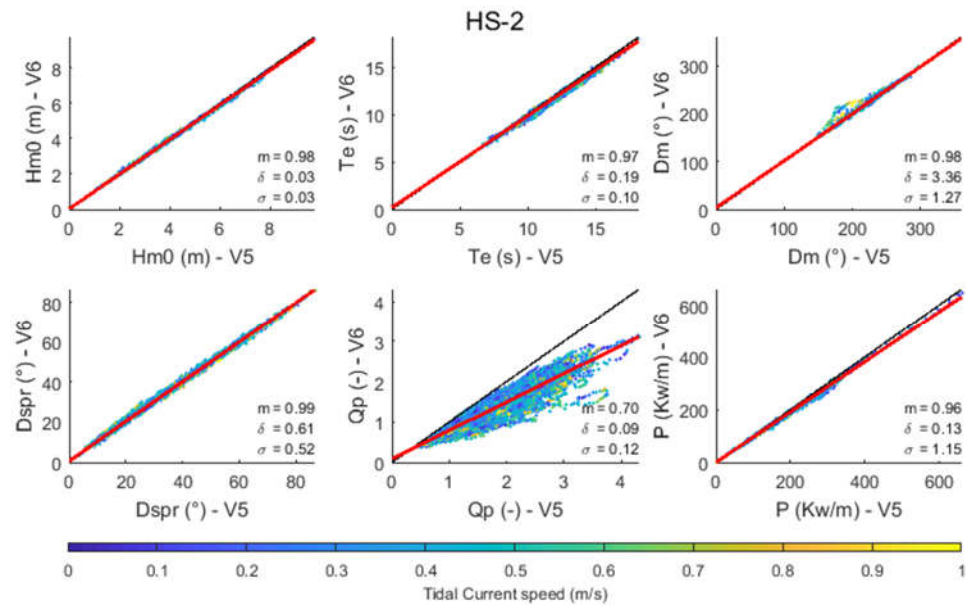


Figure B-2 Scatter plots for different wave parameters at HS-2 – V6 vs V5.
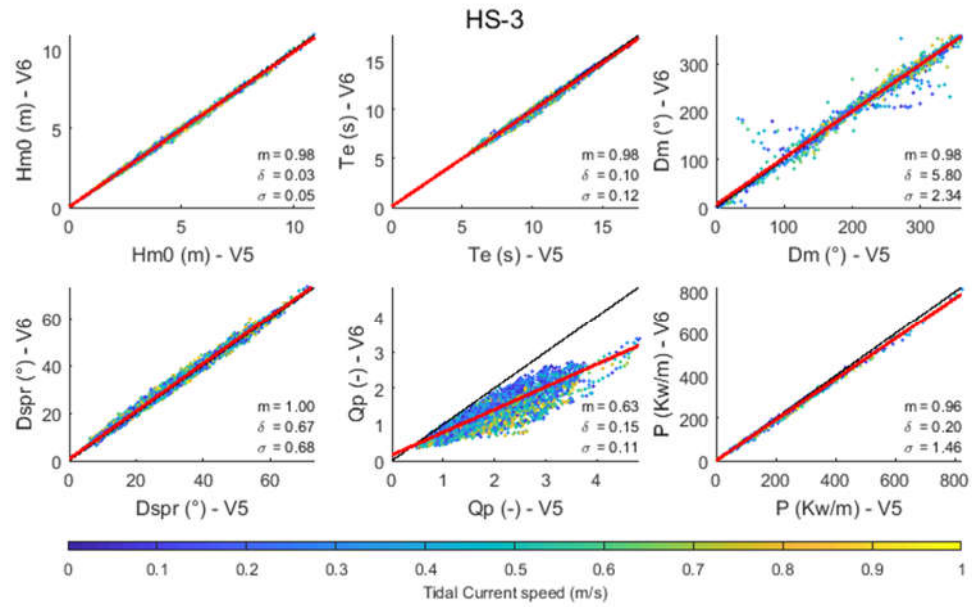
Figure B-3 Scatter plots for different wave parameters at HS-3 – V6 vs V5.
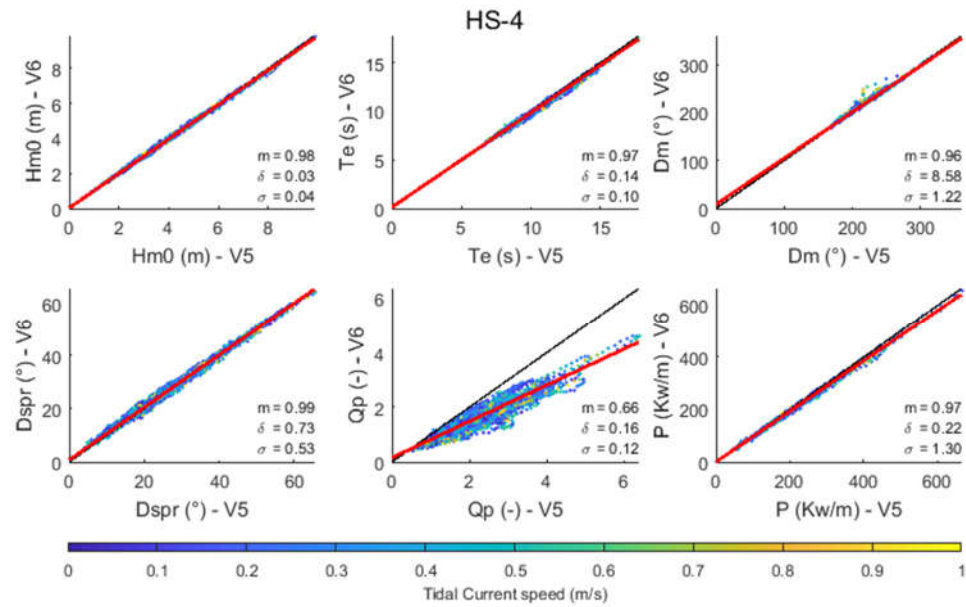


Figure B-4 Scatter plots for different wave parameters at HS-4 – V6 vs V5.

Data at location HS-5 is not available.
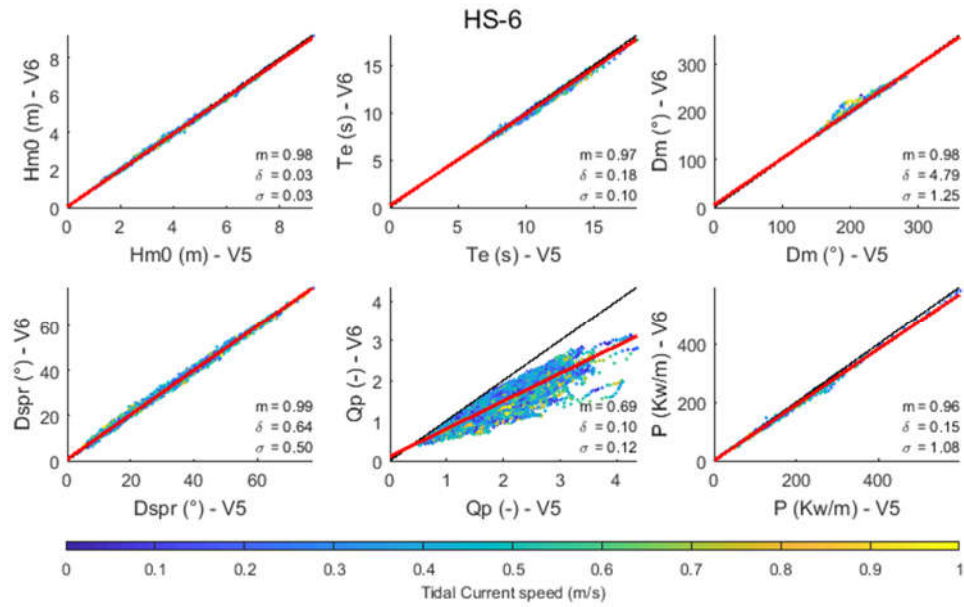
Figure B-5 Scatter plots for different wave parameters at HS-6 – V6 vs V5.
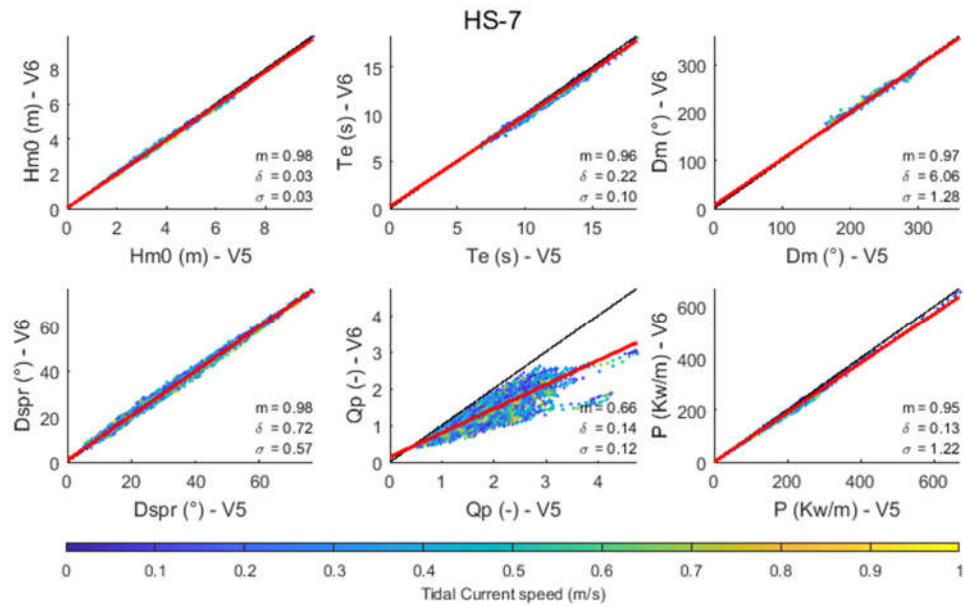


Figure B-6 Scatter plots for different wave parameters at HS-7 – V6 vs V5.
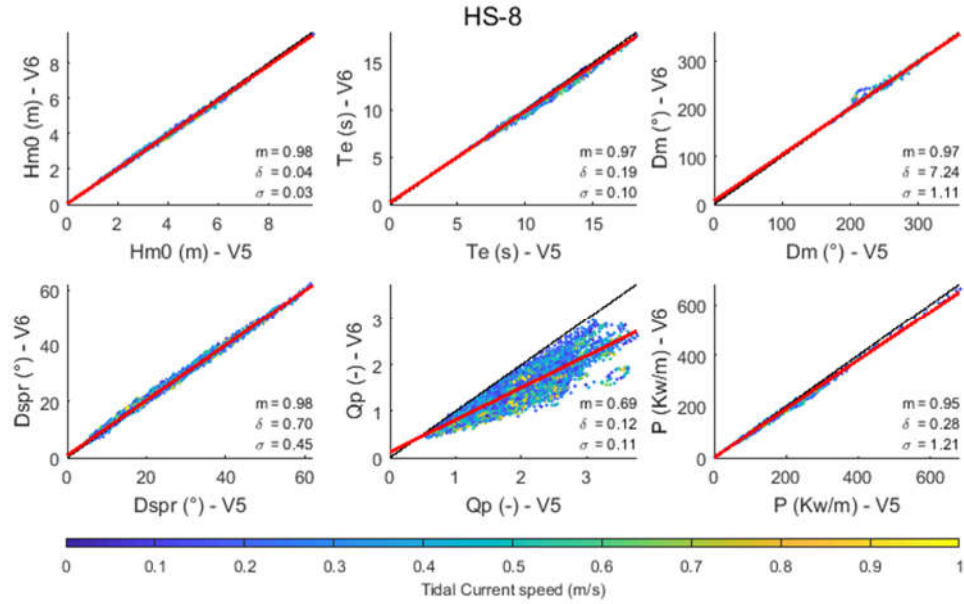
Figure B-7 Scatter plots for different wave parameters at HS-8 – V6 vs V5.
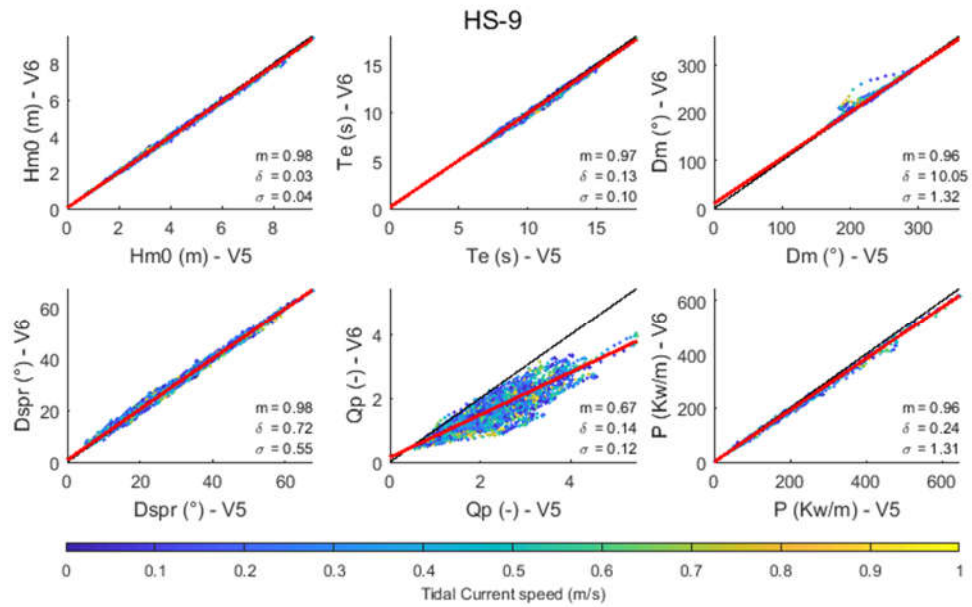


Figure B-8 Scatter plots for different wave parameters at HS-9 – V6 vs V5.
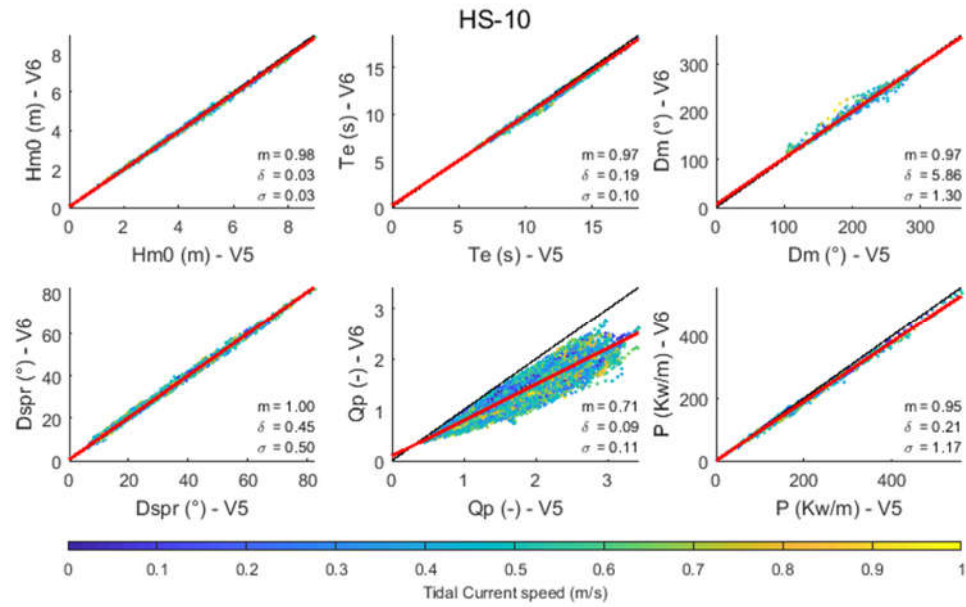
Figure B-9 Scatter plots for different wave parameters at HS-10 – V6 vs V5.
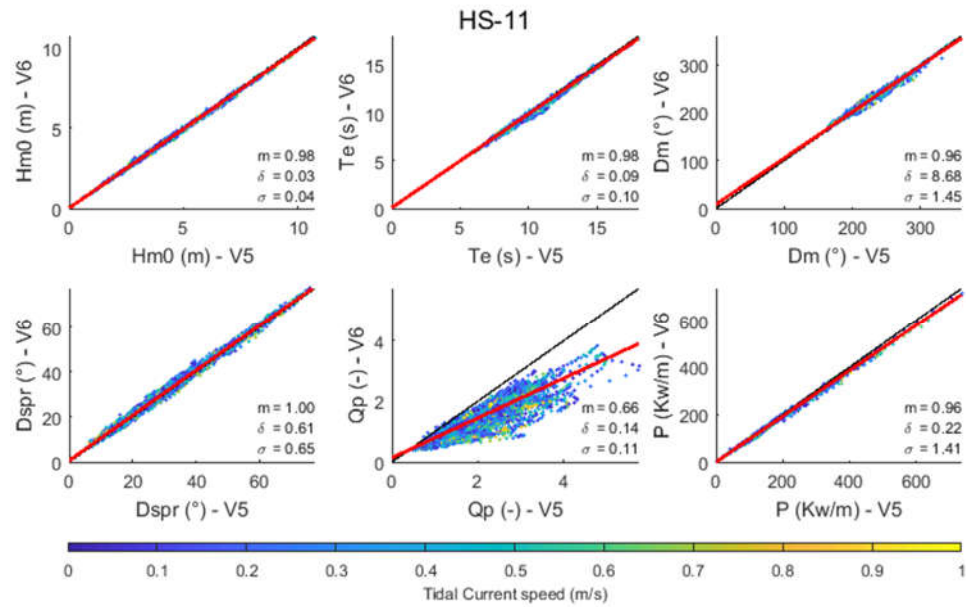


Figure B-10 Scatter plots for different wave parameters at HS-11 – V6 vs V5.
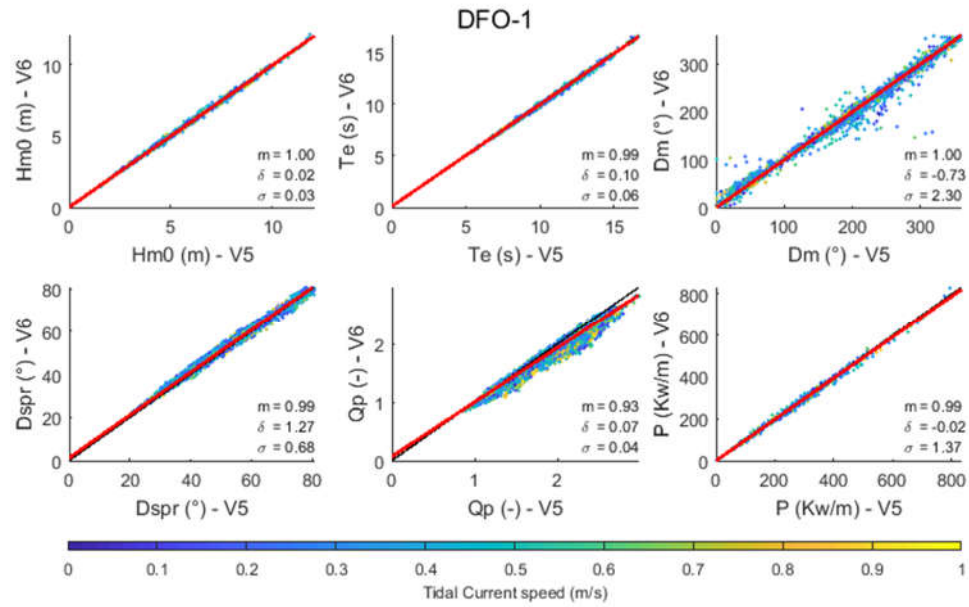
Figure B-11 Scatter plots for different wave parameters at DFO-1 – V6 vs V5.
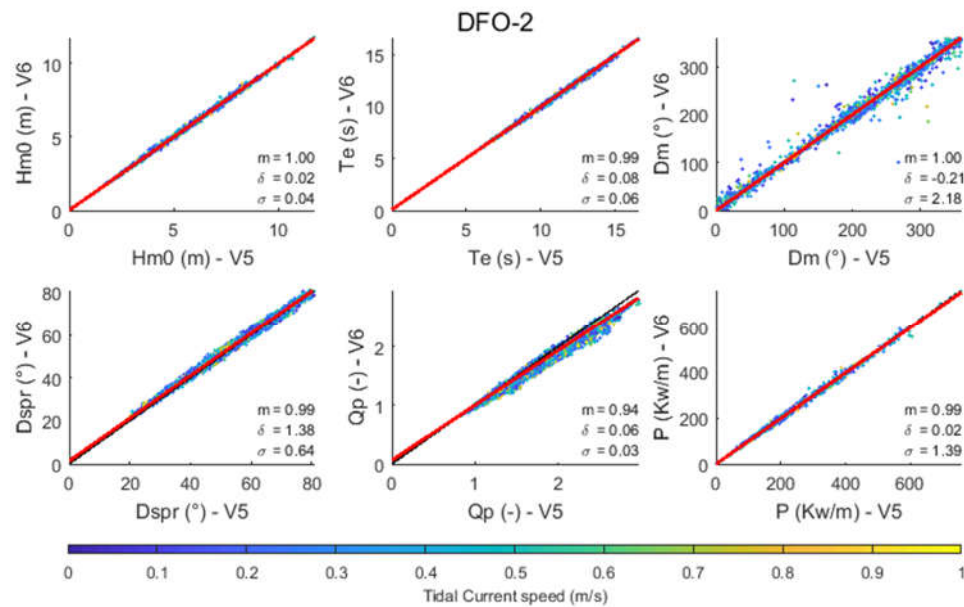


Figure B-12 Scatter plots for different wave parameters at DFO-2 – V6 vs V5.
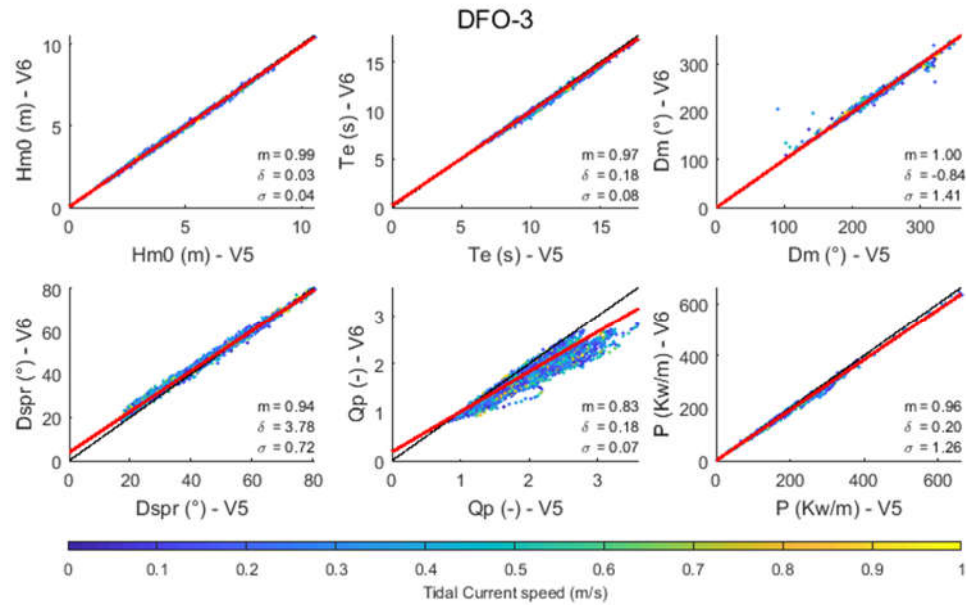
Figure B-13 Scatter plots for different wave parameters at DFO-3 – V6 vs V5.
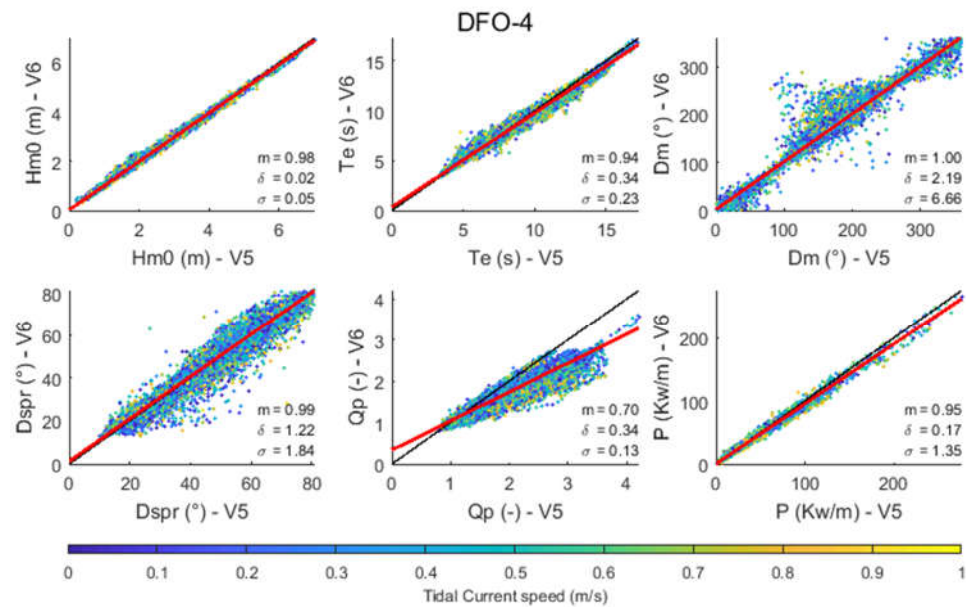


Figure B-14 Scatter plots for different wave parameters at DFO-4 – V6 vs V5.
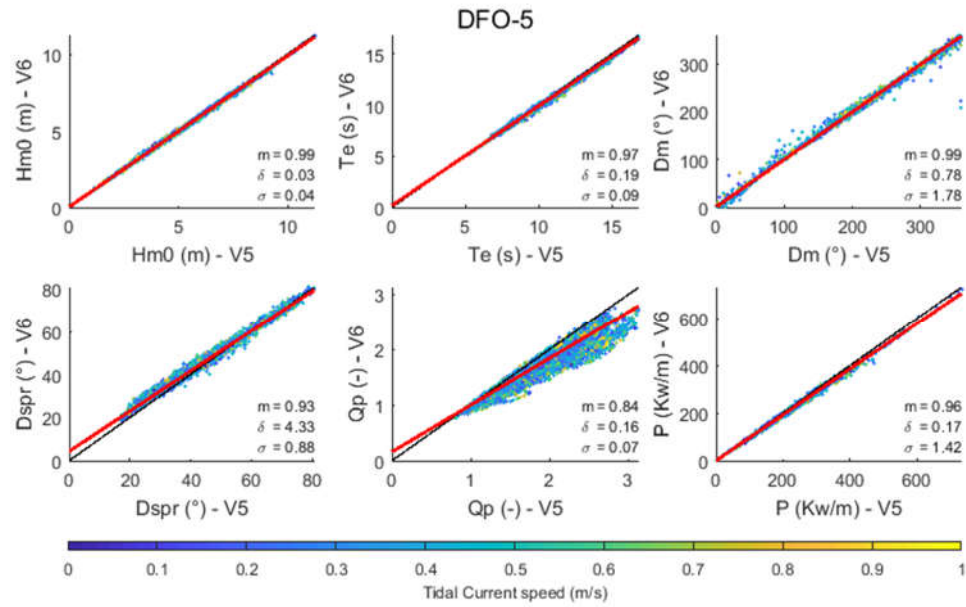
Figure B-15 Scatter plots for different wave parameters at DFO-5 – V6 vs V5.
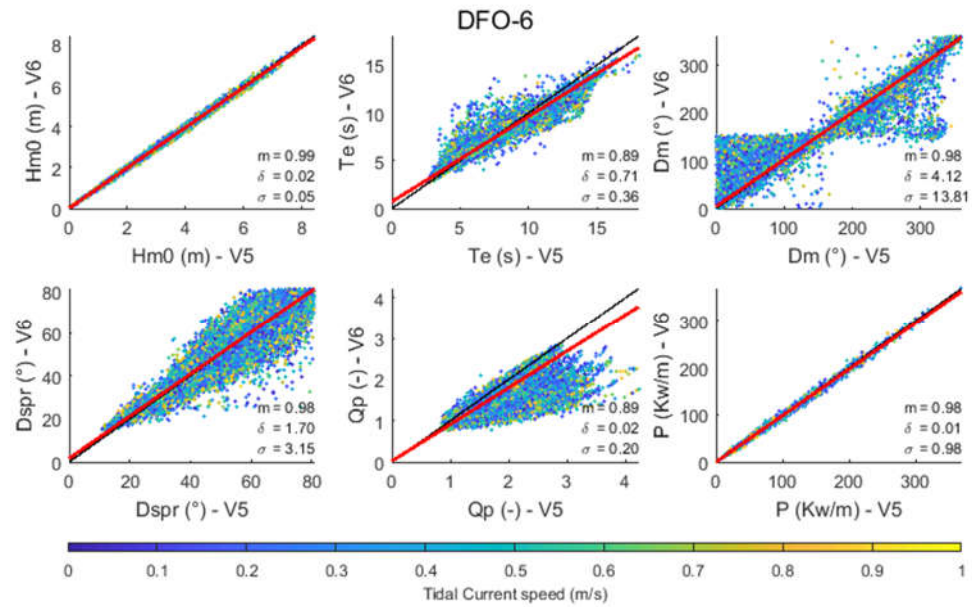


Figure B-16 Scatter plots for different wave parameters at DFO-6 – V6 vs V5.
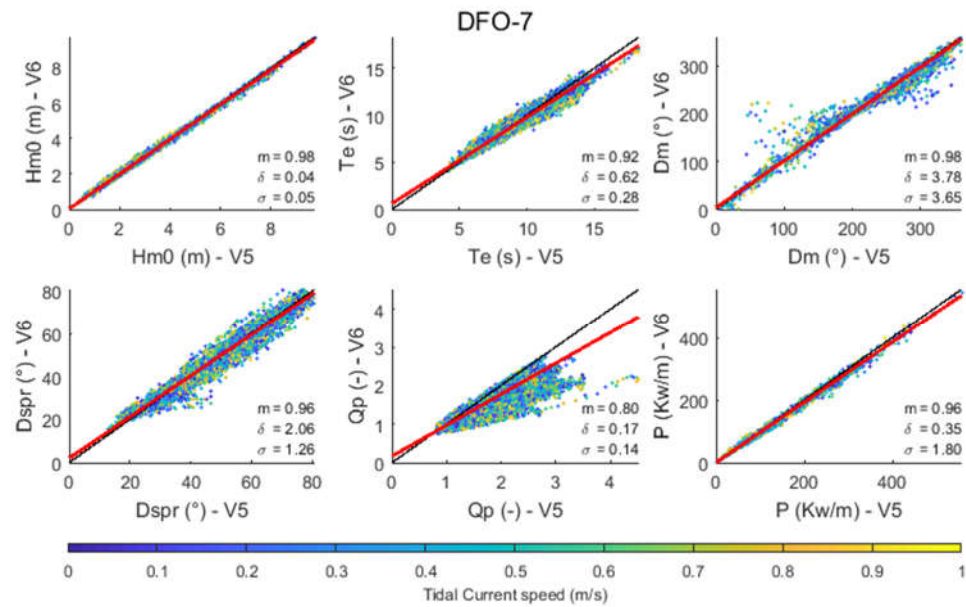
Figure B-17 Scatter plots for different wave parameters at DFO-7 – V6 vs V5.
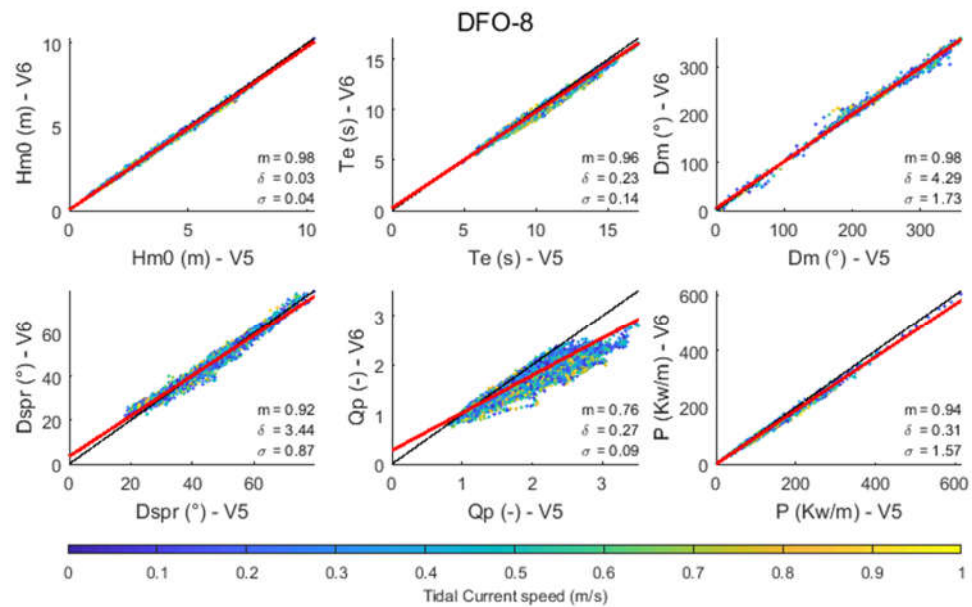


Figure B-18 Scatter plots for different wave parameters at DFO-8 – V6 vs V5.
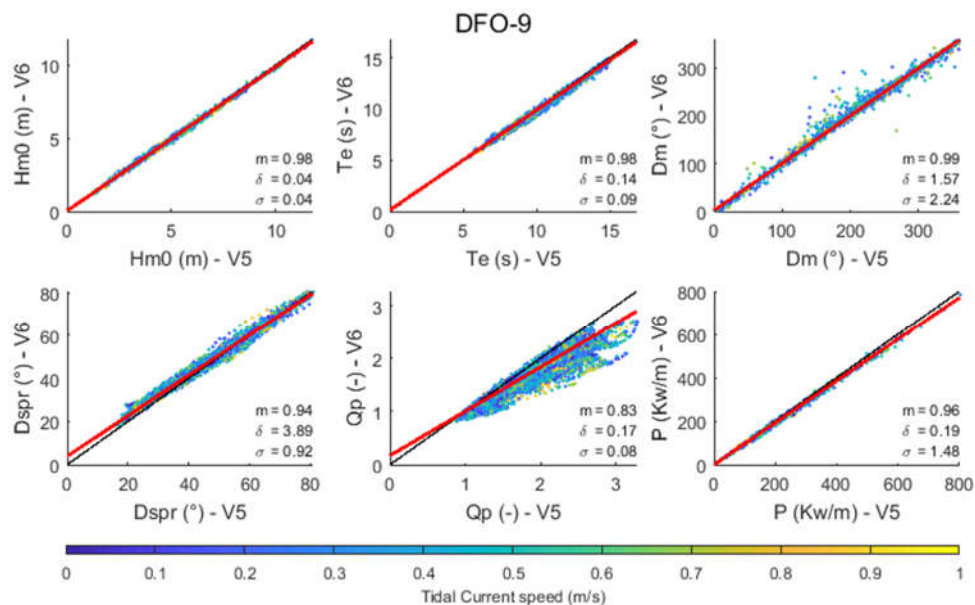
Figure B-19 Scatter plots for different wave parameters at DFO-9 – V6 vs V5.
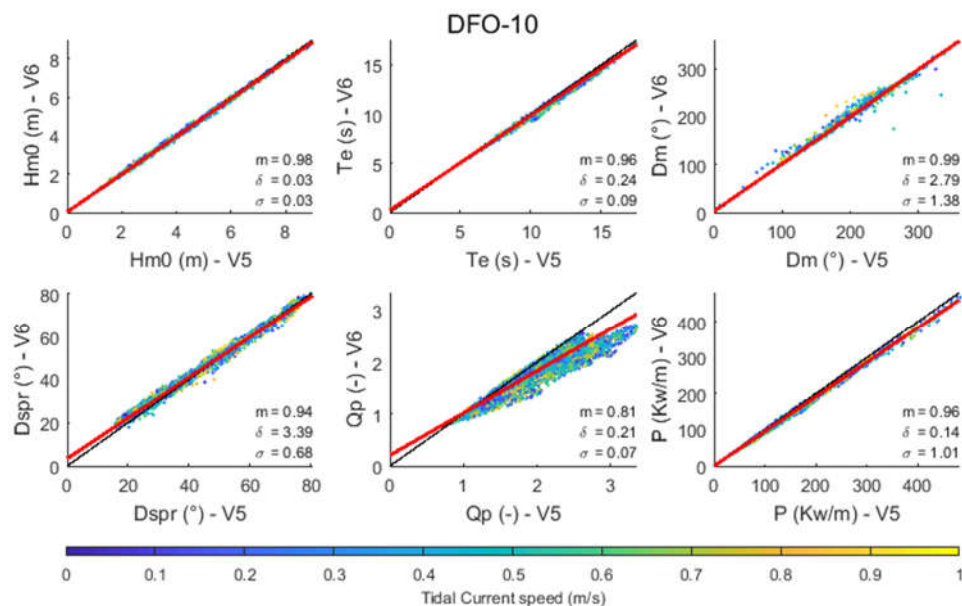


Figure B-20 Scatter plots for different wave parameters at DFO-10 – V6 vs V5.
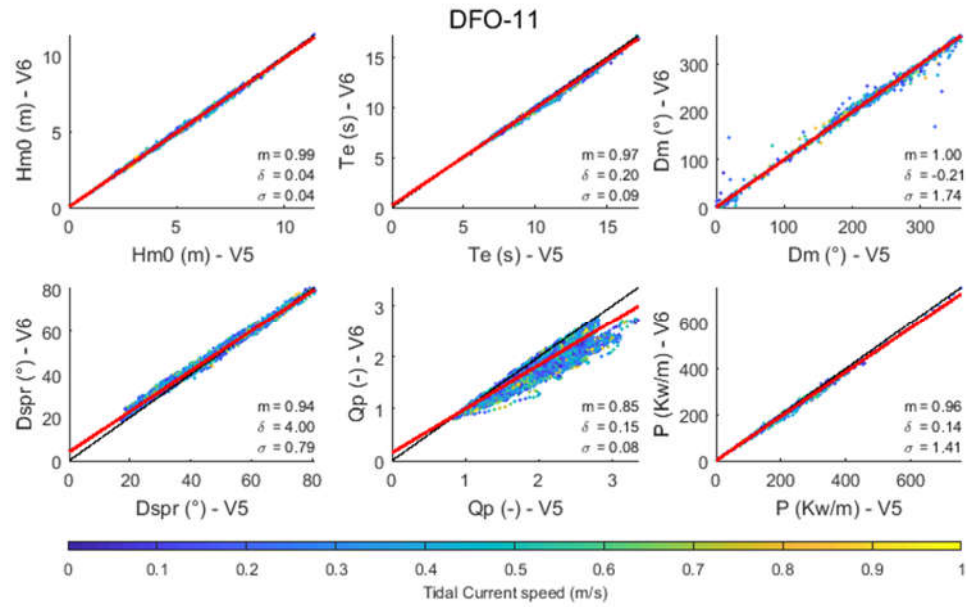
Figure B-21 Scatter plots for different wave parameters at DFO-11 – V6 vs V5.
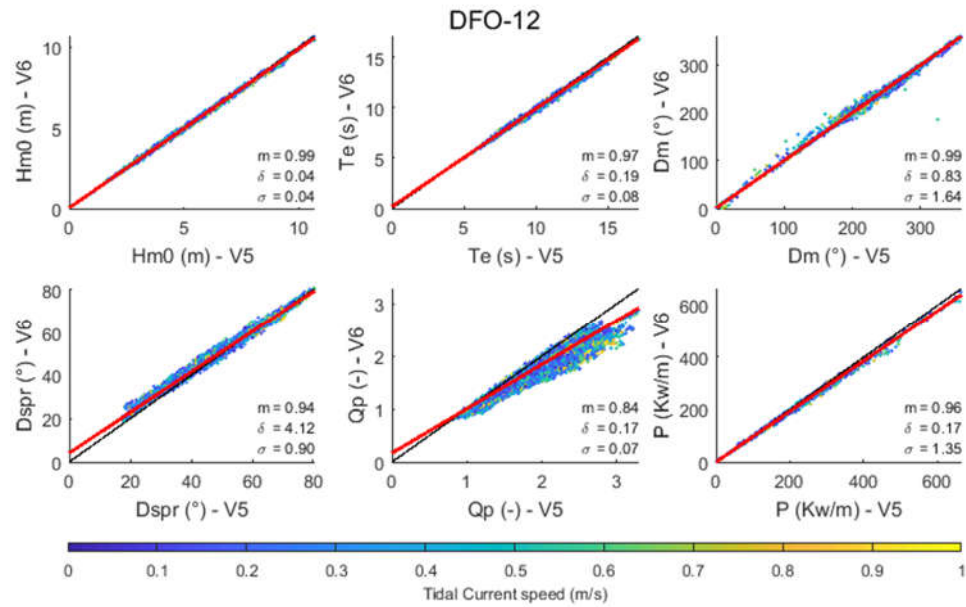


Figure B-22 Scatter plots for different wave parameters at DFO-12 – V6 vs V5.
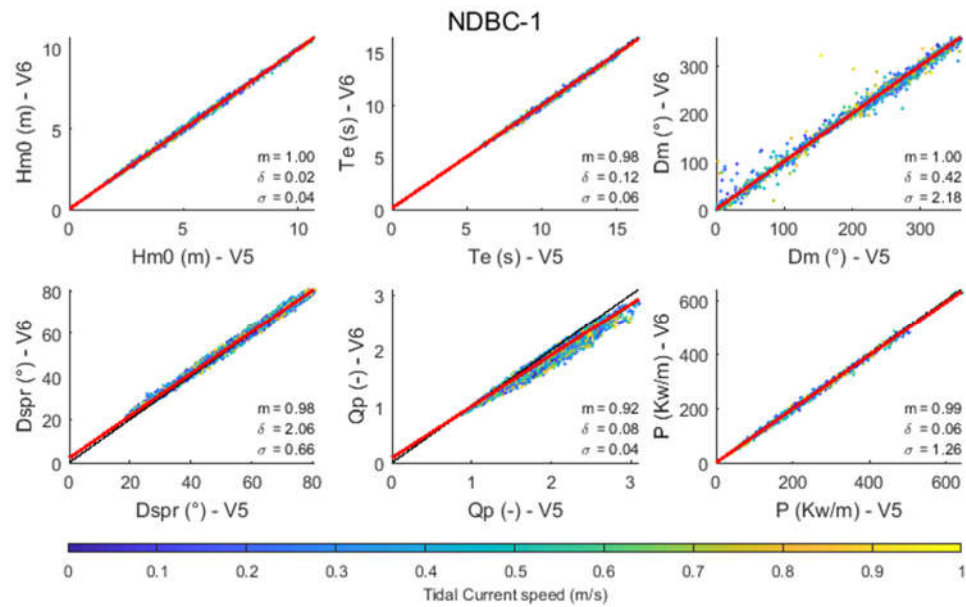
Figure B-23 Scatter plots for different wave parameters at NDBC-1 – V6 vs V5.
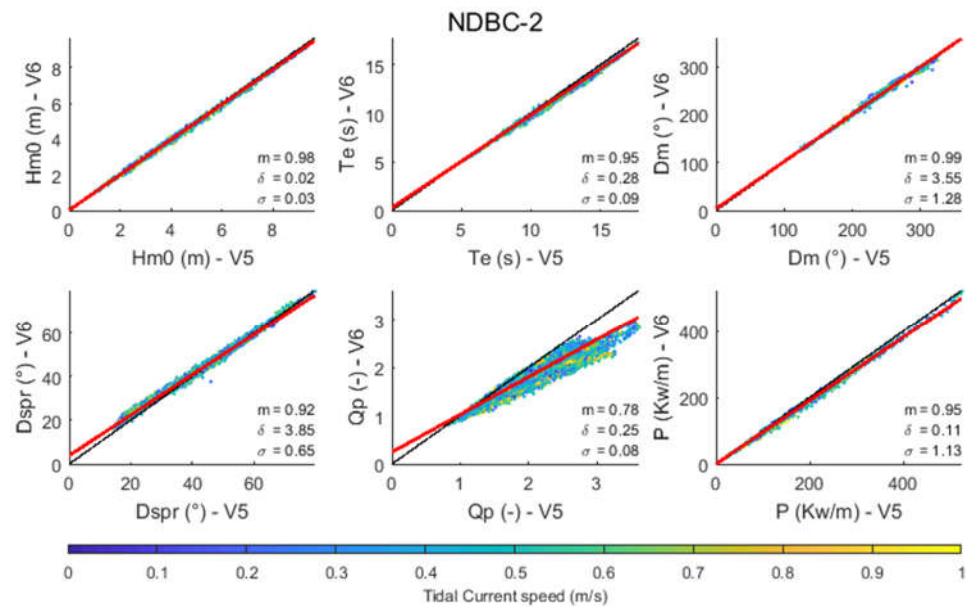


Figure B-24 Scatter plots for different wave parameters at NDBC-2 – V6 vs V5.
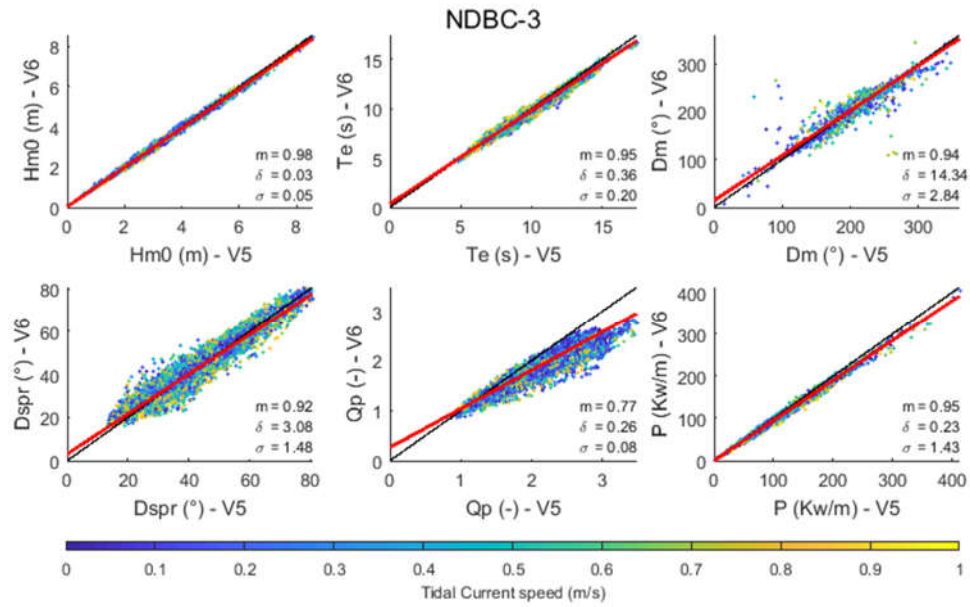
Figure B-25 Scatter plots for different wave parameters at NDBC-3 – V6 vs V5.
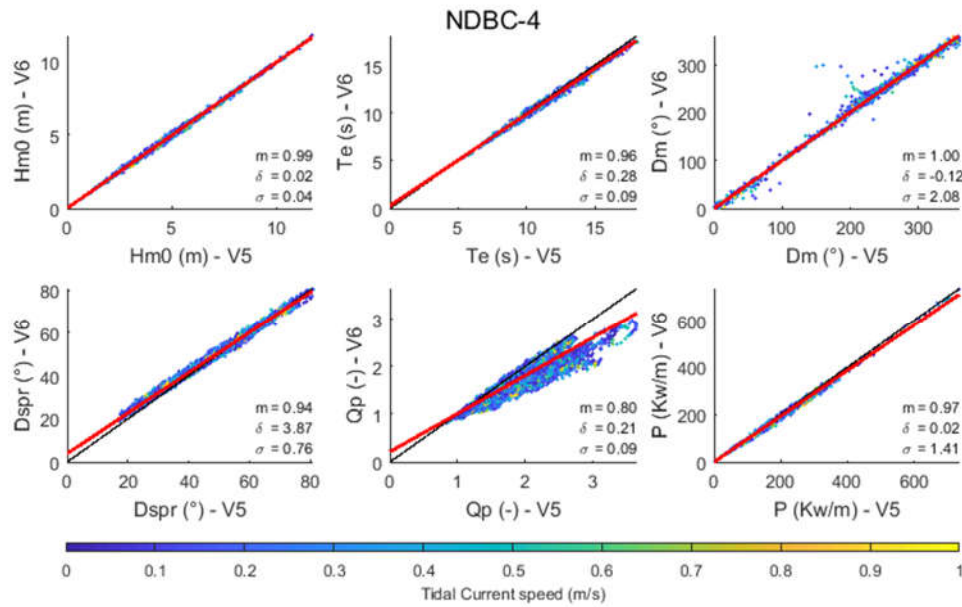


Figure B-26 Scatter plots for different wave parameters at NDBC-4 – V6 vs V5.
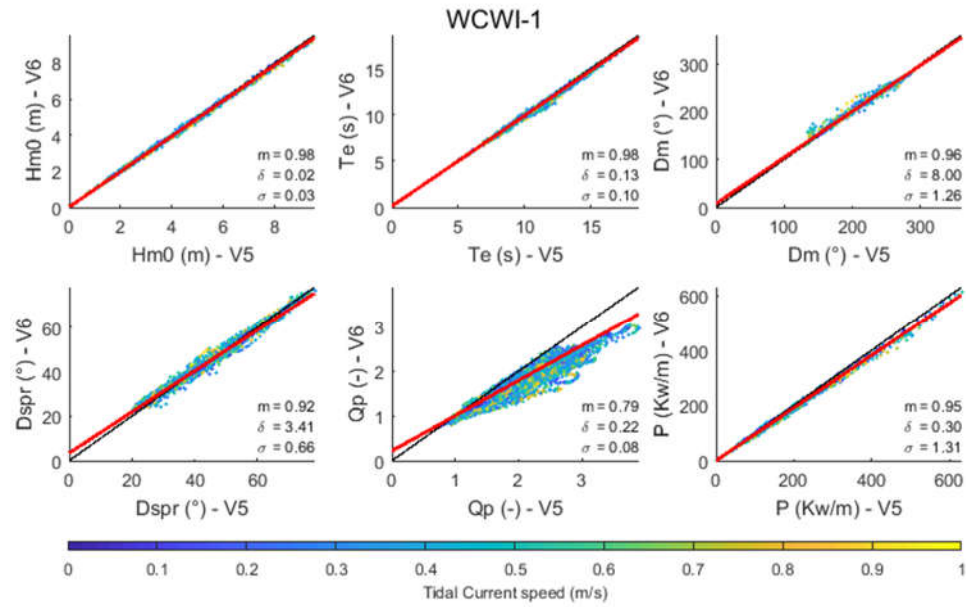
Figure B-27 Scatter plots for different wave parameters at WCWI-1 – V6 vs V5.
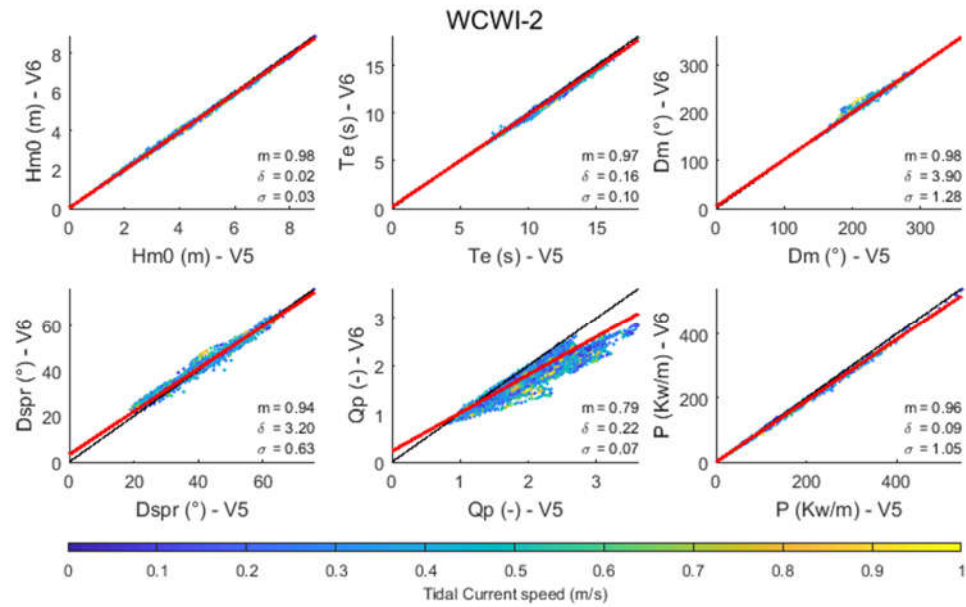


Figure B-28 Scatter plots for different wave parameters at WCWI-2 – V6 vs V5.
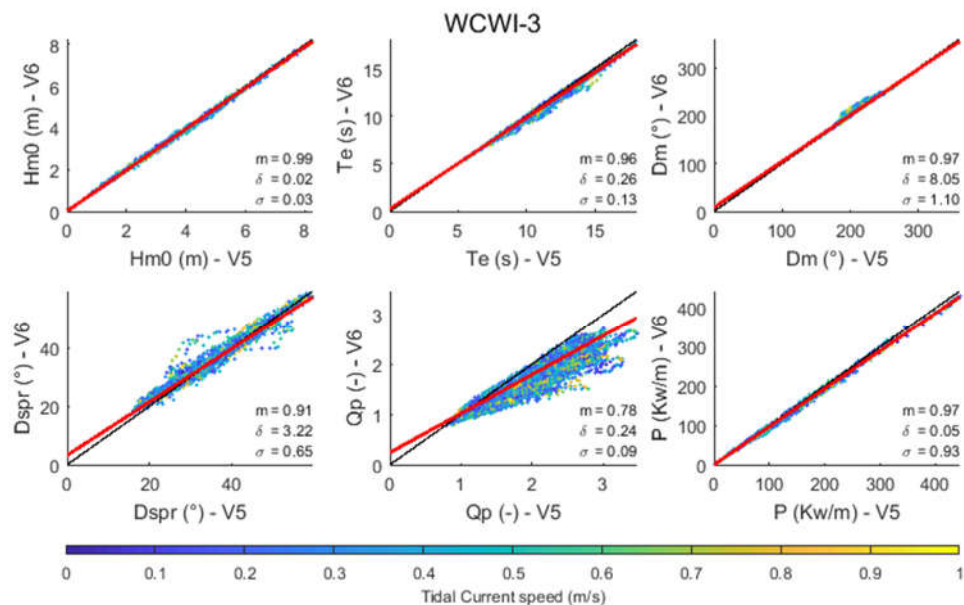
Figure B-29 Scatter plots for different wave parameters at WCWI-3 – V6 vs V5.
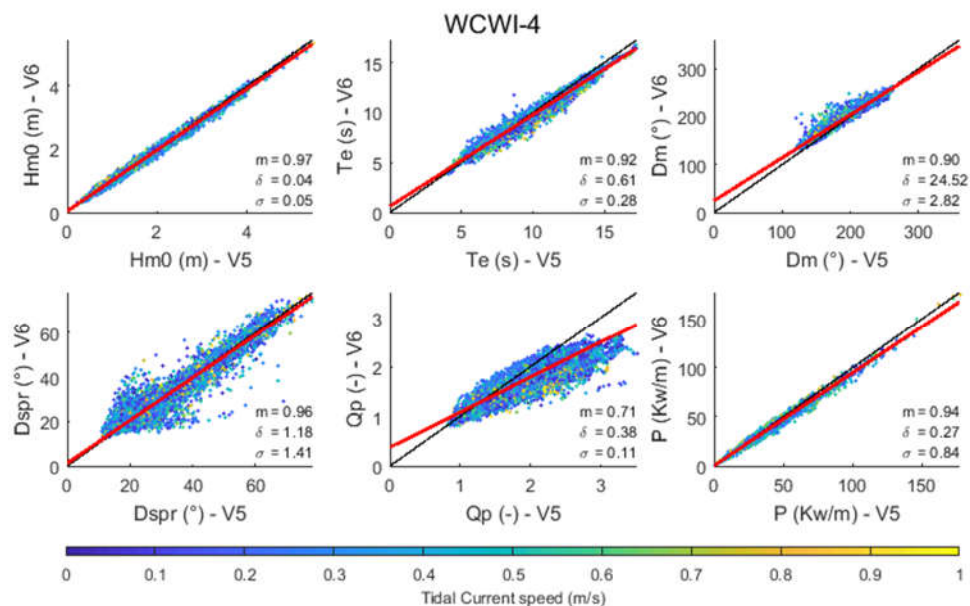


Figure B-30 Scatter plots for different wave parameters at WCWI-4 – V6 vs V5.
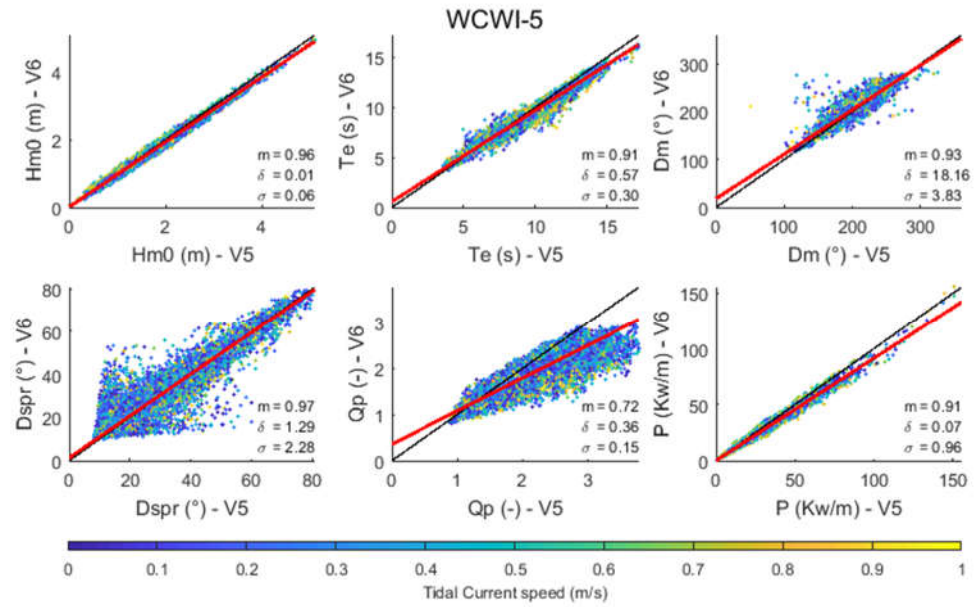
Figure B-31 Scatter plots for different wave parameters at WCWI-5 – V6 vs V5.

# Appendix C    Time series of wave parameters and power semi-centered at the biggest positive and negative difference of wave power density between models
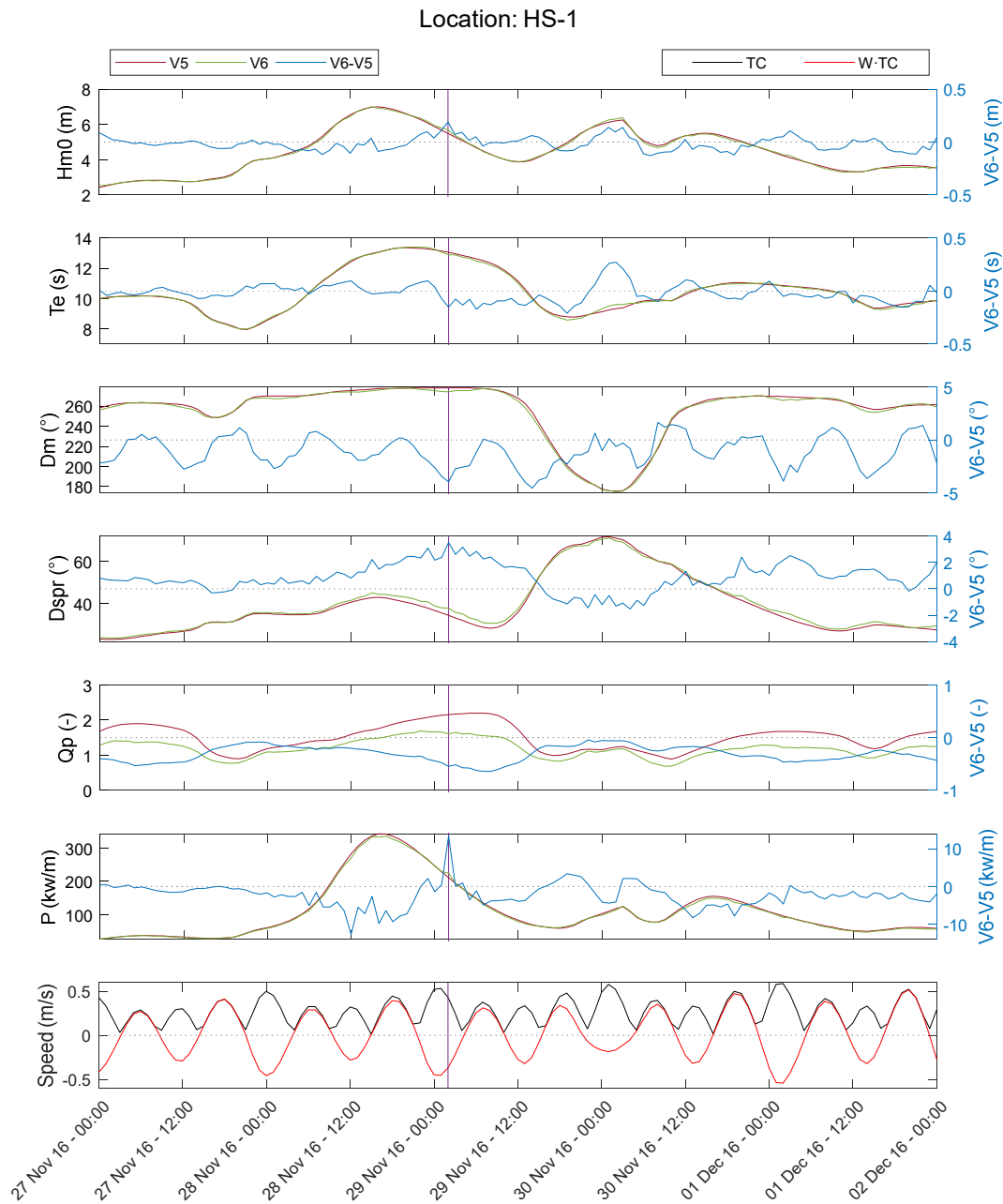


Figure C-1 Time series of wave parameters, wave power and tidal currents including the maximum positive difference in wave power density between V6 and V5 (purple line) at HS-1.
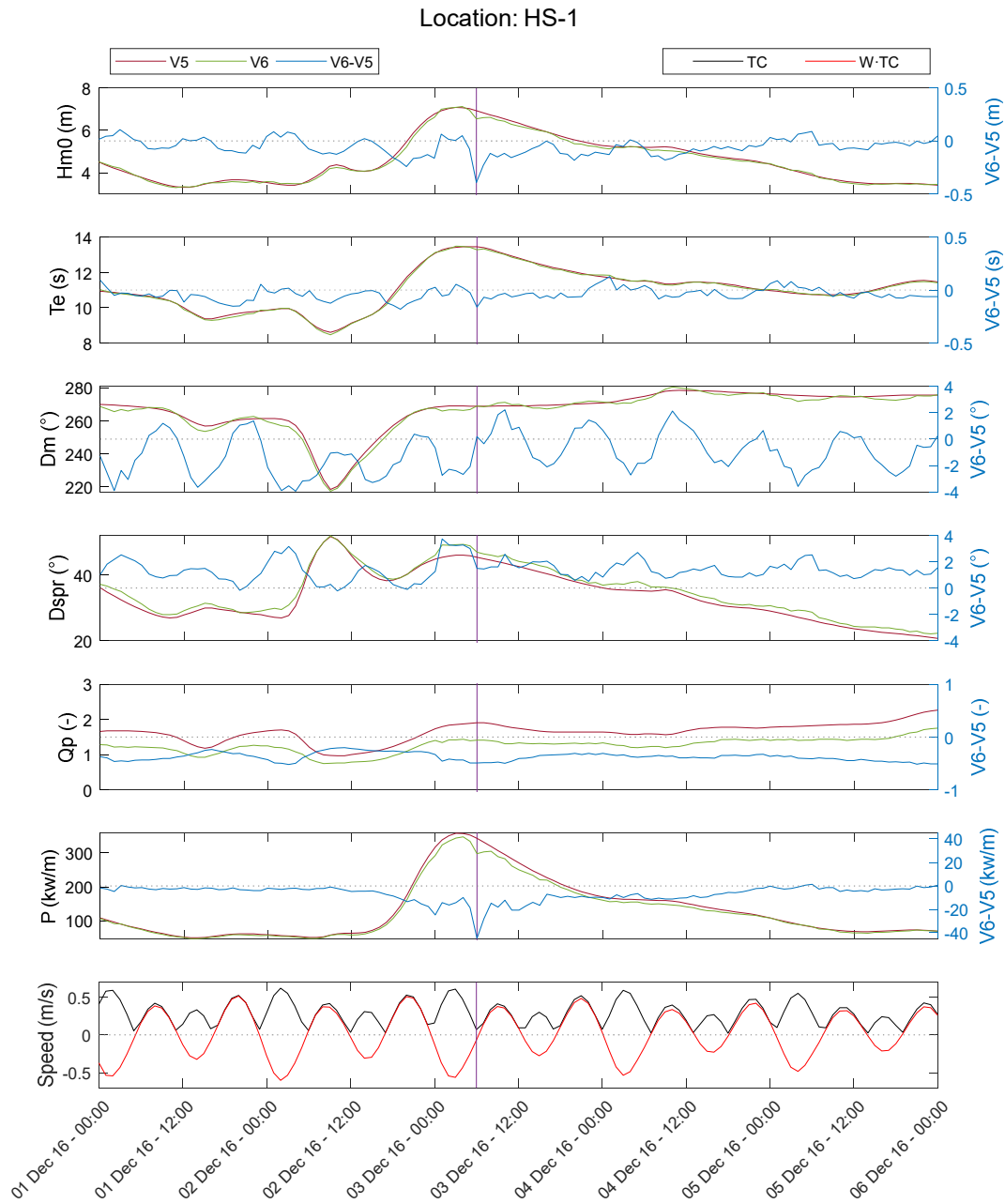
Figure C-2 Time series of wave parameters, wave power and tidal currents including the maximum negative difference in wave power density between V6 and V5 (purple line) at HS-1.
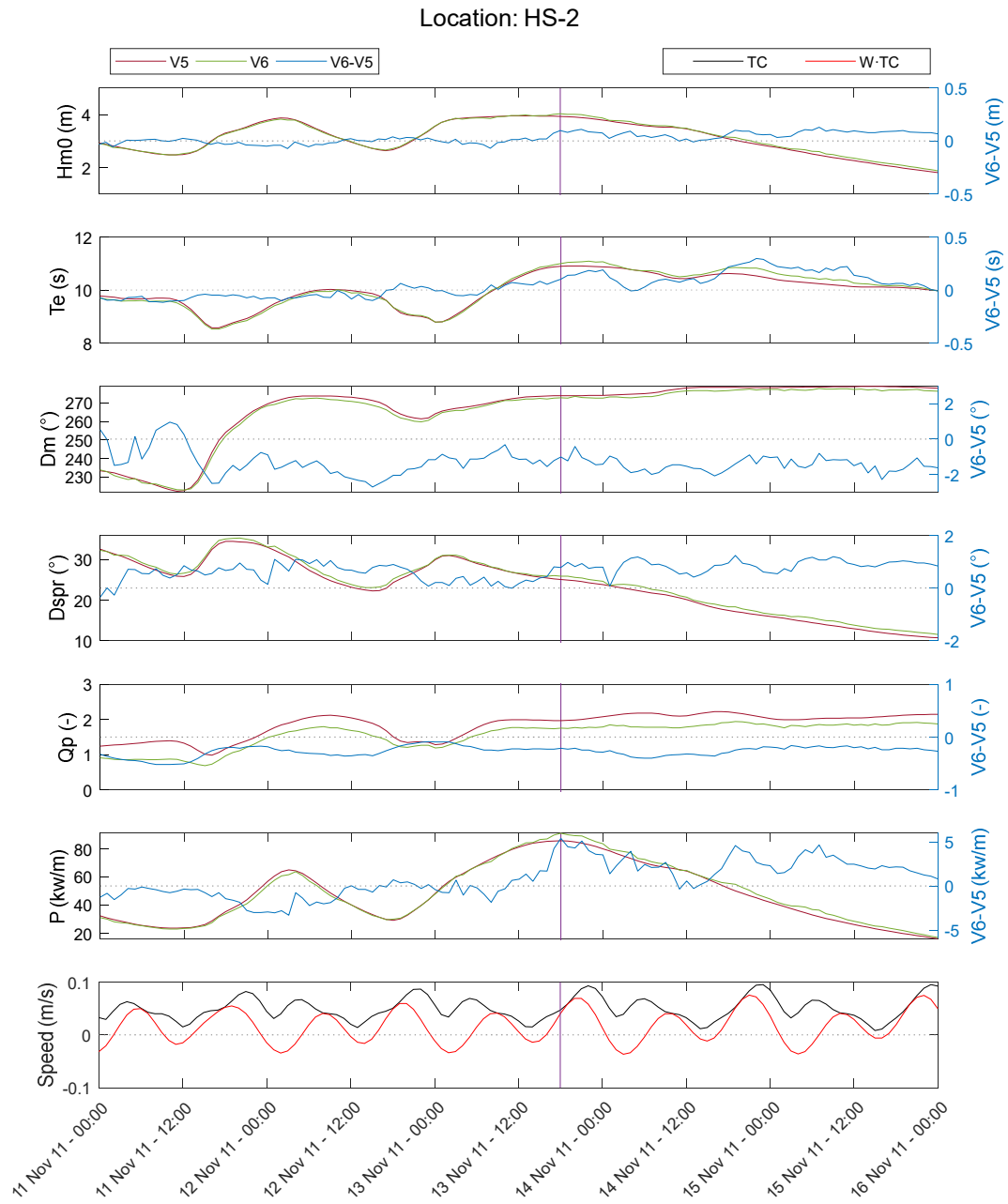
Figure C-3 Time series of wave parameters, wave power and tidal currents including the maximum positive difference in wave power density between V6 and V5 (purple line) at HS-2.
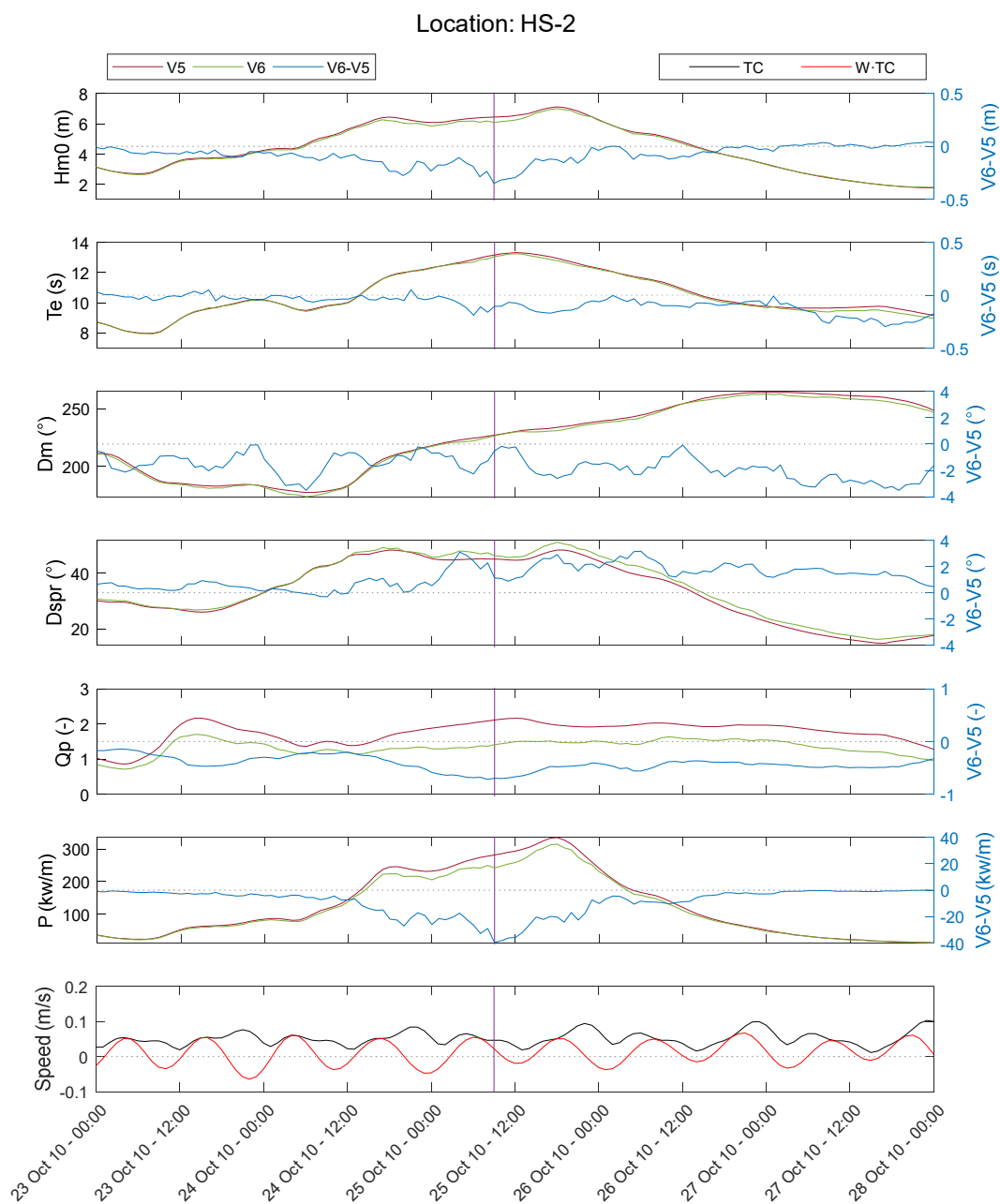
Figure C-4 Time series of wave parameters, wave power and tidal currents including the maximum negative difference in wave power density between V6 and V5 (purple line) at HS-2.
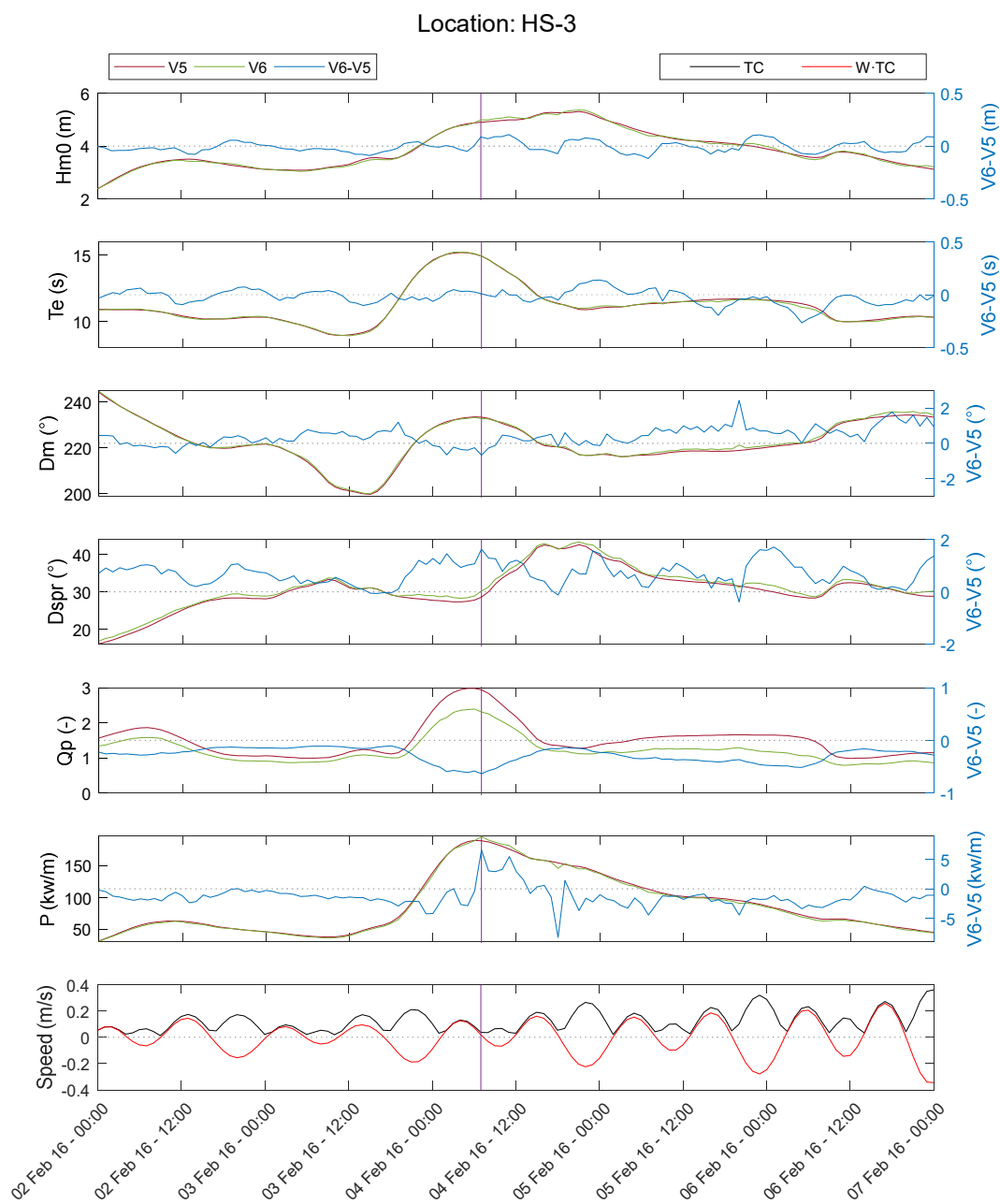
Figure C-5 Time series of wave parameters, wave power and tidal currents including the maximum positive difference in wave power density between V6 and V5 (purple line) at HS-3.
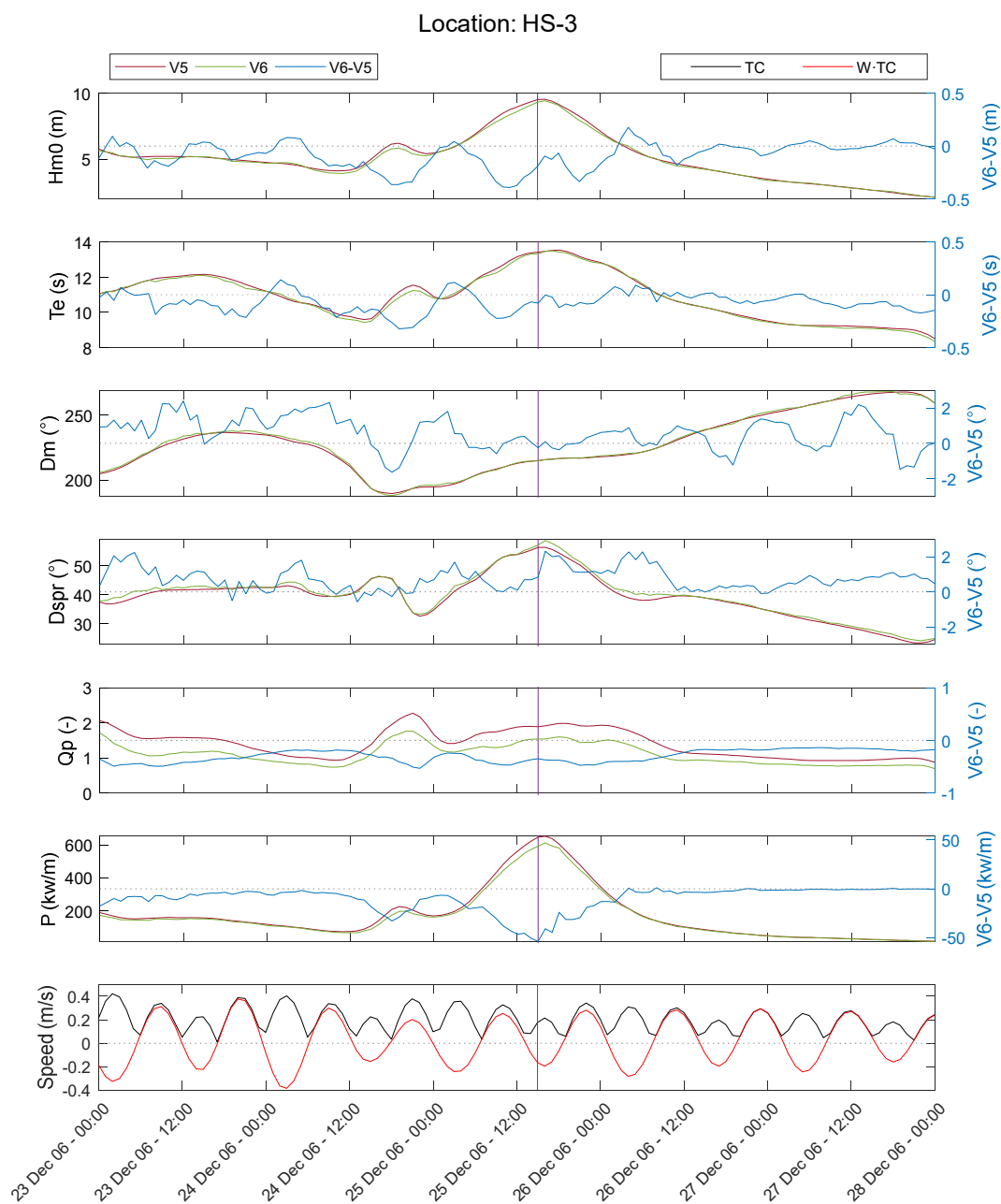
Figure C-6 Time series of wave parameters, wave power and tidal currents including the maximum negative difference in wave power density between V6 and V5 (purple line) at HS-3.
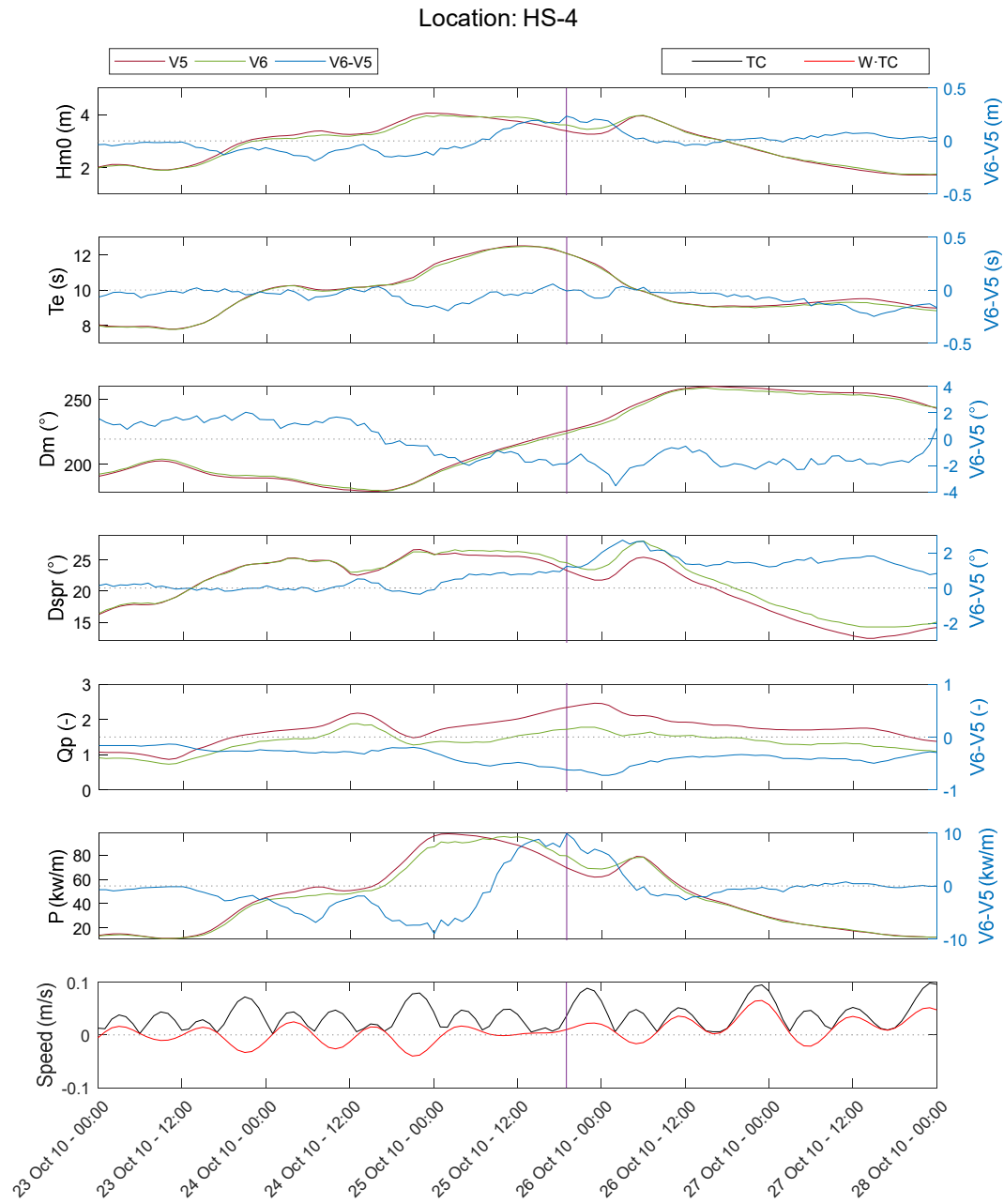
Figure C-7 Time series of wave parameters, wave power and tidal currents including the maximum positive difference in wave power density between V6 and V5 (purple line) at HS-4.
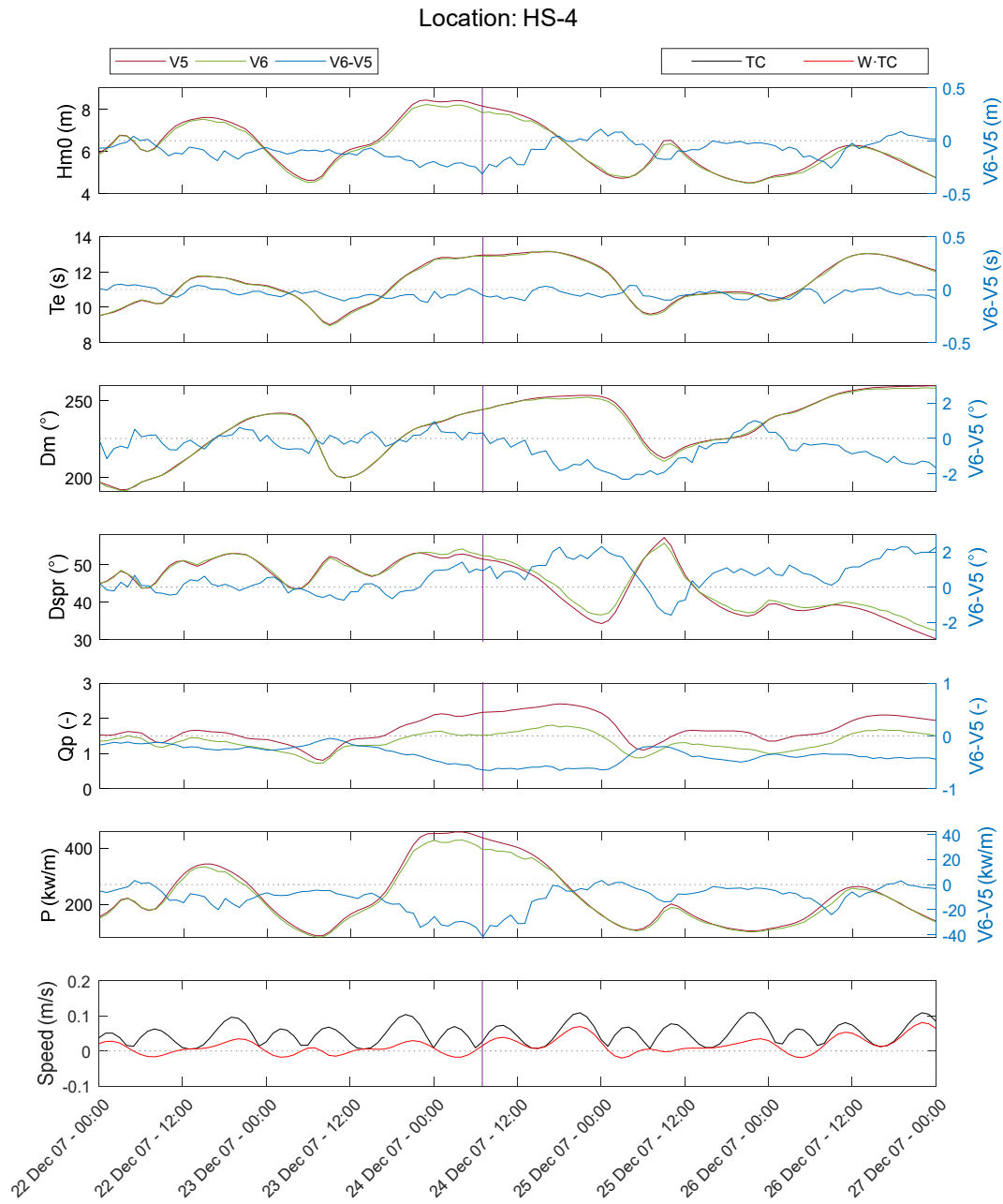
Figure C-8 Time series of wave parameters, wave power and tidal currents including the maximum negative difference in wave power density between V6 and V5 (purple line) at HS-4.

Data for HS-5 is not available.
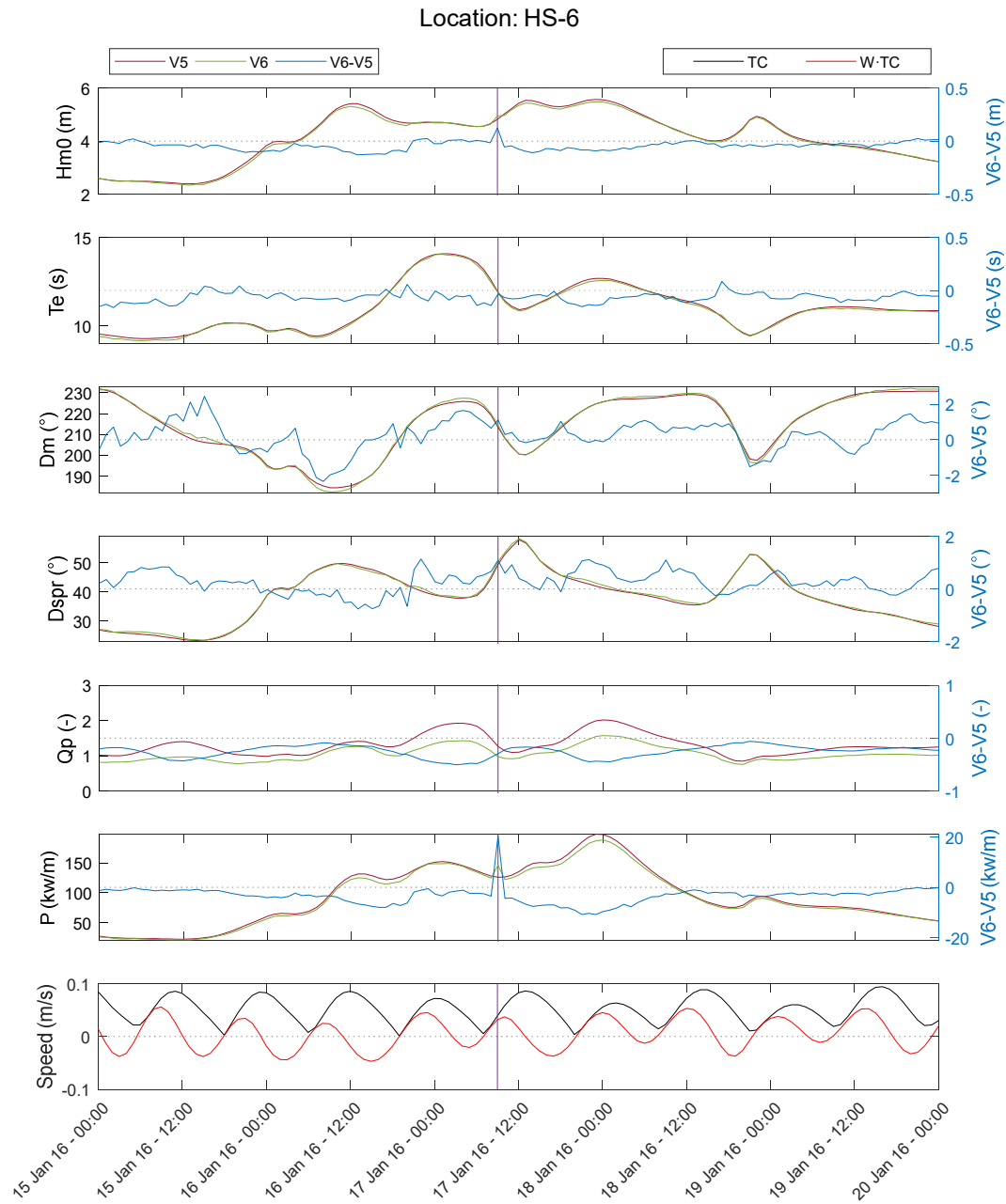
Figure C-9 Time series of wave parameters, wave power and tidal currents including the maximum positive difference in wave power density between V6 and V5 (purple line) at HS-6.
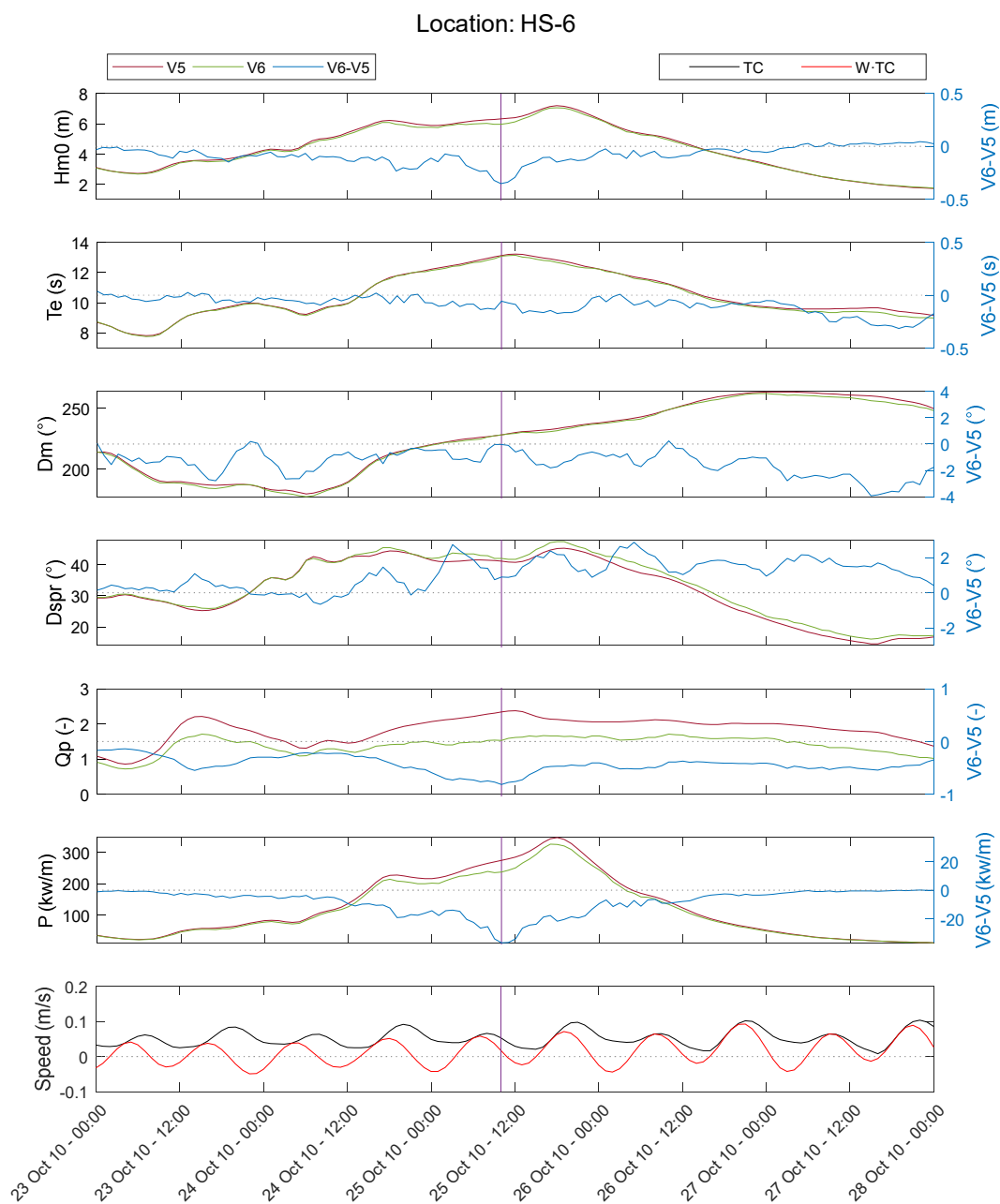
Figure C-10 Time series of wave parameters, wave power and tidal currents including the maximum negative difference in wave power density between V6 and V5 (purple line) at HS-6.
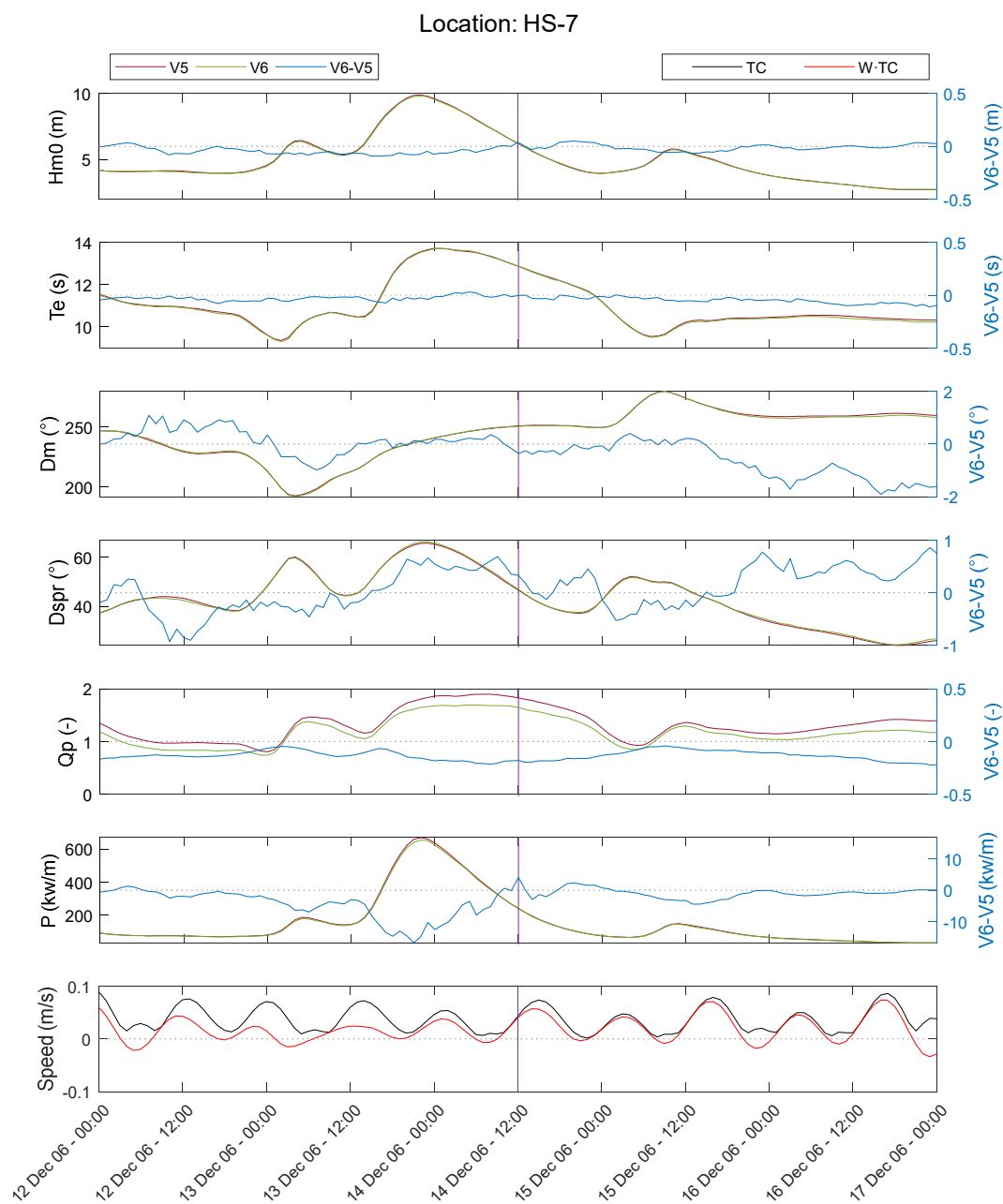
Figure C-11 Time series of wave parameters, wave power and tidal currents including the maximum positive difference in wave power density between V6 and V5 (purple line) at HS-7.
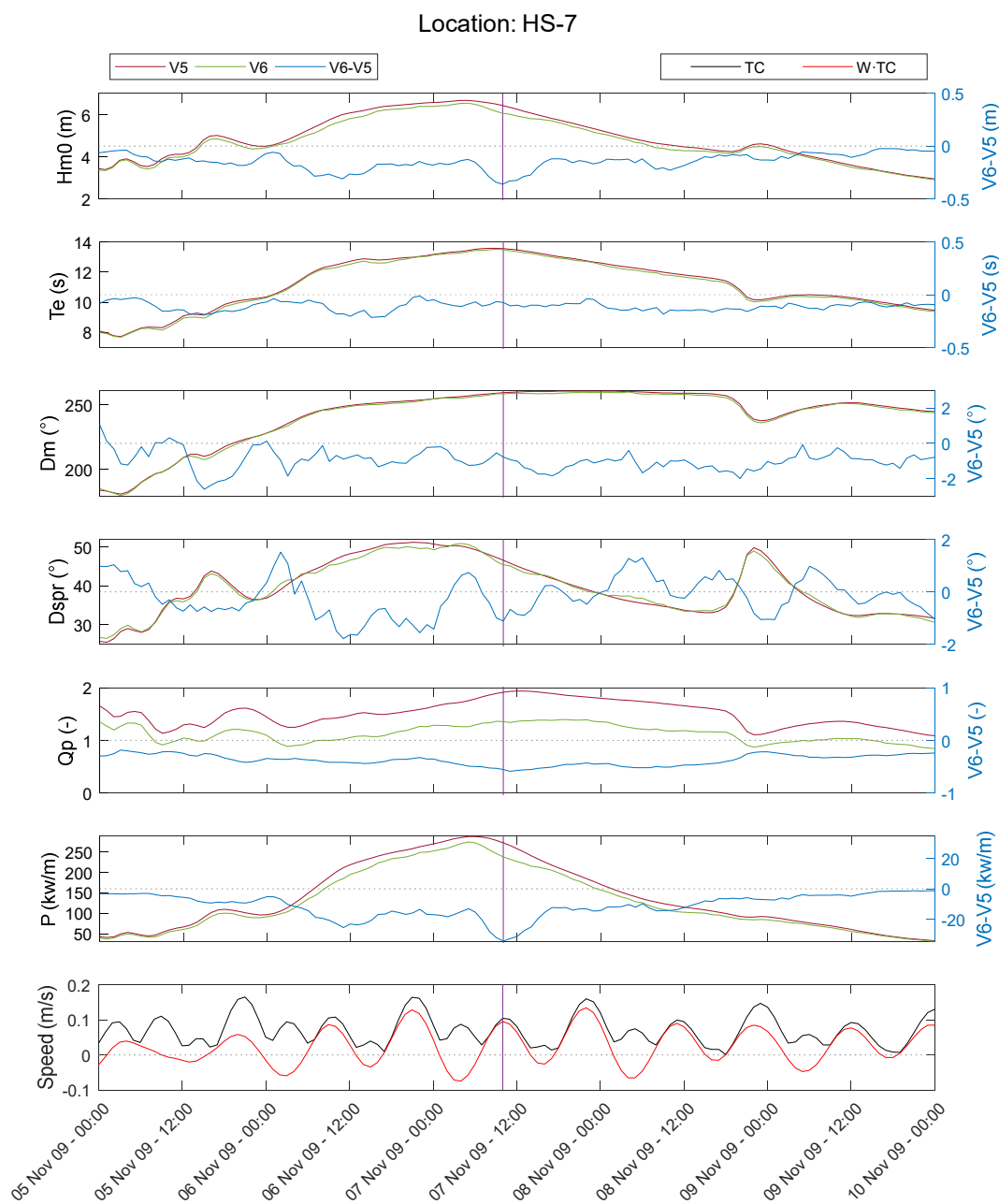
Figure C-12 Time series of wave parameters, wave power and tidal currents including the maximum negative difference in wave power density between V6 and V5 (purple line) at HS-7.
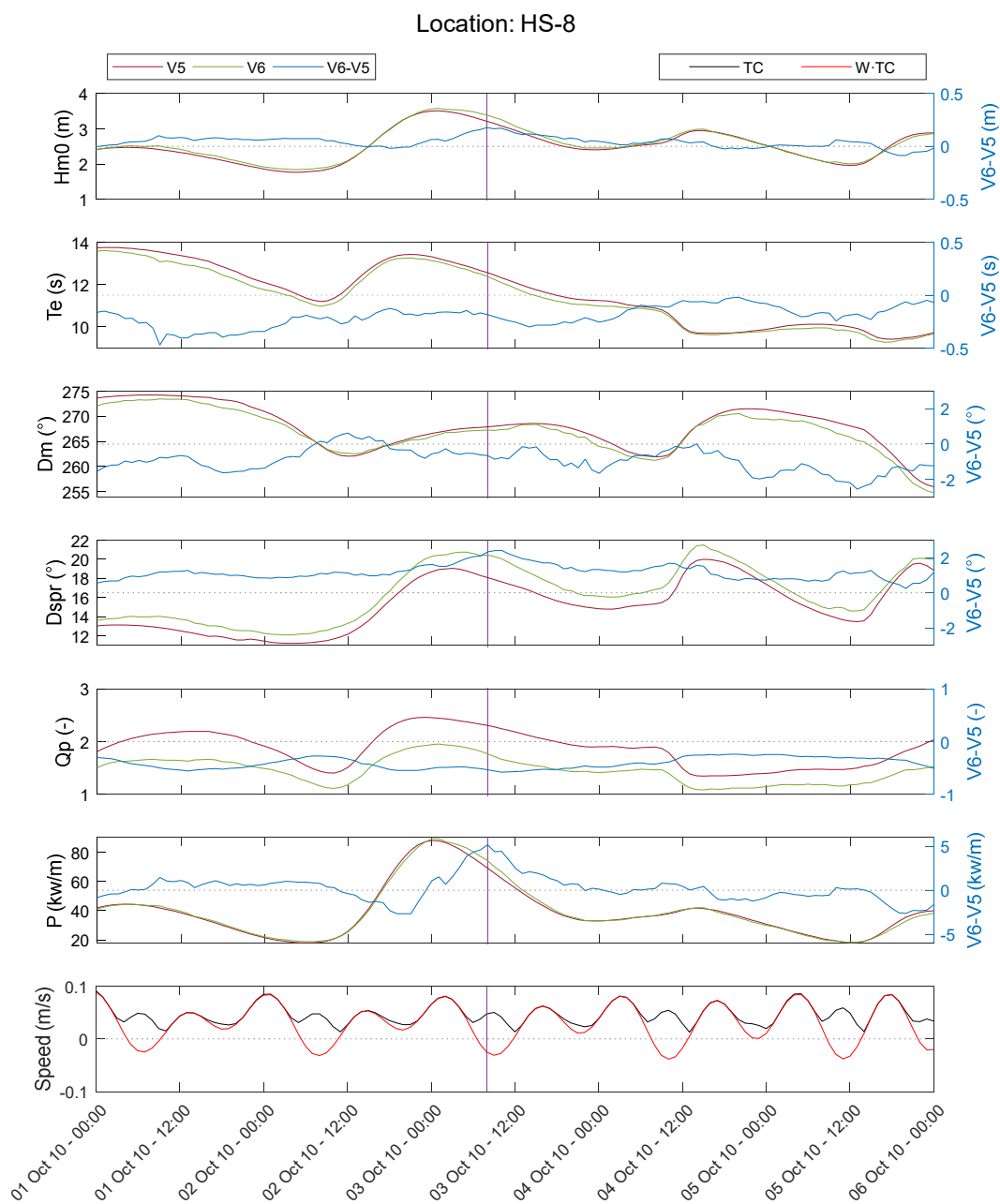
Figure C-13 Time series of wave parameters, wave power and tidal currents including the maximum positive difference in wave power density between V6 and V5 (purple line) at HS-8.
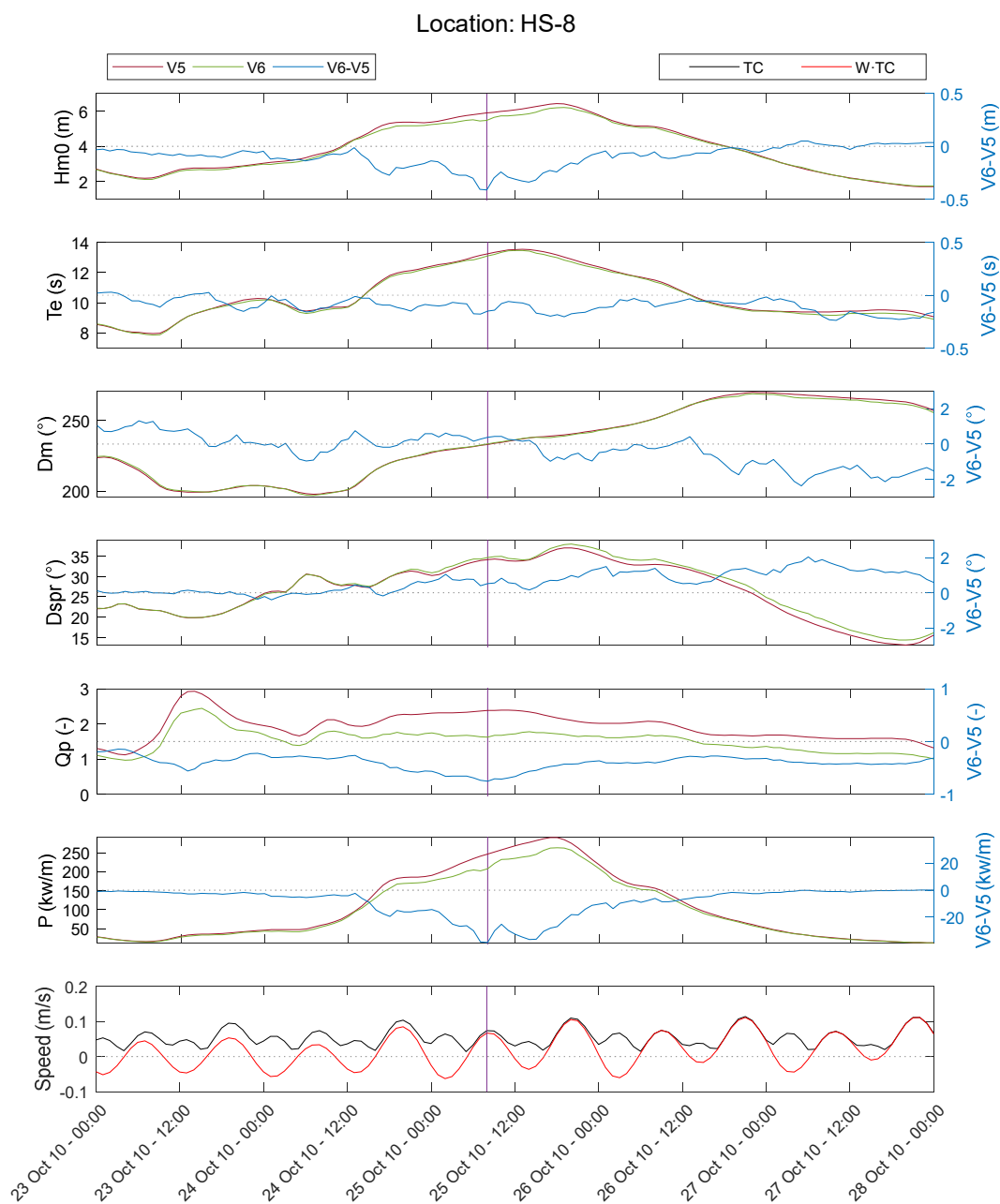
Figure C-14 Time series of wave parameters, wave power and tidal currents including the maximum negative difference in wave power density between V6 and V5 (purple line) at HS-8.
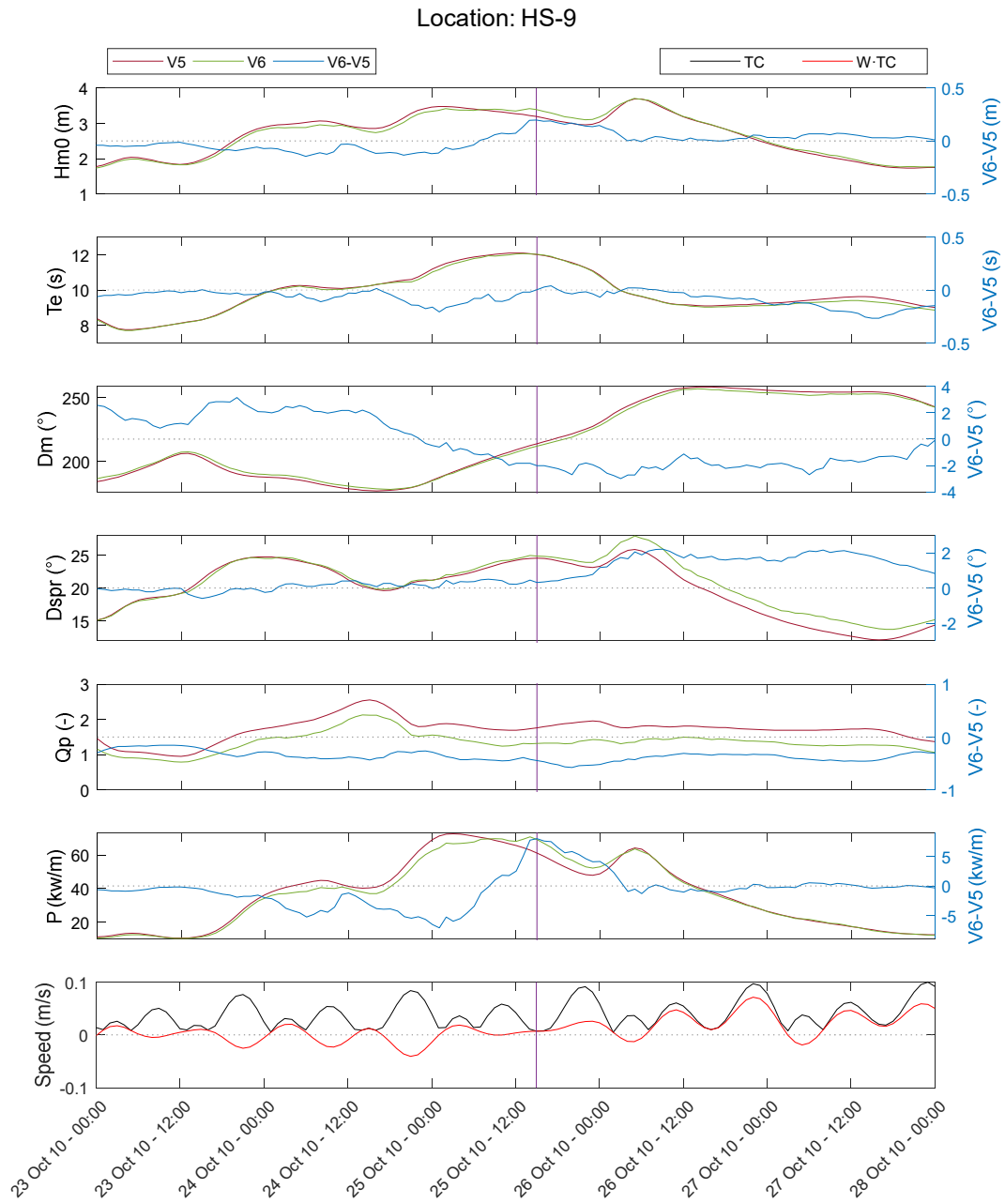
Figure C-15 Time series of wave parameters, wave power and tidal currents including the maximum positive difference in wave power density between V6 and V5 (purple line) at HS-9.
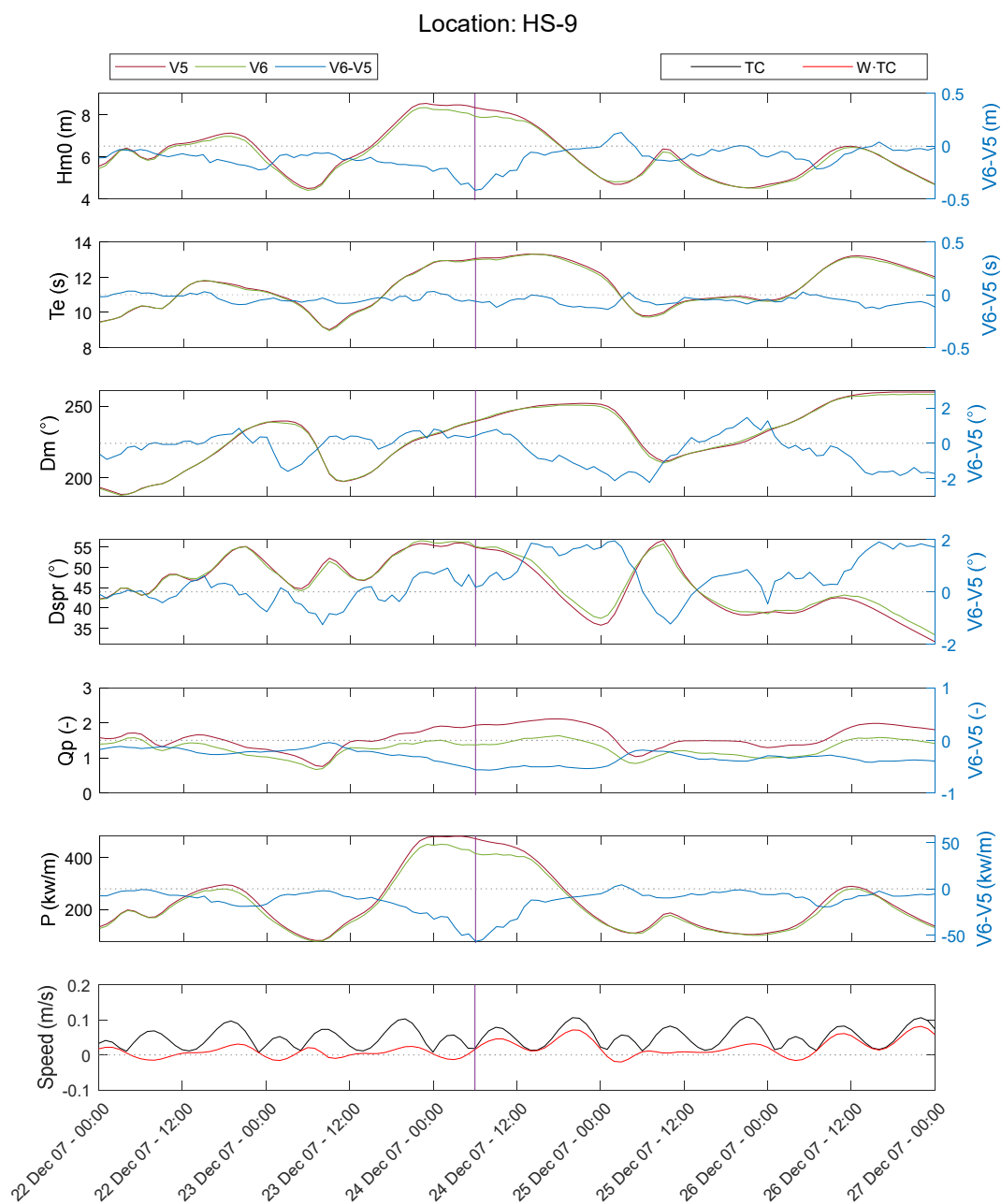
Figure C-16 Time series of wave parameters, wave power and tidal currents including the maximum negative difference in wave power density between V6 and V5 (purple line) at HS-9.
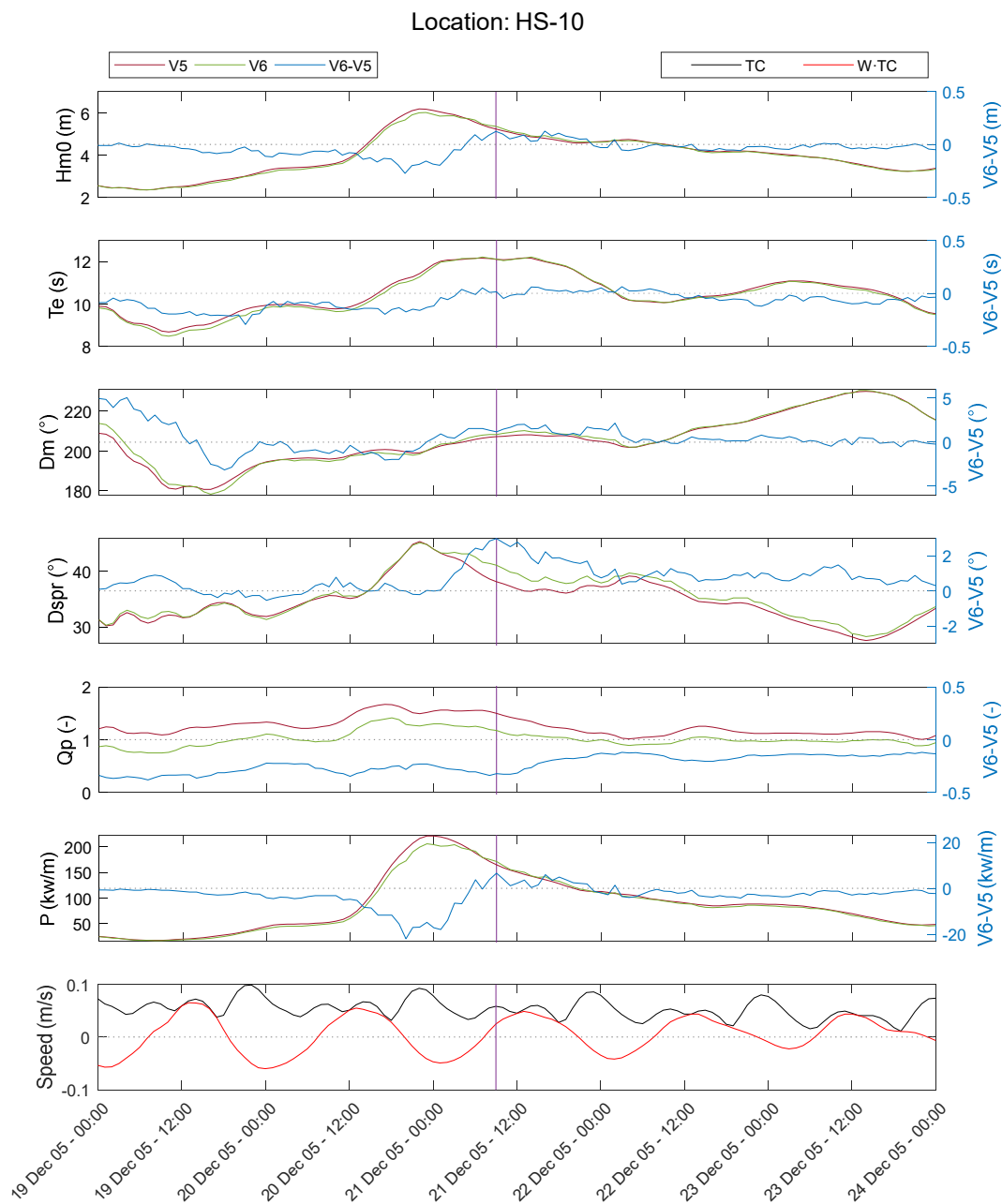
Figure C-17 Time series of wave parameters, wave power and tidal currents including the maximum positive difference in wave power density between V6 and V5 (purple line) at HS-10.
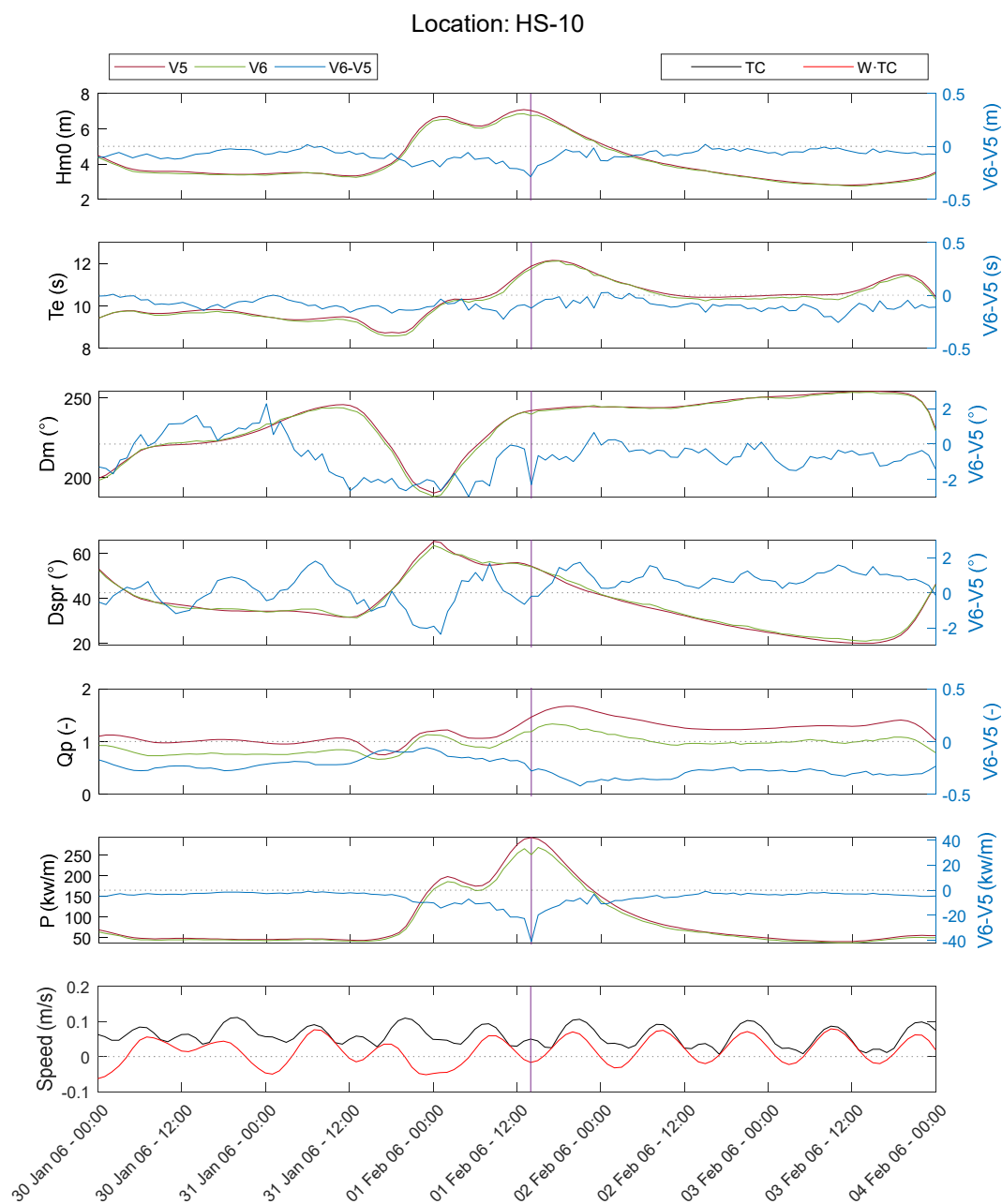
Figure C-18 Time series of wave parameters, wave power and tidal currents including the maximum negative difference in wave power density between V6 and V5 (purple line) at HS-10.
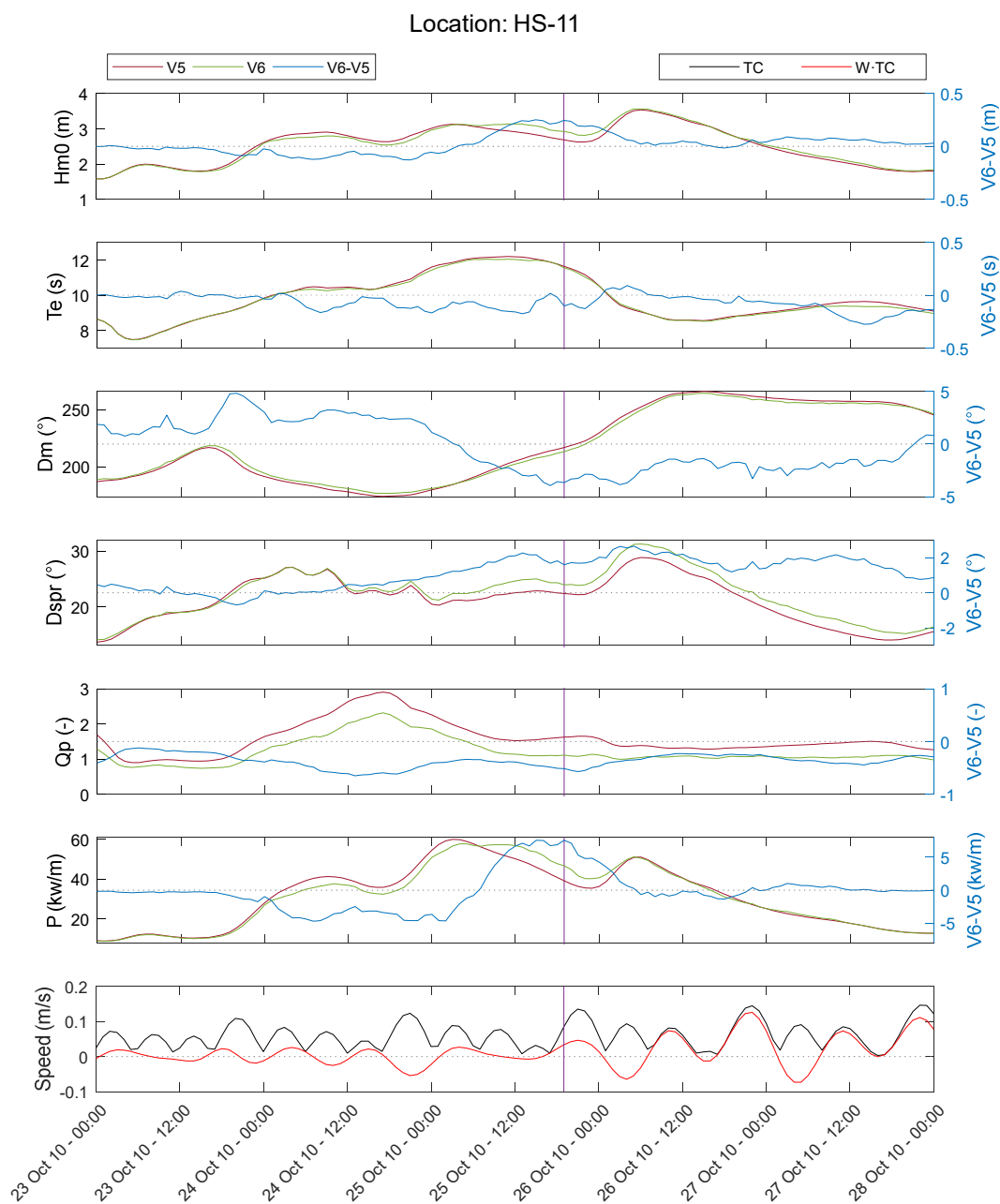
Figure C-19 Time series of wave parameters, wave power and tidal currents including the maximum positive difference in wave power density between V6 and V5 (purple line) at HS-11.
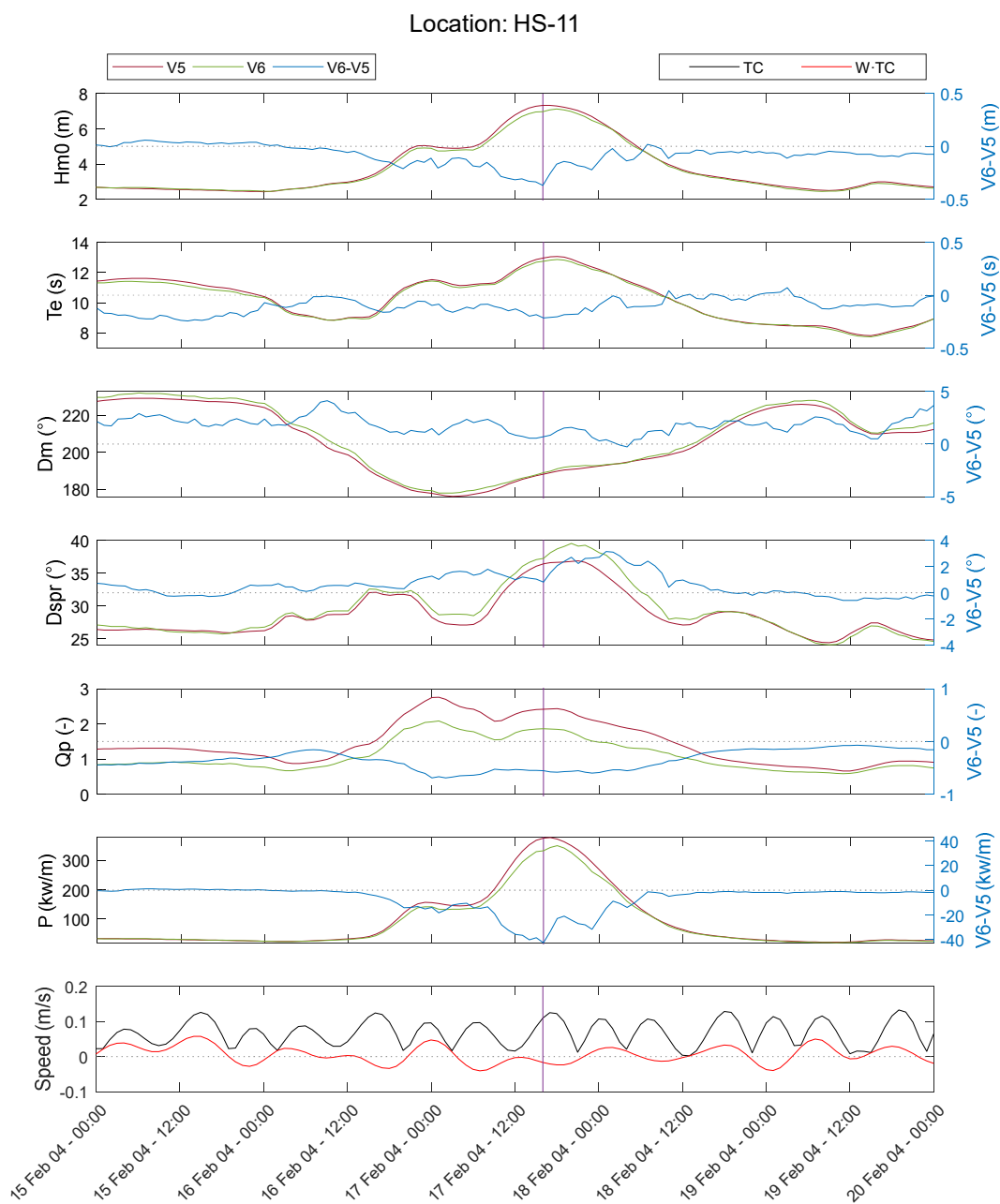
Figure C-20 Time series of wave parameters, wave power and tidal currents including the maximum negative difference in wave power density between V6 and V5 (purple line) at HS-11.

# Appendix D    Directional wave spectra at the biggest positive and negative differences of wave power density between models

Figure D-1 V6's wave spectrum, and difference between V6's and V5's wave spectra at the maximum positive (top plots) and negative (bottom plots) difference in wave power density between the two models – HS-1

Location: HS-2

**13/11/2011 18:00**

| | WCWI-v6 | WCWI-v5 |
|---|---|---|
| Hm0 (m) | 4.03 | 3.93 |
| Te (s) | 11.0 | 10.9 |
| Tm01 (s) | 9.4 | 9.3 |
| Tm02 (s) | 8.3 | 8.2 |
| Tp (s) | 13.7 | 13.9 |
| Dm (°) | 273 | 274 |
| Dp (°) | 287 | 290 |
| Dspr (°) | 25.9 | 25.1 |
| Qp (-) | 1.75 | 1.97 |
| P (Kw/m) | 9.1 | 8.5 |
| u (m/s) | 0.02 | 0.00 |
| v (m/s) | 0.04 | 0.00 |

**25/10/2010 09:00**

| | WCWI-v6 | WCWI-v5 |
|---|---|---|
| Hm0 (m) | 6.09 | 6.44 |
| Te (s) | 13.1 | 13.2 |
| Tm01 (s) | 11.3 | 11.6 |
| Tm02 (s) | 10.1 | 10.4 |
| Tp (s) | 15.1 | 15.3 |
| Dm (°) | 227 | 227 |
| Dp (°) | 235 | 232 |
| Dspr (°) | 46.3 | 45.1 |
| Qp (-) | 1.41 | 2.11 |
| P (Kw/m) | 24.2 | 28.2 |
| u (m/s) | -0.01 | 0.00 |
| v (m/s) | 0.04 | 0.00 |



Figure D-2 V6's wave spectrum, and difference between V6's and V5's wave spectra at the maximum positive (top plots) and negative (bottom plots) difference in wave power density between the two models – HS-2

Location: HS-3

**04/02/2016 07:00**

| | WCWI-v6 | WCWI-v5 |
|---|---|---|
| Hm0 (m) | 5.00 | 4.91 |
| Te (s) | 14.9 | 14.9 |
| Tm01 (s) | 12.5 | 12.5 |
| Tm02 (s) | 10.5 | 10.5 |
| Tp (s) | 17.9 | 18.0 |
| Dm (°) | 233 | 233 |
| Dp (°) | 239 | 238 |
| Dspr (°) | 30.2 | 28.6 |
| Qp (-) | 2.30 | 2.93 |
| P (Kw/m) | 19.5 | 18.9 |
| u (m/s) | -0.01 | 0.00 |
| v (m/s) | 0.04 | 0.00 |

**25/12/2006 15:00**

| | WCWI-v6 | WCWI-v5 |
|---|---|---|
| Hm0 (m) | 9.34 | 9.53 |
| Te (s) | 13.3 | 13.4 |
| Tm01 (s) | 11.6 | 11.7 |
| Tm02 (s) | 10.5 | 10.6 |
| Tp (s) | 15.7 | 15.7 |
| Dm (°) | 215 | 215 |
| Dp (°) | 220 | 219 |
| Dspr (°) | 57.0 | 56.1 |
| Qp (-) | 1.54 | 1.89 |
| P (Kw/m) | 59.1 | 64.5 |
| u (m/s) | -0.10 | 0.00 |
| v (m/s) | -0.14 | 0.00 |



Figure D-3 V6's wave spectrum, and difference between V6's and V5's wave spectra at the maximum positive (top plots) and negative (bottom plots) difference in wave power density between the two models – HS-3
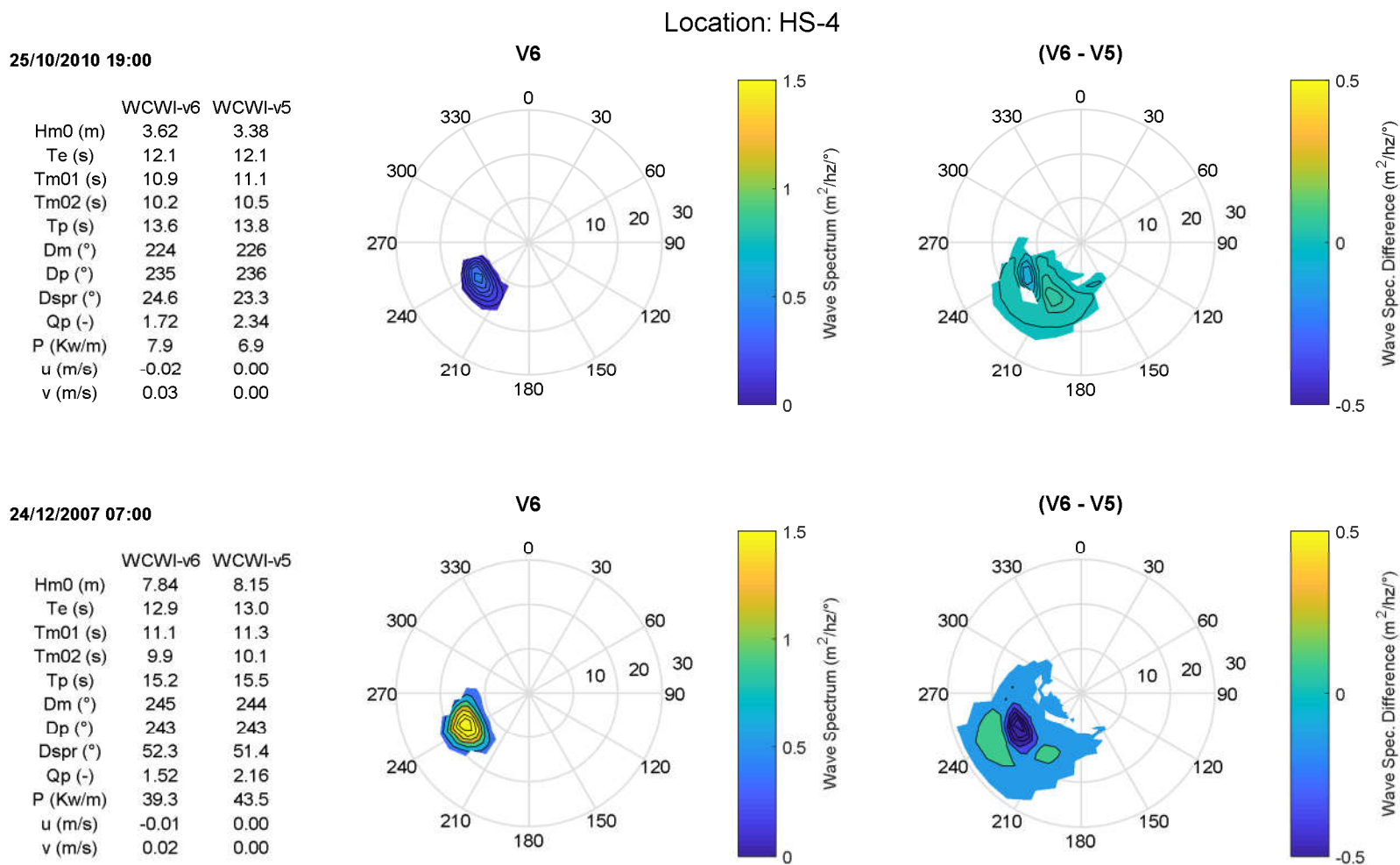
Figure D-4 V6's wave spectrum, and difference between V6's and V5's wave spectra at the maximum positive (top plots) and negative (bottom plots) difference in wave power density between the two models – HS-4

Data for HS-5 is not available.

Location: HS-6

**17/01/2016 09:00**

| | WCWI-v6 | WCWI-v5 |
|---|---|---|
| Hm0 (m) | 4.96 | 4.83 |
| Te (s) | 11.9 | 11.9 |
| Tm01 (s) | 9.4 | 9.4 |
| Tm02 (s) | 8.1 | 8.0 |
| Tp (s) | 16.6 | 17.0 |
| Dm (°) | 215 | 213 |
| Dp (°) | 243 | 245 |
| Dspr (°) | 50.4 | 49.3 |
| Qp (-) | 0.97 | 1.27 |
| P (Kw/m) | 14.6 | 12.6 |
| u (m/s) | 0.01 | 0.00 |
| v (m/s) | 0.04 | 0.00 |

V6

(V6 - V5)

**25/10/2010 10:00**

| | WCWI-v6 | WCWI-v5 |
|---|---|---|
| Hm0 (m) | 5.97 | 6.32 |
| Te (s) | 13.1 | 13.1 |
| Tm01 (s) | 11.3 | 11.6 |
| Tm02 (s) | 10.1 | 10.3 |
| Tp (s) | 15.3 | 15.4 |
| Dm (°) | 228 | 228 |
| Dp (°) | 234 | 232 |
| Dspr (°) | 42.0 | 41.2 |
| Qp (-) | 1.53 | 2.34 |
| P (Kw/m) | 23.7 | 27.4 |
| u (m/s) | -0.03 | 0.00 |
| v (m/s) | 0.05 | 0.00 |

V6

(V6 - V5)

Figure D-5 V6's wave spectrum, and difference between V6's and V5's wave spectra at the maximum positive (top plots) and negative (bottom plots) difference in wave power density between the two models – HS-6

Location: HS-7

**14/12/2006 12:00**

|            | WCWI-v6 | WCWI-v5 |
|------------|---------|---------|
| Hm0 (m)    | 6.27    | 6.23    |
| Te (s)     | 12.9    | 12.9    |
| Tm01 (s)   | 11.4    | 11.5    |
| Tm02 (s)   | 10.4    | 10.4    |
| Tp (s)     | 14.9    | 14.9    |
| Dm (°)     | 251     | 251     |
| Dp (°)     | 247     | 247     |
| Dspr (°)   | 46.8    | 46.5    |
| Qp (-)     | 1.64    | 1.82    |
| P (Kw/m)   | 24.5    | 24.1    |
| u (m/s)    | -0.00   | 0.00    |
| v (m/s)    | 0.04    | 0.00    |

**07/11/2009 10:00**

|            | WCWI-v6 | WCWI-v5 |
|------------|---------|---------|
| Hm0 (m)    | 6.06    | 6.43    |
| Te (s)     | 13.5    | 13.6    |
| Tm01 (s)   | 11.6    | 11.8    |
| Tm02 (s)   | 10.2    | 10.5    |
| Tp (s)     | 16.0    | 16.3    |
| Dm (°)     | 259     | 259     |
| Dp (°)     | 267     | 266     |
| Dspr (°)   | 45.4    | 46.5    |
| Qp (-)     | 1.36    | 1.91    |
| P (Kw/m)   | 23.7    | 27.2    |
| u (m/s)    | -0.02   | 0.00    |
| v (m/s)    | 0.10    | 0.00    |



Figure D-6 V6's wave spectrum, and difference between V6's and V5's wave spectra at the maximum positive (top plots) and negative (bottom plots) difference in wave power density between the two models – HS-7

Location: HS-8

**03/10/2010 08:00**

| | WCWI-v6 | WCWI-v5 |
|---|---|---|
| Hm0 (m) | 3.40 | 3.22 |
| Te (s) | 12.4 | 12.6 |
| Tm01 (s) | 10.9 | 11.2 |
| Tm02 (s) | 9.7 | 9.9 |
| Tp (s) | 14.1 | 14.2 |
| Dm (°) | 267 | 268 |
| Dp (°) | 273 | 274 |
| Dspr (°) | 20.4 | 18.1 |
| Qp (-) | 1.76 | 2.30 |
| P (Kw/m) | 7.4 | 6.9 |
| u (m/s) | -0.04 | 0.00 |
| v (m/s) | -0.02 | 0.00 |

**25/10/2010 08:00**

| | WCWI-v6 | WCWI-v5 |
|---|---|---|
| Hm0 (m) | 5.49 | 5.90 |
| Te (s) | 13.1 | 13.3 |
| Tm01 (s) | 11.4 | 11.8 |
| Tm02 (s) | 10.0 | 10.5 |
| Tp (s) | 15.0 | 15.1 |
| Dm (°) | 234 | 233 |
| Dp (°) | 231 | 229 |
| Dspr (°) | 34.6 | 34.1 |
| Qp (-) | 1.62 | 2.38 |
| P (Kw/m) | 20.7 | 24.6 |
| u (m/s) | 0.02 | 0.00 |
| v (m/s) | 0.07 | 0.00 |



Figure D-7 V6's wave spectrum, and difference between V6's and V5's wave spectra at the maximum positive (top plots) and negative (bottom plots) difference in wave power density between the two models – HS-8

## Location: HS-9

**25/10/2010 15:00**

|  | WCWI-v6 | WCWI-v5 |
|---|---|---|
| Hm0 (m) | 3.39 | 3.20 |
| Te (s) | 12.0 | 12.0 |
| Tm01 (s) | 10.8 | 11.0 |
| Tm02 (s) | 10.0 | 10.2 |
| Tp (s) | 13.7 | 14.0 |
| Dm (°) | 212 | 214 |
| Dp (°) | 223 | 225 |
| Dspr (°) | 24.8 | 24.5 |
| Qp (-) | 1.31 | 1.76 |
| P (Kw/m) | 6.9 | 6.1 |
| u (m/s) | 0.01 | 0.00 |
| v (m/s) | 0.00 | 0.00 |

**24/12/2007 06:00**

|  | WCWI-v6 | WCWI-v5 |
|---|---|---|
| Hm0 (m) | 7.92 | 8.34 |
| Te (s) | 13.0 | 13.1 |
| Tm01 (s) | 11.3 | 11.5 |
| Tm02 (s) | 10.1 | 10.3 |
| Tp (s) | 15.3 | 15.5 |
| Dm (°) | 240 | 239 |
| Dp (°) | 237 | 235 |
| Dspr (°) | 55.1 | 55.0 |
| Qp (-) | 1.37 | 1.93 |
| P (Kw/m) | 41.4 | 47.1 |
| u (m/s) | -0.00 | 0.00 |
| v (m/s) | 0.02 | 0.00 |



Figure D-8 V6's wave spectrum, and difference between V6's and V5's wave spectra at the maximum positive (top plots) and negative (bottom plots) difference in wave power density between the two models – HS-9

Location: HS-10

**21/12/2005 09:00**

| | WCWI-v6 | WCWI-v5 |
|---|---|---|
| Hm0 (m) | 5.36 | 5.24 |
| Te (s) | 12.1 | 12.1 |
| Tm01 (s) | 10.4 | 10.4 |
| Tm02 (s) | 9.2 | 9.2 |
| Tp (s) | 14.1 | 14.1 |
| Dm (°) | 208 | 207 |
| Dp (°) | 211 | 212 |
| Dspr (°) | 41.1 | 38.1 |
| Qp (-) | 1.17 | 1.50 |
| P (Kw/m) | 17.1 | 16.5 |
| u (m/s) | -0.00 | 0.00 |
| v (m/s) | 0.06 | 0.00 |

**01/02/2006 14:00**

| | WCWI-v6 | WCWI-v5 |
|---|---|---|
| Hm0 (m) | 6.76 | 7.05 |
| Te (s) | 11.8 | 11.9 |
| Tm01 (s) | 10.3 | 10.5 |
| Tm02 (s) | 9.3 | 9.5 |
| Tp (s) | 13.6 | 13.8 |
| Dm (°) | 240 | 242 |
| Dp (°) | 242 | 250 |
| Dspr (°) | 54.1 | 54.3 |
| Qp (-) | 1.18 | 1.46 |
| P (Kw/m) | 25.1 | 29.2 |
| u (m/s) | 0.03 | 0.00 |
| v (m/s) | -0.04 | 0.00 |

Figure D-9 V6's wave spectrum, and difference between V6's and V5's wave spectra at the maximum positive (top plots) and negative (bottom plots) difference in wave power density between the two models – HS-10

## Location: HS-11

**25/10/2010 19:00**

|          | WCWI-v6 | WCWI-v5 |
|----------|---------|---------|
| Hm0 (m)  | 2.93    | 2.68    |
| Te (s)   | 11.5    | 11.6    |
| Tm01 (s) | 10.4    | 10.6    |
| Tm02 (s) | 9.5     | 9.8     |
| Tp (s)   | 12.7    | 13.2    |
| Dm (°)   | 213     | 217     |
| Dp (°)   | 222     | 228     |
| Dspr (°) | 23.9    | 22.3    |
| Qp (-)   | 1.11    | 1.62    |
| P (Kw/m) | 4.7     | 3.9     |
| u (m/s)  | -0.02   | 0.00    |
| v (m/s)  | 0.08    | 0.00    |

**17/02/2004 16:00**

|          | WCWI-v6 | WCWI-v5 |
|----------|---------|---------|
| Hm0 (m)  | 6.97    | 7.34    |
| Te (s)   | 12.8    | 13.0    |
| Tm01 (s) | 11.0    | 11.3    |
| Tm02 (s) | 9.7     | 10.1    |
| Tp (s)   | 14.8    | 15.0    |
| Dm (°)   | 189     | 188     |
| Dp (°)   | 189     | 188     |
| Dspr (°) | 37.2    | 36.4    |
| Qp (-)   | 1.86    | 2.42    |
| P (Kw/m) | 33.2    | 37.5    |
| u (m/s)  | -0.03   | 0.00    |
| v (m/s)  | 0.10    | 0.00    |



Figure D-10 V6's wave spectrum, and difference between V6's and V5's wave spectra at the maximum positive (top plots) and negative (bottom plots) difference in wave power density between the two models – HS-11

Location: DFO-1

**25/12/2006 09:00**

|  | WCWI-v6 | WCWI-v5 |
|---|---|---|
| Hm0 (m) | 12.09 | 11.84 |
| Te (s) | 13.4 | 13.4 |
| Tm01 (s) | 12.0 | 12.0 |
| Tm02 (s) | 11.0 | 11.0 |
| Tp (s) | 15.5 | 15.5 |
| Dm (°) | 215 | 216 |
| Dp (°) | 218 | 220 |
| Dspr (°) | 96.2 | 92.9 |
| Qp (-) | 1.28 | 1.36 |
| P (Kw/m) | 83.2 | 79.4 |
| u (m/s) | 0.02 | 0.00 |
| v (m/s) | 0.03 | 0.00 |

**24/12/2007 02:00**

|  | WCWI-v6 | WCWI-v5 |
|---|---|---|
| Hm0 (m) | 9.37 | 9.70 |
| Te (s) | 12.7 | 12.7 |
| Tm01 (s) | 11.2 | 11.2 |
| Tm02 (s) | 10.1 | 10.2 |
| Tp (s) | 15.1 | 15.0 |
| Dm (°) | 251 | 251 |
| Dp (°) | 235 | 238 |
| Dspr (°) | 83.0 | 82.5 |
| Qp (-) | 1.05 | 1.27 |
| P (Kw/m) | 45.5 | 49.2 |
| u (m/s) | 0.01 | 0.00 |
| v (m/s) | -0.04 | 0.00 |



Figure D-11 V6's wave spectrum, and difference between V6's and V5's wave spectra at the maximum positive (top plots) and negative (bottom plots) difference in wave power density between the two models – DFO-1

Location: DFO-2

07/11/2009 11:00

|  | WCWI-v6 | WCWI-v5 |
|---|---|---|
| Hm0 (m) | 7.74 | 7.26 |
| Te (s) | 12.9 | 12.7 |
| Tm01 (s) | 11.3 | 11.0 |
| Tm02 (s) | 10.1 | 9.8 |
| Tp (s) | 15.3 | 15.3 |
| Dm (°) | 275 | 276 |
| Dp (°) | 268 | 286 |
| Dspr (°) | 61.7 | 56.7 |
| Qp (-) | 1.31 | 1.43 |
| P (Kw/m) | 32.7 | 28.7 |
| u (m/s) | -0.01 | 0.00 |
| v (m/s) | 0.05 | 0.00 |

17/02/2004 06:00

|  | WCWI-v6 | WCWI-v5 |
|---|---|---|
| Hm0 (m) | 10.30 | 10.68 |
| Te (s) | 12.6 | 12.6 |
| Tm01 (s) | 11.2 | 11.4 |
| Tm02 (s) | 10.3 | 10.5 |
| Tp (s) | 14.4 | 14.4 |
| Dm (°) | 204 | 204 |
| Dp (°) | 206 | 203 |
| Dspr (°) | 86.0 | 86.0 |
| Qp (-) | 1.26 | 1.42 |
| P (Kw/m) | 55.5 | 60.3 |
| u (m/s) | -0.01 | 0.00 |
| v (m/s) | 0.06 | 0.00 |



Figure D-12 V6's wave spectrum, and difference between V6's and V5's wave spectra at the maximum positive (top plots) and negative (bottom plots) difference in wave power density between the two models – DFO-2

Location: DFO-3

01/12/2017 13:00

|  | WCWI-v6 | WCWI-v5 |
|---|---|---|
| Hm0 (m) | 4.60 | 4.43 |
| Te (s) | 12.6 | 12.7 |
| Tm01 (s) | 10.6 | 10.7 |
| Tm02 (s) | 9.3 | 9.4 |
| Tp (s) | 15.5 | 15.6 |
| Dm (°) | 268 | 269 |
| Dp (°) | 275 | 276 |
| Dspr (°) | 34.3 | 31.7 |
| Qp (-) | 1.36 | 1.75 |
| P (Kw/m) | 11.8 | 11.1 |
| u (m/s) | 0.02 | 0.00 |
| v (m/s) | -0.01 | 0.00 |

V6

(V6 - V5)

25/10/2010 11:00

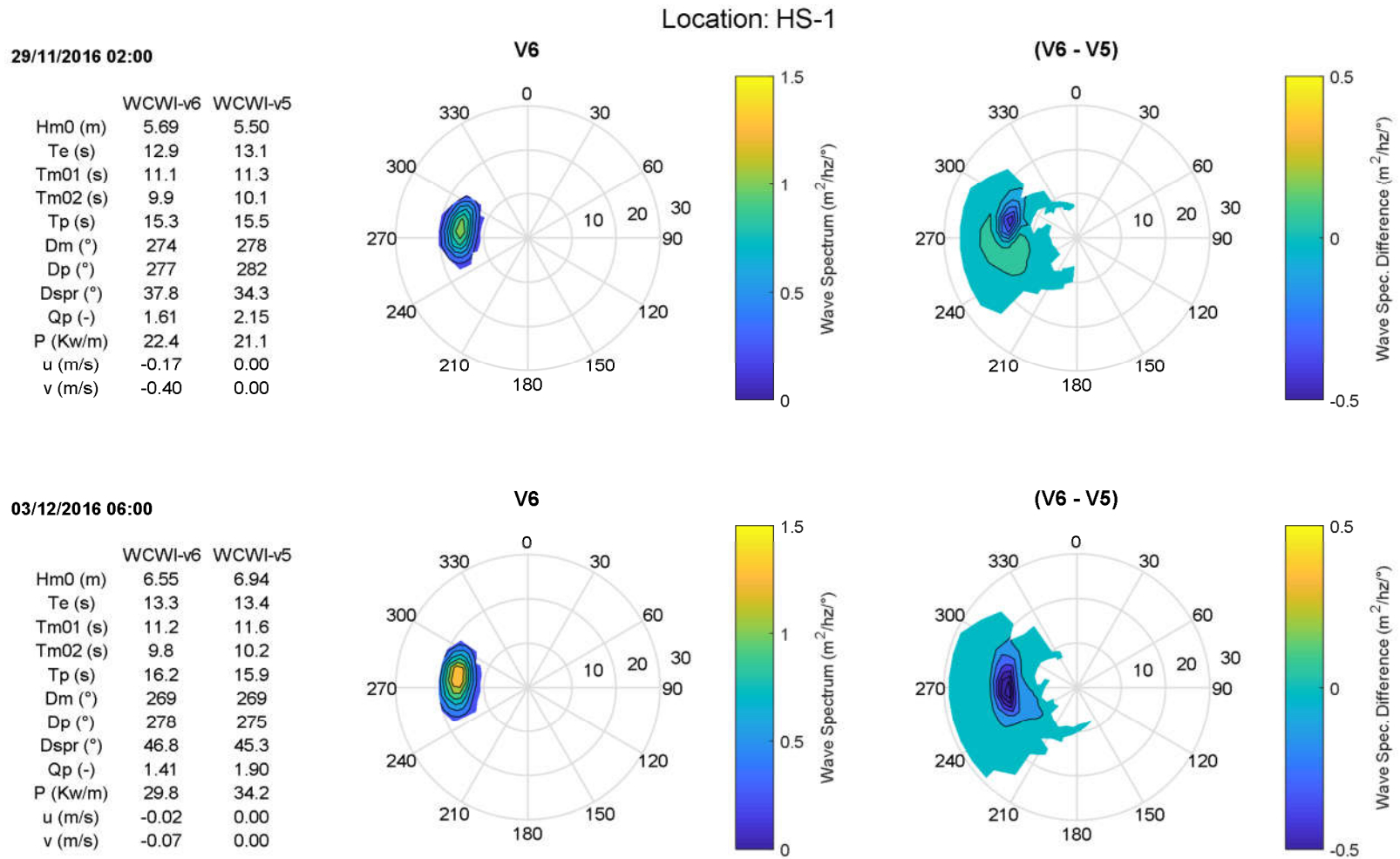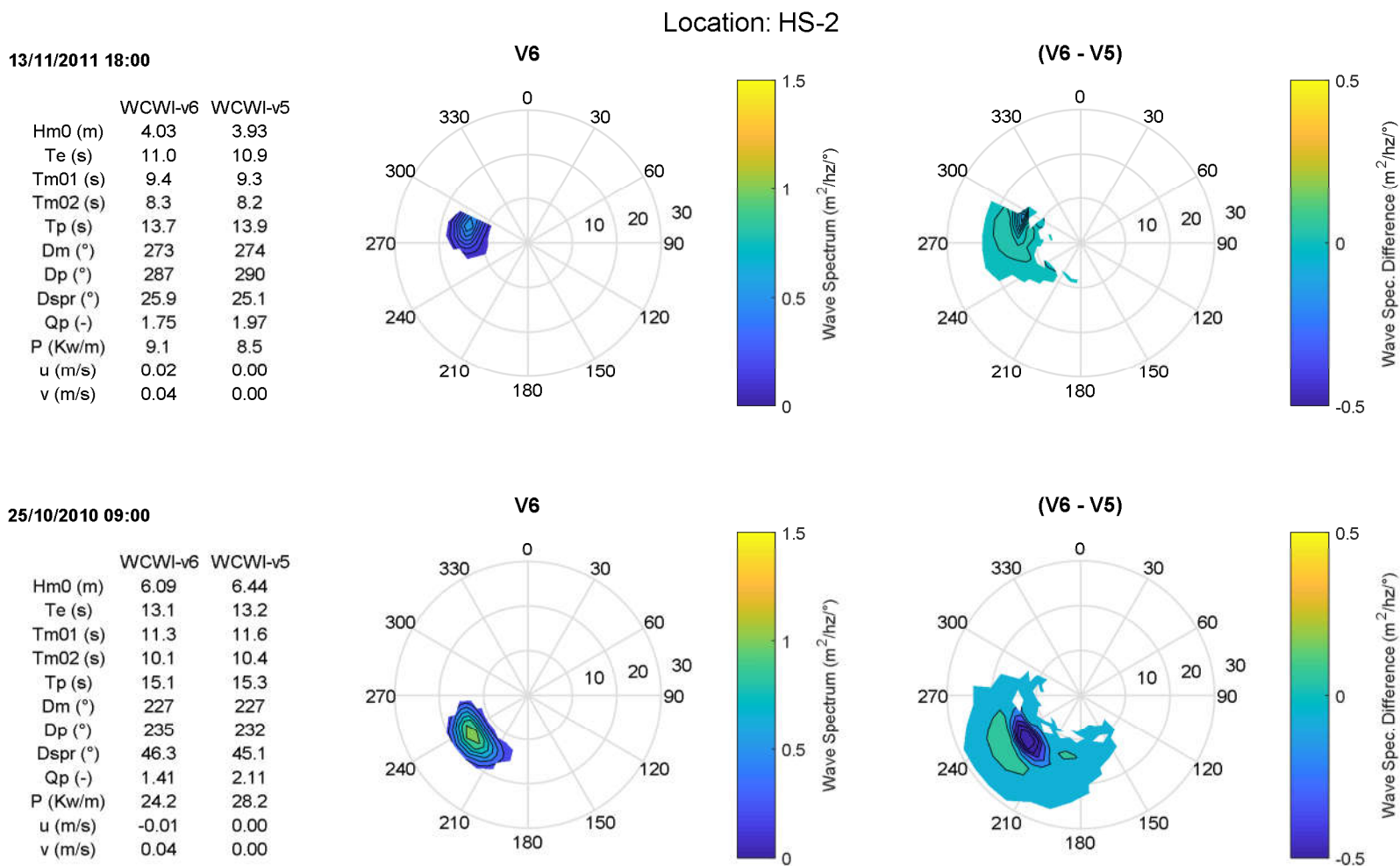|  | WCWI-v6 | WCWI-v5 |
|---|---|---|
| Hm0 (m) | 6.66 | 7.05 |
| Te (s) | 13.2 | 13.3 |
| Tm01 (s) | 11.5 | 11.8 |
| Tm02 (s) | 10.3 | 10.6 |
| Tp (s) | 15.3 | 15.3 |
| Dm (°) | 232 | 233 |
| Dp (°) | 237 | 235 |
| Dspr (°) | 50.0 | 47.8 |
| Qp (-) | 1.46 | 2.23 |
| P (Kw/m) | 25.5 | 29.5 |
| u (m/s) | -0.01 | 0.00 |
| v (m/s) | 0.03 | 0.00 |

V6

(V6 - V5)

Figure D-13 V6's wave spectrum, and difference between V6's and V5's wave spectra at the maximum positive (top plots) and negative (bottom plots) difference in wave power density between the two models – DFO-3

Location: DFO-4

|  | WCWI-v6 | WCWI-v5 |
|---|---|---|
| Hm0 (m) | 4.81 | 4.59 |
| Te (s) | 9.6 | 9.6 |
| Tm01 (s) | 8.0 | 8.0 |
| Tm02 (s) | 7.1 | 7.2 |
| Tp (s) | 12.4 | 12.6 |
| Dm (°) | 265 | 265 |
| Dp (°) | 263 | 264 |
| Dspr (°) | 30.1 | 28.4 |
| Qp (-) | 1.27 | 1.51 |
| P (Kw/m) | 11.2 | 9.1 |
| u (m/s) | 0.55 | 0.00 |
| v (m/s) | 0.04 | 0.00 |



26/12/2007 14:00

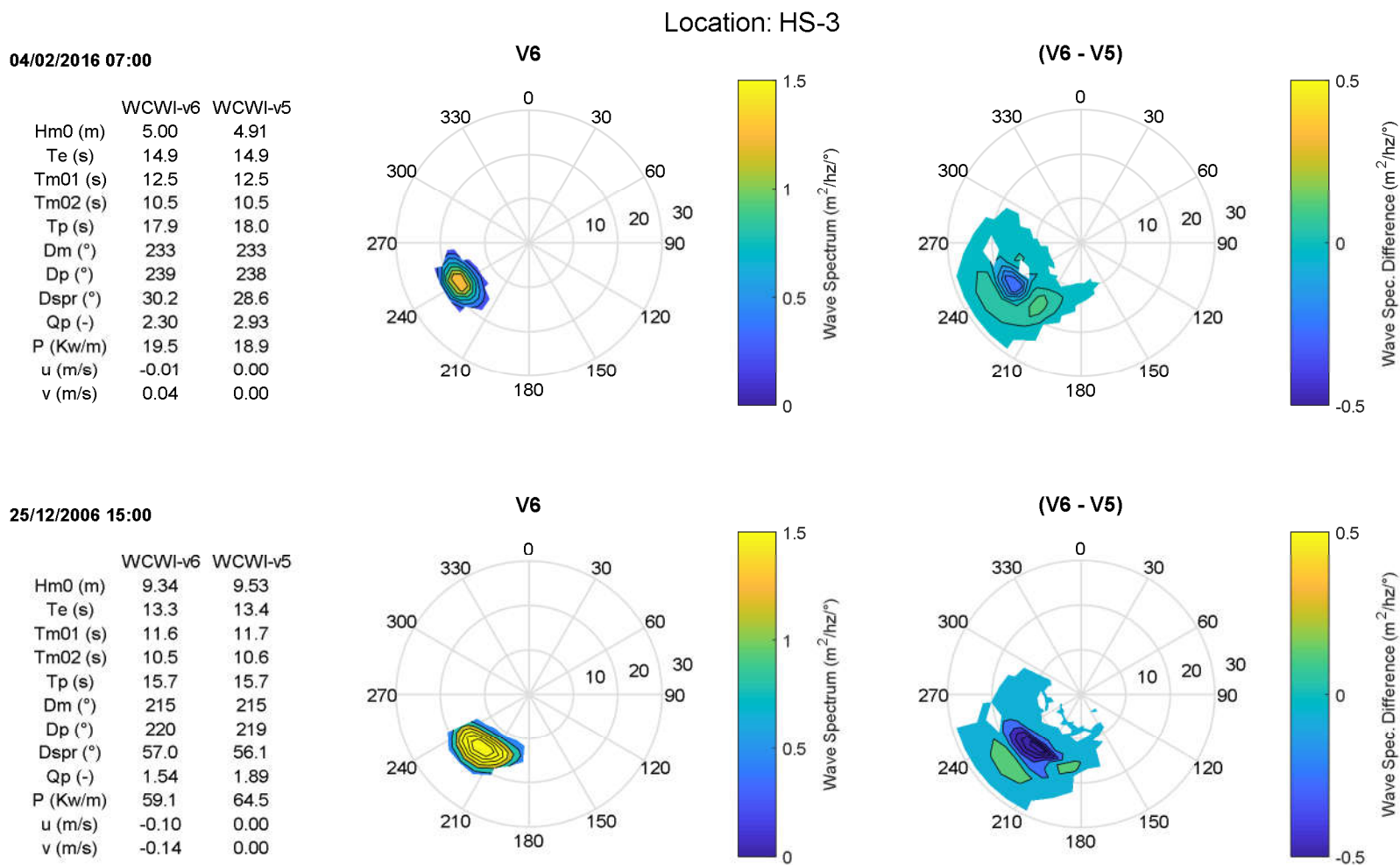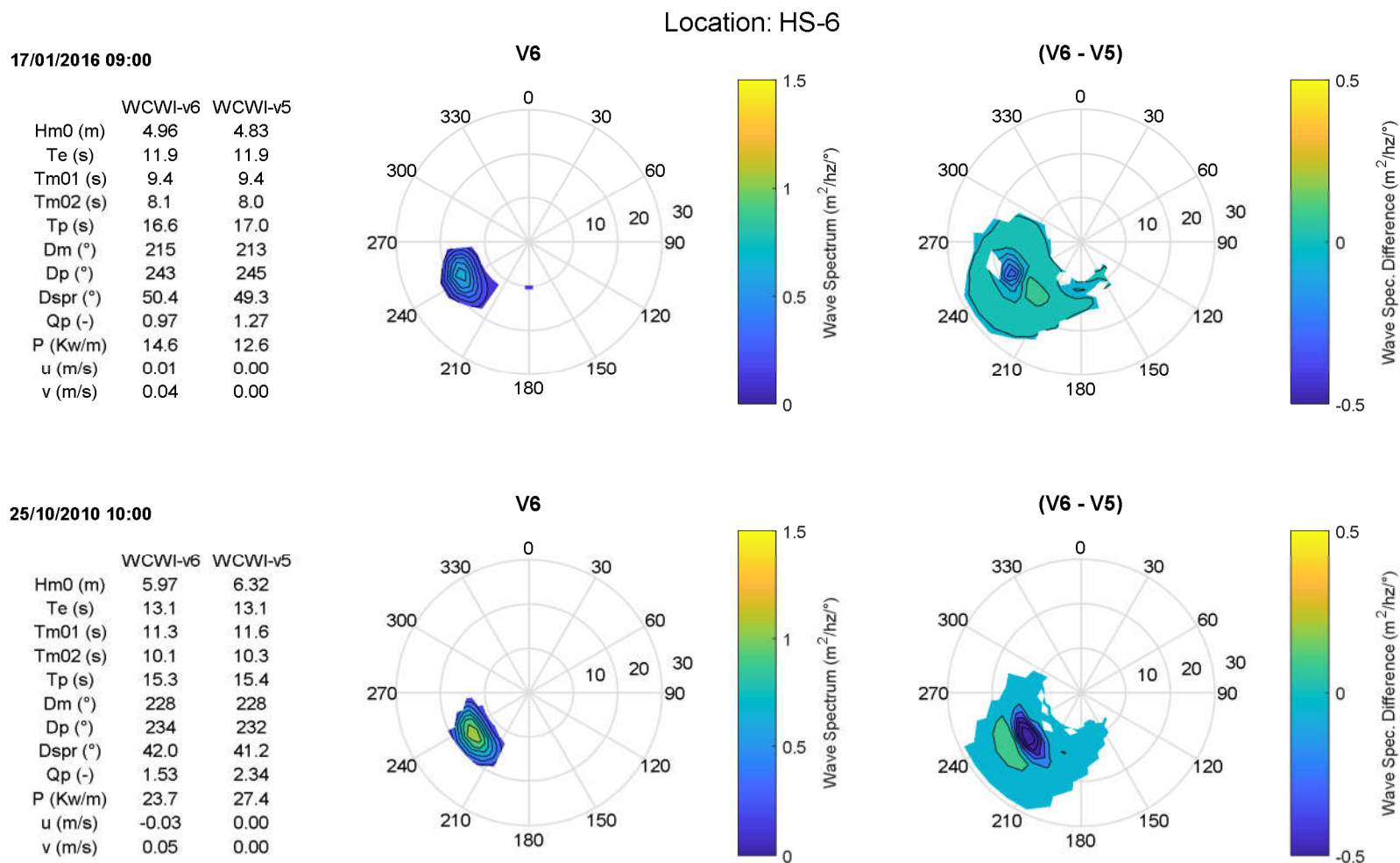|  | WCWI-v6 | WCWI-v5 |
|---|---|---|
| Hm0 (m) | 4.95 | 5.38 |
| Te (s) | 14.1 | 13.6 |
| Tm01 (s) | 12.2 | 12.0 |
| Tm02 (s) | 10.7 | 10.5 |
| Tp (s) | 16.0 | 15.5 |
| Dm (°) | 277 | 276 |
| Dp (°) | 270 | 269 |
| Dspr (°) | 20.3 | 20.7 |
| Qp (-) | 2.66 | 3.48 |
| P (Kw/m) | 15.4 | 18.8 |
| u (m/s) | -0.50 | 0.00 |
| v (m/s) | 0.02 | 0.00 |

Figure D-14 V6's wave spectrum, and difference between V6's and V5's wave spectra at the maximum positive (top plots) and negative (bottom plots) difference in wave power density between the two models – DFO-4

Location: DFO-5

**02/01/2012 02:00**

| | WCWI-v6 | WCWI-v5 |
|---|---|---|
| Hm0 (m) | 7.40 | 7.21 |
| Te (s) | 11.0 | 10.9 |
| Tm01 (s) | 9.9 | 9.8 |
| Tm02 (s) | 9.1 | 9.0 |
| Tp (s) | 12.6 | 12.6 |
| Dm (°) | 155 | 153 |
| Dp (°) | 144 | 142 |
| Dspr (°) | 60.0 | 58.3 |
| Qp (-) | 1.58 | 1.73 |
| P (Kw/m) | 25.1 | 23.8 |
| u (m/s) | -0.01 | 0.00 |
| v (m/s) | 0.03 | 0.00 |

**17/02/2004 14:00**

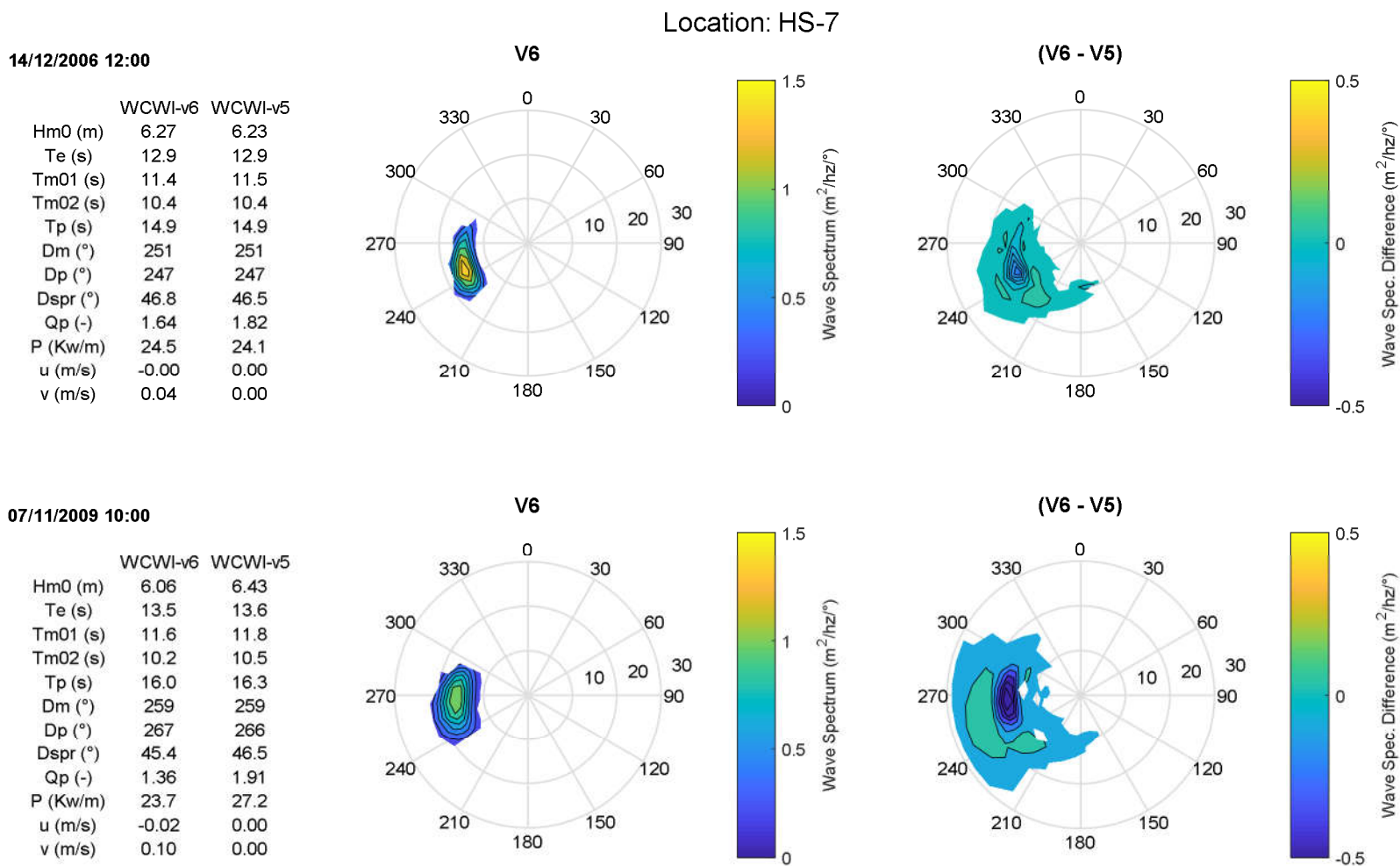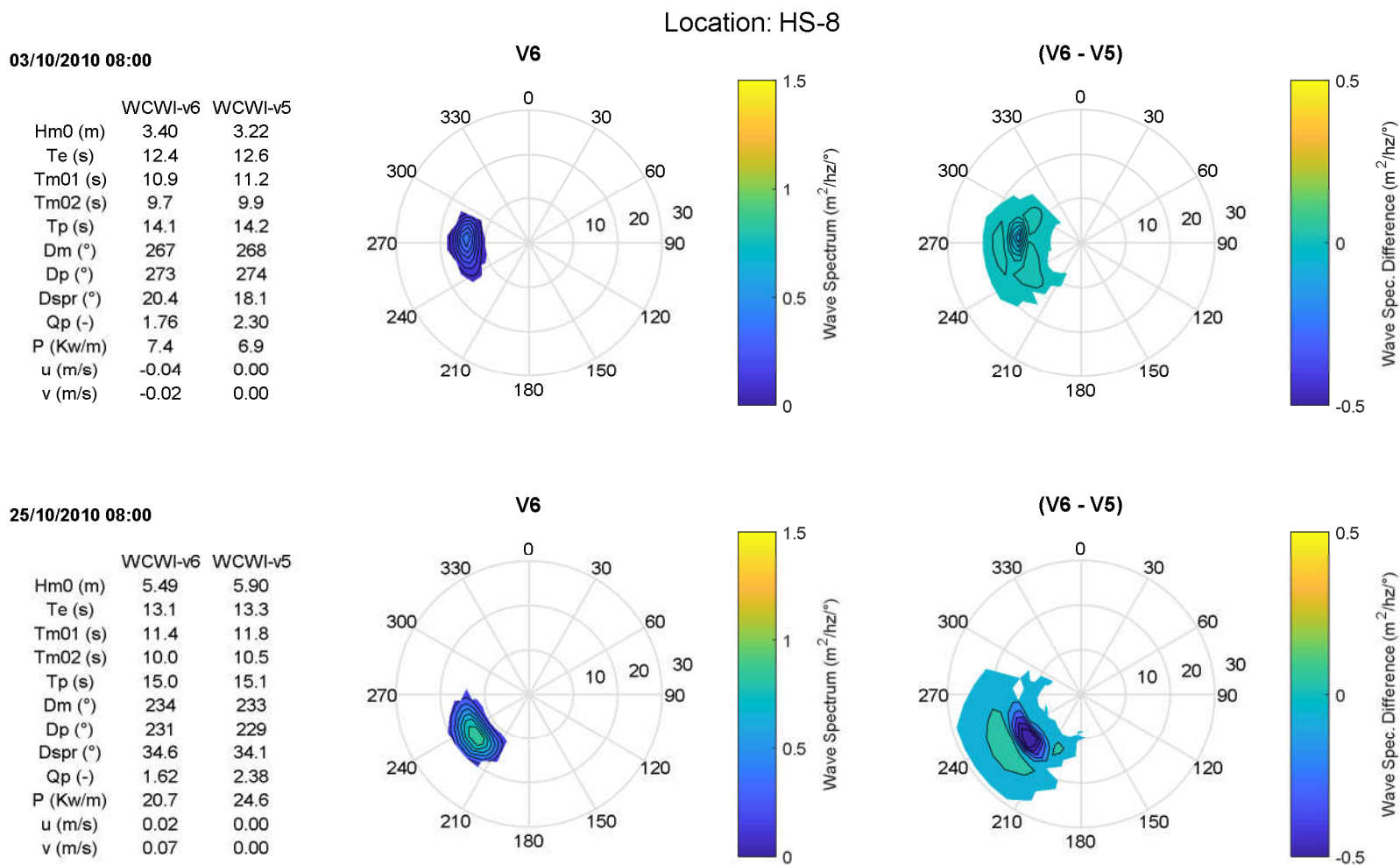| | WCWI-v6 | WCWI-v5 |
|---|---|---|
| Hm0 (m) | 8.73 | 9.29 |
| Te (s) | 12.4 | 12.6 |
| Tm01 (s) | 10.9 | 11.1 |
| Tm02 (s) | 9.8 | 10.1 |
| Tp (s) | 14.8 | 15.0 |
| Dm (°) | 189 | 192 |
| Dp (°) | 201 | 202 |
| Dspr (°) | 67.4 | 67.9 |
| Qp (-) | 1.29 | 1.68 |
| P (Kw/m) | 40.7 | 47.3 |
| u (m/s) | 0.01 | 0.00 |
| v (m/s) | 0.03 | 0.00 |



Figure D-15 V6's wave spectrum, and difference between V6's and V5's wave spectra at the maximum positive (top plots) and negative (bottom plots) difference in wave power density between the two models – DFO-5

## Location: DFO-6

**28/10/2011 06:00**

| | WCWI-v6 | WCWI-v5 |
|---|---|---|
| Hm0 (m) | 6.83 | 6.74 |
| Te (s) | 8.9 | 9.0 |
| Tm01 (s) | 8.2 | 8.3 |
| Tm02 (s) | 7.6 | 7.8 |
| Tp (s) | 9.9 | 10.0 |
| Dm (°) | 150 | 150 |
| Dp (°) | 158 | 160 |
| Dspr (°) | 41.9 | 41.2 |
| Qp (-) | 2.01 | 2.18 |
| P (Kw/m) | 21.4 | 19.6 |
| u (m/s) | -0.22 | 0.00 |
| v (m/s) | 0.25 | 0.00 |

**28/01/2017 10:00**

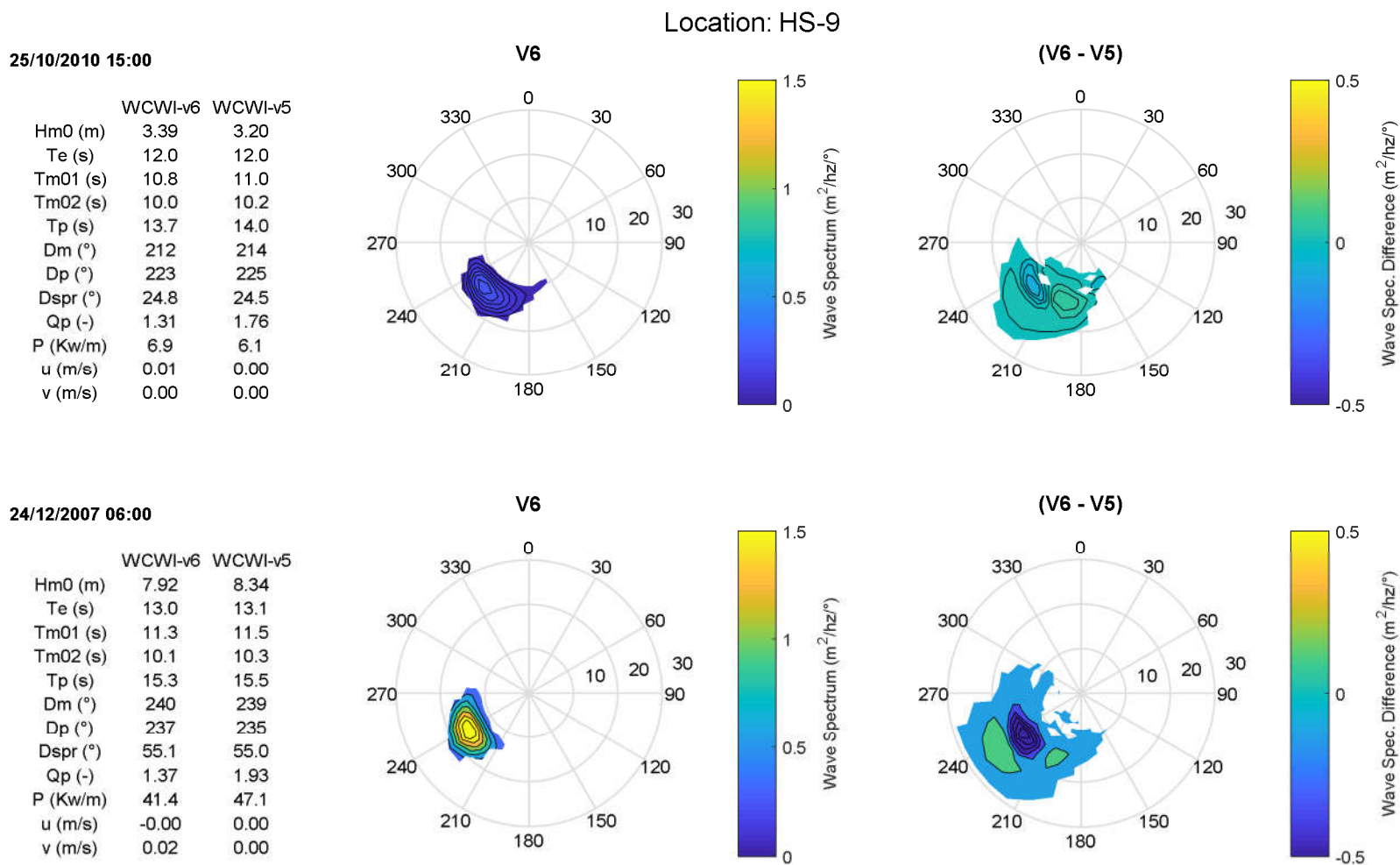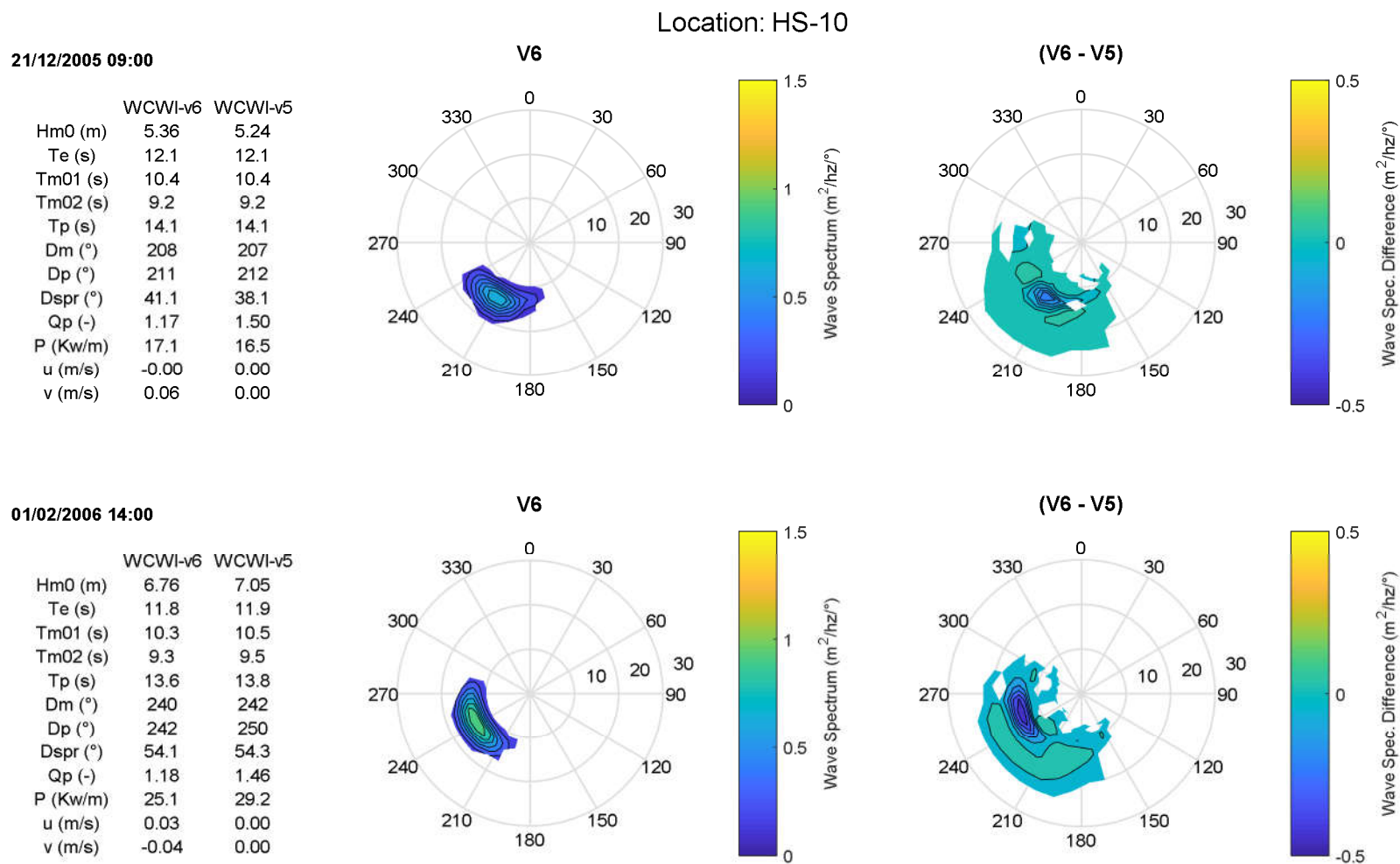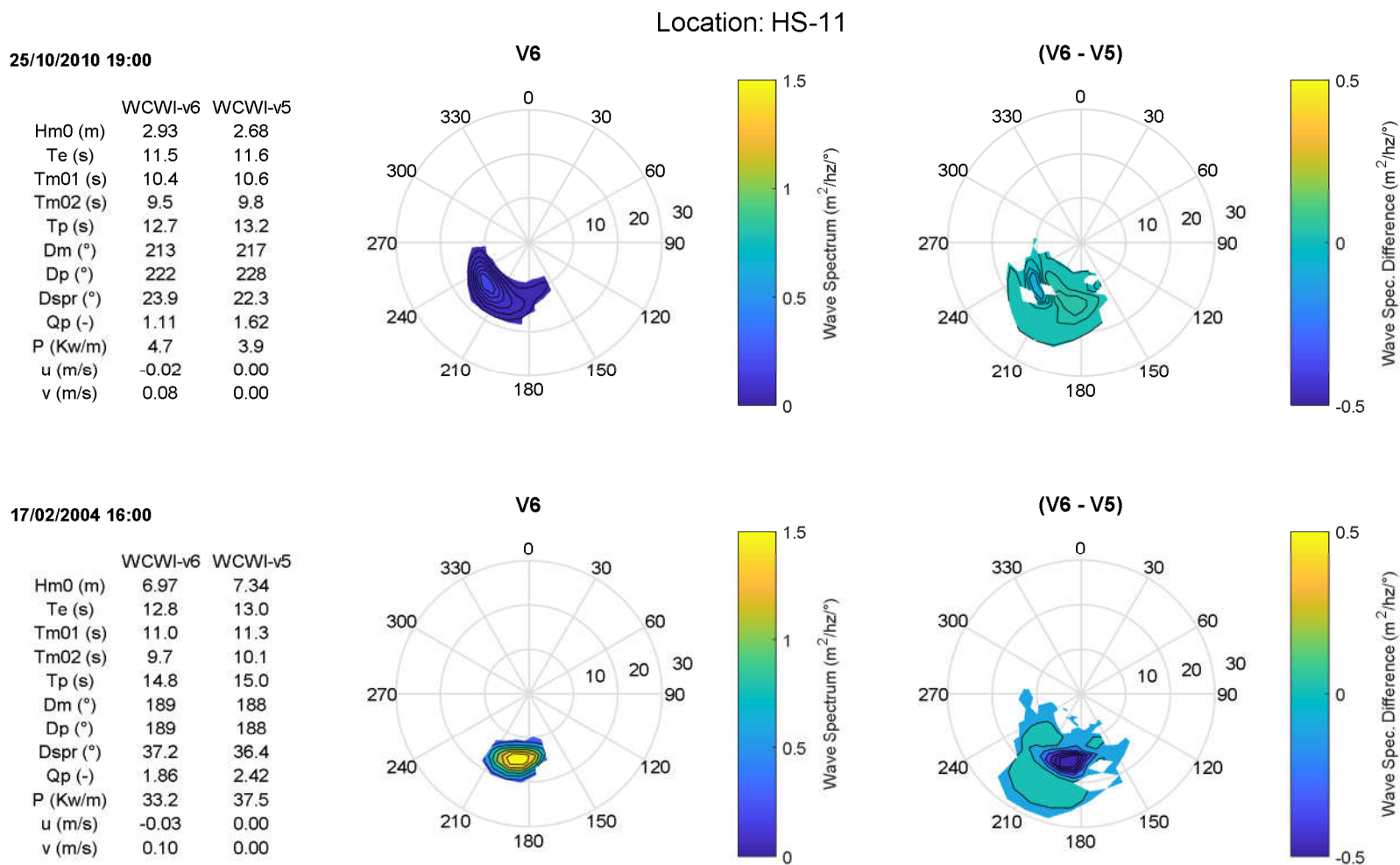| | WCWI-v6 | WCWI-v5 |
|---|---|---|
| Hm0 (m) | 6.70 | 6.96 |
| Te (s) | 9.5 | 9.7 |
| Tm01 (s) | 8.6 | 8.8 |
| Tm02 (s) | 7.9 | 8.2 |
| Tp (s) | 10.8 | 11.2 |
| Dm (°) | 158 | 157 |
| Dp (°) | 153 | 152 |
| Dspr (°) | 40.2 | 41.0 |
| Qp (-) | 1.85 | 2.04 |
| P (Kw/m) | 21.8 | 23.4 |
| u (m/s) | -0.04 | 0.00 |
| v (m/s) | 0.18 | 0.00 |

Figure D-16 V6's wave spectrum, and difference between V6's and V5's wave spectra at the maximum positive (top plots) and negative (bottom plots) difference in wave power density between the two models – DFO-6

Location: DFO-7

**24/12/2007 18:00**

| | WCWI-v6 | WCWI-v5 |
|---|---|---|
| Hm0 (m) | 4.34 | 3.98 |
| Te (s) | 11.4 | 11.1 |
| Tm01 (s) | 9.3 | 9.0 |
| Tm02 (s) | 8.1 | 7.8 |
| Tp (s) | 15.2 | 15.6 |
| Dm (°) | 228 | 234 |
| Dp (°) | 229 | 232 |
| Dspr (°) | 42.7 | 40.5 |
| Qp (-) | 1.21 | 1.81 |
| P (Kw/m) | 8.9 | 7.0 |
| u (m/s) | -0.03 | 0.00 |
| v (m/s) | 0.30 | 0.00 |

**25/01/2012 14:00**

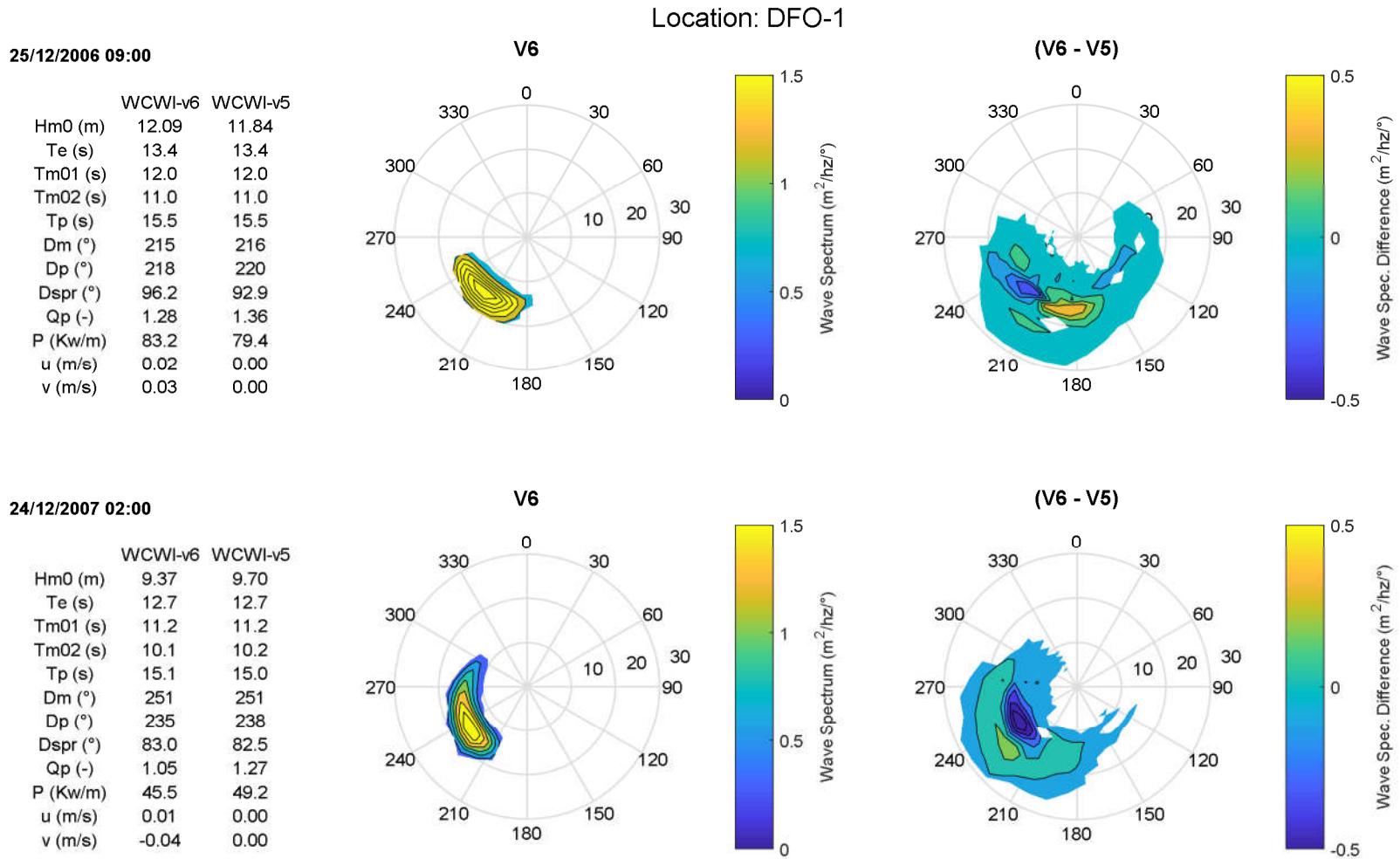| | WCWI-v6 | WCWI-v5 |
|---|---|---|
| Hm0 (m) | 6.25 | 6.79 |
| Te (s) | 12.6 | 12.7 |
| Tm01 (s) | 10.8 | 11.0 |
| Tm02 (s) | 9.5 | 9.8 |
| Tp (s) | 14.9 | 14.9 |
| Dm (°) | 210 | 212 |
| Dp (°) | 220 | 218 |
| Dspr (°) | 45.4 | 44.9 |
| Qp (-) | 1.53 | 2.18 |
| P (Kw/m) | 21.1 | 26.3 |
| u (m/s) | 0.02 | 0.00 |
| v (m/s) | -0.21 | 0.00 |



Figure D-17 V6's wave spectrum, and difference between V6's and V5's wave spectra at the maximum positive (top plots) and negative (bottom plots) difference in wave power density between the two models – DFO-7
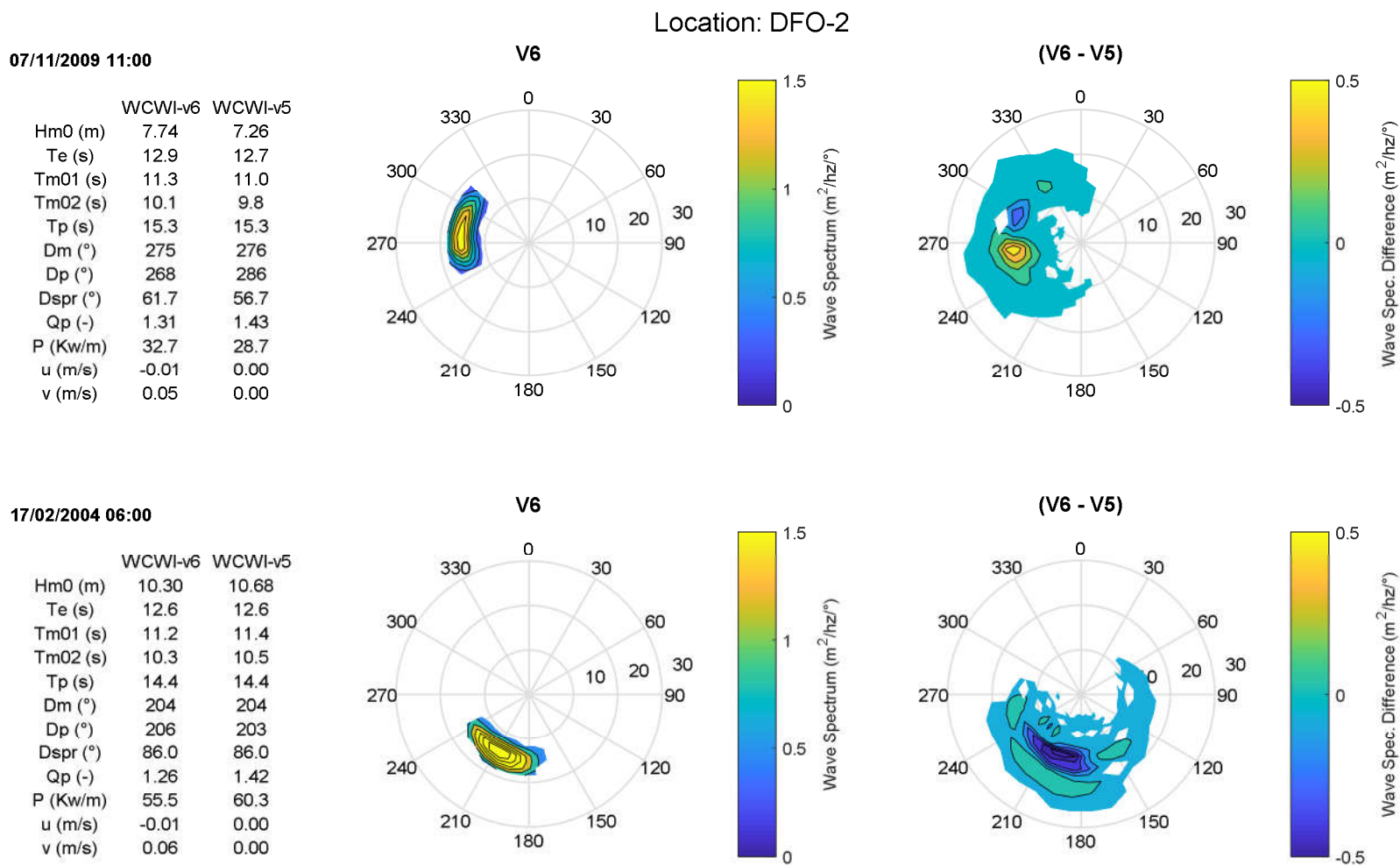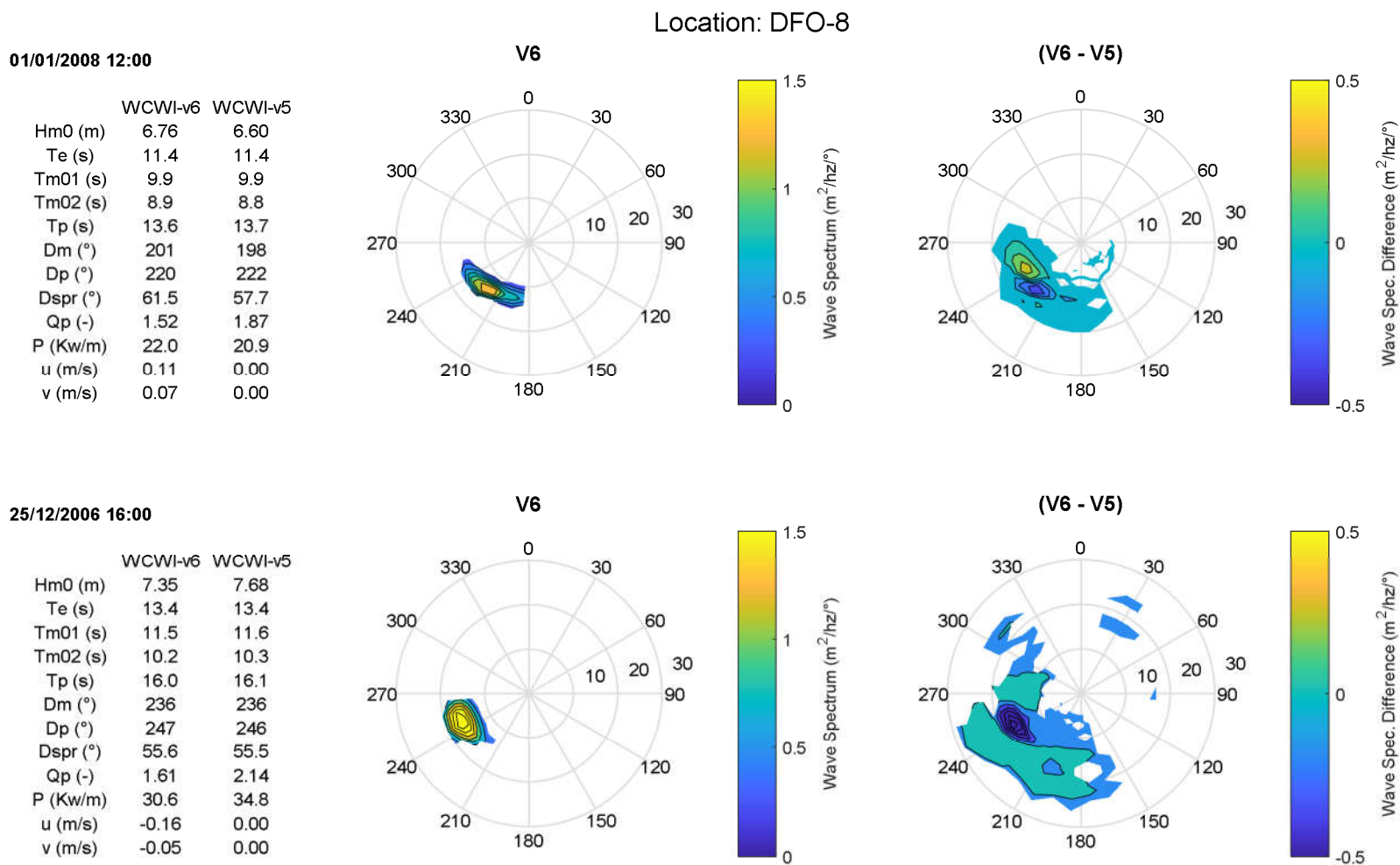
Figure D-18 V6's wave spectrum, and difference between V6's and V5's wave spectra at the maximum positive (top plots) and negative (bottom plots) difference in wave power density between the two models – DFO-8
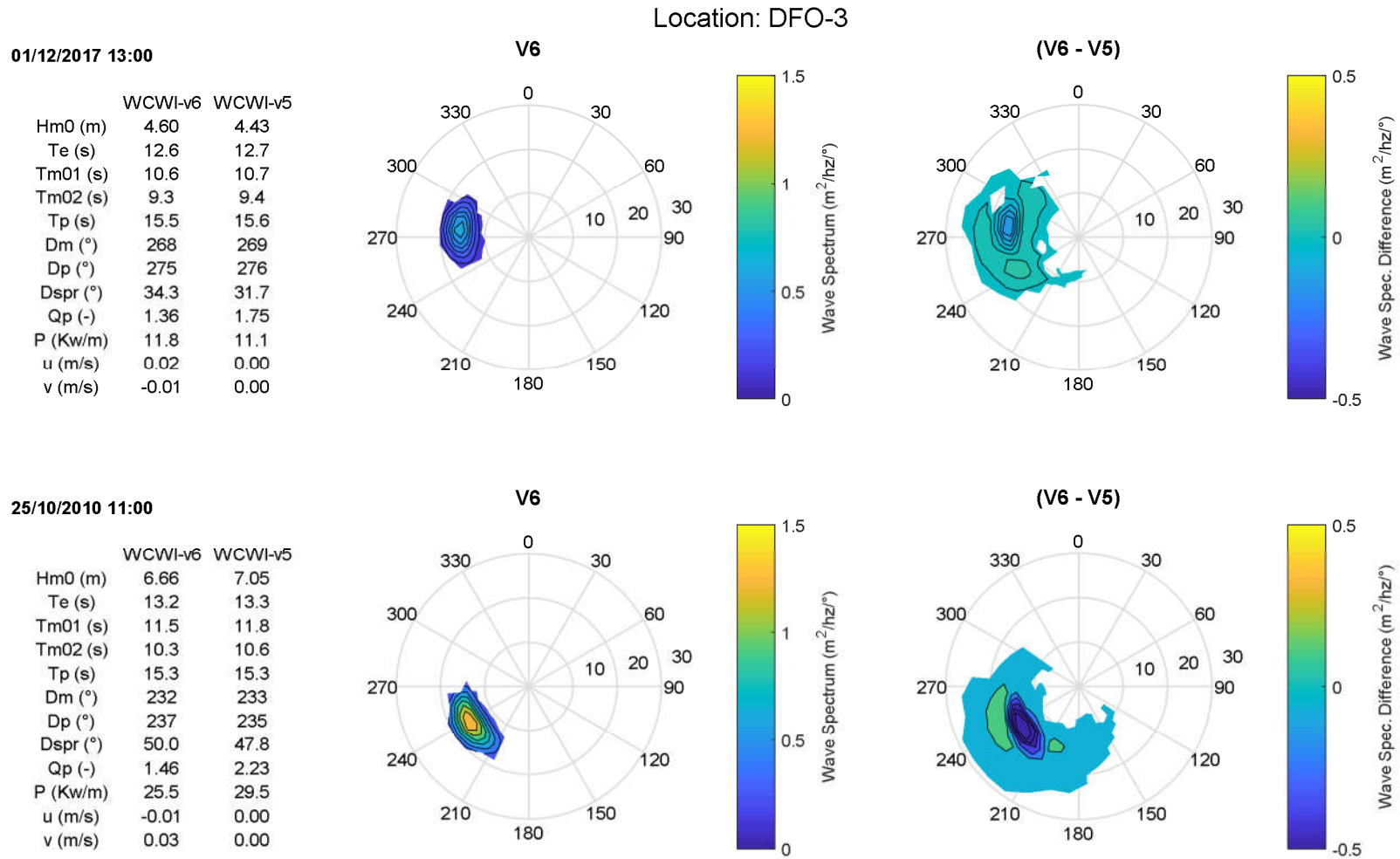
Location: DFO-9



**01/11/2010 02:00**

|  | WCWI-v6 | WCWI-v5 |
|---|---|---|
| Hm0 (m) | 8.80 | 8.63 |
| Te (s) | 11.5 | 11.6 |
| Tm01 (s) | 10.4 | 10.5 |
| Tm02 (s) | 9.6 | 9.7 |
| Tp (s) | 13.0 | 13.0 |
| Dm (°) | 177 | 174 |
| Dp (°) | 183 | 191 |
| Dspr (°) | 88.1 | 84.0 |
| Qp (-) | 1.24 | 1.50 |
| P (Kw/m) | 34.1 | 33.1 |
| u (m/s) | -0.00 | 0.00 |
| v (m/s) | 0.07 | 0.00 |

**24/12/2007 10:00**

|  | WCWI-v6 | WCWI-v5 |
|---|---|---|
| Hm0 (m) | 9.84 | 10.14 |
| Te (s) | 12.7 | 12.9 |
| Tm01 (s) | 11.3 | 11.5 |
| Tm02 (s) | 10.3 | 10.5 |
| Tp (s) | 14.6 | 15.1 |
| Dm (°) | 250 | 249 |
| Dp (°) | 237 | 234 |
| Dspr (°) | 86.4 | 86.6 |
| Qp (-) | 1.12 | 1.38 |
| P (Kw/m) | 50.0 | 54.8 |
| u (m/s) | -0.02 | 0.00 |
| v (m/s) | 0.06 | 0.00 |

Figure D-19 V6's wave spectrum, and difference between V6's and V5's wave spectra at the maximum positive (top plots) and negative (bottom plots) difference in wave power density between the two models – DFO-9
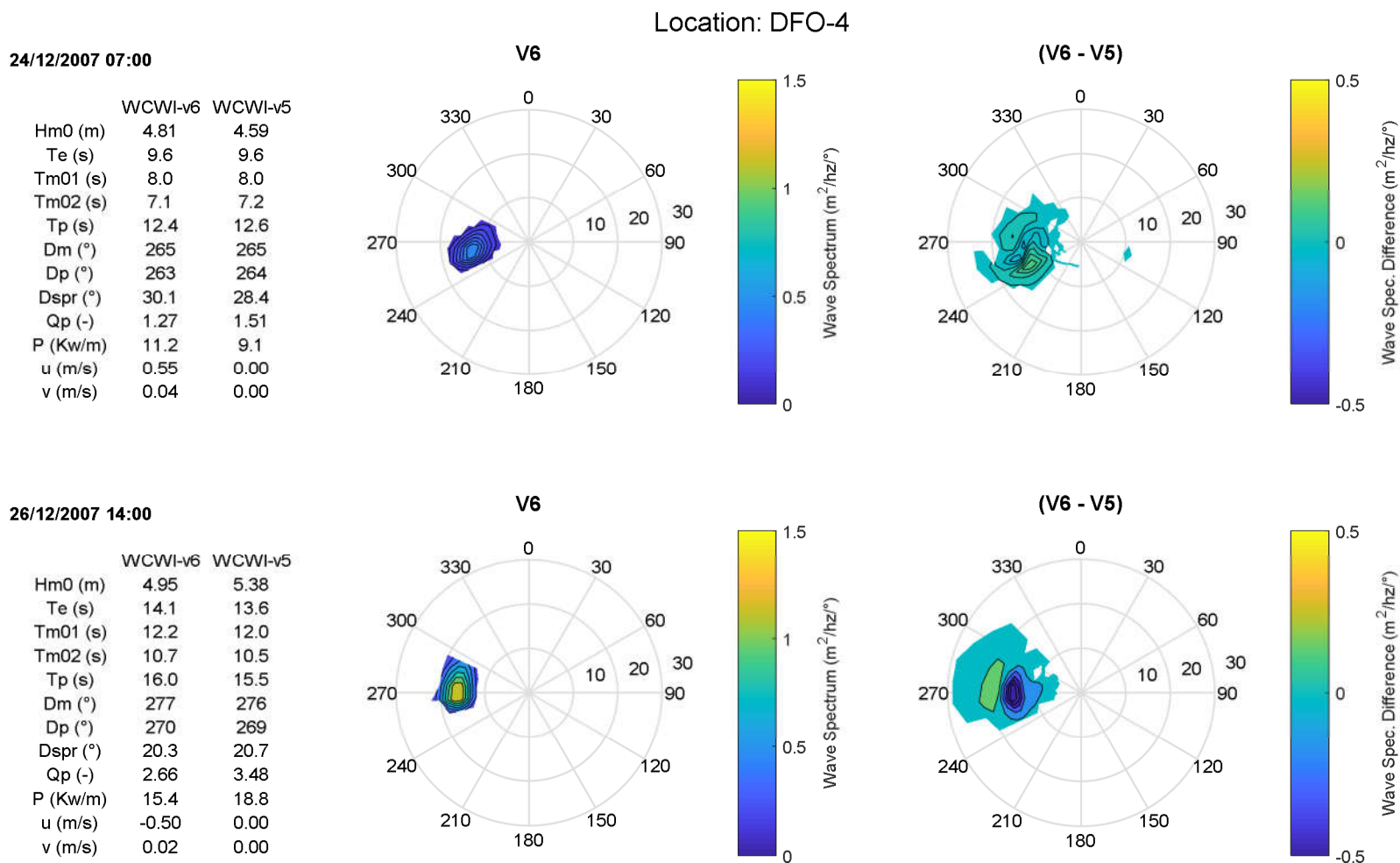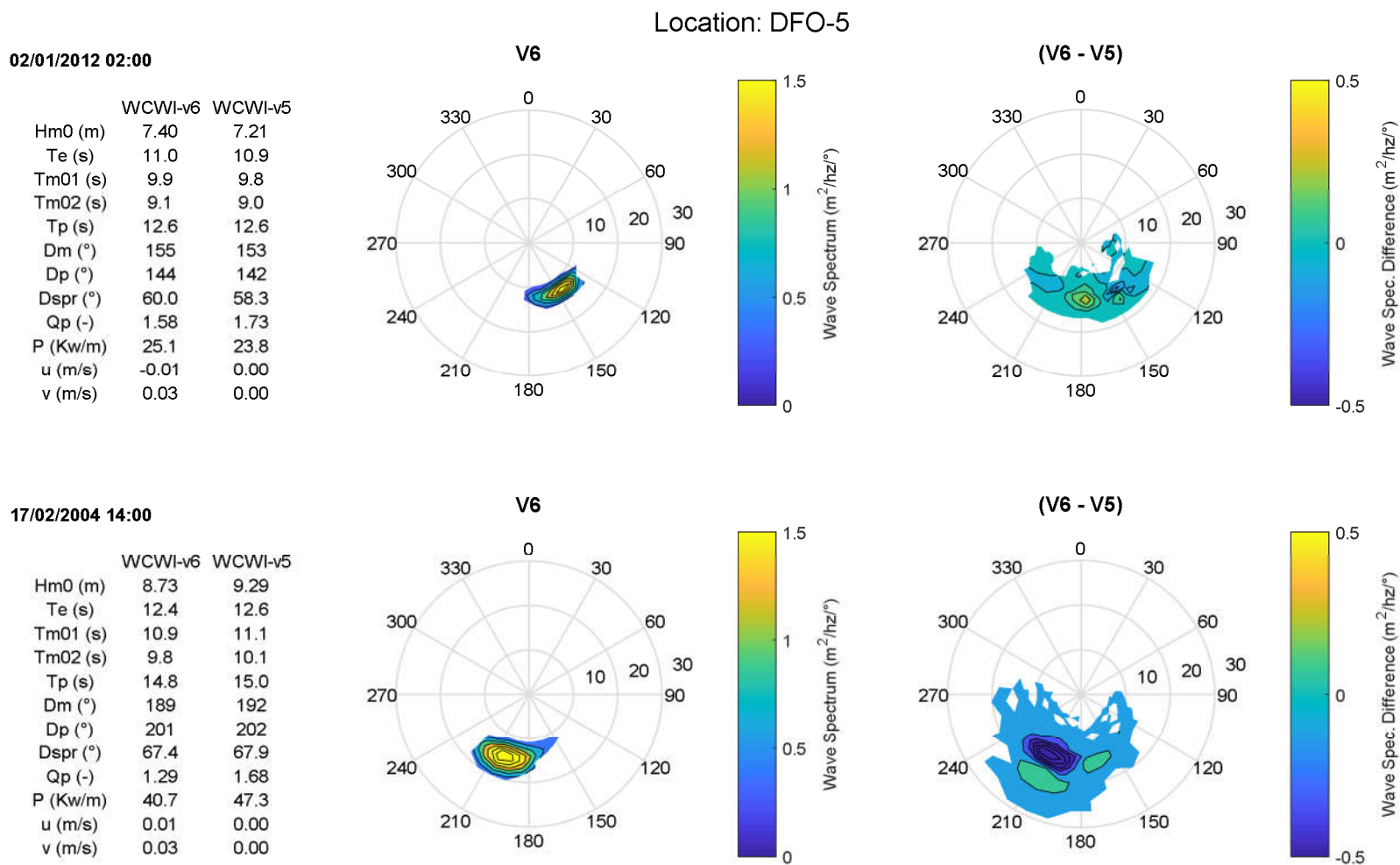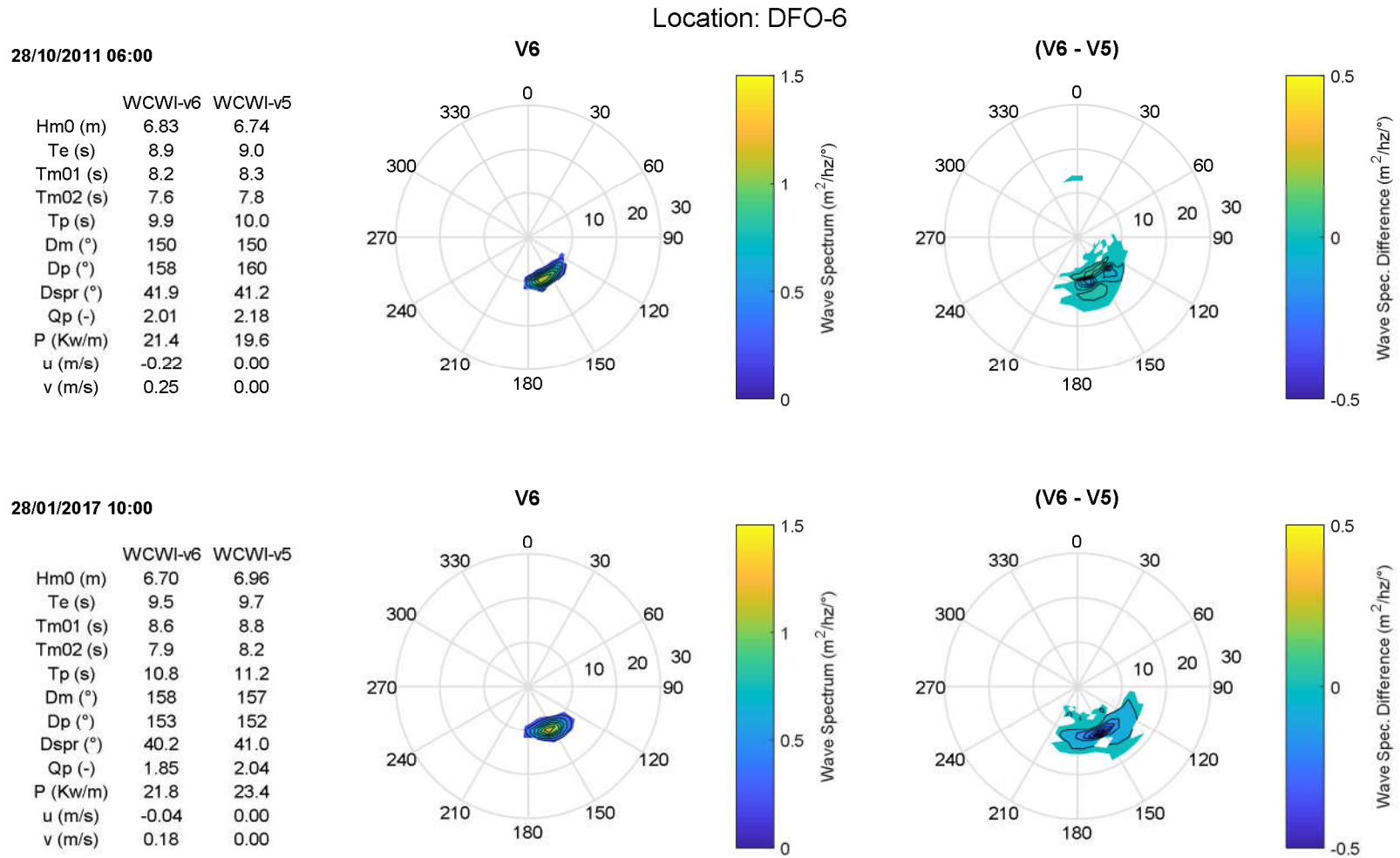
Location: DFO-10

03/12/2007 11:00

| | WCWI-v6 | WCWI-v5 |
|---|---|---|
| Hm0 (m) | 4.56 | 4.42 |
| Te (s) | 11.1 | 11.1 |
| Tm01 (s) | 9.5 | 9.5 |
| Tm02 (s) | 8.3 | 8.3 |
| Tp (s) | 13.0 | 13.0 |
| Dm (°) | 181 | 183 |
| Dp (°) | 177 | 177 |
| Dspr (°) | 39.2 | 37.2 |
| Qp (-) | 1.58 | 1.97 |
| P (Kw/m) | 10.3 | 9.8 |
| u (m/s) | 0.03 | 0.00 |
| v (m/s) | 0.03 | 0.00 |

V6

(V6 - V5)

04/02/2006 21:00

| | WCWI-v6 | WCWI-v5 |
|---|---|---|
| Hm0 (m) | 8.63 | 8.86 |
| Te (s) | 12.1 | 12.3 |
| Tm01 (s) | 10.7 | 10.9 |
| Tm02 (s) | 9.8 | 9.9 |
| Tp (s) | 14.1 | 14.3 |
| Dm (°) | 247 | 247 |
| Dp (°) | 226 | 225 |
| Dspr (°) | 78.0 | 77.6 |
| Qp (-) | 1.05 | 1.20 |
| P (Kw/m) | 40.5 | 44.1 |
| u (m/s) | -0.01 | 0.00 |
| v (m/s) | 0.04 | 0.00 |

V6

(V6 - V5)

Figure D-20 V6's wave spectrum, and difference between V6's and V5's wave spectra at the maximum positive (top plots) and negative (bottom plots) difference in wave power density between the two models – DFO-10
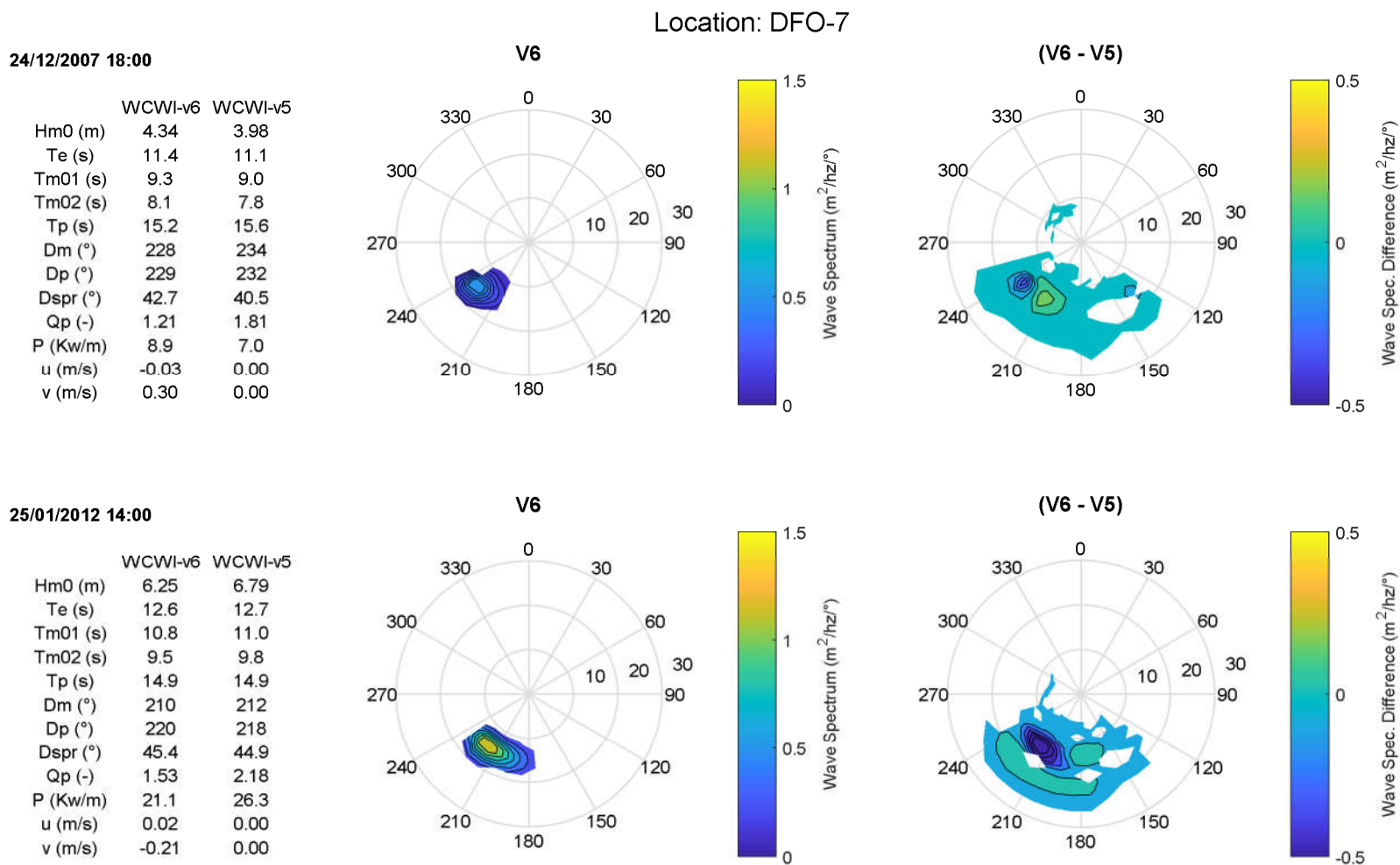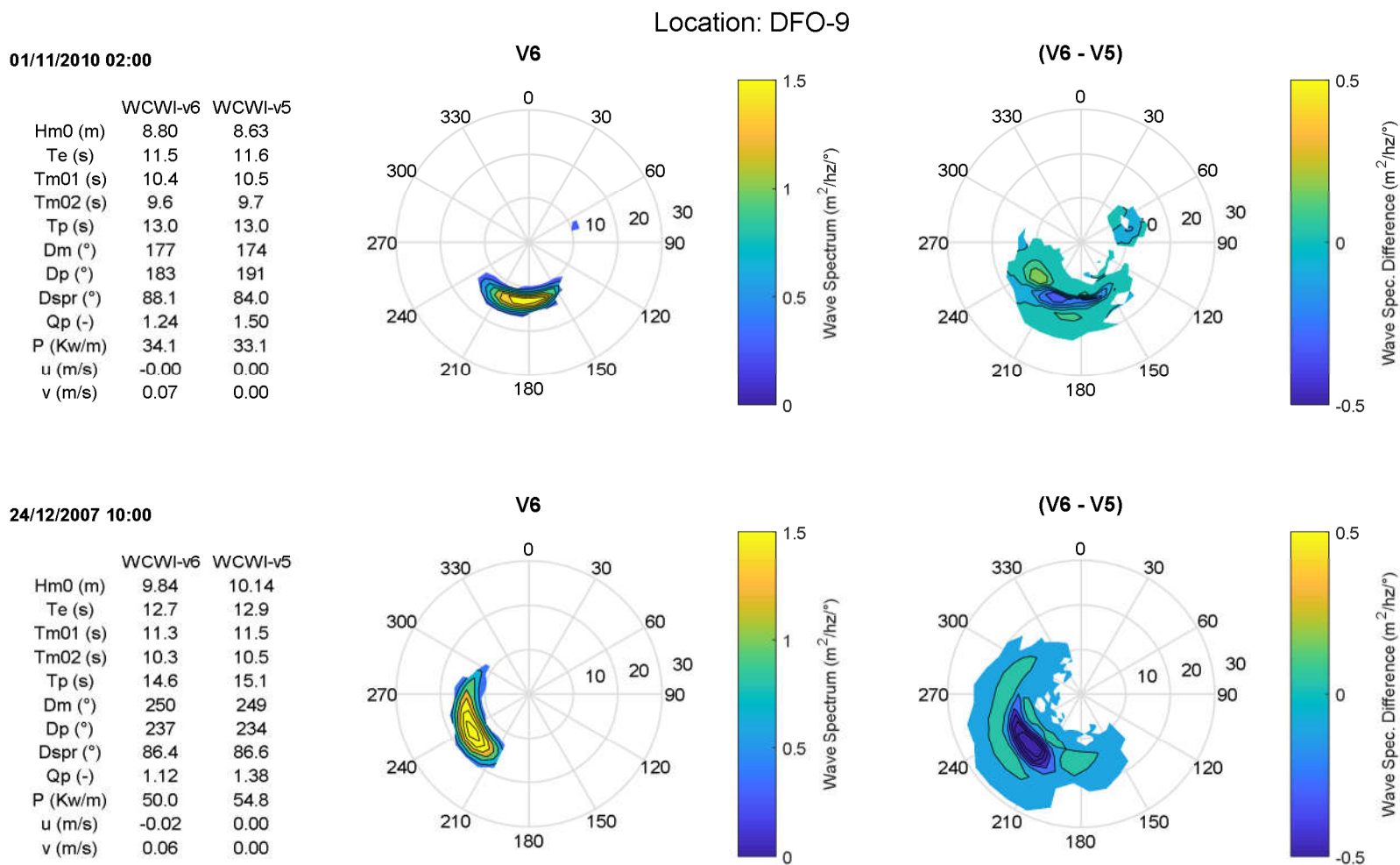
Location: DFO-11

**25/10/2010 19:00**

|  | WCWI-v6 | WCWI-v5 |
|---|---|---|
| Hm0 (m) | 5.71 | 5.38 |
| Te (s) | 12.0 | 12.3 |
| Tm01 (s) | 10.4 | 10.7 |
| Tm02 (s) | 9.3 | 9.4 |
| Tp (s) | 13.8 | 14.3 |
| Dm (°) | 227 | 233 |
| Dp (°) | 234 | 237 |
| Dspr (°) | 52.7 | 49.9 |
| Qp (-) | 1.37 | 2.04 |
| P (Kw/m) | 16.3 | 15.0 |
| u (m/s) | -0.00 | 0.00 |
| v (m/s) | 0.06 | 0.00 |
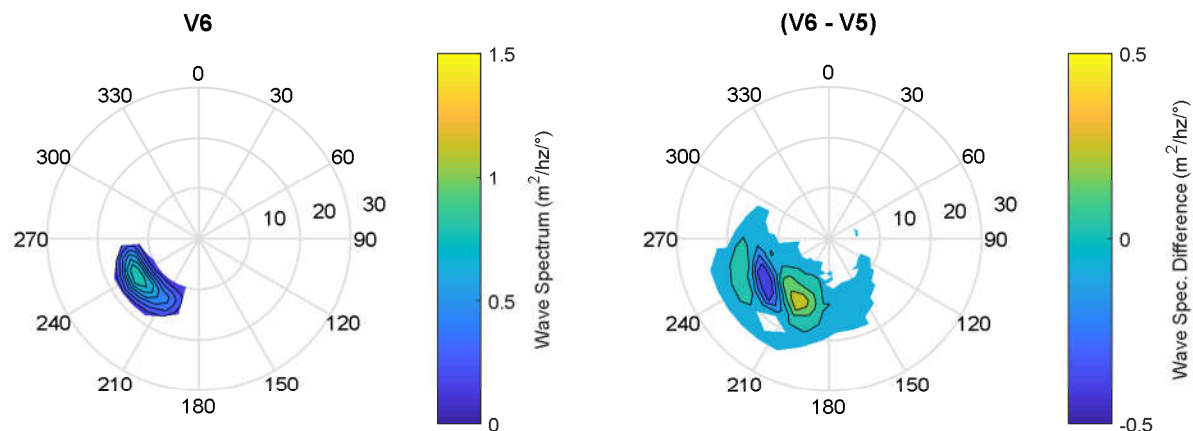
**25/12/2006 15:00**

|  | WCWI-v6 | WCWI-v5 |
|---|---|---|
| Hm0 (m) | 8.59 | 8.88 |
| Te (s) | 13.5 | 13.6 |
| Tm01 (s) | 11.7 | 11.8 |
| Tm02 (s) | 10.5 | 10.6 |
| Tp (s) | 16.2 | 16.3 |
| Dm (°) | 234 | 235 |
| Dp (°) | 245 | 246 |
| Dspr (°) | 70.7 | 70.5 |
| Qp (-) | 1.34 | 1.76 |
| P (Kw/m) | 41.9 | 45.9 |
| u (m/s) | -0.01 | 0.00 |
| v (m/s) | -0.00 | 0.00 |
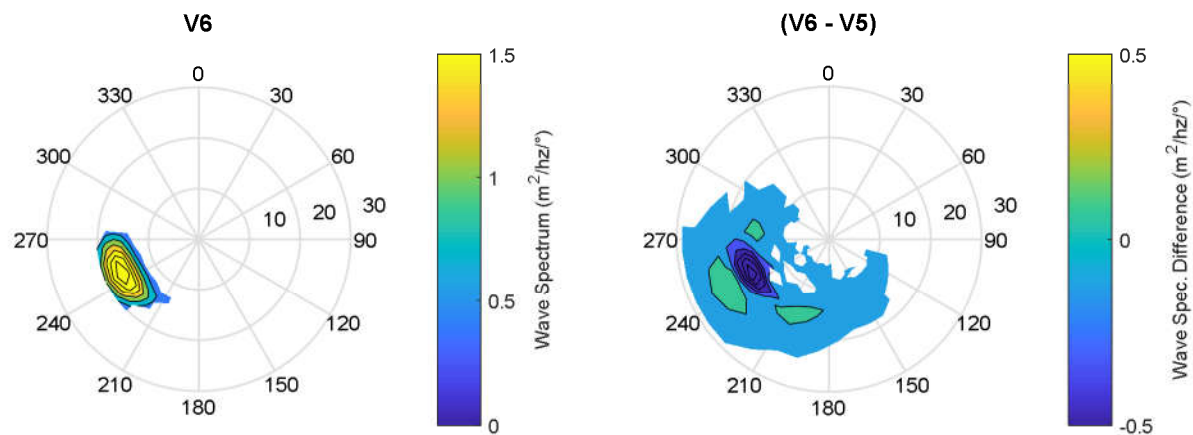


Figure D-21 V6's wave spectrum, and difference between V6's and V5's wave spectra at the maximum positive (top plots) and negative (bottom plots) difference in wave power density between the two models – DFO-11
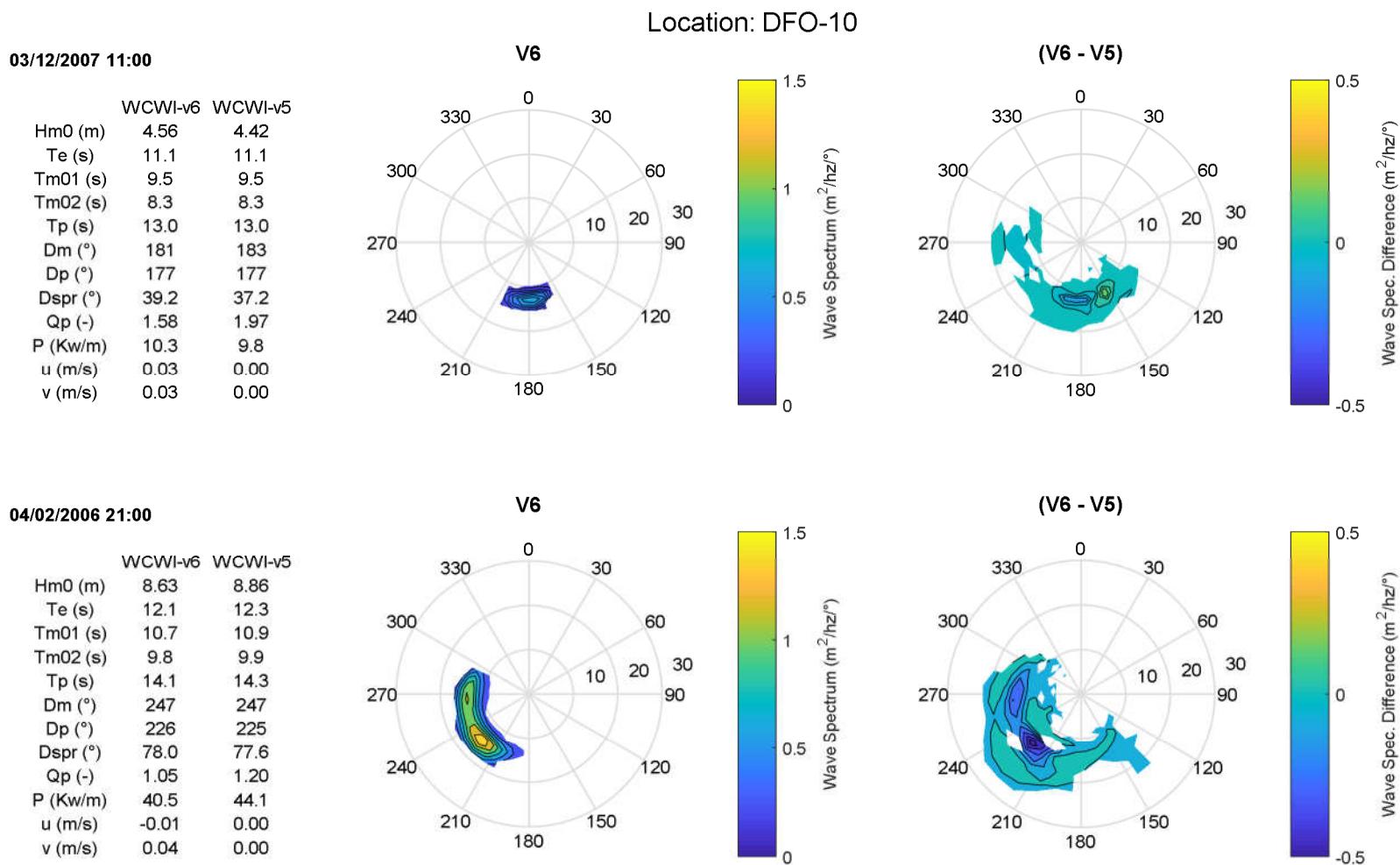
Location: DFO-12

**25/10/2010 14:00**

| | WCWI-v6 | WCWI-v5 |
|---|---|---|
| Hm0 (m) | 3.92 | 3.70 |
| Te (s) | 11.7 | 11.5 |
| Tm01 (s) | 10.3 | 10.2 |
| Tm02 (s) | 9.3 | 9.2 |
| Tp (s) | 13.6 | 13.9 |
| Dm (°) | 201 | 203 |
| Dp (°) | 223 | 225 |
| Dspr (°) | 40.4 | 39.8 |
| Qp (-) | 0.96 | 1.30 |
| P (Kw/m) | 6.9 | 5.9 |
| u (m/s) | 0.02 | 0.00 |
| v (m/s) | -0.01 | 0.00 |

**24/12/2007 06:00**

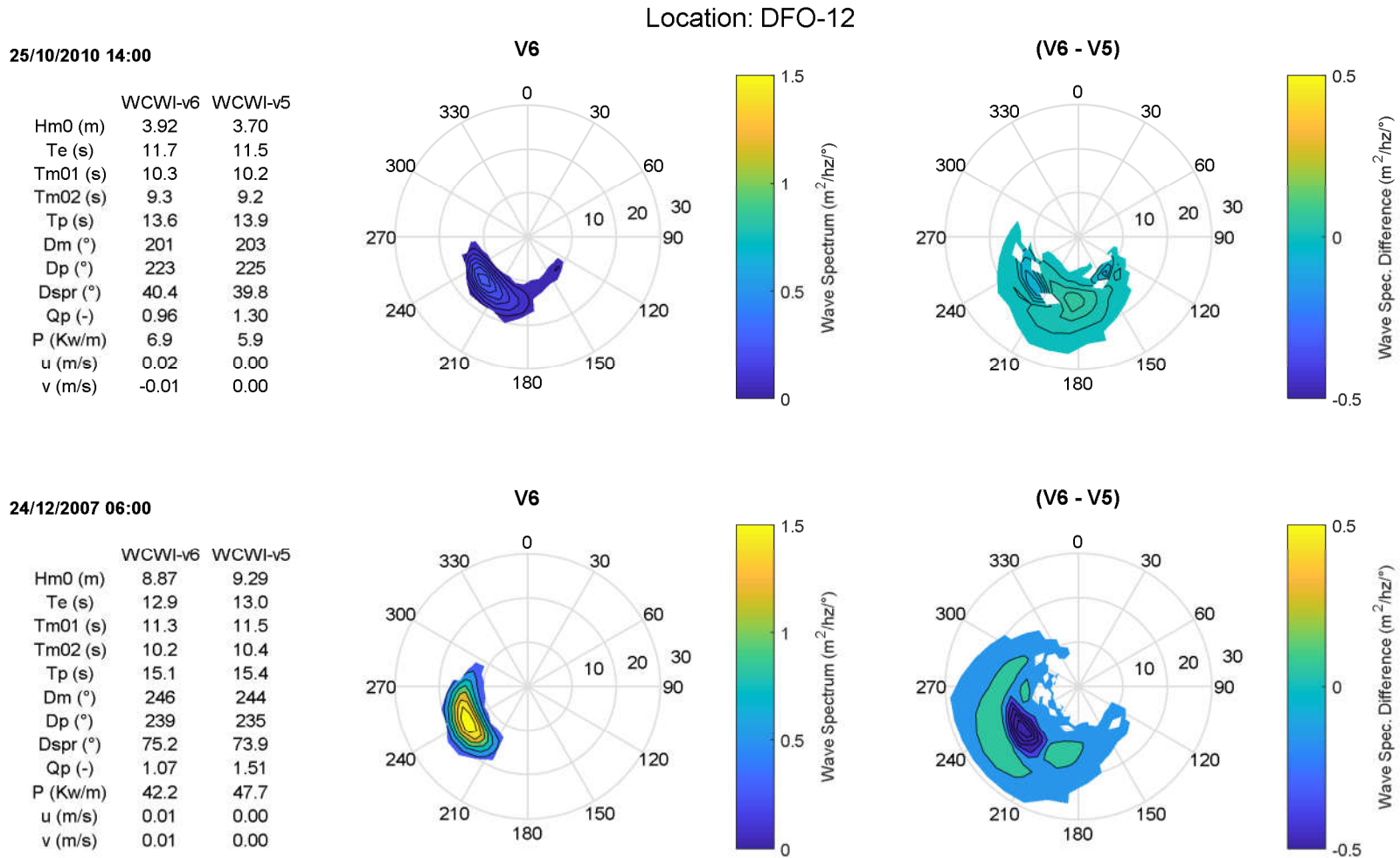| | WCWI-v6 | WCWI-v5 |
|---|---|---|
| Hm0 (m) | 8.87 | 9.29 |
| Te (s) | 12.9 | 13.0 |
| Tm01 (s) | 11.3 | 11.5 |
| Tm02 (s) | 10.2 | 10.4 |
| Tp (s) | 15.1 | 15.4 |
| Dm (°) | 246 | 244 |
| Dp (°) | 239 | 235 |
| Dspr (°) | 75.2 | 73.9 |
| Qp (-) | 1.07 | 1.51 |
| P (Kw/m) | 42.2 | 47.7 |
| u (m/s) | 0.01 | 0.00 |
| v (m/s) | 0.01 | 0.00 |



Figure D-22 V6's wave spectrum, and difference between V6's and V5's wave spectra at the maximum positive (top plots) and negative (bottom plots) difference in wave power density between the two models – DFO-12

Location: NDBC-1

**04/01/2006 15:00**

|  | WCWI-v6 | WCWI-v5 |
|---|---|---|
| Hm0 (m) | 5.97 | 5.66 |
| Te (s) | 12.3 | 12.2 |
| Tm01 (s) | 10.4 | 10.2 |
| Tm02 (s) | 9.1 | 8.9 |
| Tp (s) | 15.0 | 15.1 |
| Dm (°) | 250 | 248 |
| Dp (°) | 265 | 264 |
| Dspr (°) | 62.9 | 60.1 |
| Qp (-) | 1.21 | 1.41 |
| P (Kw/m) | 17.4 | 15.6 |
| u (m/s) | -0.00 | 0.00 |
| v (m/s) | 0.01 | 0.00 |

**05/01/2008 05:00**

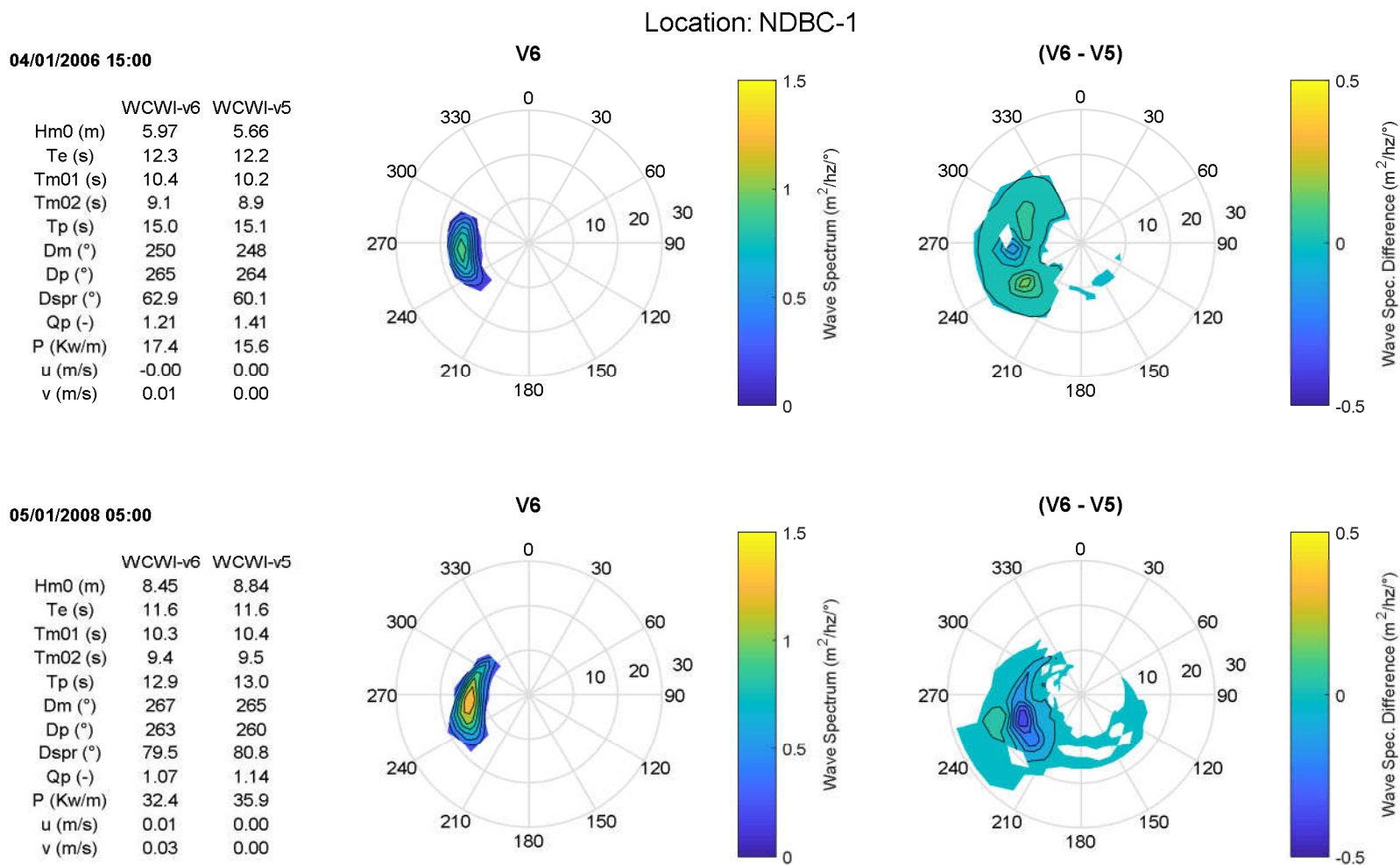|  | WCWI-v6 | WCWI-v5 |
|---|---|---|
| Hm0 (m) | 8.45 | 8.84 |
| Te (s) | 11.6 | 11.6 |
| Tm01 (s) | 10.3 | 10.4 |
| Tm02 (s) | 9.4 | 9.5 |
| Tp (s) | 12.9 | 13.0 |
| Dm (°) | 267 | 265 |
| Dp (°) | 263 | 260 |
| Dspr (°) | 79.5 | 80.8 |
| Qp (-) | 1.07 | 1.14 |
| P (Kw/m) | 32.4 | 35.9 |
| u (m/s) | 0.01 | 0.00 |
| v (m/s) | 0.03 | 0.00 |

Figure D-23 V6's wave spectrum, and difference between V6's and V5's wave spectra at the maximum positive (top plots) and negative (bottom plots) difference in wave power density between the two models – NDBC-1
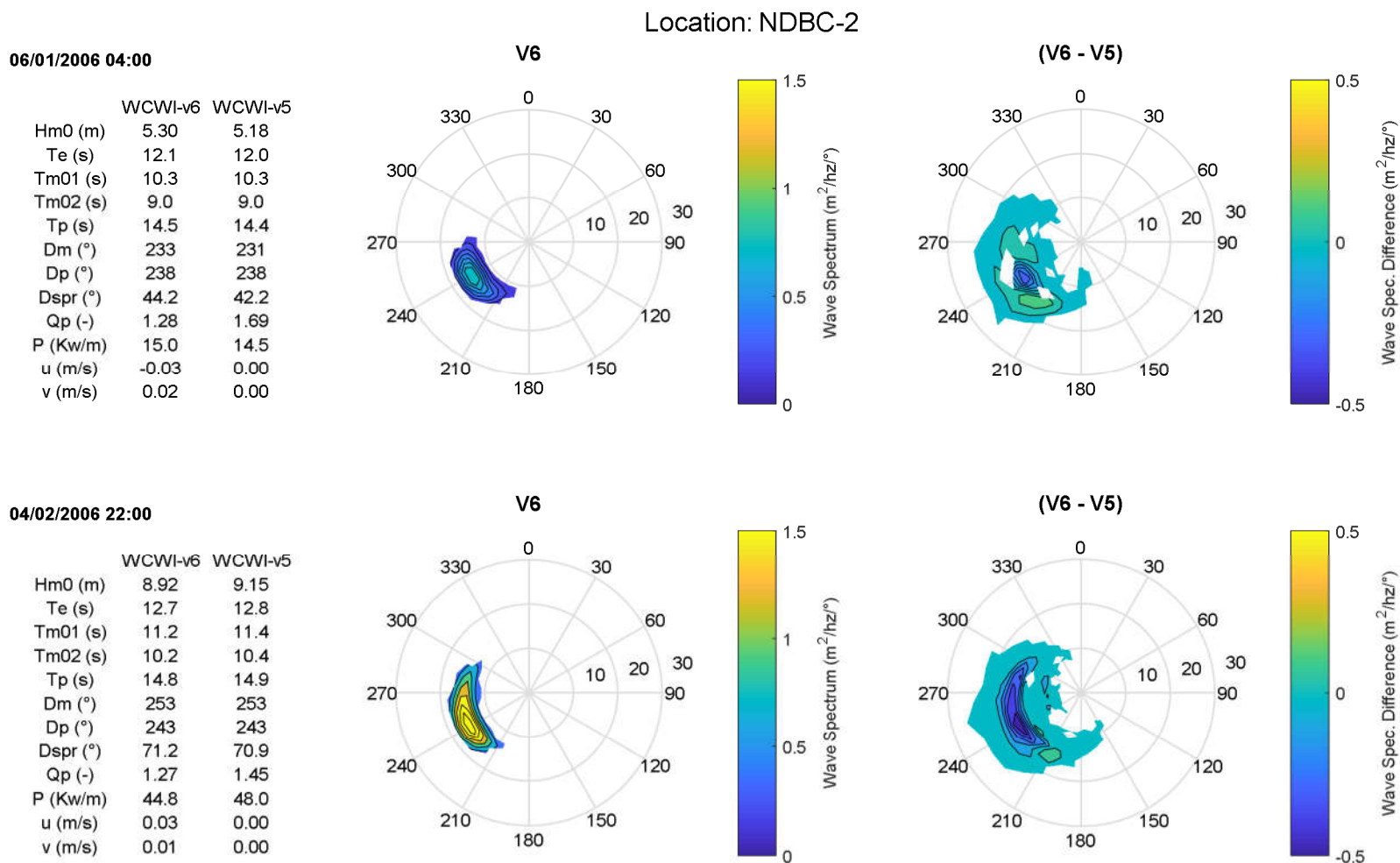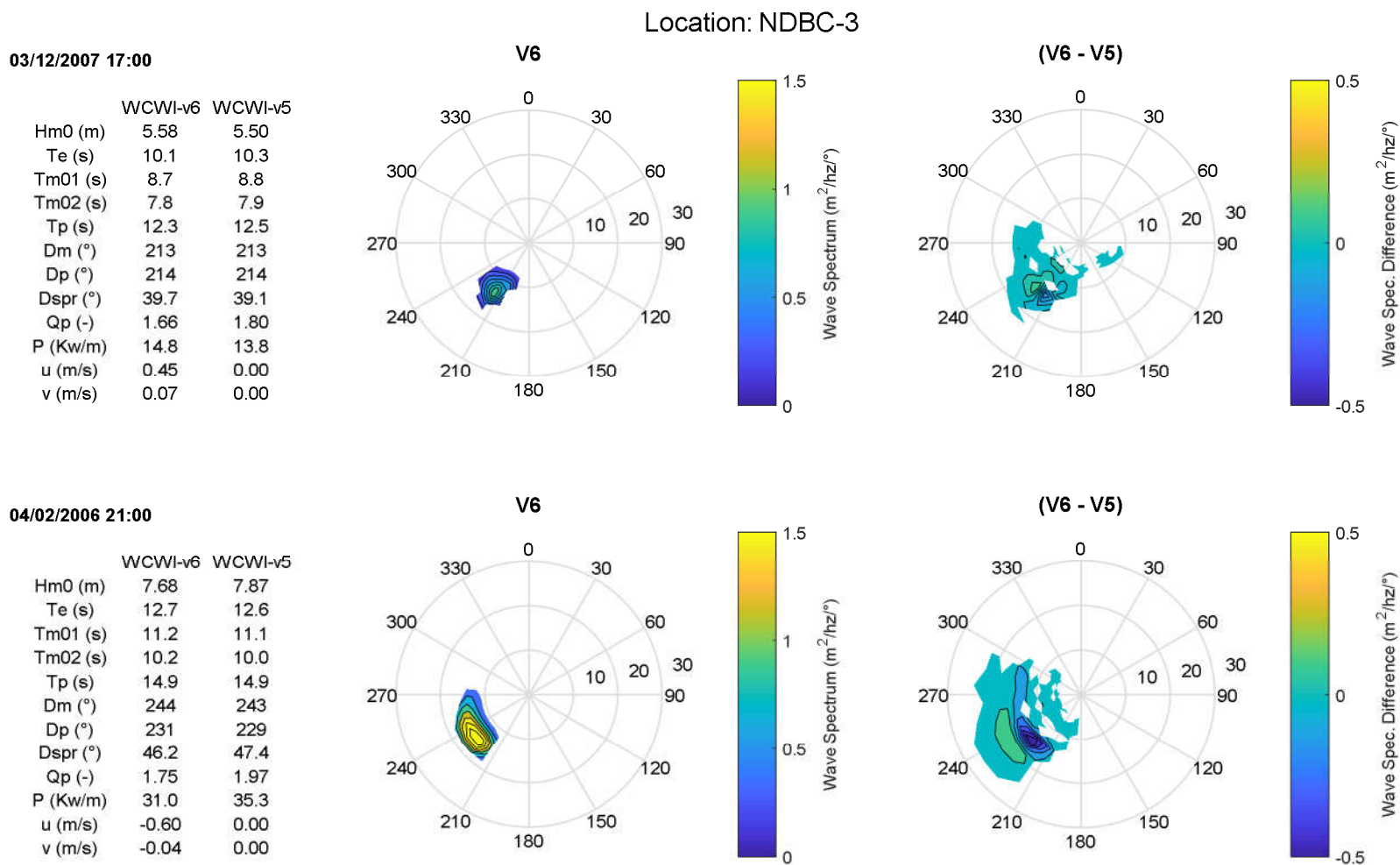
Location: NDBC-2

**06/01/2006 04:00**

|  | WCWI-v6 | WCWI-v5 |
|---|---|---|
| Hm0 (m) | 5.30 | 5.18 |
| Te (s) | 12.1 | 12.0 |
| Tm01 (s) | 10.3 | 10.3 |
| Tm02 (s) | 9.0 | 9.0 |
| Tp (s) | 14.5 | 14.4 |
| Dm (°) | 233 | 231 |
| Dp (°) | 238 | 238 |
| Dspr (°) | 44.2 | 42.2 |
| Qp (-) | 1.28 | 1.69 |
| P (Kw/m) | 15.0 | 14.5 |
| u (m/s) | -0.03 | 0.00 |
| v (m/s) | 0.02 | 0.00 |

**04/02/2006 22:00**

|  | WCWI-v6 | WCWI-v5 |
|---|---|---|
| Hm0 (m) | 8.92 | 9.15 |
| Te (s) | 12.7 | 12.8 |
| Tm01 (s) | 11.2 | 11.4 |
| Tm02 (s) | 10.2 | 10.4 |
| Tp (s) | 14.8 | 14.9 |
| Dm (°) | 253 | 253 |
| Dp (°) | 243 | 243 |
| Dspr (°) | 71.2 | 70.9 |
| Qp (-) | 1.27 | 1.45 |
| P (Kw/m) | 44.8 | 48.0 |
| u (m/s) | 0.03 | 0.00 |
| v (m/s) | 0.01 | 0.00 |



Figure D-24 V6's wave spectrum, and difference between V6's and V5's wave spectra at the maximum positive (top plots) and negative (bottom plots) difference in wave power density between the two models – NDBC-2
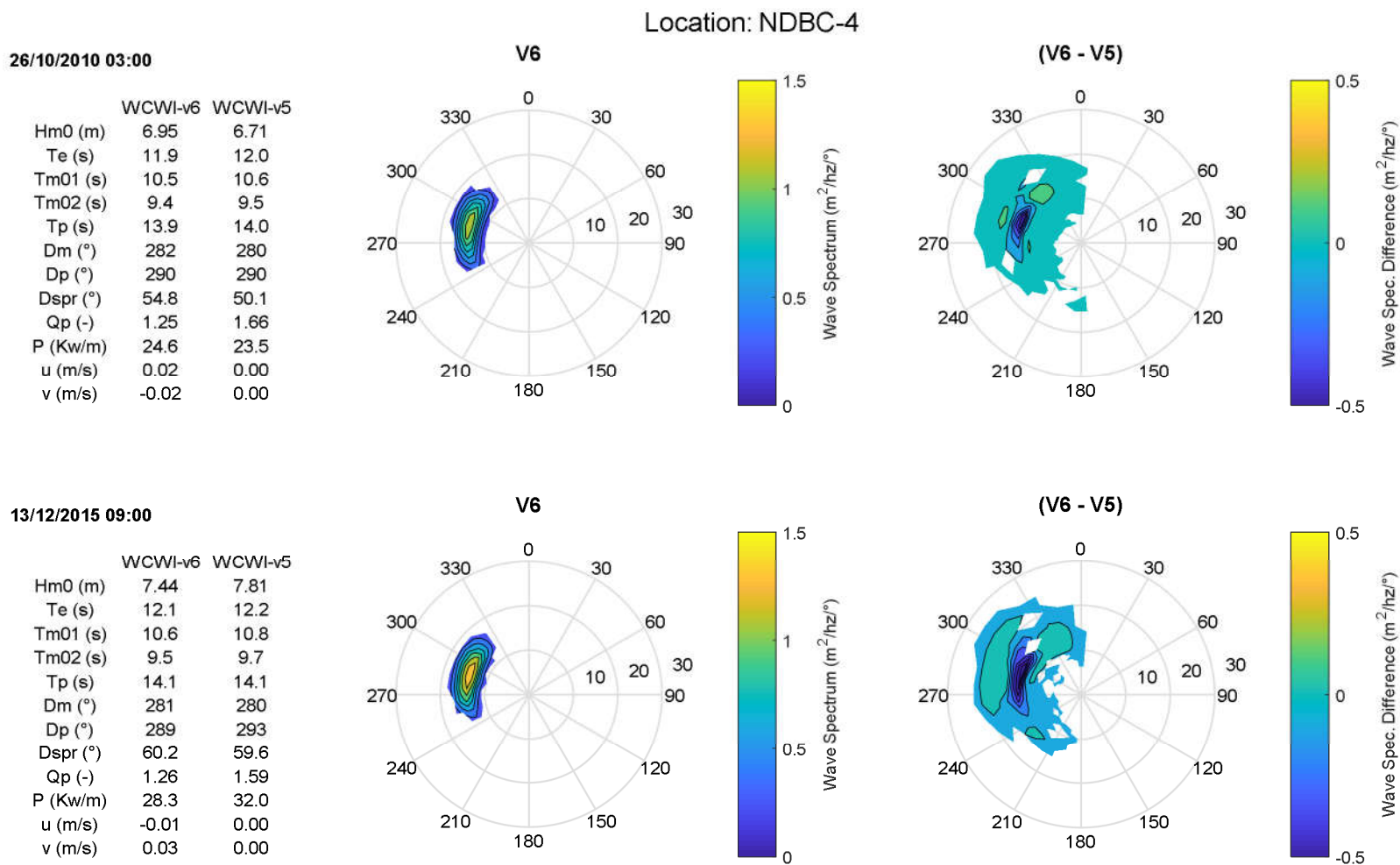
Location: NDBC-3

**03/12/2007 17:00**

| | WCWI-v6 | WCWI-v5 |
|---|---|---|
| Hm0 (m) | 5.58 | 5.50 |
| Te (s) | 10.1 | 10.3 |
| Tm01 (s) | 8.7 | 8.8 |
| Tm02 (s) | 7.8 | 7.9 |
| Tp (s) | 12.3 | 12.5 |
| Dm (°) | 213 | 213 |
| Dp (°) | 214 | 214 |
| Dspr (°) | 39.7 | 39.1 |
| Qp (-) | 1.66 | 1.80 |
| P (Kw/m) | 14.8 | 13.8 |
| u (m/s) | 0.45 | 0.00 |
| v (m/s) | 0.07 | 0.00 |

V6

(V6 - V5)

**04/02/2006 21:00**

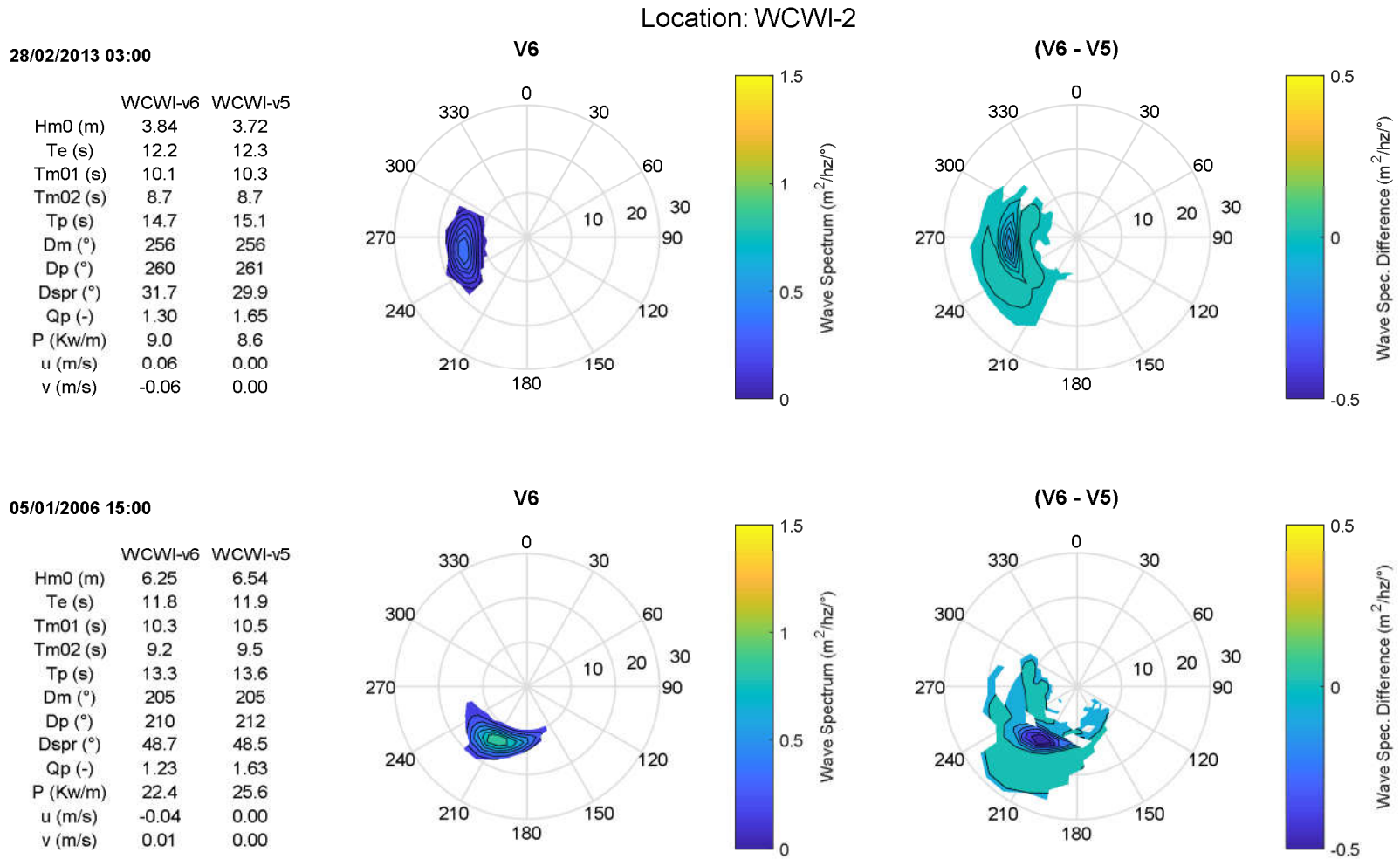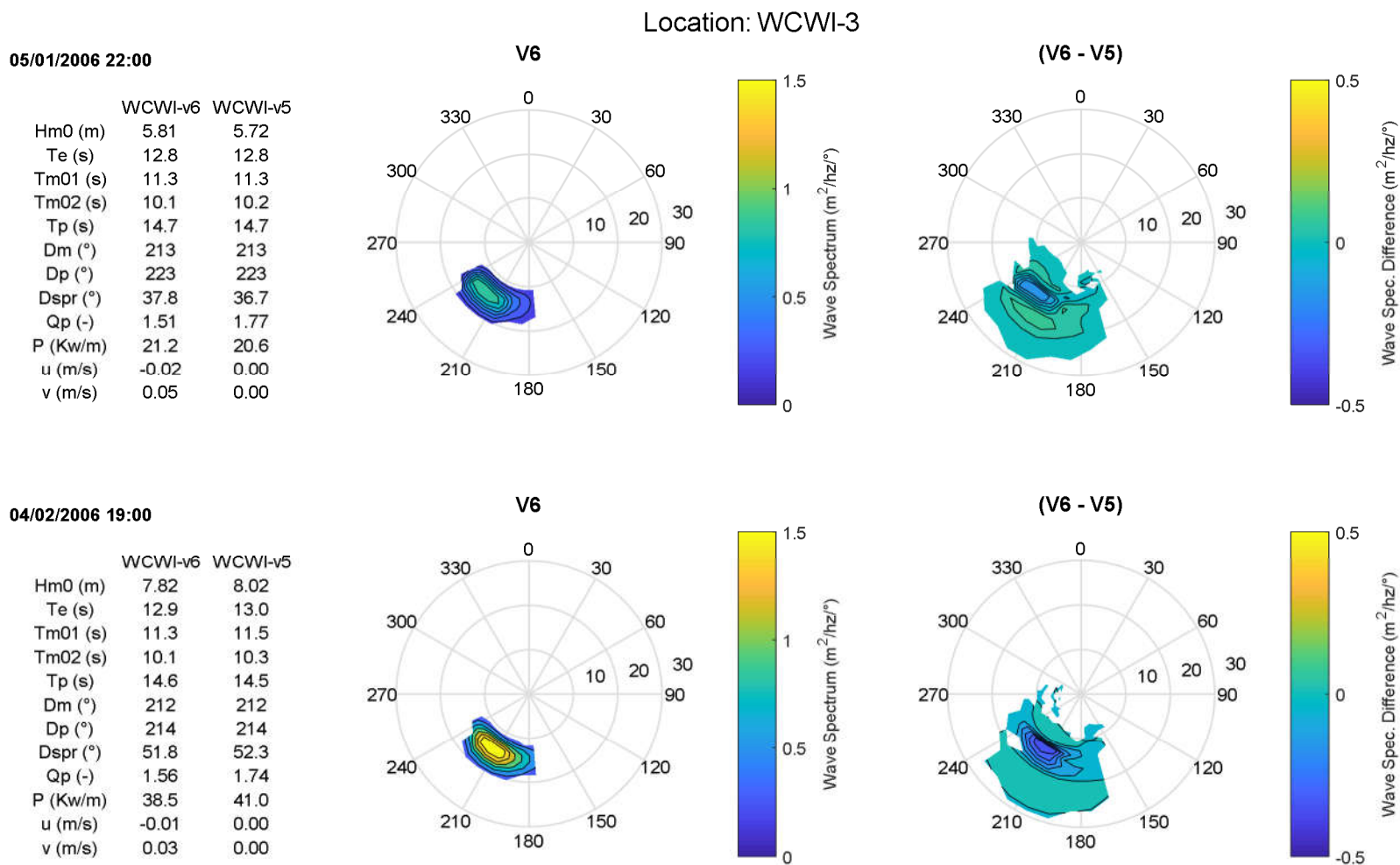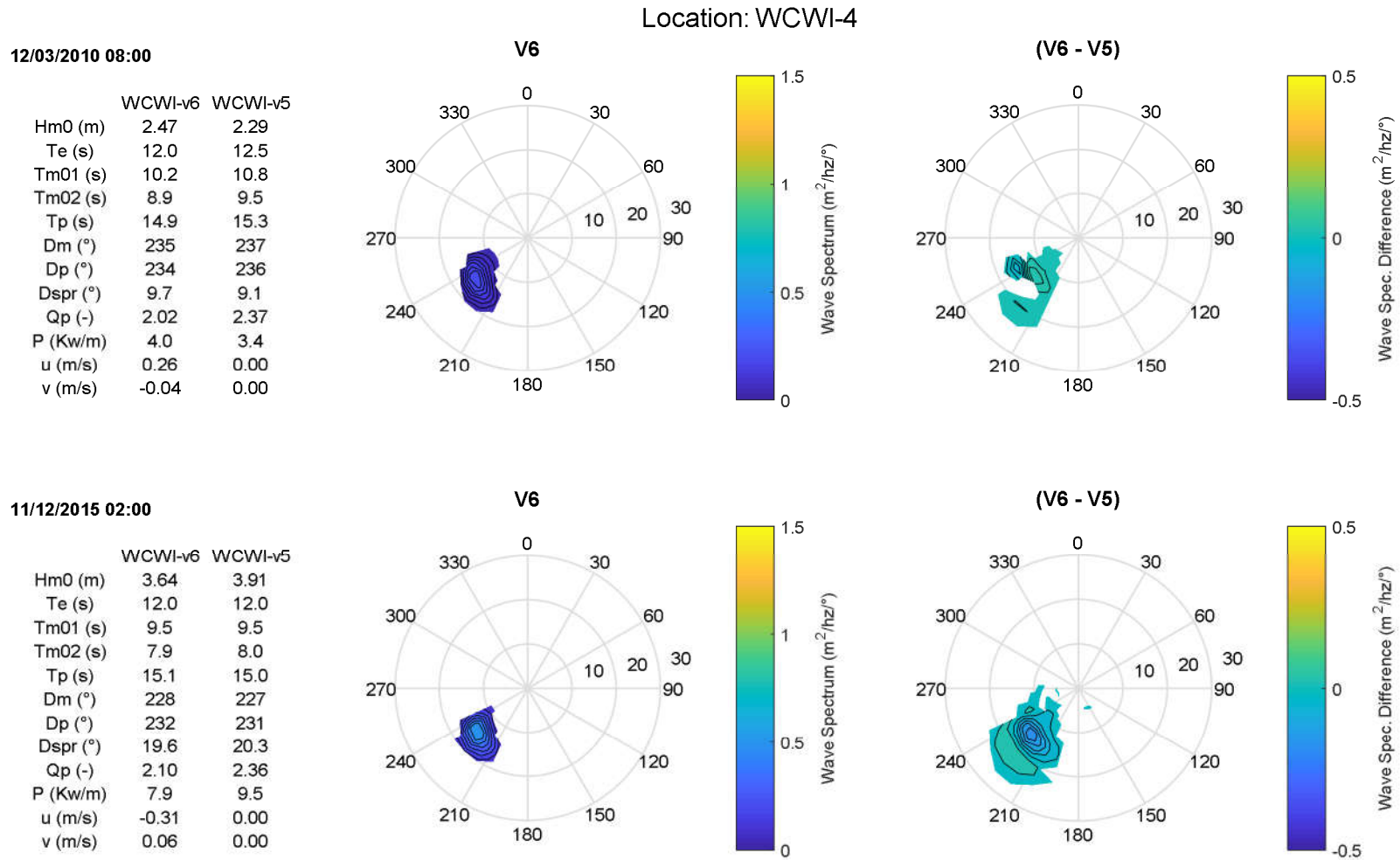| | WCWI-v6 | WCWI-v5 |
|---|---|---|
| Hm0 (m) | 7.68 | 7.87 |
| Te (s) | 12.7 | 12.6 |
| Tm01 (s) | 11.2 | 11.1 |
| Tm02 (s) | 10.2 | 10.0 |
| Tp (s) | 14.9 | 14.9 |
| Dm (°) | 244 | 243 |
| Dp (°) | 231 | 229 |
| Dspr (°) | 46.2 | 47.4 |
| Qp (-) | 1.75 | 1.97 |
| P (Kw/m) | 31.0 | 35.3 |
| u (m/s) | -0.60 | 0.00 |
| v (m/s) | -0.04 | 0.00 |

V6

(V6 - V5)

Figure D-25 V6's wave spectrum, and difference between V6's and V5's wave spectra at the maximum positive (top plots) and negative (bottom plots) difference in wave power density between the two models – NDBC-3

Location: NDBC-4

26/10/2010 03:00

| | WCWI-v6 | WCWI-v5 |
|---|---|---|
| Hm0 (m) | 6.95 | 6.71 |
| Te (s) | 11.9 | 12.0 |
| Tm01 (s) | 10.5 | 10.6 |
| Tm02 (s) | 9.4 | 9.5 |
| Tp (s) | 13.9 | 14.0 |
| Dm (°) | 282 | 280 |
| Dp (°) | 290 | 290 |
| Dspr (°) | 54.8 | 50.1 |
| Qp (-) | 1.25 | 1.66 |
| P (Kw/m) | 24.6 | 23.5 |
| u (m/s) | 0.02 | 0.00 |
| v (m/s) | -0.02 | 0.00 |

V6

(V6 - V5)

13/12/2015 09:00

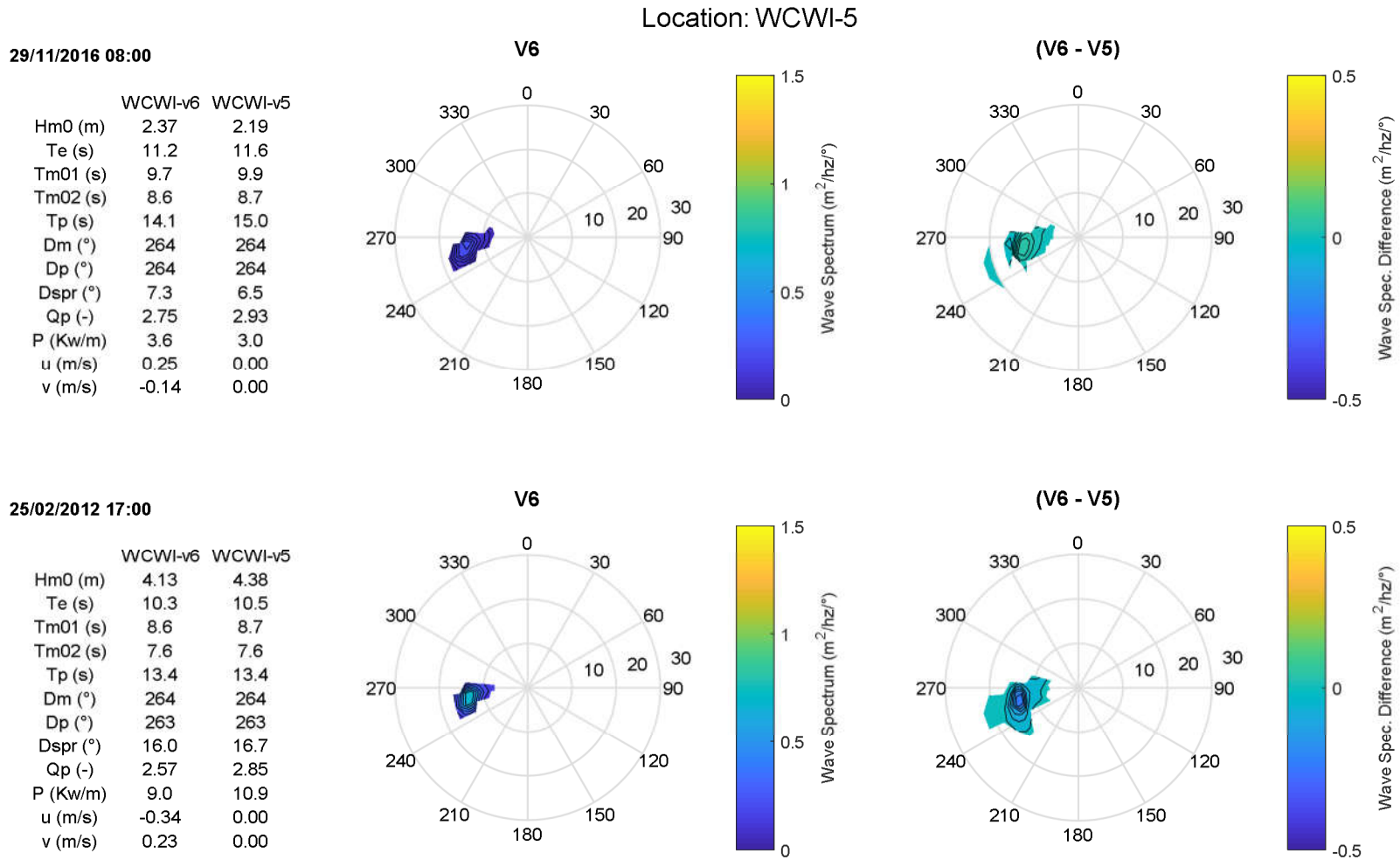| | WCWI-v6 | WCWI-v5 |
|---|---|---|
| Hm0 (m) | 7.44 | 7.81 |
| Te (s) | 12.1 | 12.2 |
| Tm01 (s) | 10.6 | 10.8 |
| Tm02 (s) | 9.5 | 9.7 |
| Tp (s) | 14.1 | 14.1 |
| Dm (°) | 281 | 280 |
| Dp (°) | 289 | 293 |
| Dspr (°) | 60.2 | 59.6 |
| Qp (-) | 1.26 | 1.59 |
| P (Kw/m) | 28.3 | 32.0 |
| u (m/s) | -0.01 | 0.00 |
| v (m/s) | 0.03 | 0.00 |

V6

(V6 - V5)



Figure D-26 V6's wave spectrum, and difference between V6's and V5's wave spectra at the maximum positive (top plots) and negative (bottom plots) difference in wave power density between the two models – NDBC-4
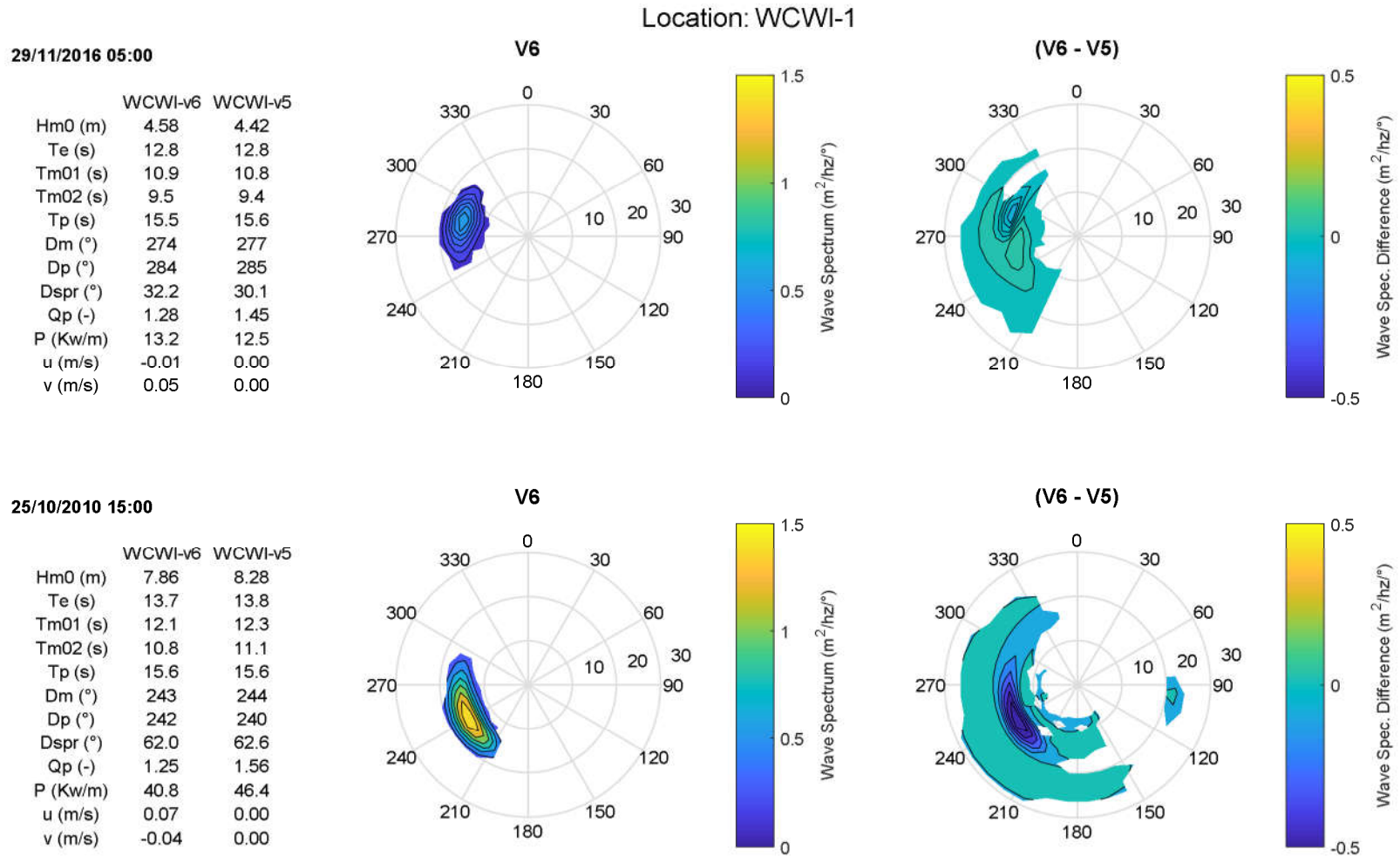
Figure D-27 V6's wave spectrum, and difference between V6's and V5's wave spectra at the maximum positive (top plots) and negative (bottom plots) difference in wave power density between the two models – WCWI-1

Location: WCWI-2

**28/02/2013 03:00**

| | WCWI-v6 | WCWI-v5 |
|---|---|---|
| Hm0 (m) | 3.84 | 3.72 |
| Te (s) | 12.2 | 12.3 |
| Tm01 (s) | 10.1 | 10.3 |
| Tm02 (s) | 8.7 | 8.7 |
| Tp (s) | 14.7 | 15.1 |
| Dm (°) | 256 | 256 |
| Dp (°) | 260 | 261 |
| Dspr (°) | 31.7 | 29.9 |
| Qp (-) | 1.30 | 1.65 |
| P (Kw/m) | 9.0 | 8.6 |
| u (m/s) | 0.06 | 0.00 |
| v (m/s) | -0.06 | 0.00 |

**05/01/2006 15:00**

| | WCWI-v6 | WCWI-v5 |
|---|---|---|
| Hm0 (m) | 6.25 | 6.54 |
| Te (s) | 11.8 | 11.9 |
| Tm01 (s) | 10.3 | 10.5 |
| Tm02 (s) | 9.2 | 9.5 |
| Tp (s) | 13.3 | 13.6 |
| Dm (°) | 205 | 205 |
| Dp (°) | 210 | 212 |
| Dspr (°) | 48.7 | 48.5 |
| Qp (-) | 1.23 | 1.63 |
| P (Kw/m) | 22.4 | 25.6 |
| u (m/s) | -0.04 | 0.00 |
| v (m/s) | 0.01 | 0.00 |



Figure D-28 V6's wave spectrum, and difference between V6's and V5's wave spectra at the maximum positive (top plots) and negative (bottom plots) difference in wave power density between the two models – WCWI-2

Location: WCWI-3

**05/01/2006 22:00**

| | WCWI-v6 | WCWI-v5 |
|---|---|---|
| Hm0 (m) | 5.81 | 5.72 |
| Te (s) | 12.8 | 12.8 |
| Tm01 (s) | 11.3 | 11.3 |
| Tm02 (s) | 10.1 | 10.2 |
| Tp (s) | 14.7 | 14.7 |
| Dm (°) | 213 | 213 |
| Dp (°) | 223 | 223 |
| Dspr (°) | 37.8 | 36.7 |
| Qp (-) | 1.51 | 1.77 |
| P (Kw/m) | 21.2 | 20.6 |
| u (m/s) | -0.02 | 0.00 |
| v (m/s) | 0.05 | 0.00 |

**04/02/2006 19:00**

| | WCWI-v6 | WCWI-v5 |
|---|---|---|
| Hm0 (m) | 7.82 | 8.02 |
| Te (s) | 12.9 | 13.0 |
| Tm01 (s) | 11.3 | 11.5 |
| Tm02 (s) | 10.1 | 10.3 |
| Tp (s) | 14.6 | 14.5 |
| Dm (°) | 212 | 212 |
| Dp (°) | 214 | 214 |
| Dspr (°) | 51.8 | 52.3 |
| Qp (-) | 1.56 | 1.74 |
| P (Kw/m) | 38.5 | 41.0 |
| u (m/s) | -0.01 | 0.00 |
| v (m/s) | 0.03 | 0.00 |



Figure D-29 V6's wave spectrum, and difference between V6's and V5's wave spectra at the maximum positive (top plots) and negative (bottom plots) difference in wave power density between the two models – WCWI-3

Location: WCWI-4

**12/03/2010 08:00**

| | WCWI-v6 | WCWI-v5 |
|---|---|---|
| Hm0 (m) | 2.47 | 2.29 |
| Te (s) | 12.0 | 12.5 |
| Tm01 (s) | 10.2 | 10.8 |
| Tm02 (s) | 8.9 | 9.5 |
| Tp (s) | 14.9 | 15.3 |
| Dm (°) | 235 | 237 |
| Dp (°) | 234 | 236 |
| Dspr (°) | 9.7 | 9.1 |
| Qp (-) | 2.02 | 2.37 |
| P (Kw/m) | 4.0 | 3.4 |
| u (m/s) | 0.26 | 0.00 |
| v (m/s) | -0.04 | 0.00 |

**11/12/2015 02:00**

| | WCWI-v6 | WCWI-v5 |
|---|---|---|
| Hm0 (m) | 3.64 | 3.91 |
| Te (s) | 12.0 | 12.0 |
| Tm01 (s) | 9.5 | 9.5 |
| Tm02 (s) | 7.9 | 8.0 |
| Tp (s) | 15.1 | 15.0 |
| Dm (°) | 228 | 227 |
| Dp (°) | 232 | 231 |
| Dspr (°) | 19.6 | 20.3 |
| Qp (-) | 2.10 | 2.36 |
| P (Kw/m) | 7.9 | 9.5 |
| u (m/s) | -0.31 | 0.00 |
| v (m/s) | 0.06 | 0.00 |



Figure D-30 V6's wave spectrum, and difference between V6's and V5's wave spectra at the maximum positive (top plots) and negative (bottom plots) difference in wave power density between the two models – WCWI-4

Location: WCWI-5

**29/11/2016 08:00**

|  | WCWI-v6 | WCWI-v5 |
|---|---|---|
| Hm0 (m) | 2.37 | 2.19 |
| Te (s) | 11.2 | 11.6 |
| Tm01 (s) | 9.7 | 9.9 |
| Tm02 (s) | 8.6 | 8.7 |
| Tp (s) | 14.1 | 15.0 |
| Dm (°) | 264 | 264 |
| Dp (°) | 264 | 264 |
| Dspr (°) | 7.3 | 6.5 |
| Qp (-) | 2.75 | 2.93 |
| P (Kw/m) | 3.6 | 3.0 |
| u (m/s) | 0.25 | 0.00 |
| v (m/s) | -0.14 | 0.00 |

**25/02/2012 17:00**

|  | WCWI-v6 | WCWI-v5 |
|---|---|---|
| Hm0 (m) | 4.13 | 4.38 |
| Te (s) | 10.3 | 10.5 |
| Tm01 (s) | 8.6 | 8.7 |
| Tm02 (s) | 7.6 | 7.6 |
| Tp (s) | 13.4 | 13.4 |
| Dm (°) | 264 | 264 |
| Dp (°) | 263 | 263 |
| Dspr (°) | 16.0 | 16.7 |
| Qp (-) | 2.57 | 2.85 |
| P (Kw/m) | 9.0 | 10.9 |
| u (m/s) | -0.34 | 0.00 |
| v (m/s) | 0.23 | 0.00 |



Figure D-31 V6's wave spectrum, and difference between V6's and V5's wave spectra at the maximum positive (top plots) and negative (bottom plots) difference in wave power density between the two models – WCWI-5

# Appendix E    Correlation analysis of $\Delta P$ and an estimation of $\Delta P$ using neural networks ($\Delta P_{nn}$)
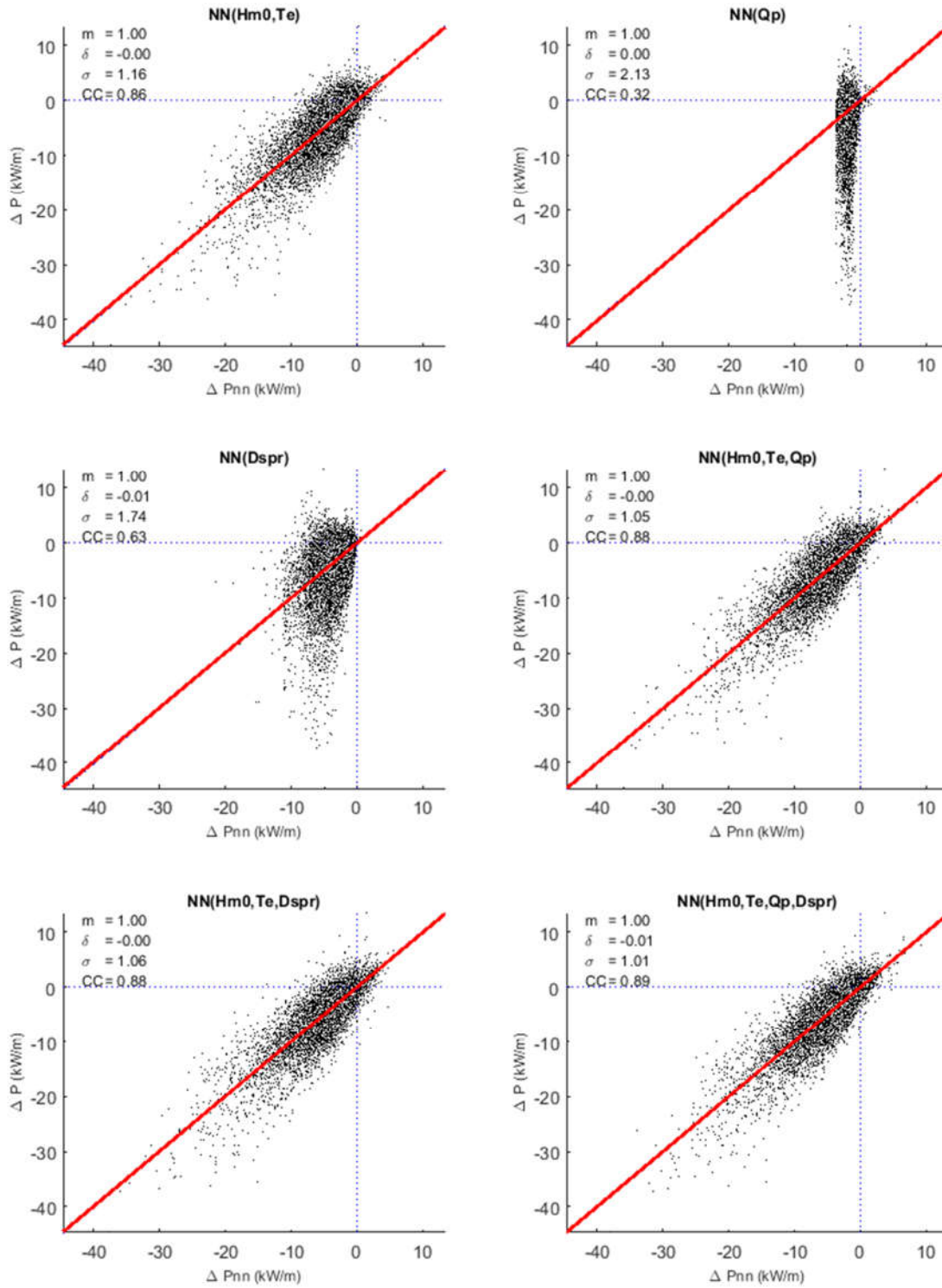
Figure E-1 Correlation analysis of $\Delta P$ and an estimation of $\Delta P$ using neural networks ($\Delta P_{nn}$) and different wave parameters from both wave models – HS-1.
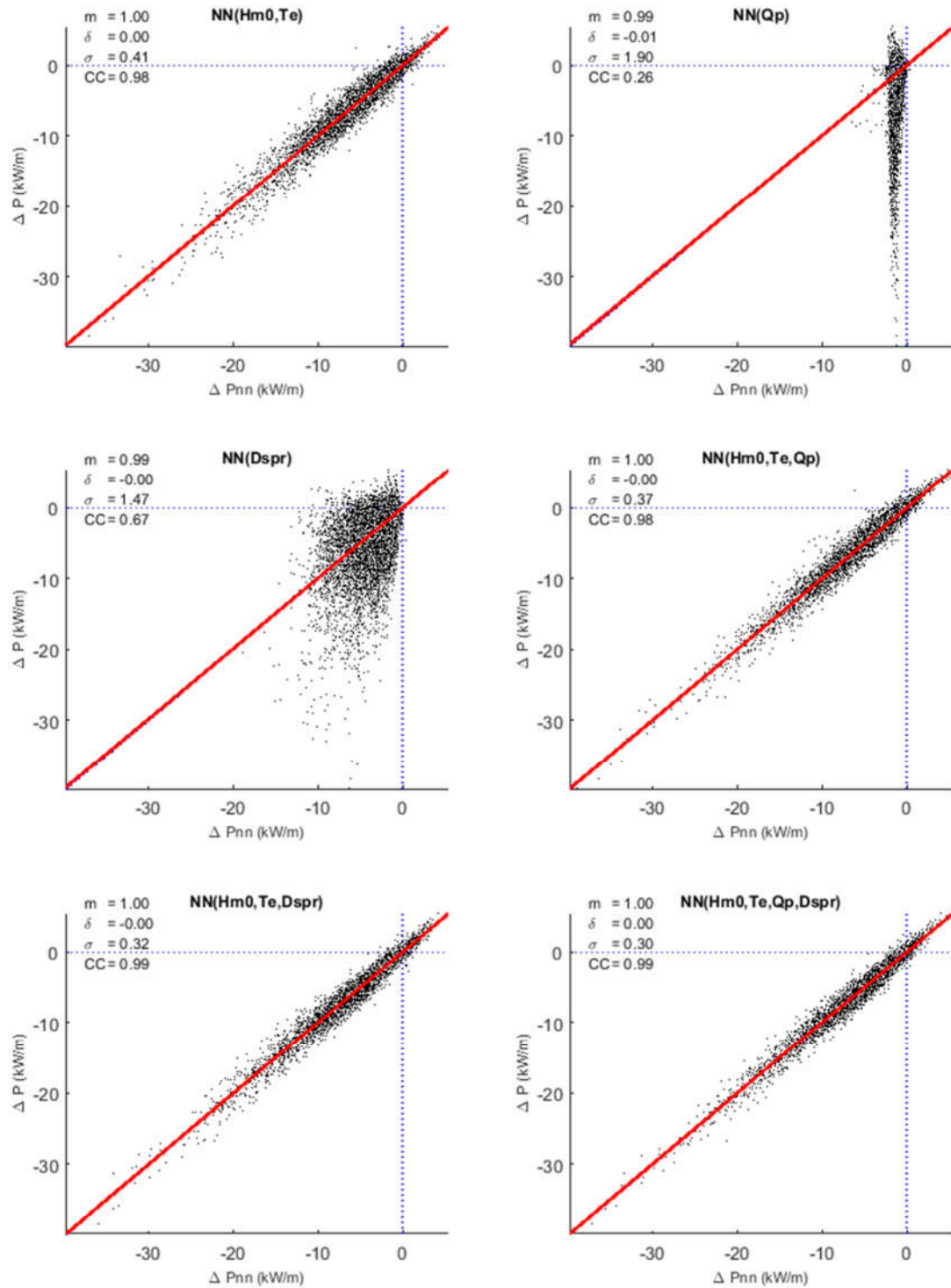
Figure E-2 Correlation analysis of $\Delta P$ and an estimation of $\Delta P$ using neural networks ($\Delta P_{nn}$) and different wave parameters from both wave models – HS-2.
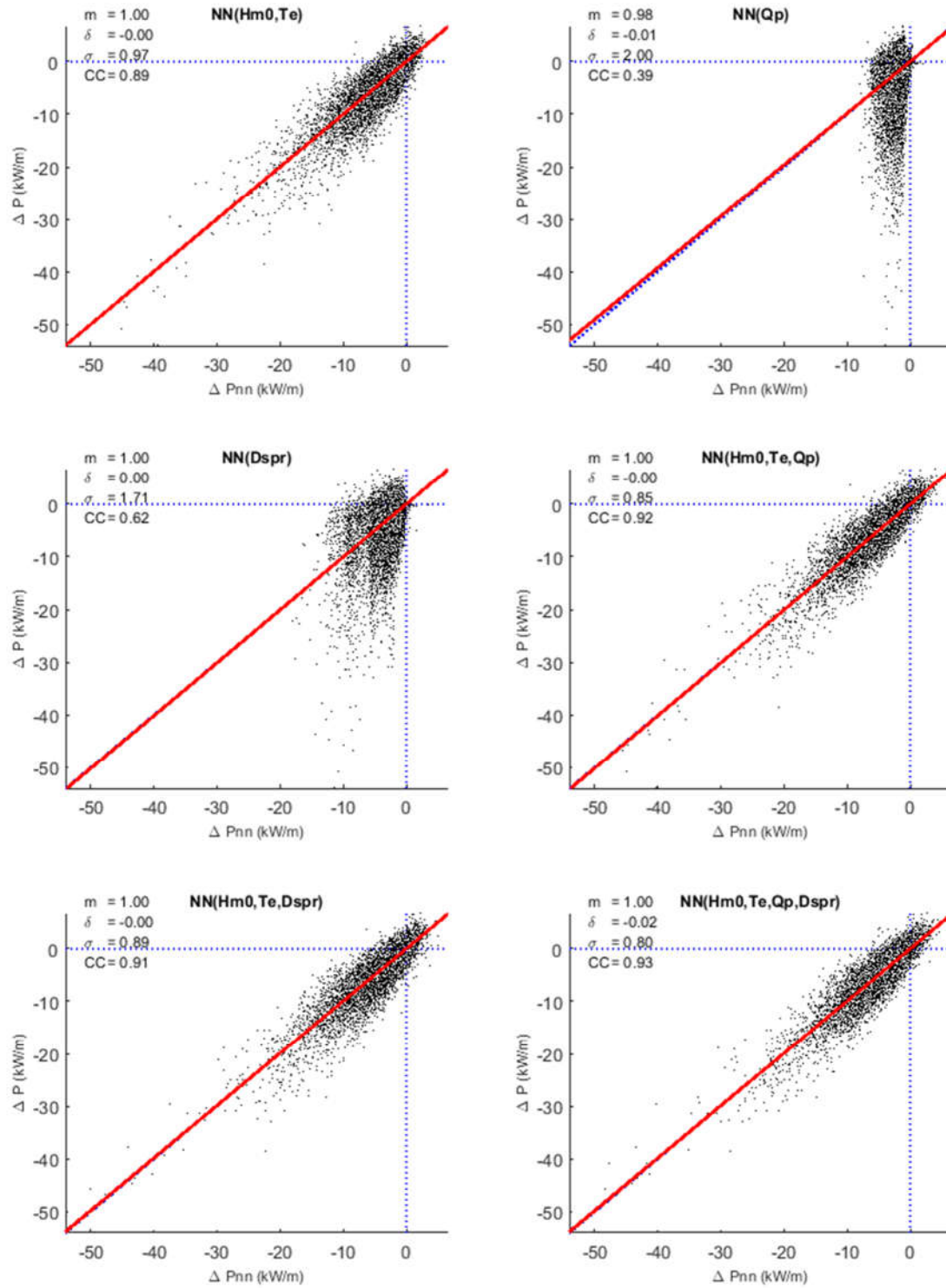
Figure E-3 Correlation analysis of $\Delta P$ and an estimation of $\Delta P$ using neural networks ($\Delta P_{nn}$) and different wave parameters from both wave models – HS-3.
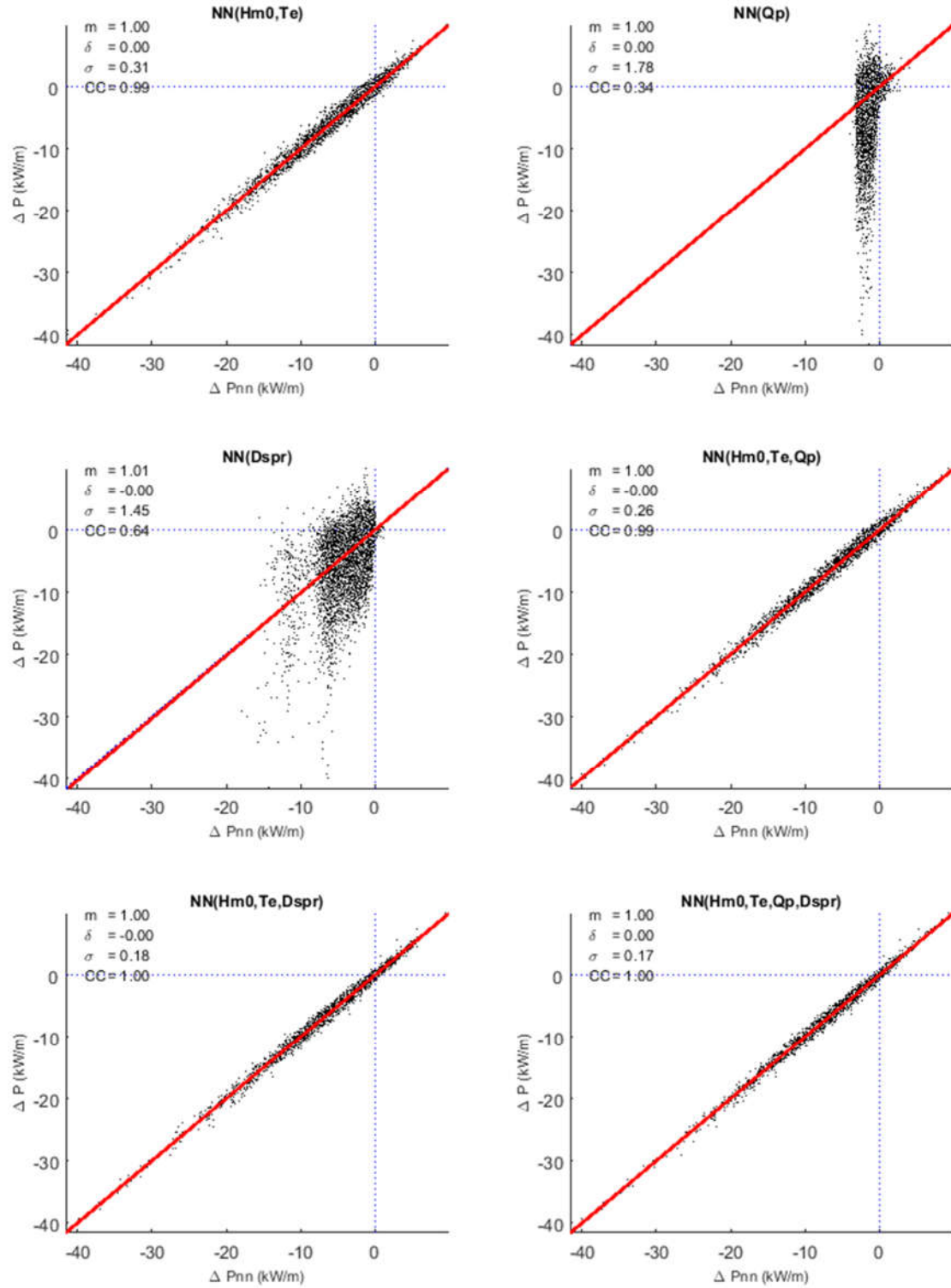
Figure E-4 Correlation analysis of $\Delta P$ and an estimation of $\Delta P$ using neural networks ($\Delta P_{nn}$) and different wave parameters from both wave models – HS-4.

Data for HS-5 is not available.
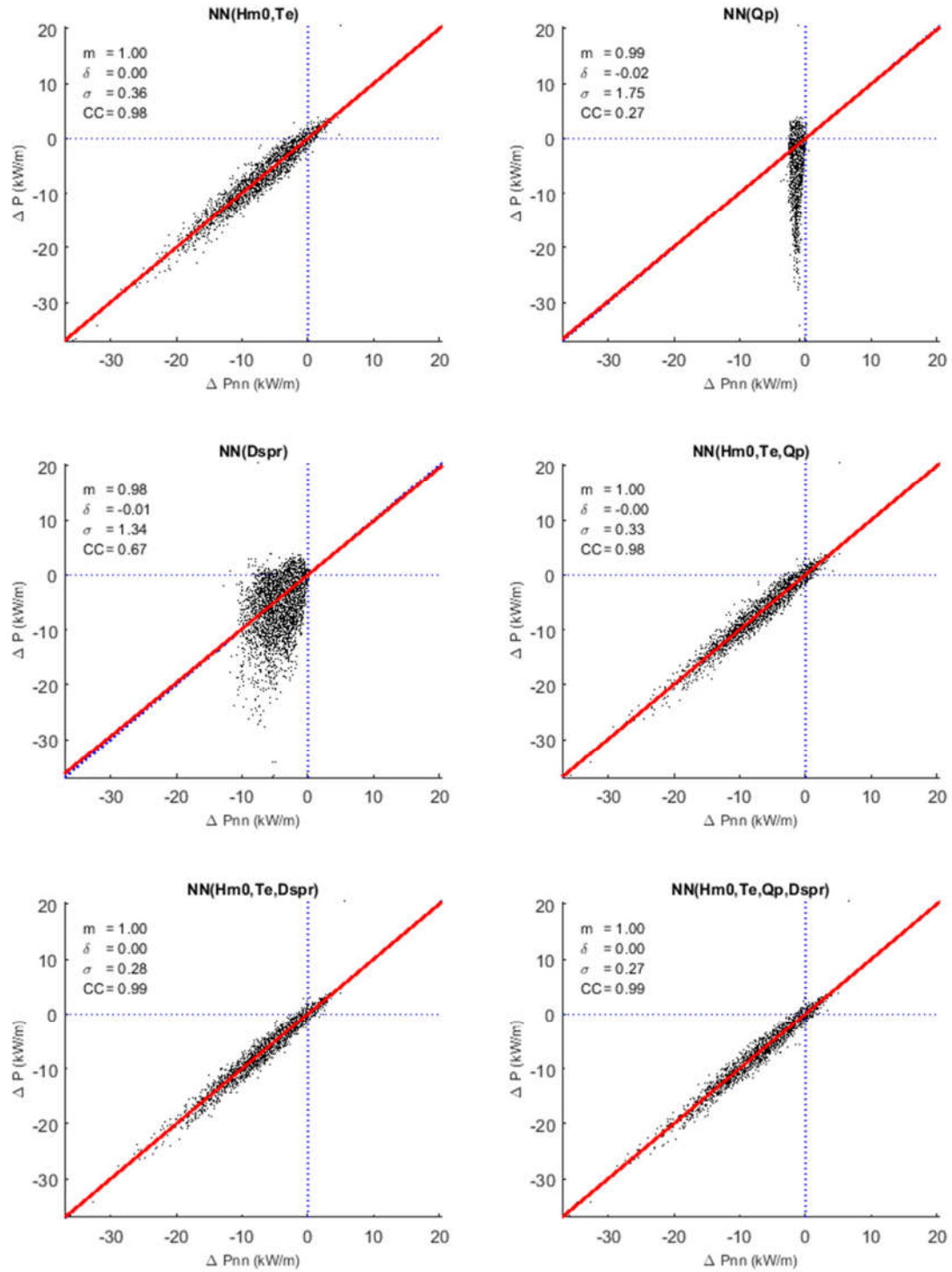
Location: HS-6



Figure E-5 Correlation analysis of $\Delta P$ and an estimation of $\Delta P$ using neural networks ($\Delta P_{nn}$) and different wave parameters from both wave models – HS-6.
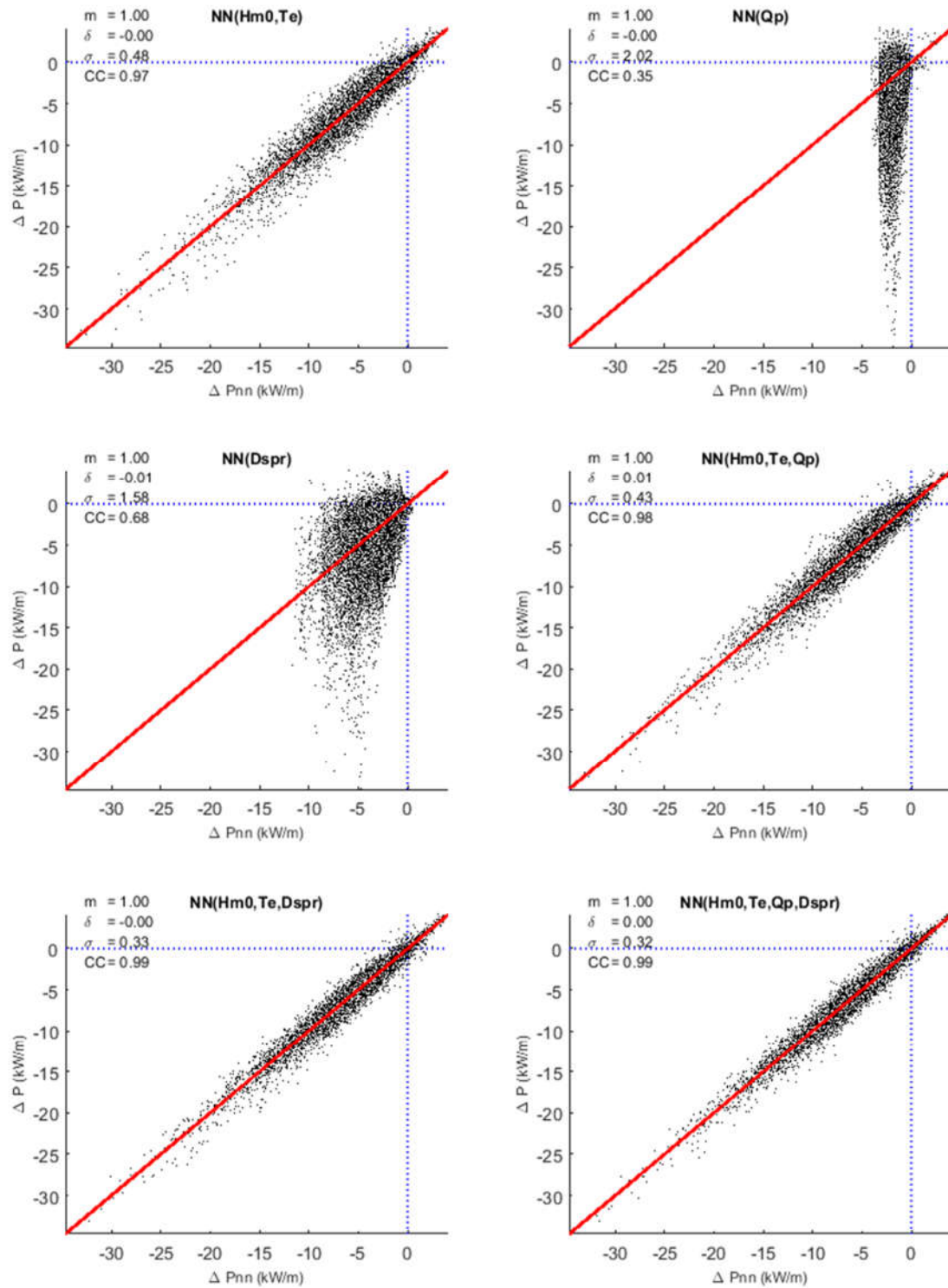
Figure E-6 Correlation analysis of $\Delta P$ and an estimation of $\Delta P$ using neural networks ($\Delta P_{nn}$) and different wave parameters from both wave models – HS-7.

Location: HS-8
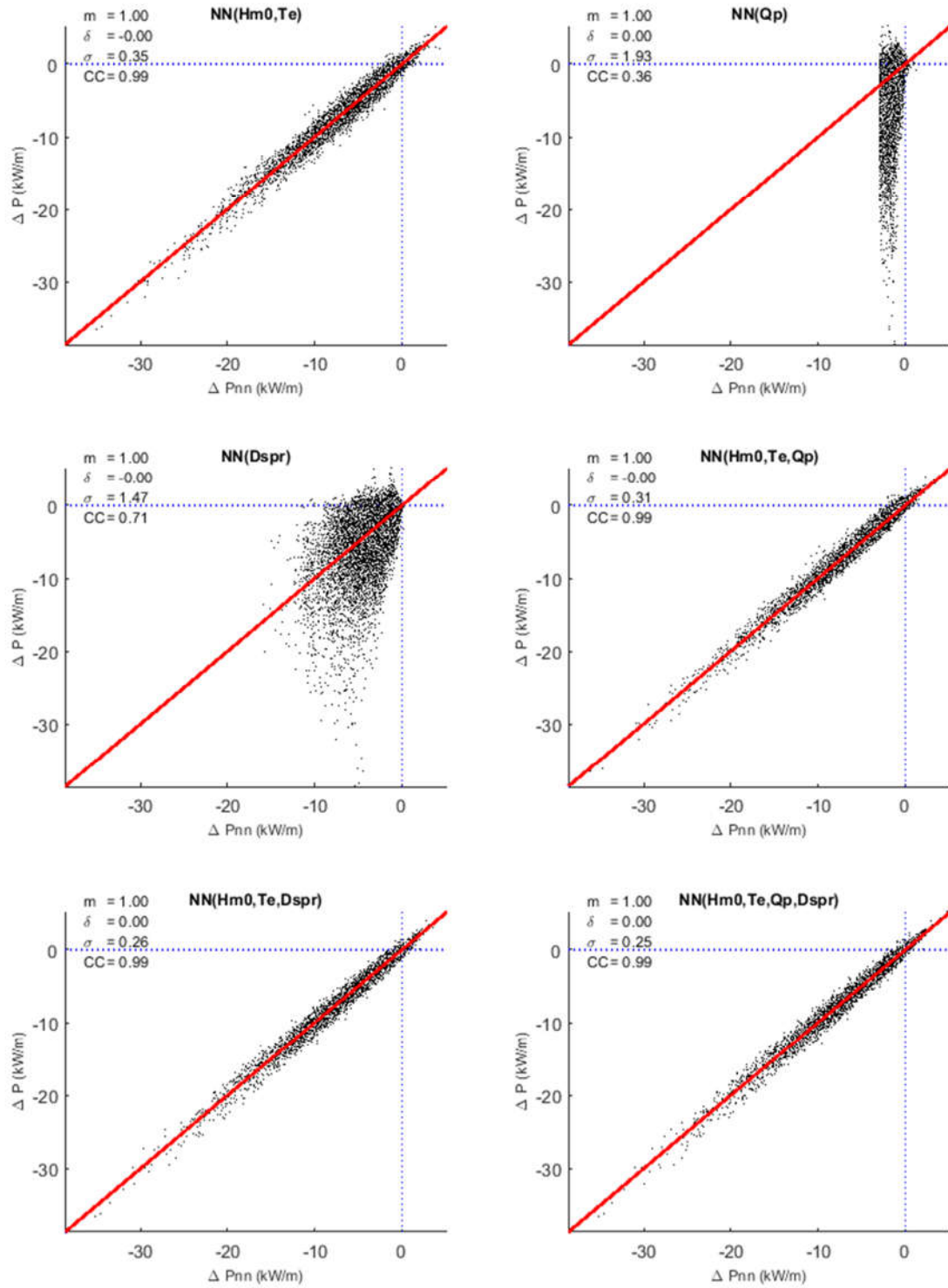


Figure E-7 Correlation analysis of $\Delta P$ and an estimation of $\Delta P$ using neural networks ($\Delta P_{nn}$) and different wave parameters from both wave models – HS-8.

Location: HS-9
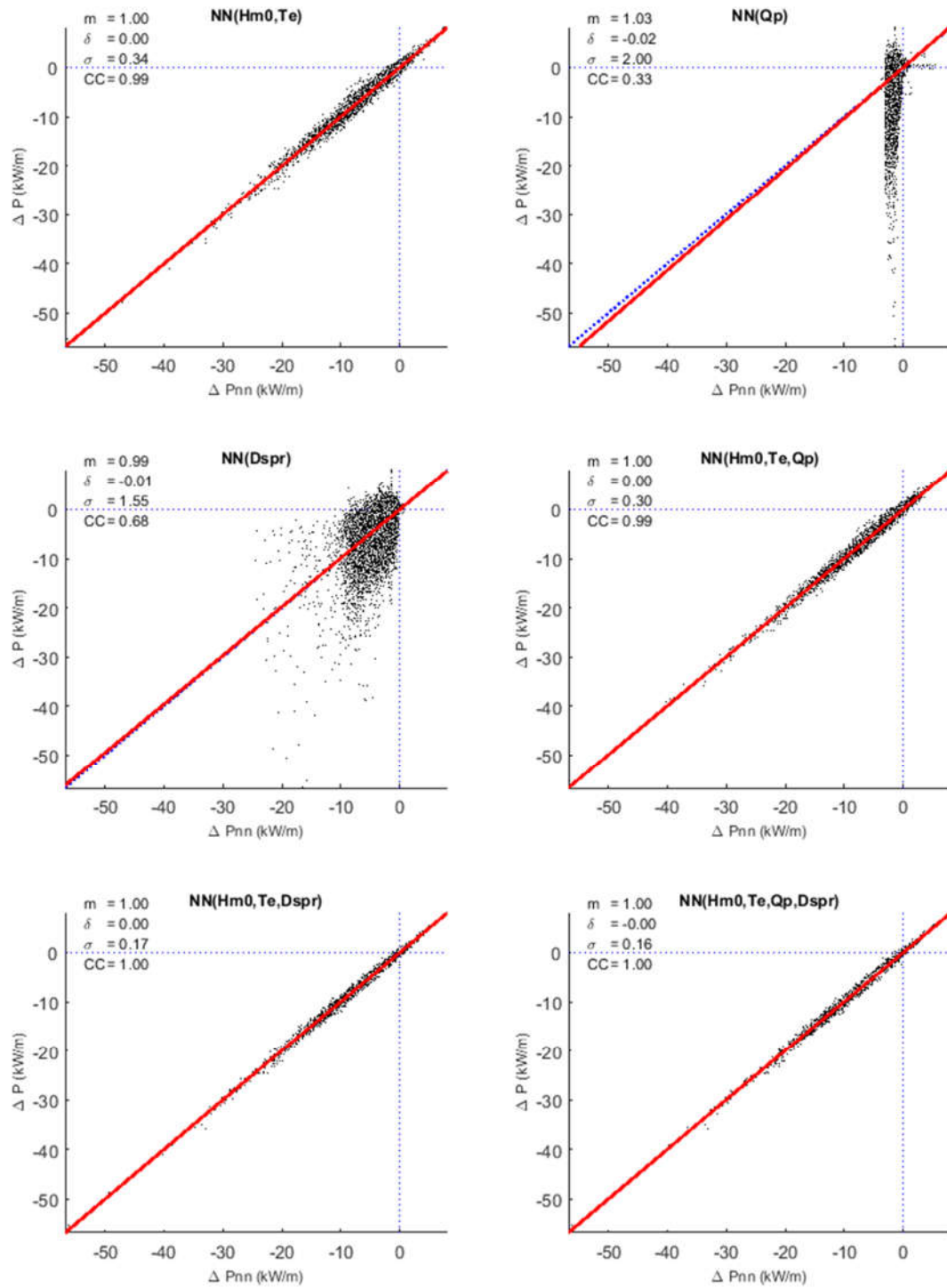


Figure E-8 Correlation analysis of $\Delta P$ and an estimation of $\Delta P$ using neural networks ($\Delta P_{nn}$) and different wave parameters from both wave models – HS-9.
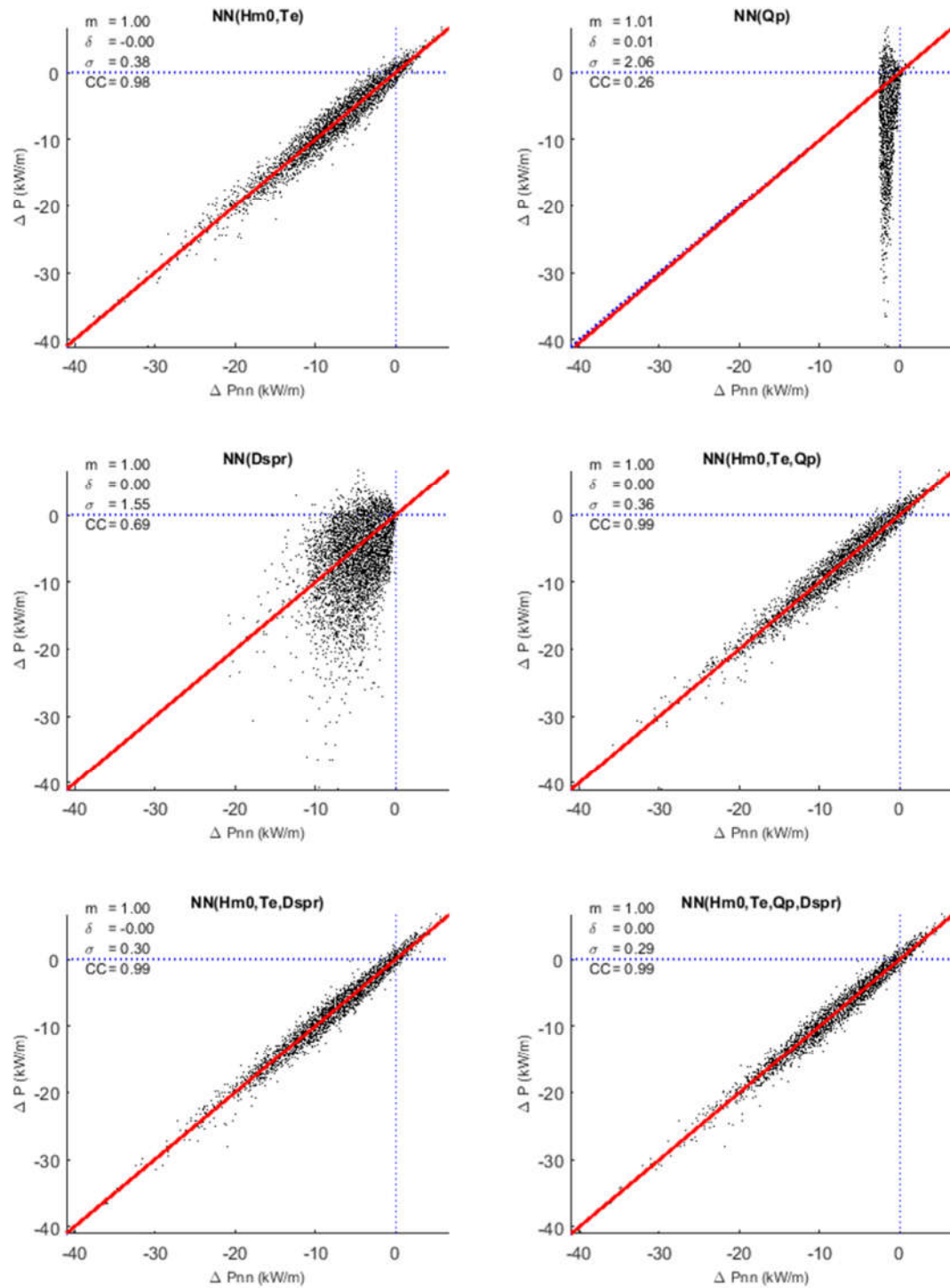
Figure E-9 Correlation analysis of $\Delta P$ and an estimation of $\Delta P$ using neural networks ($\Delta P_{nn}$) and different wave parameters from both wave models – HS-10.
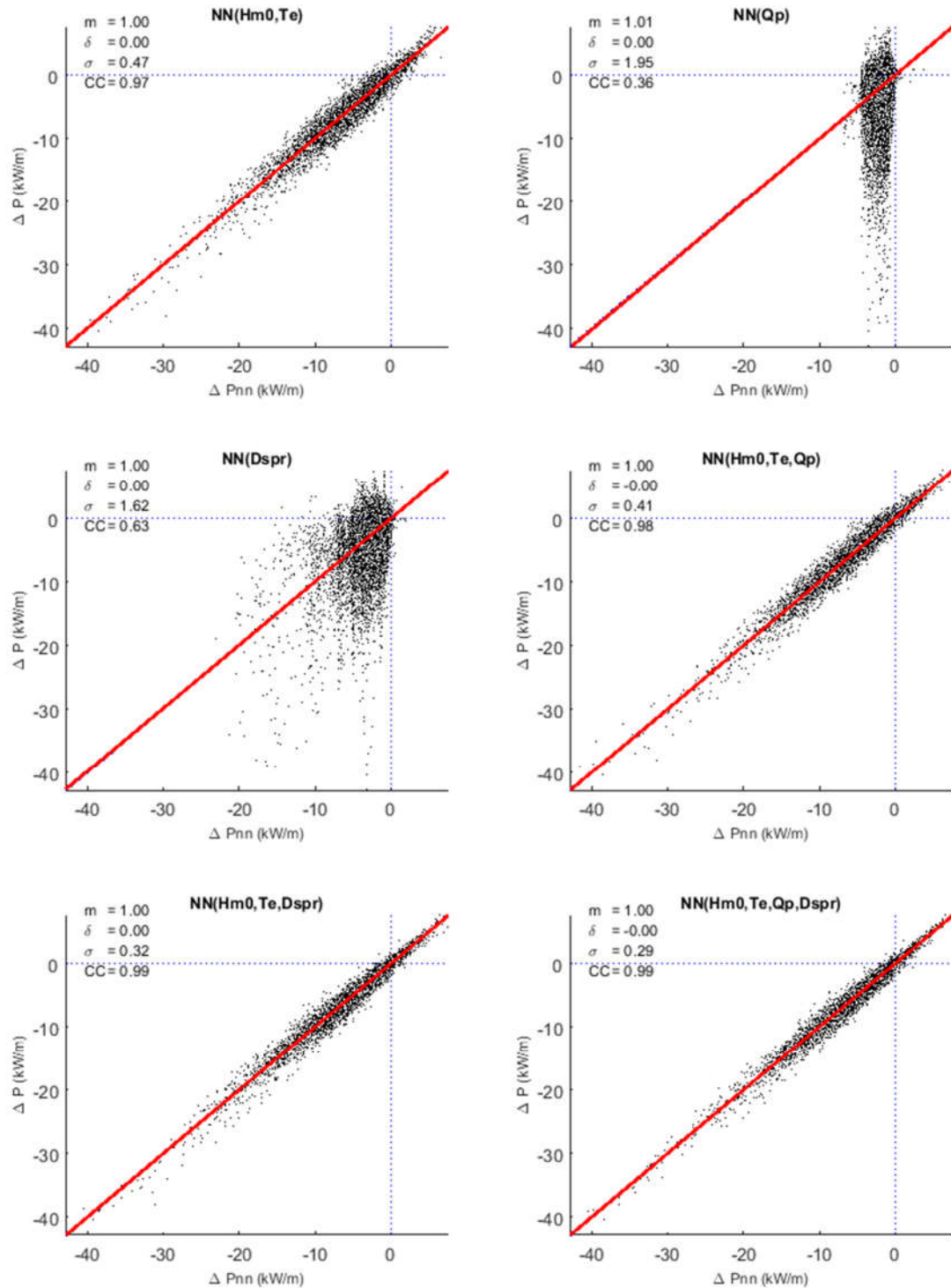
Figure E-10 Correlation analysis of $\Delta P$ and an estimation of $\Delta P$ using neural networks ($\Delta P_{nn}$) and different wave parameters from both wave models – HS-11.
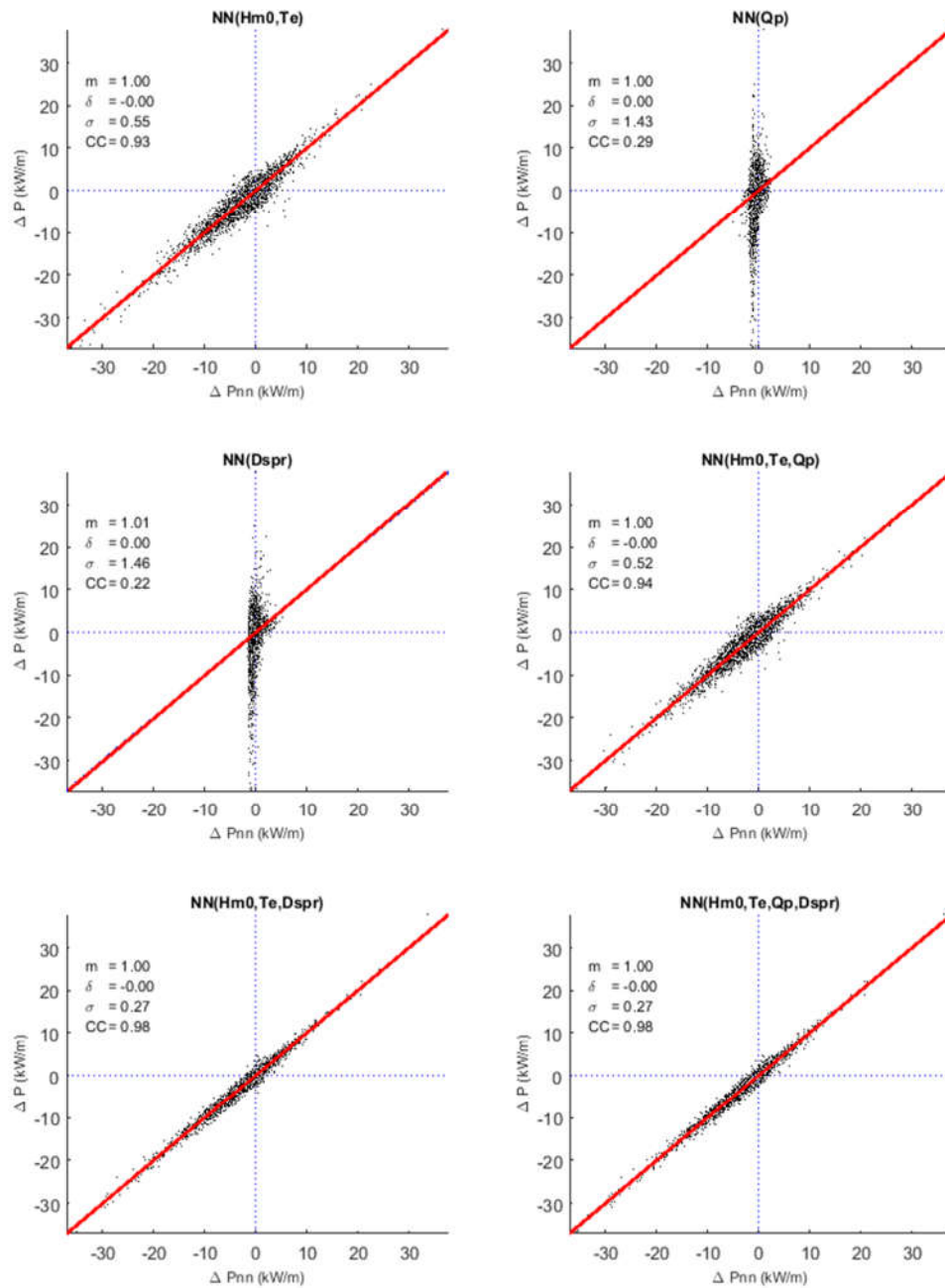
Figure E-11 Correlation analysis of $\Delta P$ and an estimation of $\Delta P$ using neural networks ($\Delta P_{nn}$) and different wave parameters from both wave models – DFO-1.
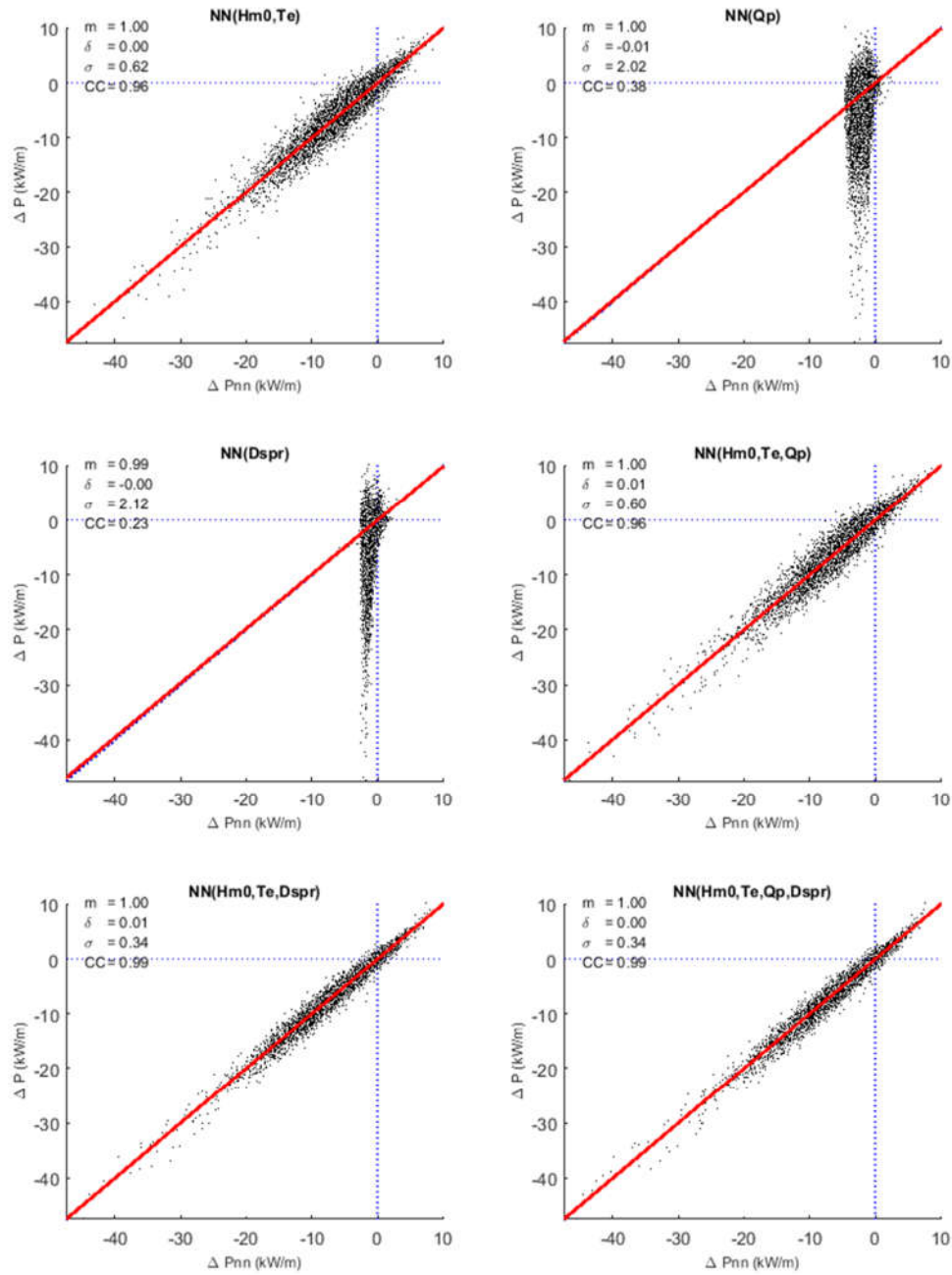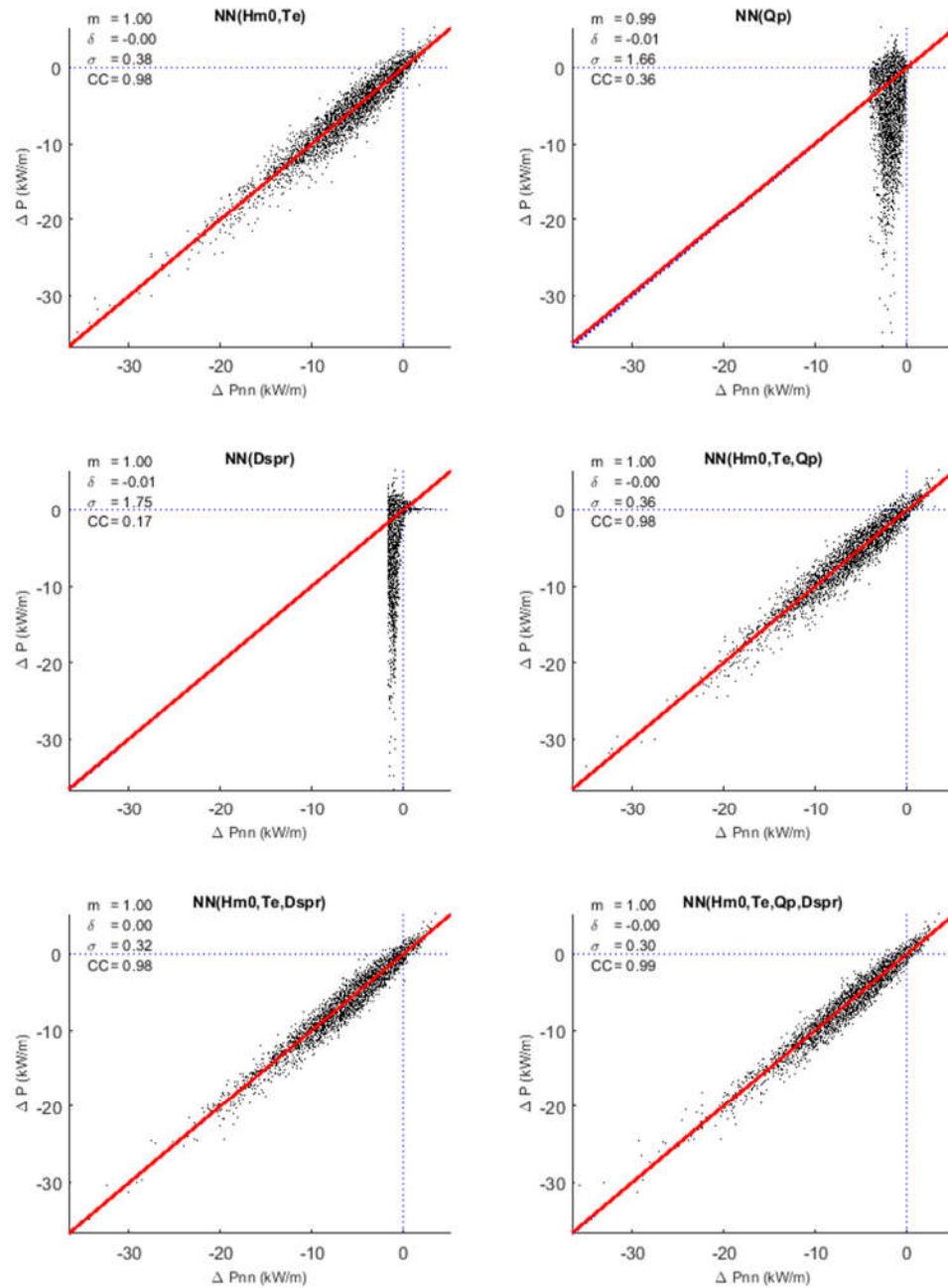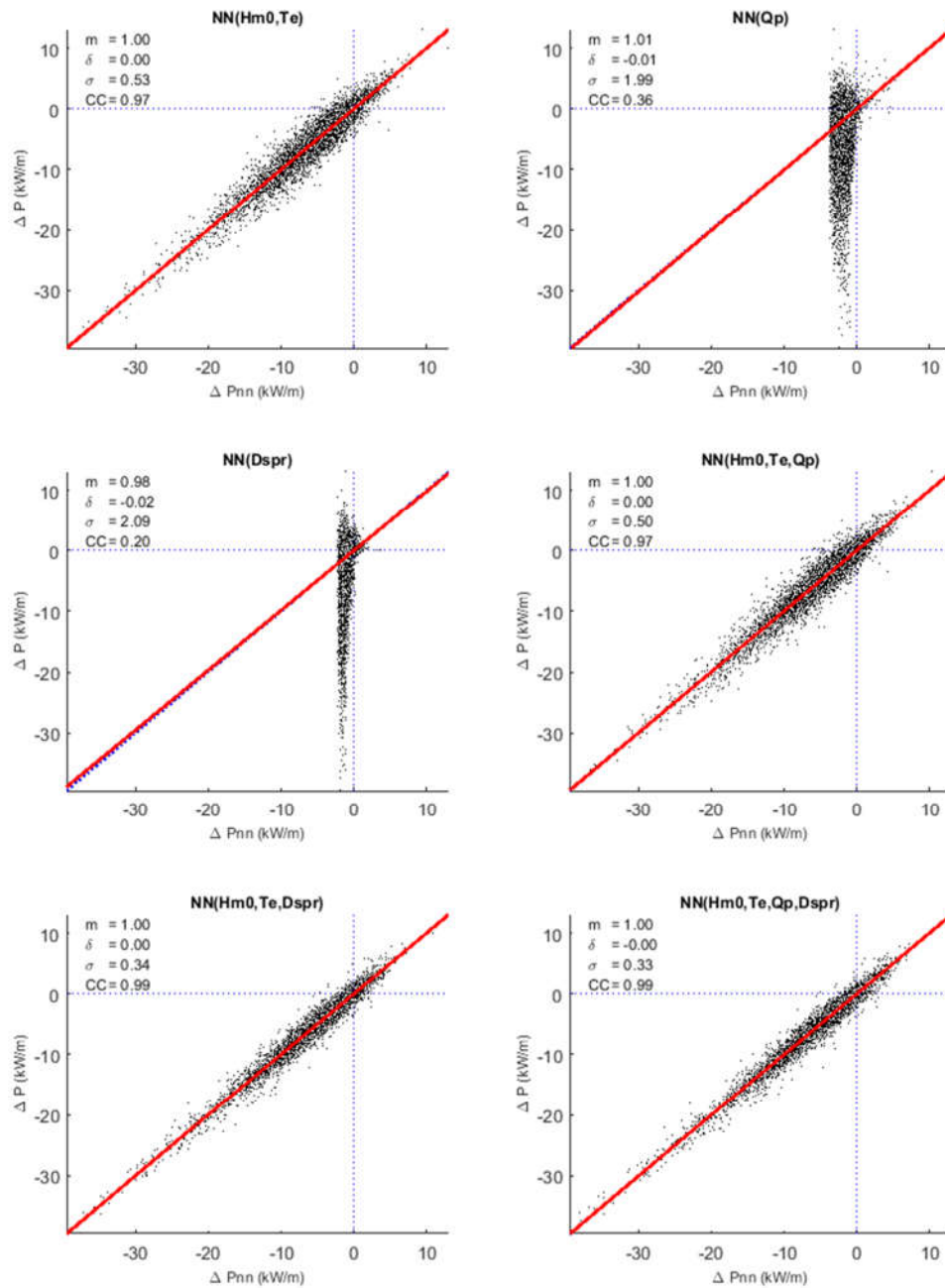
Location: DFO-2

NN(Hm0,Te)

m = 1.00
$\delta$ = 0.00
$\sigma$ = 0.49
CC = 0.94

NN(Qp)

m = 1.01
$\delta$ = 0.00
$\sigma$ = 1.39
CC = 0.29

NN(Dspr)

m = 1.00
$\delta$ = -0.01
$\sigma$ = 1.42
CC = 0.22

NN(Hm0,Te,Qp)

m = 1.00
$\delta$ = -0.00
$\sigma$ = 0.45
CC = 0.95

NN(Hm0,Te,Dspr)

m = 1.00
$\delta$ = 0.00
$\sigma$ = 0.26
CC = 0.98

NN(Hm0,Te,Qp,Dspr)

m = 1.00
$\delta$ = -0.00
$\sigma$ = 0.25
CC = 0.98
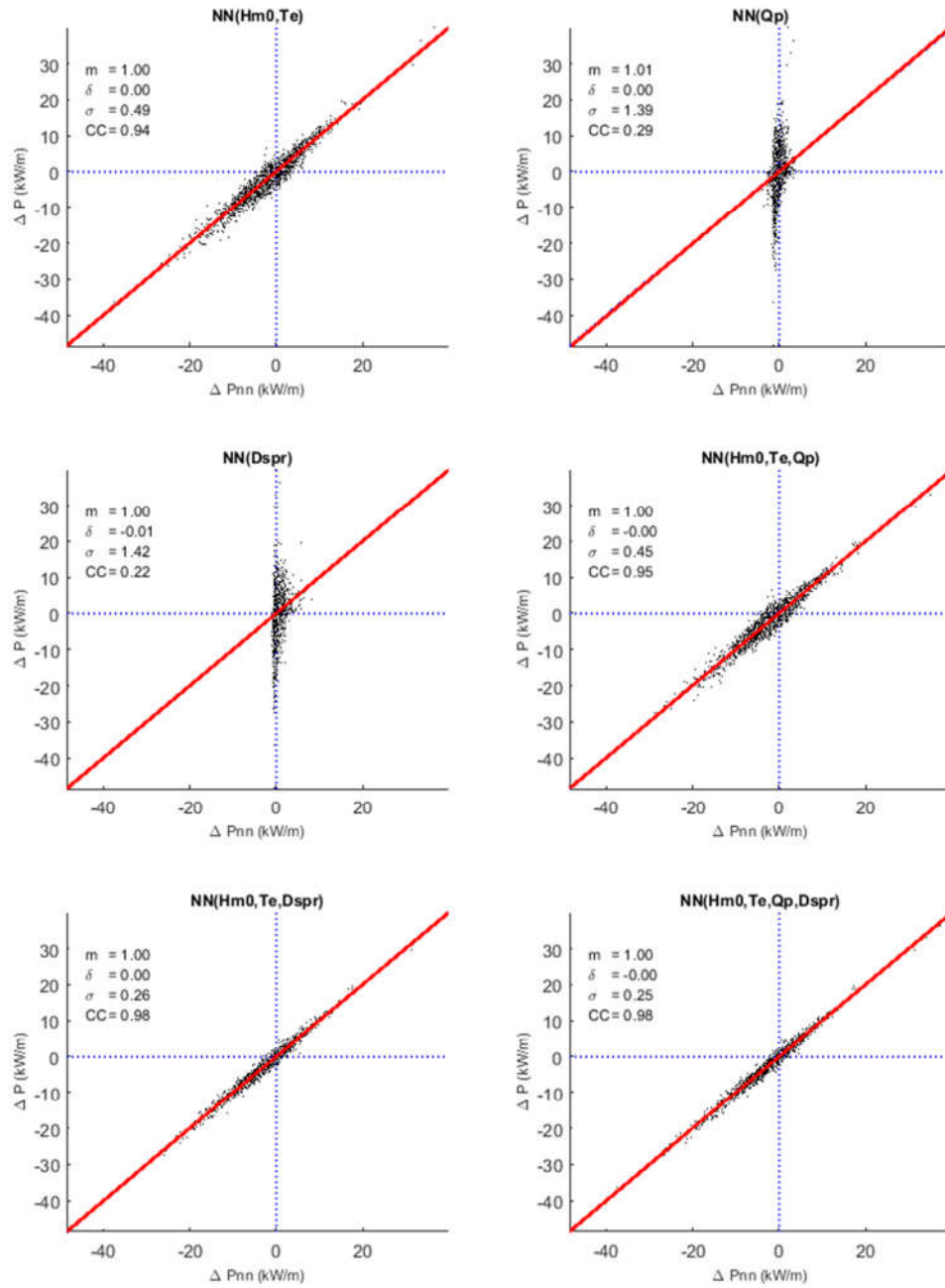
Figure E-12 Correlation analysis of $\Delta P$ and an estimation of $\Delta P$ using neural networks ($\Delta P_{nn}$) and different wave parameters from both wave models – DFO-2.
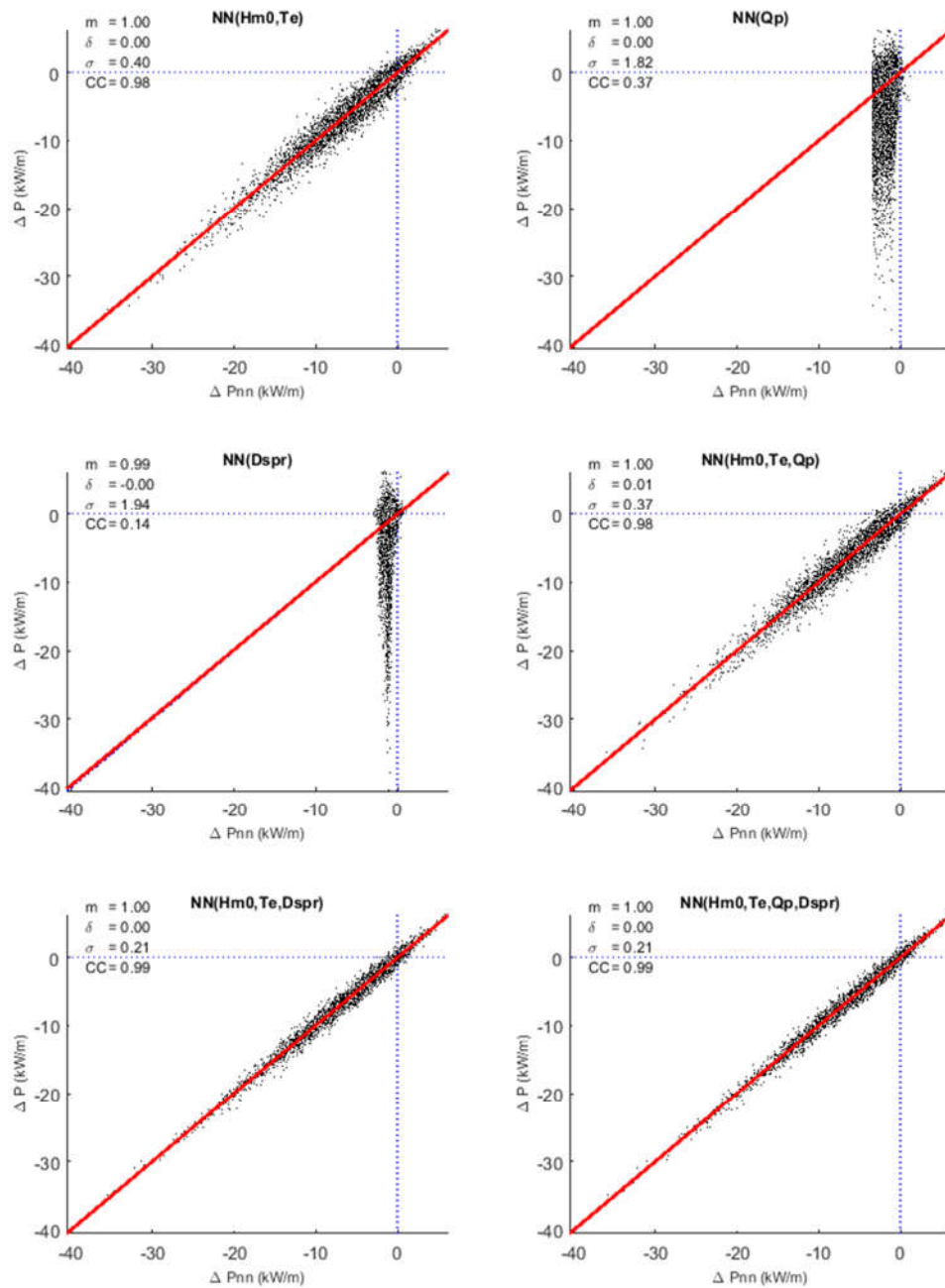
Figure E-13 Correlation analysis of $\Delta P$ and an estimation of $\Delta P$ using neural networks ($\Delta P_{nn}$) and different wave parameters from both wave models – DFO-3.
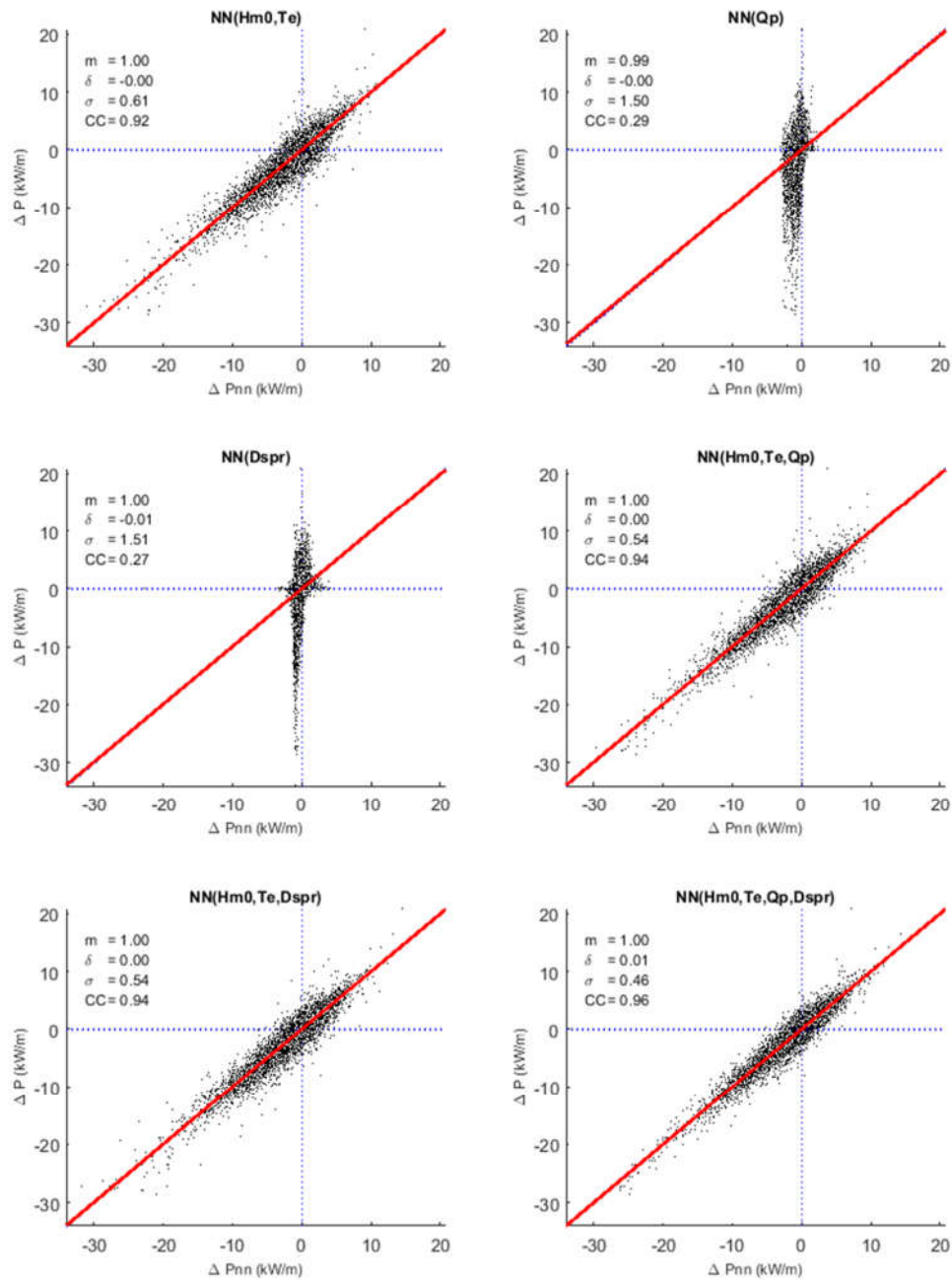
Figure E-14 Correlation analysis of $\Delta P$ and an estimation of $\Delta P$ using neural networks ($\Delta P_{nn}$) and different wave parameters from both wave models – DFO-4.
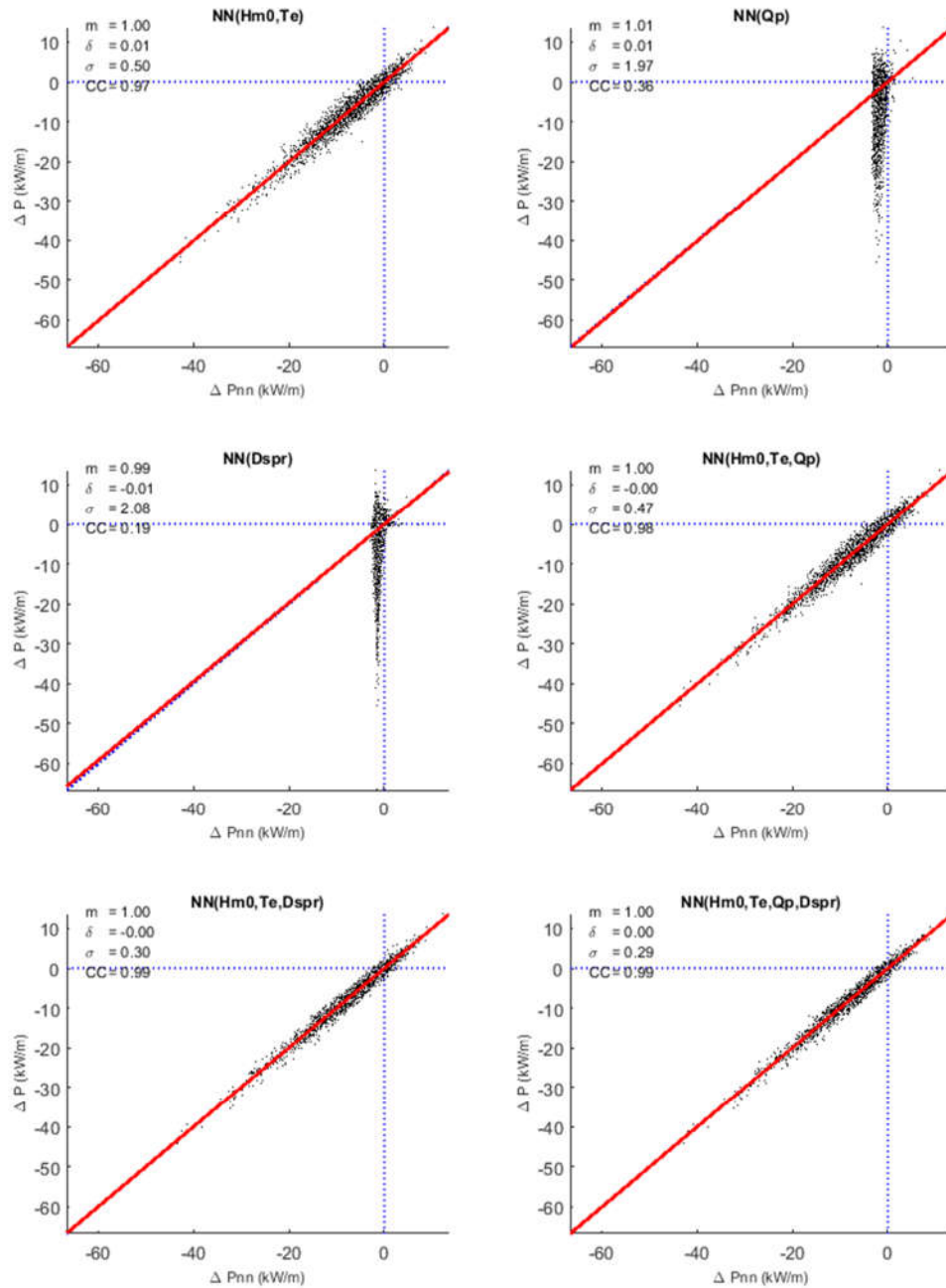
Figure E-15 Correlation analysis of $\Delta P$ and an estimation of $\Delta P$ using neural networks ($\Delta P_{nn}$) and different wave parameters from both wave models – DFO-5.
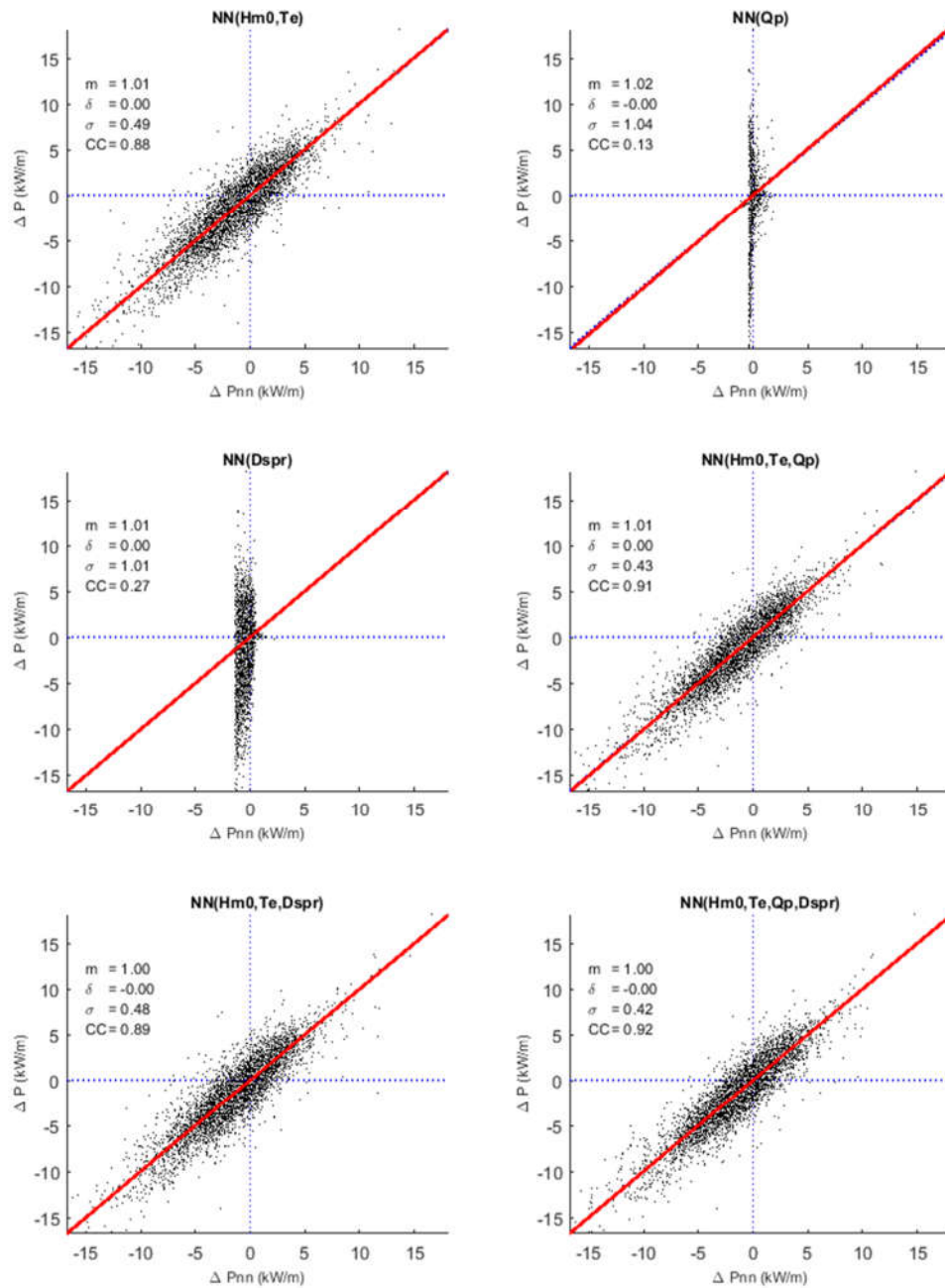
Figure E-16 Correlation analysis of $\Delta P$ and an estimation of $\Delta P$ using neural networks ($\Delta P_{nn}$) and different wave parameters from both wave models – DFO-6.
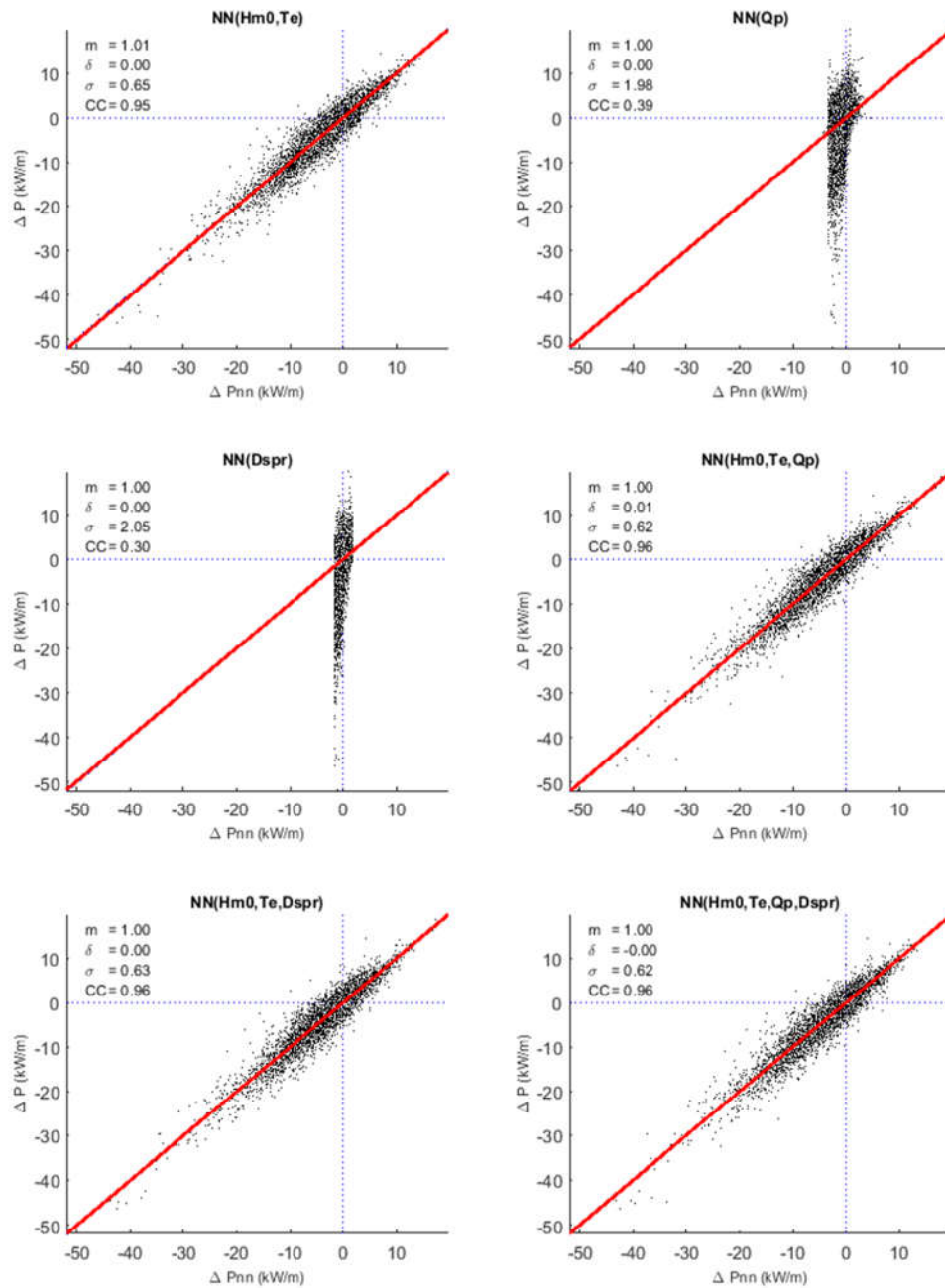
Figure E-17 Correlation analysis of $\Delta P$ and an estimation of $\Delta P$ using neural networks ($\Delta P_{nn}$) and different wave parameters from both wave models – DFO-7.
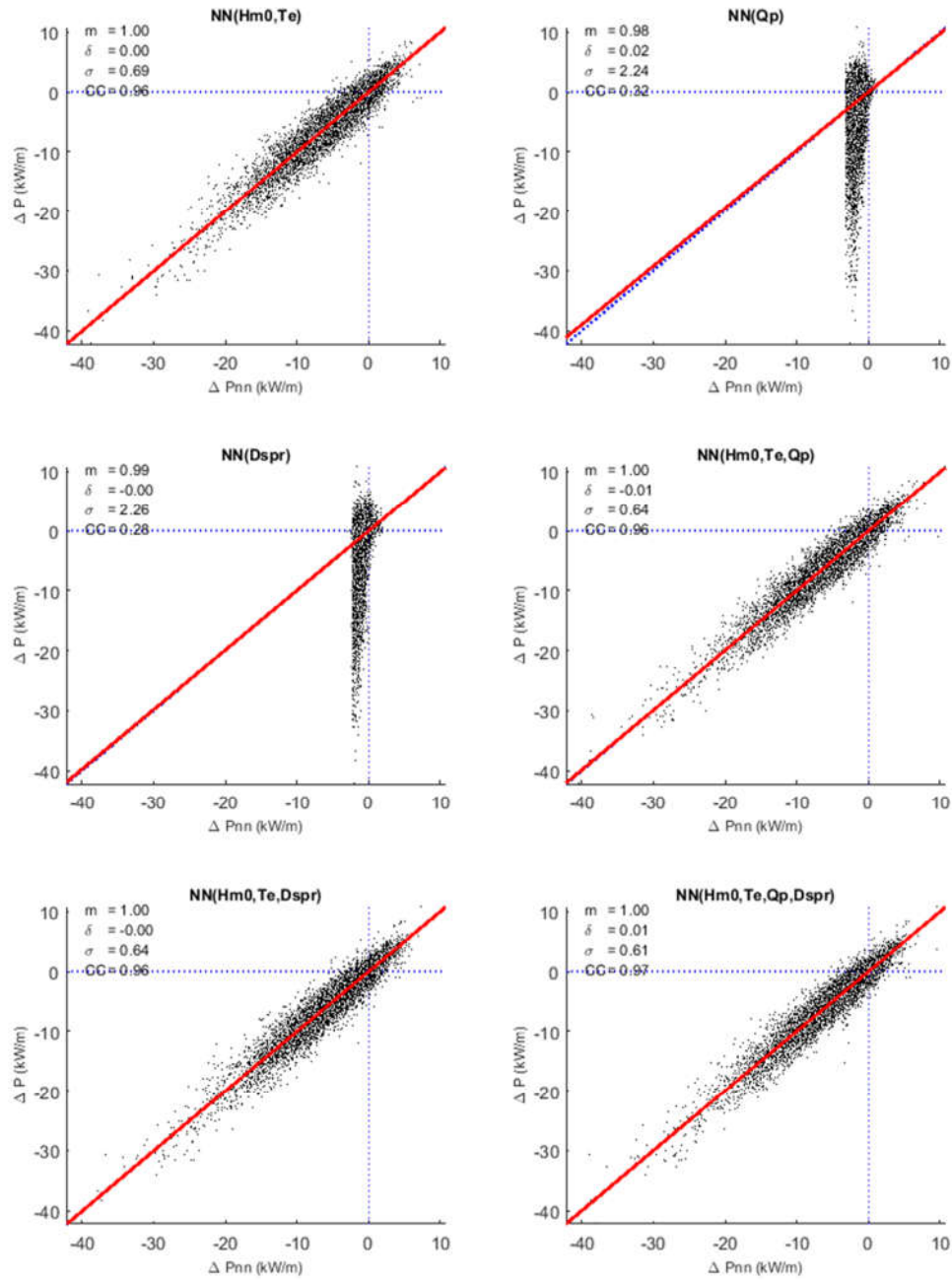
Figure E-18 Correlation analysis of $\Delta P$ and an estimation of $\Delta P$ using neural networks ($\Delta P_{nn}$) and different wave parameters from both wave models – DFO-8.

Figure E-19 Correlation analysis of $\Delta P$ and an estimation of $\Delta P$ using neural networks ($\Delta P_{nn}$) and different wave parameters from both wave models – DFO-9.

Figure E-20 Correlation analysis of $\Delta P$ and an estimation of $\Delta P$ using neural networks ($\Delta P_{nn}$) and different wave parameters from both wave models – DFO-10.

Figure E-21 Correlation analysis of $\Delta P$ and an estimation of $\Delta P$ using neural networks ($\Delta P_{nn}$) and different wave parameters from both wave models – DFO-11.
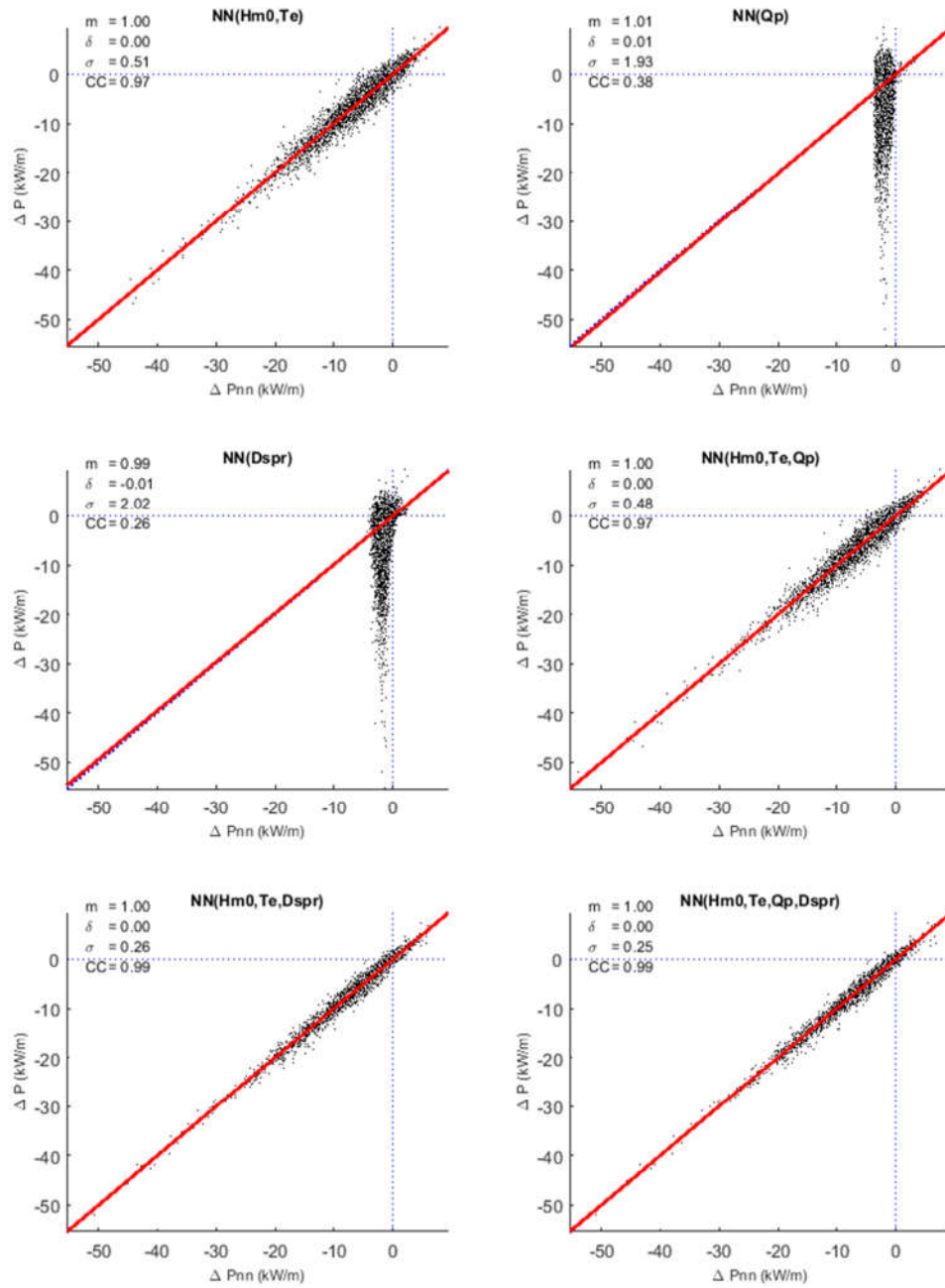
Figure E-22 Correlation analysis of $\Delta P$ and an estimation of $\Delta P$ using neural networks ($\Delta P_{nn}$) and different wave parameters from both wave models – DFO-12.
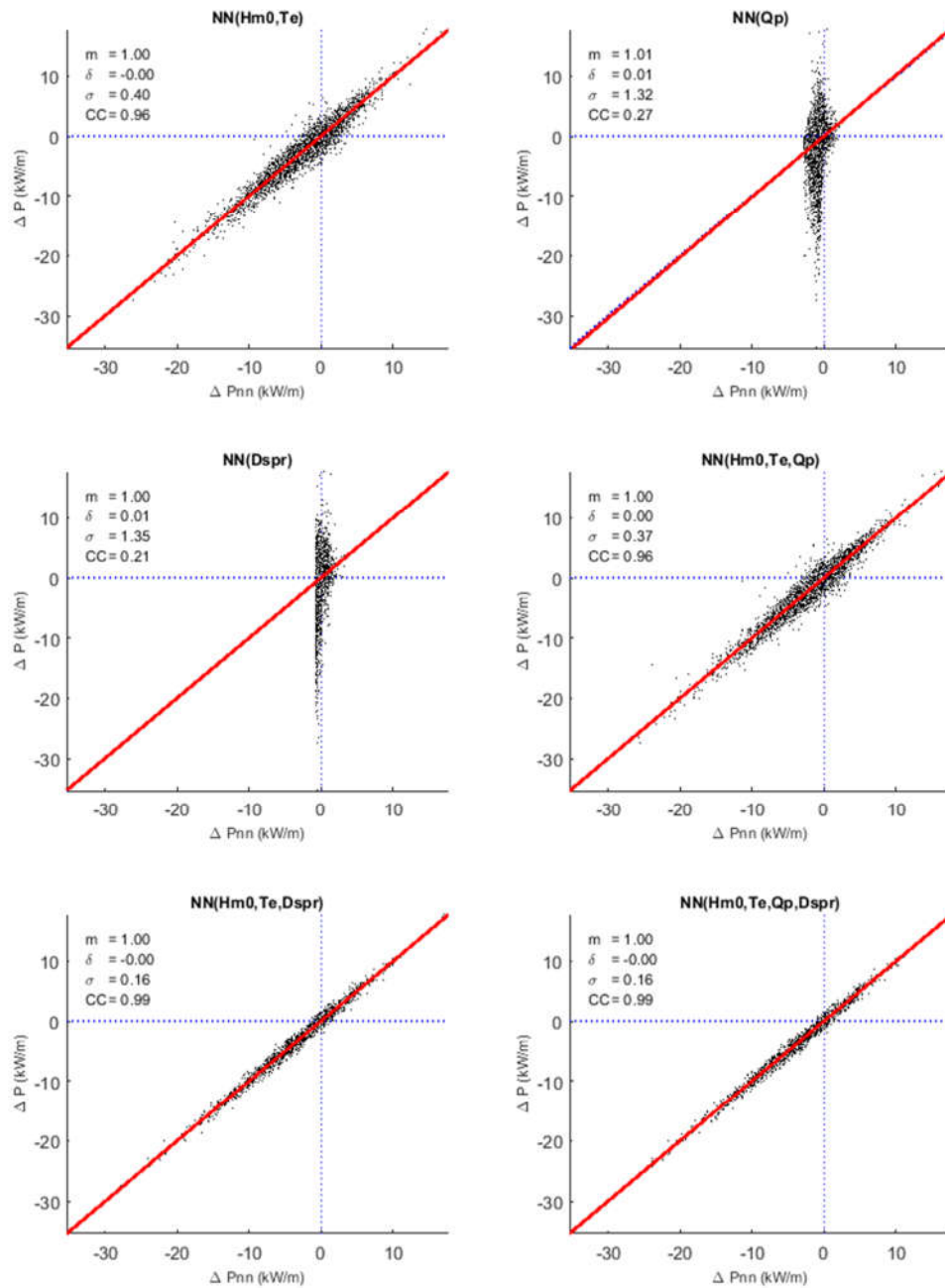
Figure E-23 Correlation analysis of $\Delta P$ and an estimation of $\Delta P$ using neural networks ($\Delta P_{nn}$) and different wave parameters from both wave models – NDBC-1.
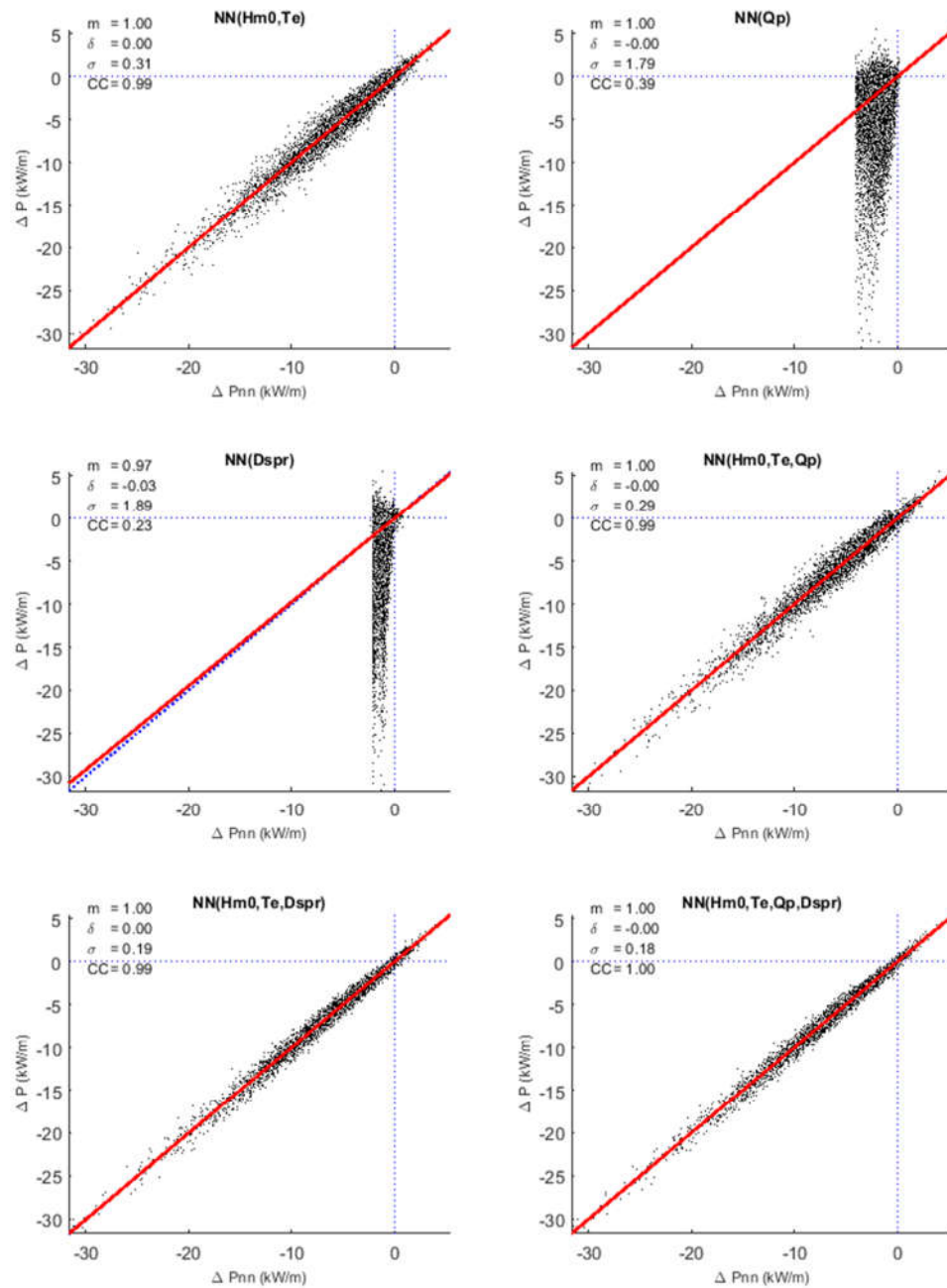
Figure E-24 Correlation analysis of $\Delta P$ and an estimation of $\Delta P$ using neural networks ($\Delta P_{nn}$) and different wave parameters from both wave models – NDBC-2.
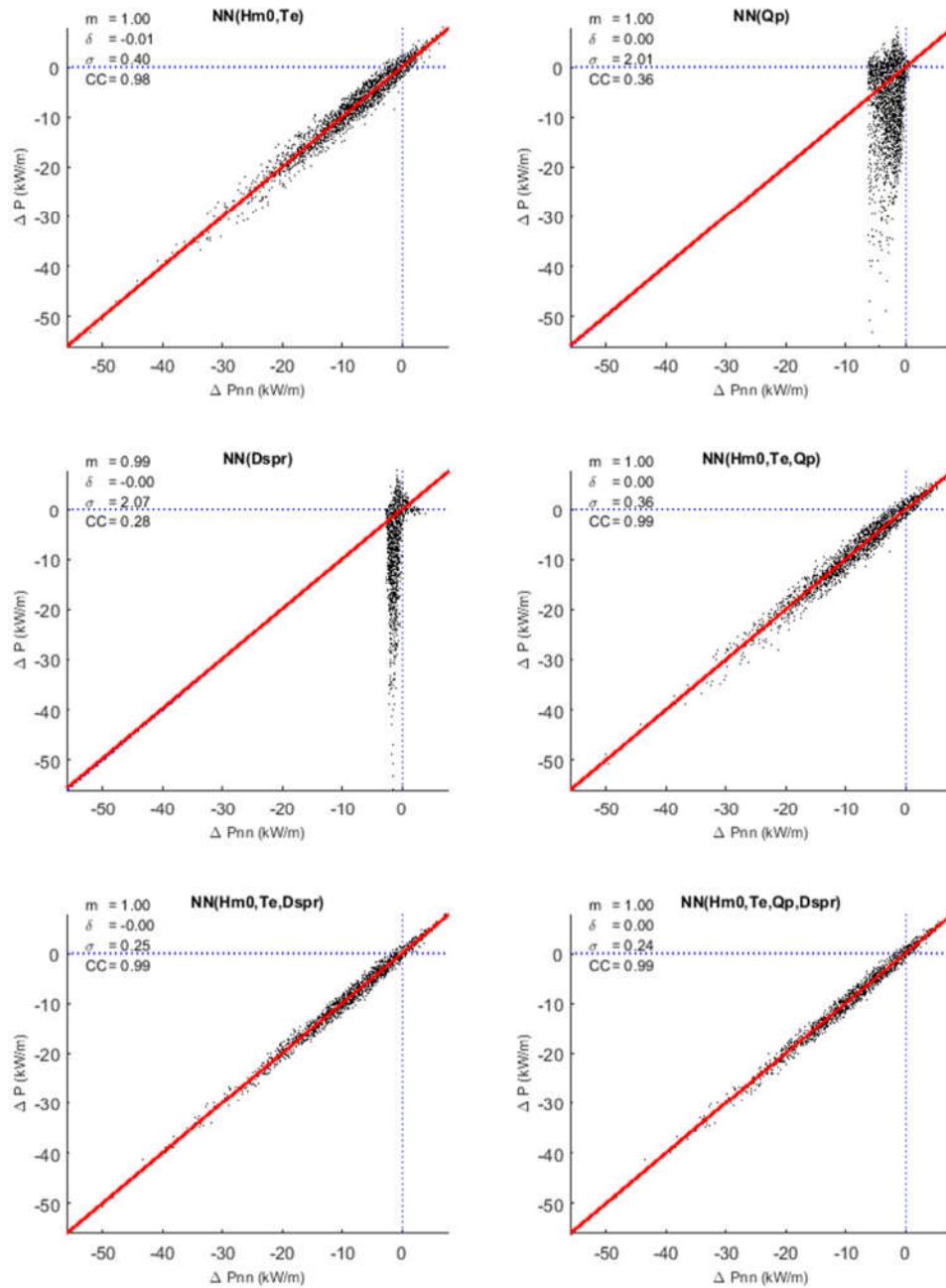
Location: NDBC-3
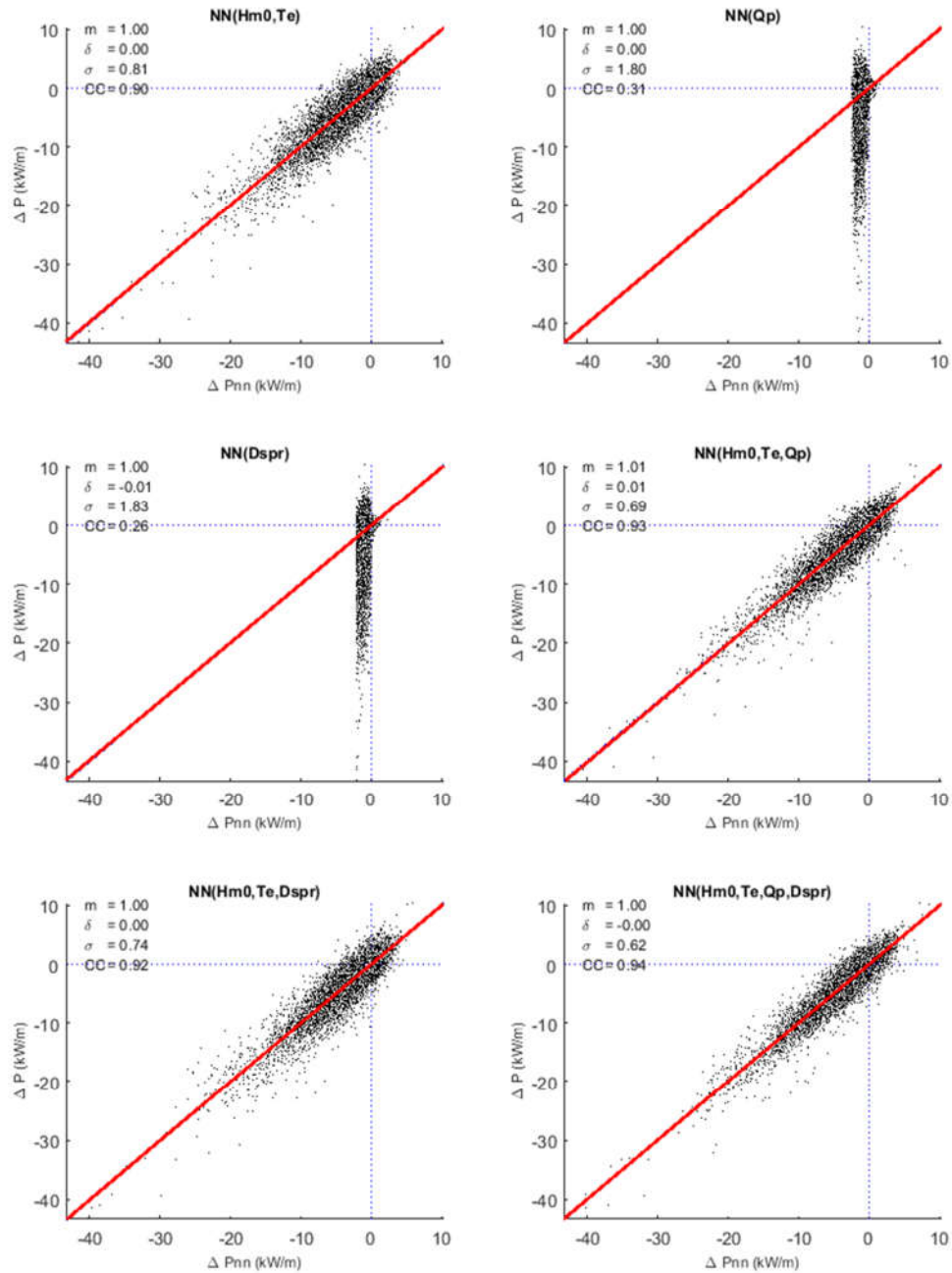


Figure E-25 Correlation analysis of $\Delta P$ and an estimation of $\Delta P$ using neural networks ($\Delta P_{nn}$) and different wave parameters from both wave models – NDBC-3.

Location: NDBC-4
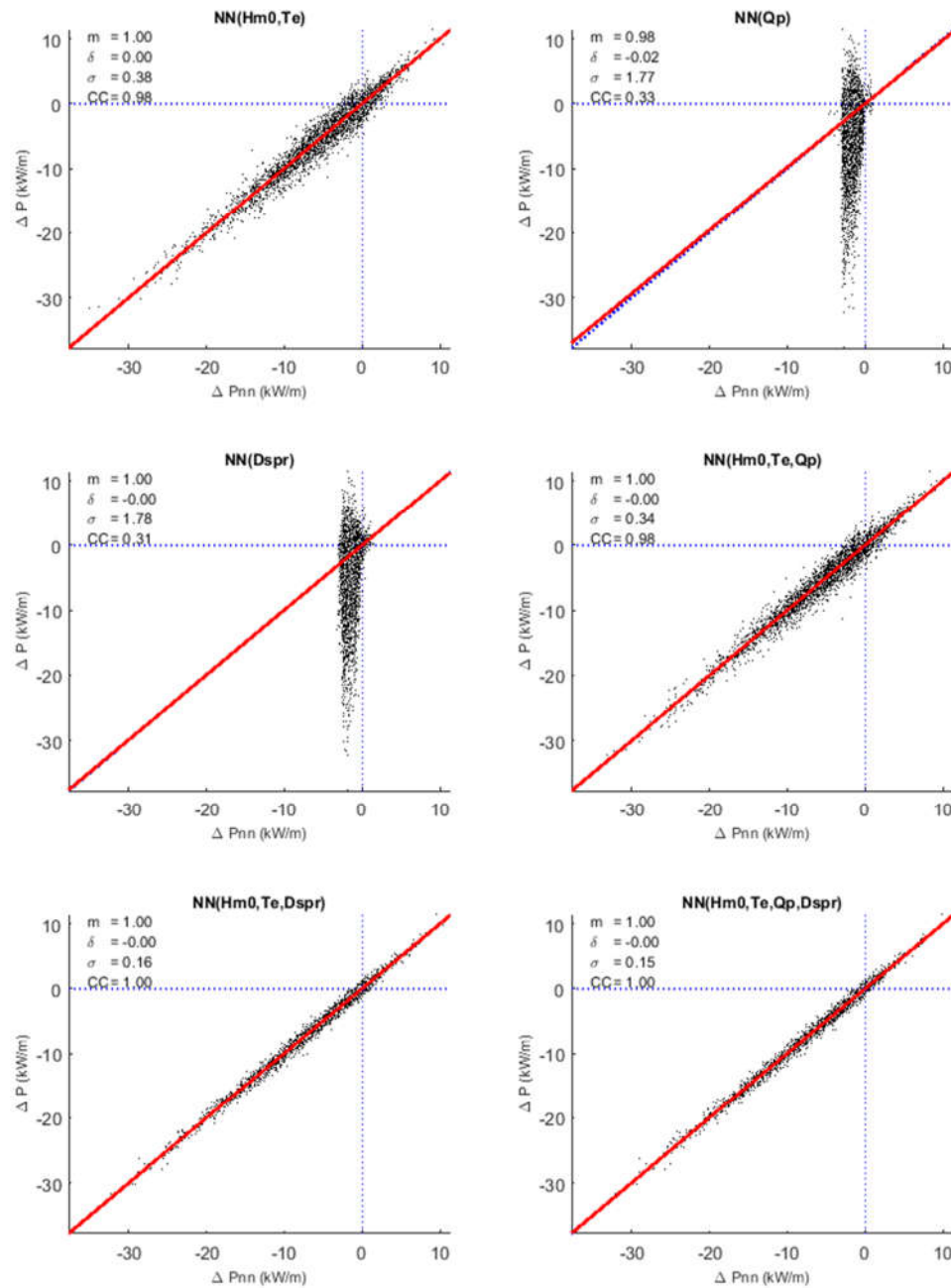


Figure E-26 Correlation analysis of $\Delta P$ and an estimation of $\Delta P$ using neural networks ($\Delta P_{nn}$) and different wave parameters from both wave models – NDBC-4.

Figure E-27 Correlation analysis of $\Delta P$ and an estimation of $\Delta P$ using neural networks ($\Delta P_{nn}$) and different wave parameters from both wave models – WCWI-1.
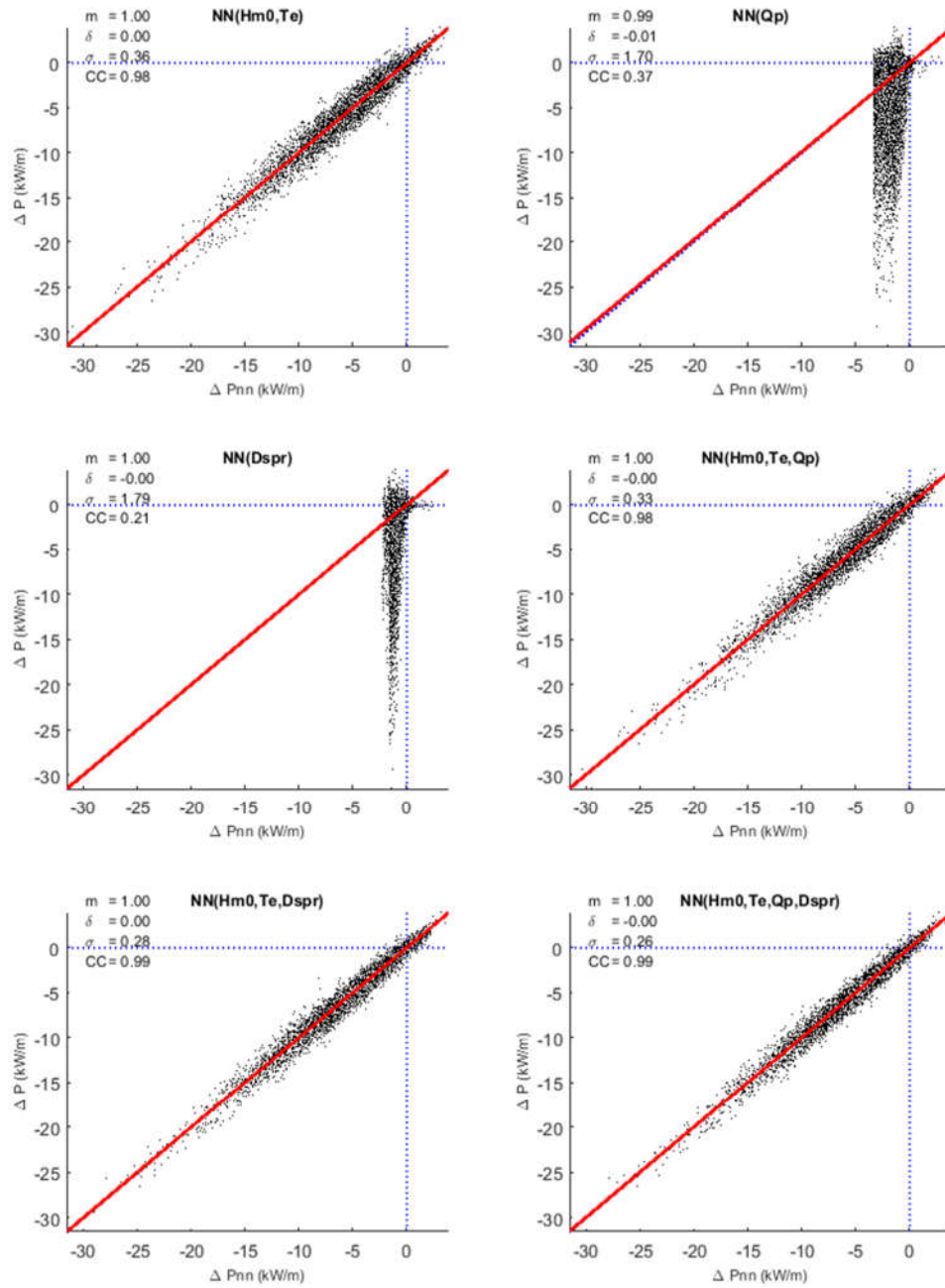
Figure E-28 Correlation analysis of $\Delta P$ and an estimation of $\Delta P$ using neural networks ($\Delta P_{nn}$) and different wave parameters from both wave models – WCWI-2.
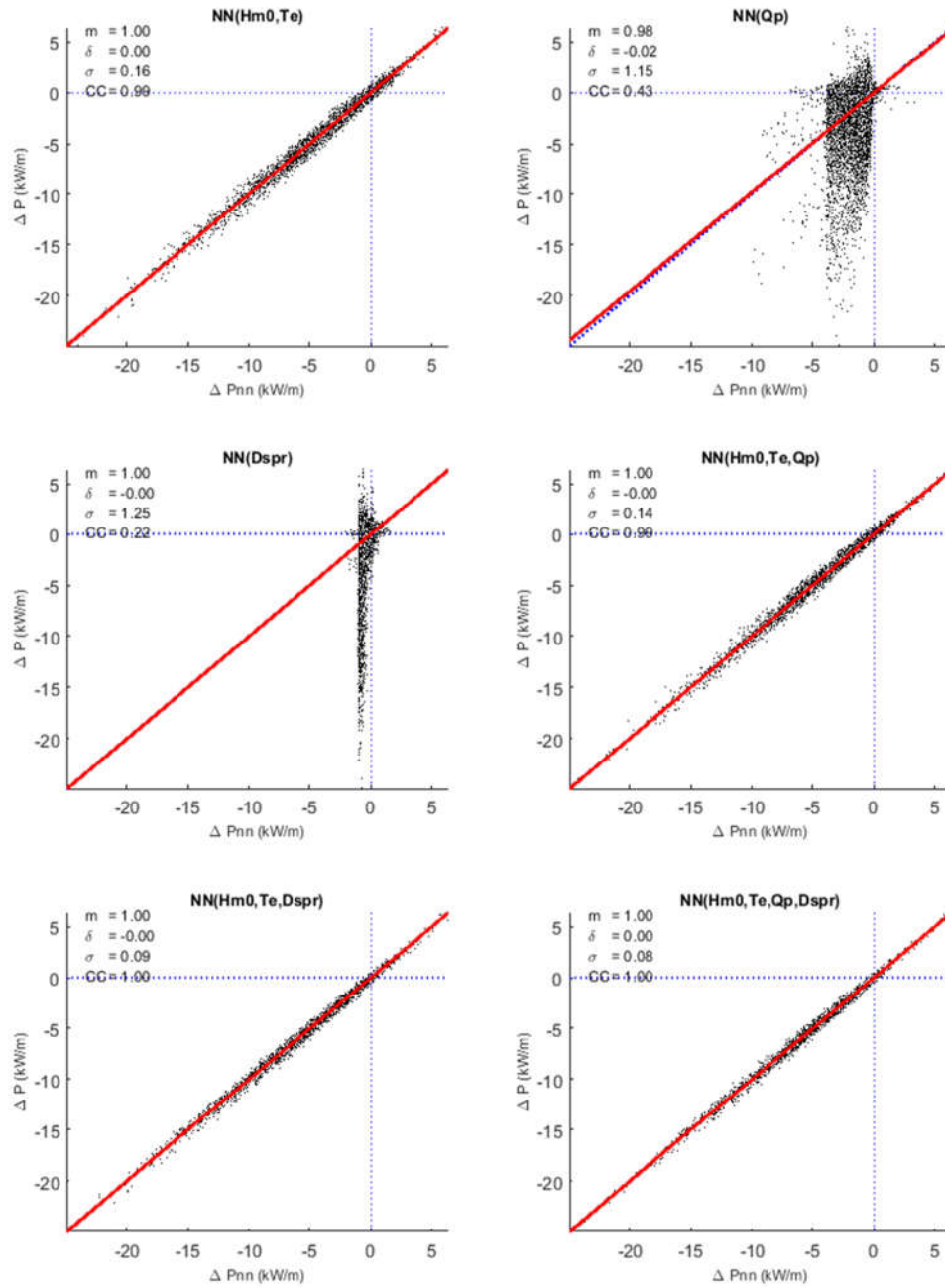
Figure E-29 Correlation analysis of $\Delta P$ and an estimation of $\Delta P$ using neural networks ($\Delta P_{nn}$) and different wave parameters from both wave models – WCWI-3.
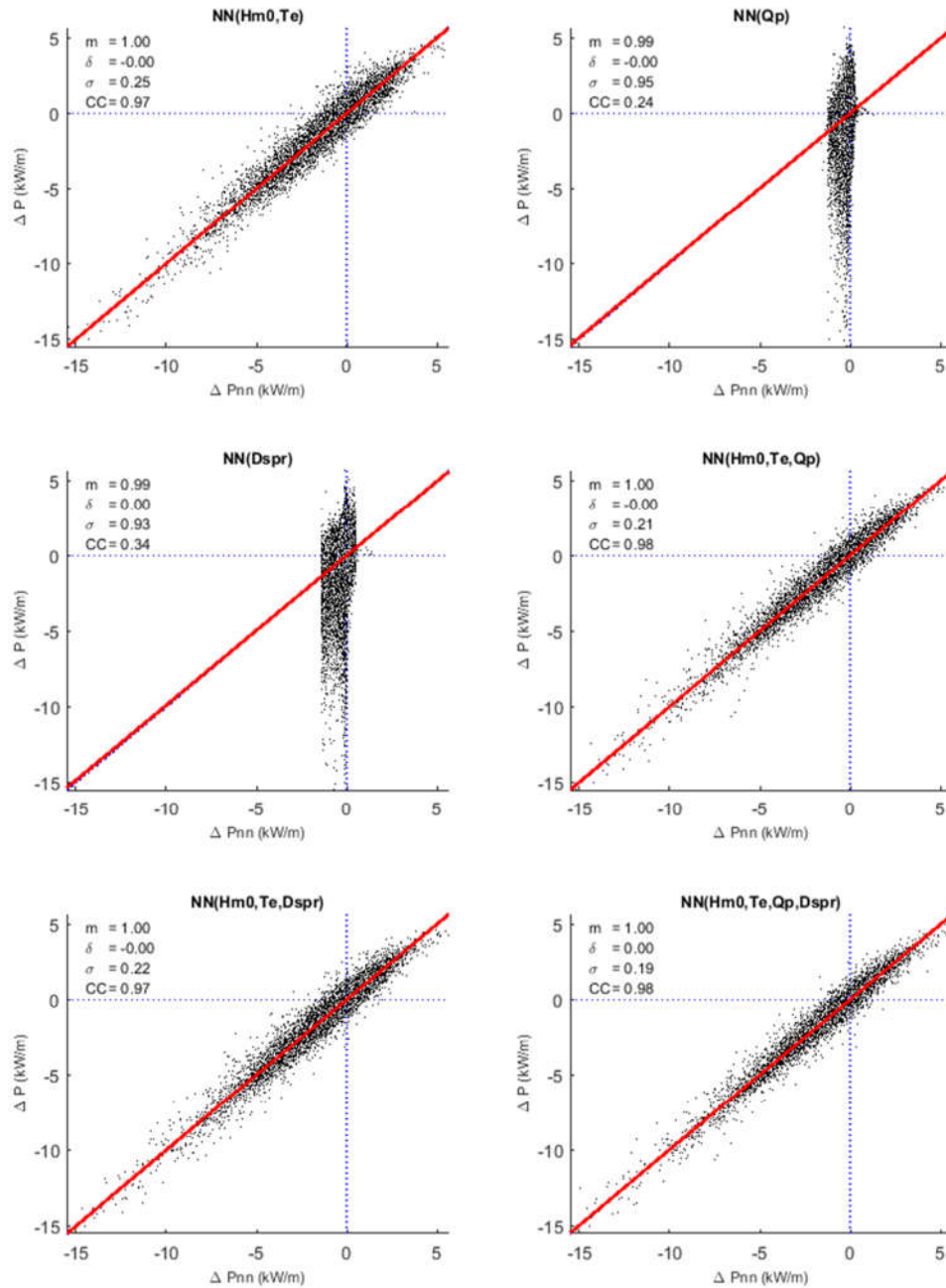
Figure E-30 Correlation analysis of $\Delta P$ and an estimation of $\Delta P$ using neural networks ($\Delta P_{nn}$) and different wave parameters from both wave models – WCWI-4.
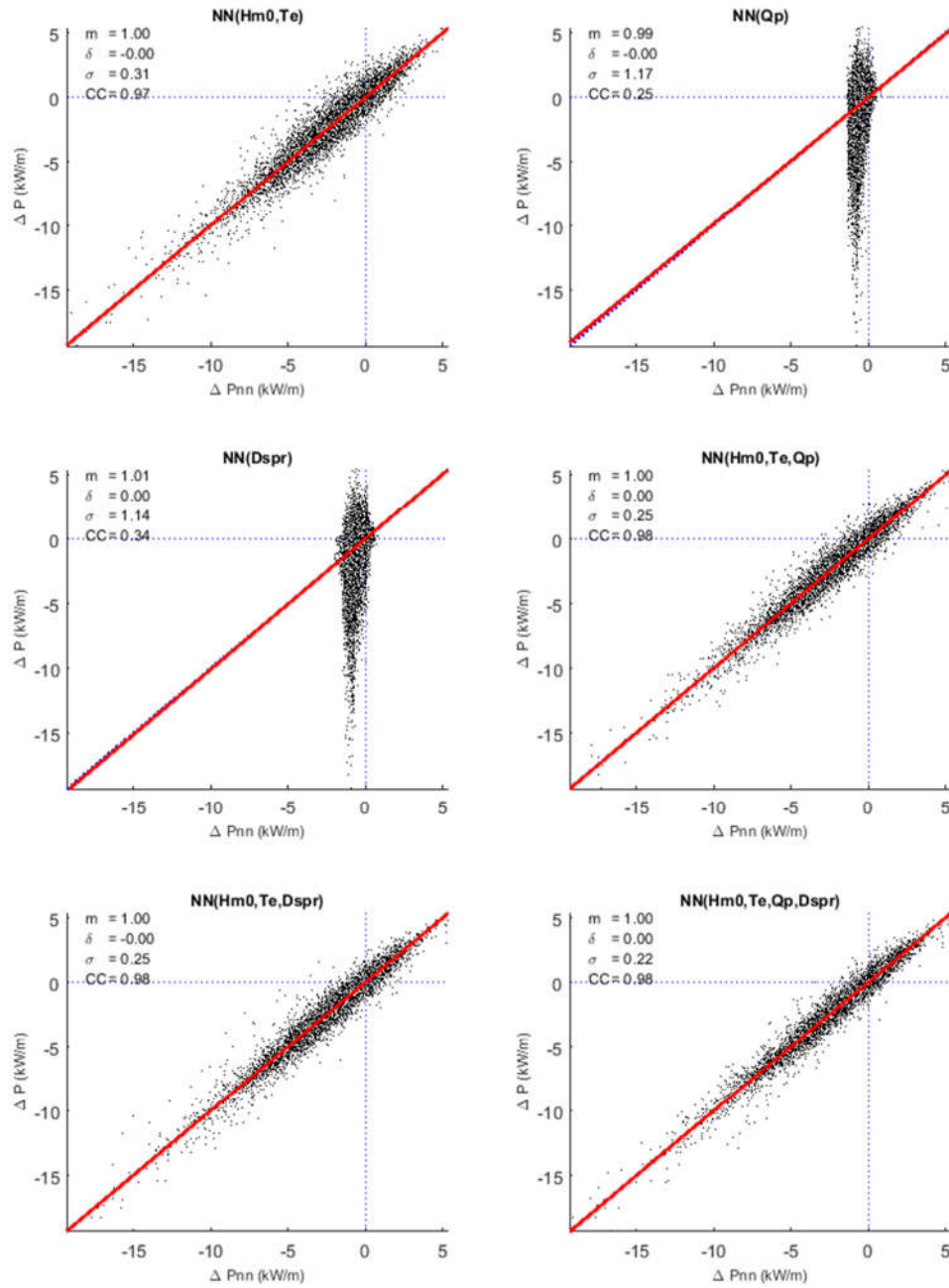
Figure E-31 Correlation analysis of $\Delta P$ and an estimation of $\Delta P$ using neural networks $(\Delta P_{nn})$ and different wave parameters from both wave models – WCWI-5.